ESIS

MICHIGAN STATE UNIVERSITY LIBRARIES

3 1293 01570 6322

This is to certify that the

dissertation entitled

AN EXPERIMENTAL EVALUATION OF A 12.5-CM DIAMETER MULTIPOLAR MICROWAVE ELECTRON CYCLOTRON RESONANCE PLASMA SOURCE

presented by

Peng Un Mak

has been accepted towards fulfillment
of the requirements for

Ph.D. degree in Electrical Eng

Major professor

Date 8/18/97

MSU is an Affirmative Action/Equal Opportunity Institution

O-12771

LIBRARY
Michigan State
University

PLACE IN RETURN BOX to remove this checkout from your record.
TO AVOID FINES return on or before date due.

DATE DUE	DATE DUE	DATE DUE
NOV 0 2 2006		
APR 1 2 2 0		
NOV 2 7 2002		
0331 05		
OCT 0 2 2006 0922 09		

MSU is An Affirmative Action/Equal Opportunity Institution
c:\circ\datedue.pm3-p.1

AN EXPERIMENTAL EVALUATION OF A 12.5-CM DIAMETER MULTIPOLAR MICROWAVE ELECTRON CYCLOTRON RESONANCE PLASMA SOURCE

VOLUME I

By

Peng Un Mak

A DISSERTATION

Submitted to
Michigan State University
in partial fulfillment of the requirements
for the degree of

DOCTOR OF PHILOSOPHY

Department of Electrical Engineering

1997

ABSTRACT

AN EXPERIMENTAL EVALUATION OF A 12.5-CM DIAMETER MULTIPOLAR MICROWAVE ELECTRON CYCLOTRON RESONANCE PLASMA SOURCE

By

Peng Un Mak

Using the 17.78 cm dia. resonant cavity, a new baseplate has been built to accommodate a 12.5 cm dia. plasma discharge at the bottom of the cavity. This plasma discharge, called MPDR™-13, was comprehensively investigated by several experimental techniques versus a number of selected input variables. The experimental techniques include the micro-coax electric field probes, a gridded energy analyzer, single and double Langmuir probes. The input variables consisted of the variations of reactor design (side feed, end feed, and four different strong magnet configurations), input microwave power, chamber pressure, and the microwave tuning positions. Experiments were carried out mostly in argon gas. This plasma source behavior and performance were evaluated by the measurements of the magnitude and spatial variation of the electric field in the applicator, and the measurements of the plasma density, electron temperature, plasma potential and the ion energy in the downstream discharge region. Microwave coupling efficiency and ion production cost are two main measures of the source performance.

Experimental results demonstrate that both the side feed excited with TE_{211} mode and end feed excited with TM_{011} mode operating with the 8P/8M magnet configuration provide the best overall performance. Both show similar, excellent coupling efficiencies (~98%) and ion production costs. High plasma density ($>10^{11}/cm^3$), low ion impinging energy (12 to 25 eV) on a substrate were readily achieved in both reactors. However, it is easier to maintain a discharge at very low pressure regimes (< 1 mTorr) with the side feed applicator while the end feed applicator produces a more uniform plasma.

Based on the electric field measurements, a microwave equivalent circuit for the end feed applicator was developed. The high density behavior of the MPDR™-13 was also experimentally investigated by examining discharge hysteresis phenomena versus the tuning, pressure, and input power. Control strategies using plasma internal variables for reproducible plasma process was demonstrated in an argon soft sputter oxide application. Finally, a comparison of the experimental performance for four different ECR reactors with the performance predicted by global discharge models indicates that these global models are useful in understanding the plasma source behavior and in plasma reactor design.

Copyright by
PENG UN MAK
@1997

To my family who gives me an
enormous amount of love.

ACKNOWLEDEMENTS

I would like to thank Dr. Jes Asmussen, my advisor, who provided me with a good kaleidoscopic study environment to learn and to perform research and thank for his constant encouragement and continuous support. Special thanks also go to Drs. Timothy A. Grotjohn and Don Reinhard for their constructive discussions and invaluable times throughout the years. Particular for Dr. Tim Grotjohn's help in both computer skill and experimental support. I would also like to thank Drs. Jeffrey A. Hopwood and Fan-Cheung Sze for their great help in my initial experiments. I still remember the enjoyable times I worked with Drs. Geoffrey T. Salbert and Gregory L. King, their excellent discussions, and nice personalities. Special thanks are extended to the faculty and staff of department of Electrical Engineering at Michigan State University. Particular thanks should go to Mr. Brian L. Wright and Ms. Roxanne Peacock for their incredible miscellaneous, and indispensable help in preparing various experimental tasks during these years. I would like to thank Mr. Craig Gunn for his patience in reading part of my thesis. Finally, I would like to thank you Drs. Aaron Galonsky and Richard Harkewicz for their kindness on being my committee members in short notice and their patience to proof-read my long overdue manuscript.

This work is supported in part by grants from State of Michigan Research Excellence Fund and General Motors, Corp.

Table of Contents

List of Tables ..... **xii**

List of Figures ..... **xiv**

Chapter 1
Introduction ---------- **1**

1.1 Motivation of High Density Plasma Sources ---------- 1

1.2 Research Tasks and Objectives ---------- 4

1.3 Dissertation Outline ---------- 6

Chapter 2
Review of the High Density Plasma Sources ---------- **9**

2.1 Introduction ---------- 9

2.2 Structure of the Plasma Processing Machine ----------14

2.3 Common Features in Current HDP Sources ----------21

2.4 ECR High Density Plasma Sources ----------22

2.4.1 Divergent Field ECR Plasma Sources ---------- 22

2.4.2 Uniform Distributed ECR Plasma Sources ---------- 26

2.4.3 Slot-Antenna Type ECR Plasma Sources (ECR SLAN) ---------- 29

2.4.4 Horn Waveguide Type ECR Plasma Sources ---------- 31

2.4.5 Microwave Multipolar ECR Plasma Sources (ECR-MPDR™) ---------- 34

2.5 Non ECR High Density Plasma Sources ----------35

2.5.1 Spiral Inductive Coupled Plasma Sources ---------- 36

2.5.2 Helical Resonator Type Reactors ---------- 39

2.5.3 Helicon Type Reactors ---------- 41

2.5.4 Microwave Plasma Sources ---------- 42

2.6 Concluding Remarks ----------46

Chapter 3
Microwave Plasma Processing Machines ---------- 48

3.1 Introduction to MSU Reactors ----------48

3.2 The Standard Structure of Microwave Plasma Processing System ---51

3.2.1 Microwave power supply ---------- 51

3.2.2 Microwave power transmission system with oscillator protection and power monitor circuits ---------- 55

3.2.3 MPDR™-13 reactor ---------- 60

3.2.4 Gas flow and vacuum system ---------- 72

Chapter 4
The System Reactor Variables ---------- 75

4.1 Introduction to the Plasma System Diagram ----------75

4.2 Independently Controlled Input Variables (U) ----------79

4.2.1 Macroscopic controllable input variables (U_1) ---------- 79

4.2.2 Reactor geometry variables (U_2) ---------- 81

4.3 Internal Dependent Variables (X) ----------84

4.4 Output Variables --- Reactor Figures of Merit (Y_1) ----------85

4.4.1 Power coupling efficiency Eff_{coup} ---------- 85

4.4.2 Ion production cost η_{ion} ---------- 89

4.5 Summary ----------90

Chapter 5
The Experimental Techniques ---------- 93

5.1 Introduction ----------93

5.2 Visual Plasma Pictures ----------95

5.3 Micro-coax Electric Probe ----------96

5.3.1 Absolute electric field measurement ---------- 101

5.4 Langmuir Probe Techniques ----------104

5.4.1 Introduction ---------- 104

5.4.2 Double Langmuir probe ---------- 106

5.4.3 Single Langmuir probe ---------- 113

5.4.4 Spatial probe measurement and array of probes ---------- 117

5.4.5 Practical problems and measurement limitations ---------- 122

5.5 Gridded Energy Analyzer ----------123

Chapter 6
Static Magnetic Fields in MPDR™-13 ECR Plasma Source - 131

6.1 Introduction ----------131

6.2 Selection of Magnets and Magnet Configurations ----------133
6.2.1 Introduction ---------- 133
6.2.2 Selection of magnets ---------- 134
6.2.3 Magnet configurations ---------- 136

6.3 Simulation on Static Magnetic Flux Density, B-Field ----------138
6.3.1 Formulation principle ---------- 138
6.3.2 Simulation result ---------- 144

6.4 Measurement of B-Fields ----------162
6.4.1 Iron powder method ---------- 162
6.4.2 Hall-effect probe B-field measurement ---------- 164

6.5 Concluding Remarks ----------167

Chapter 7
The Behavior and Performance of MPDR™-13 ECR Plasma Source
---------- - 170

7.1 Introduction ----------170

7.2 Electric Field Measurements ----------177
7.2.1 Introduction ---------- 177
7.2.2 End feed applicator ---------- 180
7.2.3 Side feed applicator ---------- 194
7.2.4 Summary and discussion of electric field measurements ---------- 214

7.3 Ion Density Measurements ----------220
7.3.1 End feed applicator ---------- 221
7.3.2 Side feed applicator ---------- 227
7.3.3 Comparison of density performance ---------- 238
7.3.4 Influence on ion density by substrate bias ---------- 247
7.3.5 Influence on ion density by downstream confinement magnetic fields ---- 248

7.4 Plasma Potential and Electron Energy Measurements ----------253
7.4.1 Introduction ---------- 253
7.4.2 Electron energy distribution function (EEDF) ---------- 254
7.4.3 Plasma potential and Electron temperature ---------- 258

7.5 Ion Energy Measurements ----------266
7.5.1 Ion energy distribution function (IEDF) and bias effect ---------- 267
7.5.2 Spatial ion energy variations ---------- 275
7.5.3 Ion energy versus pressure and power ---------- 277
7.5.4 Ion energy in pure hydrogen plasma discharges ---------- 281

7.6 Concluding Remarks ----------286

Chapter 8
Microwave Equivalent Circuit for the ECR End Feed Applicator ---------- 291

8.1 Introduction ----------291
8.2 Microwave Equivalent Circuit Components and Their Characteristics 292
8.3 Equivalent Circuit Discussion ----------298
8.4 Concluding Remarks and Proposed Design Improvement --------300

Chapter 9
Experimental Hysteresis of Multipolar ECR Plasma Source and Control Sensors ---------- 305

9.1 Introduction ----------305
9.2 Experimental Hysteresis Results ----------307
9.2.1 End feed hysteresis versus cavity height ---------- 308
9.2.2 Side feed hysteresis on cavity height, probe depth and chamber pressure - 321
9.2.3 Application to plasma control sensors ---------- 327
9.3 Argon Soft Sputter Control Processing Example ----------331
9.3.1 Experiment preparation and sensors selection ---------- 331
9.3.2 Experimental sequence and result ---------- 334
9.4 Concluding Remarks ----------336

Chapter 10
Plasma Global Model and Comparison of Various ECR Plasma Sources ---------- 338

10.1 Introduction ----------338
10.2 Review of the Simple Global Plasma Model ----------339
10.2.1 Charged particle balance and average electron temperature ---------- 340
10.2.2 Power balance and plasma load line ---------- 347
10.3 Performance Comparison Between Global Plasma Model Predictions and Experimental Data ----------350
10.3.1 Performance comparison between global discharge model predictions and measured data of MPDR™-13 ---------- 350
10.3.2 Performance comparison between global discharge model predictions and experimental data from four different ECR plasma sources ---------- 354
10.4 Concluding Remarks ----------360

Chapter 11
Summary ---------- 364

11.1 Work Done Highlights ----------364

11.2 Recommendation for Future Research ----------370

11.2.1 Diagnostic techniques ---------- 370

11.2.2 Microwave input coupling structure variations ---------- 371

11.2.3 Plasma source operating with pulse-time power supply ---------- 372

11.2.4 Reactor geometry design ---------- 372

11.3 Conclusion and Outlook ----------374

Appendix A
Calibration of E-probe in an Electromagnetic Cavity ----- 375

A.1 Introduction ----------375

A.2 Quality Factors in Empty Cavity ----------375

A.3 Formulation of the Proportional Constant for Absolute Electric Field Measurement ----------380

Appendix B
Measurements of Cavity Wall Thickness and Electrodes Lengths in Langmuir Probe Array ---------- 383

B.1 The End Feed Cavity Wall Thickness Near the E-field Sampling Holes ----------383

B.2 Measured Electrode Lengths in Array of Probes ----------386

Appendix C
Visual Images of Microwave Gas Discharges ---------- 388

C.1 Introduction ----------388

C.2 Experimental Set Up ----------389

C.3 Experimental Results ----------392

C.3.1 Side feed images for different ECR magnet configurations ---------- 393

C.3.2 End feed 8P/8M ECR plasma images ---------- 397

C.3.3 Non magnetized microwave cavity plasma images ---------- 403

C.4 Discussion and Summary ----------403

Appendix D
Low Pressure Microwave Cavity Plasma Discharges ----- 410

D.1 Introduction ----------410

D.2 Experimentals and Comparison Principle ----------411

D.3 Results and Discussions ----------413

D.3.1 Plasma density and electron temperature ---------- 413

D.3.2 Electric field comparison ---------- 417

D.4 Concluding Remarks----------420

BIBLIOGRAPHY ---------- 422

List of Tables

Chapter 4

Table 4.1 Important Input Variables (U) 90

Table 4.2 Important Internal Variables (X) 91

Table 4.3 Important Output Variables (Y) 92

Chapter 5

Table 5.1 Experimental techniques and their outcomes. 94

Chapter 6

Table 6.1 Calculated ECR area for different magnet configurations 161

Chapter 7

Table 7.1 Important Input Variables (U) for end feed applicator 172

Table 7.2 Important Input Variables (U) for side feed applicator 173

Table 7.3 Impressed electric field for 8P/8M end feed excitation 191

Table 7.4 End feed power coupling efficiencies and loaded quality factors 193

Table 7.5 Impressed electric fields for 8P/8M side feed excitation 201

Table 7.6 Cavity heights for multipolar ECR magnetic field in side feed plasma Loaded cavity 203

Table 7.7 Comparison of E-field strengths for different multipolar magnet type ECR configurations for the side feed applicator 207

Table 7.8 Power coupling efficiencies and loaded cavity quality factors for different multipolar magnet type ECR configurations in side feed applicator 213

Table 7.9 Uniformity of relative ion saturation currents.....240

Chapter 8

Table 8.1 First few guided wavelengths (λg) for propagating modes or characteristic decay lengths (d) for evanescent modes in regions II and III. 295

Chapter 9

Table 9.1 Measured transition locations for mode 2 plasma hysteresis on cavity height in end feed applicator. 315

Table 9.2 Soft sputter oxide removal experiments.....335

Chapter 10

Table 10.1 Geometric dimensions of various ECR plasma sources. 355

Appendix A

Table A.1 Sample powers for two different probes 382

Table A.2 Proportional constants for two E-probes 382

Appendix B

Table B.1 Wall thickness (in inch) around the E-field sampling holes 384

Table B.2 Electrode lengths in Langmuir probe array 387

List of Figures

Chapter 1

Figure 1.1 Historical development in semiconductor commercial products. 2

Chapter 2

Figure 2.1 Typical parallel plate plasma etching configuration. 11

Figure 2.2 Typical low pressure plasma processing machine. 15

Figure 2.3 Classification of reactor: (a) end-excited, (b) side-excited. 16

Figure 2.4 (a) The Generic Plasma Reactor (end-excited case); (b) The Generic Plasma Reactor (end-excited case); 18

Figure 2.5 Divergent ECR Plasma Source (Low profile type). 23

Figure 2.6 (a) Cylindrical DECR source machine [43], (b) Schematic representation of Planar UDECR source machine [45]. 27

Figure 2.7 (a) Slot antenna plasma source (ECR version) [46], (b) ECR magnet configurations. 30

Figure 2.8 Horn-shaped ECR plasma source with TM_{01} field pattern [51]. 32

Figure 2.9 (a) Spiral Inductive Coupled plasma source [57], (b) Single spiral coil configuration, (c) Multi-spiral coil configuration [62]. 37

Figure 2.10 Helical resonator plasma source [66]. 40

Figure 2.11 Helicon plasma source [70]. 43

Figure 2.12 Large area surface wave discharge [75] 45

Chapter 3

Figure 3.1 (a) Original ion source schematic (1980-1982), (b) Improved MPDR (mid-1980s). 49

Figure 3.2 (a) Traditional, and (b) alternate oscillator protection and power monitoring circuit. 57

Figure 3.3 Cross sectional view of side-feed MPDR reactor with processing chamber. The insert shows the end-feed excitation method. 61

Figure 3.4 Cross sectional view of MPDR reactor in Figure 3.3 at z = -1.27 cm (center plane of magnets) with standard 8 pole/8 magnet multipolar ECR magnet configuration. 65

Figure 3.5 Gas flow and vacuum system of MPDR-13 plasma system 69

Figure 3.6 Schematic view of MPCS in MPDR-13 relative to ECR magnets.. 71

Chapter 4

Figure 4.1 Generic plasma reactor system block diagram 76

Figure 4.2 System variables of a HDP Reactor for a plasma etching application. 78

Figure 4.3 Chamber pressure vs. argon flow rate 80

Figure 4.4 Cross sectional view (z = -1.27 cm) of four variations of ECR magnetic configurations (abbreviations are in parentheses). 83

Figure 4.5 Power transfer path in plasma reactor system 86

Chapter 5

Figure 5.1 Cut-away view of the microwave cavity applicator. 97

Figure 5.2 Detail of E-probe measurement system. 98

Figure 5.3 (a) Schematic circuit for Double Langmuir Probe measurement, (b) Typical measured double probe I-V characteristics. 107

Figure 5.4 Schematic of the potential distribution between the probes of a floating double probe system. (a) applied voltage $V_{pr} = 0$, (b) at the linear region, (c) over the saturation region. 110

Figure 5.5 Schematic set up of single Langmuir probe measurement. 116

Figure 5.6 Top view of the Langmuir probe array locations with 8P/8M ECR configurations. 120

Figure 5.7 Schematics of the electronic circuit for arrays of probes. 121

Figure 5.8 Schematic circuit for sampling ion energies impinging on a substrate. 125

Figure 5.9 Resolution of energy analyzer versus mesh wire diameter. 129

Chapter 6

Figure 6.1 (a) Typical Hysteresis cycle for a ferromagnetic material, (b) Demagnetization curve with load line. 135

Figure 6.2 (a) Symmetry of ECR magnet configurations, (b) Schematic of the simulation region. 141

Figure 6.3 (a) The contour plot of static B-field in Gauss at $\phi = 0^o$ plane in 8P/8M (in front of a magnet) 145

Figure 6.3 (b) The contour plot of total B-field vs. r-ϕ plane at z = -1.27 cm in 8P/8M 146

Figure 6.3 (c) Mesh and contour plot of the total magnetic flux B vs. r-ϕ at z = -1.27 cm (8P/8M case) 147

Figure 6.3 (d) The combined mesh, contour and needle plots of the total magnetic flux B vs. r-z plane at $\phi = 0^o$ (8P/8M case). 148

Figure 6.4 (a) The contour plot of static B-field in Gauss at $\phi = 0^o$ plane in 4P/4M (in front of a magnet) 149

Figure 6.4 (b) The contour plot of total B-field vs. r-ϕ plane at z = -1.27 cm in 4P/4M 150

Figure 6.4 (c) Mesh and contour plot of the total magnetic flux B vs. r-ϕ at z = -1.27 cm (4P/4M case) 151

Figure 6.4 (d) The combined mesh, contour and needle plots of the total magnetic flux B vs. r-z plane at $\phi = 0^o$ (4P/4M case) 152

Figure 6.5 (a) The contour plot of static B-field in Gauss at f = 0o plane in 4P/8M (in front of a magnet) 153

Figure 6.5 (b) The contour plot of total B-field vs. r-ϕ plane at z = -1.27 cm in 4P/8M 154

Figure 6.5 (c) Mesh and contour plot of the total magnetic flux B vs. r-ϕ at z = -1.27 cm (4P/8M case) 155

Figure 6.5 (d) The combined mesh, contour and needle plots of the total magnetic flux B vs. r-z plane at $\phi = 0^o$ (4P/8M case) 156

Figure 6.6 (a) The contour plot of static B-field in Gauss at $\phi = 0^o$ plane in allN/8M (in front of a magnet) 157

Figure 6.6 (b) The contour plot of total B-field vs. r-ϕ plane at z = -1.27 cm in allN/8M 158

Figure 6.6 (c) Mesh and contour plot of the total magnetic flux B vs. r-ϕ at z = -1.27 cm (allN/8M case) 159

Figure 6.6 (d) The combined mesh, contour and needle plots of the total magnetic flux B vs. r-z plane at $\phi = 0^o$ (allNP/8M case) 160

Figure 6.7 Visual iron powder pattern of 8P/8M ECR configuration. 163

Figure 6.8 Comparison of measured B and calculated B in 8P/8M configuration vs. r at z = -1.27 cm and along $\phi = 0^o$. 165

Figure 6.9 Comparison of measured B and calculated B in 8P/8M configuration vs. r at z = -1.27 cm and along $\phi = 22.5^o$. 166

Chapter 7

Figure 7.1 System variables investigated in this chapter. 171

Figure 7.2 Electromagnetic mode chart for an ideal circular cylindrical cavity (dia. = 17.78 cm). 178

Figure 7.3 The measured radial component electric field pattern in end feed applicator vs. Φ, (a) for mode 1, (b) for mode 2. 182

Figure 7.4 The measured radial component electric field pattern in end feed applicator vs. H, (a) for mode 1, (b) for mode 2. 183

Figure 7.5 Quartz bell jar dimensions (not in scale) and the locations for calculation of the impressed electric field. 188

Figure 7.6 End feed absolute radial component electric field strength at the wall (H =38 mm). (a) vs. absorbed power at operating pressure of 5 mTorr, and (b) vs. pressure at absorbed power of 270 W. 190

Figure 7.7 Measured EM mode pattern in side-feed, 8P/8M MPDR with short resonant mode excitation. 196

Figure 7.8 Measured EM mode pattern in side-feed, 8P/8M MPDR with long resonant mode excitation. 197

Figure 7.9 Side feed absolute radial component electric field strength at the wall (H = 54 mm) (a) vs. power at p = 0.8 mTorr, and (b) vs. pressure at power of 328 W. 200

Figure 7.10 Measured EM mode pattern in side-feed, 4P/8M MPDR with short resonant mode excitation. 204

Figure 7.11 Measured EM mode pattern in side-feed, 4P/8M MPDR with long resonant mode excitation. 205

Figure 7.12 Measured EM mode pattern in side-feed, 4P/4M MPDR (a) short resonant mode, (b) long resonant mode. 206

Figure 7.13 Measured EM mode pattern in side-feed, allN/8M MPDR with long resonant mode excitation. 210

Figure 7.14 Measured EM mode pattern in side-feed, allN/8M MPDR with short resonant mode excitation. 211

Figure 7.15 End feed downstream (0, 0, 3 cm) ion density versus microwave absorbed power at pressure 5 mTorr of argon discharge. 222

Figure 7.16 End feed ion density at (0, 0, 3 cm) versus chamber pressure at absorbed power approximately 270 W argon discharge. 224

Figure 7.17 End feed ion density versus downstream position at 3 mTorr pressure with 270 W absorbed power at mode 1. 225

Figure 7.18 End feed (8P/8M ECR plasma source) downstream (z = 8 cm) cross sectional ion density profile in mode1 with absorbed power 270 W and pressure 5 mTorr. 226

Figure 7.19 Side feed ion density (0,0, 3 cm) versus microwave absorbed power for different multipolar magnetic ECR configurations and for the TE_{211} and TE_{311} EM mode excitations..... 228

Figure 7.20 Side feed 8P/8M ion density (0, 0, 2 cm) versus chamber pressure for two different EM modes, absorbed power around 235 W..... 230

Figure 7.21 Side feed 8P/8M ion density (0, 0, 1 cm) versus argon flow rate at a fixed chamber pressure of 1.21 mTorr, absorbed power was around 240 W and two different EM modes. 231

Figure 7.22 Side feed ion density versus downstream position for four different ECR magnetic configurations. 233

Figure 7.23 Locations (o: 30 points) for spatial ion density measurement in side feed for the 8P/8M and 4P/8M configurations. 234

Figure 7.24 Side feed radial ion density (z =1 to 5 cm) for the 8P/8M configuration. 236

Figure 7.25 Side feed radial ion density (z =1 to 5 cm) for the 4P/8M configuration. 237

Figure 7.26 Ion saturation currents measuring locations at z = 1cm. 239

Figure 7.27 End feed 8P/8M ion production cost at z = 3 cm plane for mode 1 and mode 2. (a) vs. pressure at constant absorbed power ~ 270 W, (b) vs. power at constant p = 5 mTorr. 242

Figure 7.28 Side feed ion production cost at z = 3 cm plane versus absorbed power for different multipolar magnetic type ECR configurations, at 0.78 mTorr pressure. 244

Figure 7.29 Side feed 8P/8M ion production cost at z = 3 cm plane or TE_{211} and TE_{311} modes at absorbed power ~ 235 W. 246

Figure 7.30 (a) Measurement configuration of aluminum substrate with the double Langmuir probe, (b) Side feed downstream ion density (0, 0, 8 cm) vs. substrate bias with 8P/8M magnet configuration, TE_{211} mode, 1 mTorr and absorbed power ~ 490 W..... 249

Figure 7.31 Side feed ion density (x $10^{10}/cm^3$) within a quadrant at z = 8 cm w/o MPCS..... 251

Figure 7.32 Side feed ion density (x $10^{10}/cm^3$) within a quadrant at z = 8 cm w/MPCS shown in Figure 3.6. 252

Figure 7.33 Typical measured EEDF in side feed argon discharge with 8P/8M ECR magnet configuration. 255

Figure 7.34 Typical measured EEDF in side feed argon discharge with 4P/8M ECR magnet configuration. 256

Figure 7.35 Side feed plasma potential and electron temperature versus chamber pressure for 4P/8M and 8P/8M configurations. 259

Figure 7.36 Side feed plasma potential and electron temperature versus power at 1 mTorr argon discharge for 4P/8M and 8P/8M configurations. 261

Figure 7.37 Plasma potential and electron temperature in side feed applicator vs. downstream position for 4P/8M and 8P/8M configurations.... 262

Figure 7.38 Plasma potential and electron temperature in side feed applicator vs. radial position. 264

Figure 7.39 End feed electron temperatures (0, 0, 3 cm) (a) vs. pressure at absorbed power ~ 270W, (b) vs. absorbed power at fixed 5 mTorr.... 265

Figure 7.40 Typical ion energy distribution impinging on a grounded substrate. . 268

Figure 7.41 IEDF vs. z in 8P/8M, side feed reactor with TE_{211} mode. 269

Figure 7.42 IEDF vs. p in 4P/8M, side feed reactor, TE_{211} mode..... 270

Figure 7.43 Measured IEDF of allN/8M configuration in side feed applicator. 272

Figure 7.44 IEDF versus dc bias on the substrate..... 274

Figure 7.45 Average ion energy and FWHH vs. downstream position in side feed plasma source. 276

Figure 7.46 Average ion energy and FWHH vs. pressure in side feed plasma source..... 278

Figure 7.47 Average ion energy and FWHH in end feed reactor with TM_{011} mode at (0, 0, 6 cm); (a) vs. chamber pressure at absorbed power of 270 W, (b) vs. incident power at 3 mTorr pressure. 279

Figure 7.48 Average ion energy and FWHH vs. incident power in side feed plasma source. 280

Figure 7.49 Spatial variations of average ion energy and FWHH in a 4.0 mTorr hydrogen discharge in 8P/8M side feed applicator with TE_{211} mode excitation, (a) vs. r at z = 6 cm, (b) vs. z at r =0..... 282

Figure 7.50 Average ion energy and FWHH of hydrogen versus incident power.. 283

Figure 7.51 Average ion energy and FWHH of hydrogen versus chamber pressure..... 284

Chapter 8

Figure 8.1 Microwave equivalent circuit for end feed MPDR. 293

Figure 8.2 Normalized TE and TM wave impedances versus normalized frequency. 302

Figure 8.3 (a) Schematic of optimum stepped transmission line transformer, (b) A proposed version of end feed applicator. 304

Chapter 9

Figure 9.1 Schematic of a hysteresis cycle in plasma system variables. 307

Figure 9.2 Absorbed power vs. cavity height for an end feed ECR MPDR-13 argon discharge. The chamber pressure was fixed at 5 mTorr, microwave incident power was fixed at ~ 274 W. 309

Figure 9.3 Ion density at (0, 0, 3 cm) vs. cavity height for an end feed ECR MPDR-13 argon discharge. The chamber pressure was fixed at 5 mTorr, microwave incident power was fixed at ~ 274 W..... 310

Figure 9.4 Ion density at (0, 0, 3 cm) vs. cavity height at different incident power for an end feed ECR MPDR-13 argon discharge. The chamber pressure was fixed at 5 mTorr..... 312

Figure 9.5 Ion density at (0, 0, 3 cm) vs. cavity height at different chamber pressure for an end feed ECR MPDR-13 argon discharge. The microwave incident power was fixed at ~275 W. 313

Figure 9.6 Schematic to illustrate the boundaries of a resonant mode..... 314

Figure 9.7 Response surface methodology model of minimum and maximum cavity heights for a high density plasma source operation. 316

Figure 9.8 Plasma loss load lines for two different pressures for end feed reactor with 8P/8M ECR magnet..... 319

Figure 9.9 Side feed 8P/8M MPDR-13 hysteresis on cavity height, (a) absorbed power vs. cavity height, (b) ion saturation current vs. cavity height..... 323

Figure 9.10 Side feed 8P/8M MPDR-13 hysteresis on depth of input coupling probe (a) absorbed power vs. L_p, (b) ion saturation current vs. L_p. ... 324

Figure 9.11 Side feed 8P/8M MPDR-13 hysteresis on chamber pressure. 325

Figure 9.12 Microwave plasma processing control diagram. 328

Figure 9.13 Response surface methodology model of the radial electric field at the wall (r = 8.89 cm, $\Phi = 90^0$, H= 38 mm) for a high density plasma source operation (mode 1 in end feed). (a) vs. L_s and p at P_{inc} = 240 W, (b) vs. L_s and P_{inc} at p = 4 mTorr. 330

Figure 9.14 Experimental set up for soft sputter experiments. 332

Figure 9.15 9-point locations for oxide thickness measurements 333

Chapter 10

Figure 10.1 Assumed density profile in simple plasma global model 342

Figure 10.2 A comparison of experimental electron temperatures (data points) with the electron temperatures (solid curve) predicted from the global plasma model..... 345

Figure 10.3 Comparison of electron temperatures between global model prediction and measured data in different plasma sources. 346

Figure 10.4 Collisional and kinetic energy losses per electron-ion pair created versus electron temperature in argon. 349

Figure 10.5 Characteristic discharge length vs. pressure in MPDR-13. 351

Figure 10.6 Plasma density vs. discharge absorbed power as calculated from the global plasma model in MPDR-13 reactor. 353

Figure 10.7 $\langle P_a \rangle$ vs. n_i in different argon discharges and plasma load loss lines calculated from global discharge models. 357

Figure 10.8 Ion production costs vs. pressure for different ECR plasma sources. 358

Figure 10.9 Strategy to design low pressure high density plasma source using global model at the initial stage. 362

Chapter 11

Figure 11.1 Several possible scale-up versions of MPDR. 373

Appendix A

Figure A.1 The empty cavity configuration for E-field calibration. 376

Appendix C

Figure C.1 Discharge picture-taking schematic in MPDR-13. 390

Figure C.2 Discharge pictures for different ECR magnet configurations in side feed applicator operating at TE_{211} mode 394

Figure C.3 Discharge pictures for different ECR magnet configurations in side feed applicator operating at TE_{311} mode 396

Figure C.4 High density and low density operation mode plasma images in end feed applicator with 8P/8M ECR magnet configuration 398

Figure C.5 End feed visual images vs. pressure 400

Figure C.6 Visual images vs. rotation of ECR magnets in end feed plasma source 401

Figure C.7 Sample electric field power and percent of reflected power vs. rotation angle of ECR magnets. 402

Figure C.8 Plasma pictures vs. pressure in non magnetized end feed reactor at mode 1 404

Figure C.9 Plasma pictures vs. pressure in non magnetized end feed reactor at mode 2 405

Figure C.10 Demonstration of the plasma movement due to the E x B drift. .. 407

Figure C.11 Detail images vs. pressure in the end feed plasma with 8P/8M ECR magnet configuration 409

Appendix D

Figure D.1 Comparison of experimental electron temperatures (both ECR & no magnet) with global discharge model prediction in argon discharge. 414

Figure D.2 Plasma density vs. absorbed power (argon pressure as a parameter) for the un-magnetized MPDR-13 plasma source. 415

Figure D.3 Measured EM mode pattern in the un-magnetized MPDR-13 plasma source. 416

Figure D.4 Comparison of the measured electric field of 8P/8M ECR multipolar plasma source and the expected values sustained only by pure ohmic heating. 418

Figure D.5 Comparison of the measured electric field of the un-magnetized microwave cavity plasma source and the expected values sustained only by pure ohmic heating..... 419

Chapter 1

Introduction

- 1.1 Motivation of High Density Plasma Sources
- 1.2 Research Tasks and Objectives
- 1.3 Dissertation Outline

Chapter 1

Introduction

1.1 Motivation of High Density Plasma Sources

The explosive development of modern semiconductor electronic circuits after World War II has set a never-ending information journey for the human civilization. Nowadays, most of the instruments, computers, and communication equipment are embedded with many tiny semiconductor devices and advanced circuit technology as a key console control and/or displays in every aspect of society, from transportation to banking, from defense to medicine, and from households to space exploration. The billions of devices buried in the integrated circuits that control the TV sets, automobiles, telephones, calculators, and computers are just part of the common applications that have caused a phenomenal semiconductor industry success.

Endless demands for better performance, lighter weight, and smaller size (combined with the fierce global competition) fuel the rapid development both in the semiconductor process and circuit designs. For example, Figure 1.1 illustrates the development of two major semiconductor products, Dynamic Random Access Memory (DRAM) and Central Processing Unit (CPU), which represent the

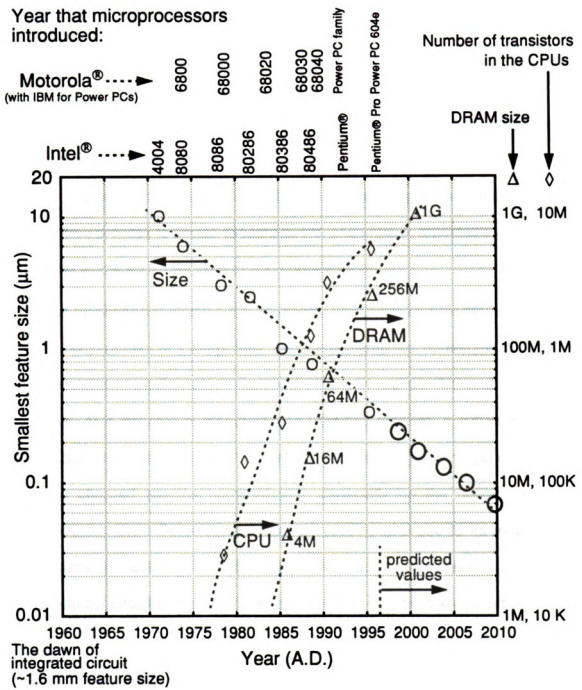

Data sources:

(1) Solid State Technol. 40(5), 1997

(2) Intel museum web site: http://www/intel.com/intel/museum/

(3) Motorola Historical Timeline web site: http://www.mot.com/General/Timeline/

(4) The IBM PowerPC Microprocessor web site: http://www.chips.ibm.com/products/ppc/

Figure 1.1 Historical development in semiconductor commercial products.

technologies of storing information and processing information speed. The minimum feature size of DRAMs and CPUs on the market has reduced significantly from 1.25 μm in the early 1980s to 0.35 μm currently. The continuous need to reduce size in the commercial products has driven the device feature size to enter the deep submicron devices (below 0.25 μm) era [1, 2]. The usual plasma process requirements include controlled ion energy, species density control, damage-free process to device delicate layers, and uniform repeatable processing across the whole substrate (200 to 300 mm diameter).

As mentioned in Section 2.1, traditional wet chemical processing does not meet the requirement of 1 μm or less, and the conventional barrel-type dry etcher fails to meet the requirements below the 0.5 μm regime. Although ion beam etching [3, 4] is capable of manufacturing ultra-fine features, it suffers from two major disadvantages. The first one is the relatively high damage caused by energetic charged species bombardment, especially on the delicate shallow semiconductor layer. Secondly, the slow processing rate due to its relative low charge density available is unsuitable for high throughput processing. As critical semiconductor circuit dimensions continue to shrink exponentially (a factor of ~0.7 every three years), people starts to look for better semiconductor processing machines [5]. Various low pressure High Density Plasma (HDP) sources have been created in recent years to keep pace with these repeatable-process requirements and recently (1993 - 1996) have demonstrated improved performance over earlier generations of plasma processing machines.

1.2 Research Tasks and Objectives

As a result of my fascination with the ever-expanding pace of electronic technology in the last two decades, my research work at Michigan State University (MSU) focused on the investigation of the high density plasma processing machines for Ultra Large Scale Integrated (ULSI) circuit fabrications. The intent of this thesis research was to examine the basic properties of the low pressure high density plasma discharges, as opposed to the materials that may be processed by the discharges. Hopefully, the final material product will ultimately be improved by better understanding the fundamentals of discharge performance.

In order to achieve the previously mentioned desired process demands, my study consists of three parts: (1) to redesign an electron cyclotron resonance (ECR) plasma source at MSU, called MPDR™-13 hereafter, (2) to provide an understanding between the Electromagnetic (EM) fields and the plasma discharge by experimentally characterizing the new ECR plasma source, and (3) to supply valuable information for repeatable processing operation and for optimization of the ECR processing machine for better performance. In addition, this thesis also reviews and explores other opportunities (non ECR) to create high density plasma at low pressure.

Redesigning a new baseplate for the 17.78-cm i.d. cylindrical microwave applicator requires a broad spectrum knowledge that includes basic vacuum techniques, mechanics and electromagnetism to ensure the absence of vacuum leaks, a sound stable structure, compliance with microwave radiation safety and

cooling protection for heat-sensitive materials such as permanent magnets and O-ring gasket. One of the most important parts in ECR reactor design is the static magnetic field strengths and patterns. Computer programs were written to perform numerical solutions for the magnetic fields in several different magnetic configurations.

Since the direct relationship between the plasma input and output variables of a plasma source is very complicated, the introduction of internal variables establishes the vital bridge between them. For example, device damage is directly related to the ion energy impinging onto the substrate. The anisotropy of device features is mainly determined by the magnitude and angle of incidence of ion energies plus the number of collisions between radical species across the plasma sheath. The processing rate is proportional to the local reactive species and ion density. By varying the input variables (e.g. power, pressure, tuning, etc.), the internal and output plasma variables were measured. These included the electromagnetic fields inside the applicator, plasma density, plasma potential, electron temperatures, ion energy impinging on a substrate, and the ion energy distribution function measurements. The experimental diagnostic techniques associated in the experimental studies on the new discharges were single and double Langmuir probes, plasma visualization pictures, micro-coax electric field probes, and a gridded energy analyzer.

Besides the usual plasma performance, the hysteresis and multiple steady states of this plasma source were experimentally investigated in response to

changes in cavity tuning and chamber pressure. This experimental knowledge will lead to reproducible plasma processing.

1.3 Dissertation Outline

This dissertation concentrates on experimental investigation of the microwave cavity plasma source developed in MSU.

- Chapter 2 consists of three portions. The first part introduces the generic concepts for both end-excited and side-excited plasma processing machines. Their basic building blocks and functions are discussed and several state-of-the-art high density plasma sources are reviewed for low pressure, large area single wafer processing. The second portion reviews the current low pressure high density ECR plasma sources and the last part describes the non ECR HDP sources.

- Chapter 3 details the physical structure of the redesigned MPDR™-13 experimental system used in this research.

- Chapter 4 treats the reactor as a "black box". A generic block diagram is given in terms of input, internal and output variable categories. The input, internal and output variables used in this study are then precisely defined. Criteria for evaluating HDPs are also stated in this chapter.

- Chapter 5 briefly describes various experimental techniques used in this thesis. The plasma source is characterized by micro-coaxial electric field probes, Langmuir probes and a gridded energy analyzer. Their operating principles are briefly discussed and their limitations or sources of error are also given.

- The formulation and results of static magnetic field simulations are given in Chapter 6 for different strong, permanent magnet configurations. Simulated magnetic field result is also compared with some experimental data.

- Chapter 7 presents the electric fields and discharge performance of the MPDR™-13 under well-matched power conditions. The internal variables include (1) electric fields at the applicator wall, (2) estimated impressed electric fields at the discharges, (3) plasma potential, (4) electron temperature, and (5) electron and ion energy distribution function measurements at different input conditions that contain input power, chamber pressure, side feed and end feed applicator, and different ECR magnet configurations. The output variables in this chapter are downstream ion densities, microwave coupling efficiencies, and ion production costs. Beside the argon gas, data on pure hydrogen (H_2) gas discharge is also briefly presented.

- Chapter 8 derives the microwave equivalent circuits for the end feed applicator from the electromagnetic field measurements. Each equivalent circuit component is described and discussed. An impedance matching structure for future or larger applicator is proposed.

- Chapter 9 supplements Chapter 7 by presenting the experimental plasma hysteresis and operation modes on the tuning and chamber pressure. Identification of "high density" and "low density" plasma operation modes for stable plasma source control is presented. A repeatable plasma process is also demonstrated by performing argon soft-sputter experiments on silicon wafers.

- Chapter 10 first reviews the simple global discharge models. The predictions from global models are then compared to the measured data of MPDR™-13 and from four different state-of-the-art ECR plasma sources. A proposed initial plasma reactor design using simple global discharge model is also given at the end of the chapter.

- Chapter 11 concludes this thesis with a summary of important results and suggestions for both improving ECR plasma source and future research.

- Appendix A gives details of the mathematical formulation of the calibration of micro-coaxial electric probe method.

- Appendix B lists the aluminum cavity wall thickness near the E-field sample holes and the electrode lengths for the array of probes.

- Appendix C presents and compares the visual plasma pictures of various discharges in MPDR™-13.

- Appendix D summarizes the preliminary data performed in MPDR™-13 without any magnetic field. The collisionless heating is observed when the operating pressure is varied from 45 mTorr to several mTorr.

This work was performed under the guidance of Dr. Jes Asmussen, Professor and Chairperson of the Electrical Engineering Department at Michigan State University. The research presented in this dissertation has resulted in a series of publications in refereed journals [6-11], and presented at several professional conferences [12-24].

Chapter 2

Review of the High Density Plasma Sources

- 2.1 Introduction
- 2.2 Structure of Plasma Processing Machine
- 2.3 Common Features in Current HDP Sources
- 2.4 ECR High Density Plasma Sources
    - 2.4.1 Divergent Field ECR Plasma Sources
    - 2.4.2 Uniform Distributed ECR Plasma Sources
    - 2.4.3 Slot-Antenna Type ECR Plasma Sources (ECR SLAN)
    - 2.4.4 Horn Waveguide Type ECR Plasma Sources
    - 2.4.5 Microwave Multipolar ECR Plasma Sources (ECR-MPDR)
- 2.5 Non ECR High Density Plasma Sources
    - 2.5.1 Spiral Inductively Coupled Plasma Sources
    - 2.5.2 Helical Resonator Type Reactor
    - 2.5.3 Helicon Type Reactors
    - 2.5.4 Microwave Plasma Sources
- 2.6 Concluding Remarks

Chapter 2

Review of the High Density Plasma Sources

2.1 Introduction

Integrated circuit fabrication consists of performing a series of meticulous processes on semiconductor substrates. These processes include lithography, oxidation, dopant/impurity diffusion, implantation, etching, deposition, metallization, etc. Etching is one of the indispensable processes in the fabrication of integrated circuits. The etching process removes unprotected material faithfully according to a mask pattern placed on the top of the substrate. The removal rate of substrate material, the etch uniformity across a large diameter substrate or several wafers, the selectivity of substrate material over the mask material, the resulting side wall pattern, the side and bottom wall roughness and substrate damage are all important concerns when evaluating the etching process.

Wet chemical etching processes have been used since the dawn of Integrated Circuit (IC) production in the early 1960s [25]. In wet etching processes, wafers are usually placed in a solution that etches the unprotected material in all directions. It works fine for circuit dimensions above several microns. The fatal drawback of pure chemical etching is the resulting isotropic

etching characteristic. Wet-etched linewidths must be several times the removal film thickness due to the undercutting inherent in isotropic etching. This prevents the wet etch process from achieving small feature size patterns. Thus as smaller feature sizes, required by the ever-increasing higher density circuit fabrication, are reduced below several microns a better etching method is needed.

Plasma etching technologies using parallel plate or barrel reactors were developed in the1970s to conquer this problem. They can fabricate fine features by ionizing the gas molecules into etchant radicals, ions and electrons which then react with the substrate surface material. The reaction products are usually volatile and pumped away, leaving no chemical waste product. Being more friendly to environmental concerns than wet etching processes is an additional advantage for plasma etching processes. Plasma etching or as it is often called "dry etching", is now the commonly used method to produce the small features (micron or submicron) required by state-of-the-art IC fabrications. By controlling the velocities of the ions and radicals the plasma etching process is capable of yielding the anisotropic, minimal damage submicron etching.

Before the mid 1980s, traditional dry etching machines usually employed parallel plate or barrel reactors. In each of these reactors, rf power (often 13.56 MHz) is capacitively coupled to plasma discharges at gas pressures of 0.05 Torr to a few Torr, with wafers located on one of the electrodes (see Figure 2.1). Depending on the operating pressure, ions/radicals may suffer collisional scattering when they fall through the sheath to reach wafer surface. Because of this random scattering in the sheath, the lower the operating pressure, the smaller

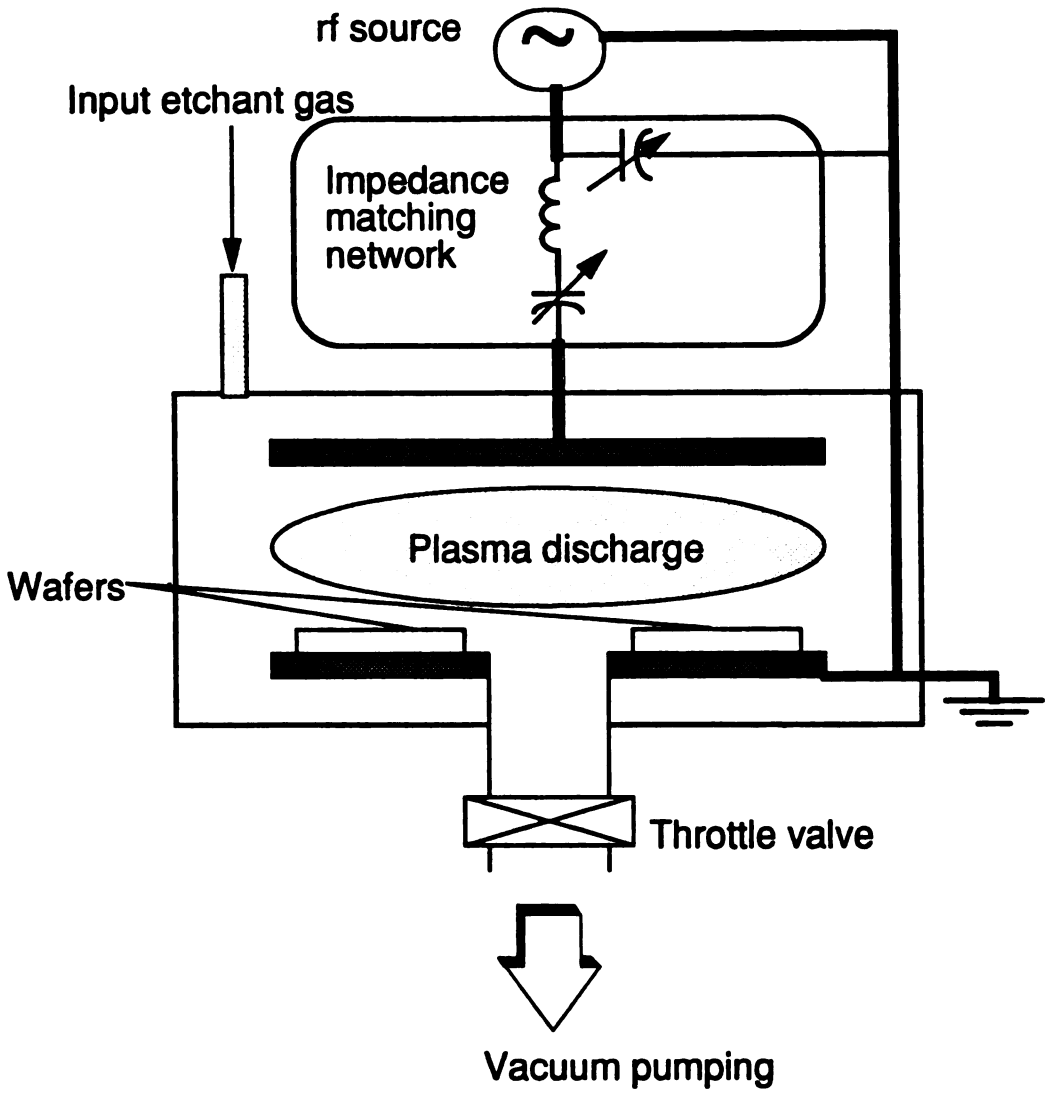

Figure 2.1 Typical parallel plate plasma etching configuration.

pattern it can faithfully fabricate. However, when the processing pressure falls below 0.1 Torr, the gas discharges generated by these traditional plasma etching machines are difficult to ignite and maintain. Also the capacitive power coupling mechanism produces high induced voltages and energetic ions that may cause significant damage to dielectrics such as silicon oxide. Additionally, the lower the pressure, the lower the availability of gas etchants, and the slower the etching rate. Trade-offs between high processing rate and small size etch capability create problems for reliable submicron etching processes in traditional dry etching machines. Moreover, the direct contact between a large area parallel plate power electrode with plasma often causes sputtering of the electrode material onto the wafer, and thus causes undesired process contamination. On the other hand, possible deposition of other materials onto the electrode and the lack of independent control of the induced voltages on substrates influence the consistency of the process. Therefore, it was recognized in mid-1980's that parallel plate etching reactors and associated processes would not be able to achieve the high throughput, submicron damage-free etching criteria required for the next generation of sophisticated microprocessors, memory chips or Application-Specific-Integrated Circuits (ASIC).

Pioneering experiments in the 1970's by Susuki et al. [26] and Musil et al. [27] successfully demonstrated that low pressure, high density microwave electrodeless discharges were capable of many potential plasma processing applications such as submicron etching and thin film deposition. When the stringent demand for reliable manufacturing submicron process was imposed as

the IC manufacturing standard in the mid-1980s, considerable attention was focused upon the development of low pressure high density plasma sources. The search for improved, low pressure, high density plasma sources was accelerated in the late 1980's by the process requirements imposed by several potential plasma processing applications. These applications included (1) large single wafer, submicron etching of silicon [28], (2) low damage etching for III-V electronic and photonic structures [29], and (3) the development of ion /free radical sources for various molecular-beam-epitaxy (MBE) and accelerator applications [30]. As a result, a new generation of low pressure, HDP sources for large area, single wafer, submicron processing were created during the past decade.

In this chapter, the important generic characteristics of a high density plasma processing machine [31] are introduced. Afterward some common features of HDP sources are presented. Then several representative ECR and non-ECR HDP sources will be briefly described. The ECR variants include the divergent field ECR sources, distributed ECR sources, ECR-SLAN reactors, horn waveguide type ECR plasma sources, and microwave multipolar ECR plasma sources. On the other hand, the non-ECR variants contain spiral inductively coupled sources, helical resonator sources, helicon sources, and an assortment of microwave plasma sources. A systematic comparison of measured plasma properties among selected ECR plasma sources are deliberately delayed and are covered in detail in Chapter 10 where some of the experimental results of this thesis are also presented.

2.2 Structure of the Plasma Processing Machine

While many HDP sources differ by the method (excitation frequency and applicator technology) of electromagnetic power coupling, it is interesting to note that the output plasmas have similar properties [11]. For a systematic study, HDP sources are viewed as a subsystem of a larger EM wave/vacuum processing system. This processing system is identified here as a low pressure plasma processing machine.

Although there are many ways in which to construct a plasma processing machine, Figure 2.2 shows the basic building blocks or subsystems of a typical machine. Such a system usually consists of an EM power supply, a power monitoring and oscillator protection circuit, the input gas handling system with the throttle valve and exhaust pumping system, and the HDP reactor. The definition of a HDP reactor here contains an impedance matching circuit, the plasma applicator, the discharge chamber, the processing chamber, the substrate and substrate holder. In most systems, the substrate potential is adjusted by a separately applied rf bias and the substrate temperature is controlled by a substrate cooler or heater.

Different HDP sources appear to be very different from one another. However, they can be separated into either the end-excited or the side-excited generic sources shown in Figure 2.3 [11]. Each HDP reactor has several common key subsystems. They are the electromagnetic applicator (1), and impedance matching circuit (2), the discharge excitation volume or chamber (3), the process chamber (4), and the substrate (5). The HDP source usually consists of (1) to (3).

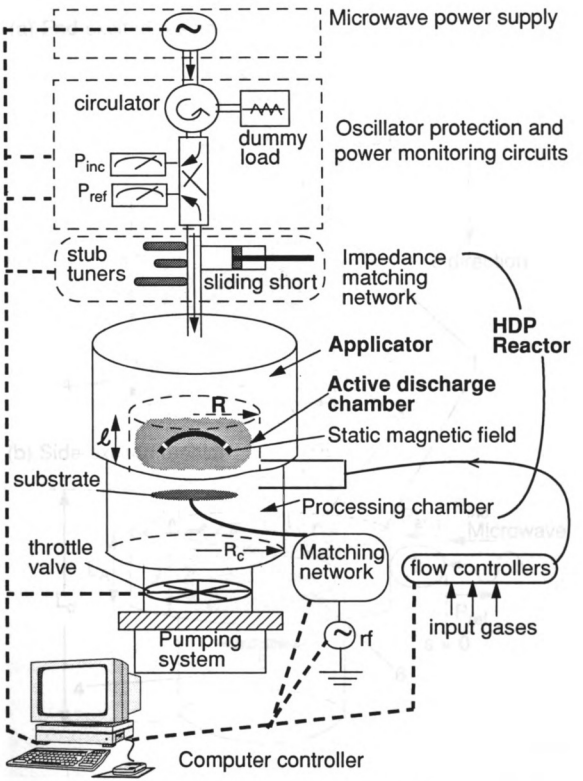

Figure 2.2 Typical low pressure plasma processing machine.

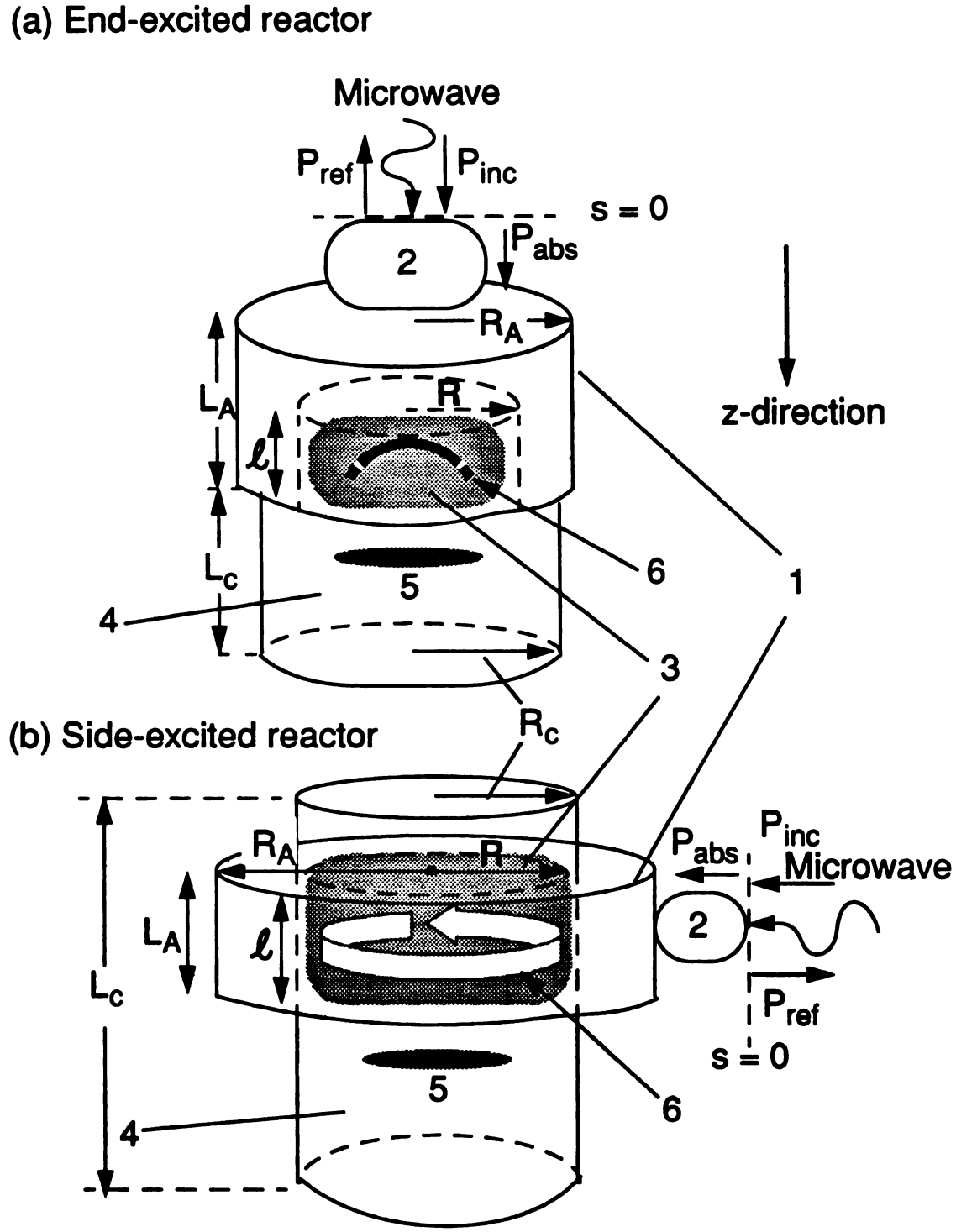

Figure 2.3 Classification of reactor: (a) end-excited, (b) side-excited.

If this is an ECR plasma source, an ECR region (6) is located somewhere inside the discharge excitation chamber. Electromagnetic energy coupling is controlled by the impedance matching network and the applicator electromagnetic field excitation. The electromagnetic energy is coupled through a dielectric window (flat, dome or cylinder shape) from the end for the end-excited reactor, or from the side (perpendicular to the z-axis direction) for the side-excited reactor. The microwave power coupled into the plasma loaded applicator, P_{abs} shown in Figure 2.3, is determined by measuring the difference between the incident power, P_{inc}, and the reflected power, P_{ref}. As indicated in Figure 2.2 the operation of this machine can be automated by computer control. Thus the process sequence, i.e. the start up, gas flow, impedance matching, process cycle, shut down, etc. is usually regulated by computer control.

The cross sections of the two generic HDP reactor concepts for plasma processing are displayed in Figure 2.4. The plasma source is where electromagnetic energy is focused by the applicator into the discharge chamber creating a high density plasma in a volume above the $z = 0$ plane. The processing chamber is where the plasma processing takes place on a substrate surface. The process surface, referred to here as the substrate and shown in Figure 2.4 as a disk, is positioned at a downstream distance z inside the process chamber. The processing chamber and the plasma source are connected at the $z = 0$ plane where discharge diffuses into the process chamber through the "open-ended" plasma source. Input gases flow either just into the discharge chamber only or can be injected into both the discharge chamber and the process chamber. Input

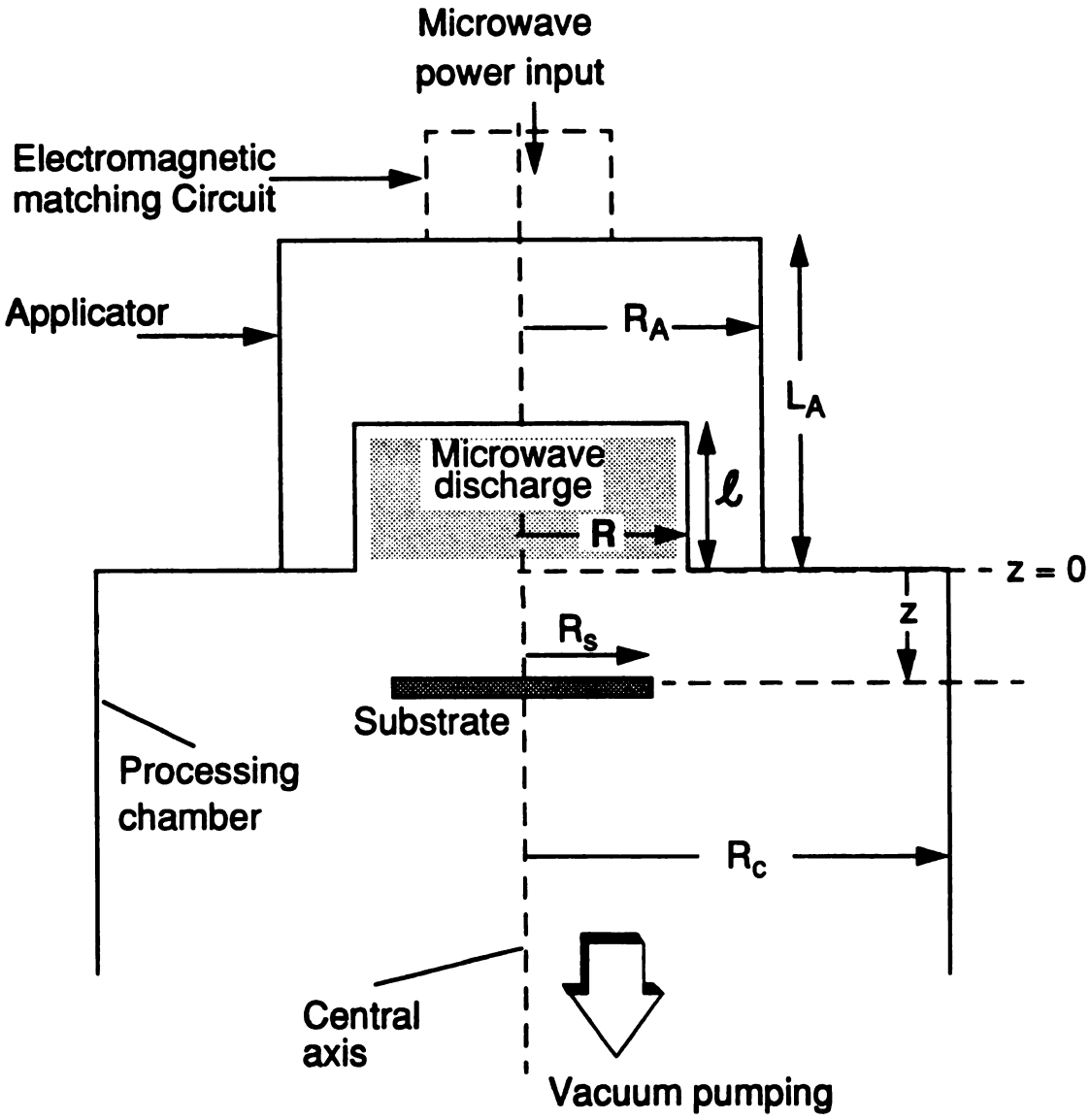

Figure 2.4 (a) The Generic Plasma Reactor (end-excited case);

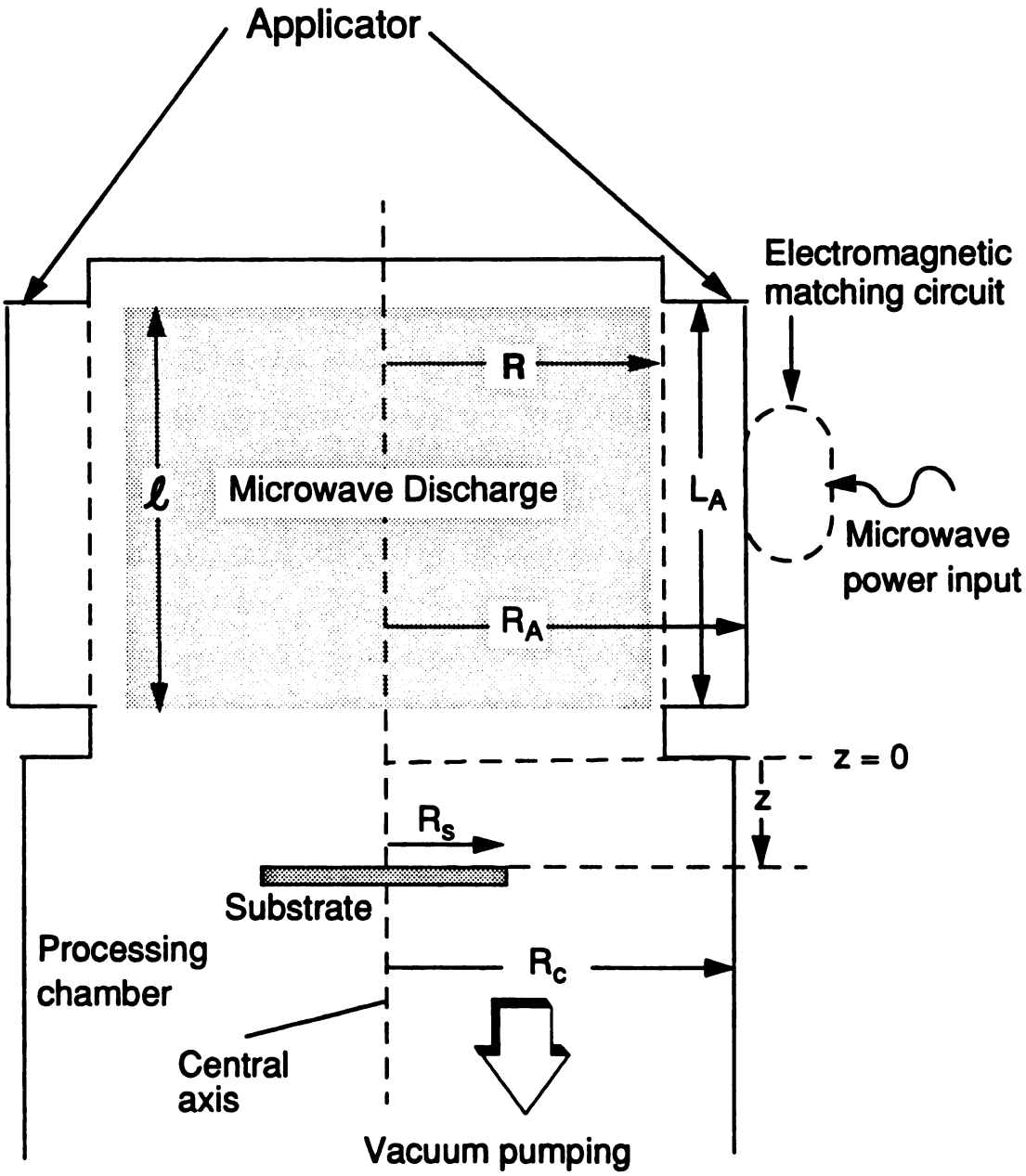

Figure 2.4 (b) The Generic Plasma Reactor (side-excited case).

and process gases exit out the process chamber via the reactor pumping systems. In some large area side-excited plasma sources, such as the DECR described in Section 2.4.2, a quiescent discharge is achieved in the central portion of the discharge chamber for processing applications.

For the sake of simplicity, a cylindrical geometry with a longitudinal axis z is assumed throughout this thesis. The discharge is mainly excited in the cylindrical volume defined by R and ℓ as shown in Figures 2.4 (a) and 2.4 (b). The ions, electrons and radicals created in the discharge then diffuse together with the remaining molecules downstream into the process chamber. The substrate holder, which is usually located downstream in the process chamber, is temperature controlled. Rf and/or dc energy is coupled into the processing chamber and produces a controllable bias on the substrate holder.

Each of HDP subsystems, i.e. the applicator, the discharge chamber, the process chamber and the substrate, have certain critical dimensions. The active discharge volume is defined by a cylinder with a radius R and length ℓ. The length ℓ is defined as the distance from the top of the discharge to the discharge opening at $z = 0$ plane. The process chamber is also a cylinder of radius R_c and length L_c. Similarly the applicator has a height of L_A and a radius R_A. The substrate, which is assumed to be a macroscopically flat surface, has a radius of R_s and is located at a distance z downstream from the $z = 0$ plane. These dimensions are the critical dimensions associated with the design of the reactor.

2.3 Common Features in Current HDP Sources

Besides the common physical structures described in Section 2.2, low pressure HDP sources also share with each other common electro-chemical characteristics [11]. One of these is the special advantageous process environment generated by their high density plasmas. The low neutral pressures of 10^{-4} to 10^{-2} Torr, high plasma densities of 10^{11} to $10^{12}/cm^3$ with low plasma sheath potential (<30V) provide a unique, beneficial environment for material processing. Under these operating conditions, the ion mean free path is much larger than the size of plasma sheath. Therefore, ions seldom suffer a collision as they pass through the sheath and strike the substrate surface with normal incidence. Moreover, by impressing a separate capacitively coupled rf bias on the substrate electrode the magnitude and the direction of the ion velocity is controlled as the ions are accelerated through the sheath onto the substrate. This plasma source configuration allows an independent adjustment of ion-bombarding energy by the adjustment of the bias on the substrate electrode. The combination of the controllable, collimated low energy flux of ions and the abundant neutral radicals that strike the substrate surface produces the conditions to achieve submicron anisotropic etching [32] and film deposition [33].

Another common feature of these sources is that microwave or rf power is coupled into the discharge through a dielectric window rather than by direct insertion of a large area power electrode into the discharge. As a result it drastically reduces the capacitive power coupling, and hence lowers the energy of ions and the plasma sheath potentials adjacent to the substrate and discharge

chamber wall surfaces. Hence, the source lifetime, substrate damage and contamination are greatly improved in these low pressure HDP sources.

Unless otherwise stated, the following HDP representatives described in Sections 2.4 - 2.5 closely follow the plasma processing machine concepts described in previous section. For example, they all have a temperature controlled substrate holder located in the process chamber. An independent dc or rf (usually 13.56 MHz) bias with matching network provides the flexible control of impinging ion energies.

2.4 ECR High Density Plasma Sources

Some researchers may have a different point of view on how to define an ECR plasma. In this thesis the definition of an ECR plasma is generalized to include all low pressure discharges which have an electron cyclotron resonance zone, i.e., a region where the excitation angular frequency equals the cyclotron frequency [34] ($\omega \cong \omega_{ce}$), within the discharge chamber.

2.4.1 Divergent Field ECR Plasma Sources

The most widely used ECR plasma reactor is the divergent (magnetic) field system [35]. This reactor concept, shown in Figure 2.5, was first employed by Suzuki et al. [26] and Musil et al. [27] in their pioneering processing experiments.

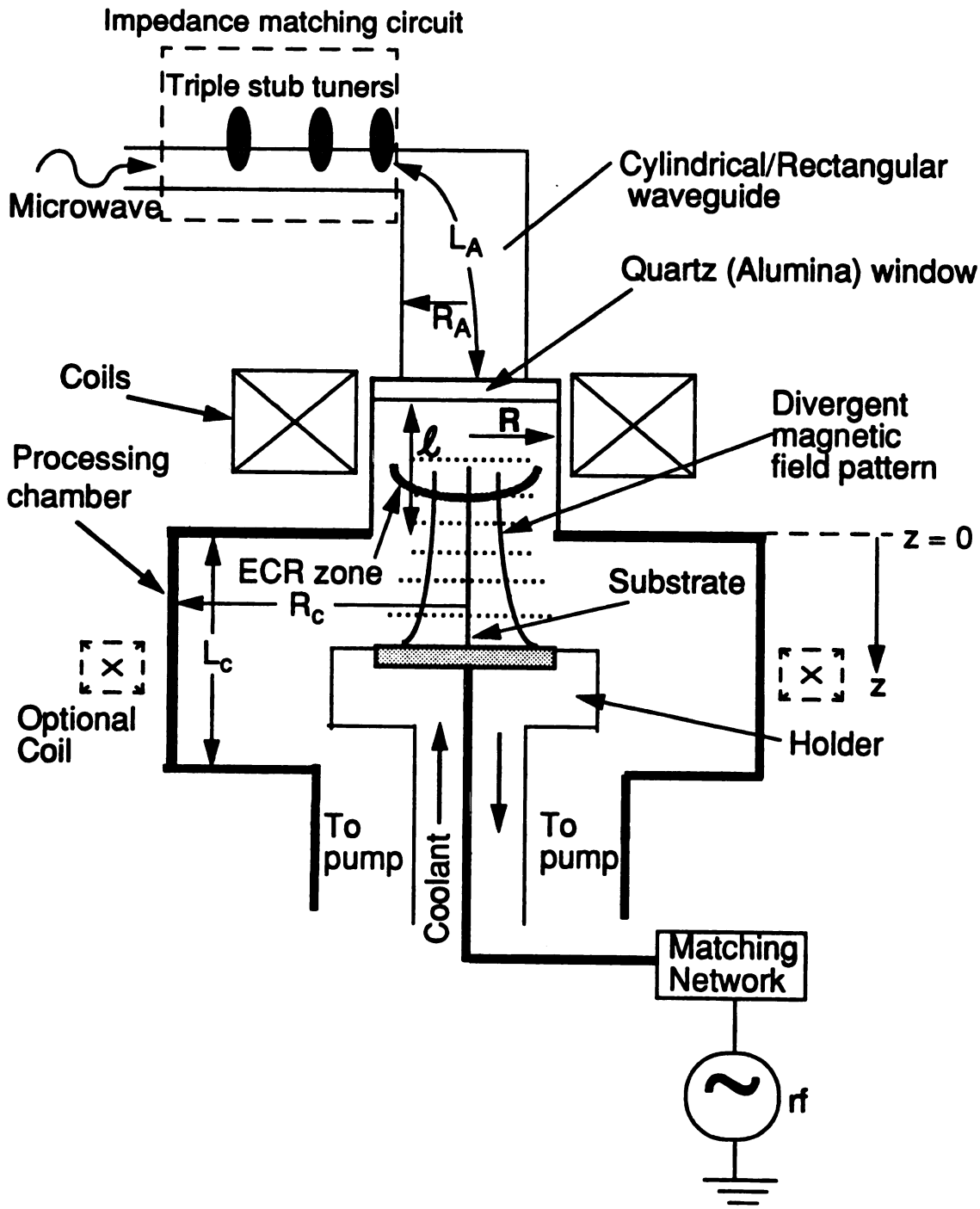

Figure 2.5 Divergent ECR Plasma Source (Low profile type).

Thus it became the standard ECR source that many researchers used to investigate new etching and thin film deposition processes. The early designs which had a high aspect ratio (ℓ >> R) were commonly used [35]. However, as understanding of the application requirements as well as knowledge of the source operation improved, the divergent field concept was redesigned to the low aspect ratio (R ~ ℓ or R > ℓ) ECR version shown in Figure 2.5. This plasma reactor is now commonly used in the investigation on many plasma processing applications. Using 2.45 GHz excitation these reactors have been built as large as 26 cm in diameter [36].

As shown in Figure 2.5, this type of reactor belongs to the end-excited group and consists of a circular waveguide applicator terminated by a dielectric microwave window which allows the microwave energy to propagate into the low pressure discharge chamber for plasma excitation. An axially variable 875 Gauss ECR layer is created across the discharge chamber cross section by adjusting the current in one or more coils, which closely surround to the discharge chamber. The coil locations and their current magnitudes are usually positioned and adjusted so that the magnetic field is the highest at the microwave coupling window and then decreases along the reactor axis downstream from the window, creating a magnetic beach condition for easy Right Hand Polarized (RHP) microwave coupling [37, 38]. The impedance matching circuit usually consists of a three stub tuner and/or a mode converter [35] to match the discharge to the TE_{11} or TM_{01} mode propagating in the input microwave wavguide applicator.

The solenoidal, axial magnetic field in this reactor often produces problems in some process applications. First the excitation charge density nonuniformities that exist in the discharge chamber are directly transferred along magnetic field lines into the process chamber and onto the substrate. Additionally the divergent magnetic field lines cut through the substrate surface at angles that vary with the radial position. Ions are carried along by the electrons as they diffuse along the magnetic field lines and thus the ions strike the substrate with different angles of incidence versus the radial position on the substrate. In anisotropic etching applications, this results in etched patterns that vary across the wafer. Clearly, this is undesirable. Therefore, an additional coil is sometimes placed close to the plane of the substrate, as shown in Figure 2.5, to control the magnetic fields/ion trajectories near the substrate surface.

A potentially important innovation in divergent field ECR plasma reactor designs is the use of permanent magnets located behind the microwave window to produce the divergent ECR magnetic fields [39, 40]. For example, Mantei et al. used a 15 x 15 x 9 cm, 18 k Gauss block of Nd-Fe-B magnets to create an ECR zone which is 8 cm from the magnet face, allowing the coupling window and waveguide to be inserted adjacent to the magnet poles. This design which readily produces plasma densities greater than 2 x $10^{11}/cm^3$ has the advantage of creating the magnetic field without using an electromagnet and its associated electrical power supply.

2.4.2 Uniform Distributed ECR Plasma Sources

The cylindrical distributed ECR (DECR), displayed in Figure 2.6 (a), employs the magnetic multipolar plasma cusp configuration. The magnetic fields (shown in dashed line in Figure 2.6 (a) not only create ECR regions near the chamber wall but also provide a plasma confinement function [41, 42]. A cylindrical metal chamber surrounded by rows of strong permanent magnets along the length of the wall houses the discharges generated by the ECR cusps and lobes. There is no clear-cut boundary between processing chamber and the discharge chamber. Plasma then drifts into the center low magnetic field region by the gradient of the B-field and by diffusion processes. Due to the large distance between the ECR region and center low magnetic field region, a very uniform processing region (1% over 15 cm dia.) can be achieved [43, 44] by placing the substrate at the center of the plasma volume. The input microwave power is distributed to a number of cylindrical stainless steel transmission-line antennas (8 mm diameter, 10 to 40 cm long) which are inserted into the discharge near the chamber wall. The impedance matching circuit includes a tuning circuit and a power distributor (both not shown), which are located in front of the coaxial feedthrough for each antenna.

Uniform DECR (UDECR) [45] is an updated version of DECR. Instead of inserting antennas directly over the magnets next to ECR zones as is done in the DECR case, the UDECR (shown in Figure 2.6 (b)) places the antennas between the magnets next to the chamber wall. This relocation of antennas reduces the

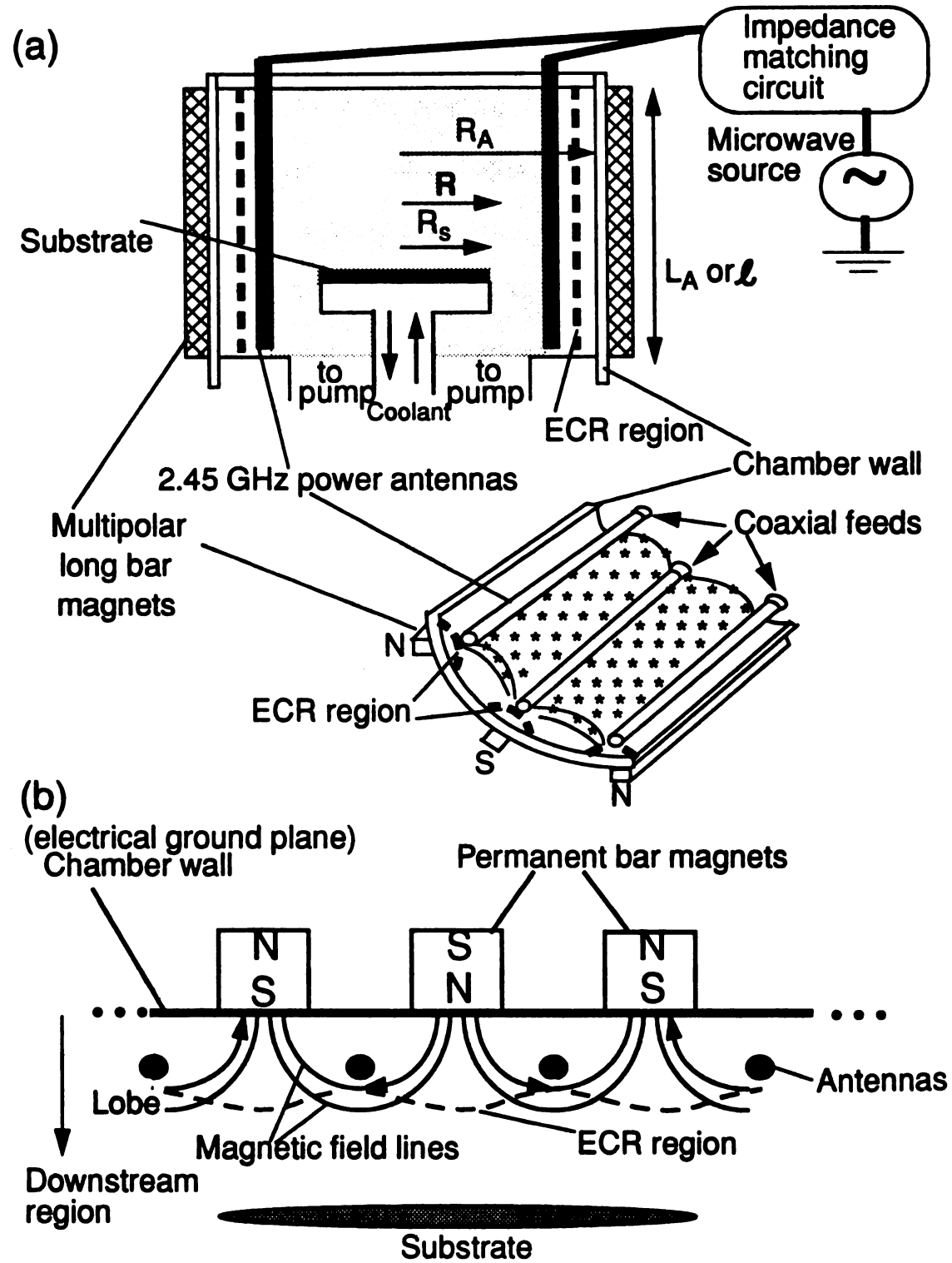

Figure 2.6 (a) Cylindrical DECR source machine [43], (b) Schematic representation of Planar UDECR source machine [45].

sputtering of antenna material by the energetic electrons. In addition, the UDECR employs the stronger NdFeB permanent magnets. As a result, the ECR regions are pushed more inwards into the chamber than in the DECR case. This allows plasma to readily diffuse into the center region (in side-excited case) or downstream region (in end-excited case) rather than to recombine on the chamber walls. The impedance matching circuit is similar to DECR situated in front of the coaxial feedthrough for each antenna.

Both DECR and UDECR can be either cylindrical chamber type (side-excited applicator, see Figure 2.6 (a)) and planar type (end-excited applicator, see Figure 2.6 (b)). In side-excited configuration, antennas are placed around the side of cylindrical chamber to distribute microwave energy into the ECR cusps along their full lengths. While in the end-excited configuration, antennas are positioned near the top end of the chamber wall to deposit energy into the ECR regions nearby. Both cases are easy to scale up by increasing the number of antenna-magnet bars. However, the direct contact between the antennas and discharge poses some potential drawbacks. For example, possible contamination from sputtering antenna material can occur during reactive species etching processes. During the deposition process, the antennas themselves can also be contaminated with non-conducting deposits, causing abnormal operation. Additionally, microwaves cannot propagate along the antennas without absorption. Hence, the plasma is not uniform along the z-axis in both side-excited and end-excited cases.

2.4.3 Slot-Antenna Type ECR Plasma Sources (ECR SLAN)

The slot antenna ECR plasma side-excited reactor concept is based upon the slot antenna (SLAN) microwave applicator concept development by Engemann [46-48]. This concept has some similarities to the Lisitano-type plasma source [49] except that the applicator is not immersed in the discharge. A cross-sectional view of a 2.45 GHz ECR SLAN plasma reactor concept is shown in Figure 2.7 (a). The ECR SLAN consists of an annular waveguide or ring cavity with axial slot antennas positioned azimuthally at equally spaced locations around a quartz cylindrical discharge chamber. Microwave energy is coupled into the ring cavity from a rectangular waveguide via a variable length coupling probe and a movable shorting plunger, which are the impedance matching network for this plasma source. These two degrees of freedom enable this plasma loaded applicator to be matched for various experimental plasma conditions. The coupling probe couples microwave energy into the ring cavity exciting a standing wave field pattern that induces large electric field displacement currents in each slot antenna.

The circumferential length of the middle line of the cavity is approximately an integral multiple of the guided wavelength ($n \bullet \lambda_g$). The distance between the coupling probe and the nearest slot is $\lambda_g/4$. The slots, which are about half wavelength high (i.e. ~ 6.12 cm), are separated approximately by a circumferential distance of λ_g. The ECR SLAN reactor has been built in two diameters (1) 4 cm (called μSLAN), and (2) 16 cm (SLAN-1). The number of slots along the perimeter depends on the diameter of the desired discharge. Figure 2.7 (a), displays a ring

(a)

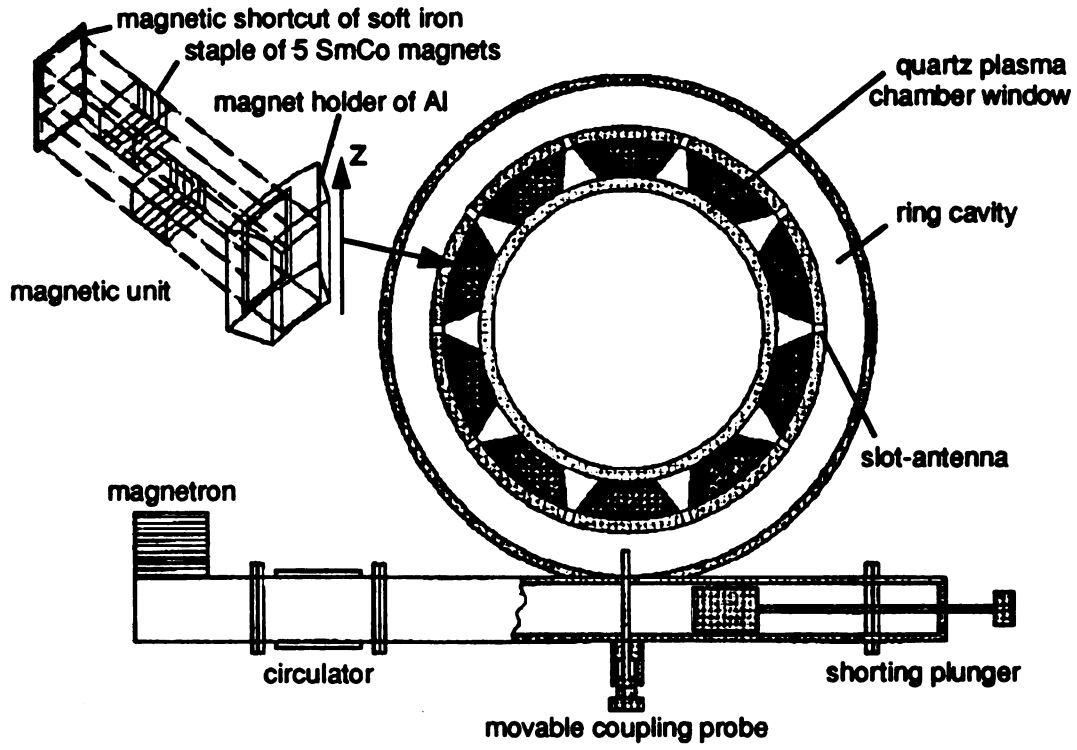

(b)

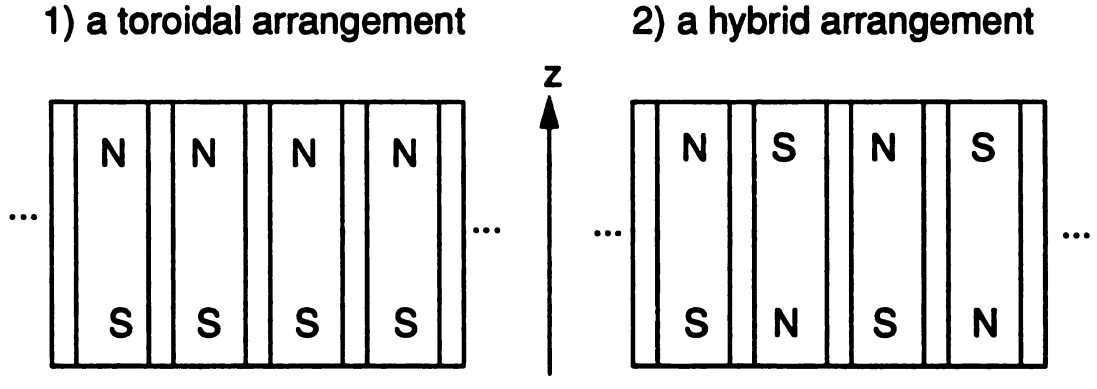

Figure 2.7 (a) Slot antenna plasma source (ECR version) [46], (b) ECR magnet configurations.
Non-ECR version is the same but without the magnets.

resonator of 10 λ_g in circumference. Each of these slot antenna radiates coherent (in phase) microwave energy through the quartz tube window into the discharge volume.

In the ECR version of SLAN SmCo permanent magnets are, as shown in Figure 2.7 (a), placed exactly half way between each slot. A U-shaped magnet is formed from a soft ion sheet and SmCo magnet. One coupling slot with two adjacent magnets forms an approximate slot/horn antenna. This magnet arrangement pushes the magnetic field from the slot into the discharge as far as possible. As shown in Figure 2.7 (b), two types of ECR magnetic confinement arrangements have been employed: (1) a toroidal arrangement when all magnet U have the same N-S pole arrangement and (2) a hybrid arrangement where N-S poles alternate from one adjacent magnet U to another as one moves around the perimeter of the quartz discharge chamber.

2.4.4 Horn Waveguide Type ECR Plasma Sources

This end-excited plasma source [50], shown in Figure 2.8, employs a circular horn or cone shaped waveguide applicator to transmit microwave energy into the large area (300 mm in diameter) dome shaped discharge. A movable shorting plunger and a microwave feed constitute the impedance matching circuit. The microwave feed (not shown in detail) is probably a waveguide to coaxial coupled probe similar to the coupling probe element in SLAN impedance matching network. The dome shaped quartz window which is inserted in the end

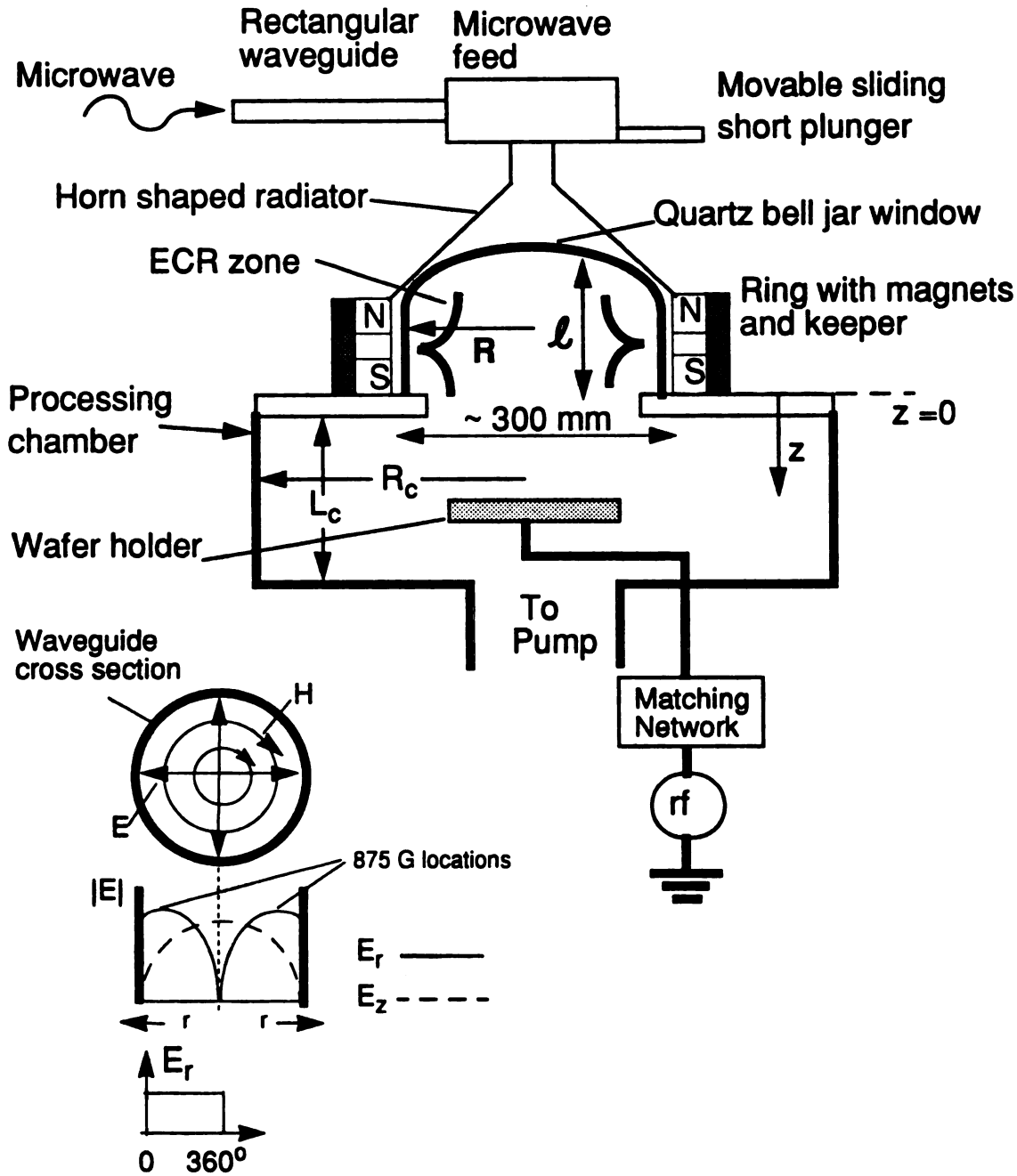

Figure 2.8 Horn-shaped ECR plasma source with TM_{01} field pattern [51].

of circular waveguide serves as the discharge excitation chamber. The ECR zones are generated inside the excitation chamber by mounting a ring of permanent magnets on the outside of the waveguide. The permanent magnet configuration has been arranged such that all magnets have the same N-S pole arrangement, as shown in Figure 2.8.

For better discharge uniformity, the microwave feed couples the rectangular waveguide TE_{01} mode energy from the microwave power supply into TM_{01} mode inside the horn shaped applicator. The ECR zone is deliberately placed on the area where the maximum radial electric field component of the TM_{01} wave occurs for more effective plasma generation [34]. Two major modes of operation, the ring mode and the bulk mode, are reported [51]. These are classified according to the visual pictures of plasmas, where the ring mode has its brightest region in a ring shape located near the ECR zone and the bulk mode burns strongly in the center region of the source, outside the ECR heating volume. The ring mode often appears below ~0.1 mTorr while bulk mode usually appears in as the pressure goes above ~ 1 mTorr. At a fixed pressure, say 0.75 mTorr, the ring mode usually occurs from microwave input power 120 W to 480 W. And above 480 W the bulk mode emerges with the ring mode to coexist in the plasma. The operational modes dependence on power and pressure was explained by the different heating regions that are caused by the different components of TM_{01} mode electric field. The ring mode is mainly heated by the radial component of electric field which has a peak coinciding to the ECR zone location. On the other hand, the bulk mode is mainly heated by the longitudinal electric field which has a maximum at the center

of the chamber. This is also consistent with the idea that it is easier to sustain the discharge with ECR heating at lower pressure or lower power. It appears that the bulk mode may be sustained by non-ECR heating process.

At a 0.75 mTorr oxygen plasma, Langmuir probe data indicates an ion density of approximately 5 x $10^{10}/cm^3$ and an electron temperature of 5 eV with 1.2 kW input power. Due to the lack of published argon plasma discharge data, its performance is not compared with other ECR sources in Chapter 10.

2.4.5 Microwave Multipolar ECR Plasma Sources (ECR-MPDR™)

The microwave multipolar ECR plasma source [31] or as it is often called the microwave plasma disk reactor (MPDR™) is the plasma machine investigated in this thesis. This type of plasma source, which is shown in Figures 3.3 and 3.4, can be built in many different sizes. Thus the different plasma sources are named according to the diameter of their discharges. Discharges come with either a disk shape or dome shape surround by multipolar ECR permanent magnets. In particular, 5 cm (MPDR™-5) [52], 9 cm (MPDR™-9) [53], 12.5 cm (MPDR™-13) [6], and 24 cm (MPDR™ 325) [54] diameter discharges have been built, investigated and commercialized with 2.45 GHz excitation. Depending upon the cavity diameter, the discharge can be excited by 2.45 GHz microwave power with one or more controlled multi-modes inside the applicator cavity. Large diameter reactors can also be excited with 915 MHz microwave energy [55]. Discharges with diameters of 30 - 60 cm appear to be feasible.

One of the common features in these machines is that they all employ a cylindrical cavity applicator with a coaxial launcher either coming from the side or from the end of a cylindrical cavity. An adjustable coaxial input probe accompanied with a movable sliding short form the impedance matching circuit inside the applicator. This internally tuned design is unique and provides the two degrees of freedom necessary to match the plasma loaded cavity to the input transmission line characteristic impedance.

Another common feature is the use of a multipolar magnetic field configuration by strong permanent magnets. An even number of magnets are arranged on an iron keeper with alternate poles forming a circumferential circle. Depending on the size of the discharge, the number of magnets varies accordingly. Another optional set of multipolar magnets can be located downstream to reduce radial charged particle diffusion and improve plasma uniformity near the substrate surface. However, the strong ECR and confining multipolar magnetic field exist mostly at the discharge and plasma chamber circumferences and the processing region is virtually magnetic field free. More details of this configuration is discussed in Chapter 3.

2.5 Non ECR High Density Plasma Sources

Due to the wide-spread industrial use of rf technology (below 500 MHz, and 13.56 MHz in particular), many new large area non-ECR high density plasma source designs [56] that employ rf frequency energy have emerged over the last

seven years. Three important representatives will be briefly discussed next. On the other hand, the continued improvement of microwave excited discharges without magnetic field has also made an assortment of microwave plasma sources competitive with other HDP sources. Three of them are mentioned in later subsections.

2.5.1 Spiral Inductive Coupled Plasma Sources

Figure 2.9 (a) shows a schematic cross sectional view of an end-excited planar Inductive Coupled Plasma (ICP) source. A (rectangular or circular) coil sitting on a large flat dielectric window in an "electric stovetop" spiral shape is connected to the rf power supply via the impedance matching circuit (usually tuned by variable capacitors). The coil radiates electromagnetic energy through the quartz window and mainly inductively couples energy into the plasma by an azimuthal induced electric field below the window. The shape of spiral coil is usually a 4-5 turn single-spiral coil [57-60] as shown in Figure 2.9 (b). For a single spiral coil, the end of the last turn produces minor non-symmetry. It can be corrected by either shifting the coil off the window center [61] or using a multispiral coil [62], as shown in the Figure 2.9 (c). Bimodal peak ion energy distributions have been observed in Ref. [63] when no Faraday screen was put between the coil and the window. Therefore, most designs insert the split Faraday shields to reduce the inevitable capacitive coupling effect that would cause undesirable ion energy distributions and energetic electron sputtering of the quartz wall.

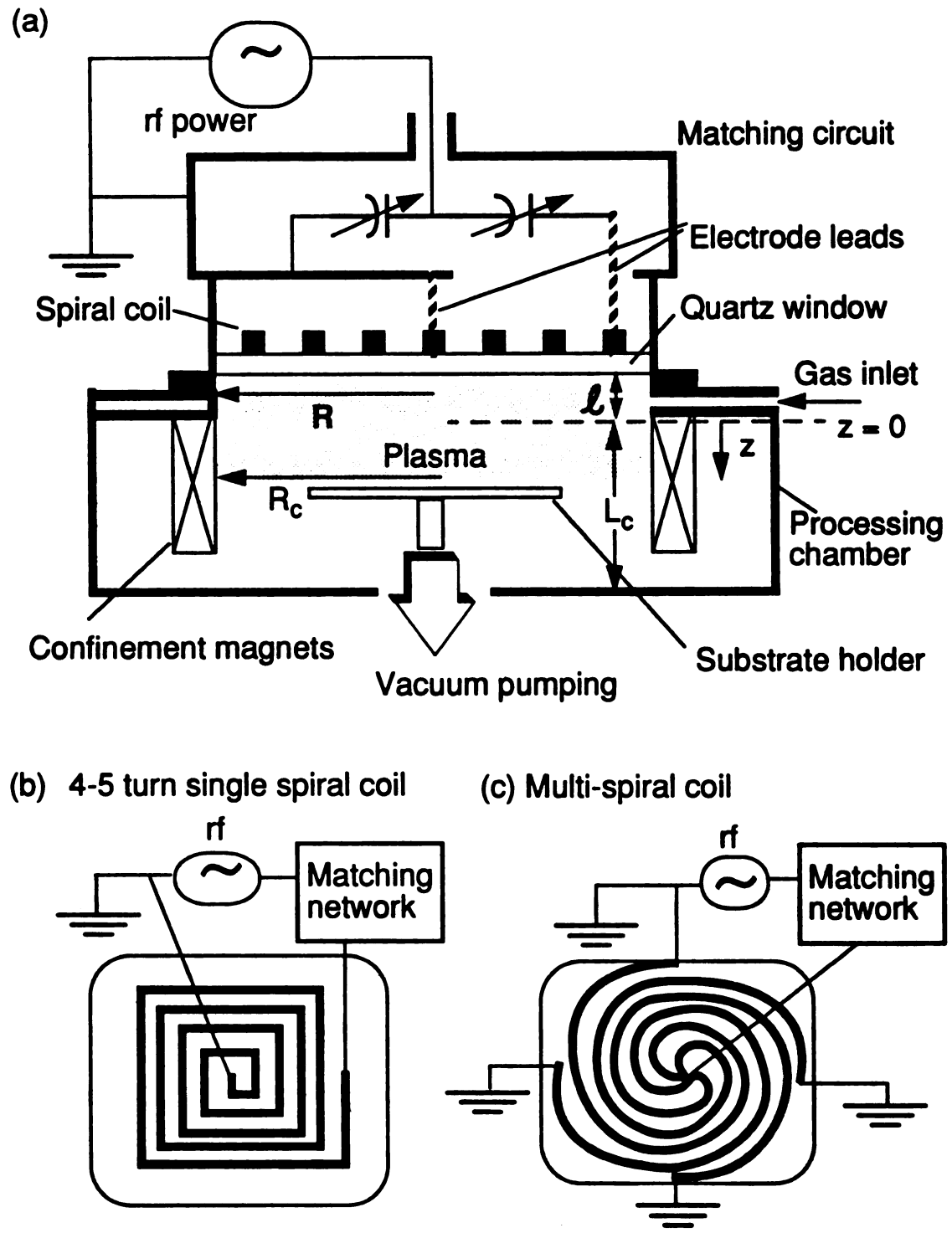

Figure 2.9 (a) Spiral Inductive Coupled plasma source [57], (b) Single spiral coil configuration, (c) Multi-spiral coil configuration [62].

Hence, the discharge becomes mainly inductive and that is why it is often called ICP. However, adding Faraday shields in the reactor reduces the power coupling efficiency [59] due to inevitable losses in the shields. The coil inductor and the capacitors in the impedance matching circuit act like a LC transformer circuit and therefore this source is sometimes called Transformer Coupled Plasma (TCP) source by Lam Research Corp. [64].

The rf induction fields usually penetrate into the plasma at several skin depths (~6 cm) [57, 58], which depend upon operating plasma parameters. This distance is equivalent to the lower boundary ($z = 0$ defined in the general reactor concept of Section 2.2) of the active discharge excitation. Then the ions, electrons and radicals diffuse freely to a downstream processing area, where sometimes an additional multipolar confinement magnetic bucket is placed to reduce radial diffusion. For a 4-5 turn single-spiral coil with downstream confinement magnets, the 5 mTorr oxygen plasma has a density of $3x10^{11}/cm^3$ with 2.5% uniformity over 20 cm diameter.

This type of HDP is easy to build for relatively large processing areas (up to 300 mm dia.) but suffers a thermo-mechanical problem when further scale-up is needed. When the size further increases, the flat dielectric flat-plate becomes rather thick (> 3 cm) and is difficult to cool. In the thick window configuration, it is difficult to efficiently couple the rf induction energy into and ionize the gas in the discharge chamber.

Nowadays, various versions of ICP sources have been and are being developed. A potential important innovation [65] in the ICP plasma source design

employs a large hemispherical bell jar wrapped surrounded by an inductive coil to produce large area of uniform plasma at the base (around 360 mm diameter). The 20-turn copper coil is powered from 250 W to 1.5 kW of 460 kHz rf power. Tuning is done by impedance matching circuit containing lumped inductors and capacitors. The wafer electrode can be independently biased with 13.56 MHz rf energy. The dome shape has reliably reduced the mechanical stress of the dielectric window exerted by the pressure. The selected frequency and dome shaped window design are quite suitable when the reactor is further scaled up while keeping the window wall thin (~0.6 cm). This design can easily generate a $2x10^{11}/cm^3$ plasma density at 5 mTorr over 200 diameter area with 2 to 3% radial uniformity for 2 kW of UHF power.

2.5.2 Helical Resonator Type Reactors

The relatively large area helical resonator was developed by Flamm et al. [66] and is manufactured by Prototech Research Inc., Tempe, AZ. As shown in Figure 2.10, this is a side-excited plasma source confined in a cylindrical quartz tube which is wrapped on the sides with a rf (13.56 MHz, up to 5 KW) powered solenoidal helix coil. Both the coil and dielectric window are liquid cooled. If the length of the helix is approximately an integral number of quarter wavelengths of the rf field, this becomes a resonant, slow-wave, plasma-loaded structure [67]. Therefore, rf energy is coupled into plasma within the discharge chamber. Similar to the spiral ICP, a Faraday shield (thin cylinder with the multi-slots parallel to the

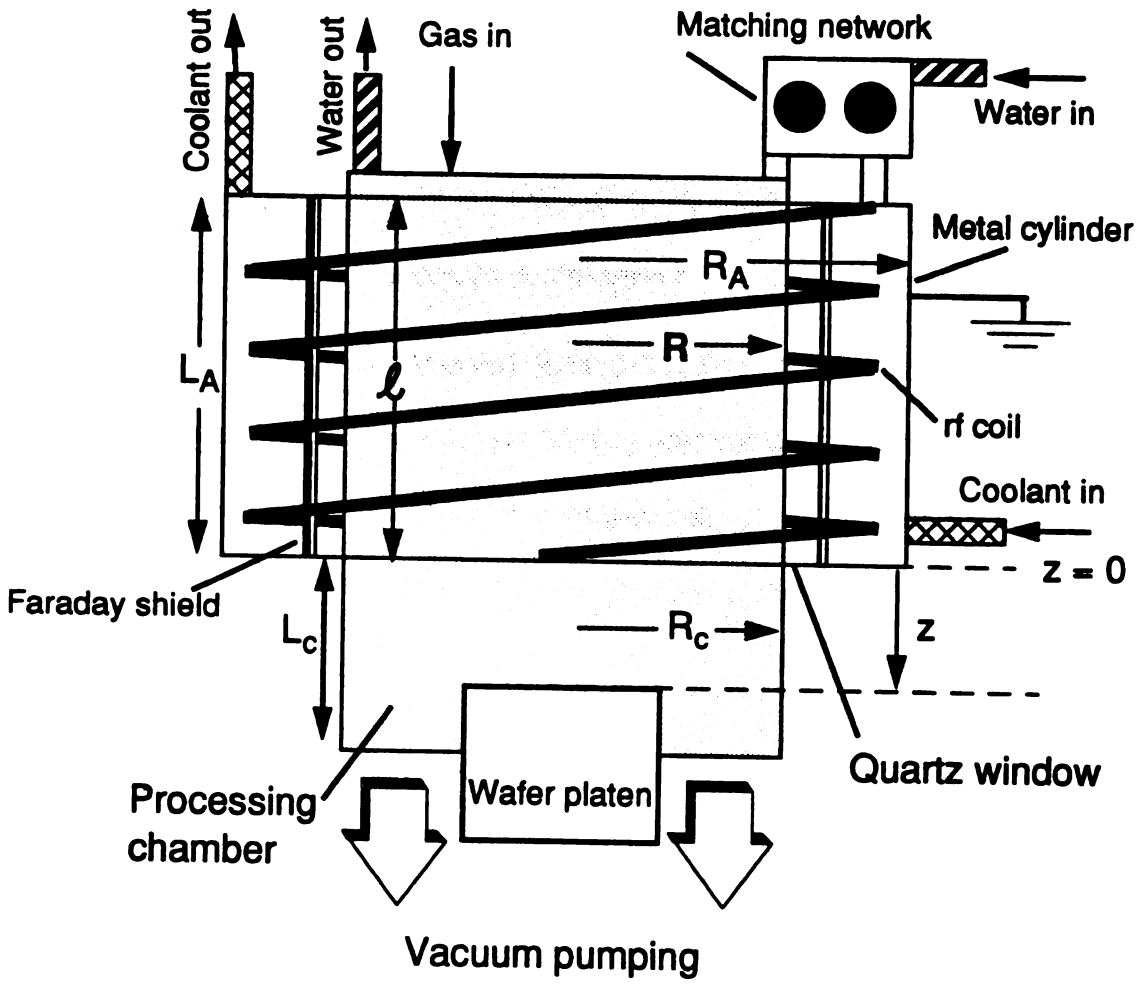

Figure 2.10 Helical resonator plasma source [66].

z-axis) is inserted between the coil and the quartz window to reduce capacitive coupling. A grounded metallic cylinder covers the whole source to shield off the rf energy. A standard rf matching network (controlled by variable capacitors) is located externally to match the different plasma-loaded resonator impedances. A temperature controlled wafer platen located in the downstream processing chamber can also be biased with rf (13.56 MHz, up to 600W) energy to adjust the impinging ion energy. Scale-up is easily done by increasing the size of chamber and varying the length of the coil by an integral number of quarter wavelengths.

The ion density is reported [68] in mid-$10^{11}/cm^3$ range and electron temperatures are around 5-7 eV. The best uniformity is at around 1% across 125 mm diameter at 3.5 mTorr, with 3 kW of input source power and with 53 W of rf-bias power.

2.5.3 Helicon Type Reactors

An efficient rf plasma discharge excited by helicon waves was first studied by Boswell [69] in 1970. After almost two decades, this source is scaled up for large area plasma processing applications [70]. Unlike the spiral ICP source or Helical reactor, energy is not coming from the peripheral region in Helicon reactor. Instead, the helicon plasma source can be sustained through the helicon wave excited inside the plasma excitation chamber. This source can be either inductive, or capacitive coupled depending upon the operation helicon wave modes [71]. A detailed discussion of this type of HDP source is beyond the scope of this study.

Interested readers should refer to the intensive studies performed by the research groups led by Chen et al. [72] at UCLA, and by Shoji et al. [73] in Japan.

Figure 2.11 displays a typical helicon plasma source for single-wafer plasma processing. The weak (30-300 G) axial static magnetic field generated by the upper two solenoid magnets is necessary to excite the helicon waves. Usually, the m=0 or m=+1 helicon wave mode is excited for uniform plasma operation. The high density plasma discharge generated in this side-excited plasma source chamber freely diffuses downstream into the plasma processing chamber. The bottom two sets of magnets shown in Figure 2.11 reduce diffusion losses and improve plasma density and uniformity near the substrate in the downstream processing chamber. Typical plasma densities in the downstream chamber are around $10^{11}/cm^3$ with < 3% uniformity over 150 mm dia. with 500 W of rf source power.

2.5.4 Microwave Plasma Sources

2.5.4.A Non-ECR MPDR™

Similar to the multipolar ECR reactor, this machine contains the exact elements/subsystems as described in Section 2.4.5 and shown in Figure 3.3, but without the ECR magnets. This high density resonant discharge has been recently operated [23] even at low pressure (< 3 mTorr). The details of some experiments are discussed in Appendix D. It is shown that this source is capable of operating with high densities (> 10^{11} /cm^3) at pressures as low as 4 mTorr.

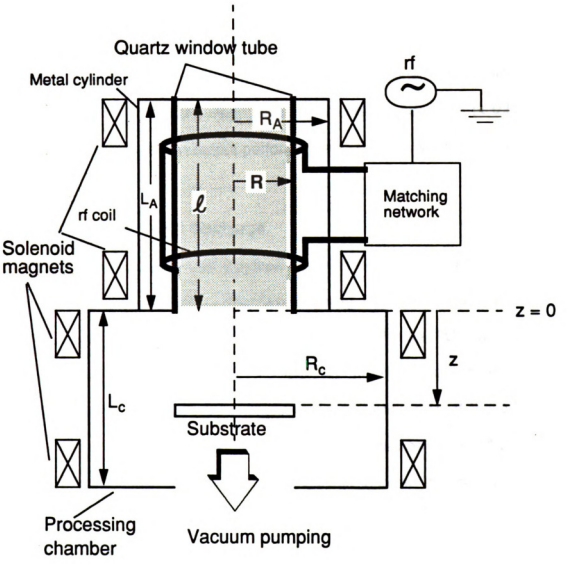

Figure 2.11 Helicon plasma source [70].

2.5.4.B Non-ECR SLAN

Similar to the ECR SLAN reactor [47, 48], this machine contains the identical elements/subsystems but without the ECR magnets. The non-ECR SLAN reactor has been built in three diameters: (1) 4 cm (called μSLAN), (2) 16 cm (SLAN-1), and (3) 66 cm (SLAN-II). Generally speaking, the non-ECR SLAN requires higher pressure or higher power to ignite and maintain the discharge than its counter-part ECR-SLAN version. Except for ultra-low pressure (< 0.5 mTorr) operation, a similar plasma output performance to ECR-SLAN was obtained [47, 48].

2.5.4.C Surface wave discharge

Surface wave sustained plasmas can also be used for large area single wafer low pressure high density plasma processing. Using the surfaguide principle [74], a 2.45 GHz microwave wave is coupled into the plasma [75] in a 12 cm tube diameter surrounded by a 18.8 cm diameter, 40 cm height metallic cylinder. The microwave is launched, shown in Figure 2.12, from the side of the plasma to excite surface waves along the discharge. Matching can be achieved by varying the opposite side waveguide plunger. Sometimes, another microwave generator connects to the other side to make surface wave excitation more symmetric. Wave propagation studies have shown that the plasma surface mode has mainly an azimuthal hexapolar ($\pi/3$ periodicity) symmetry. However, because of the diffusion, the plasma density profile is quite homogeneous, with only a slight modulated ($\pi/3$ periodicity) pattern.

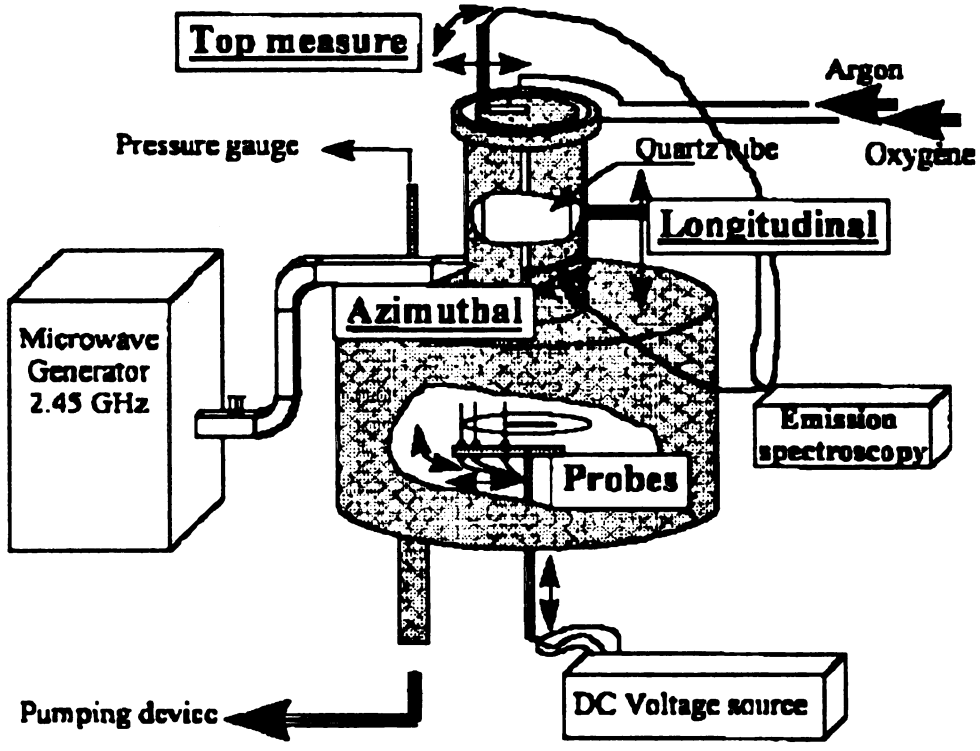

Figure 2.12 Large area surface wave discharge [75]

2.6 Concluding Remarks

In this chapter, the important plasma machine concepts for large area single-wafer processing are reviewed, and the common features of the low pressure high density plasma machines are highlighted. In addition, several ECR as well as non-ECR low pressure HDP sources are briefly discussed. Most of them meet the criteria for processing large area silicon wafers, with 0.35 μm (or below) feature sizes and high throughput [68, 76-79]. The choice of one machine over another is usually influenced by many factors, some of which may be non-technical. Practical factors such as ease of operation, reliability and ownership of patent rights heavily influence the manufacturer's decision on which machine to use.

For the design of ECR HDP, using electrical coils to generate ECR zone seems obsolete due to the cost and maintenance. Instead, state-of-the-art strong permanent magnets are becoming the popular method of producing strong static magnetic field. Also the processing confinement magnetic bucket has become a standard to improve the plasma uniformity in the downstream processing region.

Finally, ECR and helicon machine designs may continue to be improved respectively by ECR zone optimization and careful antenna launcher/source design for energy deposition into the interior of the plasma discharge. Also, the non-ECR HDP designs may work with the trade-off between better efficiency and capacitively shielding. For spiral ICP and helical resonator sources, they are relatively easy to scale and build. However, rf energy in these non-propagating wave based inductive discharges is usually confined near the window wall, which

poses a slight disadvantage of possible sputtering wall materials [80]. In this thesis, no attempt is made to name the best plasma source. Only a comparison among ECR HDP sources based on plasma load line and ion production cost is made in Chapter 10.

Chapter 3

Microwave Plasma Processing Machines

- 3.1 Introduction to MSU Reactors
- 3.2 The Standard Structure of Microwave Plasma Processing System
  - 3.2.1 Microwave power supply
  - 3.2.2 Microwave power transmission system with oscillator protection and power monitor circuits
  - 3.2.3 MPDR™-13 reactor
  - 3.2.4 Gas flow and vacuum system

Chapter 3

Microwave Plasma Processing Machines

In this chapter, the brief history of the Microwave Plasma Disk Reactor (MPDR™) in MSU is presented and the basic MPDR™ processing machine is described. Additionally, the various microwave systems and vacuum apparatus used for experiments presented in this thesis are discussed. The experimental measurement methods are also presented in the Sections below.

3.1 Introduction to MSU Reactors

In 1980-1982, Root and Asmussen [81] succeeded in building an efficient electrodeless microwave ion source. This scientific engineering development sparked a long term research effort devoted to the development of microwave ion sources at MSU. Basically, the early ion source (see Figure 3.1(a)) contained a cylindrical microwave resonator (17.78 cm i.d.) enclosing a small vacuum sealed cylindrical quartz bell jar (~9 cm i.d.) located at the bottom end of the cavity. Microwave energy was introduced into the resonator by inserting an adjustable excitation antenna at the side wall, and was coupled into the disk shaped quartz bell jar and broke down the gas molecules into a microwave discharge. This research was first published [82] in 1984 and later in 1985 the first U.S. Patent

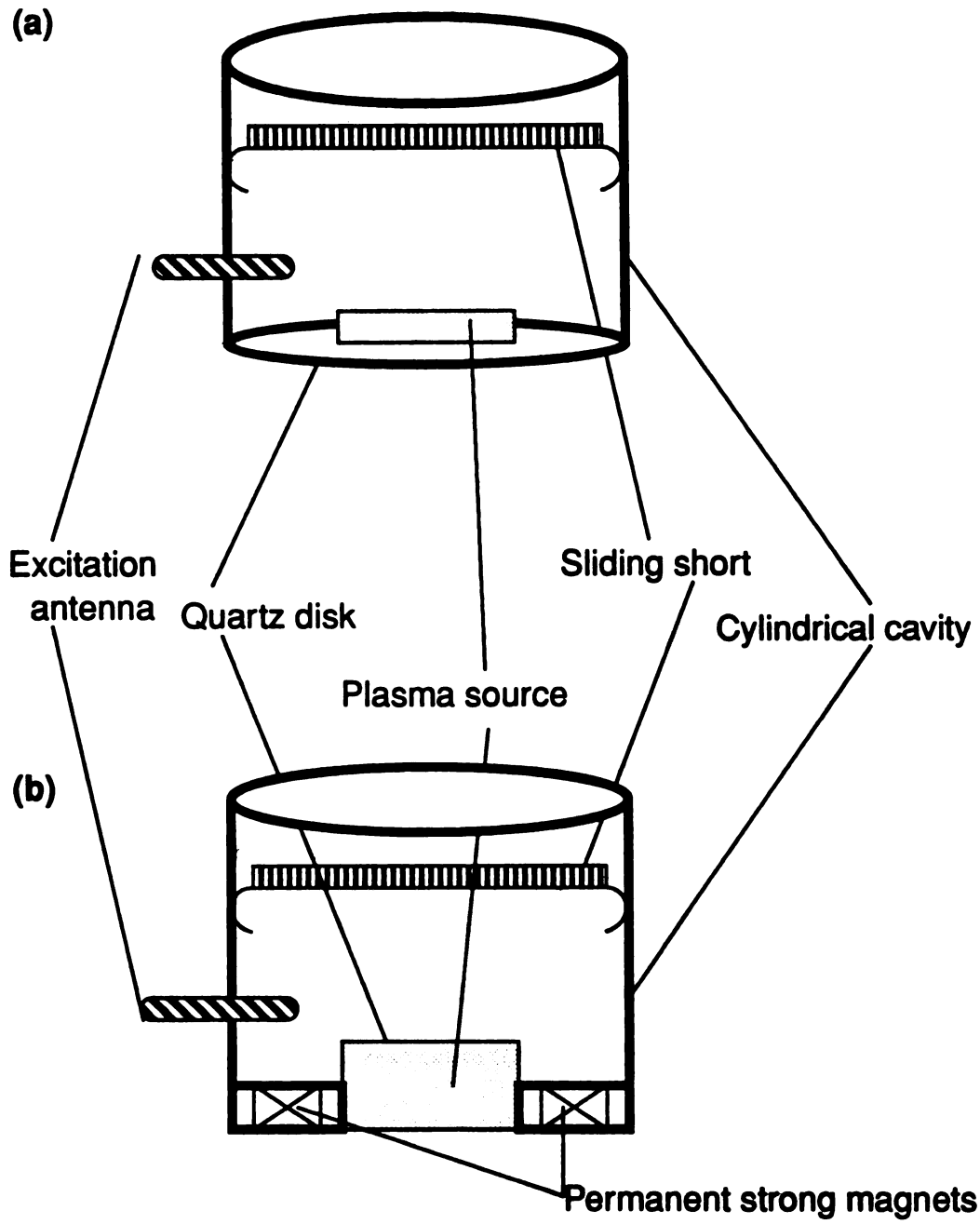

Figure 3.1 (a) Original ion source schematic (1980-1982), (b) Improved MPDR (mid-1980s).

about this type of machine [83] was granted. Because of the energy source -- microwave, the shape of the plasma -- disk, this prototype ion source is often named Microwave Plasma Disk Reactor (hereafter referred to MPDR™).

The original early prototypes of the MPDR™ strongly demonstrated two key points. First, microwave energy alone can sustain a stable plasma over a wide pressure range, from ~ 12 mTorr to around atmosphere. Another significant contribution was the electrodeless nature of the discharge and thus the plasma source was expected to have a longer operational lifetime than other discharges containing electrodes. Secondly, the unique internal tuning method [84] i.e. a sliding short to vary the cylindrical resonator height, and an adjustable side-feed probe to change the excitation antenna depth, allowed excellent microwave coupling into the gas discharge. The use of these two independent tuning adjustments provided a remarkable simple method to efficiently deliver power from the standard fifty ohm microwave transmission line into the nonlinear, dynamic plasma load.

The sensitivity in maintaining a microwave discharge at very low pressure (< 10 mTorr regime) with MPDR™ became an issue for the early plasma sources. Therefore, Dahimene and Asmussen [85] put multipolar permanent magnets directly around the quartz bell jar inside the microwave cavity. This provided Electron Cyclotron Resonance (ECR) heating to sustain a discharge at very low pressures. In addition, the multipolar magnetic field reduced the plasma diffusion to the discharge walls. The use of permanent magnets also saved space and electric power consumed by electromagnets. However, the magnets were directly

exposed to microwave radiation. This altered the electromagnetic field inside the cavity. Moreover the heating from the plasma and the electromagnetic fields might degrade the magnets. Later, Dahimene and Asmussen [85, 86] improved the ion source by relocating magnets outside the microwave excitation region in a water cooled channel. At that time, the basic structure of MPDR™ (see Figure 3.1(b)) was established.

3.2 The Standard Structure of Microwave Plasma Processing System

As mentioned in the Section 2.2, a MPDR™ system consists of four basic subsystems: a microwave power supply, oscillator protection and power monitoring circuits, microwave plasma reactor and the vacuum system. Each of these different subsystems used in the research performed in this thesis are described in some detail in the sections below.

3.2.1 Microwave power supply

In United States, the Federal Communications Commission (FCC) [87] authorizes particular frequency channels for different electromagnetic field applications. This frequency planning and spectrum allocation are carefully made so that interference between the different uses of the electromagnetic energy spectrum are minimized. Several frequency allocations are available for high power commercial heating applications. In the microwave frequency range (300

MHz to 30 GHz), 915 MHz and 2.45 GHz are the most commonly used frequencies while 13.56 MHz and 27.1 MHz are widely used for commercial heating Radio Frequency (rf, from several MHz to 300 MHz) band energy.

The role of the microwave power supply is the most often ignored factor in the application of a microwave plasma machine. The microwave power supply is not just an ON/OFF switch for the discharge. Instead it plays an important role in critical plasma processing. For example, plasma ignition, stability and repeatability depend on the quality of the microwave power supply. There are many power supply selections in the current market and how to select one depends on the application and economical budget. Adishian et al. [88] proposed four performance specifications for radio frequency power supplies. With slight modifications, the commonly used criteria for selecting a quality microwave power supply are described below.

3.2.1.A Power margin

The power margin is defined as the power output capability which exceeds rated power limit. It influences the machine uptime and availability. Of course, the higher the power margin, the better the power supply. But the cost should also be taken into consideration. Severe tube damage results from the long term use at or close to rated power. Usually, a 15% "head room" in power margin is appropriate for general application.

3.2.1.B Power regulation

The power regulation of the power supply controls output power accuracy so that the operating microwave power level will not fluctuate during the

processing cycle. Power regulation affects the repeatability and the consistency of the plasma process. One can express the regulation as a percentage deviation from the set power. Another important parameter of power regulation is how fast the set power is recovered after a power variation. Better electronic control loop design improves on the recovery rate factor. The allowable percentage deviation and recovery time are application dependent. Low ripple (< 1%) is the usual requirement for EM power regulation.

3.2.1.C Microwave cleanliness

Undesirable radiation of non-harmonic frequencies will affect plasma process repeatability. These include the 1/f noise and other spurious signals which can introduce error in real power measurement. The cleaner the output spectrum, the better the process reproducibility. For most applications, a 30 dB signal to noise ratio or greater is advised.

3.2.1.D Microwave frequency stability

Frequency stability and integrity is the ability to generate power output only at the operating frequency and suppress harmonics over a specific range of VSWR. Additionally, the output frequency should not drift over time. This frequency-shift problem is especially pronounced when operating with plasma loads which are frequency sensitive themselves. Most microwave discharge impedances are also frequency sensitive. For example, in ECR discharges, the ECR excitation or heating volume [34] moves spatially with any frequency movement. It was demonstrated in Ref. [89] that the frequency movement will broaden the ion energy distribution function. Moreover, the EM applicator may

have to be retuned back and forth to get a match for a unstable power supply. As a result, a more complex tuning strategy maybe needed for a frequency drifting power supply.

3.2.1.E Mismatch power output

When plasma changes during the process cycle (from the ignition state through processing state to shut down), the equivalent plasma impedance seen by the microwave power supply changes substantially. Occasionally, it may reach a rather large mismatch condition and a significant amount of power will be reflected back into the source, causing possible damage to the tube in the power supply. Also note that most microwave measurement circuit components are calibrated under low VSWR situations (<1.05) and their actual power values deviate from the nominal calibrated readings when they are poorly matched. The microwave circuit or the reading panel in the microwave power supply may not take this into account. Thus, as a rule of thumb, maintaining consistently low VSWR (<1.2) seen by the microwave source is vital for the accurate measurement of the actual power delivered into the reactor. Usually, a circulator is placed right at the output power port of a microwave power supply to ensure this task and redirect any reflected power into a dummy load. Some microwave power sources even have a circulator installed inside the power supply.

Most of the experiments described in this thesis were performed with a 2.45 GHz MicroNow power supply (420B1) with a rated output power of 500 W. Data from a HP 851B spectrum analyzer showed that all harmonic signals were at least 40 dB below the fundamental one. However, several spurious signals also

appeared in the spectrum at approximate locations of 2.603 GHz, 2.678 GHz, 5.122 GHz, etc. Fortunately, they are all at least 22 dB below the 2.45 GHz signal. Occasionally, a low ripple (< 1%), 3 kW, 2.45 GHz Gerling Laboratories (GL119) power supply was also used for high power operation.

3.2.2 Microwave power transmission system with oscillator protection and power monitor circuits

The microwave transmission system is the physical medium that carries microwave energy from one place to another with minimal loss. It usually involves either coaxial cables or waveguides, with appropriate connectors. For low power (less than ~900 W) applications, a low loss coaxial cable is a convenient way to transfer power into the reactor. At higher power, the current density at the inner conductor becomes too high and heats up resulting in damage to the material that fills the space between the coaxial cable conductors. Therefore, waveguides are preferred in higher power applications. Note that the longer the transmission line system, the larger the microwave loss. Therefore, the transmission section should be as **short** as possible. Some commercial systems mount the microwave power source next to HDP reactor to achieve efficient use of microwave power.

Connecting a cable or waveguide between a microwave power supply and a reactor is the simplest transmission line system required to deliver power to the discharge. However, other considerations prevent this simple method from actual use. One of them comes from the need to protect the magnetron located inside the microwave power supply from large reflected powers that may occur in the

operation of the plasma machines. Inserting one or more circulators and dummy loads can protect the magnetron from reflected power. Also note that some microwave power supplies do not provide an output power reading (e.g. MicroNow power supply "420B1") or the power panel reading is not accurate (e.g. Cheung Lab. source MPS 2450-1200). Hence, the installation of directional couplers for accurate power measurement is another item that is often added to the microwave transmission system. The two microwave power monitoring circuits that were used for the experiments performed for the research in this thesis are described below.

3.2.2.A Traditional microwave power monitoring circuit

Figure 3.2 (a) shows the traditional microwave circuit used by Hopwood [53] and Salbert 90. The output of the microwave source is first attached to a rated 500 Watt, coaxial three-port circulator (1). The function of this circulator is two-fold. First, it isolates the power supply from the large changes in the plasma load impedance. Thus, it provides better microwave frequency and power stability. Secondly, it also directs most of the reflected power into a 500 Watt capacity, 50 ohm dummy-load (7). Hence, it protects the magnetron from the influence of dramatic changes in the load impedance and prevents the reflected power from being absorbed by the magnetron.

To monitor the incident power and reflected power at the reactor entrance (s = 0 plane), a rated 500 Watt, nominally 20 dB dual directional coupler (2) is connected between the circulator (1) and a microwave cable (6). Each directional coupler coupling port is attached to a fixed attenuator (3) followed by a HP 478A

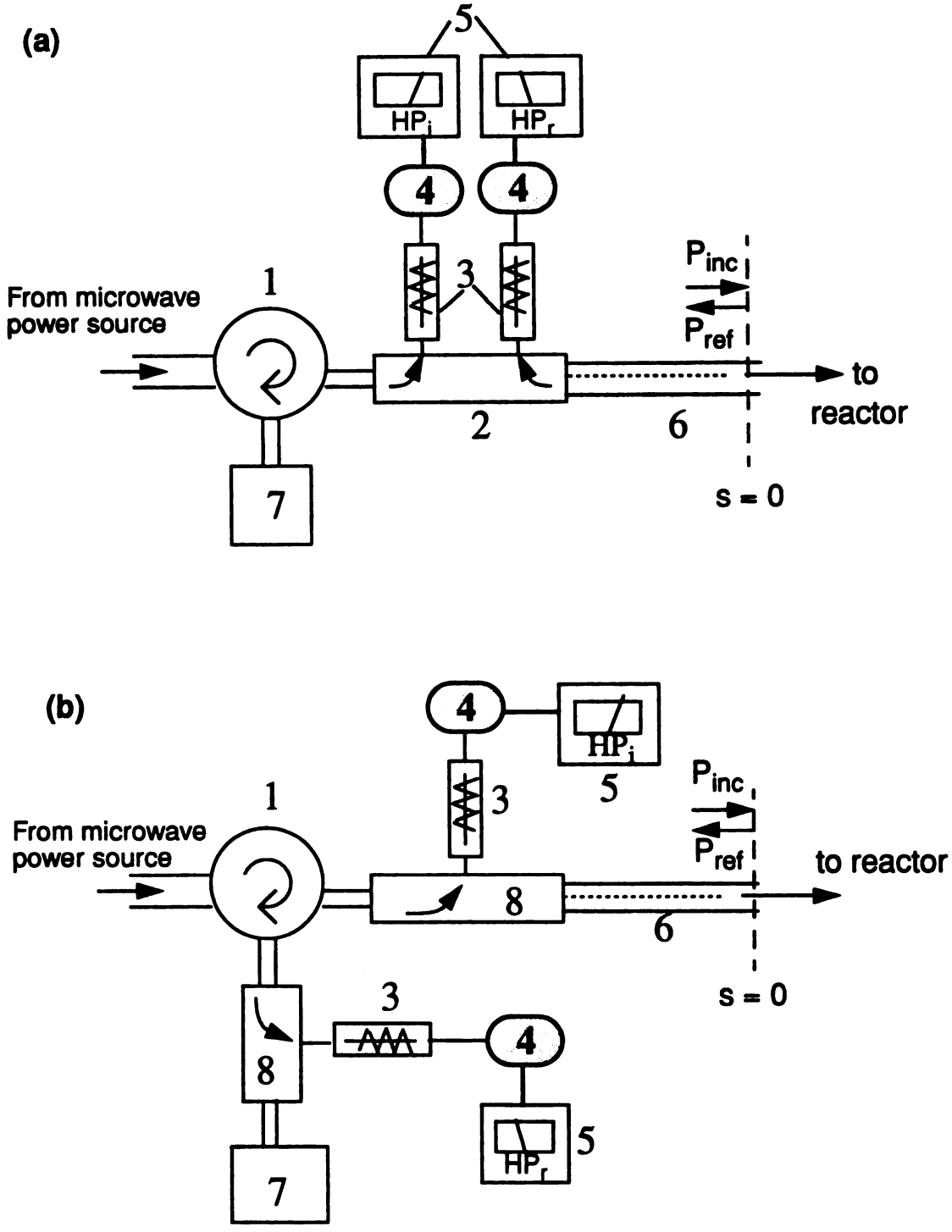

Figure 3.2 (a) Traditional, and (b) alternate oscillator protection and power monitoring circuit.

power sensor thermistor (4) and then a HP 435A power meter (5).The presence of attenuators provides protection for the delicate power sensors. Finally, a 6-foot long, 500 Watt capacity coaxial cable (6), is connected between the output of directional coupler and the entrance of reactor. Each circuit element is carefully calibrated by using power meters and a HP-8753 network analyzer operating at 2.45 GHz. The calibrated incident and reflected coupling factor of the dual coupler at 2.45 GHz are 20.9 dB and 20.7 dB respectively. And, the insertion loss of the dual directional coupler (excluding coupling power) is ~0.2 dB. Also the calibrated attenuation factors for the incident and reflected arm attenuators are 21.4 dB and 19.5 dB respectively. The calibrated cable (6) insertion loss at 2.45 GHz is 0.88 dB. That is to say about 18% of the incident power is consumed as heat in this cable.Therefore the actual power that is delivered into the reactor entrance can be traced back and hence calibrated. Finally, combining all the individual calibrated factors, the relationship between the actual power P_{inc} delivered to (or reflected power P_{ref} from) the reactor and the power readings HP_i (or HP_r) at power meters can be obtained, i.e.

$$P_{inc} = HP_i \times 10^{\left(\frac{20.9 - 0.2 - 0.88 + 21.4}{10}\right)}. \qquad (3.1)$$

That is P_{inc} ~ 13243 x HP_i. Similarly, in the reflected case,

$$P_{ref} = HP_r \times 10^{\left(\frac{20.7 + 0.88 + 19.5}{10}\right)}. \qquad (3.2)$$

And P_{ref} ~ 12823 x HP_r. This set up works fine whenever the plasma load is well-behaved (namely, less than 30% power reflected). When large amounts of

reflected power are present, accurate power measurements using this setup can not be obtained.

3.2.2.B Alternate microwave transmission set up

If the plasma discharge changes dramatically, its load impedance also changes and the above formulas (i.e. eqs. (3.1) and (3.2)) will not provide the accurate readings. This is due to the limited directivity and isolation characteristics of the dual directional couplers. For example, significant incident power may leak into the reflected power circuit and either add to or subtract from the HP_r power measurement. In some extreme mis-match cases, the ridiculous result that P_{inc} is less than P_{ref} was observed. Thus, an improved microwave circuit configuration must be employed for medium to high VSWR situations.

Figure 3.2 (b) shows another circuit configuration with similar oscillator protection and power monitoring functions. Instead of using one, single dual directional coupler (2), two single directional couplers (8) are placed at different ports of the circulator. Then, the reflected power measured is not influenced by mismatch power because of the isolation by circulator. However, the inherent finite directivity of directional coupler at the incident side still can result in small measurement errors. Under large mismatch conditions, some reflected power may leak into the HP_i side. This may lead to a slight overestimate/underestimate of incident power.

After a careful power calibration and using similar formulas with different power calibration, the new conversion formulas for this system are

$$P_{inc} \equiv (92{,}470 \times HP_i) \text{ and } P_{ref} \equiv (14{,}420 \times HP_r). \quad (3.3)$$

Note that for the most accurate measurements and the best power monitoring circuit performance, the couplers should be placed as **close** as possible to the reactor entrance, "at the plane s = 0". However, due to the mechanical convenience, the above two configurations with the long cable (6) located as shown in Figure 3.2 were used in the experiments presented in this thesis.

3.2.3 MPDR™-13 reactor

A typical plasma processing reactor has several basic components: an impedance matching network, a microwave field applicator, a plasma excitation region, a process chamber and the substrate. Static magnetic field allocation is another important component for ECR reactor. There are many different ways to combine these components. The subsections below described how these components are combined for the MPDR™-13 reactor used in this experimental study. A cross sectional view of this reactor is shown in Figure 3.3.

A cylindrical coordinate system is used throughout this thesis in which positive z will represent the distance below the bottom of ECR magnets, r is the radial distance from the center axis of the plasma and processing chamber, and Φ is the angle relative to the microwave input coupling probe (4) (also called excitation antenna) when side-feed configuration is used.

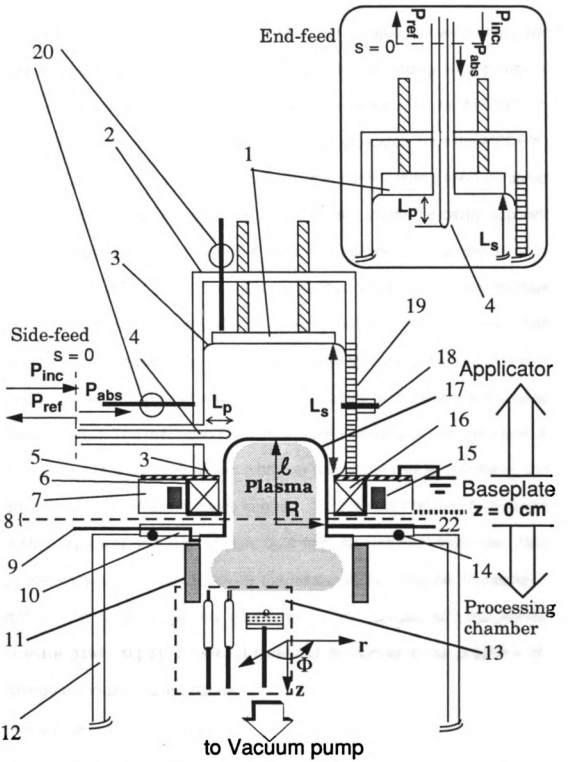

Figure 3.3 Cross sectional view of side-feed MPDR reactor with processing chamber. The insert shows the end-feed excitation method. Increasing numbers are in the counter clockwise direction.

3.2.3.A Impedance matching network

Often impedance matching networks are located between the power supply and the reactor. These include triple stub tuners, sliding short plunger or other variations of tuners that are exterior to the reactor. In the MPDR™, the impedance matching network is embedded in the applicator. Thus the MPDR™ is often called an internal tuned cavity. An adjustment of the sliding short (1) selects the electromagnetic resonance mode that is excited inside the cavity applicator while the adjustable excitation probe (4) mainly alters the impedance of the plasma loaded cavity. Their slick sliding abilities while maintaining excellent electrical contact with the cavity shell (2) are ensured by CF300-type silver plated finger stock (3). Two dial indicators (20) were used to monitor the positions of the sliding short height (L_s) relative to the bottom surface of the cavity and insertion probe depth (L_p). The resolution of the indicators is about 0.01 mm. However, the actual reading is accurate to within 0.05 mm due to the play in the sliding short gearing. The mechanical adjustable ranges (L_s, L_p) are (69-190 mm, 0-40 mm) for end feed applicator and (69-165 mm, 0-28 mm) for side-feed applicator. These two independent adjustments provide the necessary two degrees of freedom to match a wide range of plasma loaded cavity impedances with the standard microwave power supply. Additional details of the tuning in the presence of a discharge are described in Chapter 7.

3.2.3.B Cavity applicator

The microwave applicator focuses EM energy into the plasma discharge. It consists of a cylindrical EM resonator (2) (see Figure 3.3), tuning elements

(sliding short (1) and probe (4)) and a dome shaped quartz window (17). Microwave power is coupled into the plasma either by electromagnetic Ohmic heating or collisionless heating such as ECR and stochastic heating. The cylindrical cavity applicator (2) is tunable via a sliding short (1) position L_s, and movable antenna probe (4) position L_p.

Traditionally, microwave energy is introduced into MPDR™ by placing the coaxial coupling port in the cavity side wall. This configuration is called a **side-feed** reactor (Figure 3.3). The evanescent, near-field of the probe is also present in the vicinity of the probe. Thus, the non-symmetric electromagnetic (EM) excitation of the probe often occurs [90] due to the unbalance of the EM near field existing around the probe and hence this excitation unbalance may also exist within the discharge volume. This situation becomes more pronounced with high input powers or with a deep insertion of the coupling probe. Moreover, the side-feed excitation readily couples to a dipole, circumferential EM pattern excitation due to preferable excitation of TE modes. However, by careful positioning of the probe, Φ symmetric excitation also occurs. Unfortunately, for very high power excitation (> 500W) of a microwave discharge, it is difficult to excite purely Φ symmetric modes in the side-feed configuration.

One way to solve this problem is to put the coupling structure at a symmetric location. The **end-feed** cavity (see picture insert in Figure 3.3) is another cavity coupling method that more readily produces a Φ symmetric discharge excitation. The name "end-feed cavity" indicates that microwave energy is introduced through the center of sliding short at the top end of the cavity. Note

that the coupling structure moves along with the sliding short and higher order modes with two or three half wavelengths along the z-direction can be selected. This separates the probe near field from the discharge volume. Also, the end-feed readily excites symmetrical circumferential TM electromagnetic modes (see Chapters 7 & 9).

A set of 2.2 mm diameter through holes (19) are drilled around the cavity wall. Therefore, mode verification can be carried out via the small microwave power sampled by a micro-coaxial probe (18). The 17.78 cm i.d. brass (or aluminum) cavity resonator is terminated on the top by an adjustable sliding short, and on the bottom by the plasma discharge and the brass plate (5).

3.2.3.C Baseplate (ECR version) and plasma excitation chamber

Below the brass plate (5) shown in Figure 3.3 is a light-weight aluminum-stainless steel baseplate (7). This baseplate has five functions: 1) provides accommodation for the source of the static magnetic field, 2) has a number of optical access ports for plasma diagnostics, 3) allows working gases to flow through passages inside the plasma chamber, 4) delivers the cooling gas to the plasma quartz chamber, and 5) connects the microwave applicator with the processing chamber.

As shown in Figures 3.3 and 3.4, the baseplate houses a number of equally spaced strong permanent magnets (16) which are cooled by the water channel (15) running around them. Low carbon steel keepers (6) confine the

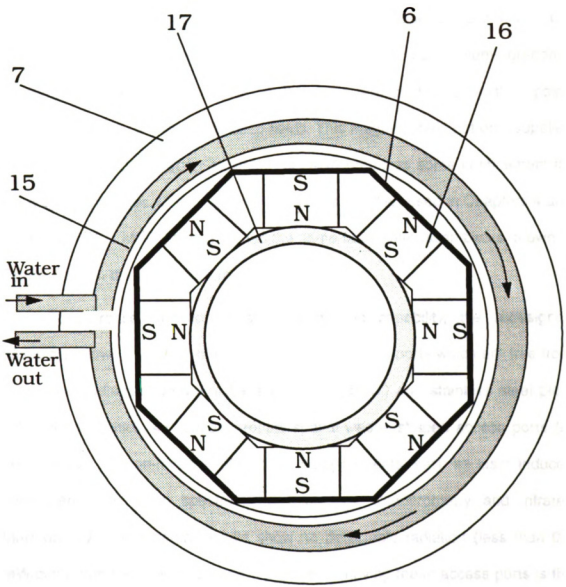

Figure 3.4 Cross sectional view of MPDR reactor in Figure 3.3 at z = -1.27 cm (center plane of magnets) with standard 8 pole/8 magnet multipolar ECR magnet configuration.

magnetic field to the discharge excitation region, so that only minimal magnetic field is present downstream in the processing chamber. The bottom plane of ECR magnets is defined as z = 0 as shown in Figure 3.3. Figure 3.4 displays a cross sectional view of the baseplate with permanent magnet assembly at z = -1.27 cm (center plane of the magnet). Eight 5.08 x 2.54 x 2.5 cm neodymium-iron-boron permanent magnets (16) are used in this ECR reactor. Moreover, their poles alternate and form the magnetic cusp fields. This magnetic field not only supplies the necessary ECR layer for excitation but also produces some confinement for the charged particles. Other ECR configurations are discussed in Chapters 4 and 6. The non ECR MPDR™ version has the same baseplate assembly as shown in Figure 3.3 with the permanent magnets removed.

To increase the non invasive diagnostic capability, the redesigned baseplate allows a number of optical diagnostic access ports which are free from microwave radiation. Between the aluminum plate (7) and stainless steel plate (10), four 1/4" thick, 45° circumferential spatial wedge-shaped access ports (8) are available for non-invasive diagnostic measurements, such as laser induced fluorescence, emission spectroscopy, microwave interferometry and infrared thermometry. Experimental results show no detectable radiation (less than 0.2 mW/cm^2) from these access ports.The price for having these access ports is the increase of the overall baseplate thickness. The quartz dome is about half inch longer than necessary and thus it provides additional recombination sites for charged and radical species. Therefore, this particular fully optical accessible

prototype ECR plasma source may not be the optimal design for process applications.

At the bottom of the baseplate, a 304 stainless steel plate (10) houses a gas feed vacuum channel (9). Pre-mixed input gases are introduced into discharge excitation region through eight equally spaced pin holes at the end of the vacuum channel (9). The baseplate is then vacuum sealed by a viton O-ring (14) far away (~19.5 cm diameter) from the discharge. This arrangement avoids the direct contact between plasma and O-ring. Hence, the reactor can survive in high microwave power operation. This also reduces contamination for processing. Furthermore, under high power operation, compressed air flows through another gas channel (22) to reach a ring consisting of eight equally spaced outlet holes and to cool the outer surface of the discharge chamber bell jar evenly.

Using the same 17.78 cm diameter microwave cylindrical cavity as was used in the earlier designs [53], the plasma excitation chamber diameter was enlarged from 9 cm to 12.5 cm. Later, diamond deposition systems used a similar discharge chamber and baseplate design [91]. In order to reduce plasma contamination from material sputtered from the metal walls, a 4.6 mm thick quartz bell jar (17) which has a dome shape on the top and a cylinder-shape on the side surrounded the 12.5-cm i.d. plasma discharge. The plasma excitation region or discharge volume V_d is defined as the discharge inside the quartz bell jar with the bottom bounded by z ~ 3 cm plane. It has the approximate dimension of radius **R** (6.2 cm) and height ℓ (~ 8 cm). This design was the first in the lab to confine the plasma excitation region completely by quartz material. The ions and electrons do

not "feel" the effects of the electrically grounded baseplate until they flow into the processing chamber.

Finally, the MPDR™ source is a very versatile machine. Carefully designed ion-extraction optics (not shown in the figure) can be attached to the exit of plasma excitation region to serve as a broad-beam ion source [52]. Highly stripped ions from ECR ion sources are important to basic science research for nuclear physics in cyclotron laboratories. For those applications, the exit of plasma excitation region usually involves design of very fine grids with precise alignment. Treatment of this type of application is not given here. Interested readers can consult reference [92].

3.2.3.D Processing chamber

Figure 3.5 displays the entire experimental vacuum system. Underneath the baseplate, the discharge can freely diffuse into a 55.3 cm height, 40.6 cm i.d., 0.32 cm thick cylindrical stainless steel (type 304) processing chamber (5), with Dovetail Seal™ on both ends, so that the O-rings stay in the groove. In order to reduce the hiding places for water and contamination, the inner surface of processing chamber has an electro-polishing pre-treatment. Four 3" dia. windows (6) on 6" Conflat® are on the walls of the processing chamber (5), located around the z ~ 15 cm plane and 90° apart. They are mainly used for optical access ports and to visually look at the plasma. One of them ($\Phi = 90^{o}$) is made of very high quality quartz to enable laser beam access with little attenuation.

Below these 3" windows at the z ~ 39 cm plane, there are two 6" dia. access doors (7) on 10" Conflat® and three 2-3/4" standard Conflat® ports (8).

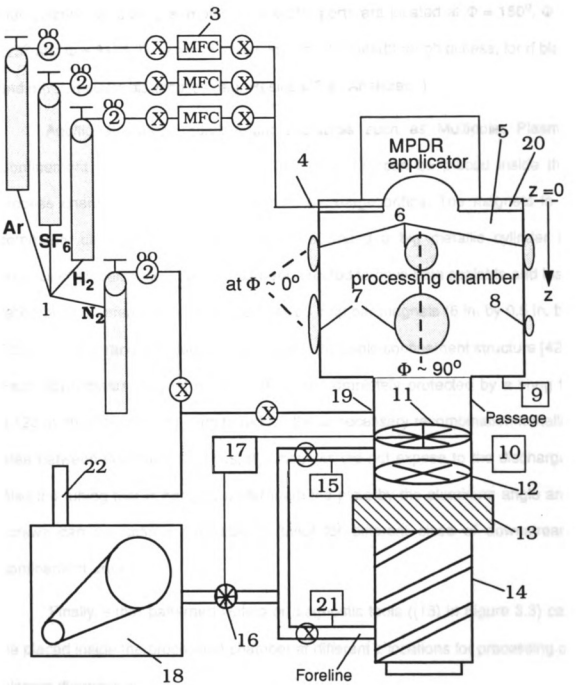

Figure 3.5 Gas flow and vacuum system of MPDR-13 plasma system

The 6" dia. doors are 90^0 apart ($\Phi = 0^0$ & $\Phi = 90^0$) and are used for vacuum manipulation or loading samples. The 2-3/4" ports are located at $\Phi = 180^0$, $\Phi = 225^0$ and $\Phi = 315^0$. They are available for electrical feedthrough access, for rf bias and other vacuum diagnostics (e.g. Residual Gas Analyzer...).

Additional plasma confinement structures such as Multipolar Plasma Confinement Structure (MPCS), (11) in Figure 3.6, can be placed inside the process chamber right below the plasma discharge orifice. The magnets in a commonly used MPCS structure [54,57] surround a big metallic cylinder in process chamber. A new design has been created to have both scalable and less recombination area functions. Eight AlNiCo5 long bar magnets (6 in. by 0.5 in. by 0.5 in.) were arranged to form a downstream multipole confinement structure [42]. Each downstream magnet is separately and completely protected by a snug fit 0.125 in. thick aluminum tubing to reduce the unnecessary recombination metallic area between the magnets. Thus, the magnets did not expose to the discharge. Also the tubing that is hanging underneath the plate by the aluminum angle and screws can be radially moveable to tailor for different sizes of downstream confinement area.

Finally, either patterned wafers or diagnostic tools ((13) in Figure 3.3) can be placed inside the processing chamber at different z locations for processing or plasma diagnostics.

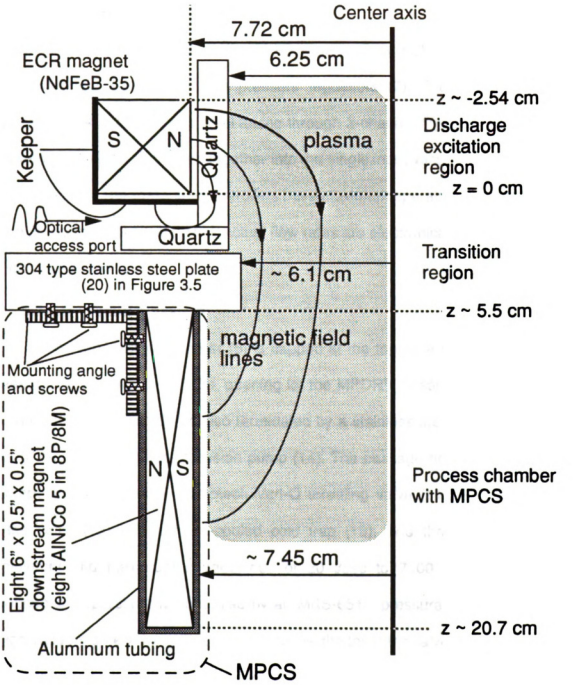

Figure 3.6 Schematic view of MPCS in MPDR-13 relative to ECR magnets.

3.2.4 Gas flow and vacuum system

3.2.4.A Gas flow

As shown in Figure 3.5, high purity (99.99%) gas cylinders (1) are first connected to appropriate Matheson model pressure regulators (2). Then the gases are guided by 1/4" o.d. stainless steel tubing through 3-channel (Tylan FC-280) mass flow controllers (3) and mixed together into the single input vacuum channel (4) of the baseplate. The mass flow controllers have maximum operating flows of 10, 20, and 50 sccm respectively. Their actual flow rates are electronically controlled by a Tylan RO-28 readout.

3.2.4.B Vacuum system

The processing chamber (5) is capped at the top by a ~1" thick stainless steel plate (20) with a ~10" dia. opening for the MPDR™ baseplate to sit on. The lower end of the chamber is also terminated by a stainless steel plate which has an 8" dia. passage to the diffusion pump (14). The passage hosts three vacuum components: an Alcatel Comptech Vari-Q throttling valve (11), a high vacuum gate valve (12) and a freon-cooled cold trap (13). The throttle valve has a minimum and maximum conductance of 20 l/sec to 7000 l/sec. The actual conductance/pressure is controlled by an MKS-651C pressure controller (17). A high vacuum gate valve (12) is installed below the throttling valve to further control the pressure manually. A freon-cooled cold trap (13) is placed between the diffusion pump (14) and the gate valve (12) to minimize the backstreaming of oil vapor. The diffusion pump is filled with inert fluid (e.g. Fomblim perfluoro polyehter PFPE 25/9, Krytox hydrocarbon-free oil 1615 or Santovac 5...) and thus is capable

of pumping reactive gases. The diffusion pump has a capability of 1250 liter/sec and is backed by an Alcatel 2033C, 11 liter/sec mechanical pump (18). An MKS-253A exhaust throttling valve (16), which is controlled by the same MKS-651C pressure controller (17), is installed at the front side of roughing pump. Its controllable conductance range is between 0.7 liter/sec and 300 liter/sec. The purpose of this throttle valve is to achieve a stable medium pressure, i.e. of the order of hundred m Torr or above, in the processing chamber when the diffusion pump is not in use.

For safety reasons, the exhaust (22) of mechanical pump is purged with dry nitrogen whenever the vacuum system is operating with dangerous gases (H_2, CH_4...). For chamber cleanliness, the same dry nitrogen is also used for venting (19) the chamber system.

3.2.4.C Vacuum measurement

Absolute pressure measurement at various locations within the vacuum system is performed by different gauges. Two thermocouple vacuum gauges (15 and 21) measure the pressure from several mTorr to 5 Torr. To monitor the approximate chamber pressure, one of these (15) is located near the passage that connects the mechanical pump directly to the process chamber. The other (21) is located at the foreline, which is the section between mechanical and diffusion pump.

For accurate chamber pressure measurement, a capacitance diaphragm (9) is installed at the bottom end of the processing chamber. This MKS-390 absolute pressure transducer, combined with MKS-270B signal conditioner, can

accurately measure pressures from 0.01 mTorr to 1 Torr. To calibrate the MKS-390, a hot filament BA-type gauge (10) is put near the passage to measure the base pressure, which is typically around 7.6×10^{-7} Torr. Whenever the readout on the MKS-290 ion gauge controller falls below 10^{-6} Torr for N_2 or Ar residual gas, the MKS-390 Baratron gauge is zeroed. The reading of the Baratron is the processing chamber pressure measurement presented in this thesis. This calibration procedure is performed whenever the chamber is previously exposed to atmosphere. Notice that re-calibration may be needed periodically (say 2 weeks) because the electronic readout will drift slightly over time.

Chapter 4

The System Reactor Variables

- 4.1 Introduction to the Plasma System Diagram
- 4.2 Independently Controlled Input Variables (**U**)
  - 4.2.1 Macroscopic controllable input variables ($\mathbf{U_1}$)
  - 4.2.2 Reactor geometry variables ($\mathbf{U_2}$)
- 4.3 Internal Dependent Variables (**X**)
- 4.4 Output Variables --- Reactor Figures of Merit ($\mathbf{Y_1}$)
  - 4.4.1 Power coupling efficiency Eff_{coup}
  - 4.4.2 Ion production cost η_{ion}
- 4.5 Summary

Chapter 4

The System Reactor Variables

4.1 Introduction to the Plasma System Diagram

Every plasma reactor consists of a nonlinear discharge which is a complex function of many experimental variables. Figure 4.1 displays the generic block diagram for a plasma reactor where the variables are arranged into three categories. Also the diagram schematically represents the nonlinear relationships between these three variable vectors, (1) the input variable vector (**U**), (2) internal variable vector (**X**), and (3) output variable vector (**Y**). The input variables are defined as the variables which can be independently controlled by a reactor operator or designer. The input variable vector **U** can be divided into four input sub-vectors; i.e. $\mathbf{U} = [\mathbf{U}_1, \mathbf{U}_2, \mathbf{U}_3, \mathbf{U}_4]$, where $\mathbf{U}_1$ consists of the controllable input variables (such as operating pressure, gas flow rate, etc.), $\mathbf{U}_2$ variables are concerned with the reactor geometry variables (size of applicator and discharge excitation, etc.), $\mathbf{U}_3$ includes the variables concerned with processing procedure (the process timing, etc.), and $\mathbf{U}_4$ includes the independent substrate variables (substrate preparation, etc.). The internal plasma variable vector (**X**) contains important internal plasma reactor states such as plasma potential, plasma

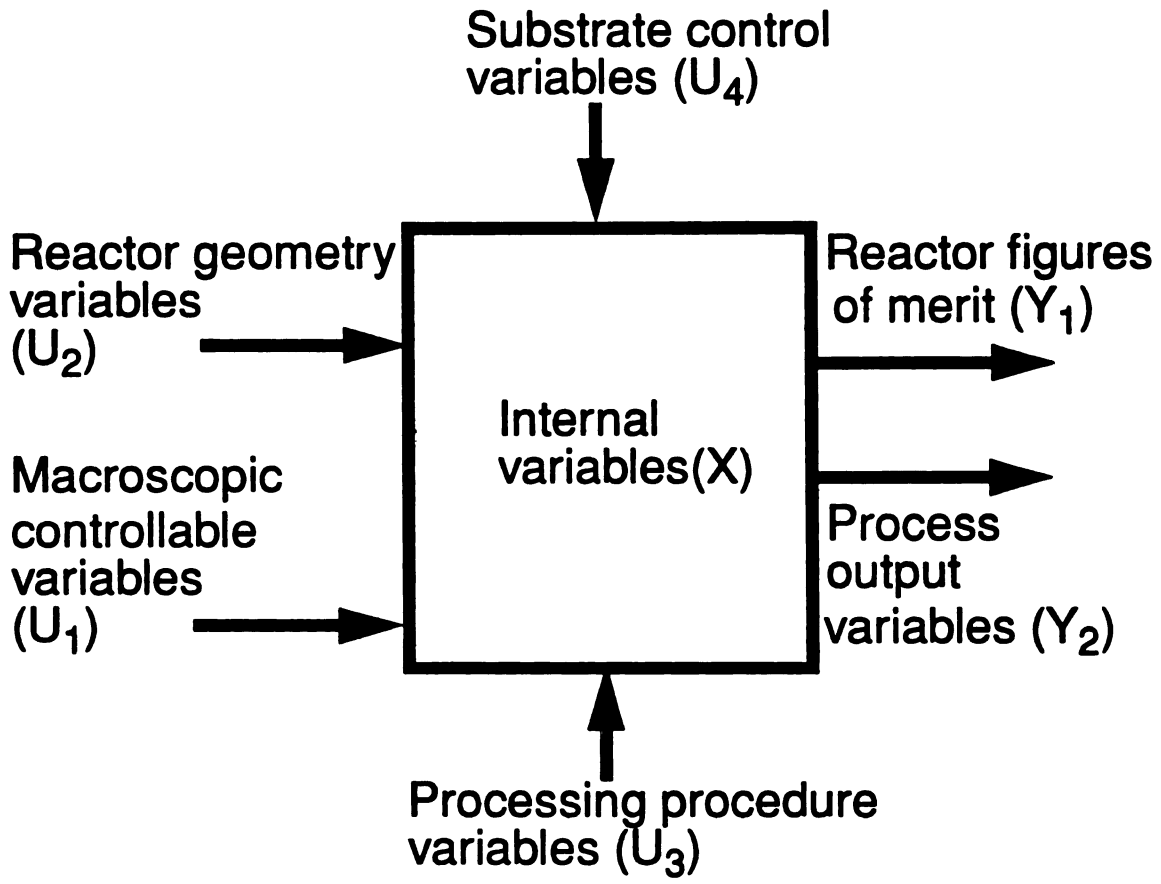

In general:

$X = f(U)$, $Y = h(X)$ and$Y = g(U)$;

where U is the input variables consisting of four groups

(i) U_1 = Macroscopic controllable input variables = $(u_1, u_2..., u_i)$;

(ii) U_2 = Reactor geometry variables = $(u_{i+1}, u_{i+2},..., u_k)$;

(iii) U_3 = Variables regarding processing procedure = $(u_{k+1}, u_{k+2},..., u_q)$;

(iv) U_4 = Substrate control variables = $(u_{q+1}, u_{q+2},..., u_r)$;

X = internal variables =$(x_1, x_2, x_3,..., x_n)$;

Y = output variables = (Y_1, Y_2);

where $Y_1 = (y_1, y_2, y_3,..., y_m)$;

$Y_2 = (y_n, y_o, y_p,..., y_s)$.

Figure 4.1 Generic plasma reactor system block diagram.

density, ion energy distribution function, etc. The output variable vector (**Y**) can be divided into two sub-vectors; i.e. $\mathbf{Y} = [\mathbf{Y_1}, \mathbf{Y_2}]$, where $\mathbf{Y_1}$ consists of all the plasma source figures of merit, and $\mathbf{Y_2}$ includes all the parameters related to the desired process outputs such as the processing rate and process uniformity, film properties, etc. As an example, Figure 4.2 shows a typical plasma reactor with appropriate variables identified for a typical semiconductor etching process application.

In order to understand the behavior of a plasma reactor, not only must the relationships between the reactor input variables and the output variables be understood, but also the relationships must also be established between the reactor internal variables and both the input and output variables. The internal variable vector is a complicated function ($\mathbf{X}=f(\mathbf{U})$) of the input variable vector. The output variable vector is a complex function of both the internal variable vector ($\mathbf{Y}=h(\mathbf{X})$) and the input variable vector ($\mathbf{Y}=g(\mathbf{U})$). Considering a typical reactor, each variable vector, **U, X, Y,** contains many variables. A comprehensive theory that describes the relationships between these variables does not exist, and particularly for microwave plasma reactors, the relationships between these variables are poorly understood. However, knowledge of these complex relationships is essential for improved reactor design and ultimately reactor control. Thus this thesis describes an experimental study which attempts to determine the relationships between selected combinations of several input variables, internal and output variables of a 12.5 cm MPDR™ discharge source. The selected variables are macroscopic controllable variables ($\mathbf{U_1}$), reactor

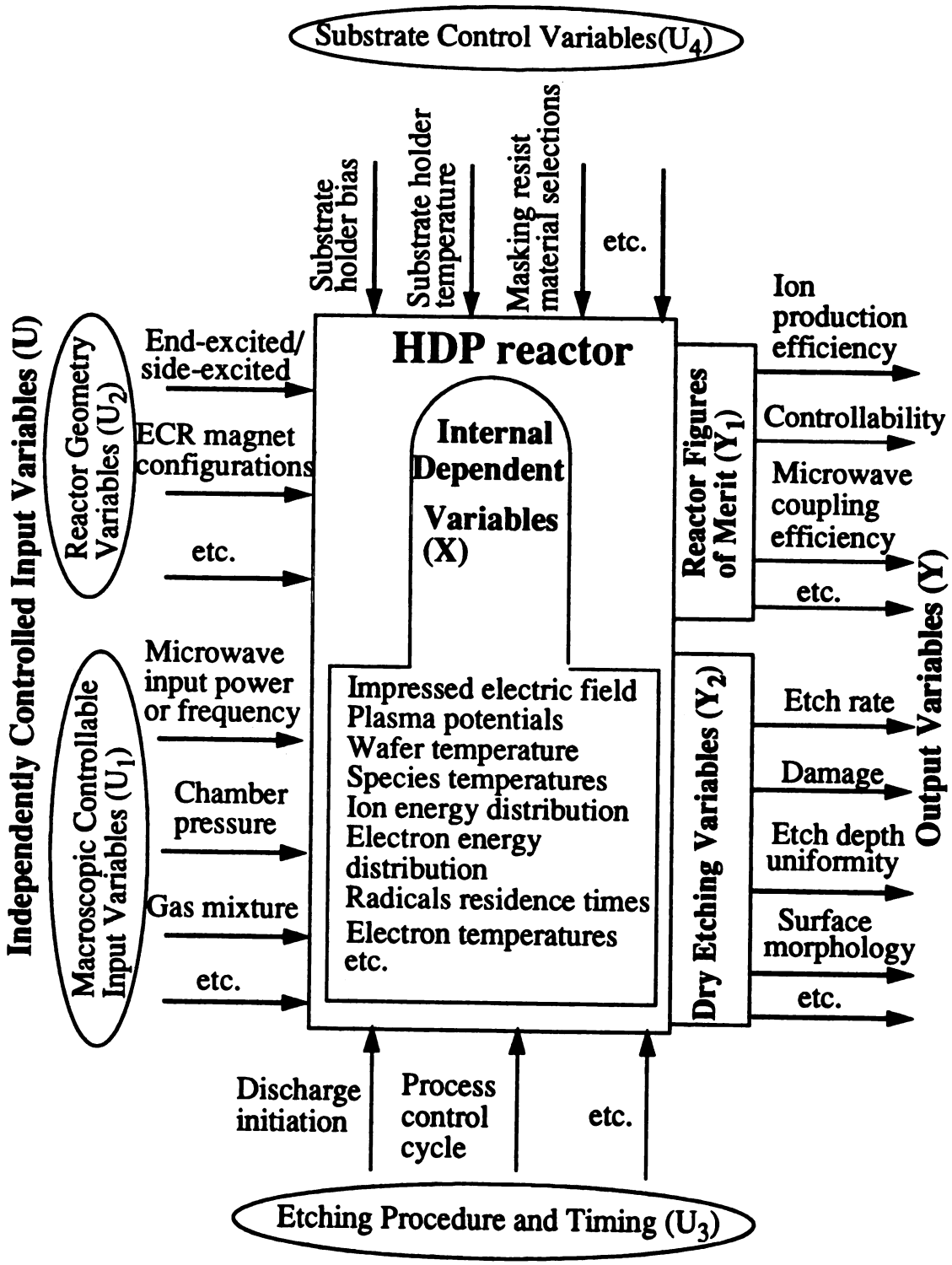

Figure 4.2 System variables of a HDP Reactor for a plasma etching application.

geometry variables (U_2), internal variables (**X**) and reactor figures of merit (Y_1). Their descriptions and varying ranges are presented in the next few sections. Their experimental relationships (**X**=f(**U**), **Y**=h(**X**) & **Y**=g(**U**)) are described in later Chapters 6, 7 and 9. A few other variables may also appear in later chapters accompanied by their appropriate definitions.

4.2 Independently Controlled Input Variables (U)

4.2.1 Macroscopic controllable input variables (U_1)

Chamber pressure (or flow rate), microwave input power and impedance matching network positions are the three major controllable input variables changing in this thesis. They are relatively easy to vary during experiments.

4.2.1.A Operation chamber pressure (p) and flow rate (f_t)

The chamber operating pressure is controlled by the total input gas flow rate, pumping speed, and the position of the throttle/gate valve. Figure 4.3 displays the pressure versus argon flow rate in the system. For experiments below 2 mTorr, the pressure was usually controlled by the gas flow rate and these two variables are tied together as a single variable. For pressure above 2 mTorr, either the gate valve or the throttle valve was varied to achieve the desired pressure. Most experiments have been conducted with pure argon as discharge gas. Occasionally, pure hydrogen gas discharge was also studied.

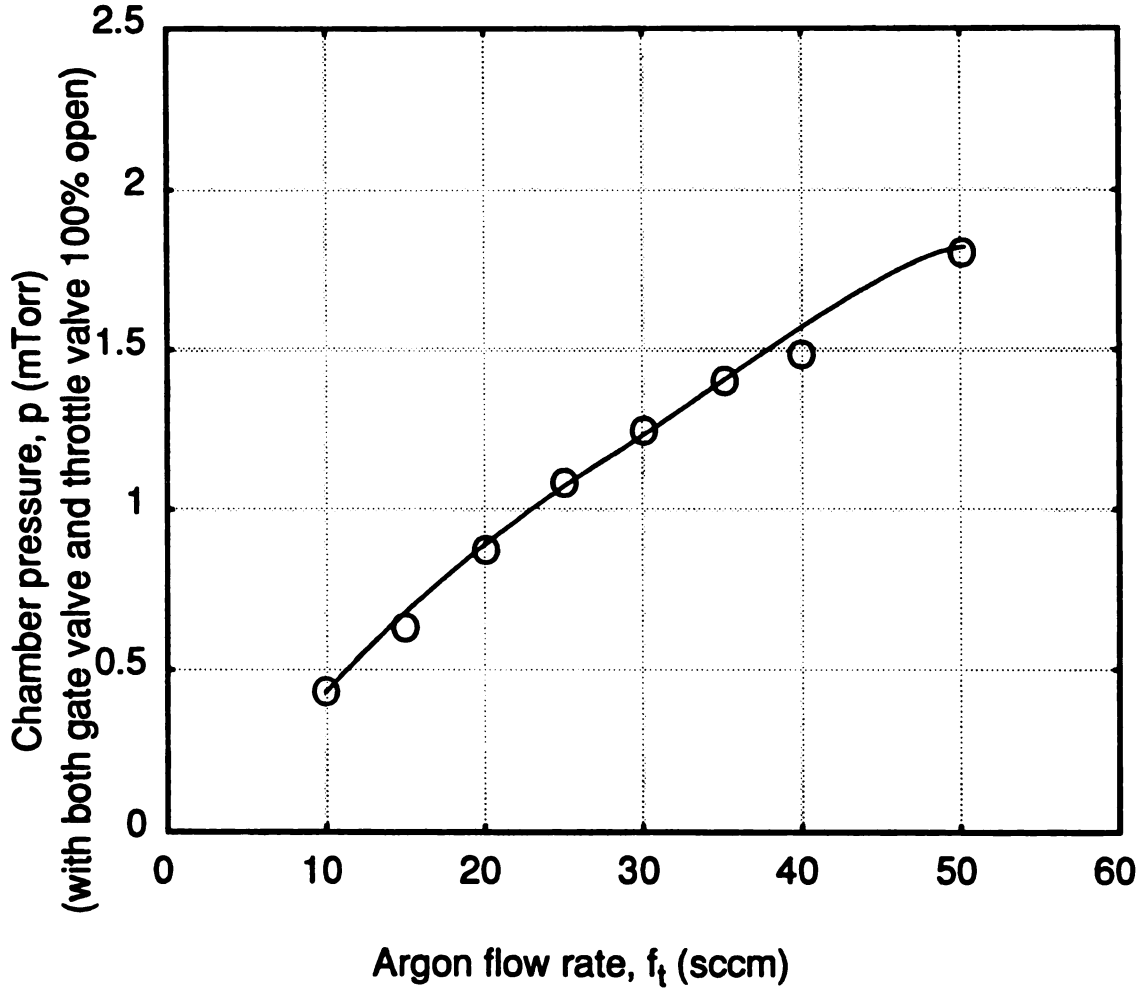

Figure 4.3 Chamber pressure vs. argon flow rate.

4.2.1.B Microwave input power level (P_{inc}), frequency (f), and waveform

The microwave input power and frequency are controlled by the turning knob/switch setting position on the microwave power supply. The accurate power absorbed by the reactor is measured at the power meters in the microwave power monitoring circuit described in Section 3.2.2. Input power ranges from 150 W to 800 W. The waveform of energy was fixed at 2.45 GHz (CW) for the experiments performed in this thesis.

4.2.1.C Impedance matching network positions

In the internally tunable cavity plasma source, the cavity height (L_s), which is adjusted by the sliding short, and the depth (L_p) of input coupling probe are the two elements that match the incoming power into plasma loaded applicator. Two different cavity shells were used for side feed and end feed applicators. For end feed applicator, the cavity height could be continuously varied from ~68 mm to 190 mm while the probe depth was continuously variable from 0 to 40 mm. The range of L_s for side feed is from ~69 mm to 165 mm. However, the L_p can only span from 0 to 28 mm due to the quartz bell jar.

4.2.2 Reactor geometry variables (U_2)

Changing geometry variables is usually difficult and costly. For example, it is not easy to run an experiment with a small applicator one day and then change to a larger cavity the next day without redesigning and changing the system components and the baseplate, etc. Therefore, only energy coupling locations,

ECR magnet configurations, and downstream confinement magnet configuration were varied in the experiments described in this thesis.

4.2.2.A Energy coupling locations, side feed or end feed

One vital variable is the coupling location in this MPDR™. Both side-feed and end-feed probe couplings were investigated. Both methods of excitation used the same coaxial coupler. That is they had identical input coaxial lines of inner diameter 3/8 in. and outer diameter 7/8 in. The side-feed probe was introduced at $\Phi = 0^0$ at a height of 44 mm from the bottom of the cavity while the end-feed probe was centered on the top end of the sliding short. The change from side-feed to end-feed allowed investigation of the differences between TE excited discharges and TM excited discharges. Moreover, the end-feed configuration was easier to perform both analytical analysis and numerical modeling of the reactor.

4.2.2.B ECR magnet configurations (4P/8M, 8P/8M, etc.)

Although the accommodation channel for ECR magnets is fixed, several ECR magnetic configurations, shown in Figure 4.4, could be obtained by either altering the relative magnetic pole directions or arranging different numbers of magnets around the accommodation. Empirical changes of the ECR magnet configuration provided interesting alteration of plasma characteristics without additional equipment investment. The permanent magnets were the NeFeB-35 type with a size of 5.08 cm x 2.54 cm x 2.5 cm.

4.2.2.C Downstream confinement magnets

Downstream confinement magnets, as mentioned in Section 3.2.3.D, can be placed into the processing chamber to improve the downstream plasma

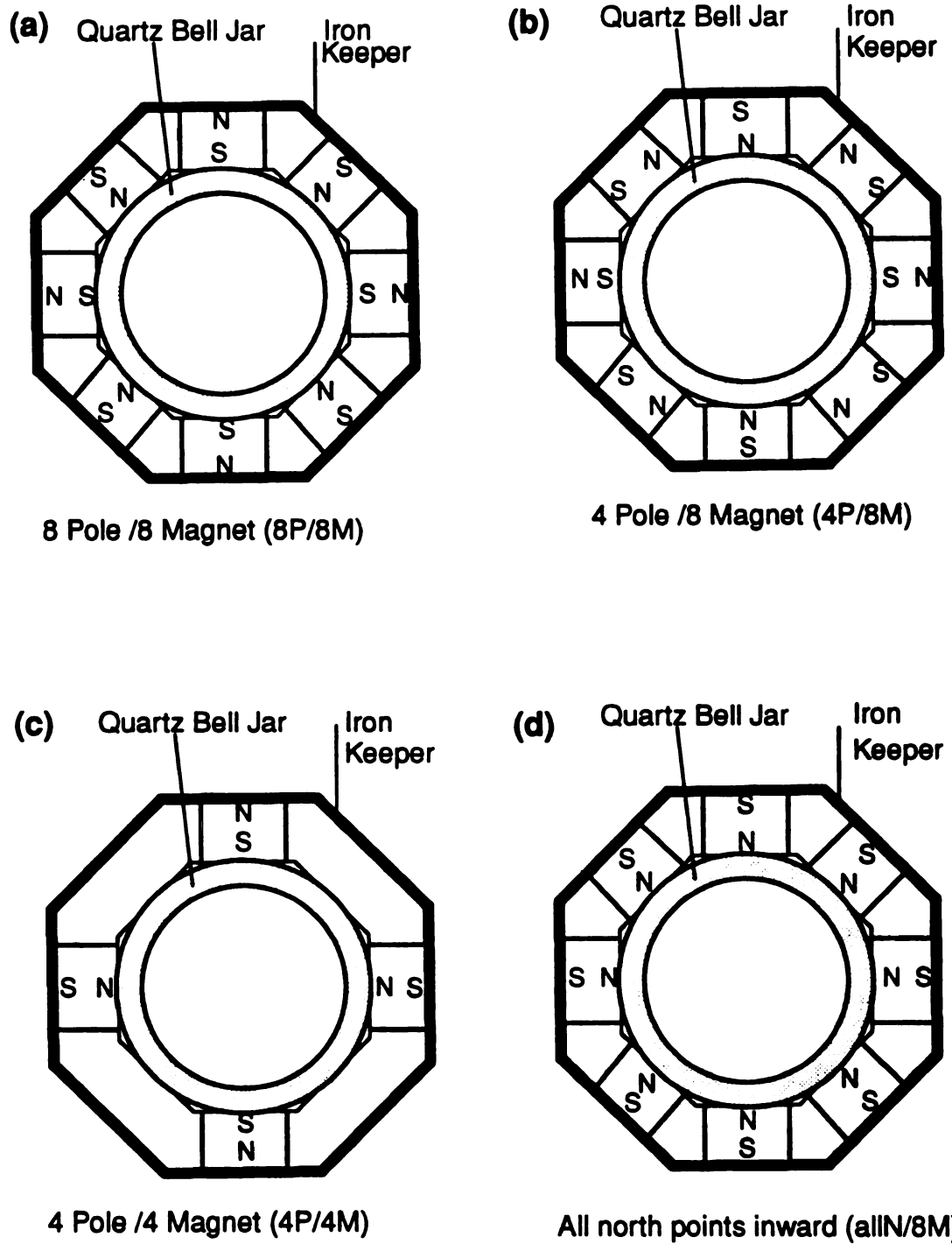

Figure 4.4 Cross sectional view (z = -1.27 cm) of four variations of ECR magnetic configurations (abbreviations are in parentheses).

uniformity. Similar to ECR magnet configurations, the permanent long bar shaped (6 in. x 0.5 in. x 0.5 in.) confinement magnets can have different magnetic configurations. Downstream magnets are usually configured in an 8P/8M multipolar fashion. This new MPCS design also allows user to readily vary the diameter of confinement region.

4.3 Internal Dependent Variables (X)

Internal variables provide the important bridge between input and output variables. They can roughly divided into three types, 1) the power related variables, 2) the electromagnetic field variables, and 3) various species spatial and energy populations inside the discharge.

The net power coupled into the reactor, i.e. total microwave power absorbed P_{abs}, is the power related variable in this thesis. P_{abs} is defined as the difference between incident and reflected power ($P_{abs} = P_{inc} - P_{ref}$). The discharge spatial average power density, $\langle P \rangle$, is defined as total microwave absorbed power P_{abs} divided by the discharge volume (V_d) in plasma chamber, i.e. $\langle P \rangle = P_{abs}/V_d$.

Electric field spatial patterns, field strength and plasma potential are the EM field variables measured in this research work. By inserting the micro-coax probe near the inside wall of the cavity, the electromagnetic mode pattern and the absolute field strength (E_r) near the cavity wall can be identified and measured. This measurement technique is described in detailed in Section 5.3. Hence, the impressed electric field that drives the plasma was estimated. On the other hand,

plasma potential (V_p) can be measured using the traditional single Langmuir probe methods described in Section 5.4.3.

Ion density (n_i) and uniformity, electron temperature, electron and ion energy distributions (EEDF & IEDF) are measured by various plasma diagnostics (described in Sections 5.4 and 5.5). Uniformity of charge density is simply defined as the derivation over the average in a cross section area.

4.4 Output Variables --- Reactor Figures of Merit (Y_1)

The reactor figures of merit usually consist of the EM power coupling efficiency and the ion production cost. Other variables such as ease of operation, cost of applicator ownership may be included. However, the criteria to judge those variables are closely related to personal preferences and are difficult to perform a fair comparison. The definitions of power coupling efficiency and ion production cost are given in the following subsections.

4.4.1 Power coupling efficiency Eff_{coup}

Figure 4.5 displays the various power paths in a plasma reactor system. Power coupling efficiency is a standard figure of merit used to evaluate the power transfer efficiency of a specific applicator. It represents how efficiently the source power is coupled into the discharge. The process of coupling microwave power into the discharge involves the inevitable power losses both in the coupling

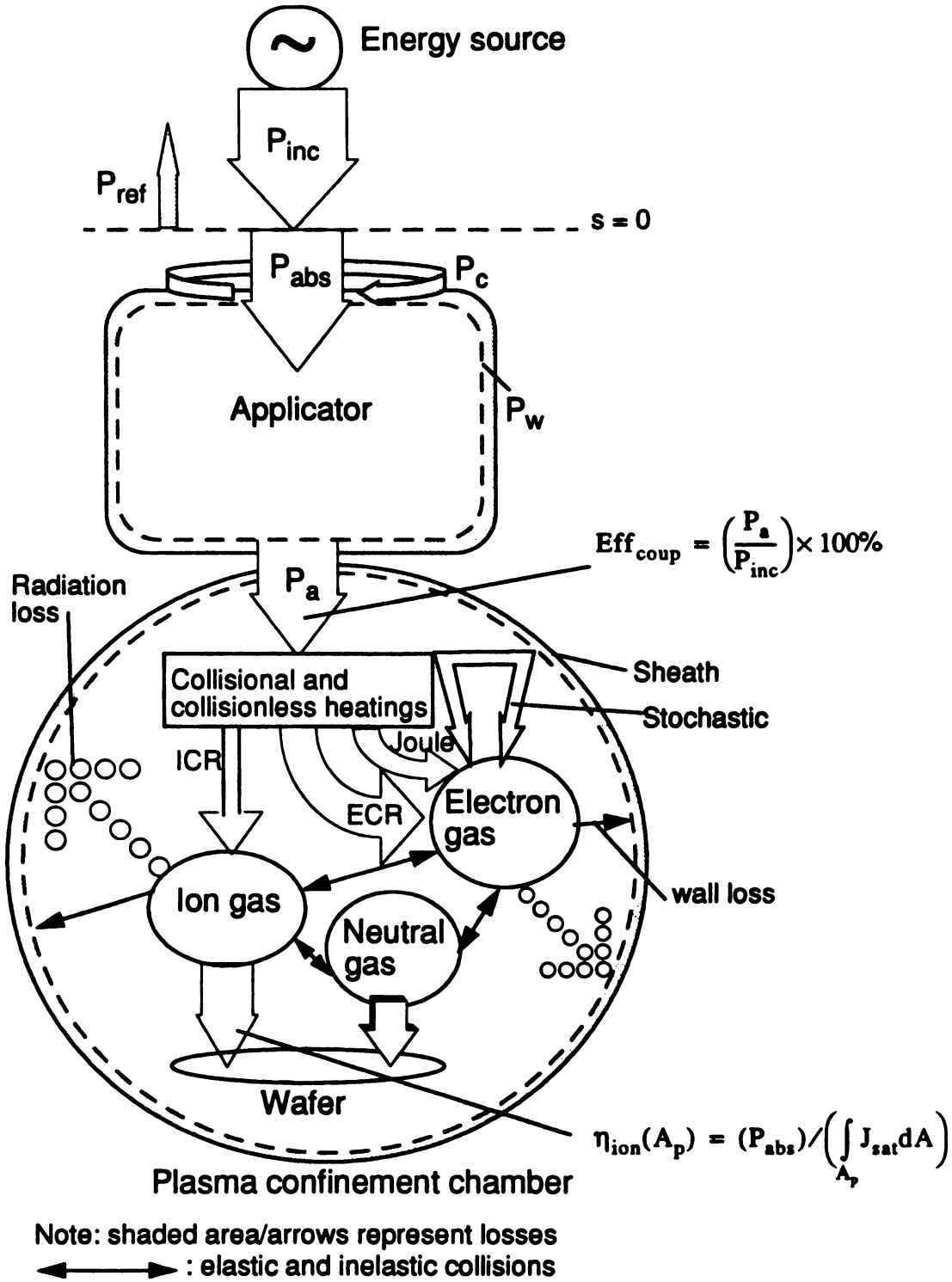

Figure 4.5 Power transfer path in plasma reactor system.

structure, P_c (antenna probe or loop or aperture, etc.), and the applicator walls, P_w. The power coupling efficiency, Eff_{coup} is defined as [93]

$$Eff_{coup} = \left(1 - \frac{P_{loss}}{P_{inc}}\right) \times 100\,\% \quad = \left(\frac{P_a}{P_{inc}}\right) \times 100\,\%, \tag{4.1}$$

where P_{loss} is the total coupling power losses, P_a represents the net power absorbed by the discharge and P_{inc} is the total power incident on the applicator. The reflected power (P_{ref}), the Ohmic heating at the applicator walls by the EM field (P_w), and the losses associated with the Ohmic heating around coupling structure (P_c) constitute the total coupling power losses ($P_{loss} = P_{ref} + P_w + P_c$) in the system. This figure of merit is probably the most neglected performance measure because of the difficulty in evaluating P_w and P_c. Both detailed EM wave distribution and absolute field strength are required in order to obtain these two losses. Therefore, studies seldom report this figure of merit. Power coupling efficiency clearly depends upon applicator type and operating mode. Depending on the applicator geometry and coupling structure, some applicators may be easier to estimate these losses than the others. Estimation of these terms in a MPDR™ cavity type reactor is investigated in Chapter 7.

An alternative method of determining the coupling efficiency is to measure the discharge loaded quality factor, Q_L, and the empty cavity quality factor Q_o. Then the coupling efficiency is written by [93]

$$Eff_{coup} = \left(1 - \frac{Q_L}{Q_o}\right) \times 100\ \%. \tag{4.2}$$

Note that Q_0 is the quality factor of the same non-ideal (finger stocks, viewing window port, etc.) empty cavity that used for plasma experiment. It can be measured by observing the microwave absorption spectrum in the oscilloscope responding to microwave sweep generator [94,95]. Then taking the frequency spectrum band width between two half-maximums divided by the center frequency gives the non-ideal quality factor Q_0 [94,95]. The discharge loaded cavity, Q_L, is calculated by [96]

$$Q_L = \omega \bullet U/\overline{P}_L, \tag{4.3}$$

where $\omega = 2\pi f$ (f is the microwave resonant frequency 2.45 x 10^9 Hz), U is the electromagnetic energy stored in the cavity applicator and $\overline{P}_L$ is the time average of total power losses in the loaded cavity. Since the plasma is a lossy material compared with the total coupling losses ($\overline{P}_L >> P_c$), it is a good approximation that $\overline{P}_L \cong P_{abs}$ for steady state operation. For sinusoidal field, U can be estimated by [97]

$$U \cong \varepsilon \bullet \int_{V_{RC}} |E|^2 dr \quad , \tag{4.4}$$

where the integration V_{RC} covers over the whole volume of the resonant cavity, including part of the plasma region, E is the electric field inside the cavity and ε is assumed to be the permittivity of free space, i.e. 8.854 x 10^{-12} F/m.

In summary, the Q_0 is measured by the frequency spectrum. Q_L is calculated by eqs. (4.3) and (4.4) with the experimental electric field and reactor absorbed power. Finally, the coupling efficiency is obtained from eq. (4.2).

4.4.2 Ion production cost η_{ion}

Ion production cost is defined as the amount of energy required to produce an output ion (expressed in eV/ion), or equivalently, it is the input power required to produce one ampere of ion output current (W/A). The lower the ion production cost, the more efficient the reactor. Ion production cost can be defined as [98]

$$\eta_{ion}(A_p) = (P_{abs}) \Big/ \left(\int_{A_p} J_{sat} dA \right), \tag{4.5}$$

where P_{abs} is the power absorbed by the reactor and A_p is the area for plasma processing. For the typical ion source employed in planar plasma processing, output spatial ion saturation current density (J_{sat}) can be estimated by moving a Langmuir probe over a horizontal plane; for example, the output planes at z = 0 or z = 3 cm in the source. Then integrating J_{sat} over the processing area gives the total ion current available at that area. Note, in order to fairly include the uniformity factor, the integration area A_p should be a contiguous area with specific uniformity (say 10%) of plasma density. Also, this ion production cost does not represent the energy cost to produce an ion since ions that diffuse toward other places (such as discharge chamber walls) are not counted. This efficiency cost does represent the energy required to create an ion that diffuses out of the source into the process chamber.

4.5 Summary

In the chapter, the generic plasma reactor system diagram is presented. The variables are classified by the input-internal-output sense. Tables 4.1, 4.2, and 4.3 summarize respectively the important input, internal and output variables used in this thesis with their descriptions and ranges

Table 4.1 Important Input Variables (U)

Input variables (U)	Variable Description	Ranges Side feed, End feed
Macroscopic controllable input variables U_1	Microwave input power, P_{inc}	200 - 750 W,150 -325 W
	Frequency, f	both fixed at 2.45 GHz (CW)
	Chamber pressure, p with	Most studies on 0.5 - 2 mTorr, 2.5 - 7 mTorr
	Flow rate, f_t	2 - 50 sccm, fixed at 50 sccm
	Electro-positive gas discharge composition	100% Argon for both
	Molecular gas mixture	pure H_2 (2-4 mTorr), none
	Impedance matching network tunings: Cavity height, L_s (mm)	L_s: ~69 -165 mm, ~68-190 mm
	Excitation probe depth, L_p (mm)	L_p: 0 - 24 mm, 0 - 40 mm

Table 4.1 (Con't).

Input variables (U)	Variable Description	Ranges Side feed, End feed
Reactor geometry variables U_2	Energy coupling locations	side feed and end feed
	ECR magnet configurations	8P/8M, allN/8M, 8P/8M 4P/8M and 4/4M, only
	Downstream confinement magnets	with and without downstream magnet for side feed
Substrate control variables U_4	Substrate holder bias	0 to -30 V for both

Table 4.2 Important Internal Variables (X)

Internal variables (X)	Measure from experiment
Electric field strength and spatial pattern at the wall, E_r and $E_r(\Phi, H)$	yes
Impressed electric field strength	No, it is estimated from the electric fields at the wall
Plasma potential, V_p	yes (side feed only)
Electron energy distribution function, EEDF	yes (side feed only)
Electron temperature, T_e	yes
Ion energy distribution function IEDF, with average ion impinging energy $\langle E \rangle_i$ and FWHH	yes

Table 4.3 Important Output Variables (Y)

Output variables (Y)	Descriptions
Plasma source output variable	Ion density $n_i(r)$, and its uniformity
Reactor figure of merit Y_1	Power coupling efficiency, Eff_{coup}
	Ion production cost, η_{ion}

Note that plasma density is normally classified as the internal variables. However, due to the close relationship between the ion density (and density uniformity) and processing rate (and process uniformity), we treat ion density as the output variables in this thesis.

Chapter 5

The Experimental Techniques

- 5.1 Introduction
- 5.2 Visual Plasma Pictures
- 5.3 Micro-coax Electric Probe
    - 5.3.1 Absolute electric field measurement
- 5.4 Langmuir Probe Techniques
    - 5.4.1 Introduction
    - 5.4.2 Double Langmuir probe
    - 5.4.3 Single Langmuir probe
    - 5.4.4 Spatial probe measurement and array of probes
    - 5.4.5 Practical problems and measurement limitations
- 5.5 Gridded Energy Analyzer

Chapter 5

The Experimental Techniques

5.1 Introduction

Science is based on experimental observations, and theories are the systematic rules concluded from numerous experiments. Experiment requires related techniques to make observations. Experimental evaluation of the gas discharge is especially needed because numerous electrons, ions and neutral species interact and react with one another in an active energy exchange environment -- plasma state. Although the current ultra high speed computer may be able to simulate many distinct physical and chemical kinetics of these enormous number of particles, the simulation results do not account for all the possible reactions that occurred inside real systems. Moreover, experiments must be performed to validate the simulations. Fortunately, there are plenty of books [99] available for various experimental plasma diagnostics. These diagnostic techniques range from an intuitive approach, such as visual plasma brightness, to the *in-situ* laser induced fluorescence, which involves much complex instrumentation and requires measurements of great precision. Some techniques are intrusive while others belong to non-invasive. Each of them provides only

partial information of the discharge plasma state, and no single measurement technique delivers a complete picture of the plasma. Therefore, researchers usually proceed with several experimental techniques that pertain to their application interests.

In this chapter, we are going to discuss the experimental diagnostic techniques that were employed in this thesis. They are visual plasma images, micro-coax electric field probe, Langmuir probes and multigrid energy analyzers. The measured plasma reactor internal variables included spatial and magnitude of the electric field at the cavity wall, plasma density, electron temperature, plasma potential, EEDF and ion energies impinging on a conducting substrate. These techniques along with their measured variables are listed in the Table 5.1.

Table 5.1 Experimental techniques and their outcomes.

Experimental techniques	Measured variables
Visual plasma images	Relative brightness, Bright zone locations and shape of a glow discharge
Micro-coax electric probe	EM field pattern/strength in the cavity applicator
Single Langmuir probe	EEDF, average electron energy, plasma potentials
Double Langmuir probe	Ion density and estimate of T_e
Multigrid energy analyzer	IEDF, average ion impinging energy$_i$

5.2 Visual Plasma Pictures

Light radiating from a gaseous plasma is a quick indication of the existence of a gas discharge. As shown in Figure 4.5, the electrons gain most of the EM power supplied by the electrical energy sources. They ionize and excite the gas atoms/molecules by random impact collisions. Then ions, neutrals and energetic electrons collide with one another and the surrounding plasma confinement wall by various processes [100] to produce a plasma state when ion-electron pairs are continuously created by ionization and destroyed by recombination. The light originates from the transition when energetic/excited ion, radical or molecule species relax back to lower energy states. The photon is emitted with an energy which equals to the different energy states of the ion, atom and molecule. The wavelength of this photon is the unique signature to a specific transition of particular ions, atoms or molecules.

The range of emitted radiation spans from far-infrared to UV spectrum. Unfortunately, human eyes are sensitive only to the visible region of wavelengths roughly between 400 nm to 700 nm. All other radiation wavelengths cannot be "seen" by human eyes and may even cause health damage. The human eye sensitivity sets the reception limit on plasma pictures. Moreover, pictures taken by regular camera depend heavily on the quality of the film and the film developing process.

Visual images of a microwave plasma discharge are roughly classified into dense (bright) and sparse (dim) plasmas. As a rule of thumb, a dense plasma probably corresponds to more energy-related processes over the sparse plasma.

A more accurate diagnostic technique examining the radiation from a gaseous discharge is the use of optical emission spectroscopy. This is partially done by my co-worker King [101]. Due to the subjectivity of the plasma photographs or pictures, they are given in the Appendix C.

5.3 Micro-coax Electric Probe

The normal component of the electric field on the inner wall of the applicator is measured by inserting, as shown in Figures 5.1 and 5.2, a micro-coaxial probe into the many small holes located around the cavity walls. The insertion (see Figure 5.2) of the small micro-coaxial probe through these wall holes couples a tiny amount of microwave power into the microwave measuring circuit. This power is proportional to the square of the normal component of the electric field [94,102,103] at each hole location. All holes in the cavity wall shown in Figure 5.1 are radially drilled with a 2.2 mm diameter drill bit (#44) to produce a snug fit for a RG405/U semi-rigid 50-Ω cable that is connected to a microwave power meter. The hole size is much smaller than the wavelength associated with the 2.45 GHz microwave energy, so that no significant perturbation to the system or radiation leakage is observed. Two different cylindrical shells with the same inner diameter (17.78 cm) were used for side-excited and end-excited plasma experiments.

The end-feed shell consists of a 1/4 inch thick aluminum shell. As shown in the inset of Figure 5.1, there are two vertical groups of holes that are 45^{0} apart.

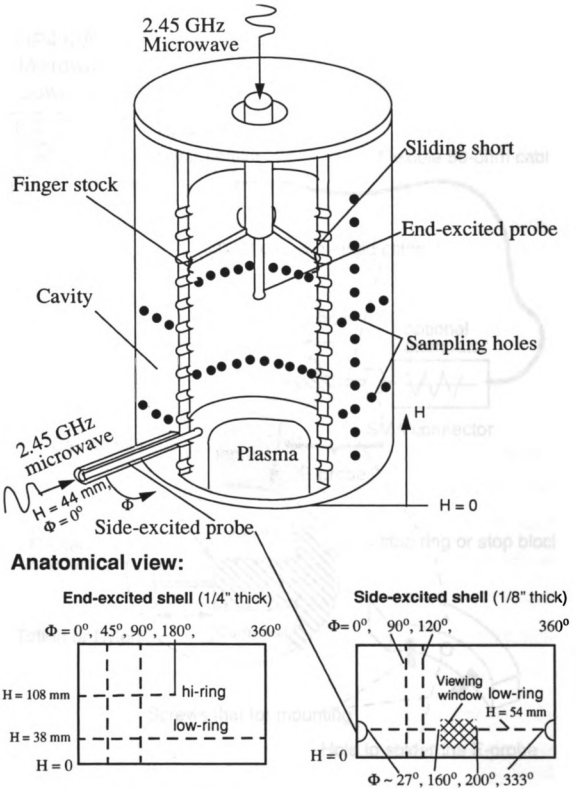

Figure 5.1 Cut-away view of the microwave cavity applicator.

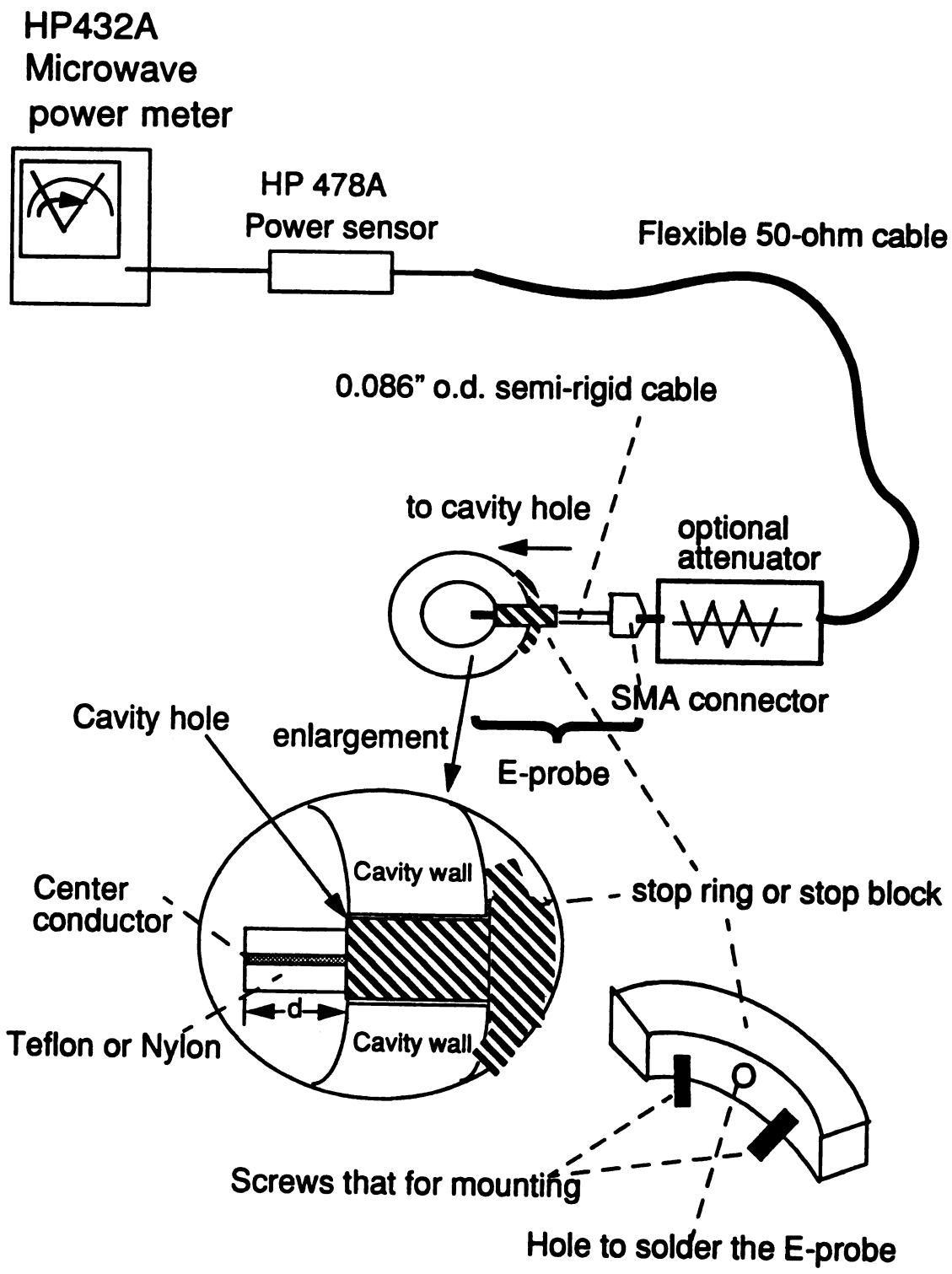

Figure 5.2 Detail of E-probe measurement system.

Each group of holes has 24 holes, 10 mm apart (center to center), starting at H = 18 mm (H = 0 is defined as the bottom of the cavity). One group of the vertical holes is located at $\Phi = 90^0$ and the other is at $\Phi = 45^0$. The $\Phi = 0^0$ reference, as shown in Figure 5.1, serves to reference the hole locations with respect to the ECR magnet locations. Furthermore, there are two horizontal series of holes located at H = 38 mm and 108 mm. The "low-ring" of holes (at H = 38 mm) has 36 equally azimuthally spaced holes, 10^0 apart from center to center. The "hi-ring" of holes (at H =108 mm) has 19 holes which are also 10^0 apart from center to center, starting from 0^0 to 180^0.

The side-feed shell consists of a 1/8 inch thick brass shell. $\Phi = 0^0$ is defined as the entrance of the excitation probe. Due to the allocations of the excitation probe and the viewing window (shown in the inset of Figure 5.1), the circumferential 36-hole series are drilled at two strip areas at the same height of H = 54 mm. Each area has 18 holes, 7.5^0 apart from center to center. One starts at $\Phi = 30^0$ and ends at $\Phi = 157.5^0$, the other occupies between 202.5^0 and 330^0. There are two vertical series of holes that are 30^0 apart, located at $\Phi = 90^0$ and $\Phi = 120^0$. The $\Phi = 90^0$ series of holes has 15 holes, 9.6 mm apart (center to center), starting at H = 25.2 mm. The $\Phi = 120^0$ series of holes has 16 operative holes, 9.2 mm apart (center to center), starting at H = 26.3 mm.

Particular attention was paid to the construction of the small micro-coaxial probe, called E-probe here-after. The outer conductor of a small micro-coax at one end was carefully trimmed so that its outer conductor was flush with the inner applicator wall surface, and its center conductor extended a small distance (typ. 1

to 2 mm) into the cavity. The longer the distance the center probe extended into the cavity, the more power it coupled from the cavity and, therefore the greater perturbation of the local fields. Thus it was important not to have a long extended center conductor protruding into the cavity. In all the experimental data, presented in this thesis, the sampled power was always less than 0.005% (or 0.04%) of the incident (or absorbed) power in order to guarantee virtually no perturbation on the excited cavity field by the E-probe measurement. This was confirmed by the fact that no measurable changes in macroscopic variables were observed during all of the experiments when inserting or removing the E-probe.

A stop-ring (collar) or a stop-block, shown in Figure 5.2, was (soldered) attached at a particular location of the E-probe so that the outside conductor of E-probe is flush with the inner cavity wall whenever the E-probe is inserted into these holes. The arc-shaped stop-blocks were fixed by inserting two screws that fit into the neighboring diagnostic holes. This ensured the consistency of the sampling depth and prevents any motions (in, out or rotation) during experiment.

On the other end of the E-probe, a SMA connector was installed, followed by an optional pad (10.38 dB or 6dB) to insure good isolation and reduce mismatch ripples for later transmission. A flexible, three-foot long, coaxial cable (RG58C/U standard) connects the E-probe to the HP478A Thermistor which acts as a microwave power sensor. Note that the power sensing unit sets the lower limit of the sampled power. The lowest limit of our HP 478A power sensor (thermistor) is to the order of 1 μW. This is the highest sensitivity of the E-probe system. The sampled power reading can be read with a HP432A power meter.

Finally, any transmission loss from the insertion end near the cavity wall to the final power sensor has to be carefully determined in order to measure the actual sampled power faithfully. The typical transmission loss of this set-up at 2.45 GHz is 1.25 dB plus any applicable attenuator loss factor.

5.3.1 Absolute electric field measurement

Two methods have been utilized to measure the normal component of the electric field at the inner conducting cavity walls, one was developed by Rogers and Asmussen (RA) [94] and the other was based upon the work of Burkart [103]. Both methods employ an E-probe to sample EM power from the small holes drilled at the cavity wall.

5.3.1.A Burkart's method

Both inner and outer conductors of the E-probe are machined with a very high-speed lathe such that both conductors are precisely flush with the inner applicator wall, with virtually no burrs. Solving Laplace's equation with appropriate boundary conditions, Burkhart developed an analytical formula [103]

$$E_r = (2\pi^2 f \varepsilon_o K_r a^2)^{-1} \sqrt{\frac{2P_s}{Z_o}} \text{ (V/m)}. \qquad (5.1)$$

For the cable (RG405/U) used in our E-probe, the dimensionless multiplier, K_r, is 3.846. Thus if the radius of inner conductor (a = 10 mils or 0.254 mm), the characteristic impedance of the cable (Z_o = 50 Ω), the operating frequency (f = 2.45 GHz), the accurate measurement of the sampled power (P_s in Watt) and the

universal constants (π and the permittivity of free space ε_0) are all known, then the normal component of the electric field, E_r, at the cavity can be determined. Note that this method is independent of the EM modes in the resonant applicator structure and no lengthy calibration procedure is required. The direct relationship in our case is

$$|E_r| \cong (1.88 \times 10^6)\sqrt{P_s} \qquad (V/m). \tag{5.2}$$

5.3.1.B Rogers and Asmussen method

The E-probe used in this method can be either a flush probe or a penetration probe (typical penetration should be less than 2 mm). However, RA method requires a calibration procedure. The idea of the procedure is briefly outlined here for clarity while a detailed explanation is given in Appendix A.

First, the discharge baseplate is removed from the cavity applicator and is replaced with a solid brass end plate. Then low 2.45 GHz power is critically coupled into the empty cavity exciting a known EM mode. The net power P_{abs} delivered into the empty cavity is lost entirely in the conducting wall losses inside the cavity. These wall losses are divided between coupling circuit losses (P_c) and EM mode wall losses (P_w). Using the end feed coaxially coupled cavity applicator, measurements of the coupling circuit Q and the empty cavity TM_{012} mode Q indicated that around one quarter to one half of P_{abs} is dissipated in the coupling circuit loss during calibration process. Thus, approximately one half to three fourths of P_{abs} is dissipated as EM mode wall loss P_w. That is

$$P_c \cong (1/4 \text{ to } 1/2) \times P_{abs} \text{ and } P_w \cong (3/4 \text{ to } 1/2) \times P_{abs}. \tag{5.3}$$

Recall EM mode wall loss, P_w, can be related to the normal component of the electric field inside the cavity applicator using conducting wall perturbation theory [96,97]

$$P_w = \int_S \left(\frac{1}{2}\Re_s |J_s|^2\right) dS \quad , \tag{5.4}$$

where $\Re_s$ is the finite resistivity of the wall material, J_s is the induced surface current density and S includes all the interior wall surface areas of the calibration applicator. When the wall surface is a very good conductor, J_s can be obtained by the EM boundary condition of $|J_s| = |n \times H_t|$, where n is the normal unit vector at the wall surface and H_t is the EM mode tangential magnetic field at the wall. Since P_{abs}, $\Re_s$, S and EM mode are known, the magnitude of the excited EM mode fields within the cavity can be determined from eqs (5.3) and (5.4).

During the calibration process, a small E-probe is inserted into a hole located away from the cavity coupling region to avoid the influence of the coupling probe near field. The power sampled, P_s, by this small E-probe is linearly proportional to the square [102]of the local normal EM-field strength, i.e. $P_s = C |E_r|^2$. Eqs. (5.3) and (5.4) establish the magnitude of the electric field at the probe position. The constant C can be determined from the P_s ($= C|E_r|^2$) measurement and, hence, the probe is calibrated (see Appendix A for detail).

Using this procedure, the upper and lower bounds of the normal electric field, E_r, are related to the sampled power by

$$|E_r| = 7.95 \times 10^5 \sqrt{P_s} \qquad (V/m) \qquad \text{for} \qquad P_w = \frac{1}{2} P_{abs}, \tag{5.5}$$

$$|E_r| = 9.19\times10^5\sqrt{P_s} \quad (V/m) \quad \text{for} \quad P_w = \frac{3}{4}P_{abs}. \tag{5.6}$$

The difference between the two measurement techniques can be explained by first noting that the value of multiplier K_r in Burkart's method is valid for an infinite flat surface. In our case, the probe is inserted into a slightly curved surface. Thus it is expected that the smaller the diameter the cylindrical cavity, the bigger the error. While the RA method requires a calibration procedure, it provides estimates of upper and lower bounds for $|E_r|$. Thus, the RA method is adopted here as the most accurate measurement technique. Unless otherwise noted, all electric field measurements with the end-feed applicator presented in this thesis are lower bound values by the RA method. This would underestimate the exact electric field values by at worst 20%. The choice of lower bound E-field values could also present a higher power coupling efficiency (see Section 4.4.1) by a few percentages (typical within 4% better).

5.4 Langmuir Probe Techniques

5.4.1 Introduction

Since the reports [104-106] proposed by Langmuir and Mott-Smith in the mid-1920s, the Langmuir probe has become one of the most widely used plasma diagnostics because it is relatively simple to construct and gives good estimates of many key local plasma parameters, such as plasma density, electron

temperature, plasma potential, etc. Basically, the technique consists of inserting one or more metallic electrodes or probes into the plasma. The probe is electrically connected to a variable-voltage power supply which can be biased with respect to a large reference electrode in contact with the plasma. The reference electrode is usually taken as the anode of the main discharge or the metallic chamber wall. Then local plasma parameters near the vicinity of the probe are extracted from the recorded current-voltage (I-V) relationship, the mass of ion, the size and shape of the probe electrode. The usual probe electrode shapes are spheres, cylinders, and planes. Several excellent references in the literature covering probe theories and measurement techniques have been presented throughout the years [107-111]. In this thesis, two different types of cylindrical probes, single and double Langmuir probes, were used in the collisionless sheath regimes for low pressure MPDR™ plasmas. The measurement techniques adopted here closely follow previous co-workers' methods [53, 112].

Both single and double Langmuir probes can be used to measure electron temperature and plasma density. However, the double probe technique has three advantages over the single probe. First, double probe system is electrically isolated and the two electrodes are simply biased with respect to one another. This can virtually measure plasma density in discharges including RF, microwave excited discharges and the plasma created at atmosphere where single probes do not work because of the lack of the large reference electrode. Secondly, the double probes "float" with the plasma. Thus they are insensitive to the changes

inside the plasma discharge because the plasma potential of two "floating" nearby electrodes almost experience the same potential change. Third, the current that a double probe draws is much lower than the electron saturation current that single probe usually collects. Thus perturbation to plasma by double probe is minimized. In this thesis, the plasma potential, electron energy distribution function (EEDF), and electron temperature are acquired by the single probe method. The ion density are obtained from the double probe technique based upon Maxwellian distribution of electrons. The fundamental principles and experimental data acquisition system of both techniques are presented in later sub-sections.

5.4.2 Double Langmuir probe

Measuring techniques and Principles: The double probe technique was first demonstrated by Johnson and Malter [113]. Figure 5.3 (a) shows the schematic of the double probe measurement system used in this thesis. Two 0.94 mm diameter cylindrical tungsten wires were partially sealed inside a high temperature pyrex tube, leaving a small portion (around 52 mm in length) exposed to the plasma discharge. The separation distance between two electrodes should be close enough so that the plasma floating potentials are essentially the same at both surfaces, yet they must be separated by a minimal separation distance which must be greater than several Debye lengths such that the plasma sheaths of each probe do not intersect. The Debye length, λ_D, is given [99] by

$$\lambda_D = 69\sqrt{T_e/n_e} \qquad \text{(m)} \tag{5.7}$$

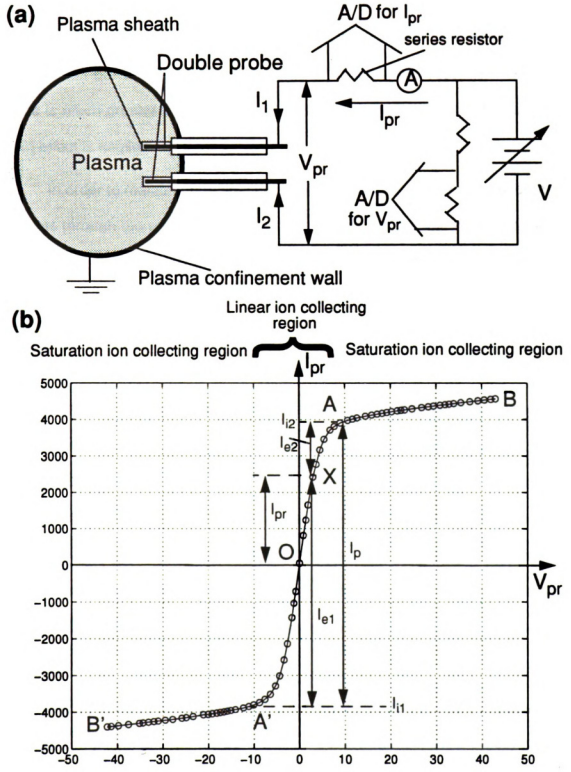

Figure 5.3 (a) Schematic circuit for Double Langmuir Probe measurement, (b) Typical measured double probe I-V characteristics.

where T_e in Kelvin and n_e in m^{-3}. The Debye length in the diagnostic region (z = 0 - 10 cm) of our high density MPDR™ plasmas is below 100 μm, which is much smaller than our double probes separation of about 4 mm. Also the size of our probe is much greater than the Debye length. Thus, orbital motion limited (OML) [109] effect is negligible.

In order to maintain the "floating" characteristics of double probes, both the currents through the probes and the voltage across the probes were recorded by a computer through a MetraByte® DAS-8 A/D (Analog to Digital) converters, which were isolated from the Langmuir probe circuit by MetraByte® ISO-4 isolation amplifiers. As shown in Figure 5.3 (a), the voltage sampled by the computer was proportional to the probe voltage plus the total voltage across the series sampling resistor and ampere meter. The voltage across the series resistor and ampere meter was deducted in a Q-Basic computer acquisition program [114] at the time when I-V data was taken. The bias (V_{pr}) was typically varied from -50 to +50 Volts. Each data point was sampled about 20-40 times and then an average value was computed and stored into the computer file. Then an estimate of electron temperature and plasma density were analyzed and deduced from another Q-Basic program [114] that uses the method outlined in the following paragraphs.

Figure 5.3 (b) displays a typical measured double probe I-V curve. The curve is composed of two regions. One is the linear ion collecting region (O-A or O-A') and the other represents the saturation ion collecting region (A-B or A'-B'). If the double probe is physically symmetric and the plasma floating potential over

the probes is the same, then the I-V curve should be symmetric around the origin. Figure 5.4 shows the potentials (V_1, V_2) reached by each probe with respect to the plasma potential, V_p. And both probes will be at a negative potential w.r.t. plasma potential due to the fast mobility of electrons over the ions [100]. That also means the ion current component collected by each probe will approximately be equal to the ion saturation current plus the electron current component which changes with the bias voltage. When the probe voltage (V_{pr}) is changed, both V_1 and V_2 change so that the electron current collected by one probe balances the ion current collected by the other. When the probe bias ($V_{pr} = V_1 - V_2$) is zero, both probes are at floating potential, V_f, which corresponds the situation in Figure 5.4 (a) or the origin (O) of Figure 5.3 (b). When V_{pr} is small, the potential distribution is displayed in Figure 5.4 (b). Probe 1 moves closer to plasma potential and collects more electrons, and probe 2 moves away from plasma potential and collects fewer electrons. The extra electrons flowing to probe 1 pass through the circuit to make up the deficiency at probe 2. Recall the conventional current follows the positive charge carrier travel direction. That results in a net current flowing into the probe 1 and leaving probe 2. This corresponds to point X in Figure 5.3 (b). When V_{pr} is large comparable to the difference between plasma and floating potential, shown in Figure 5.4 (c), probe 1 collects almost only electrons and probe 2 collects little or no electrons due to the high potential barrier there. The electron component collected in probe 1 balances the whole ion component of probe 1 and 2. This situation corresponds to point A in Figure 5.3 (b).

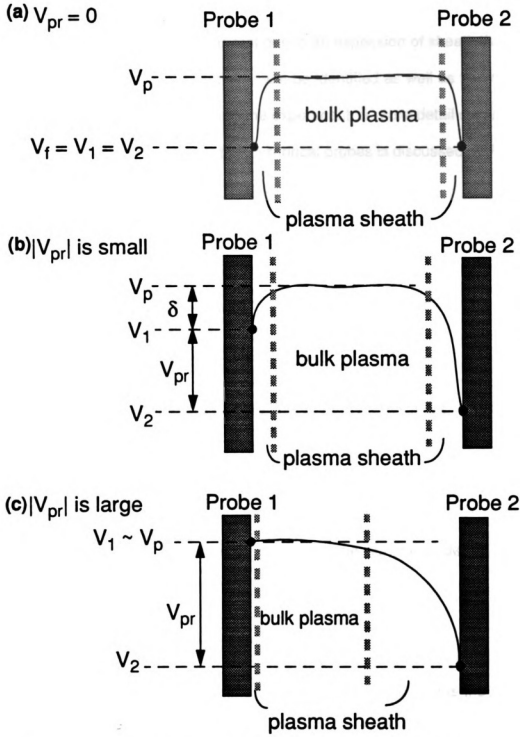

Figure 5.4 Schematic of the potential distribution between the probes of a floating double probe system. (a) applied voltage Vpr = 0, (b) at the linear region, (c) over the saturation region.

In Johnson and Malter early work [113], an assumption on the constant ion saturation currents were made. However, further increase in the bias voltage can slowly increase the collected ion current due to an expansion of sheath thickness. The knees or turning points, A and A', must be identified as well as the values of the saturation currents (I_{i1}, I_{i2}) during the experiment. A more detail discussion in non-constant ion saturation current for cylindrical probes is discussed by Peterson and Talbot [115].

Quantitatively, since both probes are insulated from ground, no net current can flow in or out the measurement system, i.e. $I_1 + I_2 = 0$. Writing each electrode current in terms of its electron and ion component,

$$(I_{i1} - I_{e1}) + (I_{i2} - I_{e2}) = 0 \tag{5.8}$$

So the total ion or electron currents collected by both probes is a constant, say I_p, as shown in Figure 5.3 (b). That is,

$$I_p = I_{i1} + I_{i2} = I_{e1} + I_{e2}\,. \tag{5.9}$$

Recall that the electron current reaching the probe surface under Maxwellian distribution assumption would be

$$I_e = I_{e0} \exp(-eV/kT_e) \tag{5.10}$$

where I_{e0} is a premultiplier constant, e is the electronic charge, V is the retarding potential with respect to the plasma potential, k is the Boltzmann constant, and T_e

is the electron temperature. Substituting eq. (5.10) into eq. (5.9) and dividing the resulting equation by I_{e2}, we have

$$I_p / I_{e2} = 1 + (I_{e1} / I_{e2}) = 1 + (I_{e10}/I_{e20})\exp\{-e(V_1 - V_2)/kTe\}. \quad (5.11)$$

As shown in Figure 5.4 (b), the applied voltages over the probes are $V_1 = V_p - \delta$, and $V_2 = V_p - \delta - V_{pr}$, respectively. Therefore, $(V_1 - V_2) = V_{pr}$, is the voltage across the probe. Take the natural logarithm of eq. (5.11), we obtain

$$\ln\{(I_p/I_{e2}) - 1\} = \ln(I_{e10}/I_{e20}) - eV_{pr}/kT_e \quad (5.12)$$

Finally, the electron temperature near the probe can be obtained by the slope of the $\ln\{(I_p/I_{e2}) - 1\}$ vs. V_{pr}.

Once the electron temperature is found, the ion density, assuming singly charged ions (which is mostly true as verified by optical emission spectroscopy [101]), at the probe vicinity can be estimated from the relationship [100]

$$I_i \sim 0.606 A_p e n_i (kT_e/m_i)^{1/2}, \quad (5.13)$$

where I_i is the ion saturation current, A_p is effective probe area, n_i is ion density, and m_i is the mass of ion. In order to find the slope in the linear ion collecting region and the knee points (A & A'), computer automated search for the best knee points by data analyzing program were performed. The best-fits for ion saturation points and the slope of ($\ln\{(I_p/I_{e2}) - 1\}$ vs. V_{pr}) were found by the minimization of the mean square error between the line formed by all the experimental data within the automated trial and error scanning knees (A & A')

and an assumed Maxwellian's one. Estimation of the ion saturation current I_i was taken by an average of the I_{i1} and I_{i2}. In the process to estimate the ion density, effective probe areas should be known in advance. The effective probe area is extended from the physical probe dimension by an order of Debye length, λ_D. which is also a function of density and electron temperature. Thus, several iterations between eq. (5.7) and eq. (5.13) were implemented in the data analyzing program. The termination criterion of iterations is set whenever the new plasma density falls within 1% of the previous one.

5.4.3 Single Langmuir probe

Principle: Plasma potential and the electron energy distribution function (EEDF) can be deduced from the second derivative of the single probe I-V characteristic. Assuming the distribution is isotropic, the electron energy distribution function, $f_e(E)$, is given by [116]

$$f_e(E) \propto (\sqrt{V_p - V})\frac{d^2 I_e}{dV^2} \tag{5.14}$$

where V_p is the plasma potential, I_e and V are electron current and voltage on the probe, and $E = e(V_p - V)$, is the retarding potential energy. Note that all the potential or voltage are with respect to the same reference ground, which in this thesis is taken as the potential at conducting process chamber wall. The more negative the bias voltage, the deeper the sampling over the high energy electron spectrum. This formula is valid only, (1) when the probe voltage is below the plasma potential, (2) when the local electron energy distribution is isotropic, and

(3) when the mean free path of electrons is much larger than the probe dimensions. In applying eq. (5.14), it is common to approximate d^2I_e/dV^2 by d^2I/dV^2 where I, the total probe current, equals the sum of I_e and the ion currents drawn by the probe. This approximation is justified by the fact that measurements were made only when the applied probe voltage was negative with respect to V_p in the region where the ion currents varied slowly.

For a Maxwell-Boltzmann distribution, the plasma potential occurs when $d^2I/dV^2 = 0$. However, in a general plasma discharge, Rundle et al. [117] suggested to take the voltage at which the highest second derivative of probe current versus probe voltage occurred as the good estimate of plasma potential. This method is adopted here in this thesis. Hence the reported plasma potentials in this thesis should be regarded as the lower bound values. All the EEDFs then have been numerically normalized so that

$$\int_0^\infty f_e(E)dE = 1. \tag{5.15}$$

Then, the average electron energies were calculated by

$$\langle E\rangle_e = \int_0^\infty E f_e(E)dE. \tag{5.16}$$

The construction of a single probe is similar to the double probe with only one electrode sticking out, approximately 6 mm in length. The rest of the 0.5 mm dia. cylindrical tungsten wire is sealed from the plasma in a pyrex glass tube.

Measuring technique: Figure 5.5 displays the schematic circuit for single probe measurement in our lab that implements the a.c. measuring technique. A small a.c. sinusoidal voltage (typical 0.35 V peak to peak, frequency at 1 kHz) is superimposed on top of the dc probe bias voltage. Then the second derivative of I vs. V is approximately proportional to the a.c. component of probe current at the second harmonic of the small a.c. oscillation frequency. An audio 1:1 transformer is employed to couple the a.c. signal into the probe circuit. A Princeton Applied Research 128A lock-in amplifier (LIA) differentially measures the voltage across a current-sampling resistor at the twice the oscillator frequency. The probe must be sputtered clean in order to produce reproductive measurements.

Quantitatively, using the notation vsin(ωt) for small a.c. voltage, probe current is a general function of total voltage,

$$I = I\,(V + v\sin(\omega t)). \tag{5.17}$$

where v and ω are the small amplitude and the driving frequency of the applied a.c. signal. Expanding eq. (5.17) in a Taylor series around the operating dc voltage V, we have

$$I = I(V) + \Delta I_{dc} + \Delta I_{ac1} + \Delta I_{ac2} + \Delta I_{ac3} + \ldots, \tag{5.18}$$

$$\text{where } \Delta I_{dc} = \frac{v^2}{4}\cdot\frac{d^2 I}{dV^2} + \frac{v^4}{64}\cdot\frac{d^4 I}{dV^4} + \frac{v^6}{2304}\cdot\frac{d^6 I}{dV^6} + \ldots, \tag{5.18A}$$

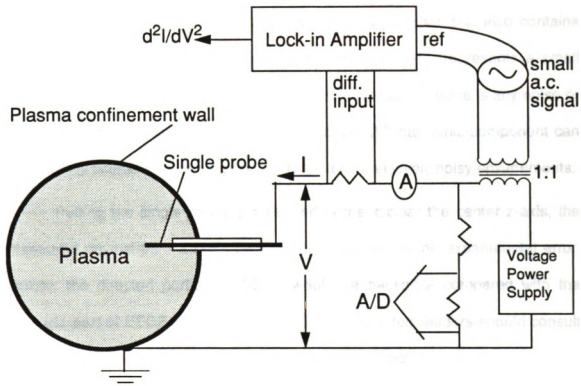

Figure 5.5 Schematic set up of single Langmuir probe measurement.

$$\Delta I_{ac1} = \left(v \cdot \frac{dI}{dV} + \frac{v^3}{8} \cdot \frac{d^3I}{dV^3} + \frac{v^5}{192} \cdot \frac{d^5I}{dV^5} + \ldots \right) \sin(\omega t), \tag{5.18B}$$

$$\Delta I_{ac2} = \left(\frac{v^2}{4} \cdot \frac{d^2I}{dV^2} + \frac{v^4}{48} \cdot \frac{d^4I}{dV^4} + \frac{v^6}{1536} \cdot \frac{d^6I}{dV^6} + \ldots \right) (-\cos(2\omega t)), \tag{5.18C}$$

$$\Delta I_{ac3} = \left(\frac{v^3}{24} \cdot \frac{d^3I}{dV^3} + \frac{v^5}{384} \cdot \frac{d^5I}{dV^5} + \ldots \right) (-\sin(3\omega t)). \tag{5.18D}$$

In the case of small signal, v << V, the higher order terms in eq. (5.19C) can be neglected without significant error. Therefore, the second harmonic component of the a.c. current simply is proportional to d^2I/dV^2, which is directly related to the EEDF from eq. (5.14). One might argue that ΔI_{dc} also contains d^2I/dV^2 term for an alternate measurement. However, ΔI_{dc} represents a small change of total dc current I and is very difficult to measure if there is any noise or fluctuations in the plasma. On the other hand, the 2nd-harmonic component can be carefully filtered and detected by the LIA even in relatively noisy environments.

Putting the single probe parallel and perpendicular the center z-axis, the measured downstream EEDFs give similar result within the experimental error. Hence, the directed portion of EEDF would be negligible compared with the isotropic part of EEDF. For anisotropic EEDFs, interested readers should consult Ref. [118] for a comprehensive discussion on this subject.

5.4.4 Spatial probe measurement and array of probes

Since Langmuir probe is such a useful tool in determining the fundamental parameters of plasma, it is strongly desired that probes be located everywhere inside the plasma to spatially extract plasma information at the same time. Also, the effect of a substrate in plasma discharges should be included during the measurements. If this goal could be achieved, then the plasma uniformity, which is of great concern for many critical processes, can be evaluated over the substrate processing region. In a simple vacuum system which does not have any vacuum

compatible movable means (such as linear or rotary feedthrough, etc.), the experimenter has to set up the probe, take a data point, purge the vacuum system, relocate the probe, pump down the system and take another set of measurements. This kind of tedious procedure is both inefficient and quite disturbing (no one can guarantee that the system returns the exact previous conditions when s/he deals with vacuum and plasma). One practical way to achieve the ideal goal is to move the probe by mechanical means such as linear or rotatable motion feedthroughs, or motorized probe carrier. Placing array of probes inside the plasma is an elegant alternate. Both were employed to take spatial probe measurements in this thesis.

For the mechanical method, a set of vacuum compatible stages and motors (Newport Corporation 860A Series Linear Motorizers) were placed into the vacuum chamber. A Langmuir probe was attached to the stages which can be moved by the motors. A computer program was written to control the motor movements remotely through the computer parallel port and vacuum feedthrough. Once the targeted location was achieved, an I-V curve scan was recorded and then the probe was moved to next position and the I-V measurements were repeated. This set up worked well initially. However, maintenance was the biggest problem. Vacuum compatible motors can not survived in plasma for a long run. The lubricant of the motors "dried up" during their exposure of the plasma and eventually the rotors stuck and could not move anymore. Furthermore, the speed of the motors is heavily dependent on both the weight it carries and the "aging" of

lubricant. It is tedious to re-calibrate the speed and then compensate for it in computer program constantly.

To include the influence of the substrate, a round shape array of probes was constructed to simulate the plasma-substrate boundary condition. As shown in Figure 5.6, thirty cylindrical tungsten probes (diameter ~ 0.508 mm) protrude out (length ~ 5 mm) on the top of a 91-mm-dia., 1/4 in-thick circular ceramic disk. The spacing between probes, d_s, is approximately 13.2 mm. Each individual probe length was listed in Appendix B for relative current calibration purpose. The probes were insulated by another ceramic disk at the bottom, and by a quartz ring on the side. The electrical signal on each wire was carried out of the processing chamber via a vacuum feedthrough. Each probe wire was connected to a switching circuit that was controlled by a personal computer. The electronic switching circuit consisted of two 74154LS Demultiplexers, six 7404 Hex Inverting Gates, eight LF347 Quad JFET Operational Amplifiers and 32 JWD172-1 Relays. They were configured as shown in Figure 5.7. The typical operation was to send out a five-bit binary signal to the demultiplexers from the computer. The demultiplexers and inverting gates then converted the binary input into one of 32 mutually exclusive outputs to select the corresponding probe in the array. The operational amplifiers after the inverting gates provided unity gain with high output current (> 18 mA) in order to drive the following relay which was selected The reason of using relays is to isolate the standard TTL circuit from the high voltage probe bias. The negative bias was set approximately to $[V_f - 10(kT_e)]$, [119], where values of V_f and T_e were estimated from the single probe measurements. After the

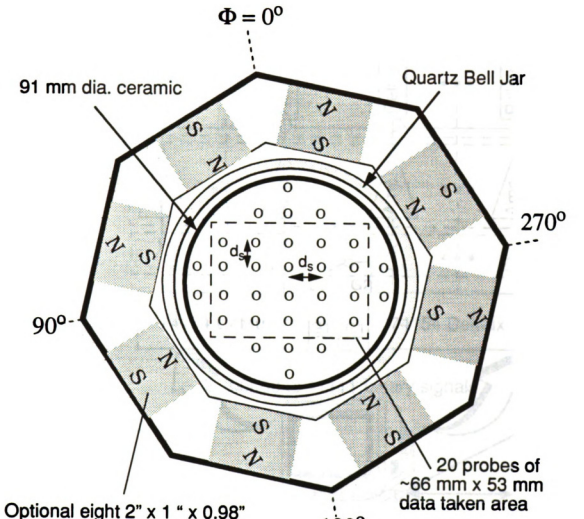

Figure 5.6 Top view of the Langmuir probe array locations with 8P/8M ECR configurations.

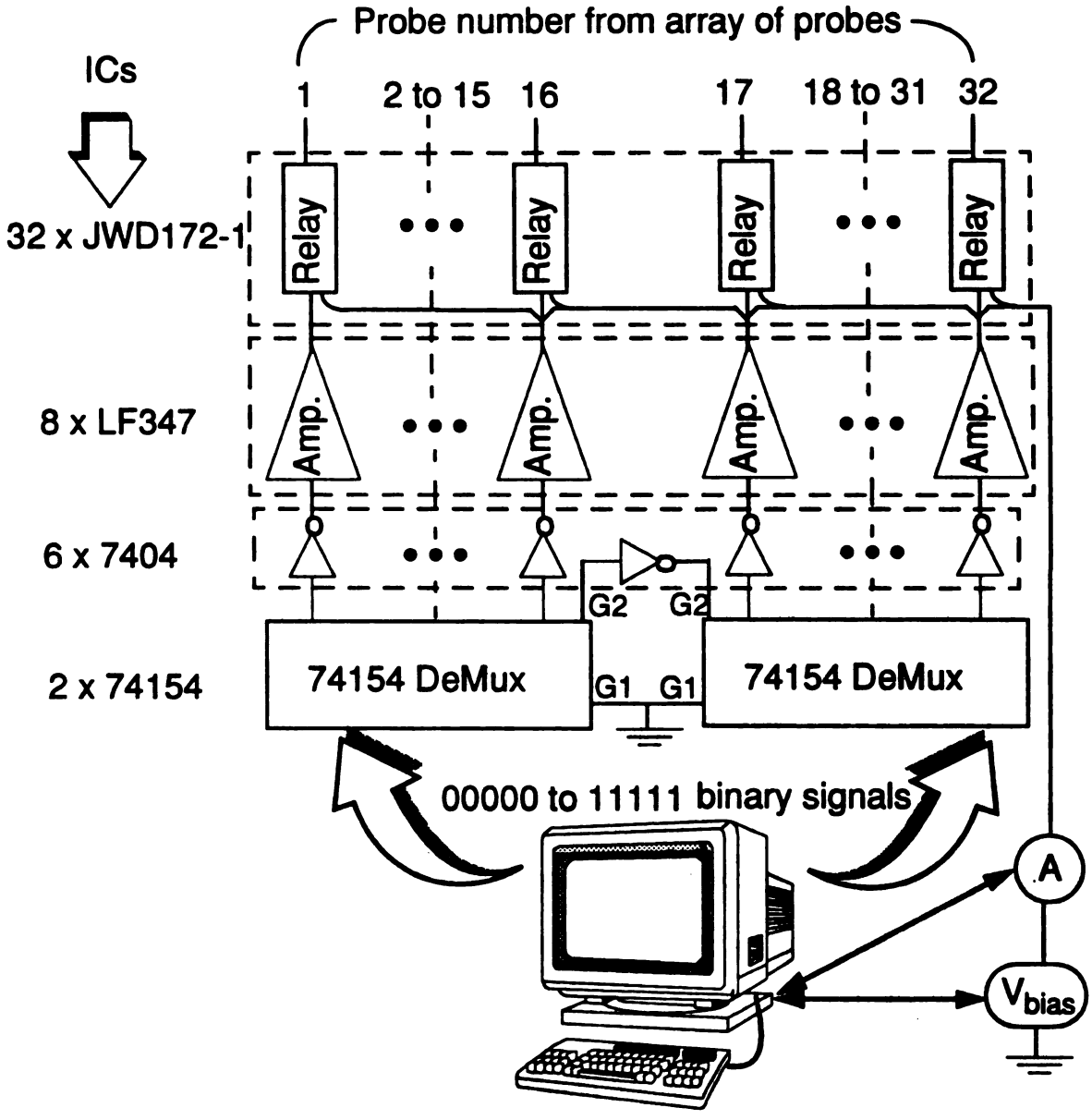

Figure 5.7 Schematics of the electronic circuit for arrays of probes.

computer recorded the current to the probe, it advanced to another binary signal to measure the current at a different probe in the array. This process repeated itself until all the desired probe saturation currents were recorded. Therefore, the uniformity of the ion density over the substrate region located at z = constant plane was automatically recorded, and calculated. Note that, only 20 probes inside the dotted rectangular region (in Figure 5.6) were used for the experiments presented in this work. This apparatus recorded *in situ* plasma ion saturation currents over an insulating substrate (a ceramic, in this case). Plasma uniformity is defined as the standard deviation divided by the average of 20 probe currents.

5.4.5 Practical problems and measurement limitations

Several experimental problems for Langmuir probes were identified. First, the arrival of a positive ion at the probe surface cannot be distinguished from the departure of an electron in the ion collection formula eq. (5.13). Electrons might be leaving the probe by either the secondary electron emission bombarded by intermediate energy ions, or the absorption of ultraviolet light at the probe surface will also eject photoelectrons. Existence of doubly or multiply charged ions will add uncertainty in ion current collection. Second, the Langmuir probe measurements were performed only in the downstream region ($z > 0$), where the strong microwave and static magnetic fields are minimal. For plasma applications in the presence of rf/microwave field or static magnetic field, the interested readers should consult Refs. [99,109] Third, in addition to the assumption of a

Maxwellian EEDF, only a small fraction of the energy distribution function of the electrons in the plasma, i.e. the high-energy tail, is sampled by the double probe method. Fourth, eq. (5.13) gives only an order of magnitude on plasma density. More accurate estimation should confer to the summary result in Appendix 4 in Ref. [108] or a recent study presented in Ref. [120]. Lastly, probes exposed to harsh plasma environment (especially sputtering situation) often behave abnormally. This is probably due to the deposition of unwanted material on the probe and its insulating support structure. The usual method of cleaning insulator-contaminated probes is to sputter-cleaning them by dc biasing them at a potential much below the plasma potential for around 1 minute between data sweeps. Thus the probe is sputtering clean through the ion bombardment. Many other experimental complications [107-109] can occur. Hence, implementing and interpreting Langmuir probes requires considerable experience. Accuracy can vary up to a factor of 10 has been reported in [120].

5.5 Gridded Energy Analyzer

Measuring techniques and principles: For the processing perspective, both the direction and the magnitude of ion energy impinging on the substrate are very important to achieve damage free anisotropic etching [121]. The usual tool to obtain this information is to measure ion energy distribution functions with an electrostatic gridded energy analyzer [122].

The gridded energy analyzer used in our laboratory was designed by my previous co-worker [53] through the machine shop supported by IBM in York Town Height, NY. The cylindrical analyzer has a size of diameter 2" and height of 0.94". As shown in Figure 5.8, the energy analyzer consists of one screening diaphragm, two gridded meshes, one collector plate and the surrounding stainless steel cylindrical housing (50 mm dia. and 19 mm high). To simulate a larger wafer effect, another thin plate can be put on the top surface to enlarge the top surface up to 150 mm dia. The first screening electrode/diaphragm is made of a 50 μm thick stainless steel, which may be electrically biased to simulate the substrate bias effect in the plasma discharge. It has a 100 μm dia. entrance orifice at the center. At low pressures the ions falls through the sheath next to the top surface. Those impinging on the holes fall through the hole and are collected by the analyzer. The study of ions flowing through a small hole can be dated back as early as in 1926 [123]. The size of the pin hole is on the order of Debye length or less in order to ensure a continuous sheath on the entrance face. Each of the two gridded meshes is made of 100 lines/inch nickel mesh welded on an circular aluminum ring shaped frame. These meshes are mounted with insulating spacers (~0.094" thick) so that they are electrically insulated with a distance of about 2.6 mm between the adjacent grids. The first grid next to the aperture entrance is also called electron repulsion grid, which was biased to a fixed negative voltage V_{er} (about - 50 V) to repel most of the electrons that had fell into the analyzer.

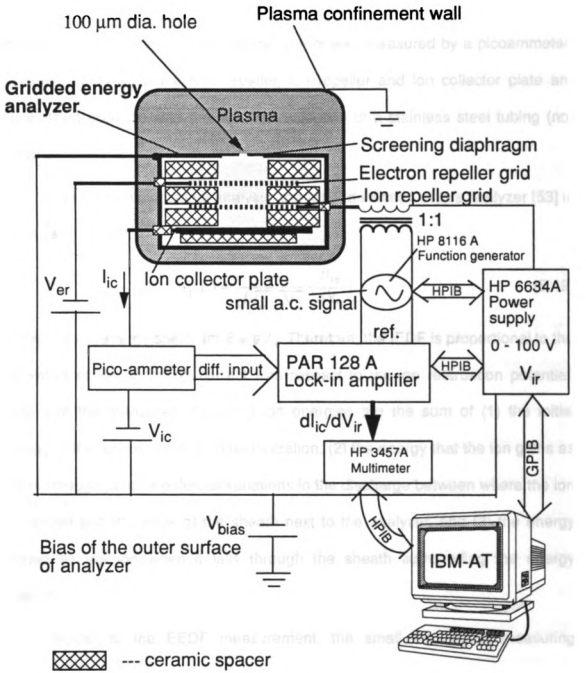

The drawing here is not in scale.

Figure 5.8 Schematic circuit for sampling ion energies impinging on a substrate.

The second grid, also known as ion retardation grid, was biased to a variable potential V_{ir} to selectively let enough high energy ions pass through and reach the ion collector plate below. The ion collection plate bias voltage V_{ic} was maintained at a constant potential of -28V and its current was measured by a picoammeter. Electrical contacts of electron repeller, ion repeller and ion collector plate are established from the side through the protection of a stainless steel tubing (not shown).

Using one dimensional analysis, the IEDF derivation of this analyzer [53] is given as

$$f_i(E) \propto \frac{1}{\sqrt{V_{ir} - V_{ic}}} \cdot \frac{dI_{ic}}{dV_{ir}}, \tag{5.19}$$

where the ion energy spectrum $E = eV_{ir}$. Therefore, the IEDF is proportional to the derivative of ion collection current with respect to the ion retardation potential. Note that the measured impinging ion energies are the sum of (1) the initial energy of the ion immediately after ionization, (2) the energy that the ion gains as it falls through plasma potential variations in the discharge between where the ion is created and the edge of the sheath next to the analyzer, and (3) the energy gained by the ion when it falls through the sheath surrounding the energy analyzer.

Similar to the EEDF measurement, the small a.c. signal measuring technique was applied to the case of IEDF. An IBM-AT computer controlled the HP 6634A power supply DC output to the ion repeller grid. A small a.c. sinusoidal signal (0.35 V peak to peak, frequency at 40 Hz from HP 8116A function

generator), controlled by computer [124] through the HPIB interface bus, was superimposed on top of the retardation potential. The PAR128A LIA differentially measured the variation in the collected ion current at the small signal fundamental frequency. Then the output of LIA, which was proportional to the dI_{ic}/dV_{ir}, fed the data to the computer which in turn computed the IEDF by eq. (5.19). All the IEDFs then have been numerically normalized so that

$$\int_0^\infty f_i(E)dE = 1. \tag{5.20}$$

The average ion energies were calculated by

$$\langle E \rangle_i = \int_0^\infty E f_i(E)dE. \tag{5.21}$$

When determining the Full Width at Half Height (FWHH) of the IEDF, the computer program assumed a 5% of the maximum peak signal as the noise level.

Limitations: There are several possible sources of error in using the energy analyzer. First, the eq. (5.19) was derived from a one dimensional analysis. It assumes all ions entering the energy analyzer fall in the same direction parallel to the normal of the top membrane. In reality, ions can impinge at angles of up to about 63.4^o from the normal direction in our gridded energy analyzer. Furthermore, the ions can travel in the radial direction by diffusion. This will contribute spread in the IEDF. Secondly, the lack of the negatively biased electron suppressor grid [122,125], which is usually located between the ion repeller and collector plate, cannot prevent secondary electrons from either of the first two grids from reaching the ion collector. This adds another uncertainty to the

measurement. Third, the grid alignment, ion charge exchange and collisions within the analyzer were not considered in eq. (5.19). Thus the FWHH of measured IEDF should be considered as the upper bound values.

Knowing the upper bound motivates us to investigate the lower bound -- i.e. the equipment resolution. The resolution of an analyzer is a function of many factors such as 1) the mesh size, 2) the inter-grid distance, 3) grid alignment, and 4) the sampling orifice design. The influence of geometrical factors on the energy resolution of a three plane grids energy analyzer was detailed in [126]. Although their gridded energy analyzer is not identical to our system, we can still use the formula as a guideline to estimate the resolution given by

$$\frac{\Delta E}{E} = \frac{\alpha s}{2\pi L}\left(1 + \frac{d}{\alpha s} + \frac{d^2}{2\alpha^2 s^2}\right)\left[1 + \frac{2d}{\alpha s}\operatorname{atan}\left(\frac{d}{\alpha s}\right) - \frac{2d}{\alpha s}\operatorname{atan}\left(\frac{2d}{\alpha s}\right)\right], \qquad (5.22)$$

where s is the spacing between neighboring wires measured from surface to surface, α is a constant of ~1.13, d is the mesh wire diameter and L is the distance between the grids. In our analyzer, s ~ 0.01" and L ~0.094".

Since our *ad hoc* analyzer has been used for many years, the fine mesh wire diameter d is unknown and difficult to measure accurately. Therefore, the resolution $\Delta E/E$ is plotted as a function of mesh wire diameter. By putting other measurable geometrical quantities into eq. (5.22), Figure 5.9 shows that there is a peak in resolution vs. wire diameter. Our estimation of wire diameter falls between 0.5 and 1 mil. Therefore, the minimum uncertainty of this energy analyzer is around 2%. Note that the analyzer using in Ref. [126] has a whole mesh as the screening entrance instead of an orifice, the above mentioned number 4 factor is

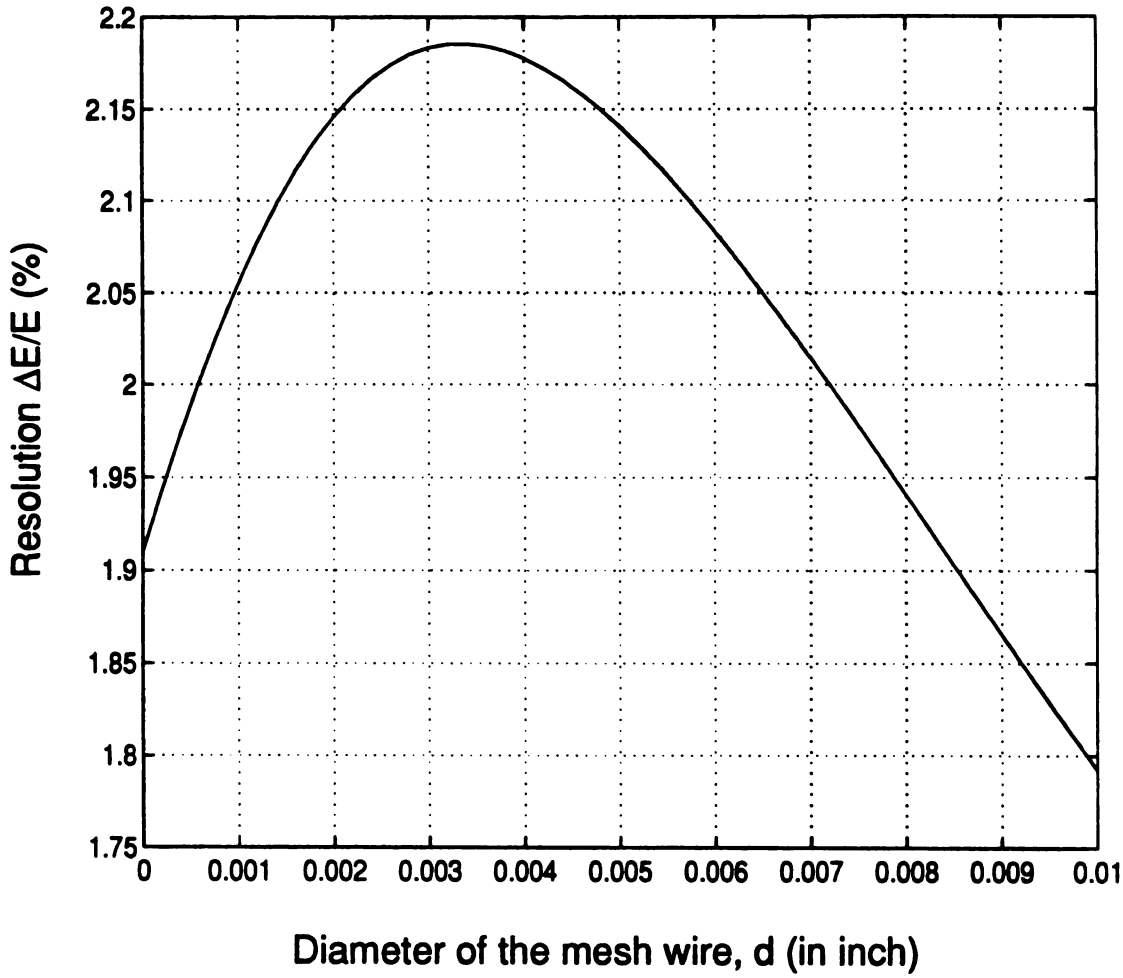

Figure 5.9 Resolution of energy analyzer versus mesh wire diameter.

not included. Moreover, perfect alignment of these grids is impossible to achieve without the special tool. Hence, 2% resolution should be considered as the best resolution in our analyzer.

The user of the energy analyzer should also be informed that the measured IEDF is contributed by several factors: 1) the plasma sheath potential plus any dc bias externally impressed on the analyzer, 2) the directed energy acquired from the spatial gradient of plasma potential before entering the sheath, 3) the ion random thermal energy, and 4) the magnetic field effect, if a static magnetic field exists. Number 3 factor has been studied by my co-worker [101] using the laser induced fluorescence technique. Finally, the absence of differentially pumping capability in our analyzer set the upper measurement pressure limit to about 10 mTorr for our energy analyzer usage in argon.

Chapter 6

Static Magnetic Fields in MPDR™-13 ECR Plasma Source

- 6.1 Introduction
- 6.2 Selection of Magnets and Magnet Configurations
  - 6.2.1 Introduction
  - 6.2.2 Selection of magnets
  - 6.2.3 Magnet configurations
- 6.3 Simulation on Magnetic Flux Density, B-field
  - 6.3.1 Formulation principle
  - 6.3.2 Simulation result
- 6.4 Measurement of B-Fields
  - 6.4.1 Iron powder method
  - 6.4.2 Hall-effect B-field measurement
- 6.5 Concluding Remarks

Chapter 6

Static Magnetic Fields in MPDR™-13 ECR Plasma Source

6.1 Introduction

Magnetism has long fascinated humans since the discovery of the remote interaction between lodestones. Using a compass to indicate the travel direction in ancient China may be the first recorded human application of magnetic material. Our scientific understanding of magnetism has only come in relatively recent times. In 1820, Hans C. Oersted discovered the phenomena between magnetism and electric currents. Later André-Marie Ampère developed a quantitative law for their relationship. The most comprehensive theory of magnetism is microscopically explained by magnetic moments and their interactions follow the rule of Quantum Mechanics.

Strong magnetic fields and their spatial variations are essential considerations in the design of an ECR plasma source. Basically, all moving charged particles are gyrating or oscillating around the magnetic field lines with an angular frequency called cyclotron frequency. The cyclotron frequency, f_c, is a function of static magnetic field i.e. $f_c = \frac{q}{2\pi m}B$, where m is the mass of the charged particle, q is the electric charge it carries, and B is the local magnetic flux

density. The magnetic flux density (B) is related to the magnetic field (H) by the relation

$$\vec{B} = \mu \vec{H}, \tag{6.1}$$

where μ is the local permeability of the medium. If the cyclotron frequency is equal to the applied electromagnetic energy frequency, synchronous pumping of energy phenomena occurs [34]. When the applied microwave energy source is oscillating at 2.45 GHz, 875 Gauss is the B-field magnitude required to accelerate the electrons at electron cyclotron resonance (ECR). Since the magnetic flux density usually varies spatially within the discharge zone, ECR only occurs at certain regions in the discharge volume. Therefore, it is important to understand how the applied static magnetic flux density varies within the plasma source. Furthermore, knowledge of the B-field pattern would help us understand the charged particle diffusion and reactor charged species confinement characteristics.

In this chapter, the commercial specification of permanent magnets is reviewed. Then several permanent magnet configurations that are experimentally investigated in this thesis are described. A FORTRAN® program [127], using numerical Finite Difference Method, is employed to simulate the three dimensional B-fields for different magnet configurations. Finally, the magnetic field simulation results are compared with some experimentally measured magnetic field data.

6.2 Selection of Magnets and Magnet Configurations

6.2.1 Introduction

Eight hundred and seventy-five Gauss is a very strong magnetic flux density in comparison to the ~ 1 Gauss magnetic fields that normally exists on the earth's surface. There are two common methods to produce the necessary ECR magnetic fields. One is by flowing a strong electric current through a coil system to produce the necessary magnetic field. The other method uses the magnetic field produced by a set of strong permanent magnets. When considering the initial set-up and maintenance costs, using permanent magnets to produce a strong magnetic field has important advantages over using the electric coil system. The coil system not only consumes large amounts of electric energy but is usually bulky and thus occupies valuable clean room space. Additionally if the current in the coil system fluctuates, this results in a corresponding movement in ECR region. This will influence discharge stability and the effect will be similar to the instabilities associated with power supply frequency variations mentioned in Section 3.2.1.D, causing an undesired spread of the ion energy distribution function. One advantage of coil system may be its simplicity of producing different magnetic field strengths while still maintaining a spatially similar magnetic pattern by just varying the amount of supply current flowing into the coil. However, the magnetic field pattern may not be changed significantly by this method.

On the other hand, once you buy the permanent magnets, they are there ready for use without extra energy supply. Therefore, as mentioned in Section 2.6,

the permanent magnet approach to generate the necessary magnetic field has become popular and is adopted here to create the ECR magnetic fields in the plasma source.

6.2.2 Selection of magnets

When designing a magnetic circuit, one needs to consider two factors. The first involves the choice of magnetic circuit elements (magnets and high permeability material, etc.) and the second is concerned with their spatial magnetic field configurations. For ECR to occur in the discharge volume, the magnetic field strength at the permanent magnet vicinity has to be at least greater than the desired ECR magnetic fields. For 2.45 GHz excitation, this minimum B-field is 875 G. However, most companies do not specify the magnetic field strength near the pole surface. It is well known that magnetic material possesses a hysteresis cycle (magnetic flux density vs. magnetic field, B vs. H as shown in Figure 6.1 (a)) as the B-field versus H-field traces out different paths of magnetization and demagnetization. Only the demagnetization curve -- the second quadrant of the loop, is useful for practical application of permanent magnets. It starts from the B-axis intercept -- B_r, called remenance, defined as the magnetic flux density that remains in permanent magnets or the maximum flux density the material is able to produce under closed circuit condition. It ends at the H-axis intercept -- H_c, called the coercive field, the value of the applied magnetic field in opposite direction required to drive the magnetization to zero. Depending

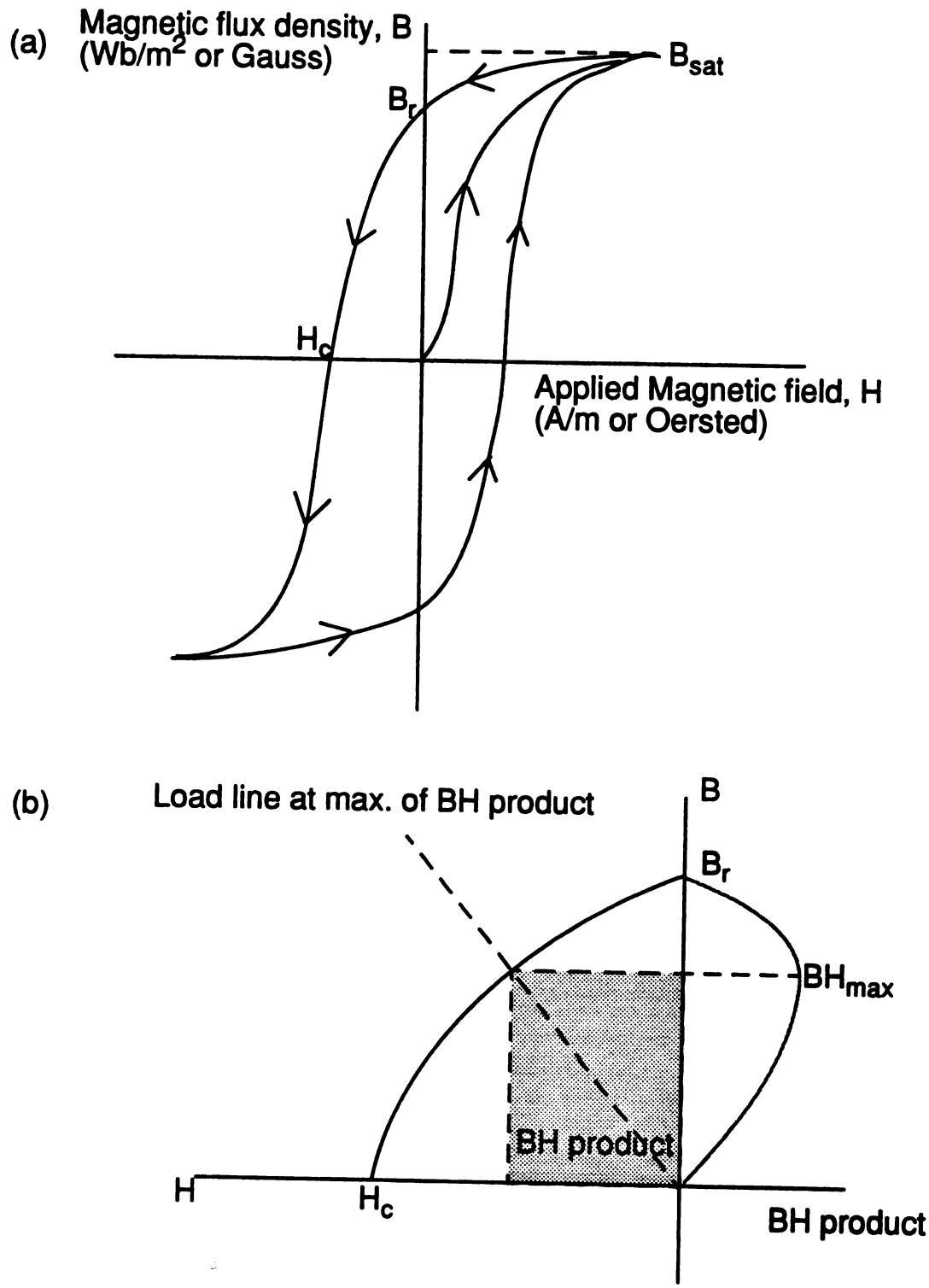

Figure 6.1 (a) Typical Hysteresis cycle for a ferromagnetic material, (b) Demagnetization curve with load line.

on the magnetic circuit design, the actual operating point will lie along this segment of demagnetization curve, shown in Figure 6.1 (b). Therefore, most commercially available permanent magnets are specified [128] by the maximum product (Mega GO) of B (in Gauss, symbol G) and H (in Oersted, symbol O) in the demagnetization region.

On February of 1990, the state-of-the-art of commercially available magnets was 35MGO for the NeoDymium-Iron-Boron (NdFeB) type of permanent magnet. From the magnetic company catalog [128], the coercive field (H_c) and the remenance (B_r) are 26000 Oersted and 11500 Gauss respectively. These magnets produce around 6.4 kG B-field at the proximity of the magnetized pole surface when the field of pole surface was measured by Hall-effect probe without any other magnetic circuit elements nearby.

Another advantage of using this type of rare-earth magnet is its toughness to demagnetize. Its aging loss is less than 0.22% after one year. However, these rare earth permanent magnets are very strong magnetically, but are weak physically. Therefore, they must be handled with great precaution to prevent injury to personnel and to prevent breaking the magnets themselves.

6.2.3 Magnet configurations

The magnet accommodation region in the MPDR™-13 reactor is a concentric ring slot channel (~3 cm high) in the baseplate with water cooling running around it. Recall that Figure 3.4 displays the cooling water channel, and

the channel filled with the benchmark ECR 8 pole/8 magnet multipolar ECR magnet configuration (abbr. as 8P/8M). Due to the fixed magnet accommodation channel in the ECR reactor, there are limited ways to arrange magnets. The four different ECR magnet configurations used in this thesis are displayed in Figure 4.4. They all constitute either eight or four 5.08 x 2.54 x 2.5 cm NdFeB-35MGO type magnets with different magnetization directions. Three of them in Figure 4.4 (a-c) belong to the multipolar magnetic type field geometry. The notation for the multipolar magnetic field configurations is number of magnetic poles, followed by number of magnets. Therefore, the shorthand notations of multipolar magnetic type configurations shown in Figure 4.4 (a-c) are 8P/8M, 4P/8M, 4P/4M. The magnetic field configuration shown in Figure 4.4 (d) has all 8 magnetic north poles facing inward. It is denoted as allN/8M and is not a multipolar magnetic field geometry.

As shown in Figure 4.4, all configurations contain four or eight magnets that are arranged equally spaced such that they inscribe a 7.4 cm radius cylindrical wall. Putting high permeability material (1/8" thick Corrosive Resistance Steel) on the outside and at the bottom of the magnets not only keeps the magnets at the arranged stable positions but also prevents the magnetic field from extending into the unwanted regions external to the plasma source. Note that the permanent magnets are located close to but outside the plasma excitation region and the magnetic fields in the discharge region are symmetric about the center axis of the cross section. The magnetic field intensity decreases from the highest value at the magnet pole surfaces to zero at the center axis. If the magnets are not

strong enough, the required 875 Gauss ECR region may be located outside of the discharge region. When stronger magnets are used, the location of 875 Gauss ECR region will be pushed further inward. However, if the 875 Gauss ECR region is too close to the center, it may result in a nonuniform plasma, dense at the center region and sparse near the wall boundary. The optimal location of the ECR zone is a matter of engineering design such that the discharge excitation and ionization balance with the charged particle loss to the wall so that a uniform steady state plasma is created across the cross section.

6.3 Simulation on Static Magnetic Flux Density, B-Field

6.3.1 Formulation principle

Governing Equation: There are at least two formulations for magnetic field analysis -- scalar and vector magnetic potential formulations. The vector magnetic potential method is versatile for all magnetic field problems while scalar magnetic potential method is suitable to the current-free regions (both conduction and displacement current free). In this thesis, the scalar magnetic potential formulation is employed owning to its simplicity and its low computational cost considerations (one degree of freedom per node for the scalar magnetic potential formulation over three for the vector potential counterpart formulation).

For current-free regions,

$$\nabla \times H = 0, \tag{6.2}$$

Any vector with zero curl may be represented as the gradient of a scalar. Thus, the magnetic field can be written as

$$H = \nabla V_m, \tag{6.3}$$

where V_m is called the scalar magnetic potential. Note that V_m is a pure fictitious mathematical quantity without any physical meaning. Substituting eq. (6.3) into eq. (6.1), the physical B-field can be directly obtained as the follows:

$$B = \mu \nabla V_m. \tag{6.4}$$

The divergence of the magnetic flux density B is zero everywhere ($\nabla \bullet B = 0$). Thus by taking the divergence of eq.(6.4), we obtain the **governing equation** for V_m,

$$\nabla \bullet (\mu \nabla V_m) = 0. \tag{6.5}$$

This equation can be numerically solved for the specific geometry where V_m is subjected to the appropriate boundary conditions. In this thesis, a cylindrical coordinate system was used and all the differentiations were approximately replaced by the finite difference method [129]. The local μ value is the average value obtained by averaging over all the neighboring nodes. Eq. (6.5) becomes a system of linear equations for V_m, which are solved by Gauss-Seidel iterative method [130]. Once V_m is calculated, the program will immediately compute the magnetic flux densities using eq. (6.4).

Boundary Conditions and simplification by symmetry: 3-D simulations are computationally expensive. Fortunately, by symmetry we can reduce the simulation region to only one slice of the 'pie' shape of the actual system. As shown in Figure 6.2 (a), only 90^0 of pie-shaped region are intensively simulated for configurations with 4-folded symmetry and 45^0 for configurations with 8-folded symmetry. The B-field for the rest of the region can be obtained by mirroring the value with respect to the symmetry planes. To avoid the unknown permeability of the rare-earth magnetic material, the simulated region will be the pie shape that excludes the region where permanent magnets occupy. We can specify the magnetic flux densities ($B = \mu\nabla V_m$) at the surfaces of each magnet as the Neuman-type Boundary Conditions there, i.e. to specify the derivatives of V_m by the B-field at the magnetic pole surfaces. By symmetry, other Natural Boundary Conditions (NBC: specify the normal derivatives of the primary variable instead of the primary variable itself) can be found. First, the B-field at center axis is zero. The ϕ component of B-field at the planes (ϕ = constant) that cut the center of the magnet is also zero. Also, if $|z|$ is large enough, the B-field at the top and bottom surface of the simulation region will go to zero. Finally, if r is large enough, the B-field at the outer surface of the simulation region becomes small and is assumed to be zero.

Note that this problem belongs to the type of Laplace equation with only NBCs specified over the boundaries. Therefore, the primary variable solution V_m is determined within an additive constant. Fortunately, the artificial quantity V_m does not have any physical meaning in this problem. Only its gradient

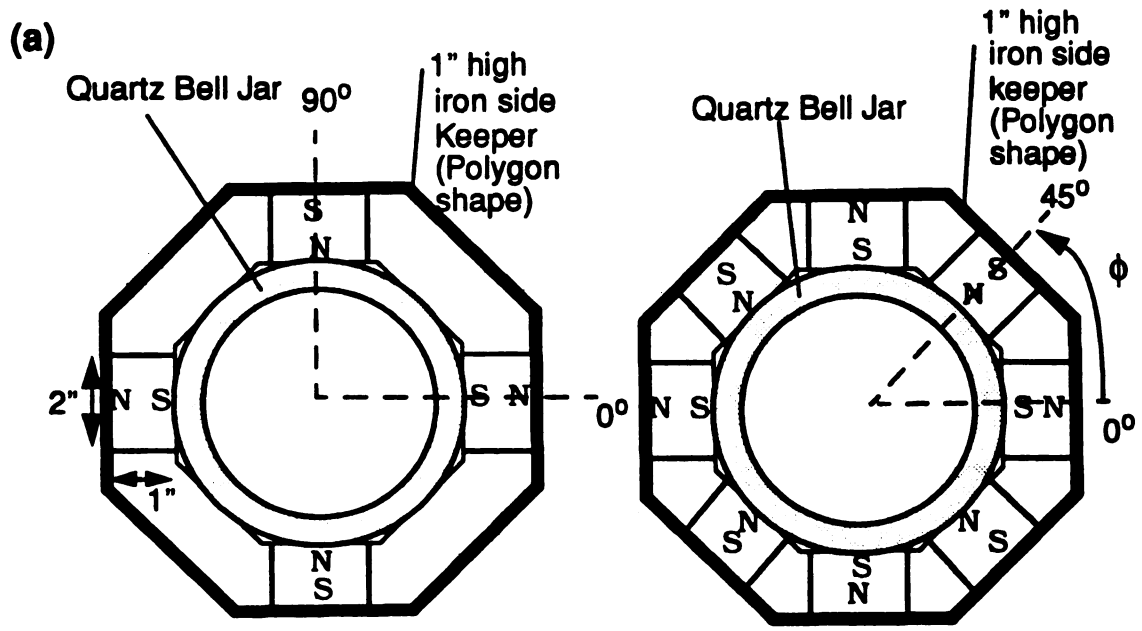

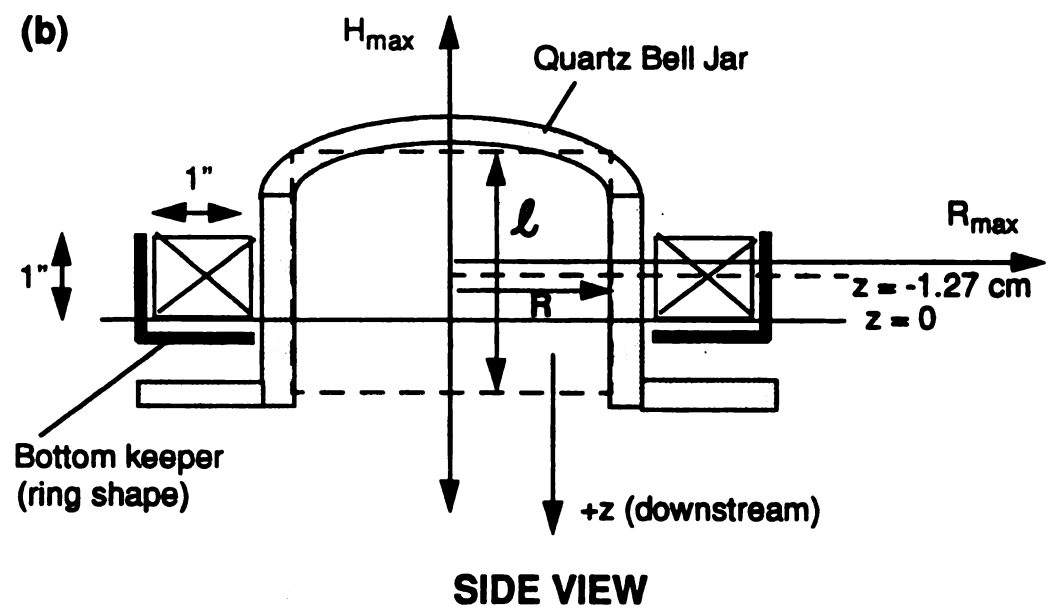

Figure 6.2 (a) Symmetry of ECR magnet configurations, (b) Schematic of the simulation region.

corresponds to the physical H- or B-fields and therefore the computed results presented here display only magnetic flux density. Since the location of the 875 Gauss ECR zone is of interest, many of the plots will detail the magnetic flux density near this region.

Geometry details: Since the field drops as we move away from the magnets in either r or z directions, a large simulation domain (Figure 6.2 (b)) is defined. It contains certain angular degree which depends on the symmetry of the configurations, and is spanned by R_{max} in radial direction and H_{max} in z-direction. Remember that the actual region of interest is the plasma excitation region confined at height ℓ and radius **R**, where the quartz bell jar seals the vacuum. Anything outside the quartz bell jar is irrelevant. The choice of R_{max} and H_{max} does not really matter provided they are large enough.

The specific grid structure used for the simulation contains 45 nodes along the radial direction, 61 nodes along azimuthal ϕ-direction and 33 nodes along z-direction. The ϕ-direction grids are uniformly spaced but are nonlinear in both radial and z-direction partitions, with emphasis on the region close to the 875 G. The gridded mesh corresponds to the following physical dimensions: (1) from 0.4 cm to 12.74 cm in r-direction, (2) 0 to 90^0 in ϕ-direction, and (3) -5.52 cm to +2.73 cm in z-direction. The discretization is partitioned as follows: in ϕ direction, $\delta\phi$ is uniformly spaced at every 1.5^0. In the r-direction, from $r = 0$ to 36 mm, $\delta r = 4$mm. When r falls between 36 mm and 74 mm, δr is 2 mm and δr becomes 2.54 mm when r is between 7.4 and 9.94 mm. δr is 4 mm again for larger r. In the z-direction, δz is 2.1 mm when z is between -27.3mm to +4.2 mm. Then $\delta z \sim 3.05$

mm elsewhere. Therefor the simulated magnet shapes are wedged shapes. Their simulated boundaries are: 7.4 cm < r <9.94 cm, -2.52 cm < z <0 cm, and $\phi \in [0^o, 18^o] \cup [30^o, 60^o] \cup [72^o, 90^o]$.

The following equations summaries the geometrical grid sizes in three directions:

$$\delta r = \left\{ \begin{array}{c} 4 \text{ mm} \quad \text{for } 0 < r < 36 \text{ mm or } r > 94 \text{ mm} \\ 2 \text{ mm} \quad \text{for } 36 \text{ mm} < r < 74 \text{ mm} \\ 2.54 \text{ mm} \quad \text{for } 74 \text{ mm} < r < 9.94 \text{ mm} \end{array} \right\}, \tag{6.6}$$

$$\delta\phi = 1.5^o \quad \text{for all } \phi, \tag{6.7}$$

$$\delta z = \left\{ \begin{array}{c} 2.1 \text{ mm} \quad \text{for } -27.3 \text{ mm} < z < 4.2 \text{ mm} \\ \sim 3.05 \text{ mm} \quad \text{otherwise} \end{array} \right\}. \tag{6.8}$$

Magnetic material characteristics: The last item that needs to be addressed is the permeability of materials. The relative permeability of most materials (including air, aluminum baseplate and quartz) in the system is one while the iron keeper material ranges from around one hundred to several thousands, depending on the applied magnetic field nearby. Unfortunately, the permeability of the iron keeper is a nonlinear function of the B-field. So the Laplace equation of eq. (6.5) described above will also be nonlinear. For simplicity, the relative permeability of the iron keepers is assumed to be 600 (μ_r = 600) for the simulation presented here. The relative permeability of the other materials is 1.

6.3.2 Simulation result

For comparison purposes, the results of all configurations are presented in range of 0^0 to 90^0. For the 8-folded symmetric configurations, data from simulated result were mirrored into the region between 45^0 and 90^0 by the symmetry plane at $\phi = 45^0$. Data are selectedly shown in different cross sections; B-field vs. r-z plane at $\phi = 0^0$ (in the normal plane of magnet) and B-field vs. r-ϕ plane at z = -1.27 cm (center plane of magnet). They are presented in three formats: the contour plot, the mesh plot, and the "needle plot". These computed B-field plots are displayed in Figures 6.3 to 6.6. The plots give the constant B-field contours in the regions where magnetic flux density are near 875 Gauss. The mesh plots display the visual pattern of the magnetic field over the two dimensional space. The needle plots represent both the magnitude (length of the needle) and direction (arrow head of the needle) of the local magnetic flux density. Figure 6.3-6.6 (a-d) show the simulated B-field result of 8P/8M, 4P/4M, 4P/8M and allN/8M respectively. Part (a) of these Figures gives both the contour and needle plots of B-field vs. r-z plane at $\phi = 0^0$. Part (b) displays the contour plot of B-field vs. r-ϕ plane at z = -1.27 cm. Part (c) presents both the mesh and contour plots of B-field vs. r-ϕ plane at z = -1.27 cm. Finally, part (d) exhibits the needle, contour and mesh plots of B-field vs. r-z plane at $\phi = 0^0$.

As the Figures show, the B-field is the highest near the magnet and rapidly decays towards the center axis. Also the gap regions between the magnets have lower values than the regions that lie directly in front of the magnets. The multipolar magnetic type ECR configurations (4P/8M, 4P/4M and 8P/8M) form

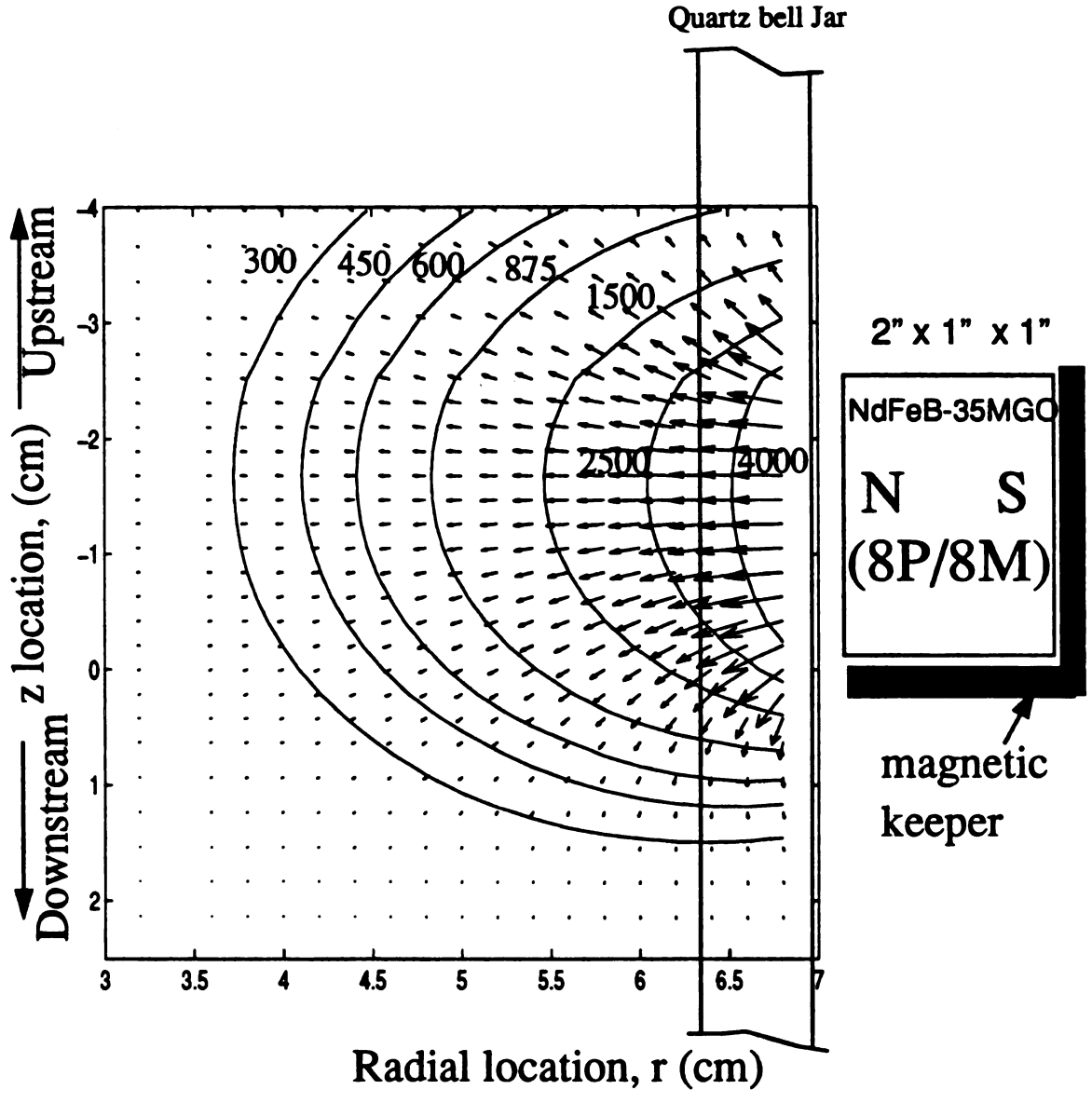

Figure 6.3 (a) The contour plot of static B-field in Gauss at $\phi = 0^0$ plane in 8P/8M (in front of a magnet).
Also, the magnetic field pattern (both the direction and magnitude) are also shown in associated needle plot.

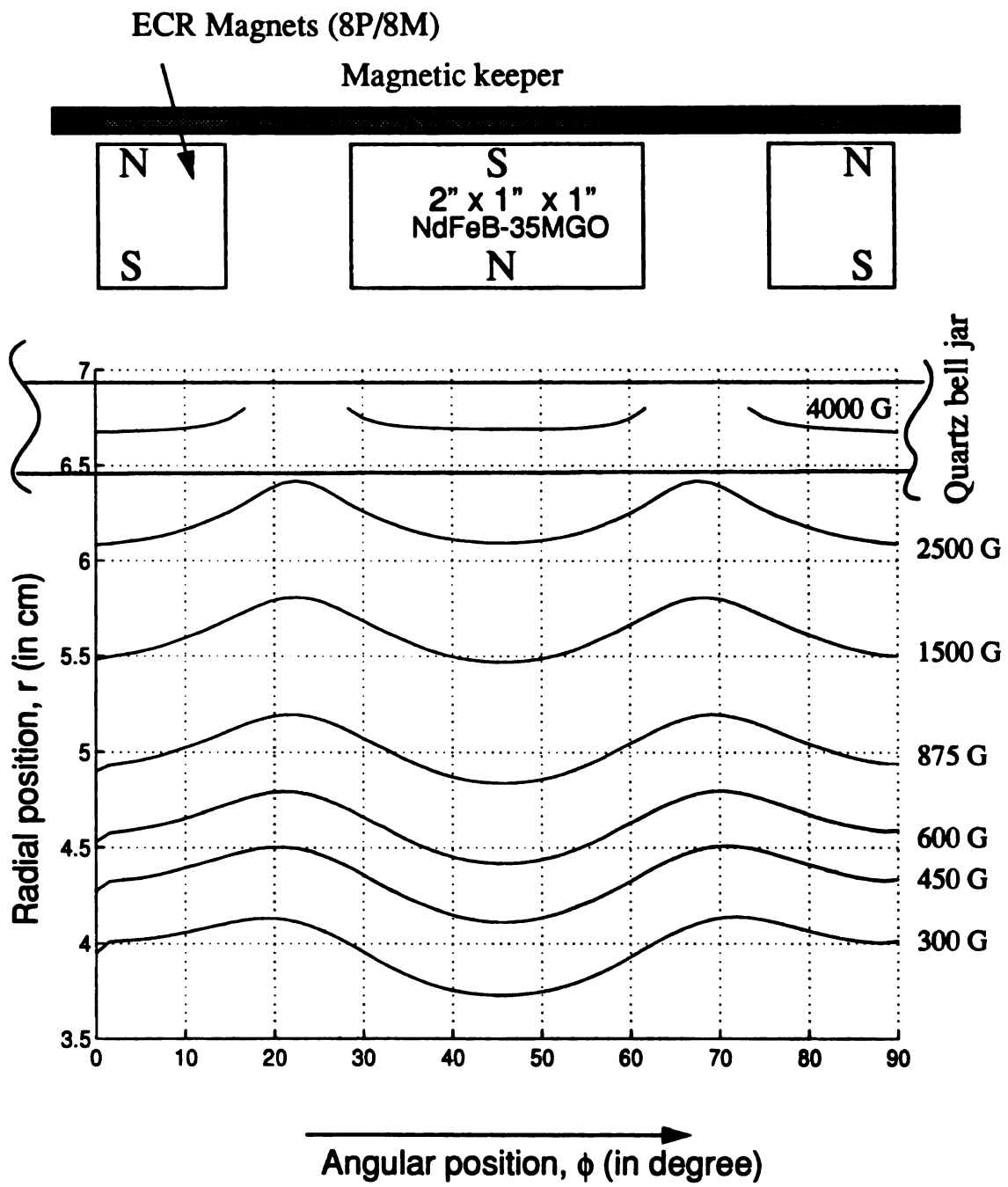

Figure 6.3 (b) The contour plot of total B-field vs. r-ϕ plane at z = -1.27 cm in 8P/8M.

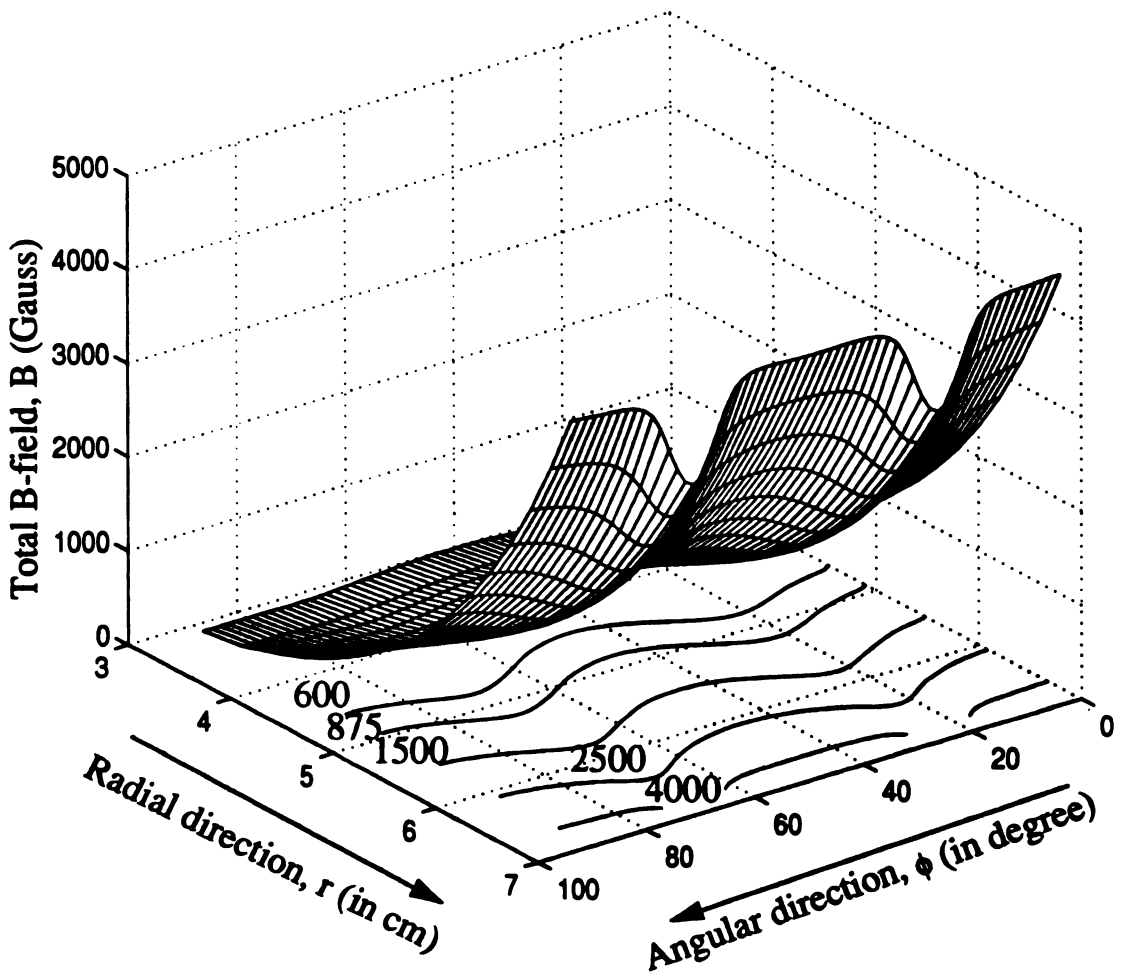

Figure 6.3 (c) Mesh and contour plot of the total magnetic flux B vs. r-ϕ at z = -1.27 cm (8P/8M case).

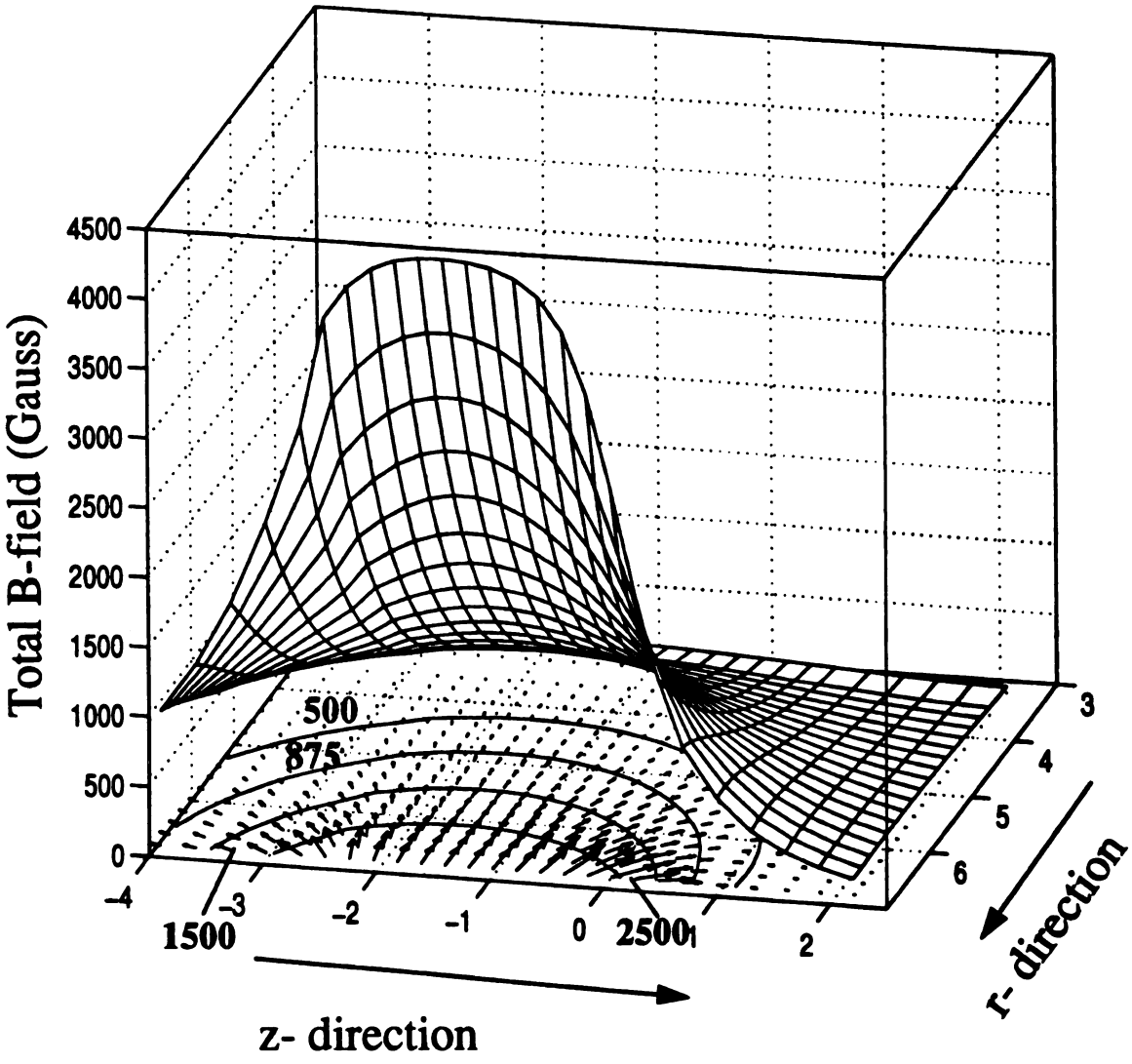

Figure 6.3 (d) The combined mesh, contour and needle plots of the total magnetic flux B vs. r-z plane at $\phi = 0^{o}$ (8P/8M case).

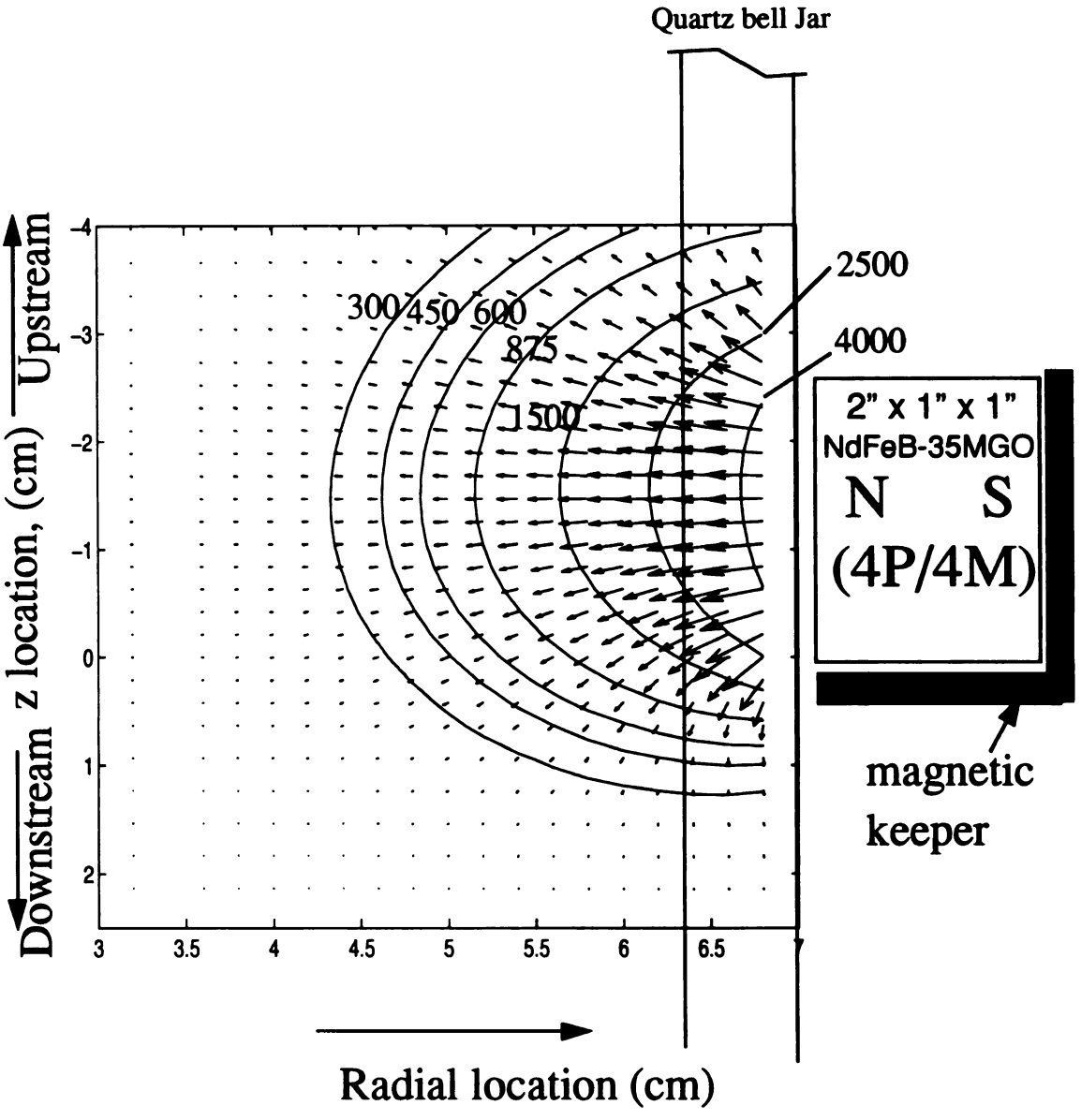

Figure 6.4 (a) The contour plot of static B-field in Gauss at $\phi = 0^0$ plane in 4P/4M (in front of a magnet).
Also, the magnetic field pattern (both the direction and magnitude) are also shown in associated needle plot.

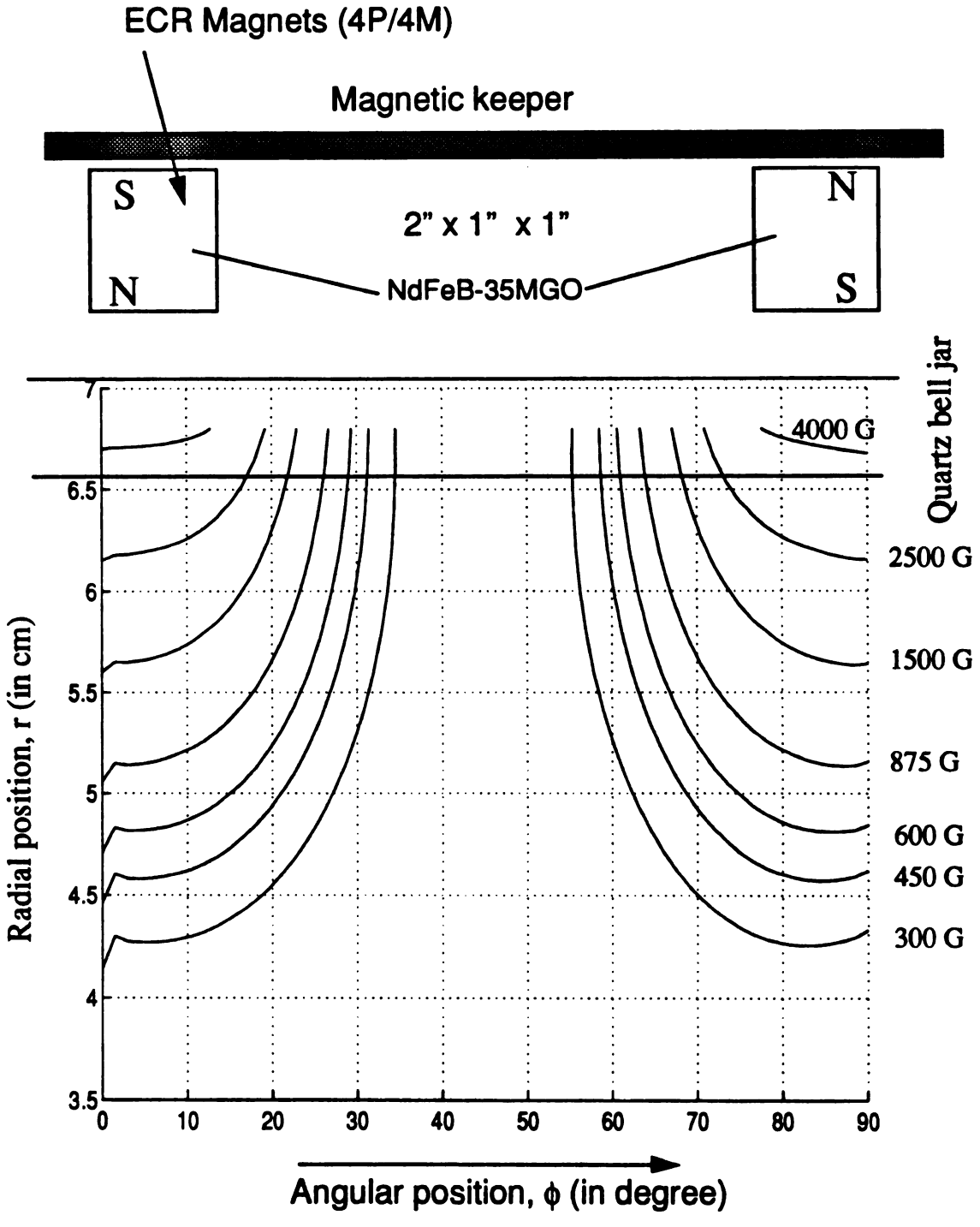

Figure 6.4 (b) The contour plot of total B-field vs. r-ϕ plane at z = -1.27 cm in 4P/4M configuration.

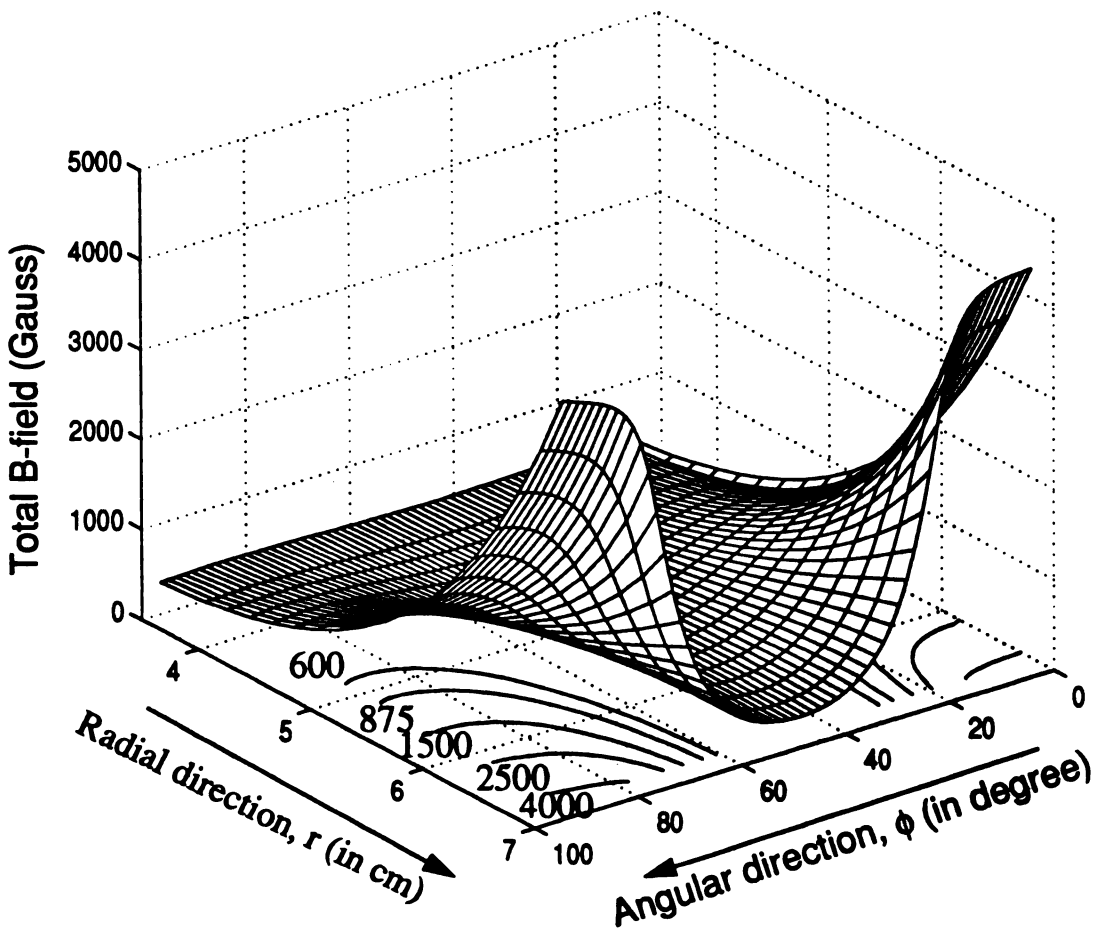

Figure 6.4 (c) Mesh and contour plot of the total magnetic flux B vs. r-ϕ at z = -1.27 cm (4P/4M case).

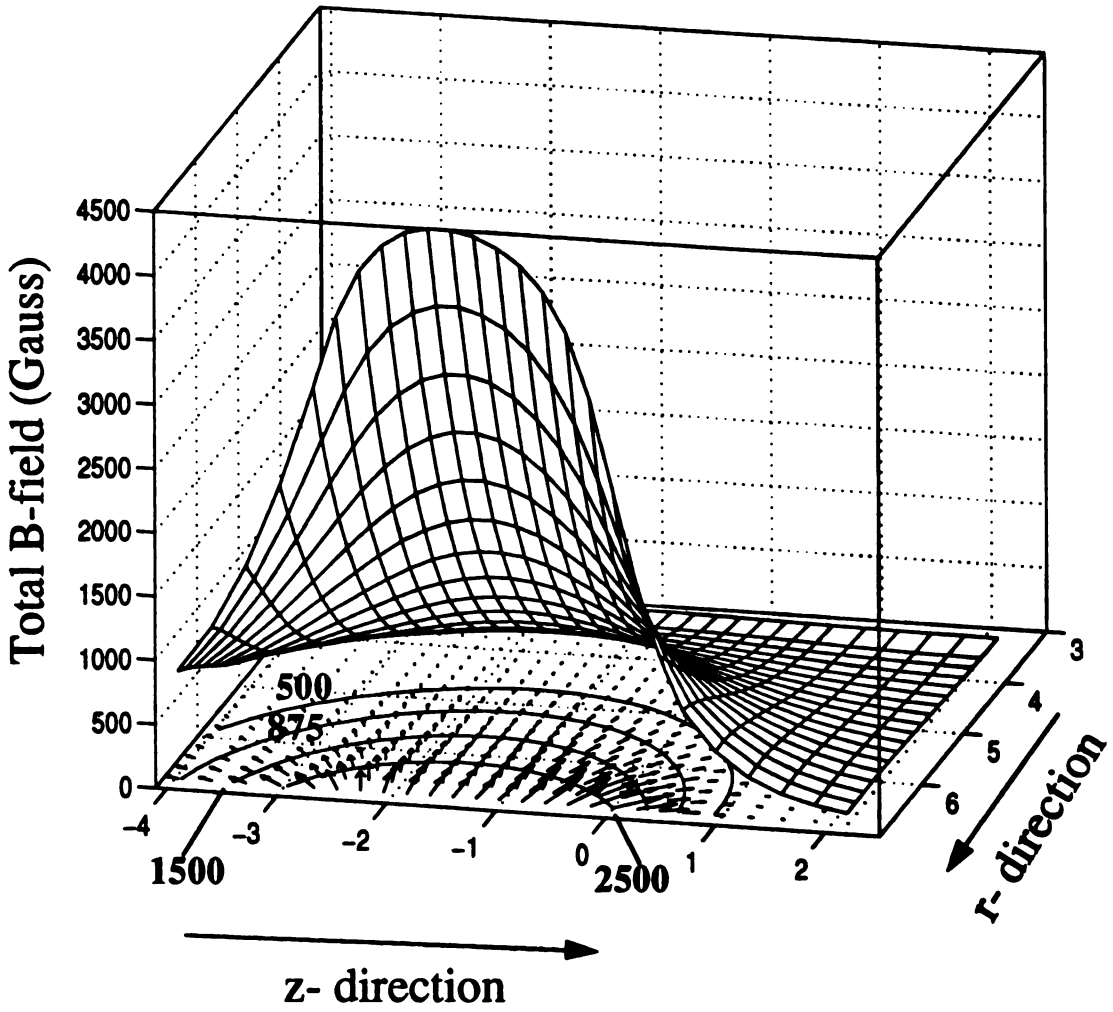

Figure 6.4 (d) The combined mesh, contour and needle plots of the total magnetic flux B vs. r-z plane at $\phi = 0^0$ (4P/4M case).

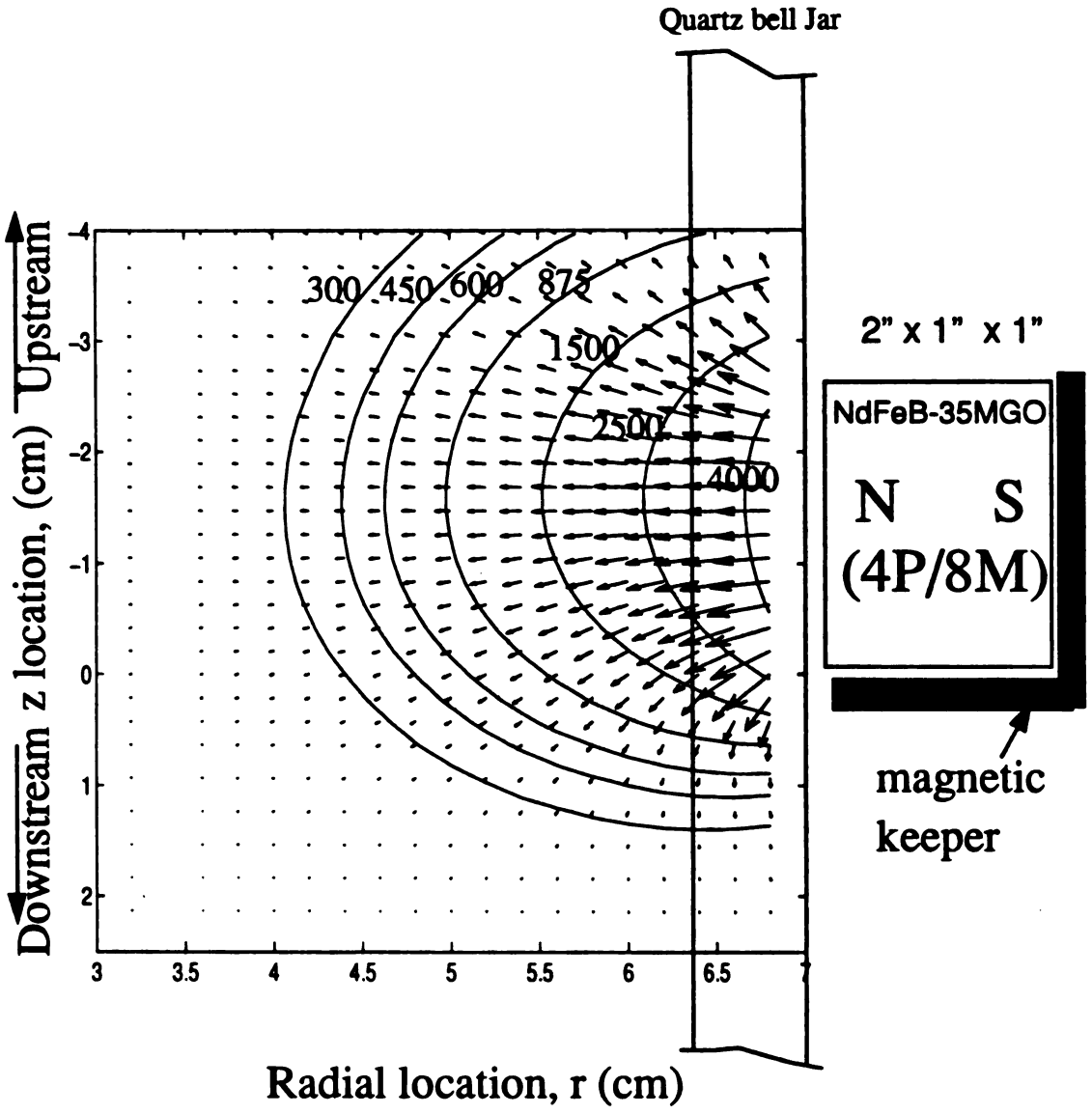

Figure 6.5 (a) The contour plot of static B-field in Gauss at $\phi = 0^0$ plane in 4P/8M (in front of a magnet).
Also, the magnetic field pattern (both the direction and magnitude) are also shown in associated needle plot.

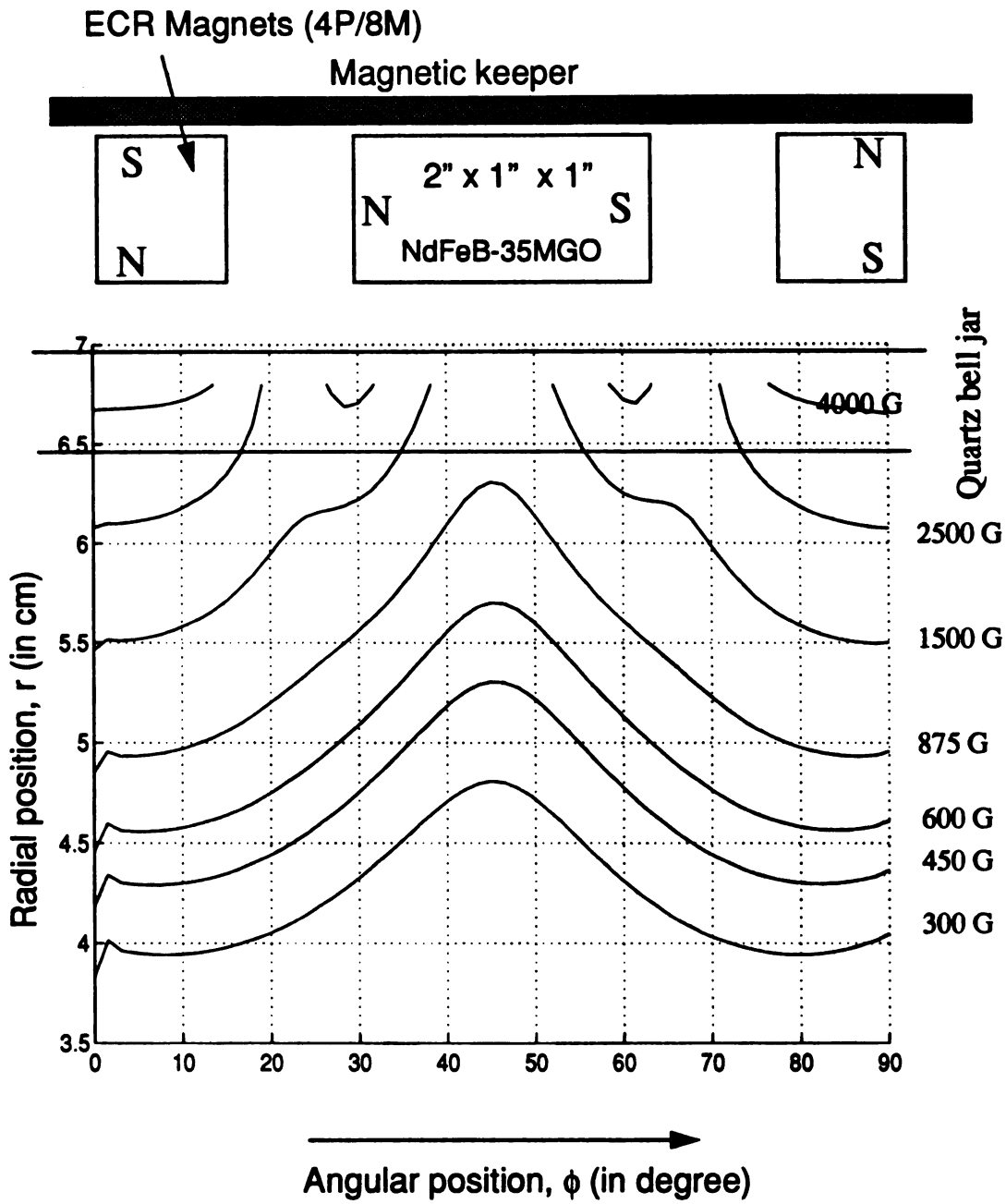

Figure 6.5 (b) The contour plot of total B-field vs. r-ϕ plane at z = -1.27 cm in 4P/8M.

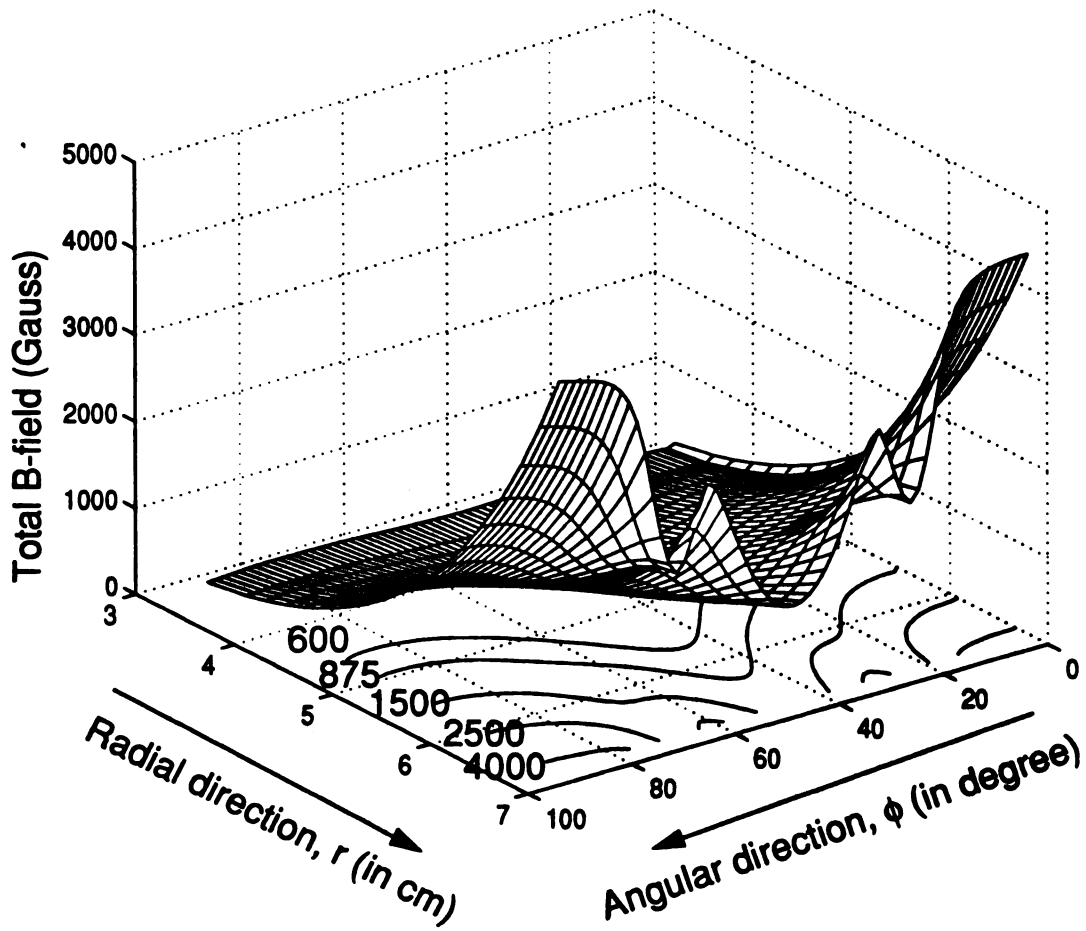

Figure 6.5 (c) Mesh and contour plot of the total magnetic flux B vs. r-ϕ plane at z = -1.27 cm (4P/8M case).

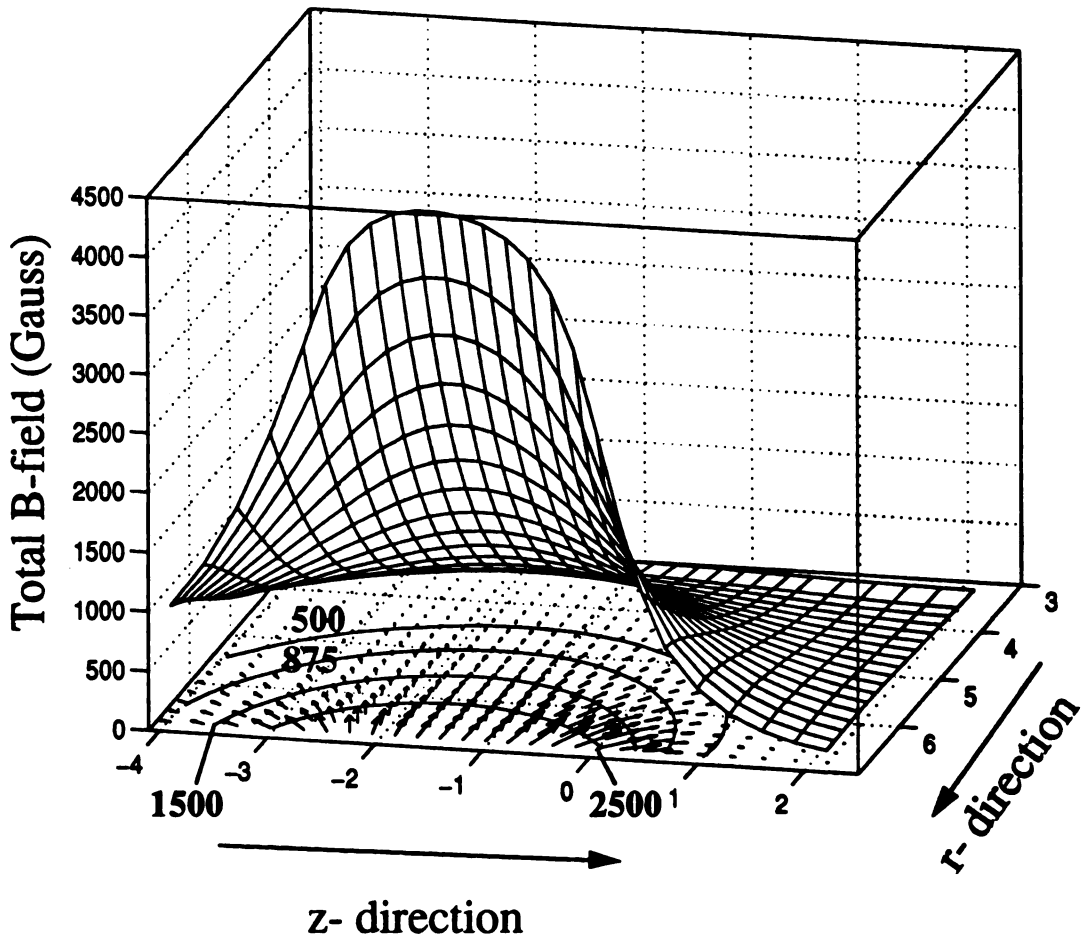

Figure 6.5 (d) The combined mesh, contour and needle plots of the total magnetic flux B vs. r-z plane at $\phi = 0^{o}$ (4P/8M case).

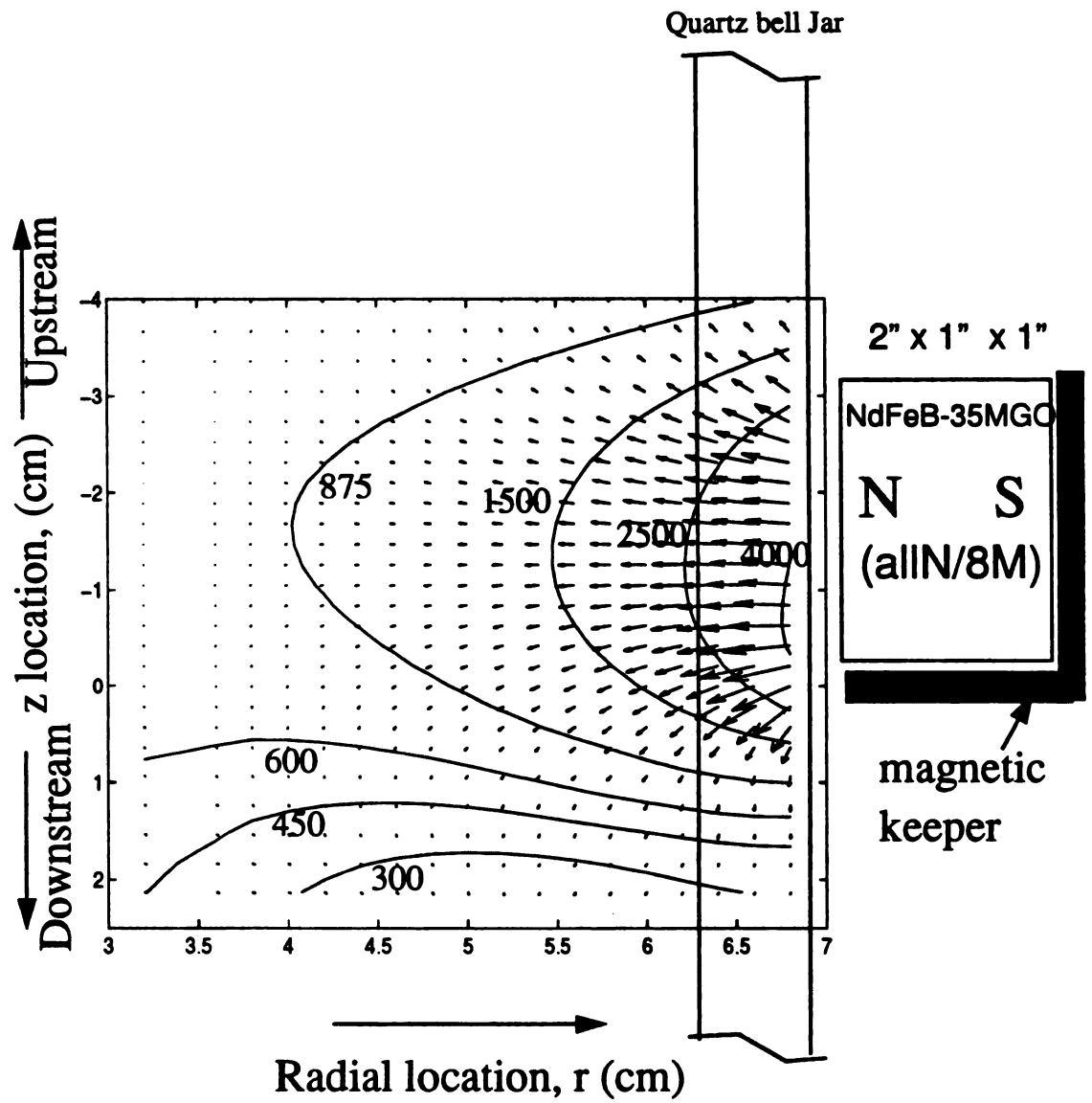

Figure 6.6 (a) The contour plot of static B-field in Gauss at $\phi = 0^0$ plane in allN/8M (in front of a magnet).
Also, the magnetic field pattern (both the direction and magnitude) are also shown in associated needle plot.

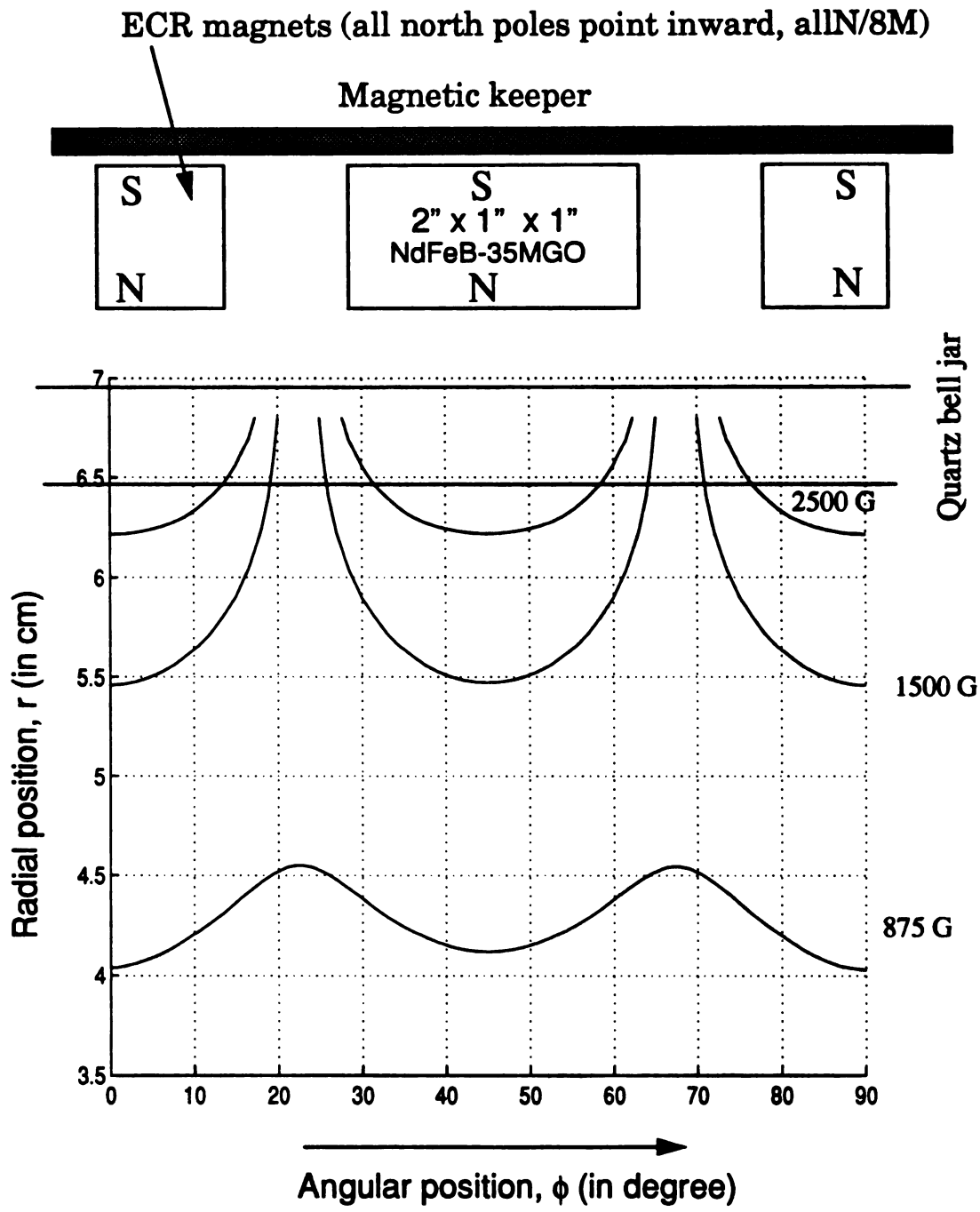

Figure 6.6 (b) The contour plot of total B-field vs. r-ϕ at z = -1.27 cm in allN/8M.

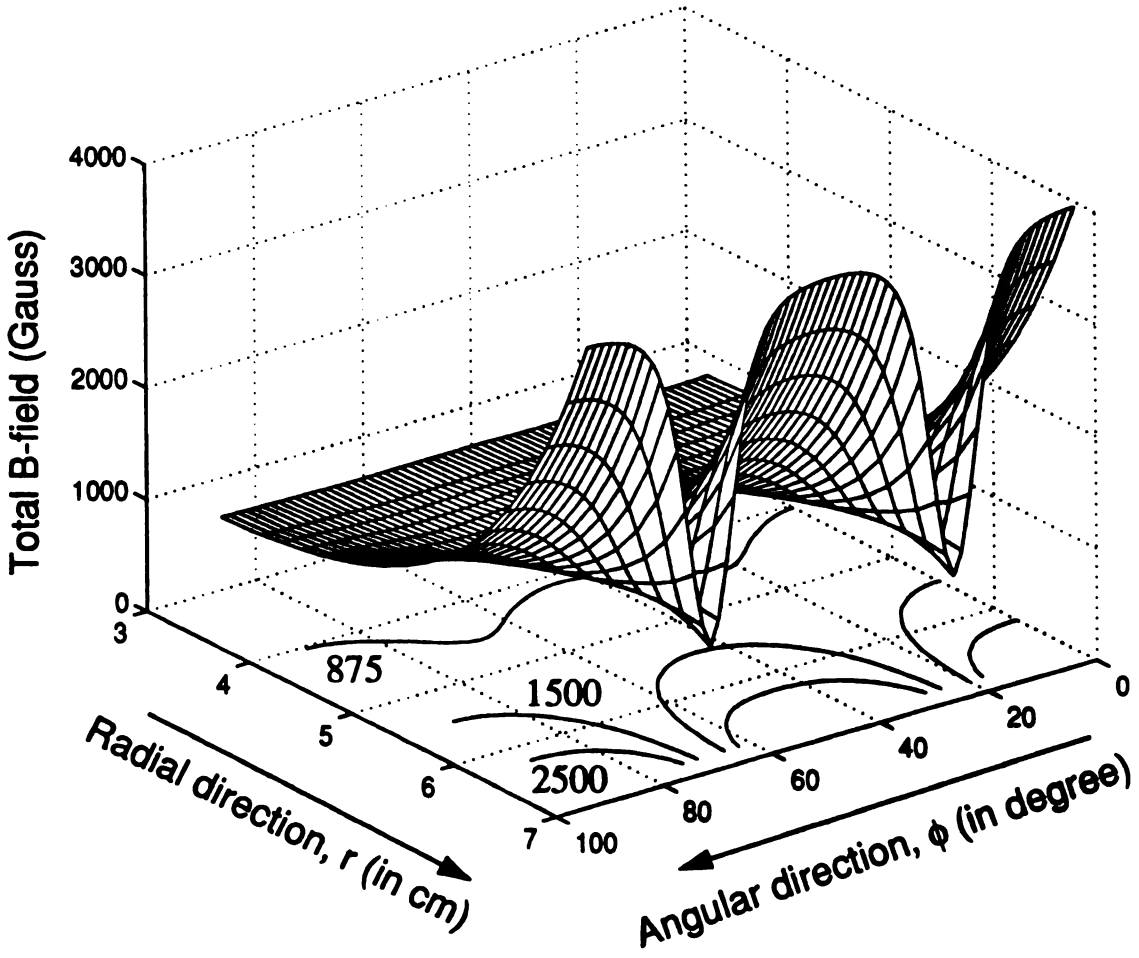

Figure 6.6 (c) Mesh and contour plot of the total magnetic flux B vs. r-ϕ plane at z = -1.27 cm (allN/8M case).

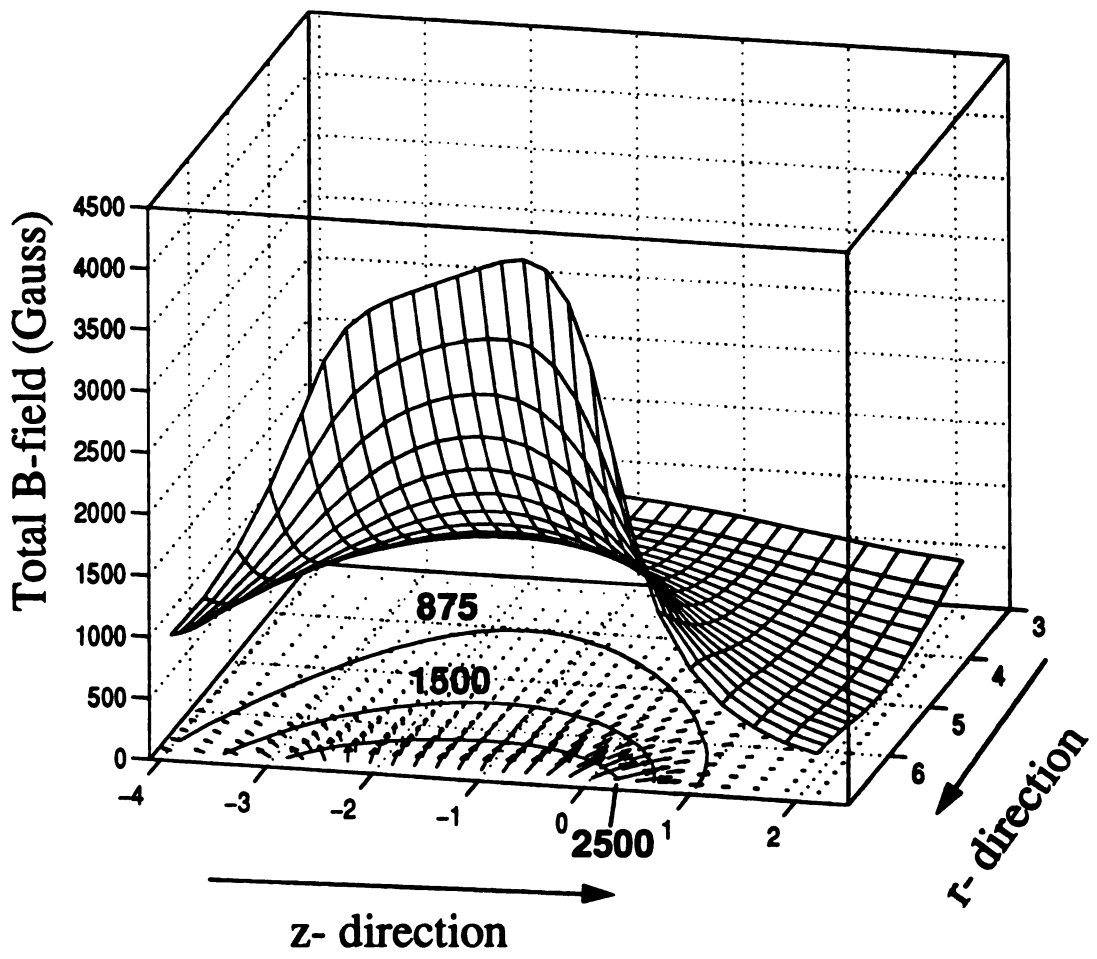

Figure 6.6 (d) The combined mesh, contour and needle plots of the total magnetic flux B vs. r-z plane at $\phi = 0^o$ (allN/8M case).

magnetic cusps between the adjacent magnets. In addition, all magnetic field configurations except the 4P/4M have a continuous contour of 875G-ECR region that lies entirely with the discharge zone at z = -12.7 cm. As shown in Figure 6.4 (b), only the 4P/4M configuration ECR surface contour does not lie entirely within the quartz cylinder at any constant z-plane. Thus as shown below, the 4P/4M configuration has the smallest ECR surface available in the discharge region.

For a more quantitative sense, Table 6.1 gives the numerical integration of the 875-Gauss area within the discharge region for these four ECR magnet configurations. Except of the 4P/4M configuration, all other three configuration have comparable ECR surfaces inside the discharge volume.

Table 6.1 Calculated ECR area for different magnet configurations

ECR configurations	8P/8M	4P/4M	4P/8M	allN/8M
ECR area (cm^2)	~86	~48	~84	~77

Note that the allN/8M does not have multipole confinement configuration. Once electrons are created in the discharge region, they can easily escape in either upstream or downstream directions. Or, in other word, the time for fast electrons spent within the active discharge volume in allN/8M configuration is much shorter than those electrons in multipolar magnetic field configurations, in which electrons can travel along the connecting magnetic field lines and hop around these magnetic cusps for further ionizations/excitations.

Another observation is on the effect of magnet keepers. As shown in the contour plots at constant ϕ plane, B-fields are much more confined and reduced in the downstream locations (defined as $z > 0$) than in the upstream locations (defined as $z < 0$). That is the reason we could not reduce simulation region in z-direction by symmetry because the bottom iron keeper did shield the magnetic fields from the downstream region.

6.4 Measurement of B-Fields

The above simulation of magnetic field seems to be plausible for estimating both the magnetic field strengths and pattern. In order to verify the simulation results, two simple experimental methods were employed to identify the experimental field pattern and measure the field strengths, and then to compare the experimental magnetic fields with the numerically simulated magnetic fields. They are the iron powder method and Hall-effect probe B-field measurement.

6.4.1 Iron powder method

Using the well-known property that magnet fields attract iron, a simple quick method is employed to observe the magnetic field pattern. First put a thin piece of fiber glass on **top** of the ECR magnets. Then shower the iron powder slowly and uniformly across the fiber glass. Due to the strong ECR magnetic field, the iron powder on the fiber glass follows the nearby magnetic field pattern.

Figure 6.7 actually shows the distribution of the iron powder, which agrees reasonably well with the simulated magnetic field pattern. For example, the B-field is maximum near the magnets corresponding to a higher density of the powder near the magnetic poles, etc. Also, the iron powder trails from one pole to another are aligned well with the simulation results. The advantage of this method is to provide quick and visual result of the magnetic field pattern but it lacks the quantitative measures required to verify the numerical simulations shown in Figure 6.3.

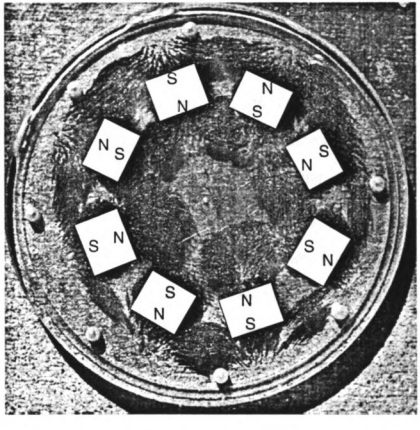

Figure 6.7 Visual iron powder pattern of 8P/8M ECR configuration.

6.4.2 Hall-effect probe B-field measurement

The magnetic deflection of flowing charge carriers in a semiconductor is known as the Hall-effect [131]. This property is usually used for measurement of the semiconductor properties. On the other hand, with a known semiconductor, it can be used as a probe [132] for measurement of local magnetic field. Using a F. W. Bell, Inc. Model 600(A) Gaussmeter with a transverse type Gaussmeter probe, the spatial magnetic field magnitudes were measured and then were compared with the simulation results. The probe was manually positioned and oriented at different locations and directions with a two-dimensional mechanical positioner. Figure 6.8 shows both the measured data in 8P/8M configuration at $\phi = 0^o$ and the simulated result. They match quite good with each other. Figure 6.9 compares the simulated curve with experimental measurement in 8P/8M configuration at the constant $\phi = 22.5^o$ plane between the magnets. They also show good agreement for small radial locations inside the discharge volume and begin to deviate from the simulation when the radial distance becomes larger.

To explain the discrepancies between the measurements and the simulated results, several factors should be taken into account. First the Gaussmeter has an accuracy of 4%. Second the simulated shape for each magnet is wedge shaped instead of the actual rectangular shape due to the cylindrical coordinate system employed in the numerical simulations. That is why significant errors occur around the gaps between the magnets at $\phi = 22.5^o$ rather than at $\phi = 0^o$. One last remark on the possible source of error comes from the presumed constant permeability of the keeper material during simulation.

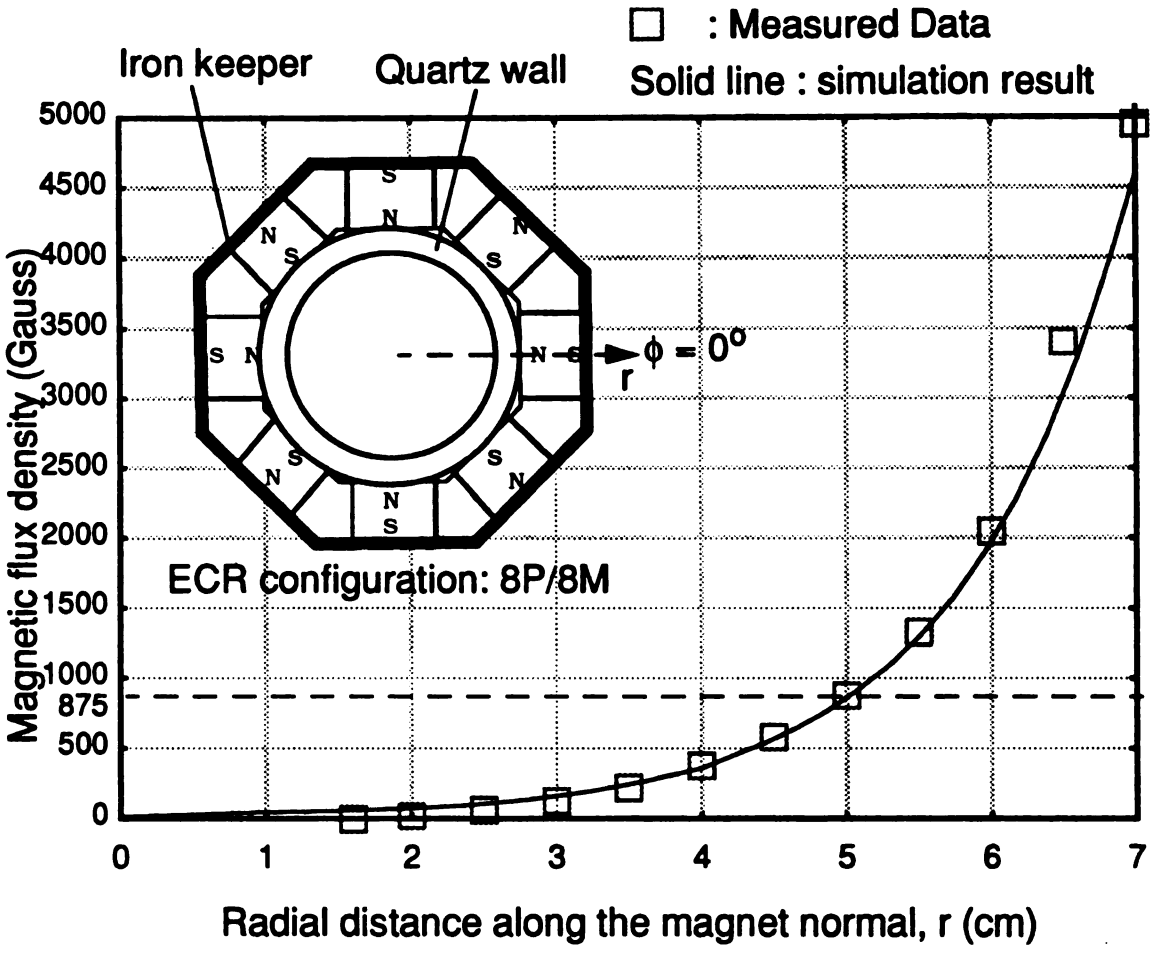

Figure 6.8 Comparison of measured B and calculated B in 8P/8M configuration vs. r at z = -1.27 cm and along $\phi = 0^{o}$.

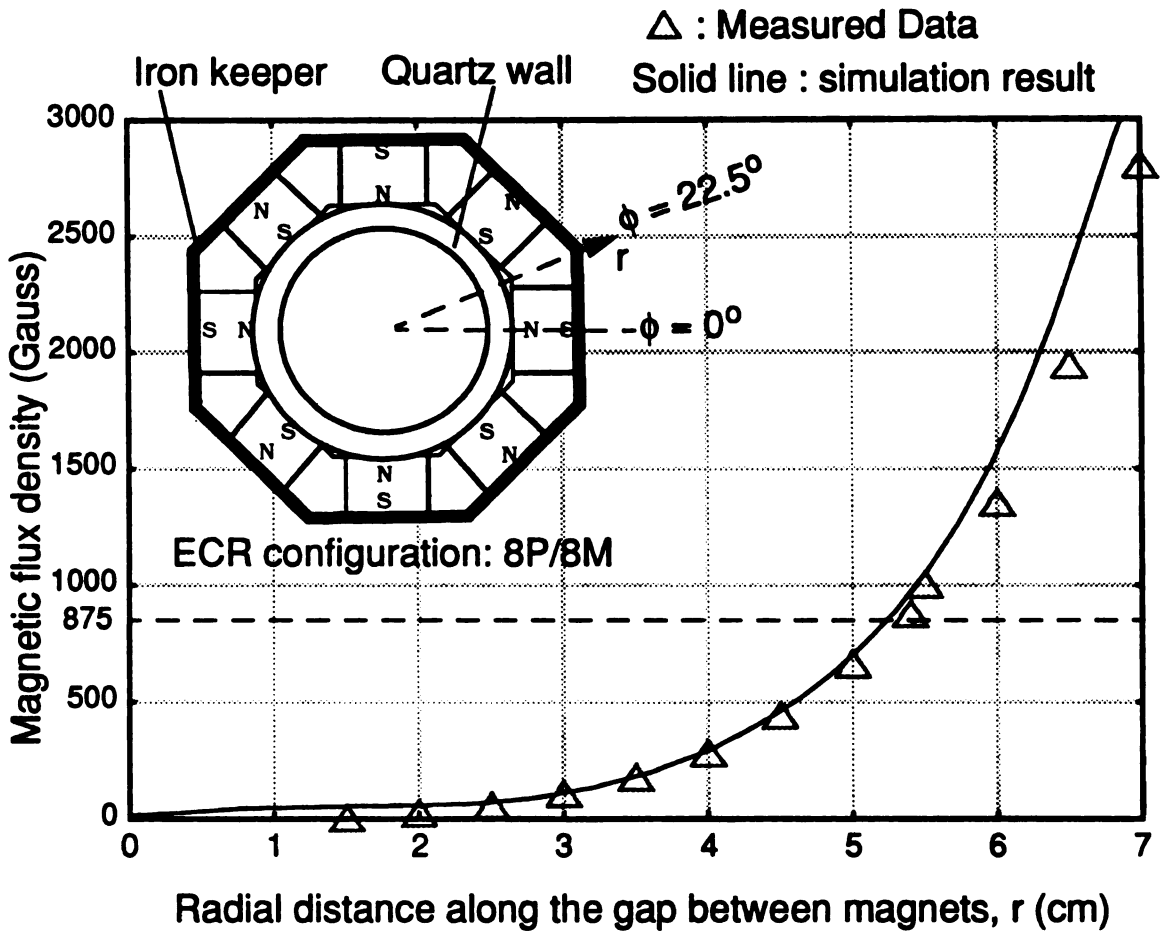

Figure 6.9 Comparison of measured B and calculated B in 8P/8M configuration vs. r at z = -1.27 cm and along $\phi = 22.5^{o}$.

Note that the μ of keeper is also a nonlinear function [133] of applied magnetic field. Iterations of complicated simulation processes are required until they reach the consistent values of V_m, μ, and B. Fortunately, the keepers occupy relatively small volume in our total simulation region and the assumed value of permeability gives an average of the nonlinear effect. Hence, the resulting error is tolerable.

6.5 Concluding Remarks

In this chapter, four different magnetic configurations employed in this thesis are described and the magnetic flux density in the discharge region is simulated for each configuration. The simulation principle, grid size, geometry and their boundary conditions are reviewed. Simulation results in several contour plots and vector plots show the B-field magnitudes and directions for various magnet configurations. Special attention is paid to the 875 Gauss regions. Finally, a comparison between some measured B-field data and the simulation results indicates good agreement between the experimental data and the predicted magnetic flux densities. Possible sources of error are also discussed.

The excellent agreement between the simulation results and measured data suggests that the numerical simulation method is valid and trustworthy. Hence, similar simulations of static magnetic fields for other ECR geometries can aid in future static magnetic field design studies. Simulations can be carried out in advance to check both the spatial B-field magnitudes and patterns for different permanent magnet geometries. In addition, it saves time and money by simulating

different types of magnets and magnet configurations before the actual physical construction of an ECR magnet configuration.

From the calculated ECR surface area, we know that the ECR region in 4P/4M configuration is the smallest among the chosen four magnet configurations. This indicates that the 4P/4M configuration has the smallest input power coupling volume. Thus for the same amount of absorbed power, the expected electric field must be higher to sustain the discharge in the 4P/4M configuration than in the other three ECR magnet configuration.

However, looking merely at the available size of ECR region is not sufficient to describe ECR coupling since the magnitude and the direction of the impressed electric field are also critical. Not all locations on an ECR surface area have the same effect on the microwave power absorption. For example, by making the simplifying assumption that the discharge under investigation is a cold magnetized plasma, the time-average power absorbed per differential volume ($\bar{P}_{abs}$) in the presence of a static magnetic field becomes [34, 134],

$$\bar{P}_{abs}(\vec{r}) = \frac{n_e \nu_e e^2}{4m_e}\left\{\left(\frac{\omega_{ce}^2 + \omega^2 + \nu_e^2}{\left(\omega_{ce}^2 + \nu_e^2 - \omega^2\right)^2 + 4\omega^2\nu_e^2}\right)\left|\vec{E}_{\perp}\right|^2 + \left(\frac{1}{\omega^2 + \nu_e^2}\right)\left|\vec{E}_{\parallel}\right|^2\right\} \quad (6.9)$$

where n_e is the electron density, ν_e is the effective collision frequency for electrons, $E_{\perp}$ is the electric field component perpendicular to the static magnetic field, and $E_{\parallel}$ is the electric field component parallel to the static magnetic field. The first term is due to the ECR heating and the second term results from purely

Joule heating. When at low pressure, i.e. $\nu_e << \omega$, there is an electron cyclotron resonance when $\omega \cong \omega_{ce}$. This resonance will be more pronounced when $E_\perp$ is not small. That is the ECR region where the a.c. electric field is perpendicular to the static magnetic field is the most "effective" ECR heating zone. Even with the same static magnetic field strengths and patterns, proper alignment the impressed electric field with the static magnetic field such that large amount of region are perpendicular to each other improves the efficiency of the ECR reactor coupling. While the three configurations (allN/8M, 8P/8M and 4P/8M) have similar available ECR surface area, it is difficult to decide which one is the best without the exact knowledge of the impressed electric fields.

On the other hand, magnetic fields in discharge region also provide confinement effect for electrons. Even though the allN/8M configuration has a comparable size of ECR region with 8P/8M and 4P/8M configurations, it does not have the multipole magnetic type field pattern as shown in Figure 6.6. Electrons are expected to be "pushed out" (upstream and downstream) of discharge region. This suggests that the fast electrons in allN/8M will not have as many chances as in multipolar magnetic type field configurations to perform ionization and excitation roles. The higher diffusion loss associated with the allN/8M configuration suggests lower steady state plasma density.

Chapter 7

The Behavior and Performance of MPDR™-13 ECR Plasma Source

- 7.1 Introduction
- 7.2 Electric Field Measurements

7.2.1 Introduction

7.2.2 End feed applicator

7.2.2.A Discharge ignition and tuning adjustments to a well-matched resonant mode in 8P/8M configuration

7.2.2.B Identification of the resonant EM modes in 8P/8M configuration

7.2.2.C Electric field strength in 8P/8M configuration

7.2.2.D Power coupling efficiency and Quality factor of the discharge loaded cavity

7.2.3 Side feed applicator

7.2.3.A Discharge ignition and tuning adjustments to a well-matched resonant mode in 8P/8M configuration

7.2.3.B Identification of the resonant EM modes in 8P/8M configuration

7.2.3.C Electric field strength in 8P/8M configuration

7.2.3.D The EM modes and electric field strengths for the different magnetic field configurations

7.2.3.E Power coupling efficiency and Quality factor of the discharge loaded cavity

7.2.4 Summary and discussion of electric field measurements

7.2.4.A Mode patterns

7.2.4.B Operation trade-off

7.2.4.C Electric field strength

7.2.4.D Microwave power coupling efficiency

• 7.3 Ion Density Measurements

7.3.1 End feed applicator

7.3.1.A Magnitude of the Ion density versus power and pressure

7.3.1.B Spatial variation of the ion density

7.3.2 Side feed applicator

7.3.2.A Ion density versus power, pressure and flow rate

7.3.2.B Spatial variation of the ion density

7.3.3 Comparison of density performance

7.3.3.A Magnitude of the ion density

7.3.3.B Cross sectional density uniformities

7.3.3.C Ion production cost

7.3.4 Influence on ion density by substrate bias

7.3.5 Influence on ion density by downstream confinement magnetic field

• 7.4 Plasma Potential and Electron Energy Measurements

7.4.1 Introduction

7.4.2 Electron energy distribution function (EEDF)

7.4.3 Plasma potential and Electron temperature

7.4.3.A Side feed applicator

7.4.3.B End feed applicator

• 7.5 Ion Energy Measurements

7.5.1 Ion energy distribution function (IEDF) and bias effect

7.5.1.A General IEDF shape and characterization

7.5.1.B IEDF vs. dc bias

7.5.2 Spatial ion energy variations

7.5.3 Ion energy versus power and pressure

7.5.4 Ion energy in pure hydrogen plasma discharges

7.5.4.A Spatial ion energy variations

7.5.4.B Ion energy versus pressure and power

7.5.4.C Summary

• 7.6 Concluding Remarks

Chapter 7

The Behavior and Performance of MPDR™-13 ECR Plasma Source

7.1 Introduction

The objectives of the experiments reported in this chapter are two-fold. First, the measured experimental data that is presented establishes the MPDR™-13 performance in electro-positive gas discharges. Secondly, several reactor design variables such the end feed versus side feed excitation, different ECR magnet configurations, and etc., are evaluated. The experimental data presented in this chapter, together with other MPDR™ experimental characterizations, which have been reported by co-workers [53,112,135] in recent years, provide a comprehensive experimental data set that establishes the performance of MPDR™ plasma sources over a wide range of input experimental conditions, plasma reactor sizes and other design variations.

In this chapter, experimental measurements of a selected group of internal variables, **X**, and output variables, **Y**, of the MPDR™ -13 are presented versus a set of multidimensional input variable space, **U**. Figure 7.1, Tables 7.1, 7.2, 4.2 and 4.3 summarize the experimental system input, internal and output variables,

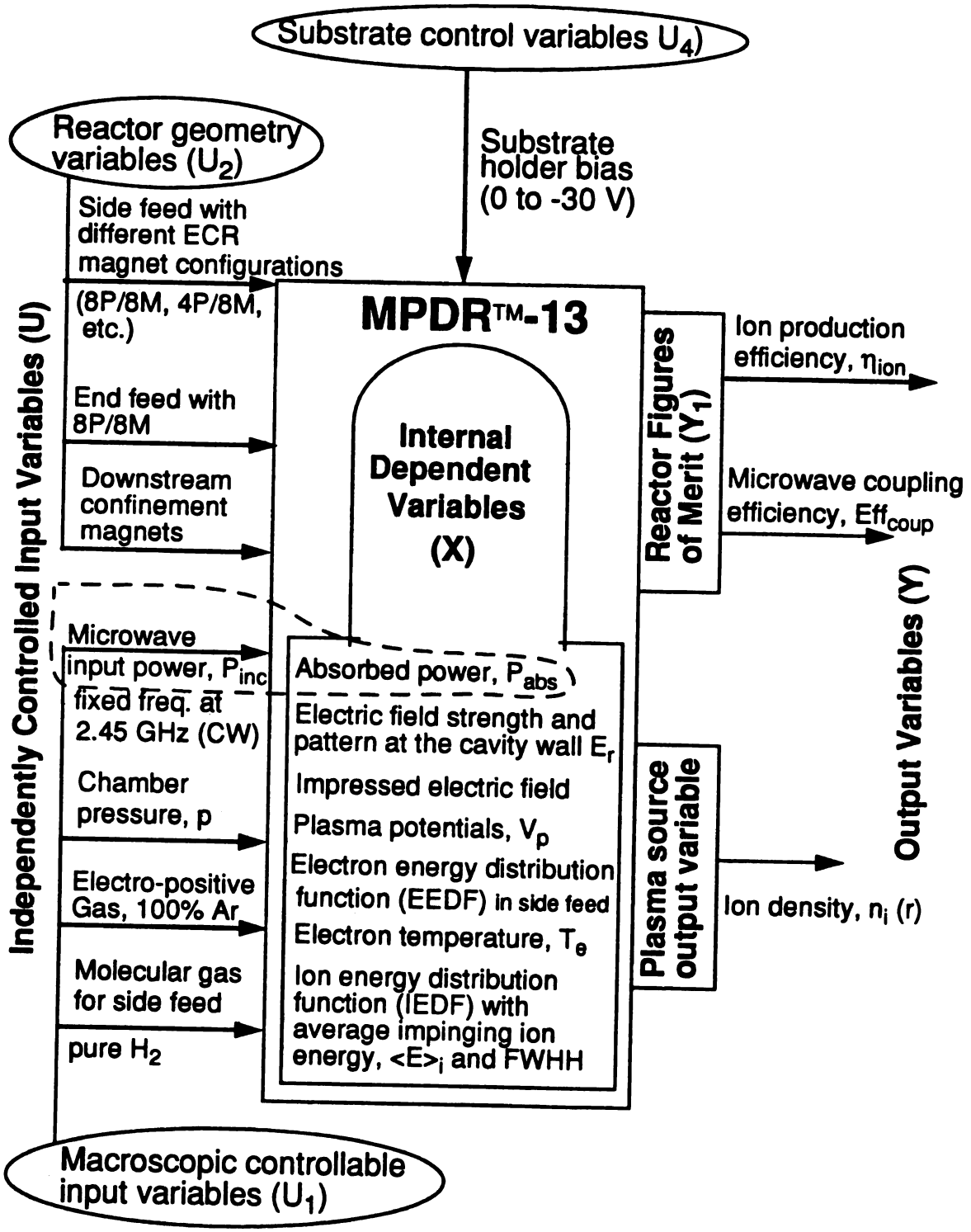

Figure 7.1 System variables investigated in this chapter.

Table 7.1 Important Input Variables (U) for end feed applicator

Input variables (U)	Variable description	Ranges for end feed applicator
Macroscopic controllable input variables U_1	Microwave absorbed power, P_{abs} and frequency, f	150- 325 W fixed at 2.45 GHz (CW)
	Input gas	fixed at100% argon
	Pressure, p with fixed flow rate, f_t	Fixed flow rate at 50 sccm as pressure varied 2.5 - 7 mTorr
Reactor geometry variables U_2	Impedance matching network tunings: Cavity height, L_s Excitation probe depth, L_p	examined range for EM resonance mode searching L_s: 67 -190 mm L_p: 0 - 40 mm
	Applicator type & size	Cylindrical 17.78 cm diameter cavity applicator
	Discharge size	Confined by dome shaped quartz tube Approximate size of a cylinder with radius 6.25 cm, height ~8 cm
	ECR magnet configurations	fixed at 8P/8M only
Substrate control variables U_4	Substrate holder bias	0 to -30 V for IEDF

Table 7.2 Important Input Variables (U) for side feed applicator

Input variables (U)	Variable description	Ranges for side feed applicator
Macroscopic controllable input variables U_1	Microwave absorbed power, P_{abs}(W) and frequency, f	200 - 720 W fixed at 2.45 GHz (CW)
	Input gases	(1) fixed at100% argon (2) pure H_2 (2 - 4 mTorr)
	Pressure, p / Flow rate, f_t	0.5 mTorr (2 sccm) to 2 mTorr (50 sccm)
Reactor geometry variables U_2	Applicator type & size	Cylindrical 17.78 cm diameter cavity applicator
	Discharge size	Confined by dome shaped quartz tube Approximate size of a cylinder with radius 6.25 cm, height ~8 cm
	Impedance matching network tuning positions: Cavity height, L_s Excitation probe depth, L_p	examined range for EM resonance mode searching L_s: 69 -165 mm L_p: 0 - 28 mm
	ECR magnet configurations	8P/8M, 4P/4M, 4P/8M, and allN/8M
	Downstream confinement magnets	(1) with and without downstream magnets (2) different diameters of downstream confinement area (3) different downstream magnetic configurations
Substrate control variables U_4	Substrate holder bias	0 to -30 V for density and IEDF

and their associated experimental ranges. The input variable space, **U**, is divided into subgroups: (1) controllable input variables, $\mathbf{U_1}$, (2) reactor geometry variables, $\mathbf{U_2}$, and (3) substrate control variables $\mathbf{U_4}$. Unless otherwise noted, all experiments were performed with the MPDR™-13 operating in a matched condition (reflected power < 5% of P_{inc}), and operating in pure electropositive argon gas discharges. For the experimental performance data presented in this chapter, the reactor absorbed power, P_{abs}, is only slightly lower than the incident power, P_{inc}. Throughout this chapter the incident power is essentially equal to the absorbed power, and thus these variables as indicated by the dashed lines in Figure 7.1, are considered as a single input variable P_{abs}.

Two different, potentially important reactor geometries, which are shown in Figure 3.3, were investigated: (1) the side feed electromagnetic excitation and (2) the end feed EM excitation. The experimental variable space for these two reactor geometries is described in Tables 7.1 and 7.2 for the respective side feed and the end feed reactor geometries. As indicated, the input variables, $\mathbf{U_1}$, that were experimentally varied for both the side feed and end feed geometries were absorbed power, discharge pressure, and cavity tuning positions (L_p, L_s). For either excitation the applicator size was fixed by employing a 17.78 cm diameter cylindrical cavity applicator and the discharge size was also fixed by employing a 12.5 cm inside diameter quartz bell jar.

Unless specifically indicated, all experiments were performed with an electropositive argon gas where the pressure was varied between 0.5 and 7 mTorr. However, the pressure and flow rate regimes were different for the two

reactor excitations. In most side feed experiments, the flow rate varied directly with pressure. Thus the pressure and flow rate were considered to be a single variable for the side feed reactor geometry. This relationship between pressure and flow rate is shown in Figure 4.3. At pressures above 2 mTorr, i.e. the pressure regime for the end feed configuration, the flow rate was fixed at 50 sccm and the throttle valve was varied to achieve a desired pressure from 2 to 7 mTorr. This flow rate was established and fixed because the maximum flow rate of the Tylan flow controller is around 50 sccm for argon gas.

It should be noted that since the experimental evaluation of the end feed and the side feed took place during different time periods, their input variable space covered a slightly different power and pressure regime. The side feed experiments were mainly performed over 0.5 to 2 mTorr pressure regime while the end feed experiments were mostly carried out over 2.5 to 7 mTorr pressure regime. The side feed absorbed power was varied from 200 to 700 W while the end feed absorbed power was varied from 150 to 325 W. The input variable space for the two sets of experiments had only a limited, common input variable operating regime and thus a direct comparison between these two reactor configurations was limited to the pressure regime of about 2 - 3 mTorr.

Besides the common input variable space, U_1, the experiments employing the side feed excitation investigated the changes in plasma source performance versus a number of additional input variables (see Table 7.2). Some important input reactor geometry variables investigated with the side feed excitation were (1) variation in ECR magnetic field configuration, i.e. 8P/8M, 4P/4M, etc., and (2)

operation with and without downstream confinement magnets. As is also indicated in Table 7.2, a number of experiments were also performed using pure hydrogen gas.

The performance of the MPDR™-13 plasma source was evaluated by experimentally measuring a selected group of internal and output variables as the input variable space was independently varied. The measured internal and output variables are listed in Tables 4.2 and 4.3. As indicated in Table 4.2, the output reactor performance was established by determining the ion production cost, η_{ion}, and microwave coupling efficiency, Eff_{coup}. Since plasma processing is not directly studied in this thesis, the ion/electron densities at the z = 0 cm or z = 3 cm plane were also considered as plasma source output variable. These output variables (**Y**) are used to understand the plasma source behavior as the experiments are varied through the multidimensional input variable space.

Important measured internal variables were either electromagnetic field related variables in the applicator or plasma species related variables at the downstream region. EM related internal variables were the spatial electric field patterns (or variation), the magnitudes of the electric field near the applicator wall and the electric field impressed on the discharge. Measurements of the electric field in the applicator were performed to understand the excited EM field patterns, and the microwave coupling efficiency, and were also used to estimate the electric field impressed within the discharge versus the multidimensional input variable space. When carefully determined, the impressed electric field aids in understanding the heating mechanisms within the discharge. Other measured

internal variables (**X**) were plasma species related. These included the plasma potential, electron energy distribution, electron temperature, ion energy distribution and the average energy of the ions impinging on a substrate. In order to minimize any perturbation of the active discharge region, all plasma diagnostic experiments (probe and ion energy) were conducted in the downstream discharge region ($z > 0$). Some of the experimental data presented in this chapter such as electron temperatures and plasma density, will be compared in Chapter 10 with the global discharge models.

7.2 Electric Field Measurements

7.2.1 Introduction

For an empty, perfectly conducting 17.78-cm i.d. circular cylindrical cavity applicator, the electromagnetic modes that are possible to excite can be displayed in "mode chart" format, i.e. cavity height vs. resonance frequency. This format is shown in Figure 7.2. In Figure 7.2, the classical electromagnetic modes for an ideal cylindrical cavity are plotted as the solid lines by using the standard EM wave textbook formulas [97], i.e.

$$f_{nlq}^{TM} = \frac{1}{2\pi R_A \sqrt{\mu\varepsilon}} \sqrt{p_{nl}^{\,2} + \left(\frac{q\pi R_A}{L_s}\right)^2}, \text{ and} \tag{7.1}$$

$$f_{nlq}^{TE} = \frac{1}{2\pi R_A \sqrt{\mu\varepsilon}} \sqrt{p'^{\,2}_{nl} + \left(\frac{q\pi R_A}{L_s}\right)^2}, \tag{7.2}$$

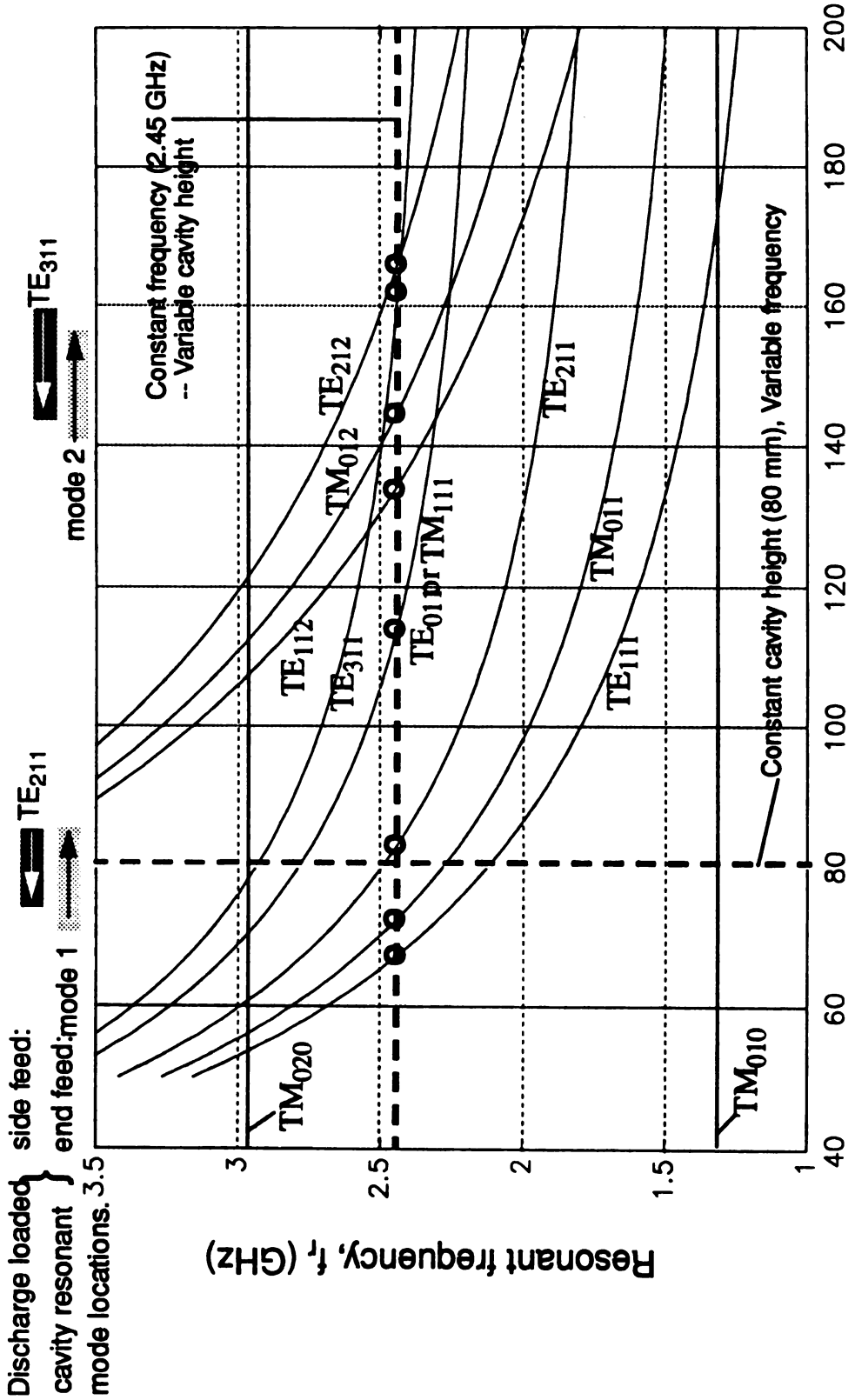

Figure 7.2 Electromagnetic mode chart for an ideal circular cylindrical cavity (dia. = 17.78 cm).

where f_{nlq} is the resonant frequency for TE_{nlq} or TM_{nlq} modes, μ and ε are the permittivity and permeability of the dielectric (or vacuum) filled inside the cavity, R_A and L_s are the applicator cavity radius and cavity height, and p_{nl} and p'_{nl} are the lth roots of Bessel function of the first kind $J_n(x) = 0$ and $J'_n(x) = 0$ respectively. The nomenclature of mode nlq is: n is the number of periodicity in the Φ direction, l is the number of zeros of the field in the radial direction, and q is the number of half waves in the z-direction.

A sinusoidal, constant 2.45 GHz frequency power source was used in the experiments conducted in this thesis. Hence, the intersections (denoted as "o" in Figure 7.2) of mode curves with the (horizontal) operating frequency line ($f = 2.45$ GHz) represent several potential excitation modes. For example, TE_{111}, TM_{011}, TE_{211}, etc. can be excited as the cavity length is increased from 6 cm to 16 cm. However, the presence of plasma discharge, the quartz discharge container, and the input coupling probe itself, etc., may alter the EM mode distribution inside the ideal cavity. Depending upon the method of cavity excitation, certain modes may more easily be excited than the others. Also some EM modes that do not exist in the ideal empty cavity may also be excited when the discharge is present. Thus the L_s locations of the EM modes shown in Figure 7.2 only serve as a very approximate guideline of the locations of the cavity experimental resonances because the excitation antenna, the quartz bell jar and the presence of the plasma discharge will all cause perturbations or shifts of the ideal cavity resonant mode curves.

The experimental measurements described in the Sections 7.2.2 - 7.2.3 are concerned with measuring the magnitude and spatial variation of the impressed electric field in the applicator when the plasma source is operating in a well matched resonant mode. As mentioned in Chapter 5, micro-coaxial E-probes measure both the excited spatial electric field patterns and electric field strengths in the plasma loaded cavity applicators. The sampling hole locations of both side-feed and end-feed cavity shells have previously been described in Section 5.3 and are illustrated in Figure 5.1. The electric field measurement techniques have also been carefully described in Section 5.3.

7.2.2 End feed applicator

7.2.2.A Discharge ignition and tuning adjustments to a well-matched resonant mode in 8P/8M configuration

The end feed discharge (see Figure 3.3) was ignited by feeding argon gas into the quartz dome, increasing the pressure to around 25 mTorr by adjusting the throttle valve, increasing the incident microwave power and then tuning the cavity applicator by varying the two degrees of freedom, i.e. L_s and L_p, to search for electromagnetic resonances. Discharges could be ignited at certain tuning positions, (L_s, L_p) when the microwave power was well-matched to a cavity resonance. After discharge ignition, the pressure was adjusted to the desired value and then the discharge loaded cavity was retuned by adjusting L_s and L_p to a well-matched operating condition (reflected power < 5% of P_{inc}). The experimental system was operated on this resonance for a few minutes and then,

if necessary, tuning adjustments were made again to reduce the reflected power to a low minimum value. Whenever an excellent match was achieved, this experimental condition was identified as a resonant operating condition.

Interestingly, as shown in Figure 7.2 the theoretical empty 17.78-cm dia. cylindrical cavity heights for TM_{011} and TM_{012} resonant modes are 72 mm and 144 mm respectively. The discharge was first ignited by adjusting L_p to ~ 30 mm and adjusting L_s close to one of these empty cavity resonant lengths and then after ignition was easily tuned by increasing L_s just a few mm to obtain a matched, high density discharge operation either at L_s ~ 78 mm or at L_s ~ 148 mm with L_p ~ 29 mm. As will be described later in Chapter 9 the resonant cavity tuning, i.e. the specific L_s and L_p required for an excellent match, varies slightly depending upon experimental conditions, such as operating pressure, $P_{abs,}$ and etc. There were only two discharge loaded cavity resonant modes excited over the tuning ranges of L_s and L_p listed in Table 7.1. These modes are identified in this thesis as mode 1 and mode 2.

7.2.2.B Identification of the resonant EM modes in 8P/8M configuration

Obtained by un-calibrated E-probe measurements, Figures 7.3 and 7.4 display the typical H and Φ variations (see Figure 5.1) of the measured radial field patterns at the cavity wall (which is proportional to $|E_r|^2$) when the discharge loaded plasma source was operating in either of the two resonant modes. The experimental measurements took place in an argon discharge at pressure of 4 mTorr and an absorbed power of 235 W. The field patterns are approximately

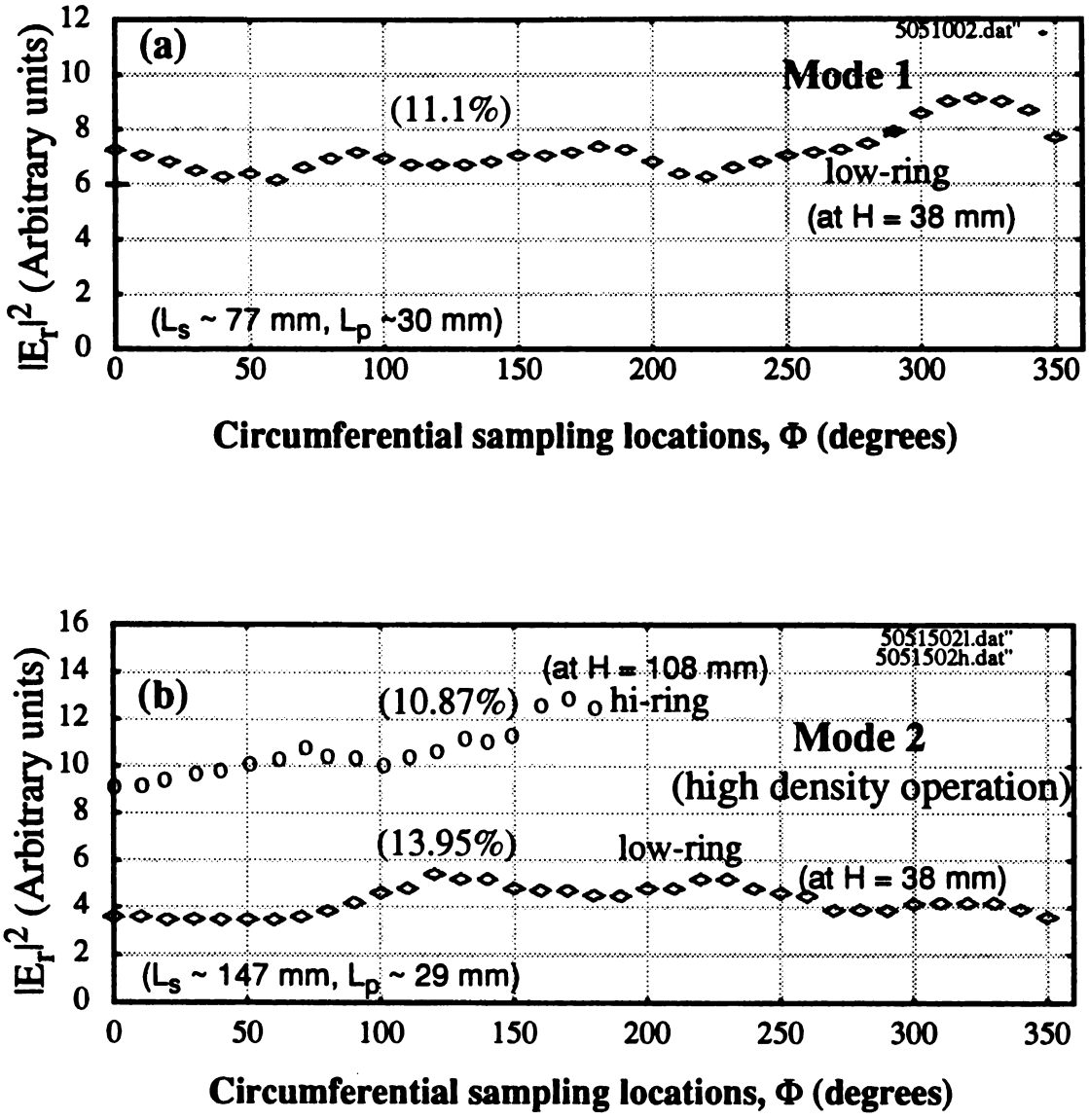

Figure 7.3 The measured radial component electric field pattern in end feed applicator vs. Φ, (a) for mode 1, (b) for mode 2..
The input variables were (1) end-feed, (2) 8P/8M MPDR™, (3) pressure of 4 mTorr and (5) absorbed power of ~235 W.

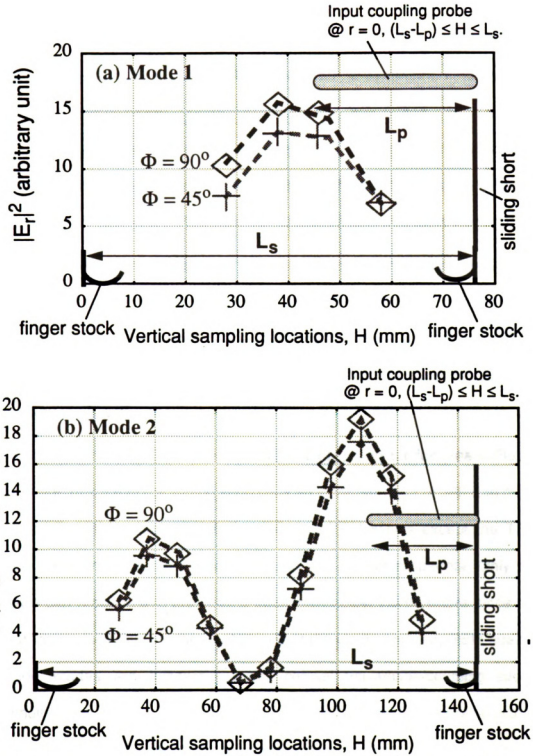

Figure 7.4 The measured radial component electric field pattern in end feed applicator vs. H, (a) for mode 1, (b) for mode 2. The input variables were (1) end-feed, (2) 8P/8M MPDR™, (3) pressure of 4 mTorr and (5) absorbed power of ~235 W.

Φ-symmetric in the circumferential direction and are approximately sinusoidal along the H-direction with one or two maxima indicating the existence of a standing wave field in the applicator. The measured Φ-symmetric field patterns suggest either one or more TM_{0y} or TE_{0x} modes (x, y = 1, 2, 3,...) are excited inside the discharge loaded cavity. If only the TE_{0x} modes were excited, one would expect that the measured radial electric field component would be essentially zero or very small. However, the measured field strengths were not low. Thus, the presence of strong E_r fields next to the wall indicates that TM_{0y} modes were excited inside the discharge loaded cavity. Whether the EM fields excited were purely TM_{0y} modes or the superposition of a combination of TM_{0y} and TE_{0x} modes is difficult to determine by only using the experimental data measured by the E-probe method.

The coaxial waveguide of the incoming coaxial probe section (see in Figure 3.3, the region of s = 0 to the sliding short) has an inner diameter of 3/8" and outer diameter of 7/8". With these small dimensions, all EM waves except the TEM wave are cut-off in the coaxial waveguide and thus do not propagate. Only the TEM wave can propagate in the coaxial input waveguide. Furthermore since the excitation probe is located at the **center** axis of the cavity and only TEM coaxial waveguide modes are incident on the coaxial waveguide/coupling probe discontinuity, Φ-symmetric TE modes are not excited by the input coupling probe. Thus, only the TM_{01} or TEM mode fields are excited inside the end feed plasma loaded cavity.

As shown in Figure 7.3, the circumferential variations of the measured circumferential field patterns were relatively "flat" (or independent of Φ). The actual "flatness", which is defined as the standard deviation over the average, is also shown in parenthesis near the data in Figure 7.3. Within the same resonant mode, the flatness varies somewhat as the fine tuning (L_s, L_p) of the cavity is varied within a resonance. This variation has several possible explanations: (1) a dominant TM_{01n} mode co-existing with dipolar TE mode(s), (2) the excitation of a dipole resonance modes within the discharge [136], or (3) slight variations of the Φ-symmetric impressed field due to a loading caused by the non perfect Φ-symmetry of ECR zones.

The vertical variation of the electric field shown in Figure 7.4 versus the H-direction suggests that two resonant modes, identified here as mode 1 and mode 2, were excited with one or two standing wave peaks along the vertical direction. Mode 1, which occurs at L_s ~ 76 mm, shows an approximate $\lambda_g/2$ standing TM_{011} wave, while mode 2, which occurs at L_s ~ 140 to 150 mm, has an approximate TM_{012} λ_g standing wave. Therefore, the measured field patterns suggest that mode 1 represents an approximate TM_{011} mode excitation while mode 2 represents an approximate TM_{012} mode excitation.

Note that the excitation probe depth, L_p, inside the cavity is constant around 29 mm for all the measurements presented in this section. The electromagnetic fields at the end of the probe are the sum of the excited standing wave cylindrical waveguide fields and the evanescent fields excited at the probe tip discontinuity. As shown in Figure 7.4 (b), the maximum electric fields in mode 2

(TM_{012}) are greater adjacent to the probe, i.e., at H ~ 110 mm than at H ~ 40 mm near the discharge. This difference in field strength is believed to be due to the additional electric field energy stored in the envanscent fields at the probe discontinuity.

As is also shown in Figure 7.4, the relative field strengths at H ~ 38 mm are slightly higher in mode 1 than in mode 2. This is believed to be caused (1) by the lower coupling wall losses in mode 1 due to the shorter applicator length, and (2) by the evanescent fields that are present at the probe tip. When in mode 1, these evanescent fields add with the standing wave fields to produce a stronger impressed electric field in the active discharge region. Thus microwave power is coupled into the discharge through both the standing wave field and the evanescent probe fields. In mode 1, these evanescent "near fields" influence the excitation of the discharge. The output discharge density, shown in Section 7.3, is slightly higher in mode 1 and the discharge also tunes differently in mode1, i.e., it has a resonance that is less sensitive to the length than mode 2 (see discussion in Chapter 9). These differences in tuning and discharge density may be caused by the probe near fields.

7.2.2.C Electric field strength in 8P/8M configuration

Measurements of the radial component of the electric field strength at the wall and the estimated impressed electric field strength in the discharge are presented in this subsection. The radial component of electric field strength at the cavity wall was determined by inserting a calibrated E-probe (see Chapter 5 for probe calibration and measurement techniques) at the applicator wall. This probe was

located at H = 38 mm, $\Phi = 90^{o}$ and 120° as shown in Figure 7.5. The average electric field from data of these two locations is presented as typical radial electric field strengths at the wall. The impressed field strength in the discharge was then estimated by (1) assuming the electromagnetic field mode spatial variation was given by the TM_{011} (or TM_{012}) mode as identified by the experimental measurement procedures described in Section 7.2.2.B, and (2) and then determining the magnitude of the TM_{011} (or TM_{012}) mode from the calibrated electric field strength measurement at the wall. The value of impressed electric field at the top interior flat edge circle of the quartz bell jar (r = 34.3 mm, H = 27.5 mm see Figure 7.5) is estimated from calculations using the theoretical formulas for the proper mode. Therefore, it is assumed [53] that the impressed electric field strengths at the top of the discharge are related by a constant to the experimentally measured radial component of electric field strength at the wall. Thus it is assumed that a knowledge of how the radial wall field strength varies with the input variables also describes how the impressed electric fields at the top of the discharge vary with the input variables. This is a direct consequence of the assumption of a "well-behaved" pure electromagnetic mode pattern in the discharge loaded cavity. This assumption may only be approximately true since (1) the EM field may be perturbed and modified by the plasma near the discharge, and (2) the evanescent "near fields" which are strong near the discharge in mode 1 do not follow the same spatial variation as in the ideal EM mode pattern. Hence, this method of determining the impressed electric field only gives an "approximate value" of the impressed electric field.

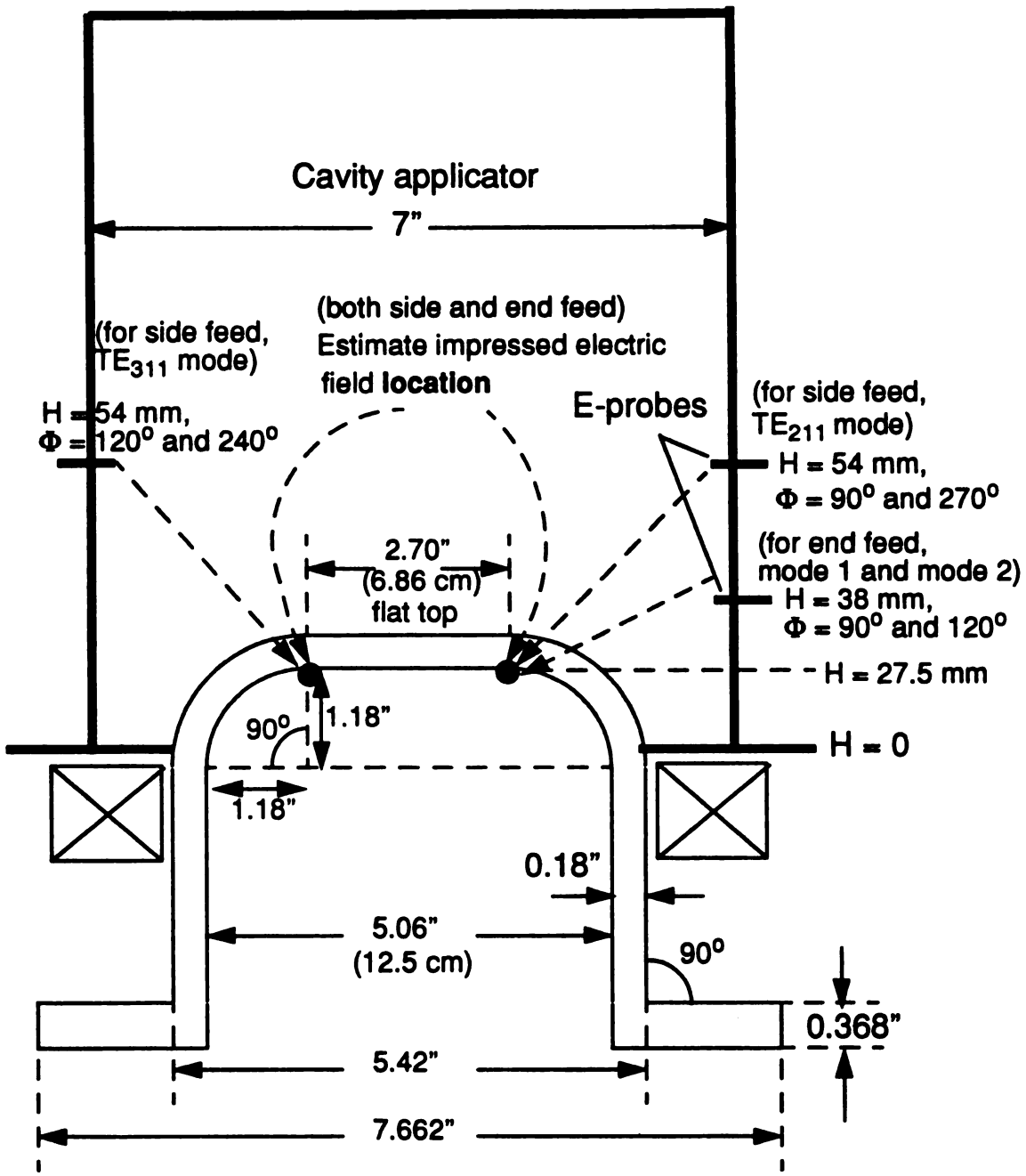

Figure 7.5 Quartz bell jar dimensions (not in scale) and the locations for calculation of the impressed electric field.

Figure 7.6 displays the applicator measured electric field strength at the wall versus chamber pressure and incident power for the two resonant modes. Both measurements were recorded at the low ring (H = 38 mm), which is closer to the plasma discharge. For both modes, the electric field decreases slightly as pressure increases and also shows an slight increase as power increases. As indicated earlier mode 1 has a higher applicator wall electric field than mode 2.

Assuming that the electromagnetic field varies either as a pure TM_{011} or TM_{012} mode, Table 7.3 gives both the tangential and the perpendicular impressed electric field strengths at r = 34.3 mm and H = 27.5 mm for different pressures and absorbed power for the 8P/8M end feed discharges. The tangential impressed electric field strengths varied from 4 to 5.1 kV/m for mode 1 and 3.3 to 3.7 kV/m for mode 2. In a similar fashion to the wall electric fields shown in Figure 7.6, the impressed electric fields are quite insensitive to the input variable space of power (185 - 324 W) and pressure (2.5 - 7 mTorr).

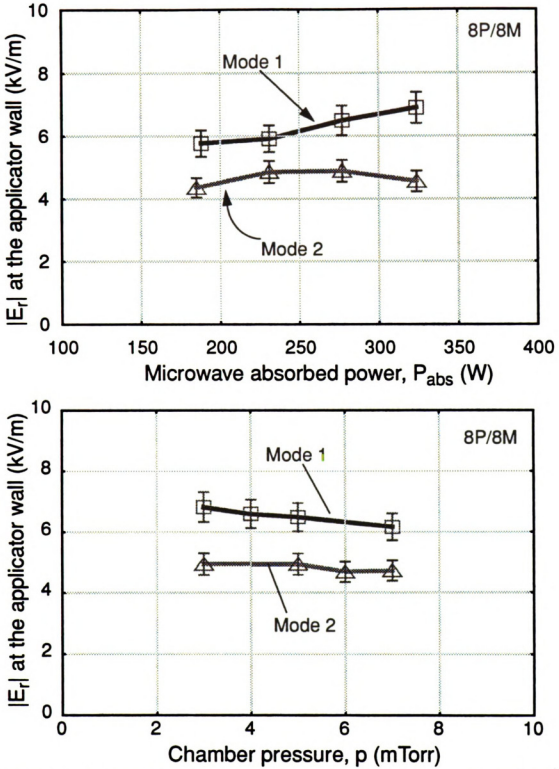

Figure 7.6 End feed absolute radial component electric field strength at the wall (H =38 mm). (a) vs. absorbed power at operating pressure of 5 mTorr, and (b) vs. pressure at absorbed power of 270 W.

Table 7.3 Impressed electric field for 8P/8M end feed excitation

Input variables		Tangential impressed electric field $\|E_r\|$ (kV/m) at (r = 34.3 mm, H = 27.5 mm)		Perpendicular impressed electric field $\|E_z\|$ (kV/m) at (r = 34.3 mm, H = 27.5 mm)	
Pressure, p (mTorr)	**Power absorbed, P_{abs} (W)**	Mode 1	Mode 2	Mode 1	Mode 2
5	185	~4	~3.3	~2.3	~1.88
	230	~4.3	~3.5	~2.44	~2.0
	270	~4.7	~3.55	~2.7	~2.03
	324	~5.0	~3.4	~2.84	~1.95
2.5	270	~5.11	~3.65	~2.9	~2.08
5		~4.68	~3.58	~2.66	~2.04
7		~4.5	~3.4	~2.56	~1.95

Note that the impressed electric fields shown in Table 7.3 for TM modes decompose into two components, one is in the direction tangential to the plasma/quartz interface and the other is in z-direction perpendicular to the plasma/quartz discharge interface. The skin depth for a tangential impressed electric field is much larger than [138] the skin depth for an electric field that is impressed perpendicular to the plasma dielectric boundary. That is, EM fields having electric field components tangential to the plasma surface penetrate deeper into the plasma before they are absorbed or reflected. Therefore, both the tangential and perpendicular component of impressed electric field strength are listed separately in Table 7.3. It is expected that the two field components will have a different impact on the discharge heating.

7.2.2.D Power coupling efficiency and Quality factor of the discharge loaded cavity

Once the electric field patterns and strengths at the applicator wall are known, the wall losses can be calculated using eq. (5.4), $P_w = \int_S \left(\frac{1}{2}\Re_s |J_s|^2\right) dS$. The resistivity ($\Re_s$) of the brass and aluminum at 2.45 GHz are ~ 0.0161Ω and ~ 0.0248 Ω respectively. Once the wall loss is determined, the power coupling efficiency can be evaluated using eq. (4.1). Neglecting the coupling losses and under essentially matched condition ($P_{inc} \cong P_{abs}$), eq. (4.1) becomes

$$Eff^{A}_{coup} \approx \left(1 - \frac{P_w}{P_{abs}}\right) \times 100\% \quad . \tag{7.3}$$

An alternative method of determining the power coupling efficiency is to measure the discharge loaded quality factor, Q_L, and the empty cavity quality factor Q_0. Then power coupling efficiency is then expressed as

$$Eff^{B}_{coup} = \left(1 - \frac{Q_L}{Q_o}\right) \times 100\% \quad , \tag{7.4}$$

where discharge loaded quality factor Q_L is determined from measured electric field strengths by eqs. (4.3) and (4.4). The empty cavity quality factor Q_0 for the non-ideal cavity (coupling probe, finger stocks, etc.) was measured to be approximately 5000 for TM_{011} and TM_{012} modes under the best polished clean conditions. Q_0 usually falls to around 3200 after experimentation since the walls oxidize and the metallic and finger stock surfaces are no longer clean. Note that the difference between power coupling efficiencies obtained by eqs. (7.3) and (7.4) is related to the excitation probe coupling losses (P_c).

Table 7.4 gives the two power coupling efficiencies and the associated Q_L versus absorbed powers and chamber pressures. The calculated value of Eff^A_{coup} is in the range of 98-99% for mode 1 and around 98% for mode 2 for the pressure of 3 to 7 mTorr and absorbed power of180 to 320 W. At the same power and pressure conditions, the value of Eff^B_{coup} has been around 98% for mode 1 and in the range of 95.4 - 97% for mode 2. The difference in these two efficiencies suggests the excitation probe coupling losses are only approximately 1%. In addition, for the loaded quality factors in Table 7.4, mode 1 excitation is more efficient than excitation in mode 2. Overall, the end feed plasma source operating in both mode 1 and mode 2 are very efficient (>95%) and the coupling efficiency is insensitive to the pressure and power input space. When operating in either mode, only a very small amount of the reactor absorbed power is lost into the wall and the coupling probe losses.

Table 7.4 End feed power coupling efficiencies and loaded quality factors

Input variables		Mode 1			Mode 2		
P_{abs} (W)	p (mTorr)	Eff^A_{coup}	Q_L	Eff^B_{coup}	Eff^A_{coup}	Q_L	Eff^B_{coup}
180	5	~98.5%	~75	~97.6%	98.3%	~138	95.7%
230		~98.7%	~62	~98%	97.9%	~147	95.4%
270		~98.7%	~63	~98%	97.8%	~122	96.2%
320		~98.6%	~60	~98%	97.8%	~92	97%
270	3	~98.5%	~60	~98%	98%	~125	96%
	5	~98.7%	~63	~98%	97.8%	~122	96.2%
	7	~98.8%	~56	~98.2%	97.7%	~115	96.4%

7.2.3 Side feed applicator

In a fashion similar to that presented for the end feed applicator in Section 7.2.2, experimental data is presented here for the side feed applicator with an 8P/8M ECR magnetic field configuration. This 8P/8M plasma source configuration is used as the "benchmark" side feed plasma source. Its performance can be directly compared with the 8P/8M end feed excitation and it also serves as the reference plasma source to evaluate the performance changes versus variation in the ECR magnet configurations. The experimental data for the other three ECR configurations (4P/4M, 4P/8M, and allN/8M) are presented and compared with the 8P/8M plasma source.

7.2.3.A Discharge ignition and tuning adjustments to a well-matched resonant mode in 8P/8M configuration

Using the same discharge ignition procedures and techniques as described in Section 7.2.2.A for the end feed applicator, microwave discharges were ignited and excited using the side feed, 8P/8M, plasma source. Only two **stable** discharge loaded cavity resonant modes were found over the L_s and L_p tuning ranges listed in Table 7.2. The final steady state discharge loaded cavity heights, L_s, for the resonant modes occurred approximately at 77 mm and 150 mm. Since there are several possible modes that are close to these cavity heights, E-probe measurements were used to identify the excited EM patterns. The mode which had the longer cavity length L_s, was initially referred to as the "long resonant mode" and the other mode excited at $L_s \sim 77$ mm was identified as the "short resonant mode".

7.2.3.B Identification of the resonant EM modes in 8P/8M configuration

Figures 7.7 and 7.8 display the un-calibrated E-field measurements at the wall for the short and long resonant modes under the following operating conditions: (a) P_{inc} ~ 240 W, (b) P_{ref} < 5% of P_{inc}, and (c) pressure ~ 0.8 m Torr with (d) 20 sccm argon flow rate. The ideal TE_{211} and TE_{311} electromagnetic cavity modes are also plotted in these Figures as the dashed lines along with the actual experimental data points which are symbolized as □. No circumferential data were available between $\Phi = 160^0$ - 200^0 and between 333^0 - 27^0 due to the presence of a screened observation window and the side excitation probe launching structure respectively. Also no longitudinal data were available near both ends (H < 24 mm or H > L_s - 24 mm) due to the finger stock at the bottom of the cavity and the sliding short. According to the circumferential variations of measured electric field patterns shown in Figures 7.7 and 7.8, the short and long resonant modes excited in the plasma loaded cavity matched, within the experimental error, favorably with TE_{21} or TE_{31} modes respectively. Moreover, the measured electric field patterns along H-direction indicate a $\lambda_g/2$ standing wave between the sliding short and the baseplate, having a peak near the middle location of the cavity height. From these two measured patterns, the short and long resonant modes excited inside the plasma loaded cavity were identified as the TE_{211} or TE_{311} EM modes respectively. The measured discharge loaded cavity heights (shown in Table 7.6 later) are slightly **lower** than the theoretical empty cavity heights of 82.5 mm (for TE_{211}) and 162 mm (for TE_{311} mode).

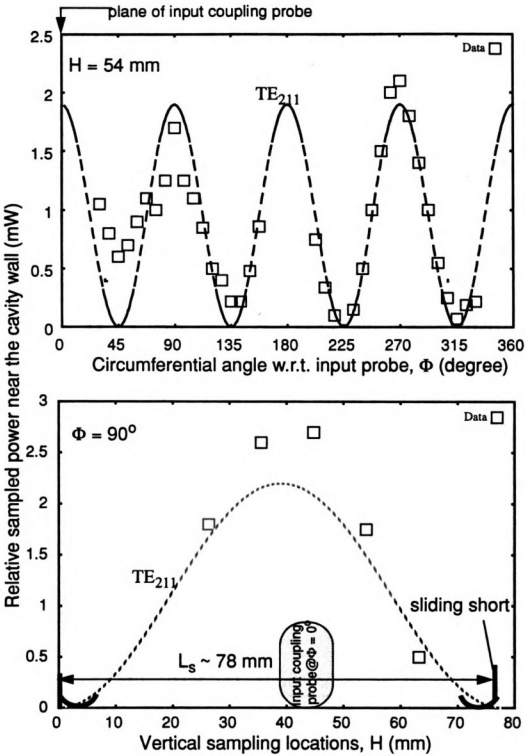

Figure 7.7 Measured EM mode pattern in side-feed, 8P/8M MPDR with short resonant mode excitation.
Absorbed power ~ 236 W, pressure 0.8 mTorr.

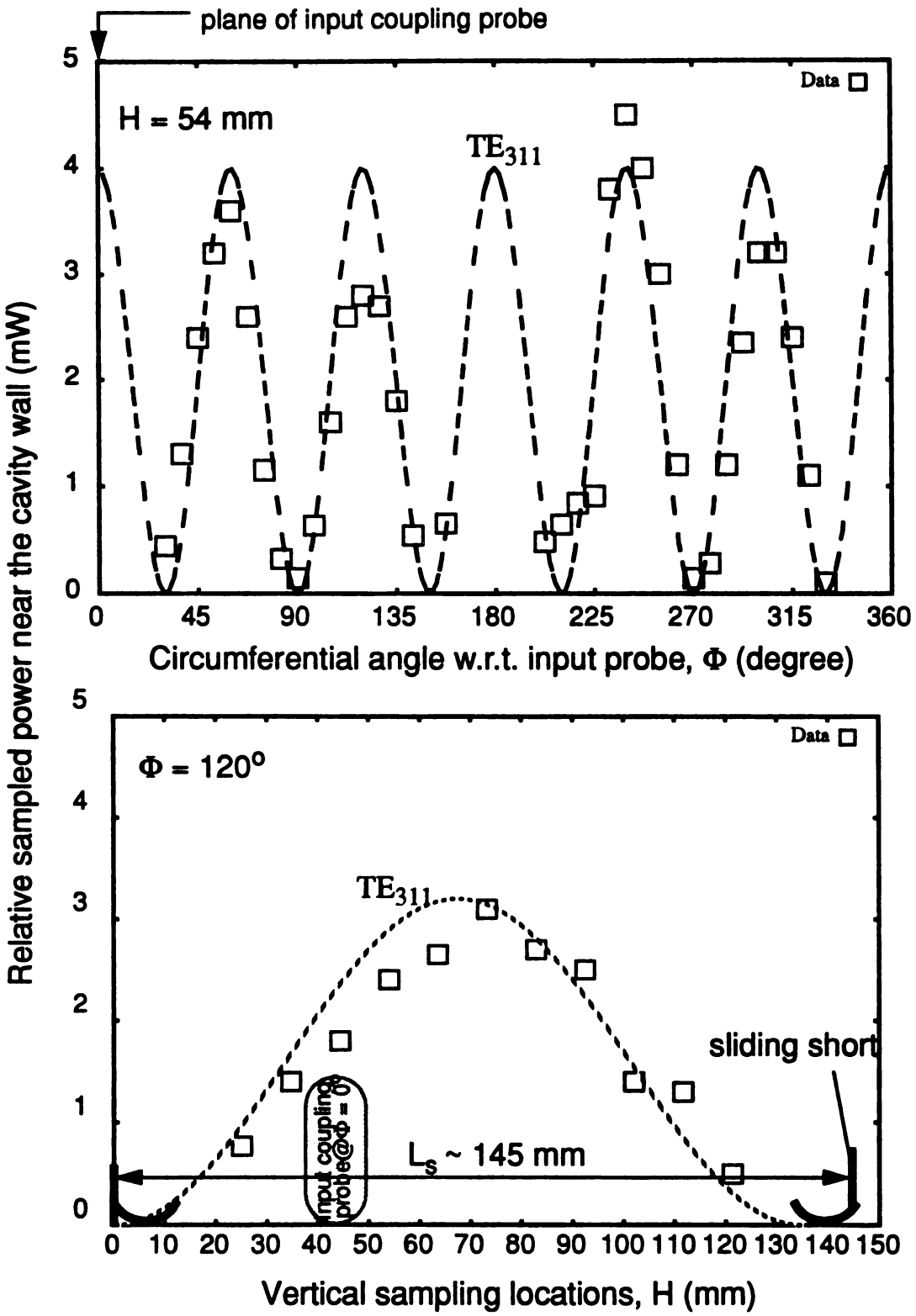

Figure 7.8 Measured EM mode pattern in side-feed, 8P/8M MPDR with long resonant mode excitation.
Absorbed power ~ 236 W, pressure 0.8 mTorr.

It should be also noted that other resonant modes (TE_{111} and TE_{112}) could be excited with the side feed excitation. However, they were difficult to ignite and operate in a stable condition. In other experimental investigations [135,139] where the antenna was located at the lower height of H ~ 37 mm, the TE_{111} and TE_{112} modes could be readily ignited and maintained. Apparently when the coupling probe is located at H = 44 mm, these modes cannot be efficiently excited. Since the side feed in this chapter was mostly at H = 44 mm, the excitation of the TE_{111} and TE_{112} modes were not investigated in detail here. It is important to note that the **launching height** of the input coupling probe in the side feed applicator is also an important geometry variable to consider when exciting specific modes.

Finally, using a smaller (9 cm i.d.) discharge [140], a Φ-symmetric TM-field pattern can be excited in a similar 17.78 cm diameter cavity applicator. This also indicates that the **size** of the discharge (in this case, the diameter of the discharge) can also influence the possible EM modes excited in the applicator.

7.2.3.C Electric field strength in 8P/8M configuration

Similar to end feed applicator, measurements of the radial component of electric field strength at the wall (by calibrated E-probe) and the estimated impressed electric field strength at the discharge are described in this section. The estimation of the impressed electric field at the discharge is based on the assumption that the TE_{211} or TE_{311} mode spatial field distributions in the applicator are related to the measured electric field strength at the walls by a constant. This constant can be determined from the classical EM wave textbook mode plots and the measured electric field strength at the walls. Therefore, both

the field strengths at the wall and of the electric field impressed on the discharge vary in a similar way versus changes in input variables. The location of impressed electric field is the same as in the end feed case but as shown in Figure 7.5 the positions where the electric field strength is measured are slightly different. The measured radial wall field strength took place at H = 38 mm for the end feed and at H = 54 mm for the side feed as shown in Figure 7.5 or Figure 5.1, due to the *de facto* existing holes on the two different applicator shells. Moreover, due to the sinusoidal variation nature of TE modes, the reported electric field strength values at the walls in side feed applicator were taken as the average of the two peaks (at $\Phi = 90^0$ and 270^0 for TE_{211} mode and at $\Phi = 120^0$ and 240^0 for TE_{311} mode, all at H = 54 mm).

Figure 7.9 displays the measured electric field strengths at the wall versus pressure and incident power for two resonant modes (TE_{211} and TE_{311} modes). For both modes, the field strengths at the wall increase slightly with the incident power and drop as pressure increases. The electric field strength at the wall in TE_{211} mode is about half of a similarly measured field for the TE_{311} mode.

Note that the electric field of pure TE modes does not have z-component, i.e. $E_z = 0$. Hence, the TE mode variation assumption implies that the estimated impressed electric field is always tangential to the plasma discharge. In addition, the variation of E_r and E_ϕ components is the sinusoidal compliment to each other (one varies with "sin" and other is "cos"). Therefore, even though the direction of the impressed electric field at r = 34.3 mm and H = 27.5 mm may be changing with circumferential angle Φ, the magnitude of the tangential impressed electric

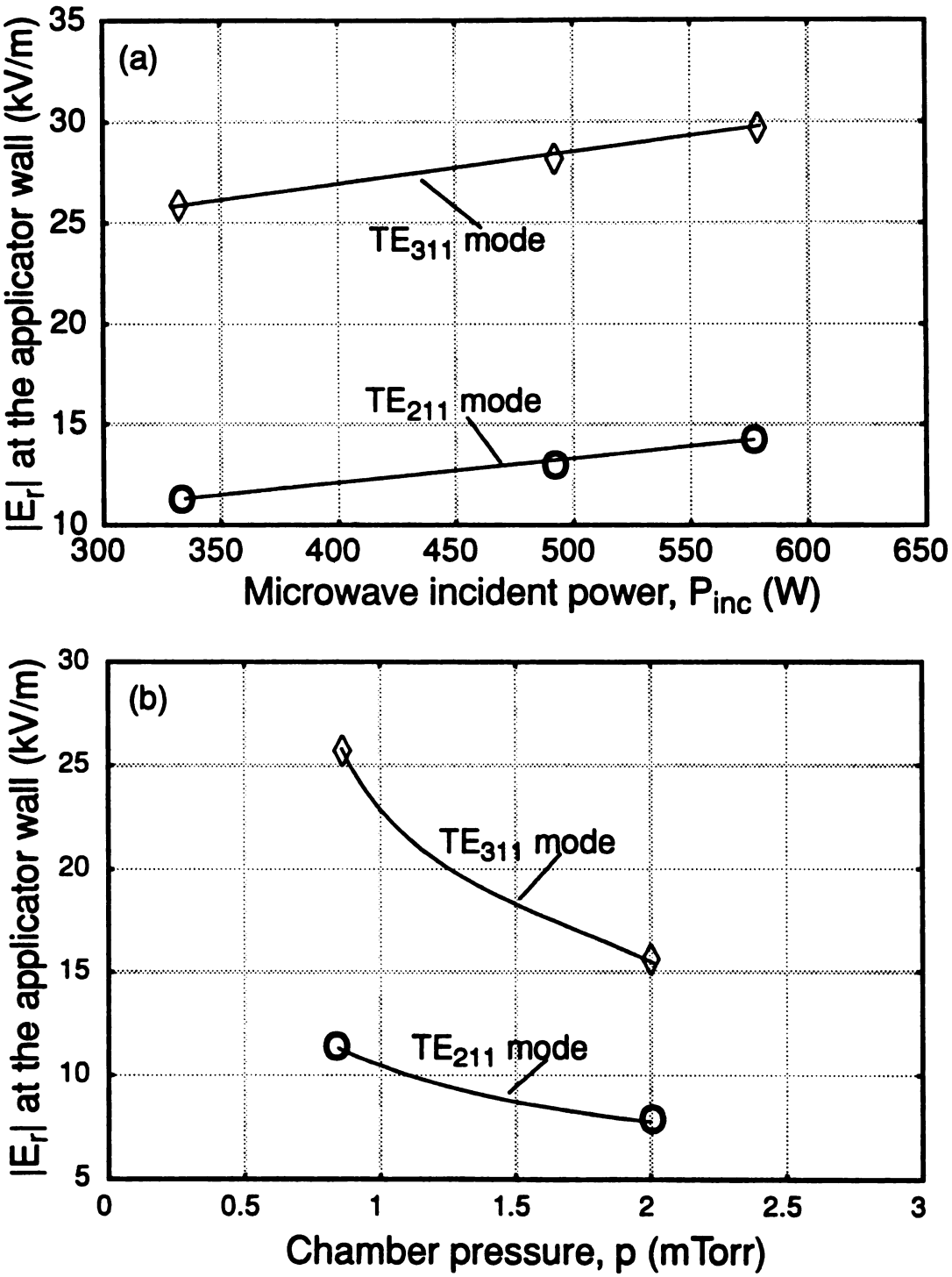

Figure 7.9 Side feed absolute radial component electric field strength at the wall (H = 54 mm) (a) vs. power at p = 0.8 mTorr, and (b) vs. pressure at power of 328 W.

field $E_t = \sqrt{E_r^2 + E_\phi^2}$ remains the same for all Φ, Therefore the side feed tangential impressed electric field strength can be readily compared with the tangential impressed Φ-symmetric electric fields reported in Table 7.3 for the end feed applicator plasma source. Table 7.5 lists the estimated tangential impressed electric field strength at the 8P/8M side feed discharges for different powers and pressures. It is interesting that even though the TE_{311} field strength at the wall is much higher than the TE_{211} mode, the estimated electric field strength at the discharge is lower. This suggests more efficient power coupling for TE_{211} mode than TE_{311} for these magnetic configurations.

Table 7.5 Impressed electric fields for 8P/8M side feed excitation

Input variables		Tangential impressed electric fields $\|E_t\|$ (kV/m) at (r = 34.3 mm, H = 27.5 mm)	
Pressure, p (mTorr)	Power Absorbed, P_{abs} (W)	TE_{211}	TE_{311}
0.8	328	~10.44	~7.1
	490	~11.9	~7.8
	574	~13.5	~8.1
0.8	328	~10.44	~7.1
2		~7.2	~4.3

7.2.3.D The EM modes and electric field strengths for the different magnetic field configurations

The electric field measurements were performed on all four different ECR configurations (4P/4M, 4P/8M and allN/8M) in the side feed applicator. Sections 7.2.3.A-C present the benchmark data for the 8P/8M side feed configuration. In this subsection, data is presented in two categories: (1) the multipolar ECR fields and (2) the non-multipolar ECR fields versus the input power (328 W and 574 W) and pressure (0.8 and 2.0 mTorr).

Multipolar ECR field configurations: Using the same discharge ignition procedures and techniques as described in Section 7.2.2.A for the end feed applicator, microwave discharges were ignited and excited in the side feed applicator using 4P/8M and 4P/4M ECR magnet configurations. Only two **stable** discharge loaded cavity resonant modes were found over the L_s and L_p tuning ranges listed in Table 7.2. The final steady state cavity height values of resonant modes occurred approximately at 77 mm and 150 mm. Since there are several possible modes that are close to these cavity heights, E-probe measurements were used to identify the excited EM pattern. The mode which had the longer cavity length L_s, was initially referred to as "the long resonant mode" and the other mode excited at L_s ~ 77 mm was identified as the "short resonant mode". Table 7.6 lists the approximate tuning locations for these three multipolar ECR magnetic field configurations including the 8P/8M benchmark case. The cavity height values in Tables 7.6 are given in a range format because the actual height depends upon the experimental conditions such as power, pressure and gas type.

Table 7.6 Cavity heights for multipolar ECR magnetic field in side feed plasma Loaded cavity

ECR Configuration	Short resonant mode	Long resonant mode
8P/8M	72 - 77 mm	134 -152 mm
4P/4M	74 - 80 mm	135 -150 mm
4P/8M	~ 76 mm	150 -153 mm

Figures 7.10 - 7.12 display the relative E-field measurements at the wall of the short and long resonant modes for pressure of 0.8 mTorr and absorbed power of 240 W. The ideal TE_{211} and TE_{311} electromagnetic cavity modes are also plotted in these Figures as the dashed lines along with the actual experimental data points which are symbolized as ❑. Like the 8P/8M case, according to the circumferential variations of measured electric field patterns, the discharge load cavity modes matched favorably with either the TE_{21} or TE_{31} modes. Moreover, the vertical variations of measured electric field patterns indicate a standing wave along the H-direction. Using the E-field pattern measurements shown in Figures 7.7-7.8 and 7.10-7.12, the discharge loaded cavity modes in all multipolar ECR magnetic configurations are identified as TE_{211} and TE_{311} modes for the short and long resonant modes respectively.

In addition, the measurements of the radial component of electric field strength at the wall (by calibrated E-probe) and the estimated impressed electric field strength were also performed for different multipolar ECR magnetic configurations. The locations of the wall electric fields presented here are identical to the benchmark 8P/8M side feed applicator and the estimated impressed

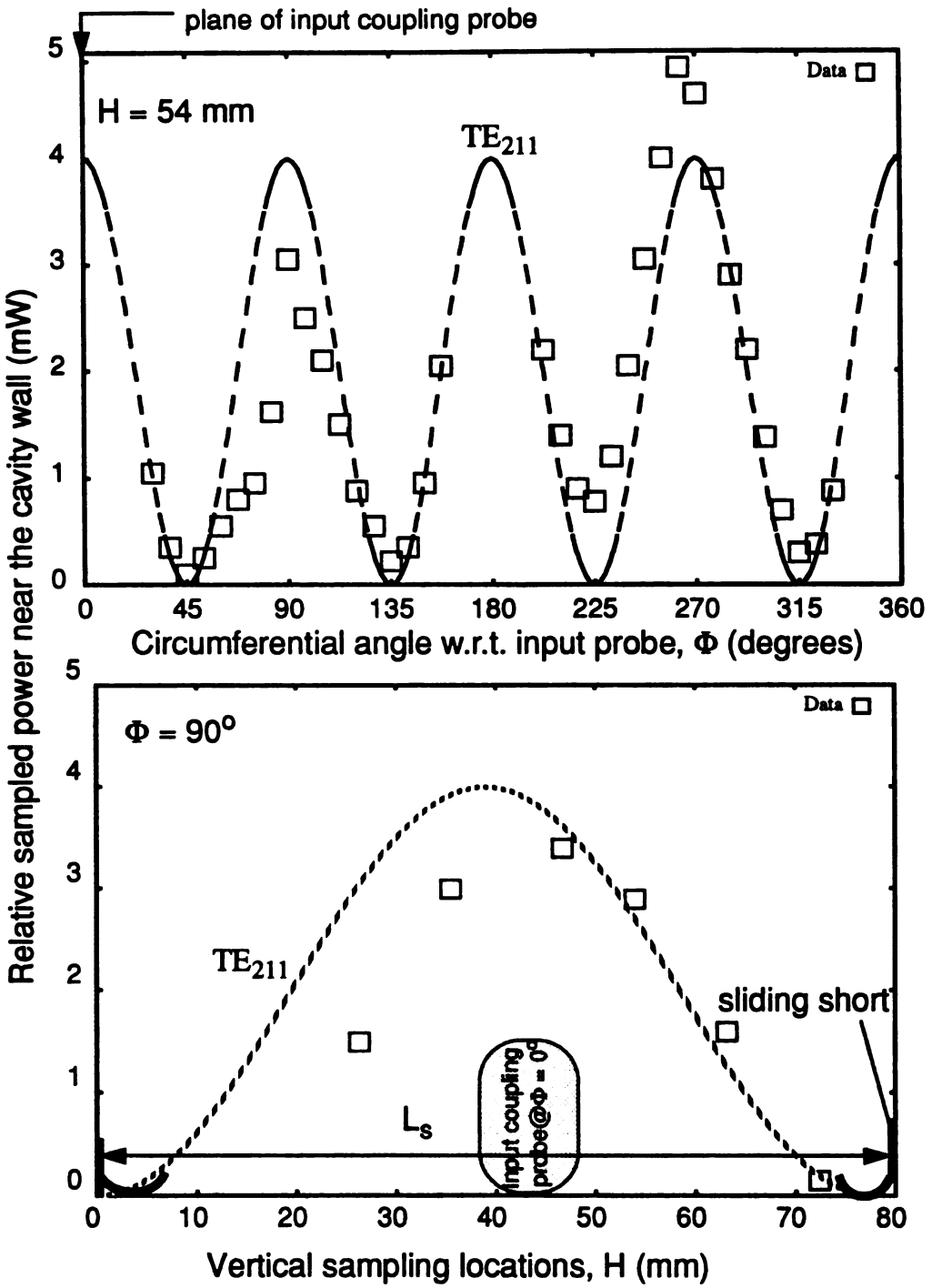

Figure 7.10 Measured EM mode pattern in side-feed, 4P/8M MPDR with short resonant mode excitation.
Absorbed power ~ 236 W, pressure 0.8 mTorr.

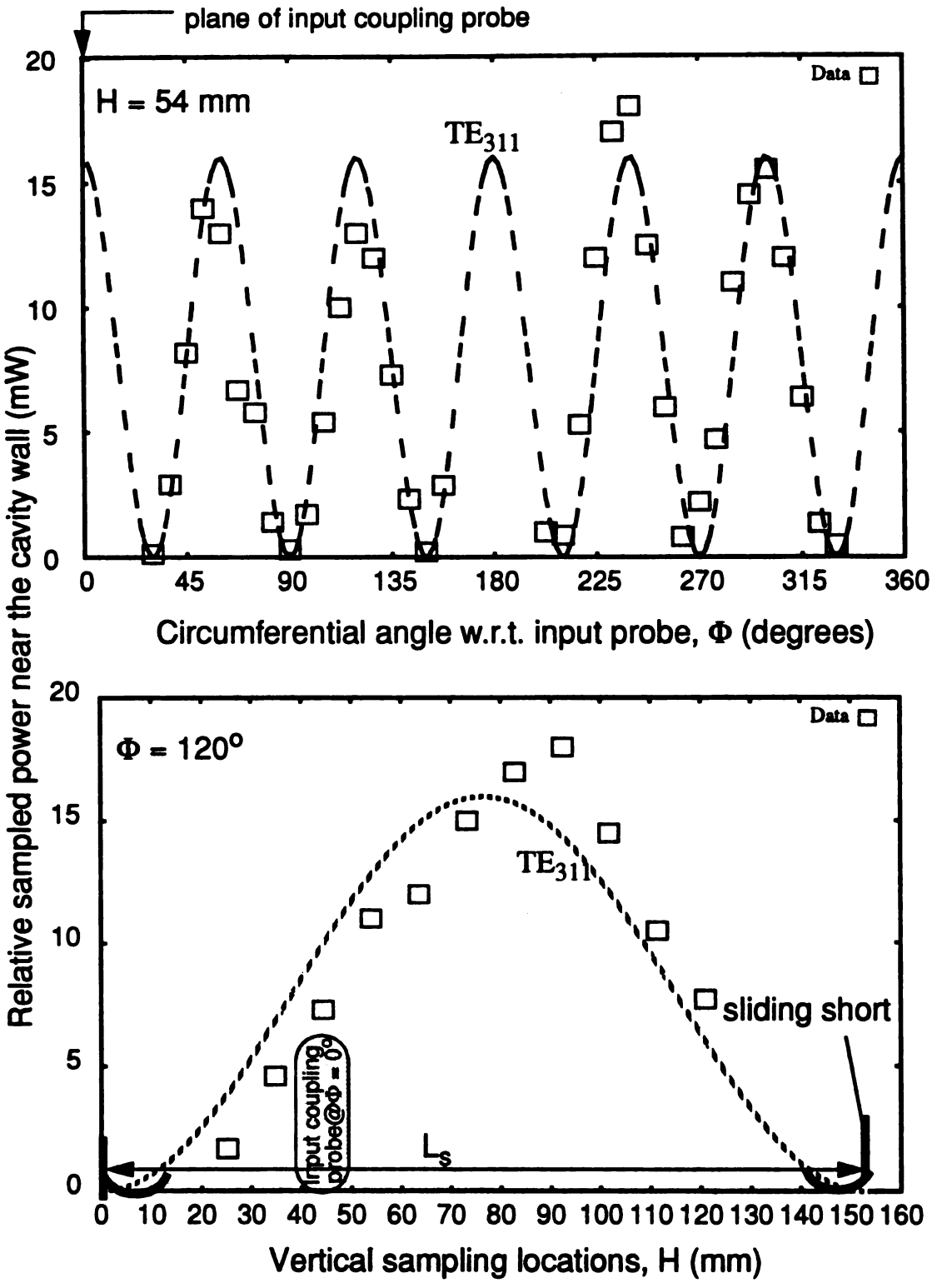

Figure 7.11 Measured EM mode pattern in side-feed, 4P/8M MPDR with long resonant mode excitation.
Absorbed power ~ 236 W, pressure 0.8 mTorr.

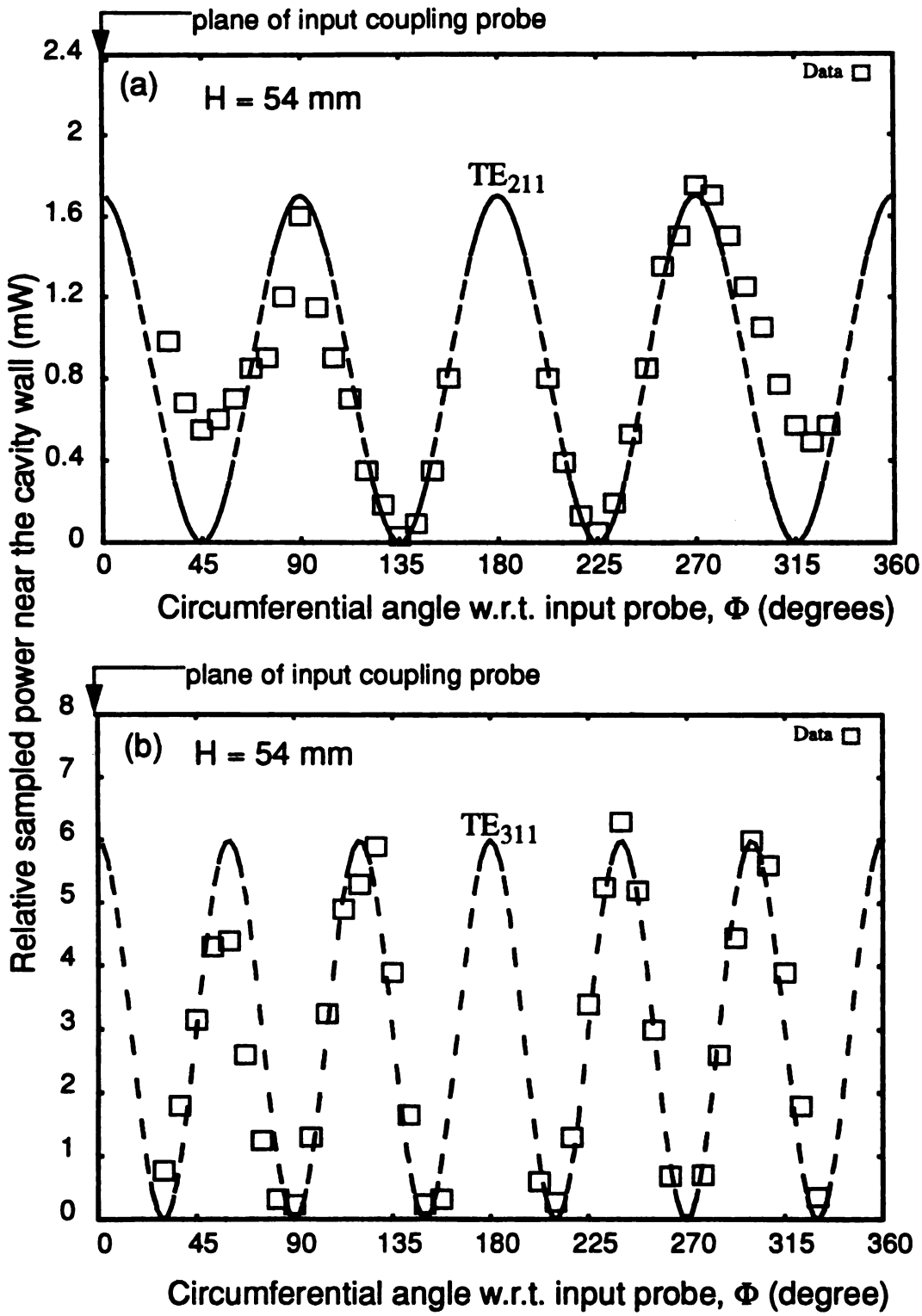

Figure 7.12 Measured EM mode pattern in side-feed, 4P/4M MPDR (a) short resonant mode, (b) long resonant mode.
Absorbed power ~ 236 W, pressure 0.8 mTorr.

locations are the same as the 8P/8M configurations of both side feed and end feed applicators. Table 7.7 compares both the electric field strengths at the wall and estimated impressed electric field on the discharge for the three multipolar ECR magnetic field configurations at the various input experimental conditions.

Table 7.7 Comparison of E-field strengths for different multipolar magnet type ECR configurations for the side feed applicator

Input variables			8P/8M	4P/8M	4P/4M
EM Modes	p (mTorr)	P_{inc} (W)	Measured $\|E_r\|$ at wall / estimated tangential impressed field $\|E_t\|$ (kV/m)		
TE_{211}	0.8	328	11.2 / ~10.44	7.9 / ~7.4	9.8 / ~9.1
		574	14.5 / ~13.5	9.1 / ~8.5	11.9 / ~11.1
TE_{311}	0.8	328	25.7/ ~7.1	16.0 / ~4.4	22.2 / ~6.1
		574	29.2 / ~8.1	22.3 / ~6.1	27.3 / ~7.56
TE_{211}	2.0	328	7.7 / ~7.2	3.7 / ~3.3	N.A.
TE_{311}	2.0	328	15.4 / ~4.3	7.5 / ~2.1	N.A.

As shown in Table 7.7, the measured electric field of the TE_{211} mode at the wall were approximately 40-50% of the values in TE_{311} mode excitation but the estimated impressed electric field at the discharges for TE_{311} mode excitation is lower (approximately 60-70%) than the values in TE_{211} mode excitation. This suggests that TE_{211} mode excitation is more efficient than the TE_{311} mode excitation. In other words, in order to have same intensity of impressed electric field at the discharge, the electric field peak magnitude at the wall of TE_{311} mode excitation must be approximately 3.4 times of the TE_{211} wall electric field

strengths. As a result, the Ohmic losses on the applicator walls in TE_{311} excitation walls are higher than the TE_{211} excitation. Hence, the expected microwave coupling efficiencies in TE_{311} mode excitation should be lower than that of TE_{211} mode excitation.

Another observation is the effect of different ECR magnet configurations. At the same power and pressure, the electric field strengths (both at the walls and at the discharges) of 8P/8M configuration is the largest, 4P/8M configuration is the lowest, and the 4P/4M configuration falls in between. The change in electric field strength from 4P/8M to 8P/8M is about 70%. That means that the TE_{211} mode couples more efficiently with the 4P/8M magnet configuration. This is probably due to the fact that the 4P/8M configuration has a larger amount ECR area where the electric field is perpendicular to the static magnetic field. The number of EM poles is the same as number of magnetic poles for 4P/8M and 4P/4M configurations. However, the amount of available ECR coupling region in the discharge for 4P/4M configuration is smaller than 4P/8M configuration. Therefore, for the same amount of absorbed power, the impressed electric field is higher for 4P/4M than 4P/8M.

Non-multipolar ECR magnet configuration: The electric field measurement techniques and experimental procedures used to study the allN/8M ECR magnet configuration are similar to those described in Section 7.2.2.A. There were still only two **stable** resonant modes over the tuning locations listed in Table 7.2. The location cavity heights are around 81 mm and ~155 mm for the short and long resonant modes.

However, when applying E-probe measurement at the wall, several unclear phenomena occurred in electric field measurements. Figures 7.13 and 7.14 show the measured E-field patterns at the walls for two resonant modes under input conditions of 0.8 mTorr and 240 W power. The dashed lines in the Figures are ideal TE_{211} and TE_{311} cavity modes plotted along with data (❑) for comparison. First, the maximum circumferential peaks did not coincide with the probe launching location ($\Phi = 0^0$) as shown in Figures 7.13 and 7.14. The circumferential maximum peaks for both the short and long resonant modes in allN/8M configuration seem to have shifted approximately 35^0 off the excitation probe. However, the E-field pattern data in long resonant mode matches favorably with the TE_{311} mode after the circumferential ~35^0 shift. Second, as shown in Figure 7.14, the data for the short resonant mode in allN/8M ECR configuration within $\Phi = 40^0$ to 80^0 had relatively large discrepancy when compared with the ideal TE_{211} mode. These behavior which was found in allN/8M ECR configurations is not fully understood. AllN/8M configuration behaved in a manner unlike the other three multipole ECR magnet configurations. Also, the visual images of allN/8M configuration shown in Appendix C (Figure C.3) did not have the bright plasma pie shapes which are located between the multipolar magnets that exist in the discharges of other three multipolar type ECR configurations. The speculation on this may be due to the lack of magnetic multipole structure to stabilize the discharge. Due to the unclear EM mode patterns, absolute electric field strength measurements in allN/8M configuration were not performed and the impressed electric field was not estimated. Thus, other electromagnetic related

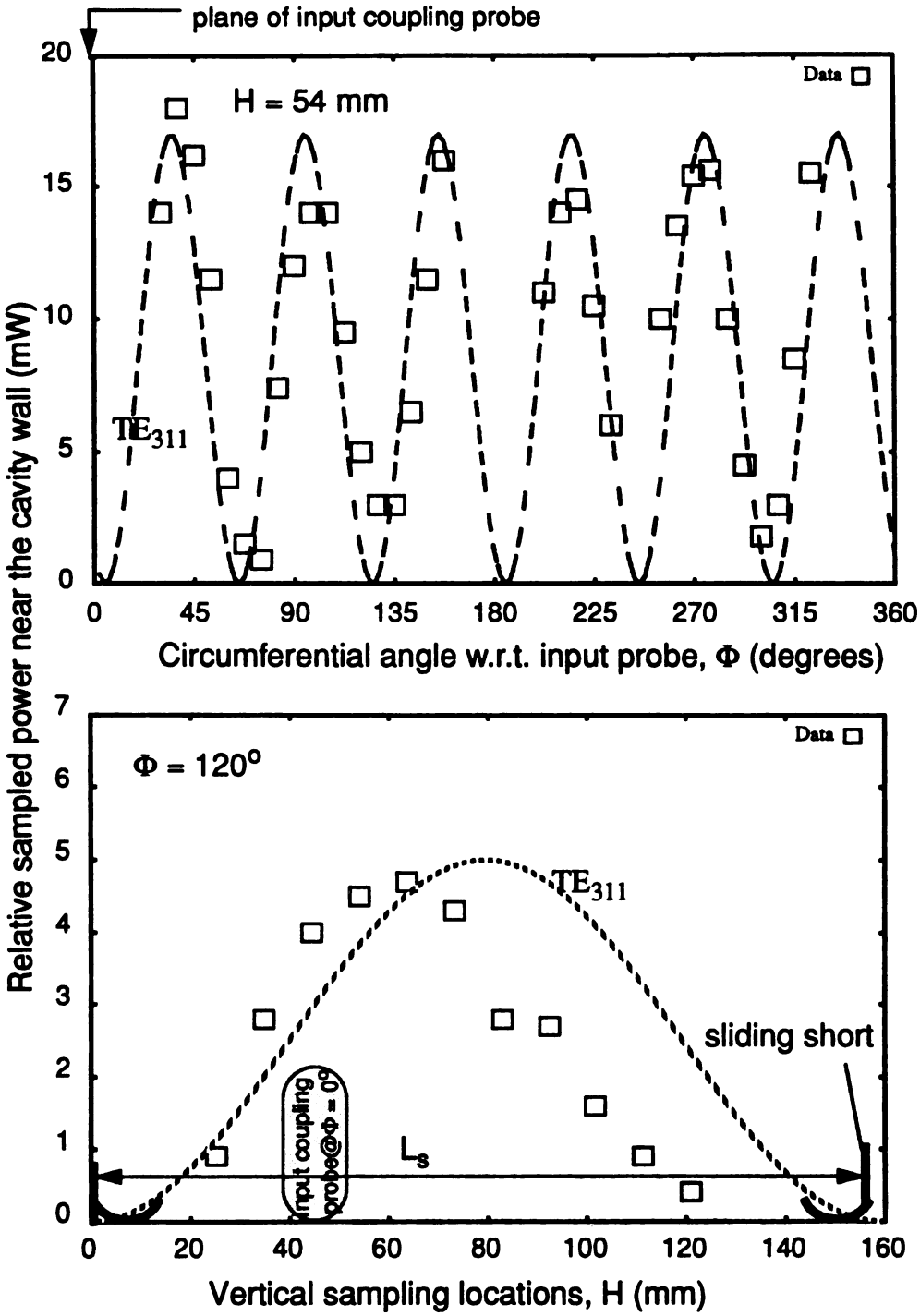

Figure 7.13 Measured EM mode pattern in side-feed, allN/8M MPDR with long resonant mode excitation.
Absorbed power ~ 236 W, pressure 0.8 mTorr.

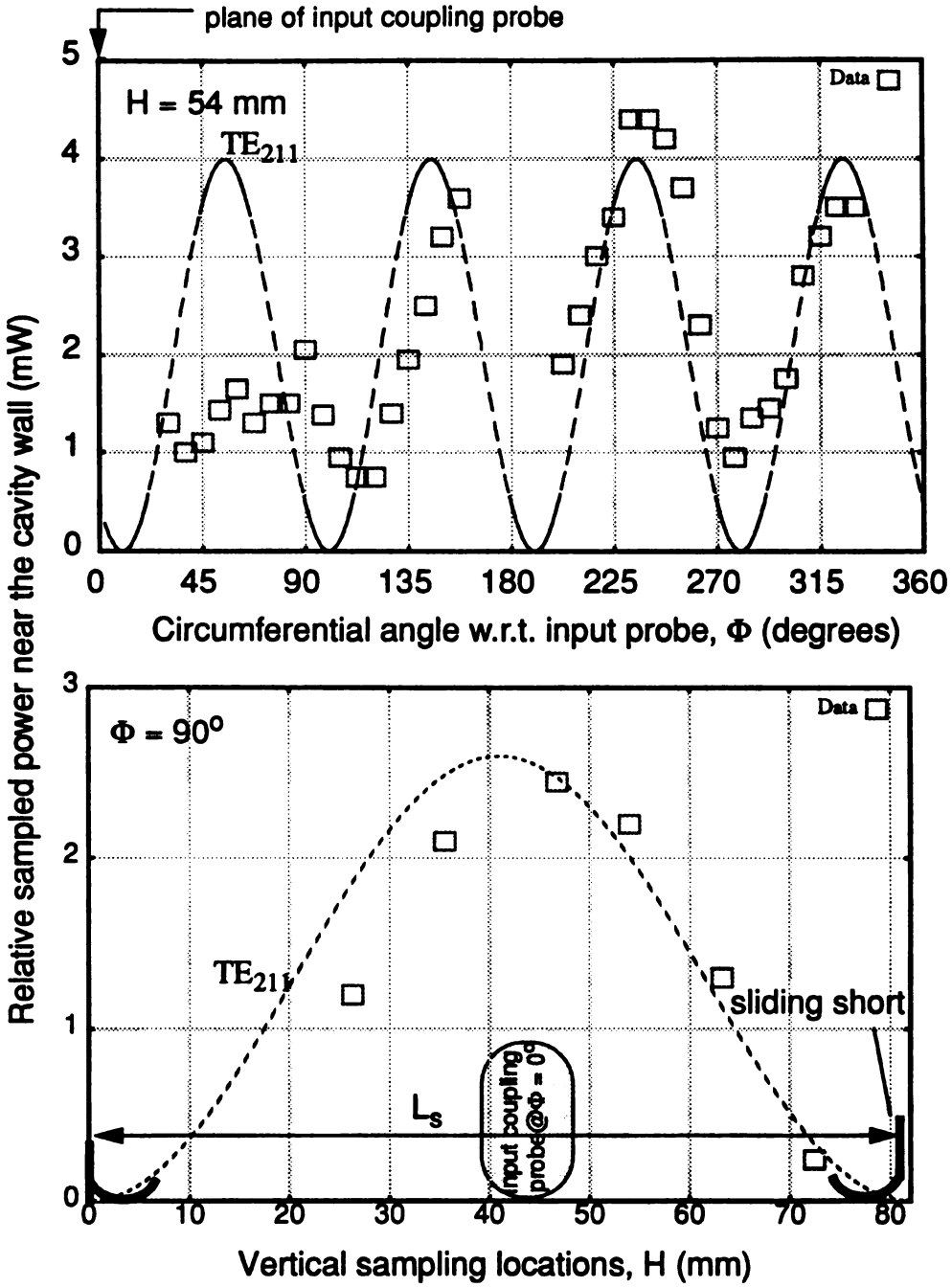

Figure 7.14 Measured EM mode pattern in side-feed, allN/8M MPDR with short resonant mode excitation.
Absorbed power ~ 236 W, pressure 0.8 mTorr.

data and discussion in side feed applicator were only focused on the three multipolar magnetic type ECR configurations.

7.2.3.E Power coupling efficiency and Quality factor of the discharge loaded cavity

Using calculation techniques similar to those described in Section 7.2.2.D for the end feed reactor, the microwave power coupling efficiencies are estimated either from quality factors or deduced by the calculated wall losses. Table 7.8 shows the power coupling efficiencies and the loaded cavity quality factors for the two resonant modes versus the three multipolar magnetic type ECR configurations and for different powers and pressures.

For all three ECR configurations, the TE_{211} mode loaded cavity quality factors are less than the corresponding quality factors for the TE_{311} mode. At 0.8 mTorr pressure and 328 W absorbed power, the TE_{211} mode loaded quality factors vary from approximately 22-28 for 4P/8M configuration to ~55 for 8P/8M configuration. The discharge loaded quality factors for TE_{311} mode are also the lowest at approximately 140 -160 for 4P/8M configuration while the highest are for 8P/8M configuration.

The power coupling efficiencies for TE_{211} mode which are in the range of 98% are better than the coupling efficiencies in the TE_{311} mode (87% to 95%). Again, this suggests that TE_{211} mode couples power more efficiently into the plasma discharge than for TE_{311} mode. For the magnetic configurations operating at the same EM mode, the 4P/8M configuration has the best power coupling efficiency and the 8P/8M has the lowest. This may due to the good match

between the number EM poles of the TE_{211} mode and number of magnetic poles for the 4P/8M magnet configuration. However, the overall coupling efficiencies are still high (> 87%) for all configurations. When pressure is increased to 2 mTorr, more efficient coupling is observed. The difference between Eff^{A}_{coup} and Eff^{B}_{coup} indicates the excitation coupling losses are only approximately 1% for TE_{211} mode and 5-10% for TE_{311} mode.

Table 7.8 Power coupling efficiencies and loaded cavity quality factors for different multipolar magnet type ECR configurations in side feed applicator

Input variables			8P/8M			4P/8M			4P/4M		
EM Modes	p (mTorr)	P_{abs} (W)	Eff^{A}	Q_L	Eff^{B}	Eff^{A}	Q_L	Eff^{B}	Eff^{A}	Q_L	Eff^{B}
TE_{211}	0.8	328	99.6 %	55	98.1 %	99.7 %	28	99%	99.6 %	43	98.5 %
		574	99.6 %	53	98.2 %	99.8 %	22	99.1 %	99.7 %	36	98.8 %
TE_{311}	0.8	328	97.7 %	377	87.4 %	99%	146	95%	98.2 %	281	90.6 %
		574	98%	278	91%	99%	162	94.6 %	98.5 %	243	92%
TE_{211}	2.0	328	99.7 %	27	99%	99.9 %	18	99.4 %	N.A.		
TE_{311}	2.0	328	99%	135	95.5 %	99.7 %	32	98.9 %			

7.2.4 Summary and discussion of electric field measurements

7.2.4.A Mode patterns

These electric field measurements demonstrate that the EM modes that are excited inside the cavity applicator depend upon the exact location of the microwave energy input coupling probe. The side feed coaxial probe applicator preferably excites TE modes while the end feed coaxial probe excites only TM modes. However these experiments together with the observations of others [141] indicate that both end feed and side feed coaxial coupling can excite TE and TM modes. Only by careful cavity applicator/coupling probe design can certain modes excitations be suppressed. For example, only TM_{01n} modes are excited if (1) the coupling probe is located exactly on the center axis of the sliding short end plate, and (2) the center conductor of the coupling probe is located exactly in the center of the input coaxial cable. If the center conductor of the coaxial probe is slightly off center or the probe is located off axis on the sliding short, the discharge loaded cavity TE modes can also be excited. However by the careful choice of the size and location of the excitation probe, one can control the EM mode(s) excitation even inside a discharge loaded cavity.

Another important observation is concerned with the difference between the actual discharge loaded cavity resonant mode height and the ideal cavity resonant mode height. As indicated in Figure 7.2, the actual discharge loaded cavity resonant height for TE modes in side feed applicator was close to but **less** than the empty cavity resonant length while the opposite happened for the TM modes excited by an end feed applicator. It is believed the shift is caused by the

non-ideal factors of the cavity applicator. By the EM perturbation theory, the insertion of input coupling probe causes the resonant cavity height to be slightly higher than the theoretical empty cavity resonant length. On the other hand, the quartz bell jar material would cause the resonant cavity height to be slightly lower. The biggest perturbation is caused by the plasma discharge itself which occupies the bottom hole of the cavity. According to the visual plasma images presented in Appendix C (figures C.2 and C.3), the side excited plasmas were very dense at the magnetic cusps especially close to the ECR magnet region and the center discharges area were sparse. That is equivalent to reducing the big bottom hole (14 cm dia.) of the cavity into a smaller hole. This explains why the side feed loaded cavity height shifts downward. One the other hand, there were additional dense plasmas near the top center of the bell jar in the end excited discharges shown in Appendix C (Figure C.5 and C.6). This is equivalent to a gaseous conductor shorting the cavity near the top bell jar location. Hence, the end feed loaded cavity height shifts upward.

7.2.4.B Operation trade-off

According to the experience developed from experimental operations, the side feed applicators can sustain a plasma discharge (the high density states) more readily at low pressure (below 2.5 mTorr) with the same input power than the end feed source. The end excited discharges tended to jump into a lower density state at low pressure operation. However, at higher power operation, the near field excited adjacent to the input excitation probe is difficult to avoid. As shown in Section 7.3, the end feed has a more uniform plasma density output than the side

feed. At low pressure, there seems to be a trade-off between plasma uniformity and the ease of operation in choosing applicator excitation.

7.2.4.C Electric field strength

The electric field strength measurements for side feed and end feed do not share the same pressure regime. However, their experimental behavior shares two common trends. First, the impressed field of the "short resonant mode" is always higher than the "long resonant mode". This is due to less wall loss and better coupling efficiency in the short resonant mode. Secondly, the higher the power, the higher the impressed field strength. In addition, under the 8P/8M and short resonant mode of both applicators with similar input power of 325 W, the total impressed electric field is E_t ~7.2 kV/m for side feed at 2 mTorr, and is ~6.27 kV/m (E_r ~ 5.1 kV/m and E_z ~3.65 kV/m) for end feed at 2.5 mTorr. This indicates that the side feed has higher **tangential** impressed electric field than the end feed and may explain why it is easier to operate the side feed at lower pressure.

Within the same end feed applicator, both the electric field strength at the walls and the estimated impressed electric field on the discharge in mode 1 is roughly 30% higher than the impressed electric field in mode 2. This indicates that near fields have an influence on the excitation of the plasma discharge.

As mentioned earlier, within the same side feed applicator and fixed multipolar ECR magnet configuration, the TE_{211} mode excitation has higher impressed electric fields (a factor of ~1.5) and lower applicator wall electric field strengths (40-50%) than the values in TE_{311} mode excitations. This suggests better coupling efficiency for TE_{211} mode excitation. On the other hand, within the

same side feed applicator and fixed EM mode excitation, the 4P/8M configuration has the lowest impressed electric field strengths, which is about ~70% of the corresponding electric fields in 8P/8M configuration. This indicates that 4P/8M ECR magnetic field configuration couples the most efficiencies with the TE_{211} mode. This high coupling efficiency is probably related to the excellent match between the multipolar ECR surface produced by the 4P/8M configuration and the multipolar electric field produced by the TE_{211} mode.

Comparison to other electric field strength measurements: Finally, it might be interesting to compare the measured electric field strengths in our plasma source to the electric field strengths measured in other MPDR™ or plasma sources. However, the reported absolute electric field strength measurements in journals are relatively sparse.

Using B-dot probe technique [142], Hopwood [57] and Wendt's group [143] have investigated the EM field strengths insides the spiral inductive coupled plasma (ICP) sources (described in Section 2.5.1) near the top of the quartz window by an protected B-dot probe. Hopwood performed studies in a square 27 cm x 27 cm x 13 cm plasma chamber for the ICP. The measured peak electric fields [57] varied from 100 V/m to 200 V/m as the incident rf power changed from 100 W to 1000 W at a fixed argon pressure of 5 mTorr. The electric field strength saturated above 600 W of rf power. At a fixed input rf power of 500 W, the measured peak electric field strength [144] varied from 350 V/m to 600V/m as pressure dropped from 10 mTorr to around 1 mTorr. Wendt's group [143] studied the cylindrical ICP with diameter 22 cm and height 13.7 cm. The reported peak

$|E_\phi|$ values were: for a fixed pressure of 10 mTorr, $|E_\phi|$ increased slightly from ~460 V/m at rf power of 50 W to ~530 V/m at rf power of 500 W; for a fixed 200 W of rf power, the $|E_\phi|$ decreased from ~ 610 V/m at 5 mTorr to around 320 V/m at 50 mTorr.

Recently, the plasma research group led by Godyak [145] made a comparison between the protected B-dot probe and a bare (and well-calibrated) B-dot probe in the spiral inductive coupled plasma discharge. Godyak concluded that the measured EM fields by the protected B-dot probe have significant perturbation by the protection gear in a protected B-dot probe. The measured electric fields from the bare and calibrated B-dot probe are around 200 and ~150 V/m for 1 and 10 mTorr at 100 W input rf power in a 19.8 cm diameter inductively coupled discharge.

These reported electric field strength values in ICP are much lower than the expected values caused by pure Ohmic heating. It is believed that other collisionless heating process such as stochastic heating occur in the ICPs. These electric field strengths are difficult to compare with the values in MPDR™-13. The direct comparison between disparate plasma systems are dubious. In the microwave MPDR™ operating at 1-10 mTorr (ν/ω) <<1 while in rf ICP sources ν is comparable with ω. In addition, the large difference in discharge volume make the comparison difficult to perform.

In a smaller discharge (9-cm diameter) MPDR™-9 [53] using the same side feed applicator, the measured electric field strength at the wall was ~18.9 kV/m for TE_{211} mode and ~46.3 kV/m for TE_{311} mode excited at 2.45GHz microwave CW

power. The experimental conditions were 8P/8M configuration with 260 W incident power and 0.9 mTorr argon. In comparison the electric wall field strength in MPDR™-13 at similar experimental conditions, the electric wall field strengths at MPDR™-9 are 70% higher for TE_{211} and 80% higher for TE_{311} than in the MPDR™-13. Some of the difference between Hopwood's measurement and the measurements reported here may be due to (1) the reported values in MPDR™-9 used the Burkart's method described in Section 5.3.1.A and the lower bound of RA methods is adopted in MPDR™-13, (2) microwave energy is more efficiently to couple into the larger discharge size (from 9 cm to 12.5 cm in diameter).

7.2.4.D Microwave power coupling efficiency

The microwave power coupling efficiencies in MPDR™ are excellent (> 87%) for both side feed and end feed geometries. Most of the power is lost in the plasma discharge instead of the applicator wall or coupling probe losses. The power coupling efficiencies change slightly as the EM modes, ECR configurations, and input power vary. The short resonant modes (TE_{211} mode and mode 1) for both side feed and end feed have better power coupling efficiencies than their long resonant mode/mode 2 counterpart. The extra section of applicator wall contributes the additional wall loss in the longer resonant mode. However, the overall power lost in the wall is still much lower than the power absorbed by the discharge.

For the similar experimental conditions, the coupling efficiency in 8P/8M side feed configuration is ~99% at TE_{211} mode, 328W power and 2.0 mTorr argon

gas, while the 8P/8M end feed configuration is ~98% at mode 1, 270 W power and 3.0 mTorr argon gas. This suggests a slight advantage for side feed in TE_{211} mode. However, when operating at the long resonant mode cavity height, the coupling efficiency for 8P/8M end feed configuration at mode 2 drops to ~96% while the 8P/8M side feed at TE_{311} mode is around 95%. As the sliding short moves up, the EM mode pattern in the end feed applicator does not change much (as shown Section 7.2.2.A). It only increases the standing wave by another $\lambda_g/2$ in axial length. However, the EM mode in side feed applicator has changed from the TE_{211} mode into the TE_{311} mode as the L_s increases. The number of EM poles does not match well with the number of magnetic poles at TE_{311} mode. Therefore, the coupling efficiency becomes smaller for TE_{311} excitation.

7.3 Ion Density Measurements

In most applications, the magnitude and uniformity of the ion density are proportional to the plasma processing rate and process output uniformity. Therefore downstream ion density is one of the most important output variables of a plasma source. The objectives of this section are (1) to investigate the magnitude of the ion density as a function of the input variables, (2) to evaluate the uniformity of the ion density profile for different ECR configurations and for different applicators (side feed vs. end feed), and (3) to calculate the ion production costs from the measured ion densities. The ion density data was obtained from the double Langmuir probe measurements carried out as described

in Section 5.4.2. The magnitude and spatial variation of the ion density versus power, and pressure are experimentally measured. The spatial variation of the radial and downstream densities is presented. Only experiments with 8P/8M configuration were conducted in end feed reactor. Data in different ECR magnet configurations are also presented in the side-feed applicator for comparison with the "benchmark" 8P/8M configuration. Only argon gas is used. Knowing the cross sectional ion density at z = 3 cm allows the calculation of ion production cost by eq. (4.5). Ion production costs are calculated versus pressure and power for each of the plasma source variations.

7.3.1 End feed applicator

The ion density reported here is usually measured for the 8P/8M end feed plasma source at r = 0, and z = 3 cm downstream location with the applicator operating in either the mode 1 or the mode 2. The absorbed power varied from 150 W to 320 W and the argon gas pressure varied from 2.5 to 7 mTorr.

7.3.1.A Magnitude of the Ion density versus power and pressure

n_i vs. power: The ion density for the end feed MPDR™-13 at z = 3 cm and r = 0 cm versus microwave absorbed power is shown in Figure 7.15 for a constant chamber pressure of 5 mTorr argon. The density of mode 1 is approximately 15% higher than mode 2 and for both modes the measured ion density increases with the absorbed microwave power. This difference may be due to (1) the wall losses are higher in mode 2 due to the larger applicator wall surfaces areas,

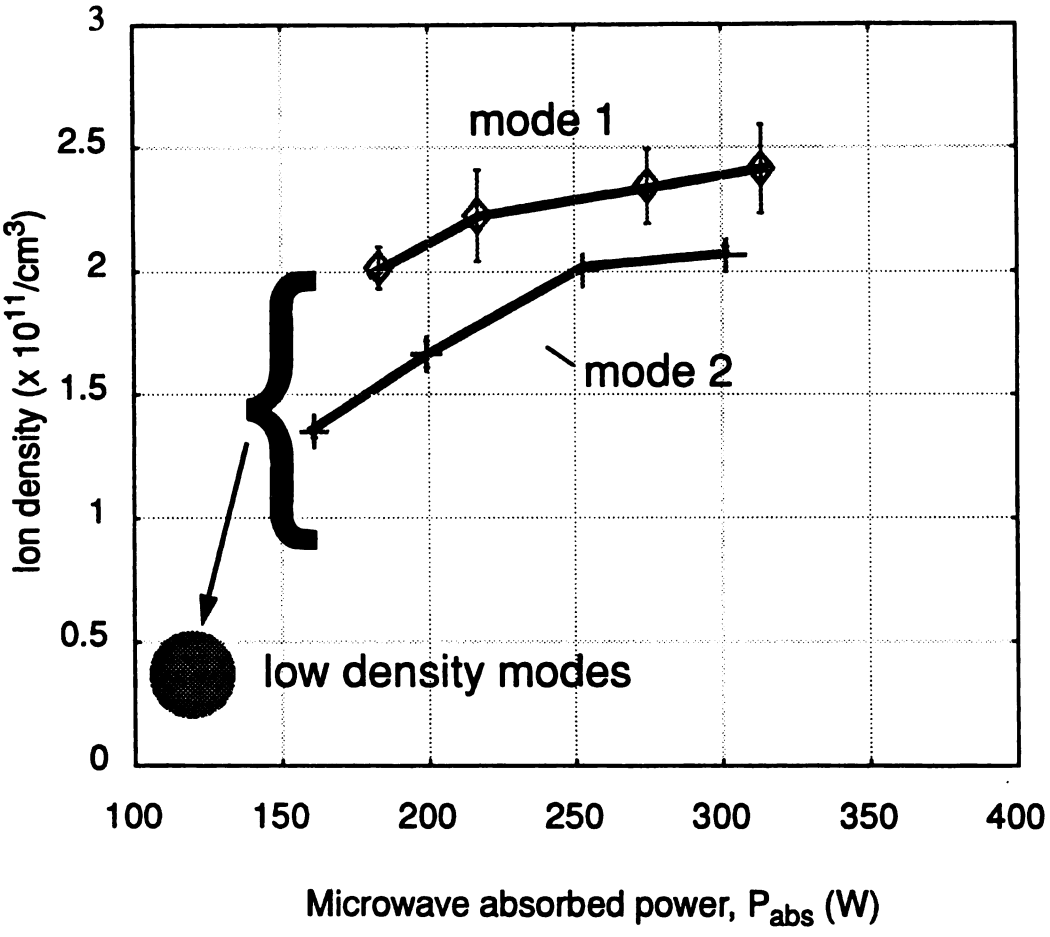

Figure 7.15 End feed downstream (0, 0, 3 cm) ion density versus microwave absorbed power at pressure 5 mTorr of argon discharge.

and (2) in mode 1 the "near fields" influence/enhance the excitation of the plasma discharge. Whenever the incident power is less than 150 W, it is not easy to maintain a well-matched discharge and a jump to a lower density operating state occurs. This lower density state is shown by the shaded area in Figure 7.15 and is denoted as the low density mode state.

n_i vs. pressure: Figure 7.16 displays the end feed MPDR™-13 at z = 3 cm and r = 0 cm versus chamber pressure at a constant absorbed power of approximately 270 W. The flow rate was fixed at 50 sccm of argon gas and the pressure was controlled by the throttle valve. As the pressure varied from 2.5 to 7 mTorr, the measured ion density slightly decreased for both mode 1 and mode 2. Again the measured ion density in mode 1 is about 12% higher than the mode 2.

When the pressure is below 2 mTorr, the well-matched end feed plasma discharge is difficult to maintain and often jumps to a lower density mode of operation. A significant amount of incident power is then reflected and the low measured ion density is represented as shaded area in Figure 7.16. These jumps in density are more carefully described in Chapter 9.

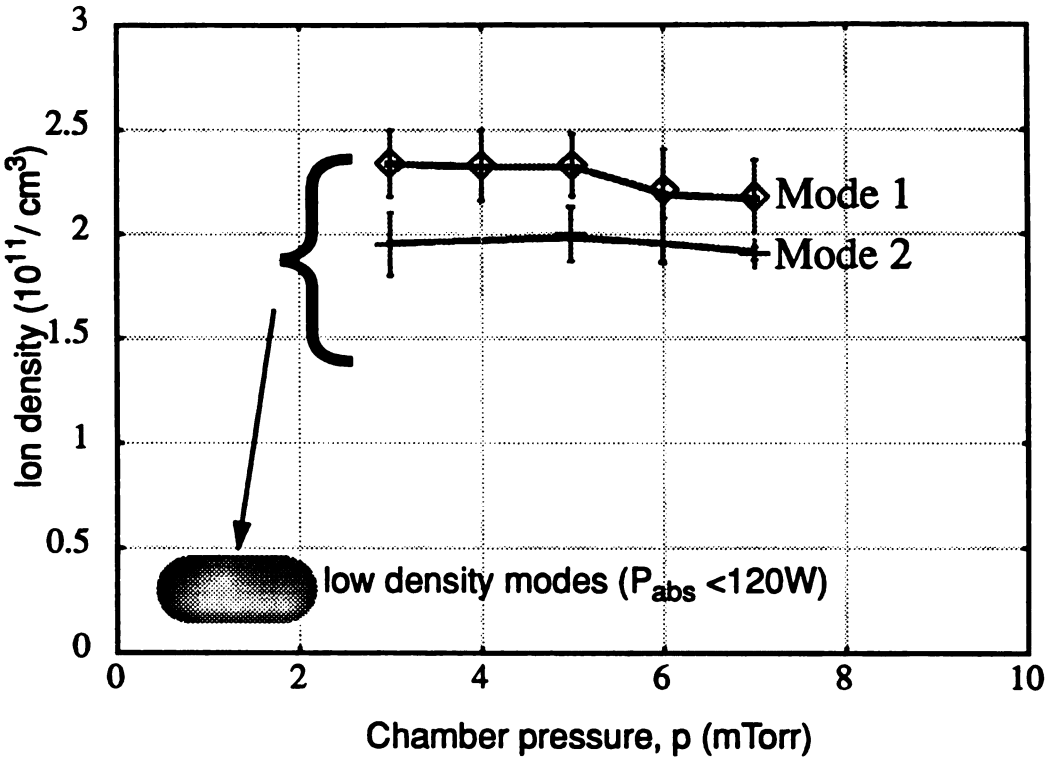

Figure 7.16 End feed ion density at (0, 0, 3 cm) versus chamber pressure at absorbed power approximately 270 W argon discharge.

7.3.1.B Spatial variation of the ion density

n_i vs. z: The variation of the end feed ion density versus z is displayed in Figure 7.17. The experimental conditions were 3 mTorr, absorbed power 270 W and operation in mode 1. The density decreases as the position z increases away from the plasma source. Specifically, the density falls to 25% of its original value from z = 1 cm to z = 9 cm. A similar density decay was also observed for all absorbed power levels and for mode 2.

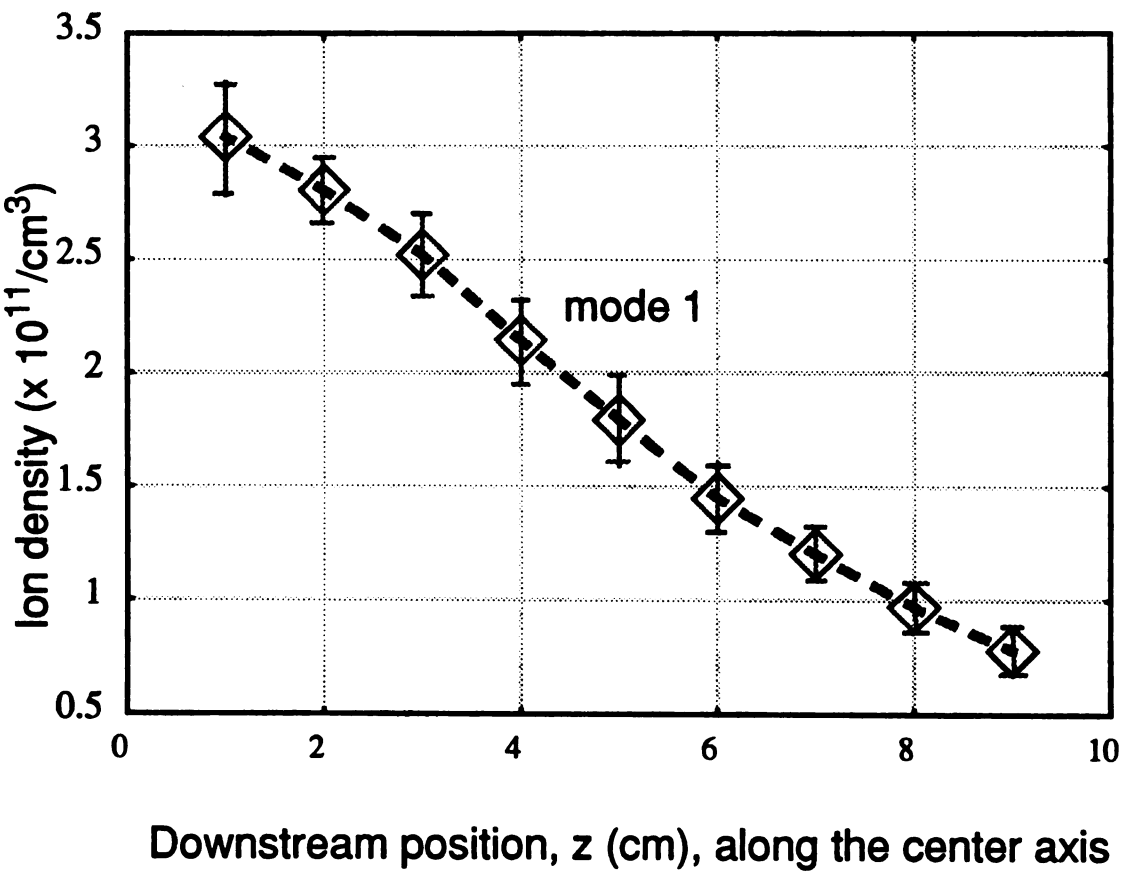

Figure 7.17 End feed ion density versus downstream position at 3 mTorr pressure with 270 W absorbed power at mode 1.

Cross sectional profile: Figure 7.18 displays the typical end feed ion density profile at z = 8 cm as measured by the Langmuir probe array shown in Section 5.4.4. The uniformity (defined as the standard deviation over the average of 20 probes) at z =8 cm, 270 W absorbed power and 5 mTorr is around 6.8% over a 66 mm x 53 mm cross section area (see dotted rectangle in Figure 5.6).

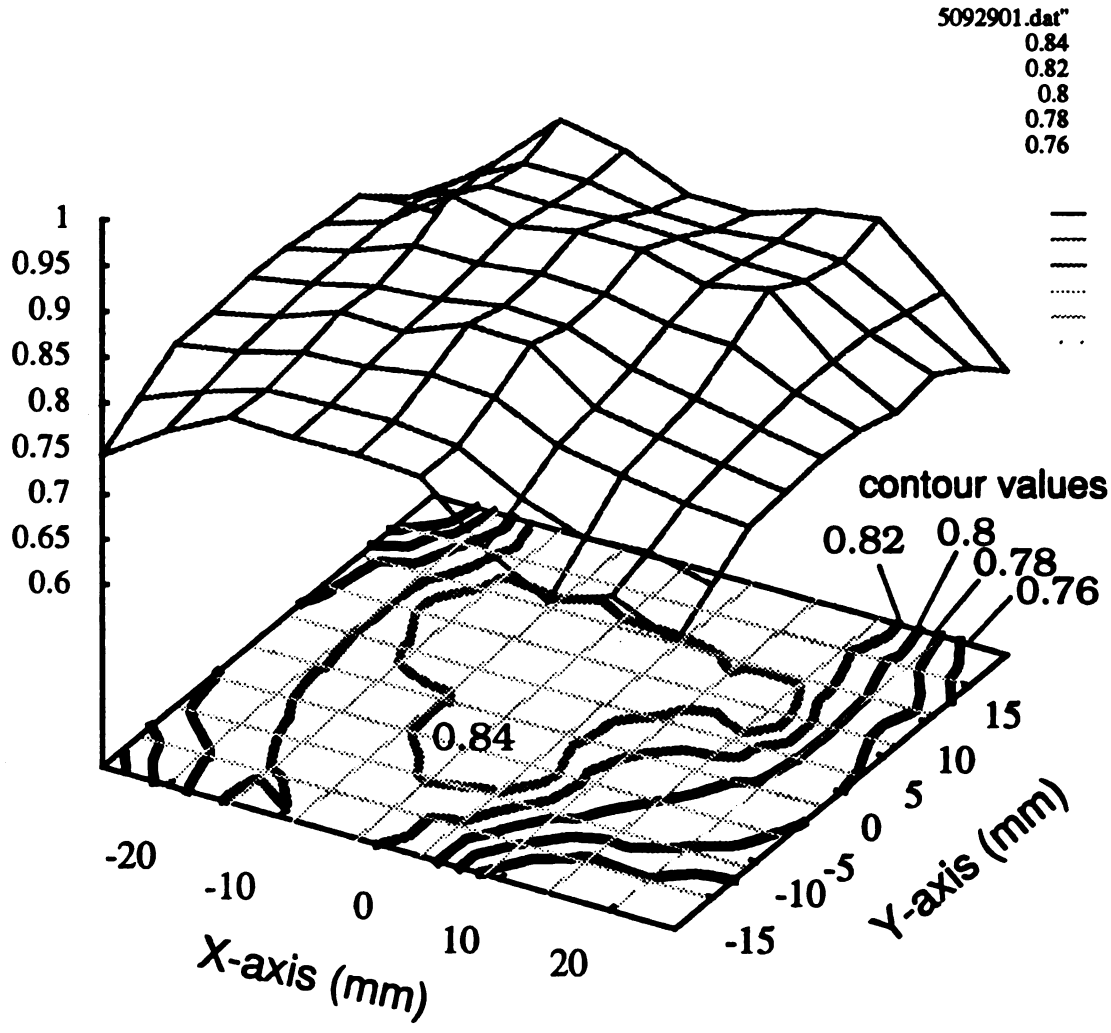

Figure 7.18 End feed (8P/8M ECR plasma source) downstream (z = 8 cm) cross sectional ion density profile in mode1 with absorbed power 270 W and pressure 5 mTorr.

The density uniformity at z =8 cm was also measured under different input conditions: absorbed power from 150 to 320 W, and pressure from 3 to 7 mTorr, for both modes (mode 1 and mode 2). Downstream uniformities are 6-7.8%, and are independent of the input experimental conditions. It is believed that near the ECR excitation region ionizing collisions influence the density profiles. Then as the plasma diffuses downstream the diffusion processes and recombination on the walls determine the density profiles. This behavior is expected since it follows the prediction from the plasma diffusion models [53,146] in low pressure regime.

7.3.2 Side feed applicator

7.3.2.A Ion density versus power, pressure and flow rate

n_i vs. power: The ion density in side feed MPDR™-13 at z = 3 cm and r = 0 cm versus incident microwave power is shown in Figure 7.19 for three different multipolar magnetic ECR configurations. Using argon gas they are either operated in a well-matched TE_{211} mode or a well-matched TE_{311} mode at pressure of 0.78 mTorr. Therefore in this figure the incident power can be considered as the absorbed power. As shown, the 8P/8M magnet configuration excited with the TE_{211} mode had the highest measured plasma density and the 4P/4M configuration, independent of TE_{211} or TE_{311} excitations, had the lowest density. The 4P/4M configuration densities were around 40% lower than the 8P/8M. The other two magnetic field configurations, i.e. the 4P/8M or 8P/8M with TE_{311} mode excitation fell in between. Note that this does not necessary mean that 8P/8M

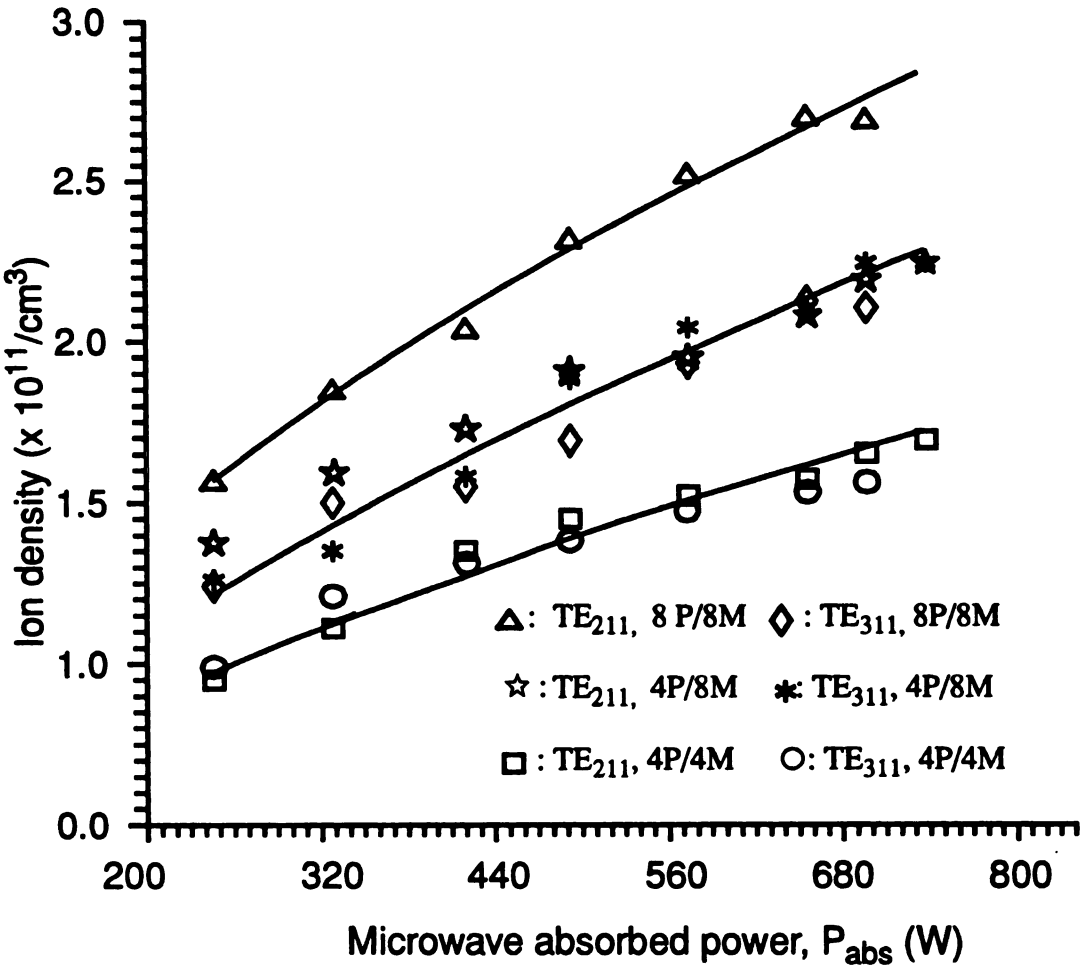

Figure 7.19 Side feed ion density (0,0, 3 cm) versus microwave absorbed power for different multipolar magnetic ECR configurations and for the TE_{211} and TE_{311} EM mode excitations.
The discharge pressure was 0.78 mTorr with 20 sccm argon gas.

configuration excited with TE_{211} mode has the highest density over the entire z = 3 cm cross section. The cross sectional density profiles vary from one magnetic field configuration to another. The spatial density profiles vs. magnetic field configuration are described in more detail in the Subsection 7.3.2.B.

Of all cases, the ion density increases when the (absorbed) power increases. As shown in later, charged particle energy measurements (Sections 7.4 and 7.5), power increases result in only slight increases of electron and ion energies. The extra deposited power is primarily used to the argon atom and ion excitations and to increase the ion density via ionizations. Therefore, this confirms that the ion density is mainly controlled by the discharge absorbed power. As can be seen from Figure 7.19, no ion saturation phenomenon occurred in MPDR™-13 when the power was operated up to 720 W.

n_i vs. pressure: Figure 7.20 shows the side feed ion density (0, 0, 2 cm) dependency versus chamber pressure for the TE_{211} and TE_{311} mode excitations. The absorbed power was constant at approximately 235 W and in 8P/8M configuration. The pressure was solely controlled by the argon gas flow rate with both the gate and throttle valves wide open. As shown, the ion density of the TE_{211} mode is ~15% higher than TE_{311} mode and the ion density increases monotonically with pressure for both EM modes.

n_i vs. flow rate: The ion density (0, 0, 1 cm) versus flow rate is shown in Figure 7.21 for both the TE_{211} and TE_{311} resonant modes. The experimental conditions were 235 W absorbed power with the plasma source operating at a fixed pressure of 1.21 mTorr. The constant pressure of 1.21 mTorr was maintained

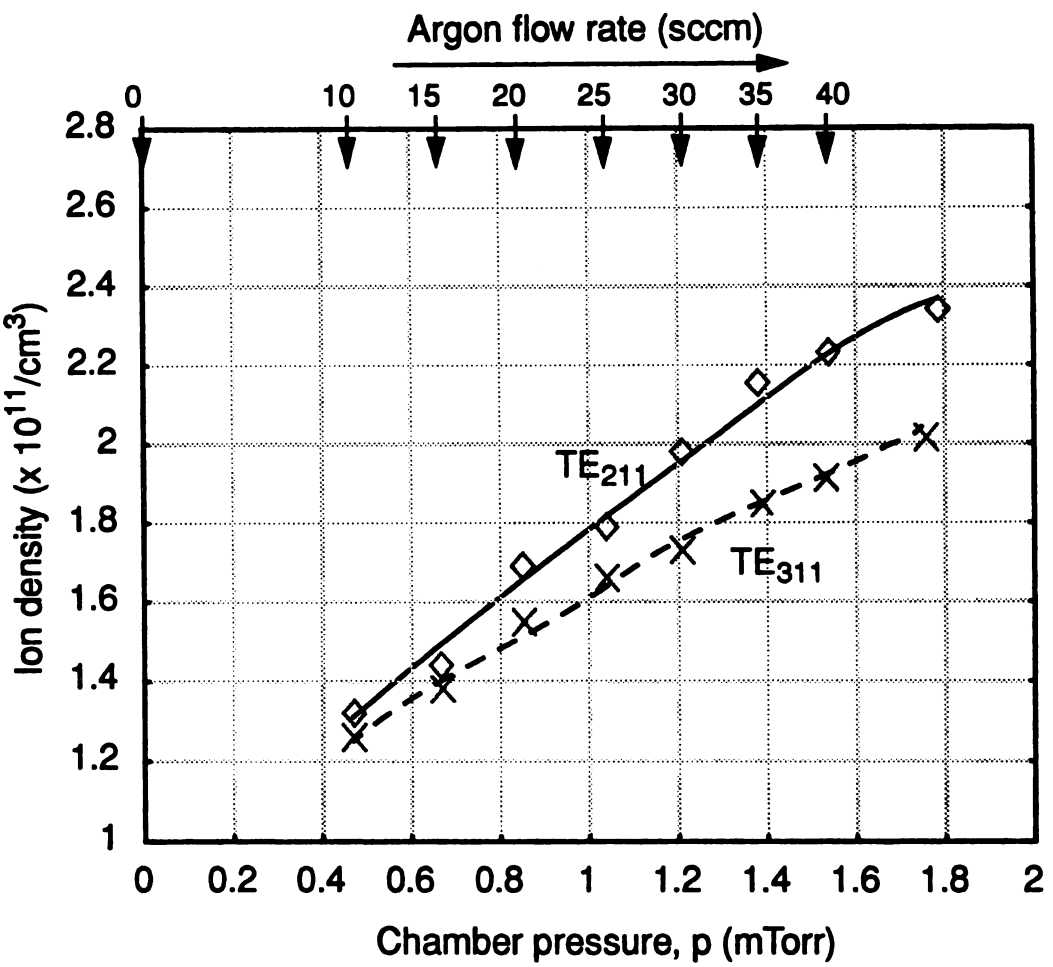

Figure 7.20 Side feed 8P/8M ion density (0, 0, 2 cm) versus chamber pressure for two different EM modes, absorbed power around 235 W.

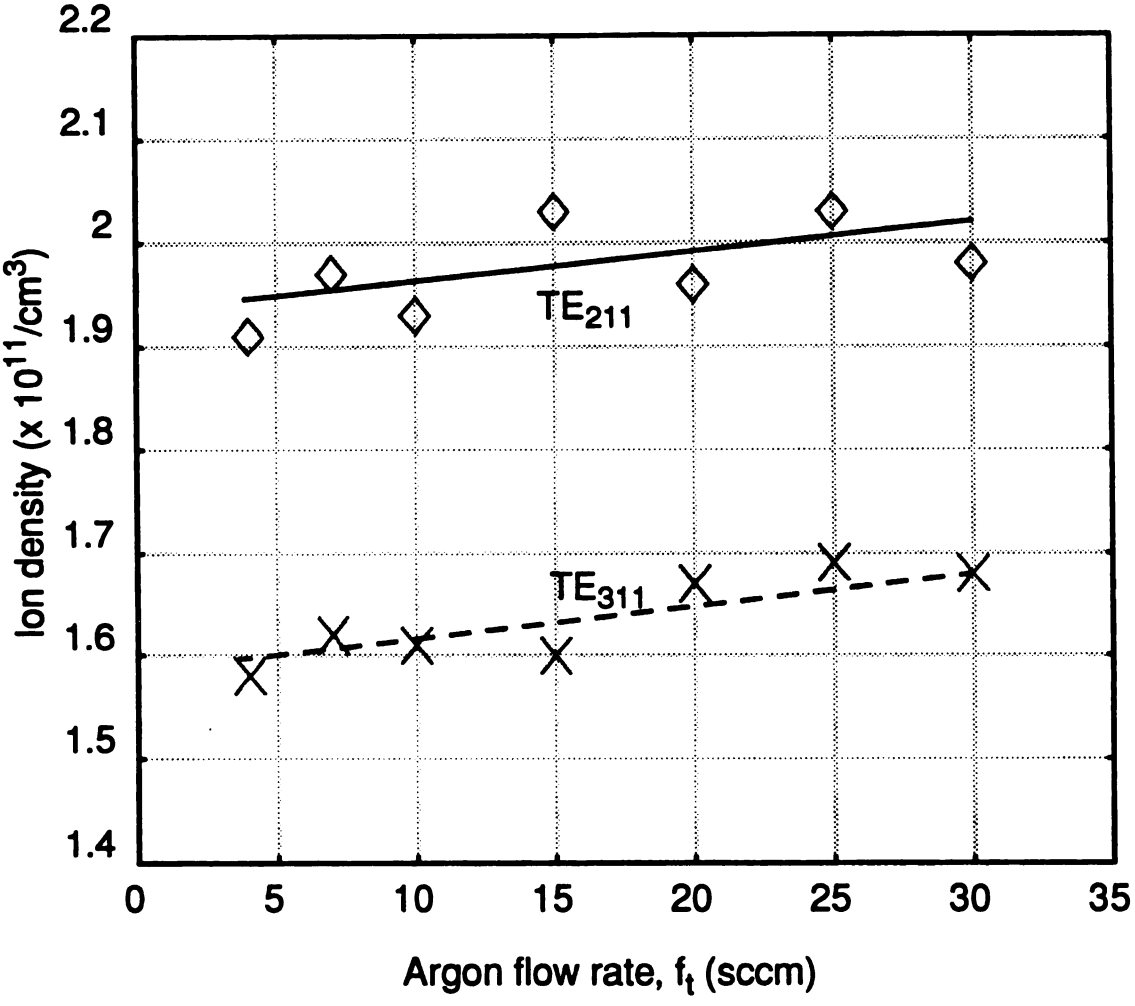

Figure 7.21 Side feed 8P/8M ion density (0, 0, 1 cm) versus argon flow rate at a fixed chamber pressure of 1.21 mTorr, absorbed power was around 240 W and two different EM modes.

by throttling the gate valve. As shown in the Figure, the measured ion density varied only ~5% while the argon flow rate changed over seven times (from 4 sccm to 30 sccm). This indicates that pressure and absorbed power are more dominate variables than the flow rate if plasma density must be changed.

7.3.2.B Spatial variation of the ion density

n_i vs. z for different ECR magnet configurations: Figure 7.22 shows the side feed ion density versus downstream location for four different magnet configurations. The absorbed power was approximately 236 W and chamber pressure 0.8 mTorr argon. The 8P/8M and the 4P/8M configurations with TE_{211} excitation have about the same densities with 8P/8M configuration density slightly higher. At the larger z values (z > 6 cm), both 4P/8M and 8P/8M showed similar uniformities and densities. The 4P/4M has a density of about 30% less than those of two configurations. Note the allN/8M configuration operating at TE_{311} excitation clearly had the lowest density; its density was around half of the density produced by the 8P/8M configuration operating at TE_{211} excitation. This is mainly because the allN/8M multipolar magnetic configuration does not have the confinement effect and has higher diffusion losses. Due to the low density of 4P/4M and allN/8M configurations, the charged particle energy measurements in side feed applicator (Sections 7.4 and 7.5) will only be focused on the 4P/8M and 8P/8M configurations.

Radial ion density profile: Due to the non Φ-symmetric EM field excitations in side feed applicator, detailed ion density radial profiles have been examined by moving the Langmuir probe at the grid point locations within a specific quadrant (shown in Figure 7.23) in each of z = constant plane (z = 1, 2, 3, 4, 5 cm). Since the ion densities of 4P/4M and allN/8M magnetic configurations or the TE_{311} mode excitation in all magnetic configurations are lower than the density in 8P/8M and 4P/8M with TE_{211} excitation, the radial ion density profiles

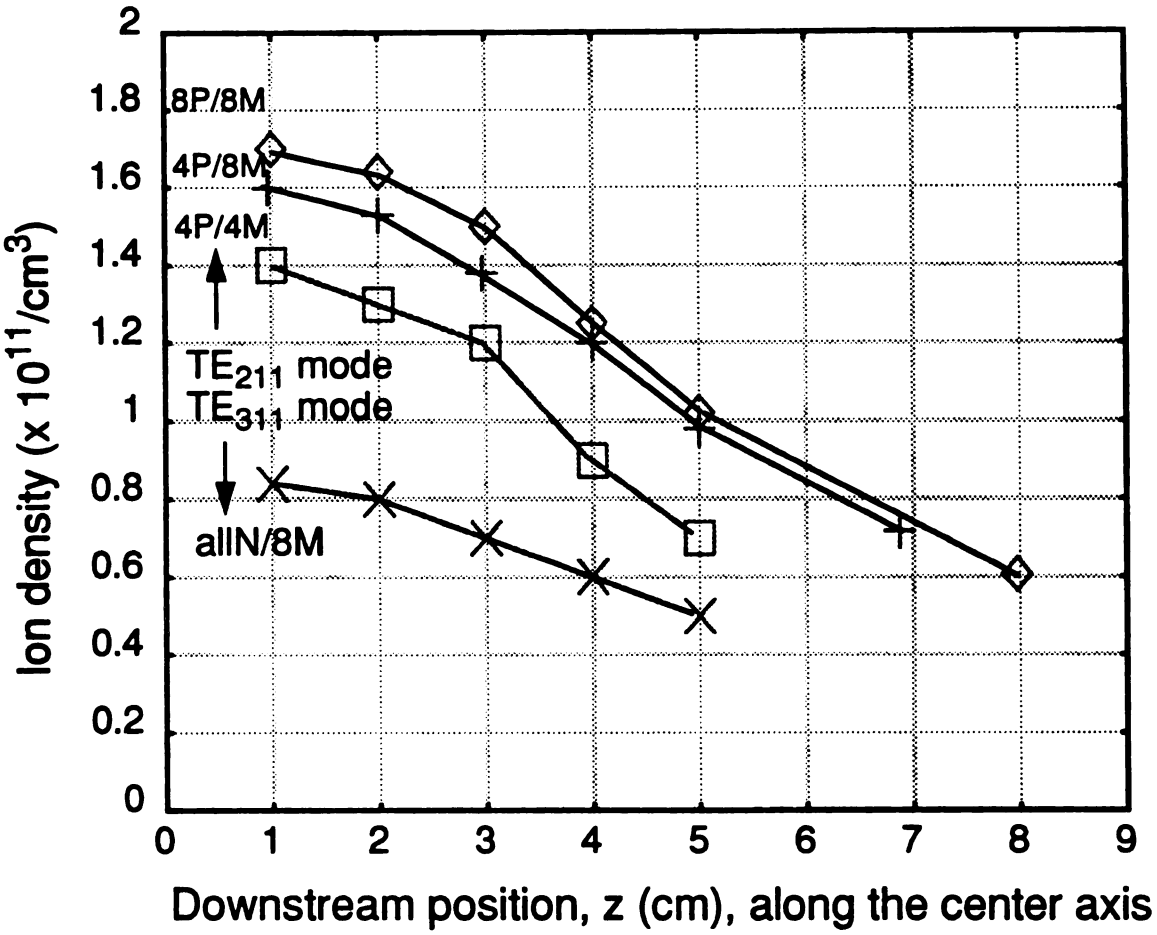

Figure 7.22 Side feed ion density versus downstream position for four different ECR magnetic configurations.
The experimental conditions were argon gas at a pressure of 0.8 mTorr approximately ~ 236 W absorbed power.

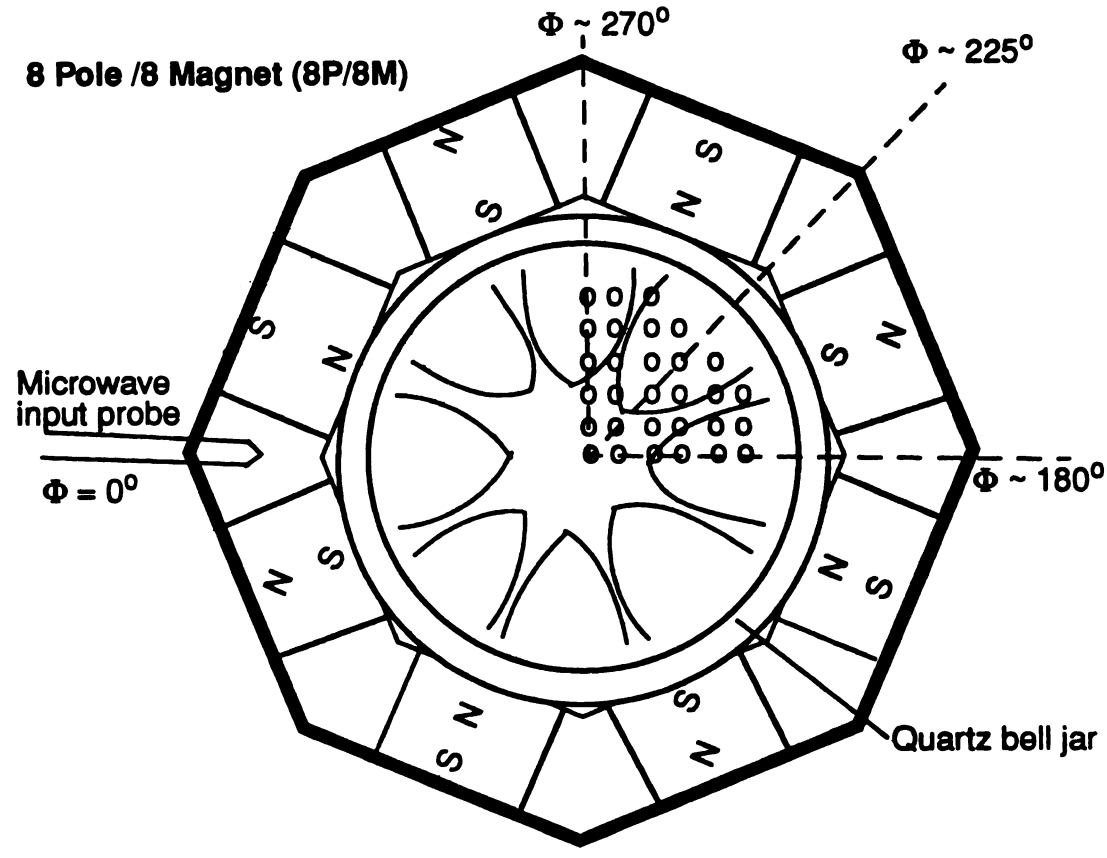

Figure 7.23 Locations (o: 30 points) for spatial ion density measurement in side feed for the 8P/8M and 4P/8M configurations.

were only measured for the 4P/8M and 8P/8M configurations with TE_{211} excitation. The measurements of the side feed radial ion density profile at different z locations are summarized in Figures 7.24 and 25 for the 4P/8M and 8P/8M configurations operating in the TE_{211} mode excitation. The experimental conditions were ~ 237 W absorbed power and with 20 sccm argon at 0.78 mTorr. The Φ direction variations in the ion densities are not completely shown in Figures 7.24 and 25. As the Φ direction is varied the ion density values do change to some extent, but the data shown in Figures 7.24 and 25 roughly represent of the data at various Φ values within the measured quadrant area, shown in Figure 7.23. The 8P/8M configuration had its highest density in the center of the discharge (shown in Figure 7.24), while the peak density for the 4P/8M configuration occurred off-center (shown in Figure 7.25) near the ECR excitation region. This density profile results from the fact that the ECR region in 4P/8M configuration shown in Figure 6.5 (b) is closer to the quartz wall than the 8P/8M configuration shown in Figure 6.3 (b). It takes further distance for the ionized species in 4P/8M ECR zone to diffuse into the center discharge region. However, as ions travel downstream they become homogeneous for all configurations and then have a regular diffusion-controlled type density profile. To quantify the effect on density uniformity, the standard deviation of ion density is calculated from density measurements over a 30 cm^2 quadrant of a 5-cm radius circular area, as shown in Figure 7.23. The 4P/8M configuration at z = 3 cm had the most uniform plasma (13.7%) with an average of about $1.4 \times 10^{11}/cm^3$.

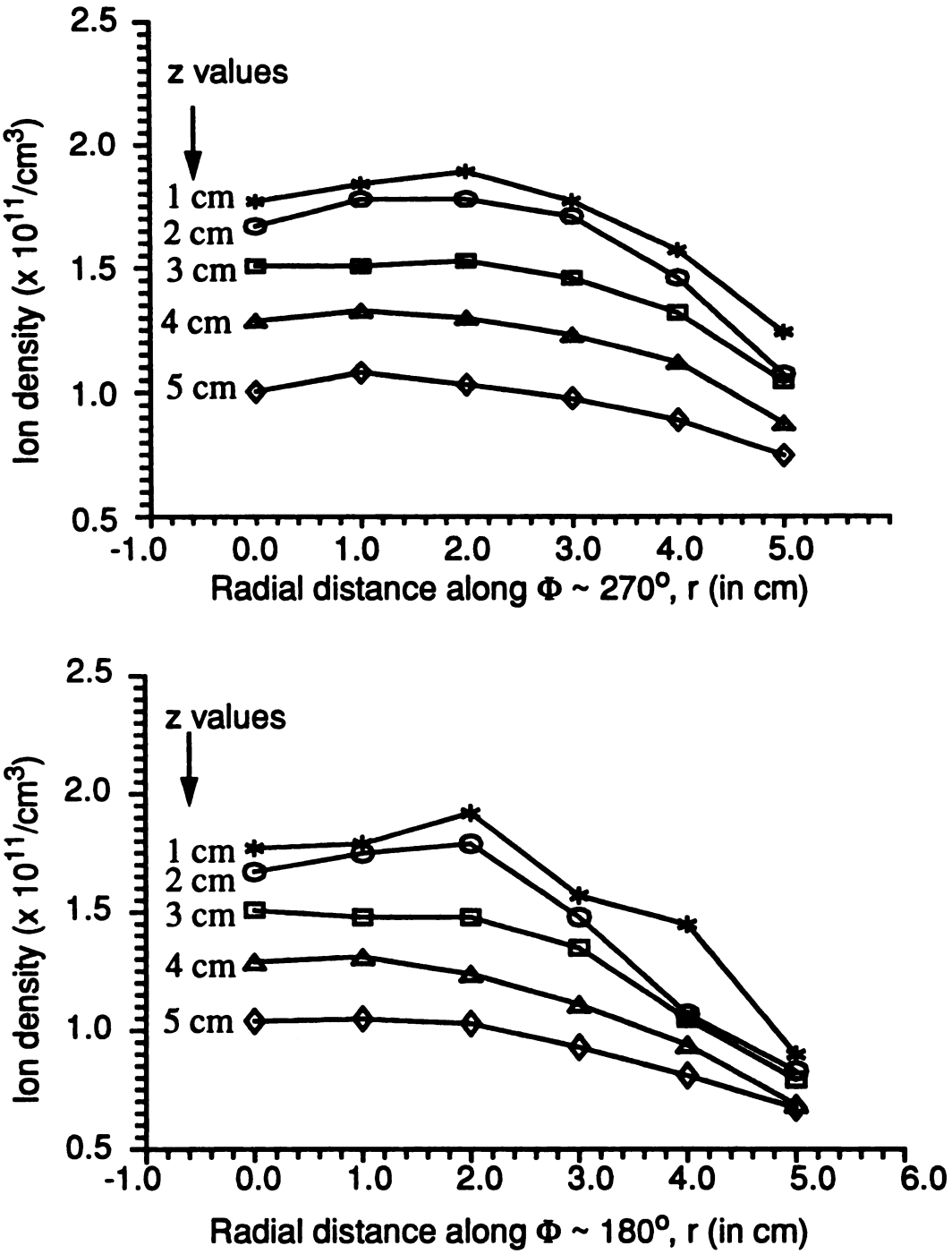

Figure 7.24 Side feed radial ion density (z =1 to 5 cm) for the 8P/8M configuration. Experimental condition: 20sccm, 0.78 mTorr argon gas, TE_{211} mode with ~ 238 W absorbed power.

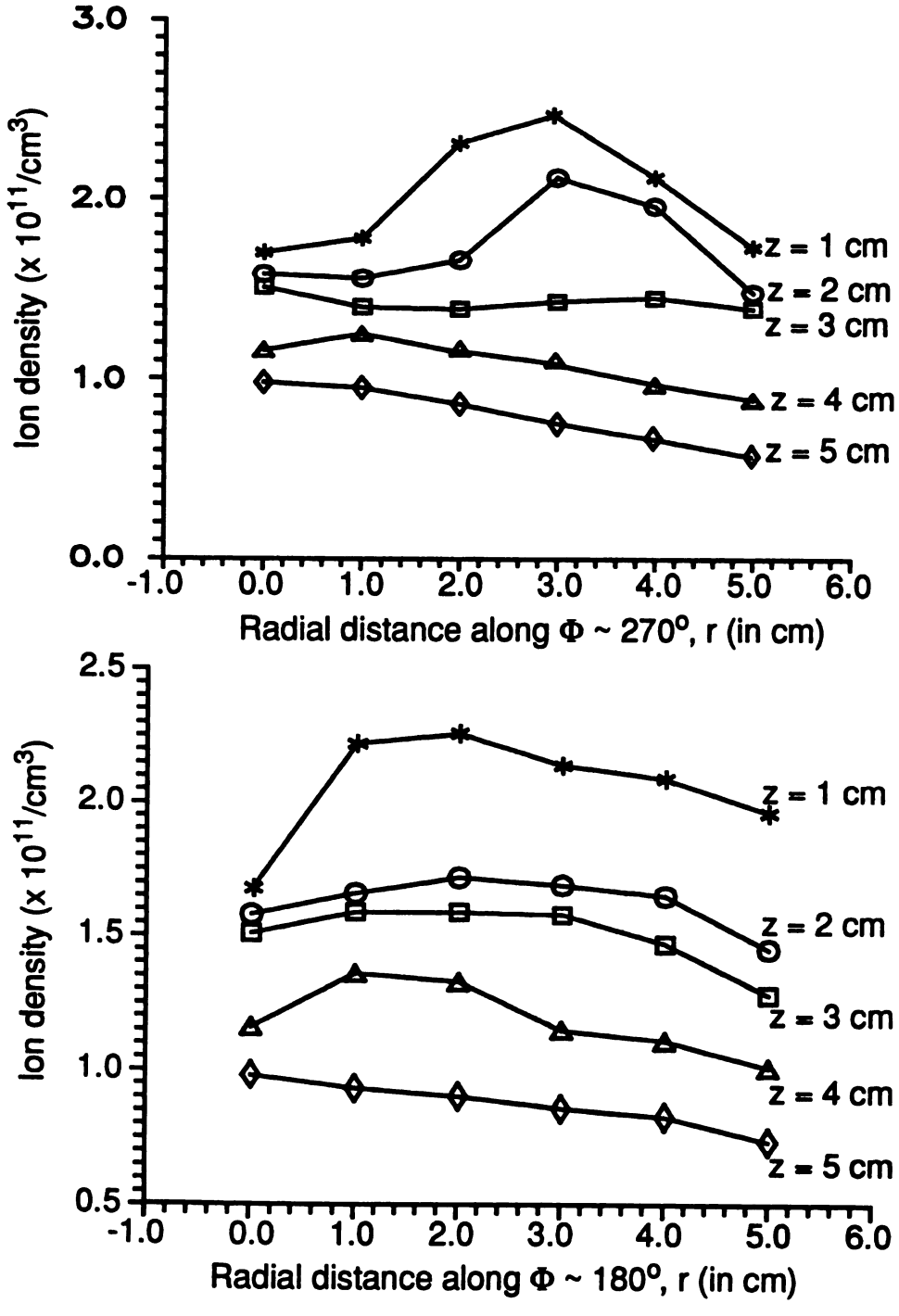

Figure 7.25 Side feed radial ion density (z =1 to 5 cm) for the 4P/8M configuration. Experimental condition: 20sccm, 0.78 m Torr argon gas, TE_{211} mode with ~ 237 W absorbed power.

7.3.3 Comparison of density performance

7.3.3.A Magnitude of the ion density

Side feed vs. end feed: The measured ion densities in both end feed and side feed plasma source which were measured under similar experimental conditions were taken for the 8P/8M ECR magnet configuration, at the location (0, 0, 2-3 cm). The measured ion density of end feed plasma source in TM_{011} mode was ~2.78 x $10^{11}/cm^3$ at 3 mTorr and 270 absorbed power while the ion density of side feed plasma source in TE_{211} mode was ~2.37 x $10^{11}/cm^3$ at 1.8 mTorr and 235 W absorbed power. They show very similar densities when operating under similar input experimental conditions.

7.3.3.B Cross sectional density uniformities in side feed and end feed of 8P/8M magnet configuration

The density uniformity near the plasma generation region (z = 1 cm) was investigated by biasing the Langmuir probe at -30V with respective to the chamber grounded wall. In these experiments, the side feed input coupling probe was at the height of H ~ 37 mm. As shown in Figure 7.26 next page, the Langmuir probe was moved along the two axes and sixteen ion saturation currents (I_{sat}) were recorded.

It is understood that ion saturation current does not fully represent the density. However, ion saturation current is a very good approximation indication on relative ion density **uniformity** provided that: (1) the measured plasma potential is relatively constant over the region of interested, and (2) the electron temperatures does not vary much over the region. From eq. (5.13), ion density is

proportional to the current collected and only inversely proportional to the square root of electron temperatures, (i.e. T_e is the 2nd order effect on n_i). Both conditions are confirmed by the data presented in Section 7.4.

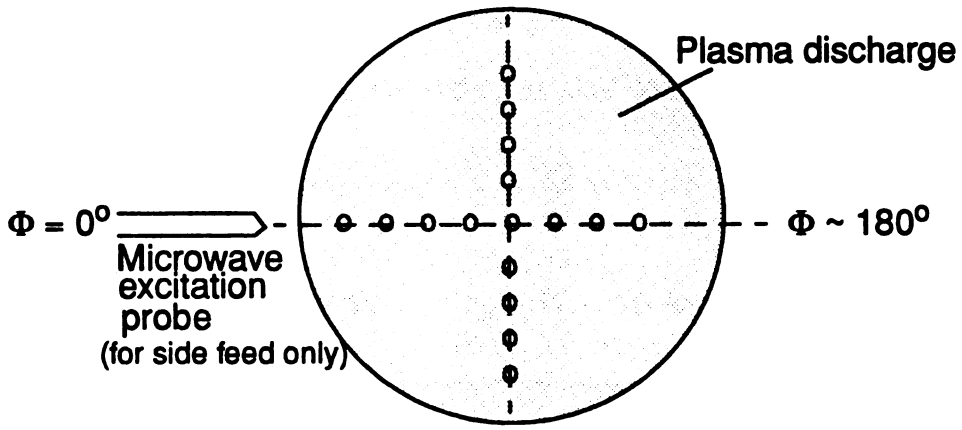

Note: 1 cm distance between data taking points (denoted o) along both directions

Figure 7.26 Ion saturation currents measuring locations at z = 1cm.

Table 7.9 lists the experimental conditions and uniformities of the measured saturation currents at z = 1 cm, which is near the plasma generation region. The "mode" described in Table 7.9 referred to the subjective visual plasma images, which were unfortunately not pictured at the time during experiments. The data was measured in the "near field" indicates that both the visual image and the measured density were lopsided with the brightest or densest discharge at $\Phi = 0^o$, i.e. brighter or denser plasma was near the input coupling probe side. "Dipole" and "quadratic" (similar to TE_{111} and TE_{211} excitations) represent two and four bright lobes observed in the plasma discharge. "Uniform" represents a quite uniform visual brightness distribution across the magnetic cusps

circumferentially. Clearly the density uniformity of "near field" modes is the worst. One of the observations from Table 7.9 indicated that the careful excitation of "uniform" mode inside side feed plasma source can yield a good uniformity of 4.9% with a sacrifice of a lower absorbed power (hence the density). However, it should be note that if the end feed is employed to excite the TM_{011} mode, improved uniformity (~2.8%) is expected due to more symmetric EM field excitation.

Table 7.9 Uniformity of relative ion saturation currents at z = 1 cm

Types	L_s (mm)	Mode	P_{ref} (W)	$<I_{sat}>$	$\sigma/<I_{sat}>$
Side feed L_p ~ 23 mm 1.0 mTorr argon gas P_{inc} ~ 246 W	62.6	Near field	33.0	~119	9.5%
	66.5	Near field	14.0	~147	10.4%
	~69.0	Dipole	5.6	~158	7.8%
	72.6	Uniform	47.6	~124	4.9%
	82.0	Quadratic	9.1	~140	8.2%
End feed L_p ~ 31mm 3.0 mTorr argon gas P_{inc} ~ 246 W	76.8	Uniform (with bright center region)	14.0	~280	2.8%

In summary, the density uniformities near the plasma source (16 data taken at z = 1 cm) are 2.8% and 8.2% for TM_{011} excitation in end feed and TE_{211}

excitation in side feed respectively. The downstream ion density uniformities at z = 8 cm are 6.8% and 14.8% (shown in later Section 7.3.5) for end feed and side feed respectively. These measurements indicated that the density in end feed plasma source is more uniform than in the side feed source.

7.3.3.C Ion production cost

A. End feed applicator

Using the measured ion density at r =0, and z = 3 cm in the end feed plasma source, the ion production cost is calculated using eq. (4.5) at z = 3 cm plane. Figure 7.27 displays the variation of ion production cost versus incident power and pressure for the 8P/8M end feed MPDR™-13 for both mode 1 and mode 2. Figure 7.27 (a) presents the ion production cost versus different pressures with a constant absorbed power of approximately 270 W. For mode 2 the ion production cost drops from ~450 eV/ion to around 420 eV/ion as pressure changes from 1 mTorr to 3 mTorr. And the ion production cost of mode 2 is stable at approximately 420 eV/ion form 3 to 7 mTorr. The ion production cost for mode 1 is at about 375 eV/ion from 3 to 7 mTorr and is ~12% lower than the corresponding ion production cost for mode 2.

Figure 7.27 (b) shows the ion production cost versus absorbed power for both mode 1 and mode 2 at a fixed pressure of 5 mTorr. For both modes, the ion production cost increases as absorbed power increases. That means that even though increasing absorbed power results in a higher ion density, the additional input watts to produce another ion downstream increase as the input power increases. Thus the efficiency producing additional ions decreases with

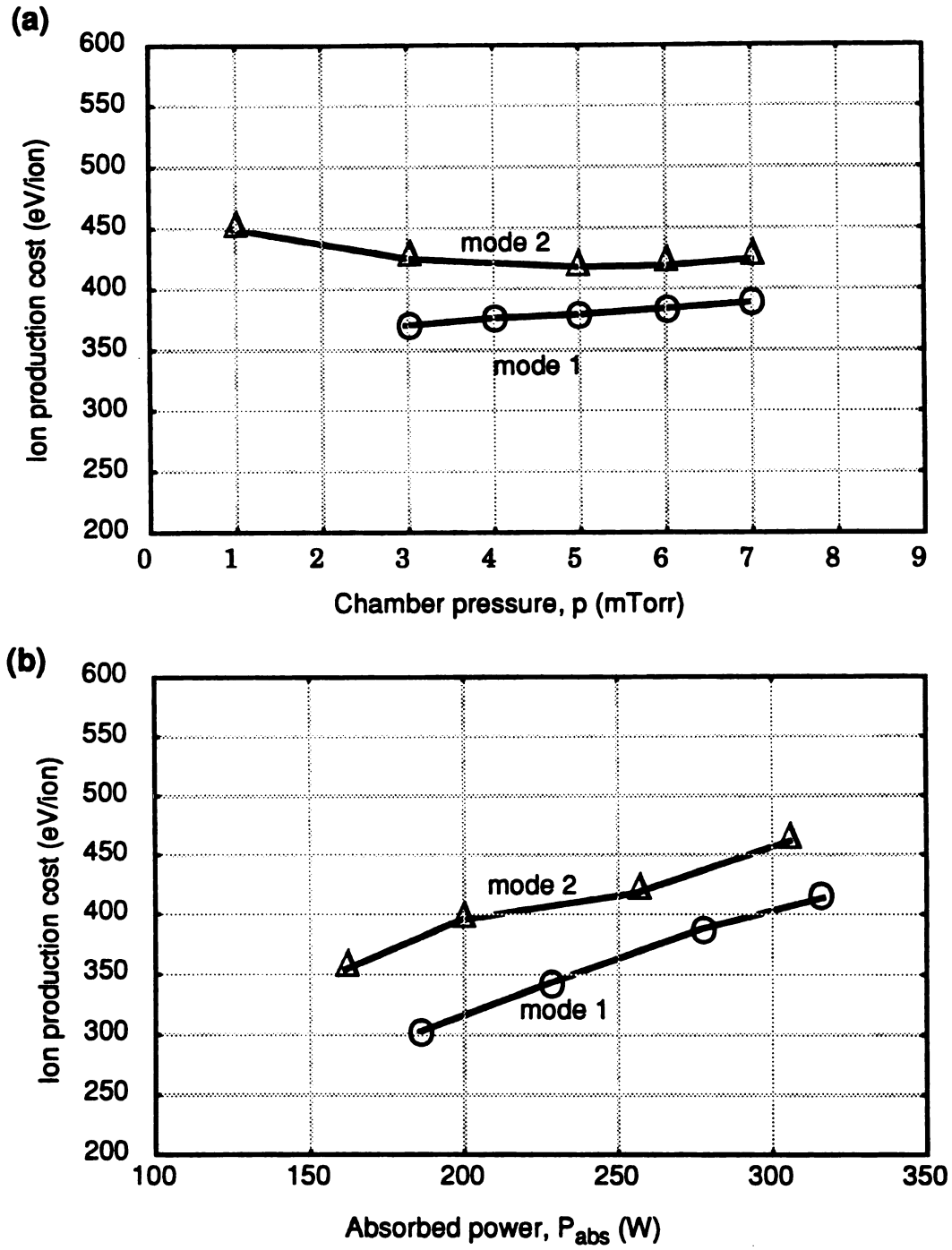

Figure 7.27 End feed 8P/8M ion production cost at z = 3 cm plane for mode 1 and mode 2. (a) vs. pressure at constant absorbed power ~ 270 W, (b) vs. power at constant p = 5 mTorr.

increasing microwave input power; i.e. the ion losses in the plasma source region increase with increasing input power.

Note that both curves in Figure 7.27 indicate that independent of the input power and pressure, mode 1 produces ions more efficiently than in mode 2. The difference in ion production cost between mode 1 and mode 2 is due to the better microwave power coupling efficiency in mode 1 than in mode 2 (see Table 7.4).

B. Side feed applicator (with different ECR magnet configurations)

The side feed MPDR™-13 ion production costs at z = 3 cm plane are shown in Figure 7.28 versus absorbed power for argon discharges at a pressure of 0.78 mTorr for three multipolar ECR magnet configurations and two EM modes. The ion production costs are calculated using eq. (4.5) based on the measured cross sectional spatial ion density data in Section 7.3.2.B. The ion production cost for the "benchmark" 8P/8M configuration are shown for both TE_{211} and TE_{311} excitations and the ion production cost for the 4P/8M and 4P/4M configurations are shown only with TE_{211} mode excitation. Similar to the end feed plasma source, all the ion production costs increase with increases in microwave absorbed power. This means that as input power increases, the plasma source is less efficient in producing additional ions at the processing region. As shown in Figure 7.28, the 8P/8M configuration operating with TE_{211} mode has the best ion production cost. This is due to both the good microwave coupling efficiency and the excellent magnetic confinement of the 8P/8M magnetic field configuration. The 8P/8M configuration operating with TE_{311} mode is not as good as TE_{211}

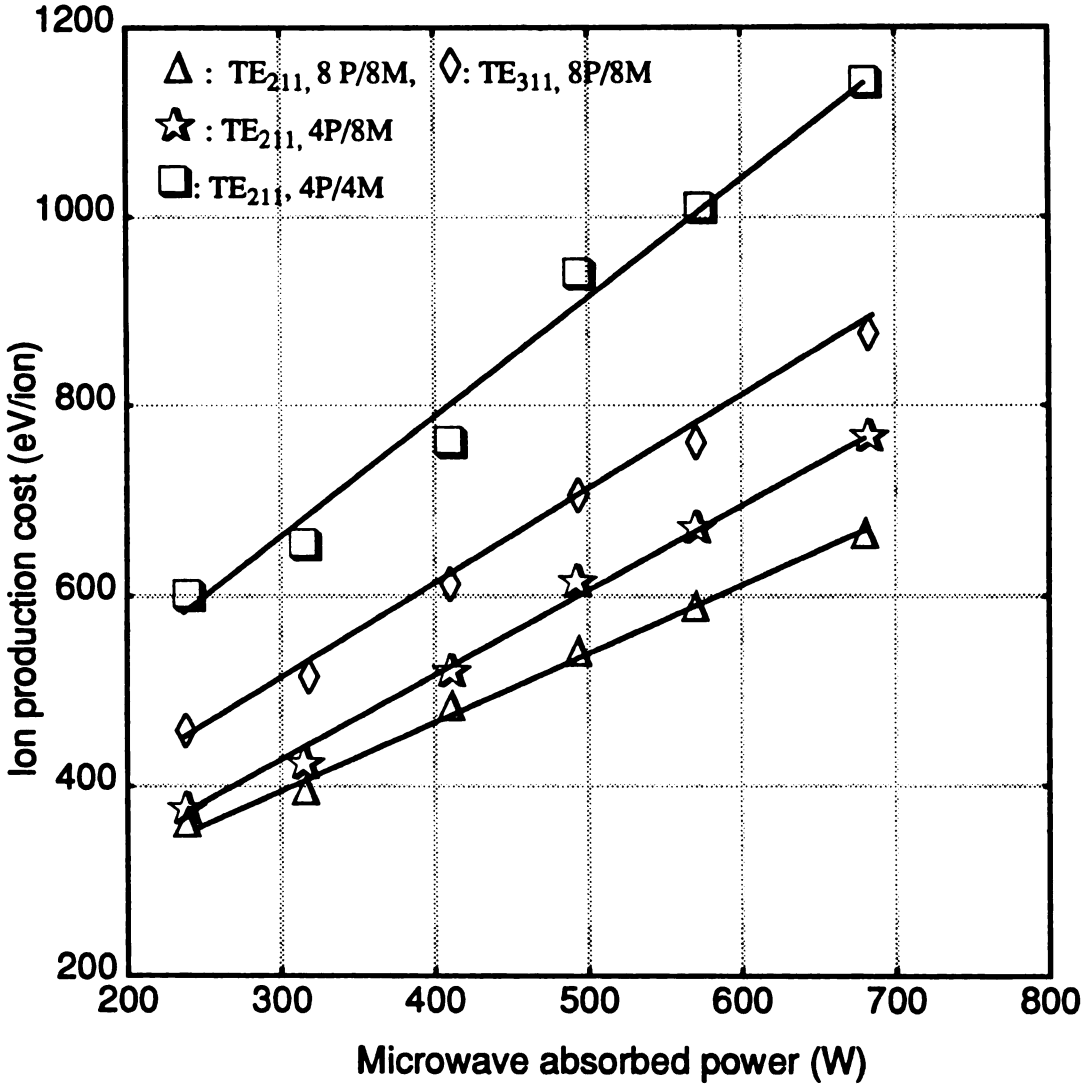

Figure 7.28 Side feed ion production cost at z = 3 cm plane versus absorbed power for different mulitpolar magnetic type ECR configurations, at 0.78 mTorr pressure.

mode because of the lower microwave power coupling efficiency described in Section 7.2.3.E.

Note that the ion production cost of the 4P/8M configuration operating with TE_{211} mode is very close to the 8P/8M configuration with TE_{211} mode when absorbed power is less than ~420W. This may due to the off-peak density profile of the 4P/8M configuration. As power is further increased, the ion production cost of the 4P/8M configuration operating with TE_{211} mode falls between the 8P/8M configuration of TE_{211} and TE_{311} modes. This is due to the fact that the 8P/8M configuration has better magnetic confinement structure than the 4P/8M.

The ion production cost for 4P/4M configuration with TE_{211} excitation is almost the double of 8P/8M configuration with TE_{211} mode. It can reach up to 1150 eV/ion at absorbed power of ~700 W. The high ion production costs in 4P/4M configuration is due to its less effective magnetic confinement and smaller ECR coupling surfaces.

Figure 7.29 displays the side feed 8P/8M ion production cost at z = 3 cm plane versus the chamber pressure at a fixed absorbed power of ~ 235 W for both TE_{211} and TE_{311} modes. Again the ion production cost in TE_{211} mode is always ~12% better than TE_{311} mode due to better (5-10%) microwave power coupling efficiencies in TE_{211} excitation. As shown in Figure 7.29, all the ion production costs decrease as the pressure is increased from 0.47 mTorr to 1.8 mTorr. In this low pressure regime, as pressure increases, the diffusion loss are reduced, hence, the ion production costs are improved as pressure increases.

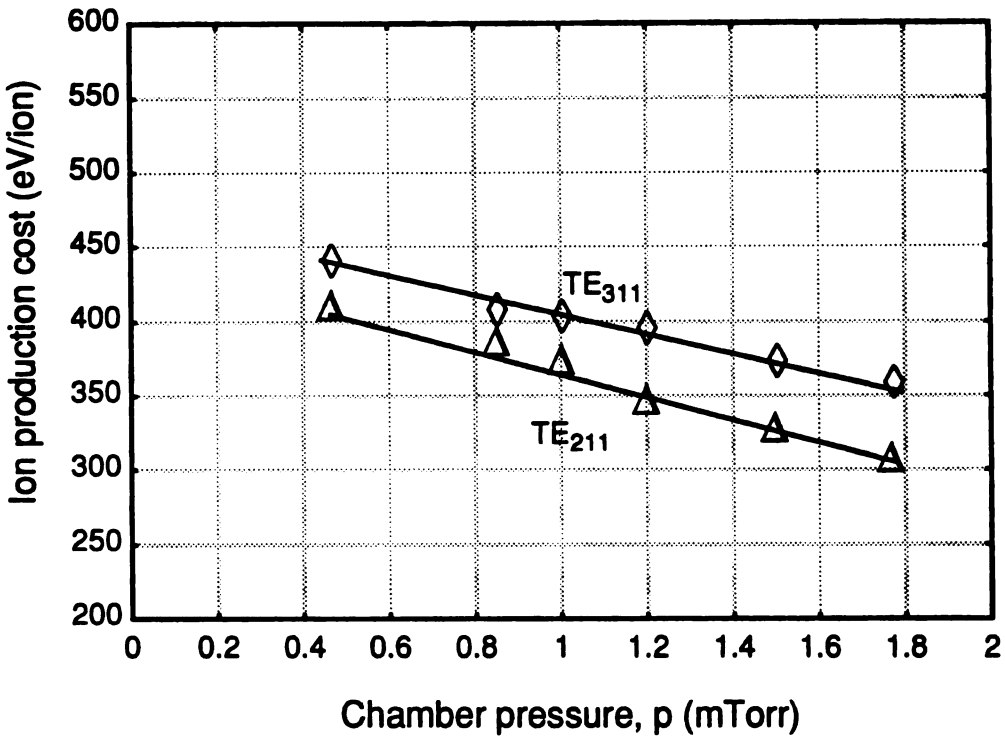

Figure 7.29 Side feed 8P/8M ion production cost at z = 3 cm plane or TE_{211} and TE_{311} modes at absorbed power ~ 235 W.

C. Comparison of the end feed and side feed ion production costs

A performance comparison between the end feed and side feed applicator can be made by comparing the source behavior with their best performance under similar experimental input conditions. The best operation in end feed is 8P/8M configuration excited with the mode 1 while the side feed is 8P/8M configuration excited with TE_{211} mode. The common data points for the two plasma sources (end feed and side feed) were at pressures 2-3 mTorr, P_{abs} ~ 235-270W, 8P/8M ECR magnet configuration and in argon gas. After slight extrapolation, the best ion production costs for the end feed (with TM_{011} excitation) and side feed (with TE_{211} excitation) plasma sources are ~340 eV/ion and ~300 eV/ion respectively. This means both side feed and end feed plasma source has similar best performance. This is attributed to (1) both end feed (with TM_{011} excitation) and side feed (with TE_{211} excitation) plasma sources have the same microwave power coupling efficiency at around 98% (see Tables 7.4 and 7.8), and (2) 8P/8M is the best magnetic configuration among the four magnet configuration investigated in this thesis.

7.3.4 Influence on ion density by substrate bias

In order to examine the effect of substrate bias on downstream ion density, a half inch thick, 3 in. diameter aluminum solid plate was drilled with 1.5-cm diameter hole at the center. A double Langmuir probe was mounted in this hole such that the top surface of the plate was approximately half inch below the probe

tips, shown in Figure 7.30 (a). Then the aluminum plate was negatively dc biased with respect to the chamber to draw ion current. Figure 7.29 (b) displayed the measured downstream ion density versus the aluminum substrate bias. The experiment was conducted at (0, 0, 8 cm), at 1 mTorr argon, 490 W absorbed power, 8P/8M ECR magnet configuration operating with TE_{211} excitation in a side feed plasma source. During the experiment, both the supply voltages and currents were also recorded. As shown in Figure 7.30 (b), even at the downstream position z = 8 cm, the substrate can pull 118 mA (or ~3.9 mA/cm^2) without significant disturbance (< 3%) to the ion density. This experiment indicates abundance of ion density is available for plasma processing in downstream region and dc substrate bias ($|V_b| < 50V$) has little effect on the downstream ion density.

7.3.5 Influence on ion density by downstream confinement magnetic fields

As mentioned in Section 3.2.3.D, downstream confinement magnets can be put into the process chamber to improve the density. Although the additional Multipolar Plasma Confinement Structure (MPCS shown in Figure 3.6) is supposed to improve both the density and its uniformity, other factors must be considered: (1) the downstream confinement magnet configuration and orientation with respective to the ECR magnet, (2) the confinement area by the MPCS, and (3) the distance between ECR magnets and downstream magnets. Two different confinement size (19 cm dia. and 14.9 cm dia.) and three (4P/8M, 8P/8M and allN/8M) configurations of MPCS with 8P/8M ECR magnet were

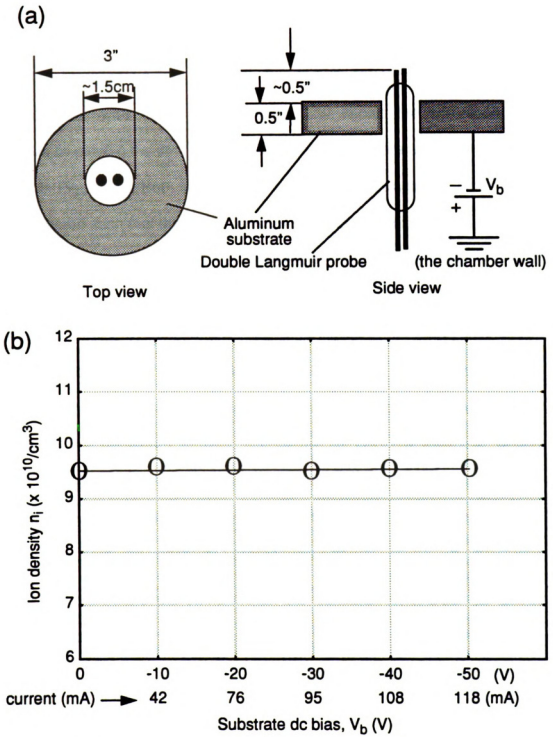

Figure 7.30 (a) Measurement configuration of aluminum substrate with the double Langmuir probe, (b) Side feed downstream ion density (0, 0, 8 cm) vs. substrate bias with 8P/8M magnet configuration, TE_{211} mode, 1 mTorr and absorbed power ~ 490 W.

evaluated.

Figure 7.31 displays the measured spatial side feed ion densities at z = 8 cm over a quadrant without the MPCS. The experimental conditions were 1 mTorr, 500 W power with TE_{211} mode. Figure 7.32 shows the corresponding ion densities by placing the 8P/8M MPCS with14.9 cm diameter confinement area, as shown in Figure 3.6. Both sets of magnets (ECR & downstream magnets) have been oriented such that they have opposite magnetic polarity with respect to each other, as shown in Figure 3.6. Downstream ion density uniformity at z = 8 cm improved from 14.8% to 11.6% with about the same average density. So far, only the above mention configuration have improved the ion density profile. The measured ion density magnitude and uniformity in most combinations of configuration and size yield the same or even worse in density uniformities when compared the measured density without the MPCS. For example, when the 8P/8M MPCS size was extended to 19 cm diameter, uniformity of 30 density data over the same 5 cm radius quadrant dropped to ~ 15.5%. If the diameter of MPCS extends too large, the uniformity become worse.

The possible explanation lies on the combination of both the ECR and MPCS magnetic fields, which is a function of the transition region thickness, their relative configurations and strengths. It is believed that when the diameter of MPCS or the thickness of transition region is large the magnetic fields that connect ECR and downstream magnets would cross the transition region, which results in more species recombination at the transition wall before they reach the processing region. Yet the optimal size and relative configuration is pending

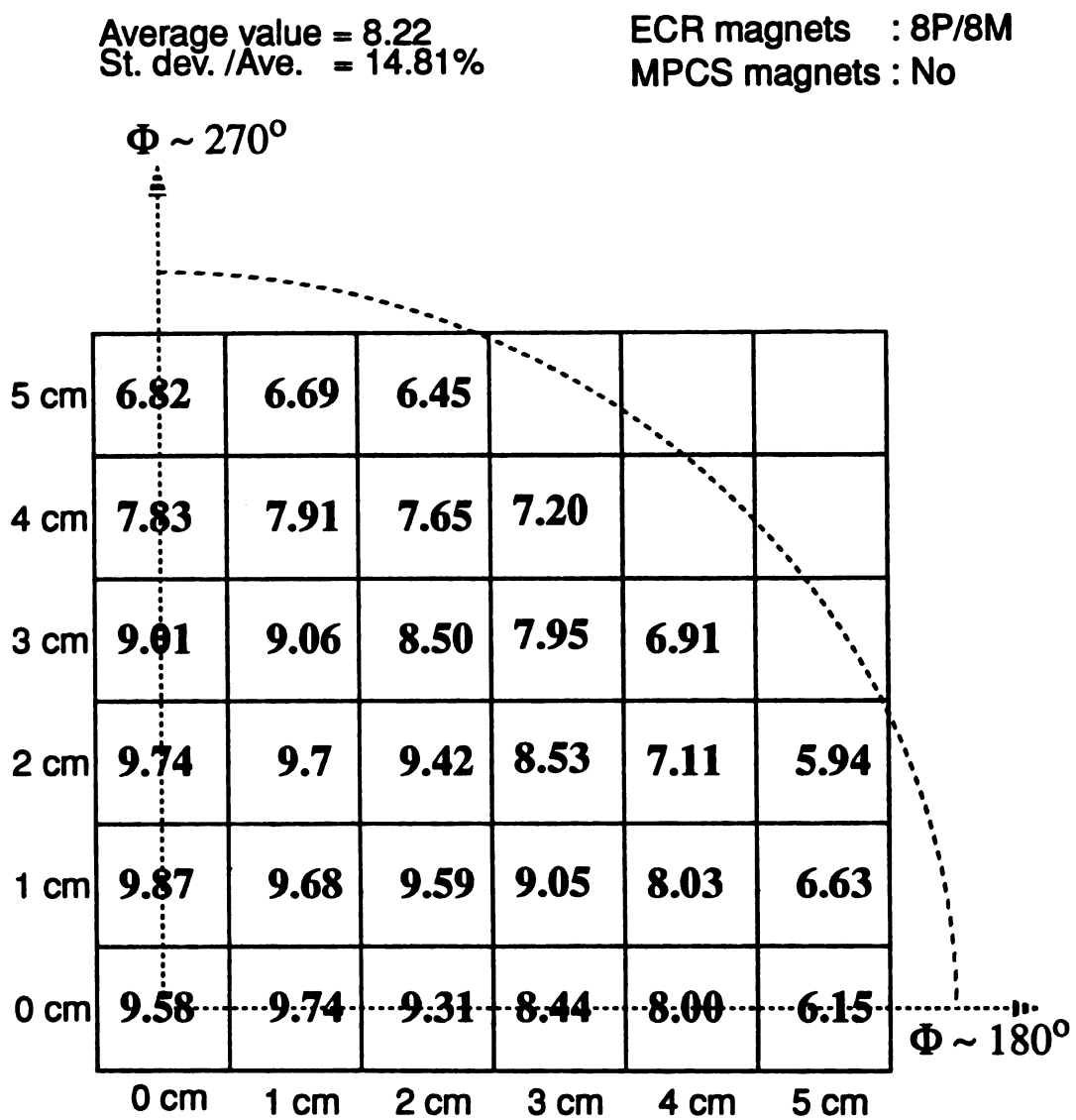

Figure 7.31 Side feed ion density (x $10^{10}/cm^3$) within a quadrant at z = 8 cm w/o MPCS.
Experimental conditions: 1.0m Torr argon, ~490 W absorbed power, and TE_{211} mode.

Average Value = 8.18
St. dev. /Ave. = 11.16%

ECR magnets : 8P/8M
MPCS magnets: 8P/8M
(14.9 cm dia.)

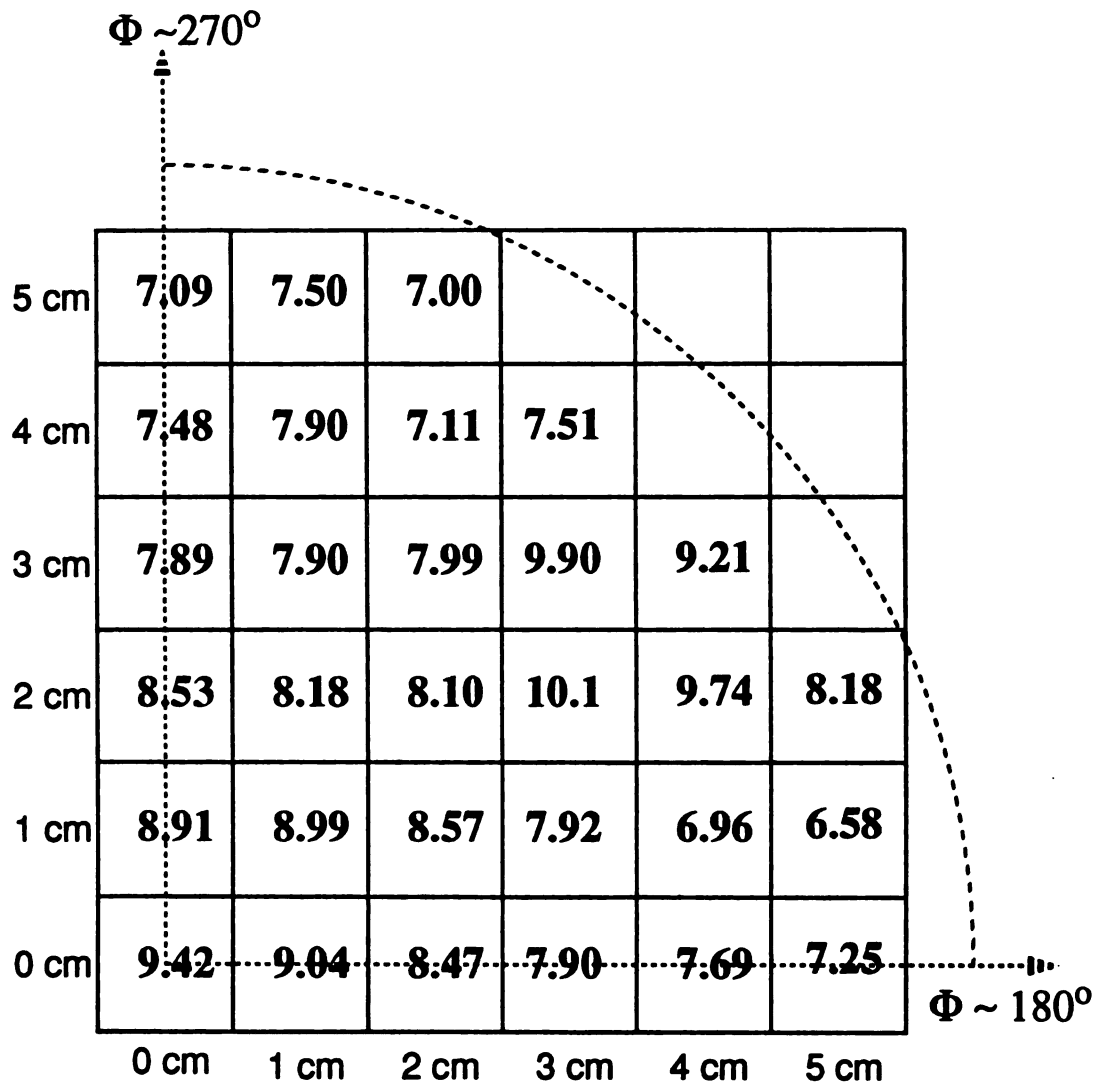

Figure 7.32 Side feed ion density (x $10^{10}/cm^3$) within a quadrant at z = 8 cm w/MPCS shown in Figure 3.6.
Experimental conditions: 1.0m Torr argon, ~490 W absorbed power, and TE_{211} mode.

for further future experiments. If the optical access ports are not required, new MPDR™s should reduce that transition region thickness or discharge height as much as possible.

7.4 Plasma Potential and Electron Energy Measurements

7.4.1 Introduction

The objectives in this section are: (1) to check on the EEDF shapes, (2) to study the plasma potential and electron temperature in response to the input variable of power, pressure and downstream position. In this section, a set of internal variables related to the electron energy of the plasma discharges is presented versus limited input variables such as pressure, power and downstream locations. The internal variables in **side feed** applicator include the EEDF, plasma potential and electron temperature and were excited only with $\mathbf{TE_{211}}$ **mode** for the following two ECR magnetic configurations, namely 4P/8M and 8P/8M. The interest on only these two ECR configurations is due to their higher measured ion densities than the other two ECR configurations (4P/4M and allN/8M) reported in Section 7.3. Only one internal variable, the electron temperature was measured for the **end feed** applicator.

The data (d^2I/dV^2 vs. V) was first obtained from the single Langmuir probe measurement technique which has been discussed in Section 5.4.3. Then a data analyzing program processed the data. The following four tasks were addressed: (1) to determine the plasma potential (V_p) by locating the maximum [117] of

d^2I/dV^2, (2) to calculate the normalized EEDF using Eq. (5.15), (3) to obtain the average electron energy by eq. (5.16), and (4) to calculate the theoretical Maxwellian and Dryvesteyn distribution curves with the same average electron energy obtained in step (3). The V_p and EEDF presented here were obtained from in steps (1) and (2) respectively. The electron temperatures were from the slope of Langmuir probe data in electron retardation region.

7.4.2 Electron energy distribution function (EEDF)

EEDF shape vs. ECR magnetic configurations: The focus here was to only measure the downstream EEDF with a few selected experiments. This measurement was made (1) to determine if the EEDF was close to Maxwellian or Druyvesteyn distribution, and (2) to examine the high energy population (if any) in the downstream processing region from the ECR acceleration region. If the measured EEDF is close to the standard distribution, the reaction rate constant in the particle kinetics can be readily calculated. Otherwise, experimental fit curve should be used in the calculation instead.

Figures 7.33 and 7.34 display the typical measured EEDFs of 8P/8M and 4P/8M ECR magnetic configurations. The experimental conditions took place at location (0, 0, z = 3 cm) argon pressure of 0.78 cm, absorbed power of 490 W in side feed TE_{211} mode argon discharges. For comparison purpose, two standard distribution curves of Maxwellian (solid line) and Druyvesteyn (dashed line) distributions with the same average measured electron energy were also plotted

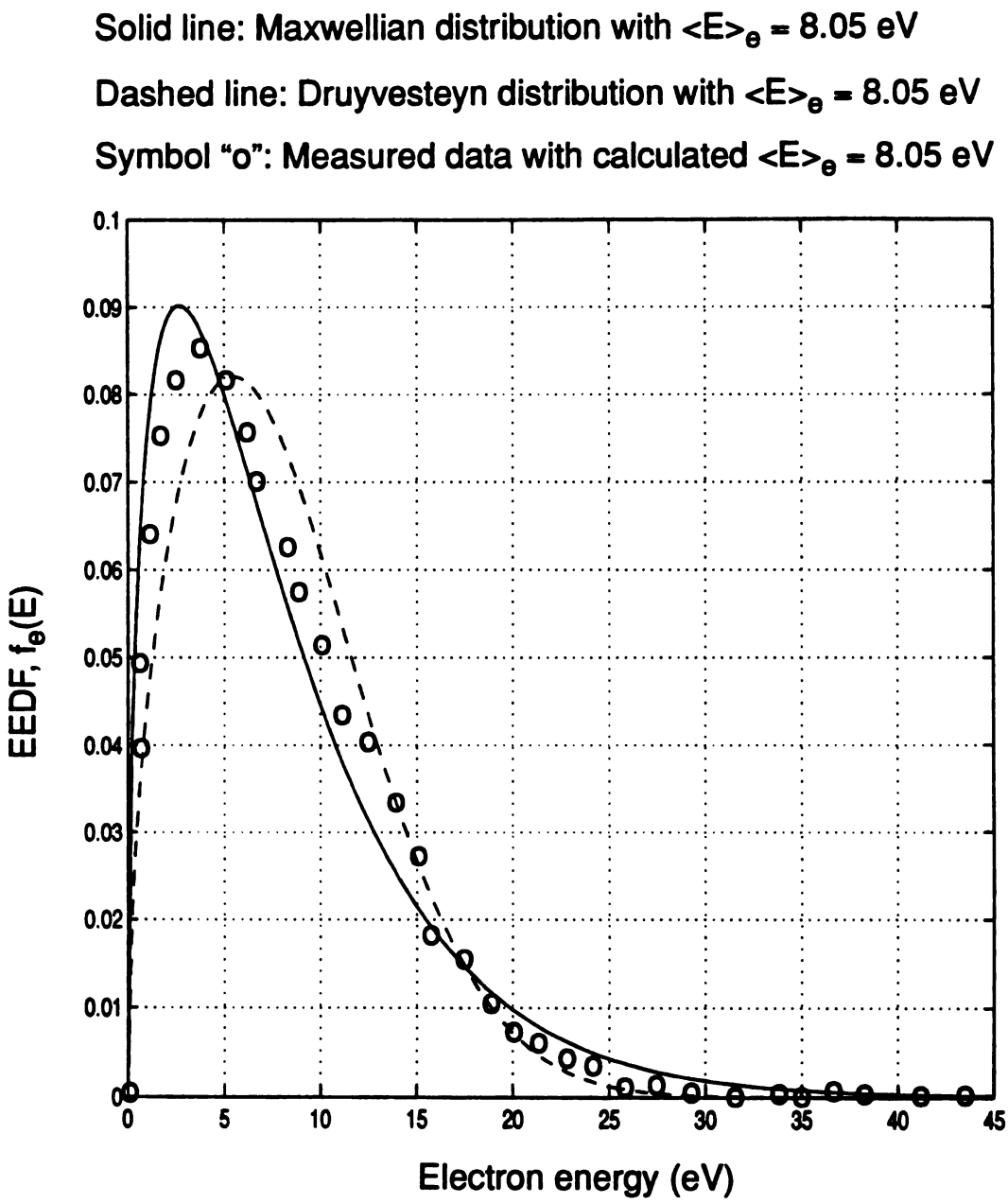

Figure 7.33 Typical measured EEDF in side feed argon discharge with 8P/8M ECR magnet configuration.
Experimental conditions: absorbed power ~ 490 W, location (0, 0, 3 cm), pressure 0.78 mTorr, TE_{211} mode.

Solid line: Maxwellian distribution with $\langle E \rangle_e$ = 7.82 eV

Dashed line: Druyvesteyn distribution with $\langle E \rangle_e$ = 7.82 eV

Symbol "o": Measured data with calculated $\langle E \rangle_e$ = 7.82 eV

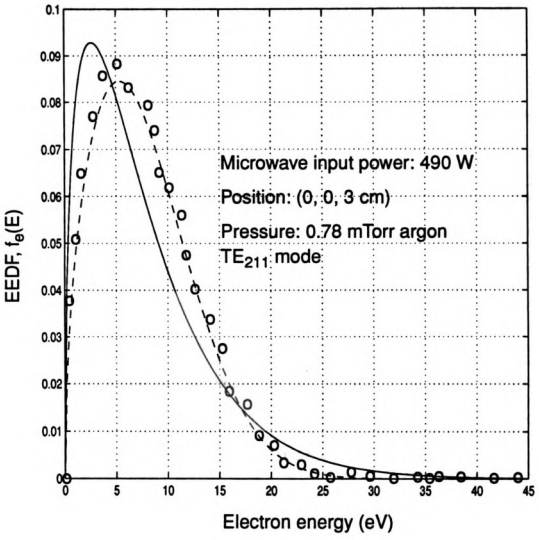

Figure 7.34 Typical measured EEDF in side feed argon discharge with 4P/8M ECR magnet configuration.
Experimental conditions: absorbed power ~ 490 W, location (0, 0, 3 cm), pressure 0.78 mTorr, TE_{211} mode.

along with the data in each figure. For the 8P/8M case as shown in Figure 7.33, its EEDF falls between the Maxwellian and Druyvesteyn distributions. The measured EEDF in 4P/8M magnet configuration roughly follows the Druyesteyn distribution as shown in Figure 7.34. The high energy electron spectrums in both cases are lower than the those in Maxwellian distribution. For both configurations, no high energy electrons were detected in the downstream region. The fast electrons lose most of their energy due to the elastic and inelastic collisions in the discharge generation region before diffusing or drifting into the downstream process chamber. However, electrons in the ECR zones may have energies much higher than those measured downstream.

These observations (EEDF shape close to Druyvesteyn or Maxwellian distributions and no high energy electron) in the TE_{211} mode exited side feed argon discharges were also found over the input variable space spanned by pressure from 0.8 to 3.5 mTorr, power from 320 to 640 W, locations from (0,0, 3 cm) to (0, 0, 7 cm). The measured shapes of these EEDFs did change to some extent, but the shape of the data shown in Figures 7.33 and 7.34 remains representative of the data for the two magnet configurations in side feed applicator as input variables are varied. The indication of no high energy electron adds another credit for the MPDR™-13 suitable to process sensitive materials.

7.4.3 Plasma potential and Electron temperature

7.4.3.A Side feed applicator

Pressure dependency of the two ECR configurations: Figure 7.35 shows the measured plasma potential and electron temperature versus the chamber pressure in 4P/8M and 8P/8M magnet configurations. The experimental conditions were side feed with TE_{211} mode, at (0, 0, z = 3 cm) location with an input power of 320 W. The plasma potential of 8P/8M configuration is always approximately 30% higher than the 4P/8M plasma potential. This may due to the strong space charge field existing in the 8P/8M configuration. Recall the measured ion density at z = 3 cm plane in 8P/8M configuration is higher at the center region while the peak density in 4P/8M occurs off center. More uniform density profile is preferably to have a lower space charge field and causes a lower plasma potential.

However, the electron temperatures in the downstream region (z > 3 cm) for these two ECR magnetic configurations are comparable with each other. Interestingly both plasma potentials and electron temperatures fall off with a similar trend with increasing pressure. They start to level when pressure is larger than 5 mTorr. This trend is consistent with the particle conservation versus pressure in plasma global model described in Chapter 10.

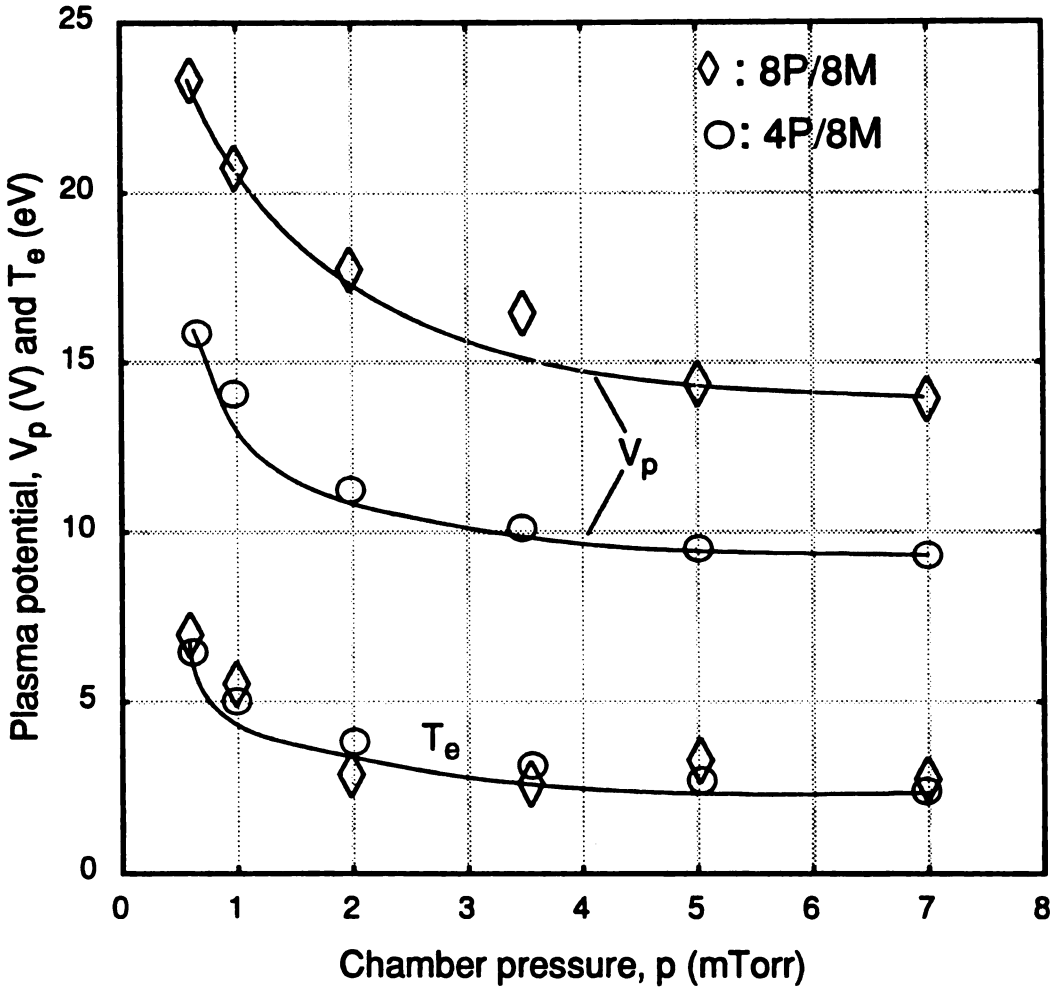

Figure 7.35 Side feed plasma potential and electron temperature versus chamber pressure for 4P/8M and 8P/8M configurations.
Argon discharge at (0, 0, z = 3 cm), side feed applicator, TE_{211} mode, P_{inc} ~ 320 W.

Power dependency of the two ECR configurations: Figure 7.36 displays the measurements of plasma potential and electron temperature versus incident power in 4P/8M and 8P/8M configurations. They were performed at the (0, 0, 3 cm) location, 1 mTorr for a side feed, well-matched TE_{211} mode argon discharge. Similarly, the plasma potential in 8P/8M configuration is larger than in 4P/8M configuration. Both have similar electron temperatures. As shown in Figure 7.36, both the plasma potential and the electron temperature are a weak function of microwave incident power. This is in reasonable agreement with the prediction of plasma global models which are described in Chapter 10.

Spatial (V_p and T_e vs. r and z) dependency for two ECR configurations: The measured spatial variation of the plasma potential and electron temperature in side feed applicator are shown in Figures 7.37 and 7.38 for 4P/8M and 8P/8M configurations. For the spatial dependency in electron temperature, only 8P/8M configuration were measured.

V_p and T_e vs. z: Figure 7.37 shows the z-dependence of V_p and T_e at 1.0 mTorr with input power of 320 W in side feed TE_{211} mode. As indicated, the plasma potential of 4P/8M is approximately 33% lower than the 8P/8M's. The plasma potential for the 8P/8M configuration at 1 mTorr, 320 W absorbed power decreased from around 21 V to approximately 17.5 V at the discharge center as the downstream position was varied from z = 3 to 8 cm. Its counterpart in 4P/8M configuration has a slight decrease from ~13.5 to ~11.2 V. The electron temperature along the z-axis decreases when it was farther away from the excitation region. For the electron temperature adjacent to the discharge region

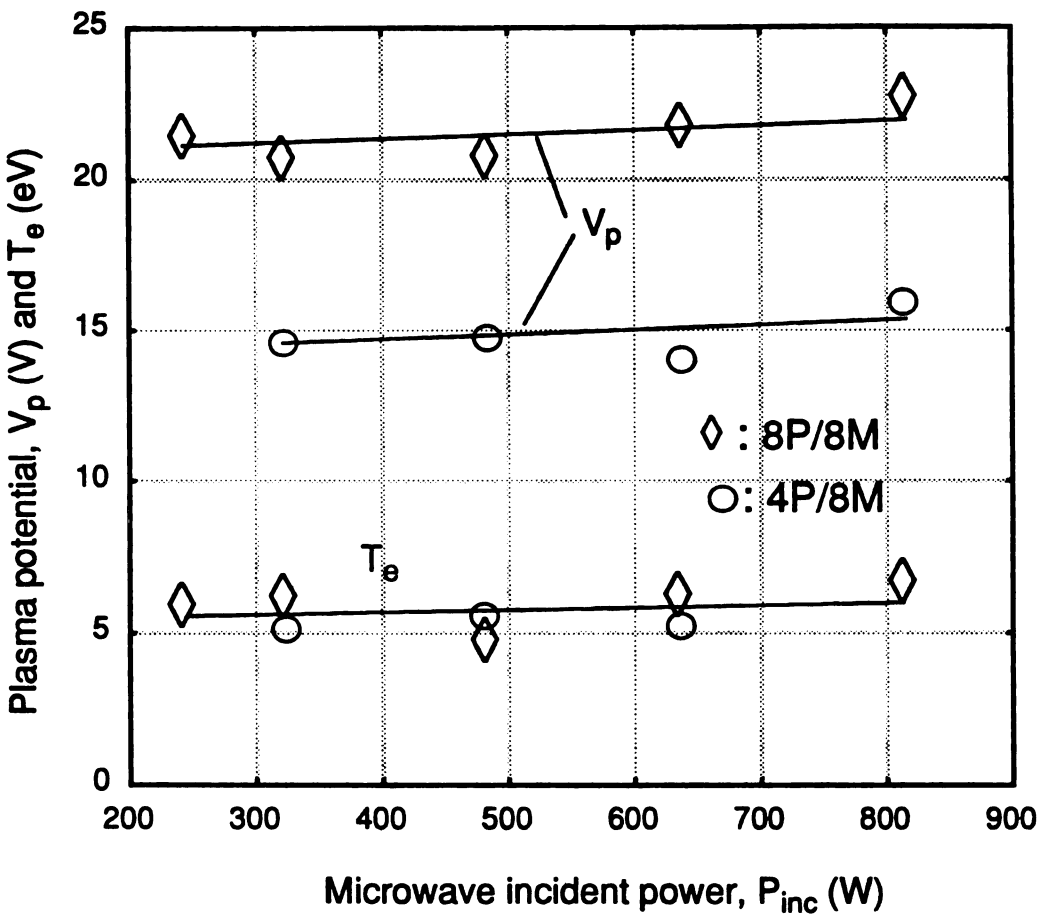

Figure 7.36 Side feed plasma potential and electron temperature versus power at 1 mTorr argon discharge for 4P/8M and 8P/8M configurations. Argon discharge at (0, 0, z = 3 cm), side feed applicator, TE_{211} mode, P_{inc} ~ 320 W.

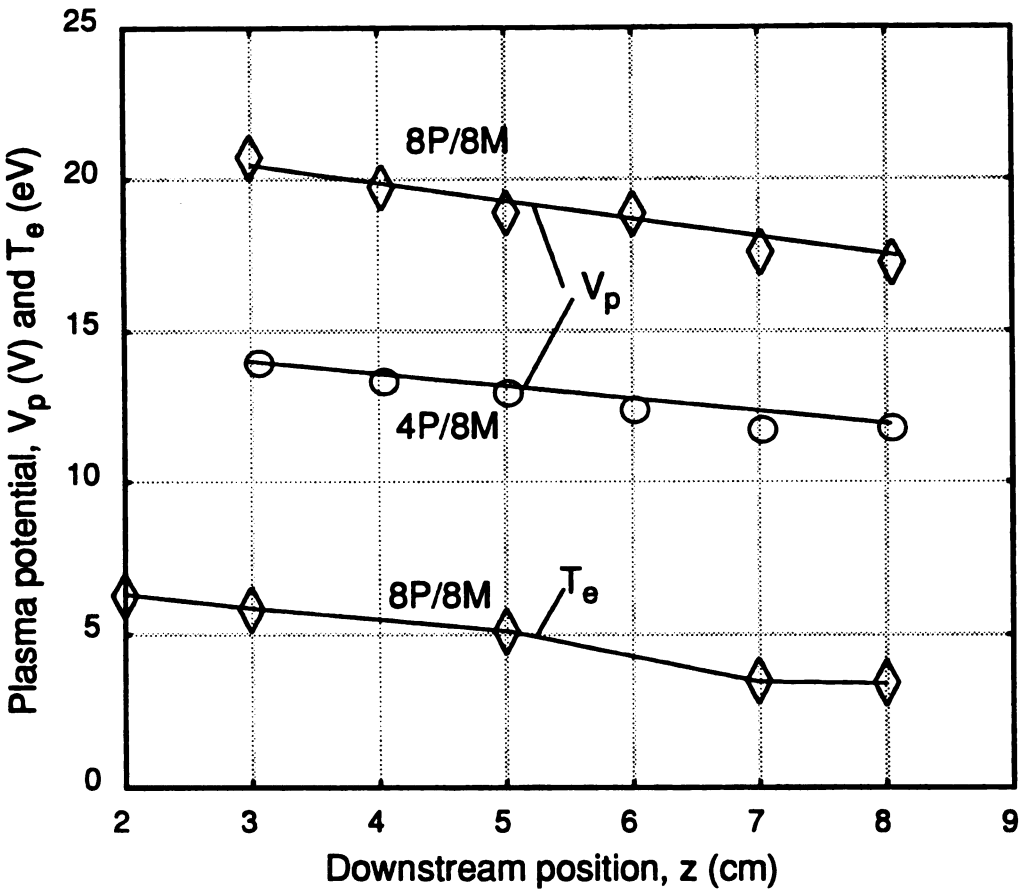

Figure 7.37 Plasma potential and electron temperature in side feed applicator vs. downstream position for 4P/8M and 8P/8M configurations.
1.0 mTorr Argon discharge, r = 0, P_{inc} ~ 320 W, Side feed applicator, TE_{211} mode excitation.

probably has more energetic electrons than in the process chamber region.

V_p and T_e vs. r: Figure 7.38 displays the plasma potential and electron temperature radial-dependency at (0, 0, z = 7.5 cm), 0.78 mTorr side feed TE_{211} mode excited discharge with absorbed power at approximately 320 W. As shown in Figure 7.38, the plasma potential of 8P/8M configuration decreases to 12 V at z = 7.5 cm as the radial position changed from r = 0 to 8 cm and is relatively flat at approximately 10 to11 V for the 4P/8M configuration. The more uniform plasma potential in the 4P/8M configuration is probably due to its more uniform ion density profile.

The electron temperature remains relatively flat between 4 - 5 eV along radial direction at z = 7.5 cm under similar experimental conditions. Note that both the plasma potential and the electron temperature do not vary significantly in radial direction. This supports the assumptions made in Section 7.3.3 that the relative ion density can be represented by the relative ion saturation current.

7.4.3.B End feed applicator

Electron temperature: End feed electron temperature data at (0, 0, 3 cm) for mode 1 and mode 2 were plotted in Figure 7.39 versus chamber pressure and reactor absorbed power in 8P/8M magnet configuration. Figure 7.39 (a) shows the T_e vs. pressure at a fixed absorbed power of 270 W. The electron temperature for both mode 1 and mode 2 is quite similar and decreases as the pressure increases. This is expected by the prediction of low pressure global discharge model. Figure 7.39 (b) displays very little power dependence on electron temperature at fixed chamber pressure of 5 mTorr. This suggests that increasing

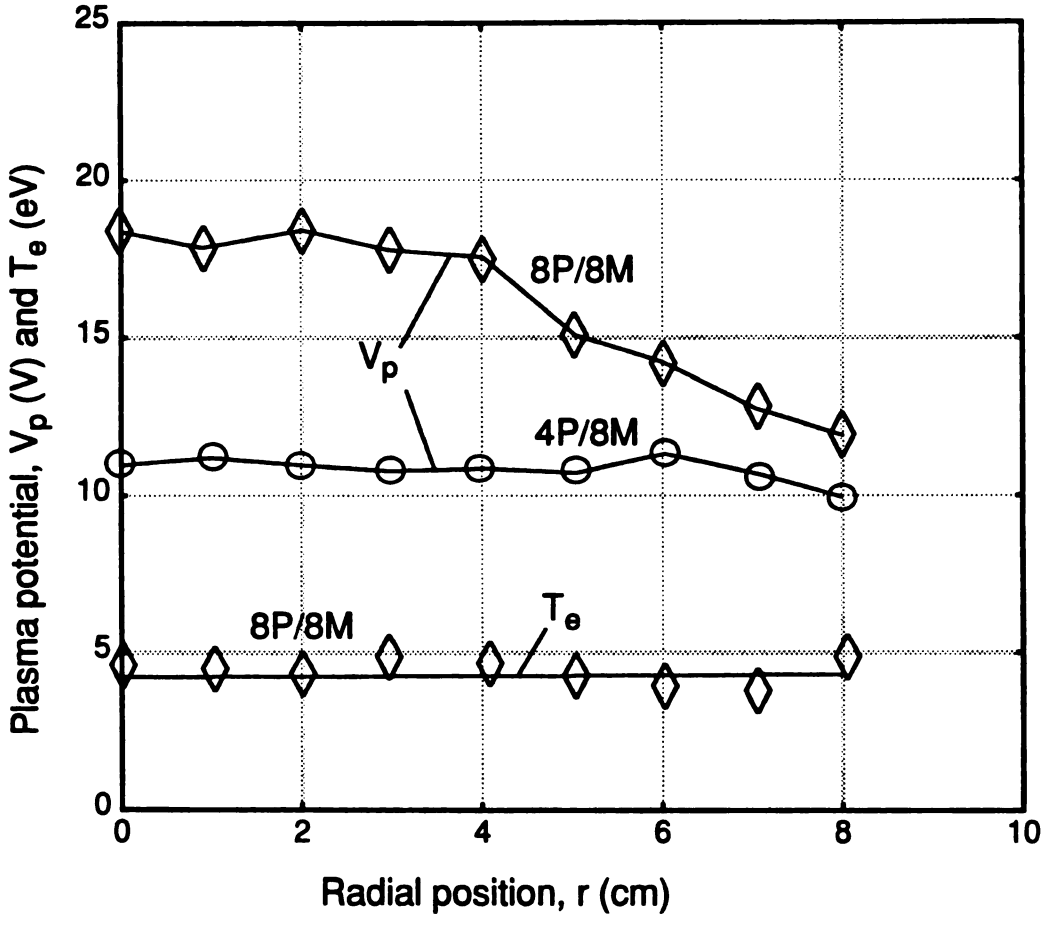

Figure 7.38 Plasma potential and electron temperature in side feed applicator vs. radial position.
0.78 mTorr Argon discharge, z = 7.5 cm, P_{inc} ~ 320 W, Side feed applicator, TE_{211} mode excitation.

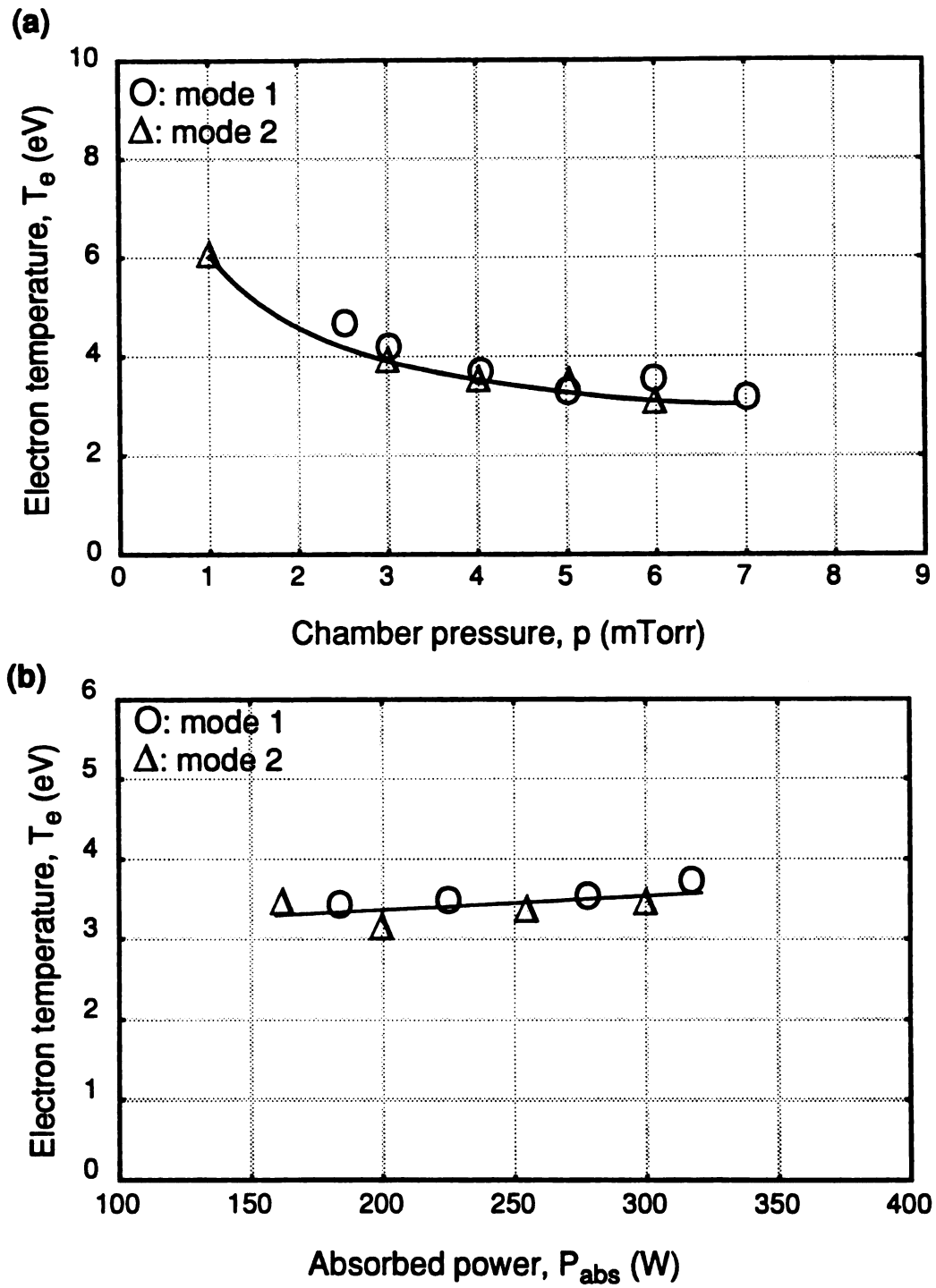

Figure 7.39 End feed electron temperatures (0, 0, 3 cm) (a) vs. pressure at absorbed power ~ 270W, (b) vs. absorbed power at fixed 5 mTorr.

absorbed power mainly increases the plasma density population.

7.5 Ion Energy Measurements

Measurements of the ion energy distribution of the ions diffusing out of the source and hitting the energy analyzer is discussed in this section. Ion energies are important since ions have a much higher mass than electrons and hence they may create damage on the outmost layer of the processing materials. Additionally, the ions with a specific narrow and low energy distributions are desirable for a number of etching applications. Throughout this section, the ion energy spectrum impinging on the substrate was measured by the gridded energy analyzer described in Section 5.5. Unless otherwise noted, the ion energy measurements were taken with the surface of the gridded energy analyzer grounded with respect to the chamber walls. Thus, the measured energies are the total ion energy that have arrived at the grounded conducting surface. Note that ion energies measured with gridded analyzer are appropriate for determining the energy of ions hitting the substrate surfaces. However, the measurement does not provide enough information to separate the plasma potential variation and sheath potential contributions to the total measured ion energy. Pure argon discharges were mostly used in this section. In end feed applicator, only ion energy measurement of 8P/8M operating at TM_{011} mode excitation is presented here because similar results were obtained with TM_{012} mode.The ion energy measurement was mostly conducted with 4P/8M and 8P/8M magnet

configurations for the side feed applicator with TE_{211} mode excitation. Finally, ion energy measurements in pure hydrogen gas discharges are briefly discussed in the last subsection.

7.5.1 Ion energy distribution function (IEDF) and bias effect

7.5.1.A General IEDF shape and characterization

Multipolar ECR magnetic configurations: Figure 7.40 shows a typical measured argon discharge IEDF in the process chamber. It was measured at (0,0, 6 cm) in an end feed 8P/8M TM_{011} mode excited discharge with pressure 2.5 mTorr and absorbed power 294 W. As shown in the figure, its shape is similar to the shifted-Gaussian distribution with a single sharp peak. The IEDF measurement for the side feed excited at different powers and pressures (see Figures 7.41 and 7.42) had similar shape that resembled this shifted-Gaussian distribution. In general, the measured ion energy distributions in 4P/8M and 8P/8M side feed plasma sources or 8P/8M end feed plasma source can be characterized by three parameters. They are (1) the average ion energy $\langle E \rangle_i$, (2) the most probable energy, and (3) the full width at half-height (FWHH) energy. For most of the measured IEDFs in MPDR™-13, the most probable energy differed from the average ion energy by only 1 to 2 eV at most. That indicates that the measured IEDFs are quite symmetric around the peak value. Thus, the average ion energy and the FWHH are sufficient to describe the ion energy distributions here.

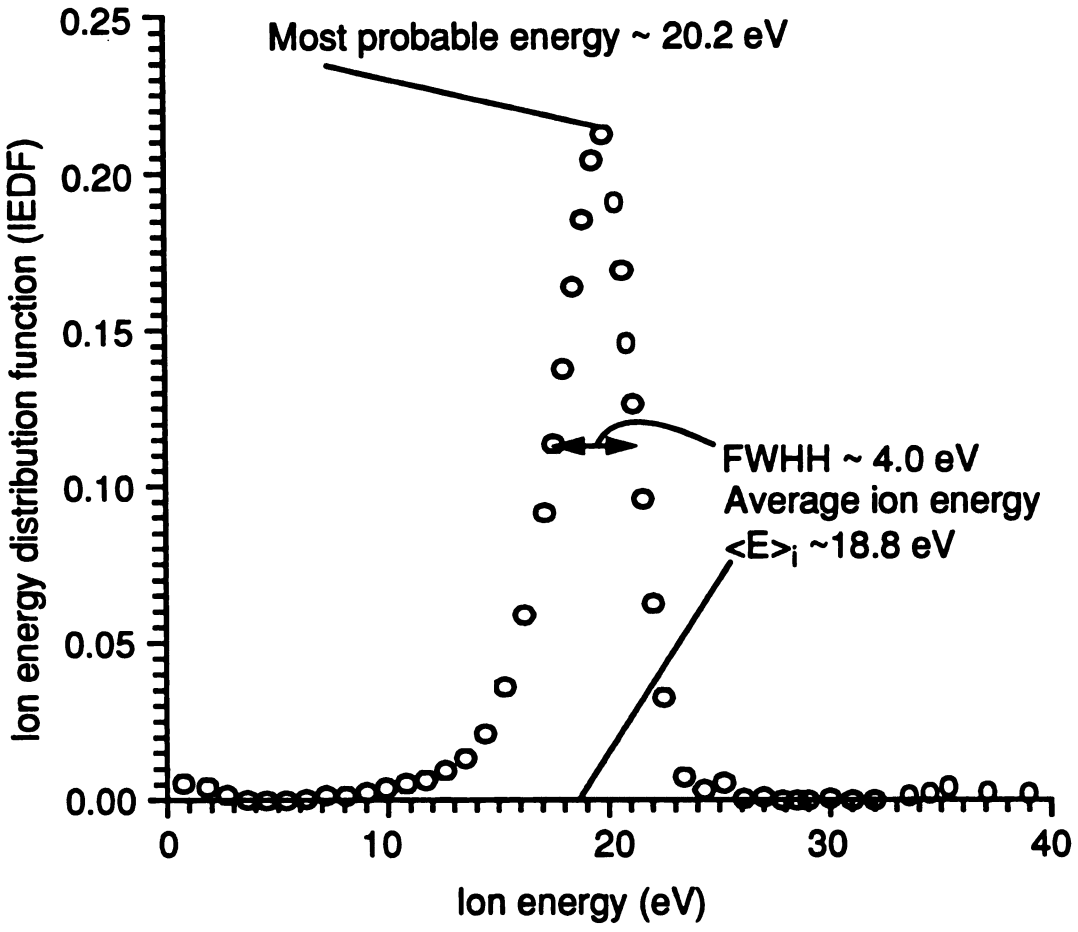

Figure 7.40 Typical ion energy distribution impinging on a grounded substrate. End feed applicator, 8P/8M, dominating TM_{011} mode, argon gas at 2.5 mTorr, P_{inc} ~ 298 W, P_{ref} ~ 4 W and location at (0, 0, 6 cm).

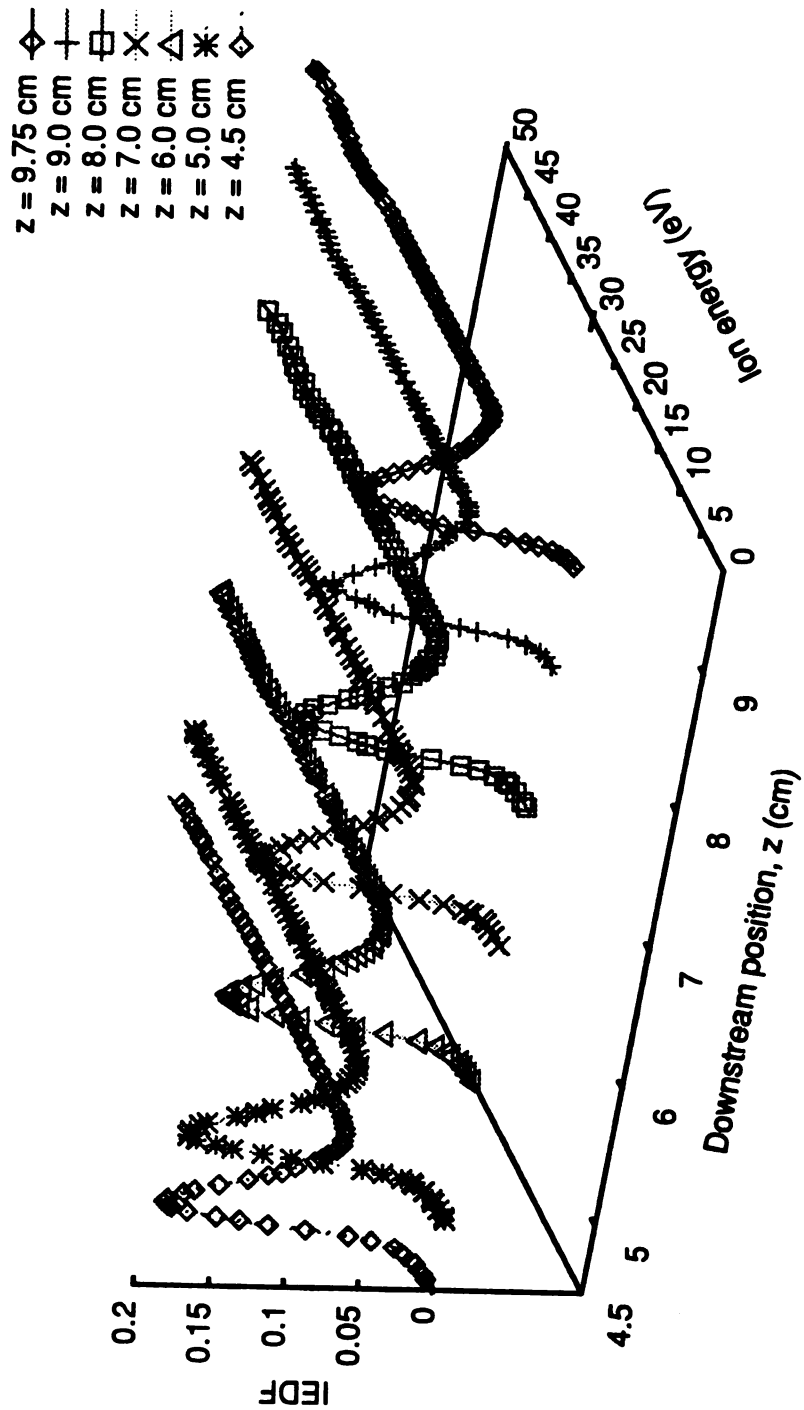

Figure 7.41 IEDF vs. z in 8P/8M, side feed reactor with TE_{211} mode.

Side applicator, TE_{211}, 8P/8M, r = 0 cm, p = 0.78 mTorr, P_{inc} = 240 W

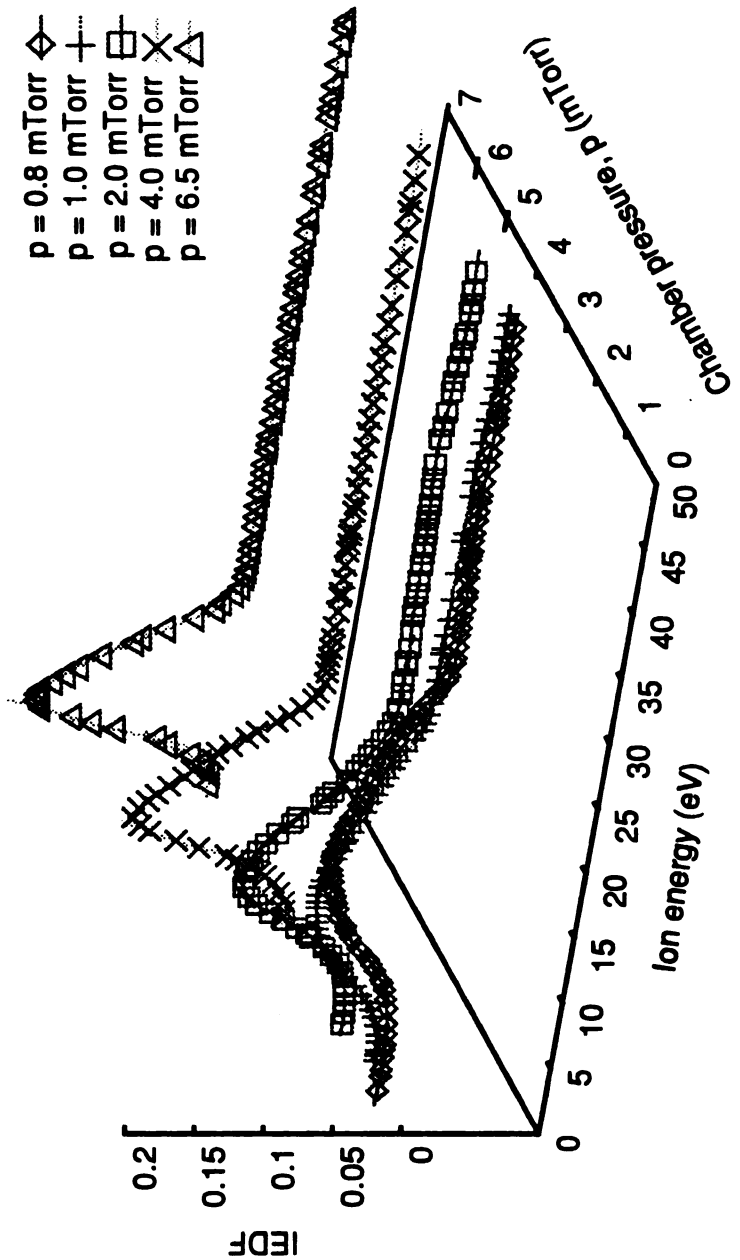

Figure 7.42 IEDF vs. p in 4P/8M, side feed reactor, TE_{211} mode.
Side applicator, TE_{211}, 4P/8M, r = 0 cm, z = 9.75 cm, P_{inc} = 240 W

Figure 7.41 shows the IEDFs vs. downstream position for an 8P/8M, TE_{211} mode excited side feed plasma source at 0.78 mTorr and 240 W power. Figure 7.42 displays the IEDFs vs. chamber pressure at (0, 0, 9.75 cm) for a 4P/8M, TE_{211} mode excited side feed plasma source at 0.78 mTorr and 240 W power. No anomalous IEDF shapes or high ion energy tails were observed in 4P/8M and 8P/8M configurations. This phenomenon also occur in the 8P/8M end feed plasma source. Therefore in later subsections, the ion energy measurements for end feed and side feed plasma sources has similar IEDF shape with only different $\langle E \rangle_i$ and FWHH. This indicates that relatively quiescent plasmas can be produced in the downstream processing region of MPDR™-13. Note that the IEDF dependence versus downstream position and pressure presented in Figures 7.41 and 7.42 will be described later in Sections 7.5.2 and 7.5.3.

Non multipolar ECR magnetic configuration: Figure 7.43 displays a typical IEDF measured at (0, 0, 10 cm) in side feed allN/8M ECR configuration with 0.8 mTorr pressure and 320 W absorbed power. Not only the spectrum is much more broadened than in 4P/8M or 8P/8M configurations but also the peak becomes relatively flat. This rectangular "window shaped" IEDF had a typical average ion energy of 25 eV with FWHH of approximately 17 eV when the experimental conditions were at the center and z = 10 cm, 0.8 mTorr argon plasma with input power of 325 W. Both the average ion energy and the FWHH are usually higher than the multipolar structure 4P/8M and 8P/8M configurations under similar experimental conditions. The speculation would be the allN/8M static magnetic field does not confine the charged particles and they diffuse along

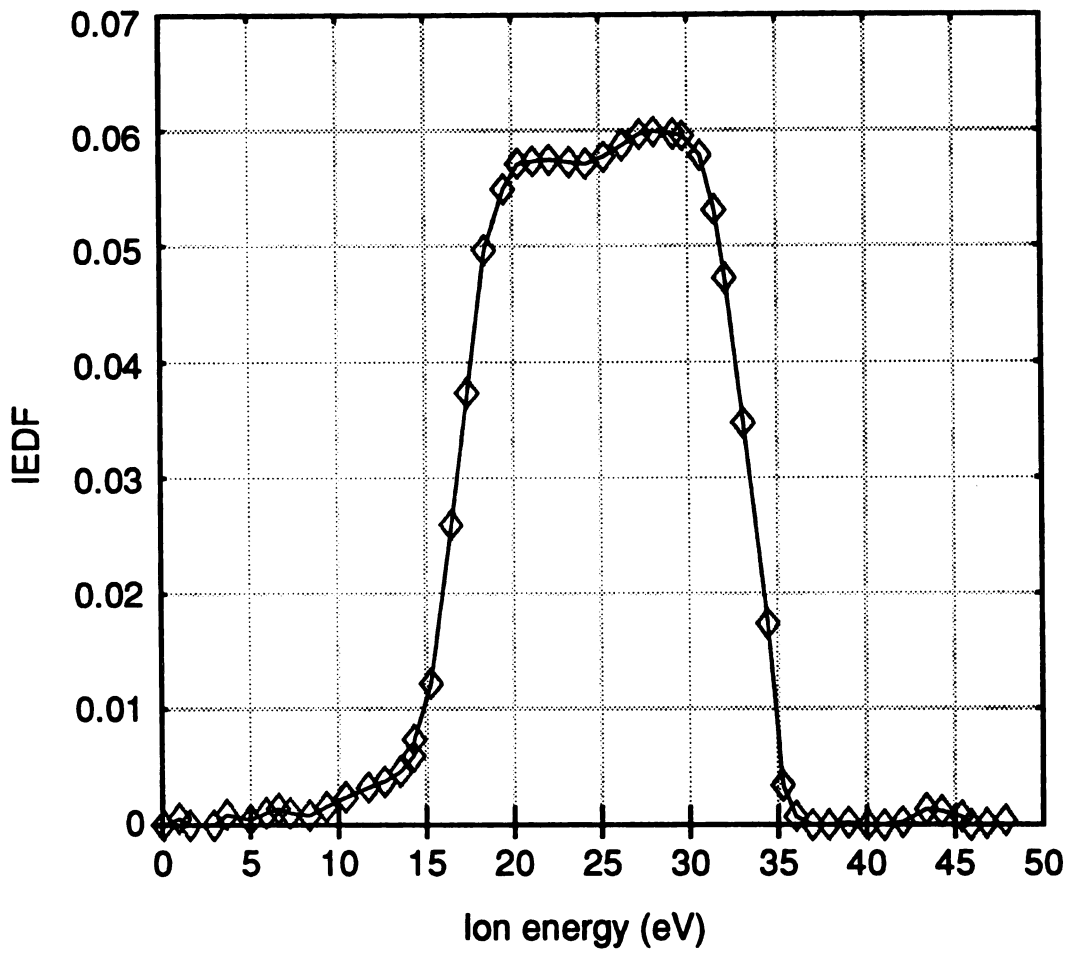

Figure 7.43 Measured IEDF of allN/8M configuration in side feed applicator.

the magnetic field line both downstream and upstream. Because of the higher diffusion loss, higher ion energies than the ion energies for the multipolar ECR magnetic field configurations is expected.

7.5.1.B IEDF vs. dc bias

A dc bias was applied to the top surface of the energy analyzer with respect to the grounded chamber wall to simulate the substrate bias effect on the IEDF. Figure 7.44 shows the measured IEDFs with bias at 0, -15 V, and -30 V. They were measured at (0, 0, 8 cm) under the 8P/8M end feed plasma source with pressure 3.0 mTorr and absorbed power of 320 W. The measured IEDF shapes and their FWHHs did not change much as the applied dc bias was varied. Only the $\langle E \rangle_i$ shifted accordingly with the applied dc bias. For example, the net effect of a -15 V dc bias to the plasma was to provide an additional 13 eV ion impinging energy. Similar results were founded in side feed plasma source. Hence, the average ion impinging energy onto a conducting substrate can be independently controlled by this simple substrate bias method.

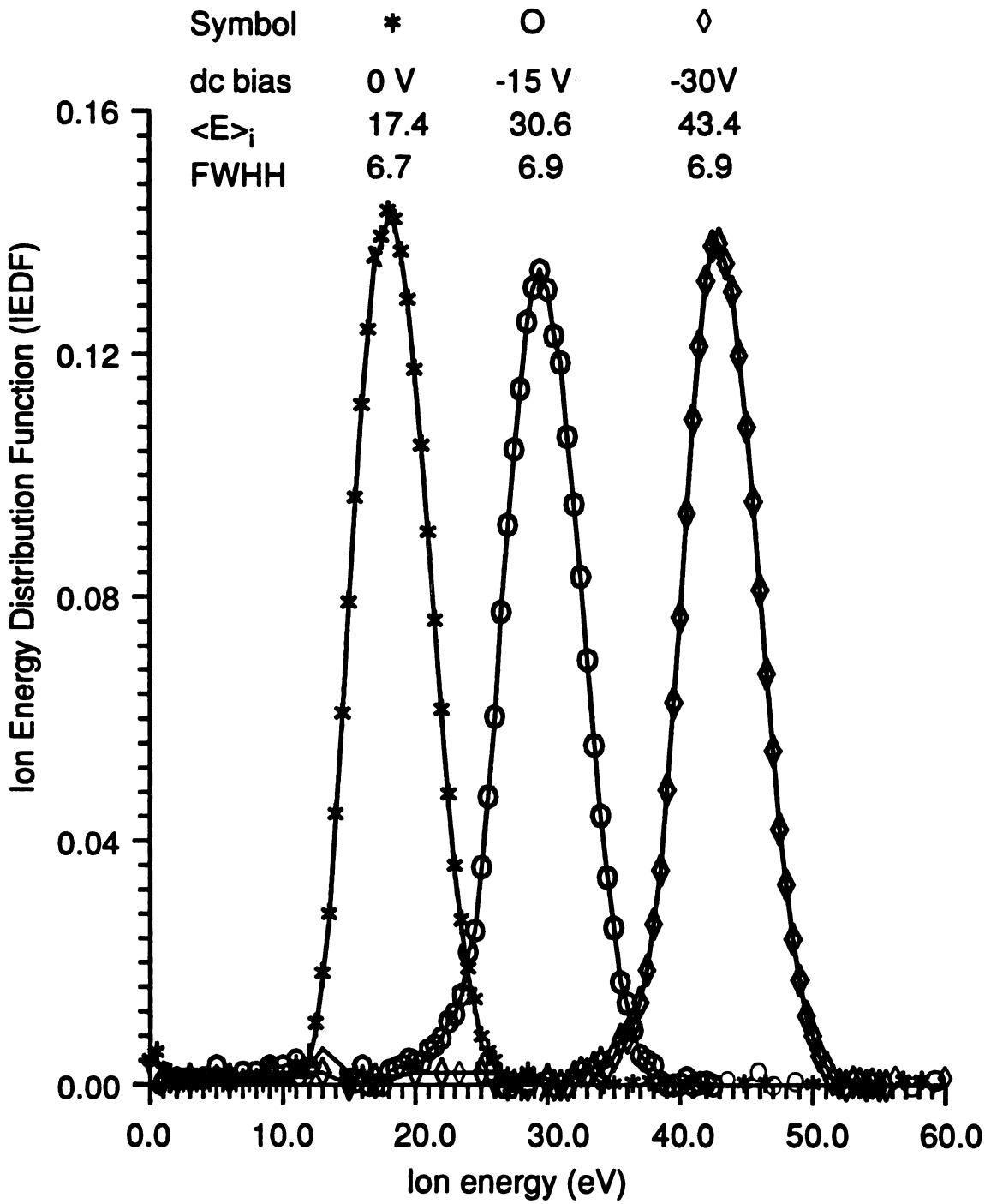

ECR magnet: 8P/8M, with TM_{011} mode in end feed applicator
Chamber pressure: 3.0 mTorr of pure argon
Position: z = 8 cm at center, P_{inc} ~ 325 W

Figure 7.44 IEDF versus dc bias on the substrate.

7.5.2 Spatial ion energy variations

Figure 7.45 display the variation of ion energy versus the downstream positions when the source was operated with TE_{211} side feed applicator for 8P/8M and 4P/8M configurations. The pressure and absorbed power were 0.77 mTorr and 236 W respectively. As shown in Figures 7.41 and 7.45, the average ion energy decreases slightly as the downstream distance increases. Also, the ion FWHH increases as the ions move away from the source. The ion energies (both $\langle E \rangle_i$ and FWHH) of the 4P/8M configuration were significantly lower than the ion energies of the 8P/8M configuration. In particular, the 8P/8M configuration operating with an input power of 240 W at 0.77 mTorr at z = 5 cm exhibited an ion distribution with an average ion energy of approximately 21 eV and a FWHH of 10 eV. The corresponding energy distribution of the 4P/8M configuration yielded a much lower average ion energy of 11 eV with a FWHH of ~6 eV.

In both magnet configurations, as the downstream position increases, the average ion energy slightly decreases, but the FWHH significantly increases. This broadening of the ion distribution is no doubt due to ion collisional processes as the ions diffuse downstream. SImilar situation also occurs in 8P/8M end feed plasma source.

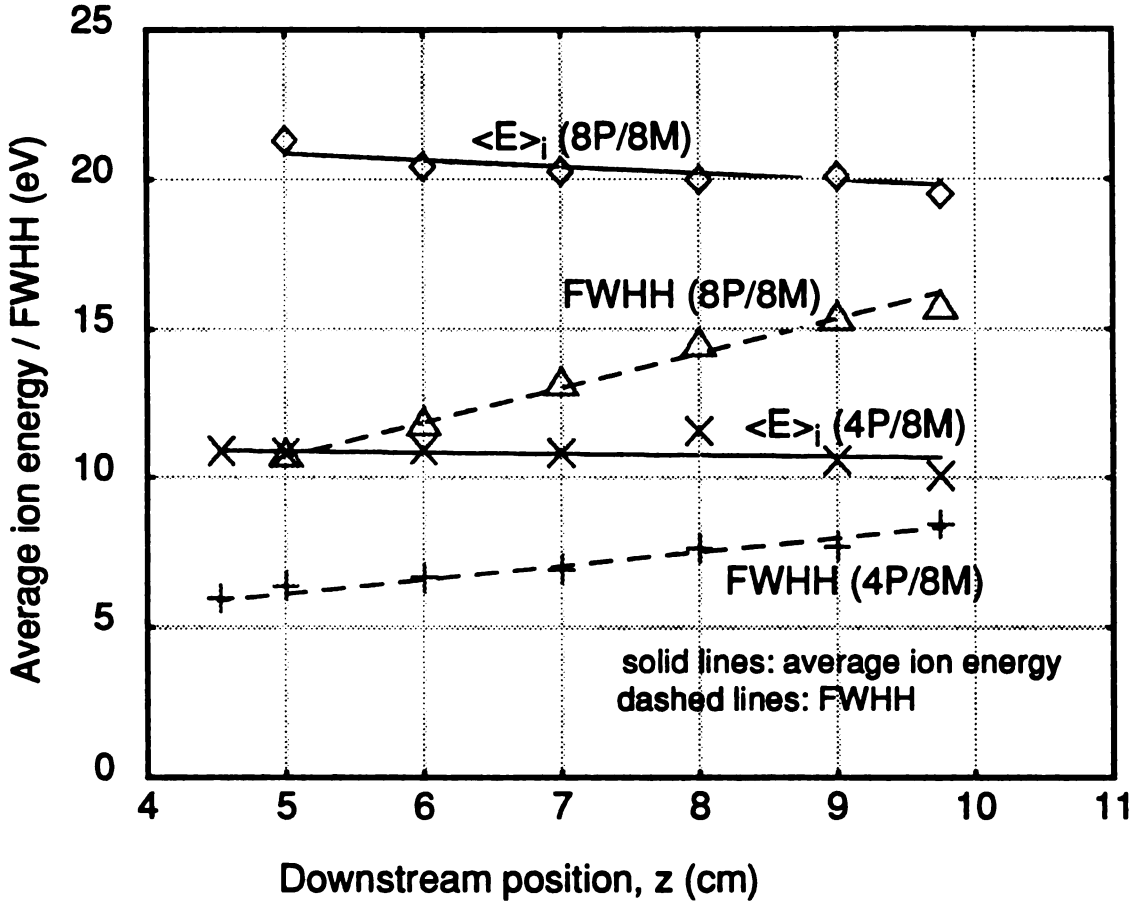

Side feed applicator, TE_{211}, r = 0, p = 0.77 mTorr, P_{inc}= 240 W

Figure 7.45 Average ion energy and FWHH vs. downstream position in side feed plasma source.

7.5.3 Ion energy versus pressure and power

Pressure increases, as shown in Figures 7.46 and 7.47 (a), result in lower average ion energies and in smaller FWHH values for both side feed and end feed reactors. The chamber pressure ranges in side feed and end feed measurements were 1-7 mTorr and 2-4 mTorr respectively. As shown in the Figures 7.42, 7.46 and 7.47 (a), both $<E>_i$ and FWHH decrease rapidly with increasing pressure. The average ion energy dependence of pressure is closely related to the plasma potential behavior versus pressure.

Figures 7.48 and 7.47 (b) indicate that the average ion energy and FWHH increase slightly as the input microwave power is increased for both side feed and end feed reactors. The power ranges for side feed and end feed measurements were 100-700W and 210 to 270 W respectively. As shown in the figures, both $<E>_i$ and FWHH increase slightly as the power increases. Since it is shown in Section 7.3 that microwave input power increases produce significant increases in ion density, the addition of microwave power considerably increases the ion density but only slightly increases the ion energy. This feature plus the bias dependence mentioned earlier (Sections 7.3.4 and 7.5.1.B) are very desirable for damage-free semiconductor wafer processing. It is desirable in these applicators to have plasma source where the flux of the ions and the ion energies distribution are separately controllable. The process rate is usually determined by ion density, which is mainly controlled by varying the power absorbed by the ECR source while the anisotropic processing task, governed by the ion energy impinging on the substrate, is primarily controlled by an independently applied substrate bias.

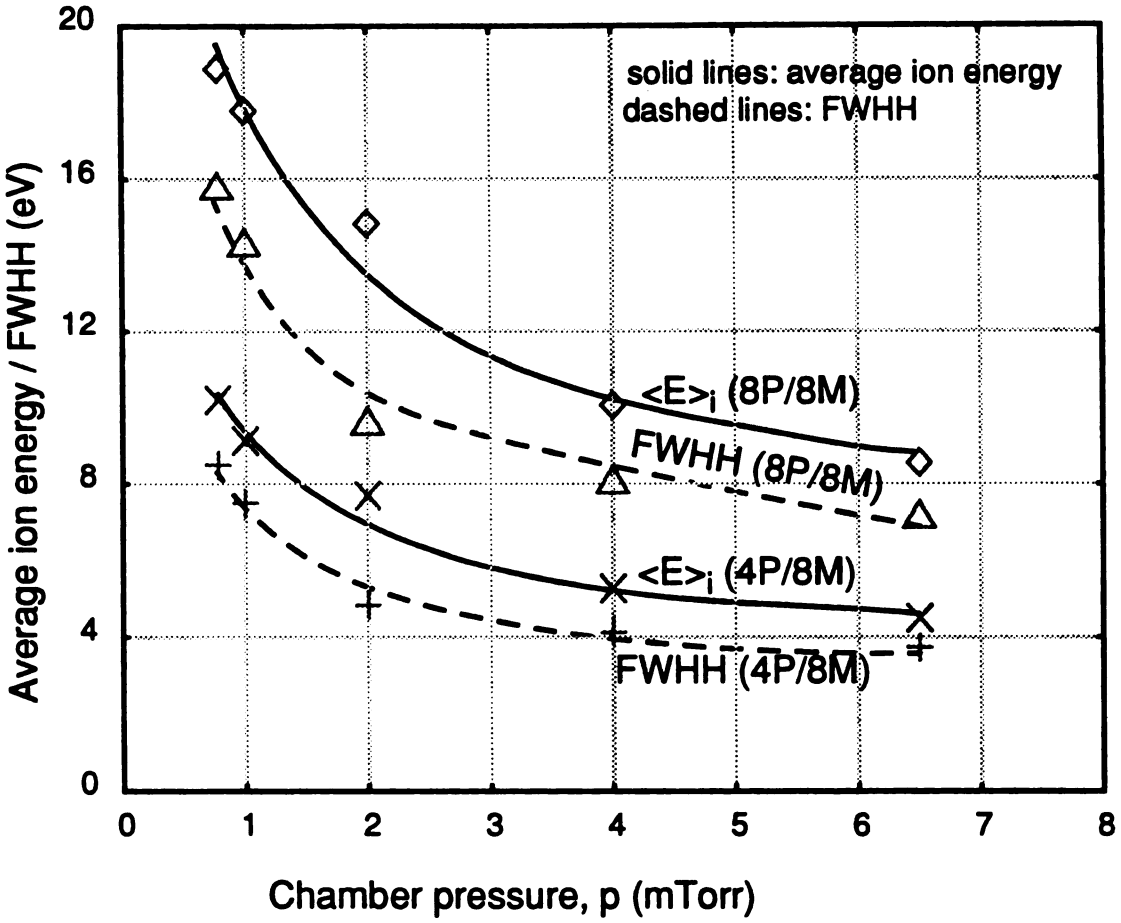

Side feed applicator, TE_{211}, r = 0, z = 9.75 cm, P_{inc} ~ 235 W

Figure 7.46 Average ion energy and FWHH vs. pressure in side feed plasma source.

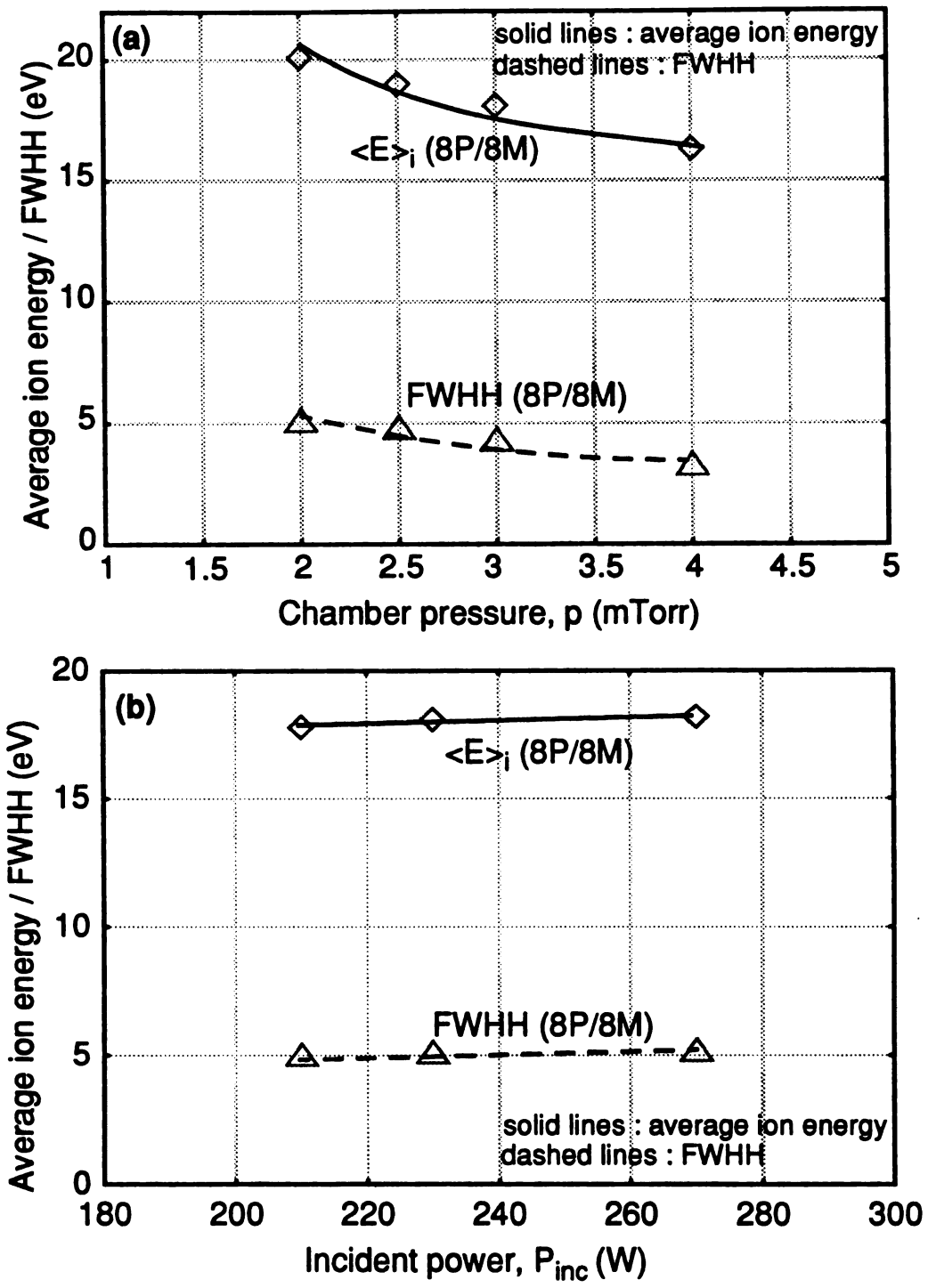

Figure 7.47 Average ion energy and FWHH in end feed reactor with TM_{011} mode at (0, 0, 6 cm); (a) vs. chamber pressure at absorbed power of 270 W, (b) vs. incident power at 3 mTorr pressure.

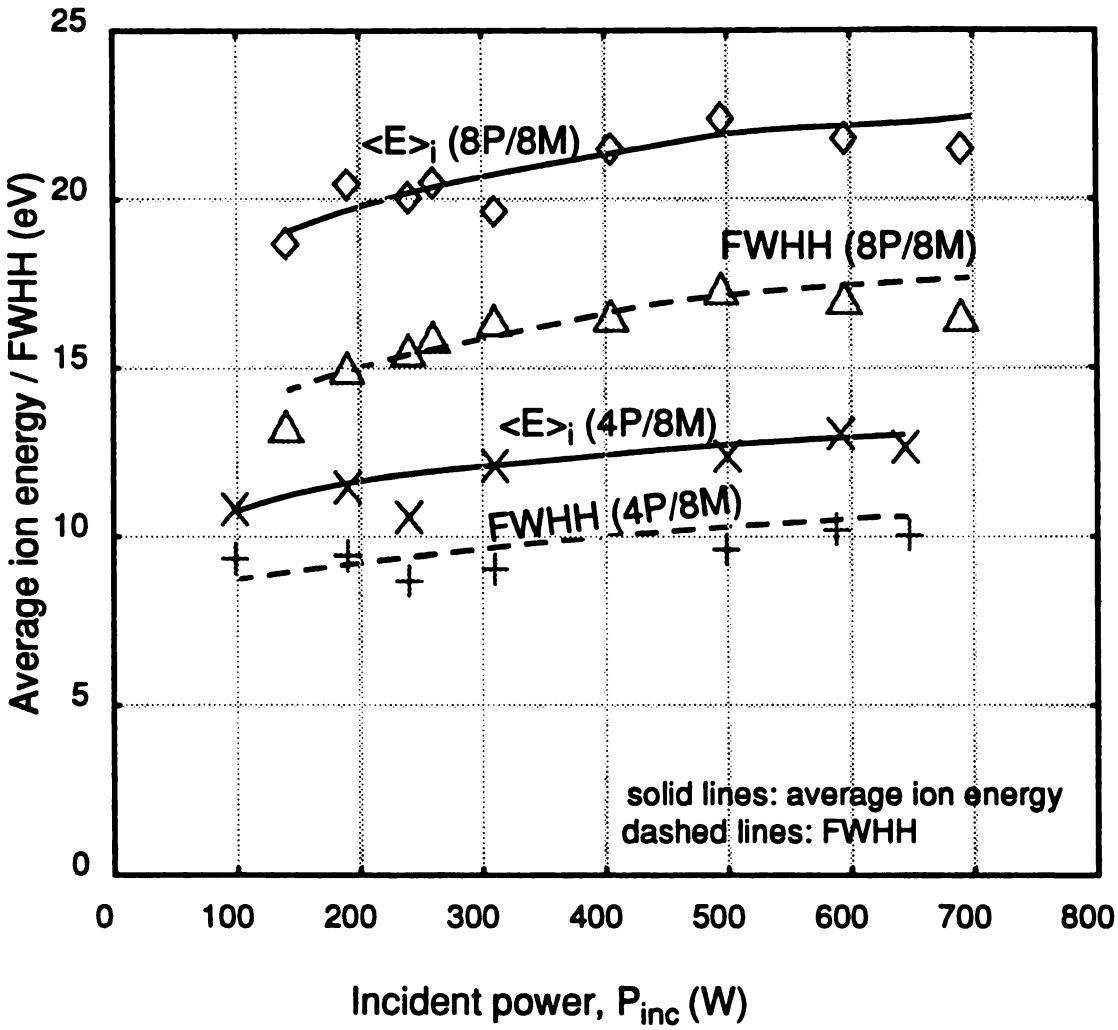

Side feed applicator, TE_{211}, p = 0.77 mTorr, r = 0, z = 9.75 cm

Figure 7.48 Average ion energy and FWHH vs. incident power in side feed plasma source.

7.5.4 Ion energy in pure hydrogen plasma discharges

Since hydrogen is a very common molecular processing gas used in plasma etching or CVD film growth, pure hydrogen gas was also introduced into the side feed MPDR™-13 for ion energy studies. Because of the lightness of hydrogen atomic or molecular ions, they have much higher mobility than the argon ions and hence more readily diffuse to the walls for recombination. Thus, higher power or higher operating pressure is required to sustain a low pressure hydrogen plasma. All the ion energy measurements in hydrogen discharges were performed in 8P/8M ECR magnet configuration operating with the side feed TE_{211} mode excitation applicator.

7.5.4.A Spatial ion energy variations

Figure 7.49 (a) indicates that the ion energies are quite uniform along the radial direction at z = 6 cm for an 8P/8M, TE_{211} mode excited side feed discharge. As shown in Figure 7.49 (b), the average ion energy decreases as z increases due to the various collisional losses. At the same time, the ion spectrum becomes broadened due to collisional processes as the ions travel downstream away from the source.

7.5.4.B Ion energy versus pressure and power

When power is increased, both the average ion energy and FWHH increase slightly as shown in Figure 7.50. This suggests that the extra power absorbed by the discharge results in higher density. This should be verified by further hydrogen ion density experiments in the future. Figure 7.51 shows the pressure dependence of average ion energy and FWHH. As expected, both the

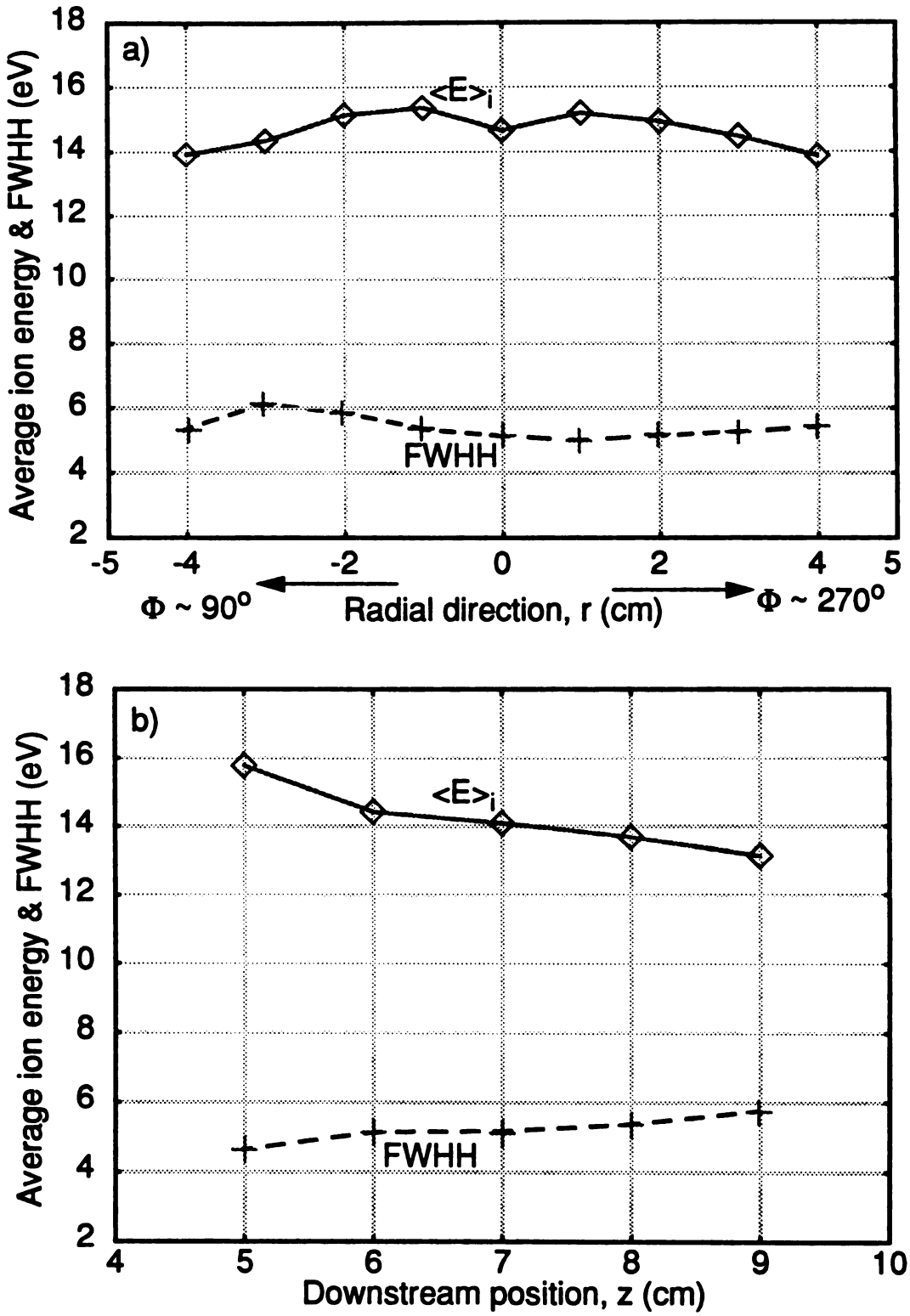

Figure 7.49 Spatial variations of average ion energy and FWHH in a 4.0 mTorr hydrogen discharge in 8P/8M side feed applicator with TE_{211} mode excitation, (a) vs. r at z = 6 cm, (b) vs. z at r =0.

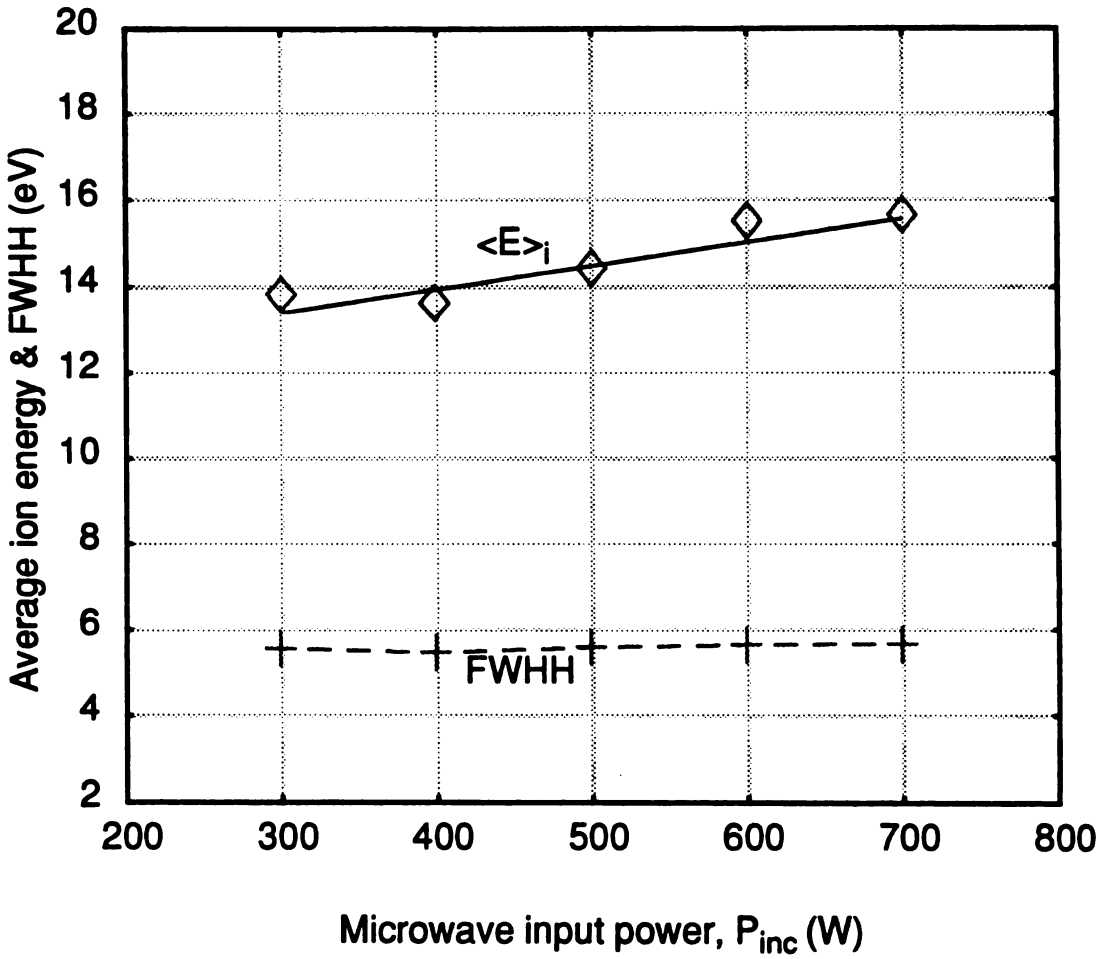

Figure 7.50 Average ion energy and FWHH of hydrogen versus incident power.

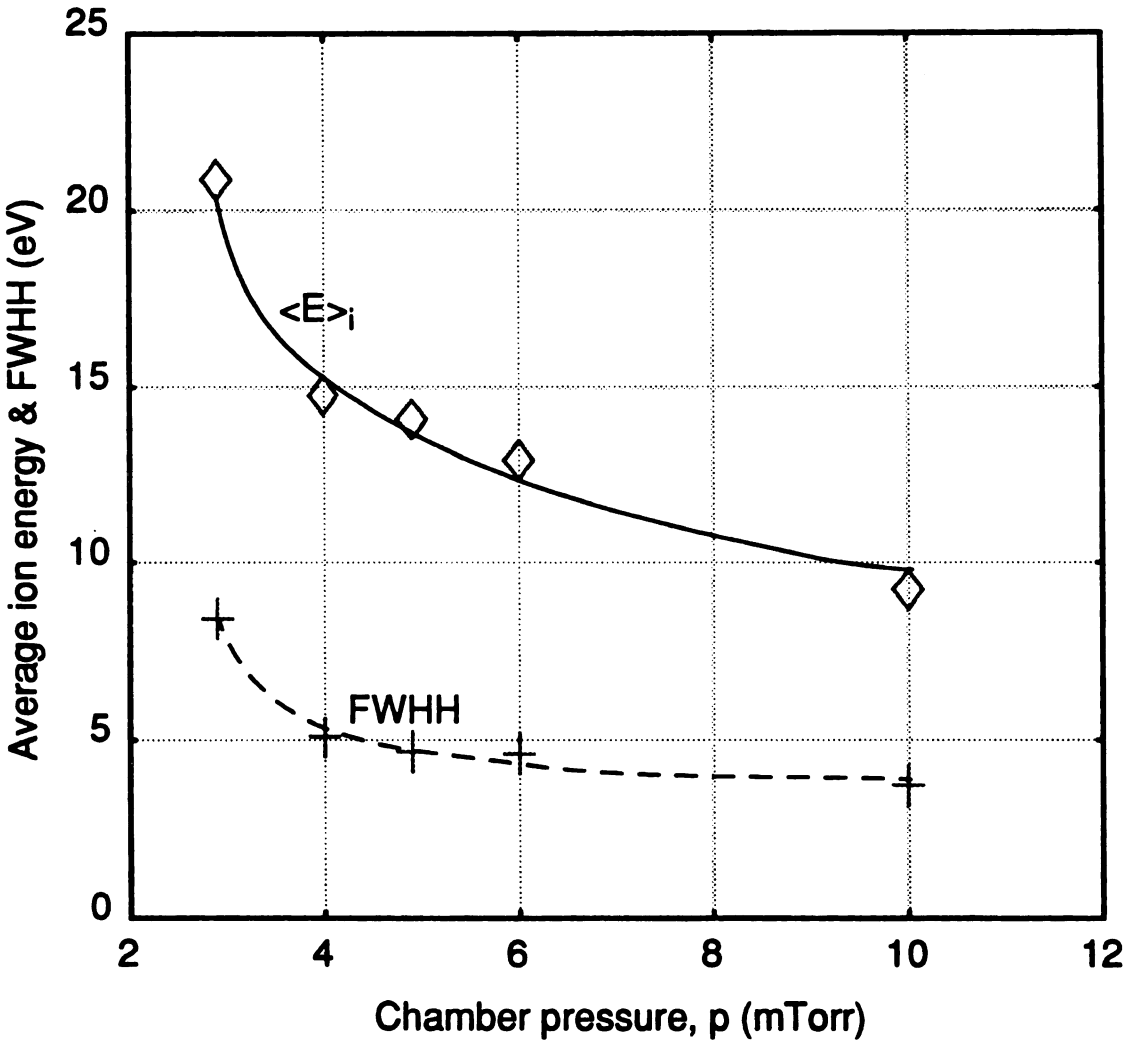

8P/8M ECR hydrogen discharge
Side feed applicator, TE_{211} mode Microwave power, P_{inc} ~ 500 W
Location z = 6 cm, at center

Figure 7.51 Average ion energy and FWHH of hydrogen versus chamber pressure.

average ion energy and FWHH decrease as pressure increases.

7.5.4.C Summary

The measured IEDF shape (not shown) of hydrogen discharges is still similar to the shifted-Gaussian distribution. The ion energy variations of pure hydrogen discharges over spatial positions, pressure and power varied in a similar way as the pure argon discharge. Even though ion energy of both argon and hydrogen discharges exhibited the similar dependency over the input variables, their magnitudes (both the average ion energy and FWHH) of hydrogen discharges were different from the argon discharges. The average ion energy in hydrogen discharge is 20% higher than that of the argon ion under similar experimental conditions. The disparate mass between hydrogen and argon ions makes hydrogen ions more easily accelerate by EM fields and have greater mobility. Thus the hydrogen ions diffuse faster to the walls than the argon ions. Also there are other inelastic collisional processes in the molecular hydrogen gas discharges. For example, hydrogen molecules can be disassociated by electron impact such as $e + H_2 \dashrightarrow 2H + e$, and etc... Therefore, it is quite complicated to understand the detail processes unless more detailed optical emission spectroscopy studies are also performed.

7.6 Concluding Remarks

The properties of a 2.45 GHz ECR plasma source with a 12.5 cm diameter discharge zone have been investigated comprehensively in this chapter by using various experimental diagnostic techniques including microwave electric field probes, Langmuir probes, and a gridded energy analyzer.

The electric field patterns and strengths were measured near the cavity wall in both end feed and side feed applicators. Both end feed and side feed discharge loaded applicators have two resonant well-matched modes over the tuning positions (L_s, L_p). For an end feed applicator, they were identified as the TM_{011} (or mode 1) and TM_{012} mode (or mode 2) excitations. The TE_{211} and TE_{311} mode excitations were found in the side feed applicator with three different multipolar ECR magnet configurations. The measured discharge loaded cavity height positions were slightly **higher** than the heights in the corresponding empty resonant cavity modes for an end feed applicator and were slightly **lower** than the heights in corresponding empty resonant cavity modes for a side feed applicator. It is believed that the dissimilar visual plasma patterns in different applicators produce different perturbations. In addition, the location of the input coupling probe is important to selectively excite EM fields in the applicator. Impressed electric field strengths were estimated based on the field strengths at the wall and the ideal unperturbed empty resonant pattern. Impressed electric fields for both end feed and side feed are low (< 10 kV/m) and indicate very efficient power coupling.

Measurements of absolute electric field strengths enable us to calculate the applicator wall surface losses and, hence, to estimate the microwave power coupling efficiencies for different applicators and mode excitations. The coupling efficiency in an end feed applicator with 8P/8M configuration varies from ~ 95% in mode 2 excitation to ~98% in mode 1 excitation. In a side feed plasma source, the coupling efficiency in a side feed applicator with 8P/8M configuration varies from ~ 90% in TE_{311} excitation to ~98% in TE_{211} excitation. The 4P/8M and 4P/4M magnet configurations in a side feed applicator have only slightly better microwave coupling efficiencies than in the 8P/8M configuration. It is believed that the number of magnetic poles is matched with the number of EM dipole mode for 4P/8M and 4P/4M magnet configurations. Overall, the coupling efficiencies in both applicators are excellent (~98%), especially in mode 1 excitation in end feed applicator and TE_{211} excitation in side feed.

The ion density in the side feed plasma source is highest in the 8P/8M magnet configuration and lowest (~50% of 8P/8M) in allN/8M configuration. This is due to the 8P/8M configuration, which has the best magnetic confinement while the allN/8M has the worst. Moreover, the measured ion densities at $z = 3$ cm plane in 8P/8M configuration peak at the center while the peak density in 4P/8M configuration is off-center. This indicates that the density profile in 4P/8M configuration is more uniform near the source region. Hence, it produces less space charge field and lowers the plasma potential and ion impinging energy. Based on the ion density measurements, the ion production costs at $z = 3$ cm were evaluated. The best ion production cost for the side feed applicator is the

8P/8M configuration with TE_{211} excitation, namely, ~300 eV/ion at absorbed power of 235 W and at pressure of 2 mTorr.

The measured ion density and ion production cost in 8P/8M end feed plasma source with mode 1 excitation is lower (~12%) than those with mode 2 excitation. This is partially due to the better coupling efficiency in mode 1 than in mode 2. The best ion production cost in an end feed applicator is the 8P/8M configuration with TM_{011} excitation, namely, ~360 eV/ion at absorbed power of 270 W and at pressure of 3 mTorr. The best operation for both applicators show similar ion production costs because of their excellent coupling efficiencies and good 8P/8M magnetic confinement. However, the measured ion density in an end feed plasma source is more uniform (2.8% vs. 8.2% at z = 1 cm and 6.8% vs. 14.8% at z = 8 cm) than densities in the side feed source. On the other hand, the side feed applicator is easier to sustain plasma discharge at low pressure (< 1 mTorr) than in the end feed. It may due to the impressed electric fields in side feed excitation are mostly tangential to the plasma boundary.

Additionally, the measured downstream ion densities at (0, 0, 8 cm) near a dc biased substrate changed very slightly when the dc bias was varied from 0 to -50 V. This demonstrates that the ion density is mainly controlled by the microwave absorbed power into the discharge without increasing the electron or ion energies, and ion energy is independently controlled by the applied substrate bias.

The measured EEDF of side feed 8P/8M configuration falls between the Maxwellian and Druyvesteyn distribution while the EEDF is similar to Druyvesteyn in the side feed 4P/8M configuration. No high electron energy population was

founded in the downstream region. The plasma potential of the side feed 4P/8M configuration is more uniform and lower than the plasma potential of side feed 8P/8M configuration due to the above-mentioned uniform plasma density profile in 4P/8M configuration. Both the plasma potential and electron temperature behave normally according to the global discharge model.

All measured ion energy exhibited a relatively low energy (< 25 eV) and narrow distribution (< 16 eV). A similar ion energy behavior versus input power and downstream position was also observed. However, the average ion energy and FWHH vary versus discharge position, operating pressure, and input power. The $\langle E \rangle_i$ and FWHH increase as pressure decreases or the z-position decreases. Increasing the input power has only resulted in slight increase in $\langle E \rangle_i$ and FWHH. Putting a dc bias over the substrate can independently control the $\langle E \rangle_i$ without altering other plasma parameters (such as ion density and FWHH). From the comparison of the plasma potential and average ion energy, they have the same order of magnitudes and trends. Therefore, the measured ion energy is dominated by the energy gained by the ion when it falls through the sheath surrounding the analyzer. The measured $\langle E \rangle_i$ and FWHH of side feed 8P/8M configuration are higher (21 eV vs. 11 eV) than side feed 4P/8M configuration. This is a consequence of the plasma potential result. The measured $\langle E \rangle_i$ of the end feed 8P/8M configuration are slightly higher (17 eV vs. 12 eV) than the side feed 8P/8M configuration. This phenomenon is not fully understood.

The measured ion energy response in hydrogen discharges has the similar behavior dependence on input variables as in argon discharge. However, the average ion energy is about 20% higher than the corresponding ion energy in argon.

In summary, the macroscopic properties of the side feed and end feed multipolar ECR plasma sources have been comprehensively measured. The typical measured downstream plasma parameters are ion density ($>10^{11}$ cm^{-3}), electron temperature (2.5 to 8 eV), plasma sheath potential (12 to 32 V) and the ion energy (12 to 26 eV) impinging on a conducting substrate. The behavior of measured plasma parameters including ion density, plasma potential, electron temperature, and ion energy follows approximately with the plasma global model predictions. All ion densities increase with increased absorbed power. Ion energy, plasma potential, and electron temperature decrease rapidly as the pressure increases.

THESIS

MICHIGAN STATE UNIVERSITY LIBRARIES

3 1293 01570 6140

LIBRARY
Michigan State
University

PLACE IN RETURN BOX to remove this checkout from your record.
TO AVOID FINES return on or before date due.

DATE DUE	DATE DUE	DATE DUE
343		
APR 08 2003		
NOV 27 2002		
0331 06		
OCT 02 2006		
092209		

MSU Is An Affirmative Action/Equal Opportunity Institution
c:\circ\datedue.pm3-p.1

AN EXPERIMENTAL EVALUATION OF A 12.5-CM DIAMETER MULTIPOLAR MICROWAVE ELECTRON CYCLOTRON RESONANCE PLASMA SOURCE

VOLUME II

By

Peng Un Mak

A DISSERTATION

Submitted to
Michigan State University
in partial fulfillment of the requirements
for the degree of

DOCTOR OF PHILOSOPHY

Department of Electrical Engineering

1997

Chapter 8

Microwave Equivalent Circuit for the ECR End Feed Applicator

- 8.1 Introduction
- 8.2 Microwave Equivalent Circuit Components and Their Characteristics
- 8.3 Equivalent Circuit Discussion
- 8.4 Concluding Remarks and Proposed Design Improvement

Chapter 8

Microwave Equivalent Circuit for the ECR End Feed Applicator

8.1 Introduction

Solving for electromagnetic fields inside a plasma reactor involves Maxwell equations, particle kinetics, and detailed wave-particle interactions [149,150]. In some complex reactors (irregular geometries, strong inhomogeneous static magnetic fields,...), analytical results are virtually impossible. Even with the recent amazing speed of the advanced computer processors, plasma simulations [151,152] consume tremendous computer time and are based on many considerably details but still incomplete models. Even of the numerical simulations provide plausible solutions, they still require experimental data for verification. From an electrical engineer's point of view, an alternate way to understand the problem is by an equivalent circuit. Although it is also an approximate method, this usually provides physical meaning and insight to user/designer without involvement of the tedious mathematical or computer tools.

In this chapter, using the electric field measurement data described in Chapter 7, the MSU end feed microwave ECR applicator is divided into four

regions. An equivalent circuit for each region is then derived. The various circuit components and their roles are also discussed. This equivalent circuit helps to identify the power transfer paths via impedance transformation techniques and provides some physical intuition and feeling of how the applicator works. This kind of knowledge can apply to other MPDR™ reactors. Recommendations of improving the design of the large area processing reactors is outlined at the end of this chapter.

8.2 Microwave Equivalent Circuit Components and Their Characteristics

By examining its physical configuration, the end feed cavity applicator can be divided into four different but interconnected microwave circuits as shown in Figure 8.1 (a): (1) a TEM coaxial transmission coaxial waveguide region I, (2) the coupling probe region II, which is represented by another coaxial waveguide, (3) a circular cylindrical waveguide region III, and (4) a plasma loaded waveguide region IV.

Region I consists of an incoming coaxial cable with inner and outer diameters of 3/8" and 7/8" respectively. It connects the microwave power supply to the input of coupling region II. The characteristic impedance of this coaxial cable is about 50 Ω which is equal to the microwave power supply internal resistance. Due to the small dimensions of the coaxial cable, only the TEM mode can propagate when the cable is excited with 2.45 GHz energy.

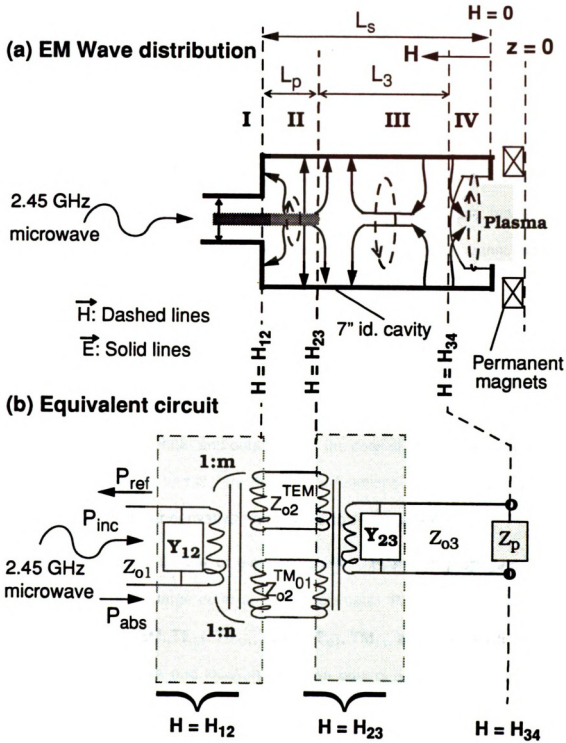

where $Y_{12}=G_{12}+jB_{12}$, $Y_{23}=G_{23}+jB_{23}$

Figure 8.1 Microwave equivalent circuit for end feed MPDR.

As shown in Figure 8.1 (b), this region ($H > H_{12}$) is represented as a transmission line with a characteristic impedance of $Z_{01} \cong 50\ \Omega$.

Coupling transitions: At the $H = H_{12}$ plane, the coaxial waveguide in region I abruptly jumps to the coaxial waveguide of region II. The coupling probe region II can be viewed as another coaxial waveguide of inner diameter of 3/8" and outer diameter of 7" with length L_p. Table 8.1 lists the possible propagating and evanescent modes in this coaxial waveguide section. These modes and guided wavelengths were obtained by solving the eigenvalues of transcendental equations [97]

$$J_n(k_c r_o) \bullet N_n(k_c r_i) - J_n(k_c r_i) \bullet N_n(k_c r_o) = 0, \text{ for TM modes} \tag{8.1}$$

$$\text{and } J_n'(k_c r_o) \bullet N_n'(k_c r_i) - J_n'(k_c r_i) \bullet N_n'(k_c r_o) = 0, \text{ for TE modes,} \tag{8.2}$$

where r_i and r_o are the inner and outer radii of the coaxial waveguide, $k_c = (2\pi)/\lambda_g$ is the wavenumber, J_n and N_n are the Bessel functions of the first and second kind, prime (') stands for derivative with respect to its argument.

As indicated a number of electromagnetic modes can propagate in this region because of the large outer conductor diameter. Possible propagating EM coaxial modes are TEM, TE_{11}, TM_{01}, TE_{21}, TE_{01}, TM_{11}, and TE_{31}. By the choice of excitation probe size and location, one can control the EM mode excitation inside this section of the applicator. Since the incoming wave in Region I is a Φ-symmetric TEM mode and the coupling aperture in the $H = H_{12}$ plane is located at the axial **center** of the coaxial waveguides, only Φ–symmetric electromagnetic modes are excited inside the coupling region II for propagation.

Table 8.1 First few guided wavelengths (λg) for propagating modes or characteristic decay lengths (δ) for evanescent modes in regions II and III.

Propagating characteristics	Mode name	Region II		Region III	
		λg (Z_{02})	d[b]	λg (Z_{03})	d[b]
Possible Propagating Waves	TEM	12.24 cm (175.6 Ω)	N.A.	N.A.	N.A.
	TE_{11}	13.37 cm (411.6 Ω)		13.38 cm (412 Ω)	
	TM_{01}	16.6 cm (277.8 Ω)		14.4 cm (320.3 Ω)	
	TE_{21}	16.48 cm (507.5 Ω)		16.48 cm (507.5 Ω)	
	TE_{01}/ TM_{11}[a]	23.0 cm (709.5 Ω/ 200.3 Ω)		22.6 cm (694.9 Ω/204.5 Ω)	
	TE_{31}	31.4 cm (967.6 Ω)		31.4 cm (967.3 Ω)	
Nonpropagating waves (Evanescent or near field modes)	TM_{02}	N.A.	1.95 cm	N.A.	2.86 cm
	TM_{21}		3.77 cm		3.77 cm
	TM_{12}/ TE_{02}[a]		1.63 cm		1.67 cm
	TE_{12}		3.38 cm		3.22 cm
	TE_{22}		1.81 cm		1.81 cm
	TE_{32}		1.35 cm		1.35 cm
	TE_{41}		3.25 cm		3.25 cm
	etc.				

a: stands for the degenerate EM modes;

b: stands for the distance at which the near fields would decay down to 37% of the original value.

This was confirmed experimentally presented in Section 7.2.2. Thus, only propagating TEM and TM_{01} coaxial waveguide modes are excited. In addition to propagating modes, Φ–symmetric localized evanescent TM fields that store reactive energy are also excited on both sides of $H = H_{12}$ and $H = H_{23}$ planes [153]. The capacitive reactance caused by the discontinuity at $H = H_{12}$ plane is not easy to estimate. The reactance at $H = H_{23}$ plane is due to the abrupt transition from coaxial waveguide of region II into the empty circular waveguide of region III. This reactance is calculated to be around 0.233 pF using the formulas and charts in Refs. [154-156].

Region II, thus, can be represented as shown in Figure 8.1 (b) by two transmission lines of length L_p in parallel. One transmission line with a characteristic impedance $Z_{02}^{TEM} \cong 176\ \Omega$ represents the TEM mode excitation, and the other with a characteristic impedance of $Z_{02}^{TM01} \cong 277.6\ \Omega$ represents the TM_{01} mode excitation. The mode couplings that occur between the different propagating modes in regions I, II and III at the $H = H_{12}$ and $H = H_{23}$ planes is represented as the two mutual coupled transformers in Figure 8.1 (b). The capacitive susceptances jB_{12} and jB_{23} are the equivalent lumped susceptances that account for the reactive energy stored in the localized evanescent fields at the discontinuity planes $H = H_{12}$ and $H = H_{23}$ respectively. The coupling wall losses in region II, which are due to the currents flowing on the probe and the conducting surfaces at the $H = H_{12}$ plane and on the outer conductor, are usually small (shown in Section 7.2.2.D) when compared with the power coupled into the plasma load. These losses are lumped together and represented as the lumped

circuit conductance G_{12}. These losses are usually referred to as the coupling circuit losses or the coupling losses. The electric field measurements in Section 7.2.2 show that the end of the center conductor in region II is always located at a maximum electric field strength for the fields excited in region III and that L_p is approximately one quarter of a TEM wavelength.

Region III, the region between $H = H_{23}$ and $H = H_{34}$ planes in Figure 8.1, consists of a 7" i.d. empty circular waveguide section. This region serves several roles. First, it transmits the impressed electric fields with the desired spatial variation into the plasma load, i.e. the electric fields impressed on the plasma load must have field components perpendicular to the static magnetic field in the ECR excitation regions. Second, its length, L_3, changes as the sliding short varies, so that an impedance match at $H = H_{12}$ is achieved. Since the electromagnetic fields in the excitation coupling region II are TM-type and Φ symmetric, only the symmetric TM_{01} fields are allowed to propagate in this empty waveguide section. Region III is represented by a TM_{01}-type transmission line of characteristic impedance $Z_{03} \cong 320\ \Omega$ and length L_3. The power loss in this region originates from the induced surface currents flowing on the low-loss conducting cylindrical wall and is represented as a lumped conductance G_{23} in the equivalent circuit in Figure 8.1 (b).

Region IV: Finally, the plasma discharge and its enclosing circular waveguide boundary ($H < H_{34}$) make up the plasma loaded waveguide region IV. This plasma loaded waveguide cannot be easily analyzed because of the dome shape discharge geometry, and the inhomogeneous static magnetic field. Indeed

the experimental data (Chapters 7 and 9) demonstrates that the discharge is very nonlinear vs. the experimental inputs. Simple analytical solutions of the electromagnetic fields in this region are not available and, thus, the details of the field structure in this region are not presented here. For simplicity, this region is represented as a lumped circuit impedance, $Z_p = R_p + jX_p$, located at the $H = H_{34}$ plane. R_p represents the equivalent resistance due to the microwave power absorbed by the discharge. X_p represents the reactive energy stored in the EM fields and the motions of charged species. This impedance varies in a complex, nonlinear fashion as the discharge responds to the changes in the input experimental variables.

8.3 Equivalent Circuit Discussion

This equivalent circuit can now be used to understand how the microwave is coupled into the discharge load. It clearly demonstrates that regions II and III are resonant impedance transforming circuits that enable the nonlinear plasma load to be matched to the 50 Ω characteristic impedance of the coaxial region I. Region II consists of two coupled transmission line circuits that either individually or collectively produce an impedance transformation that reduces the reflected power at the $H = H_{12}$ plane. Depending upon the length L_p, the impedance matching can be achieved through either circuit or possibly both circuits. The experimental measurements indicate that one optimum probe depth that yields a matched cavity applicator for both mode 1 and mode 2 resonances while still

maintaining a discharge for poorly matched conditions (see Chapter 9). This occurs when the probe depth L_p was approximately equal to 3.0 cm. In most of end feed experimental measurements presented in this thesis, the probe depth only varied slightly between 2.9 cm and 3.0 cm (although it is possible to create discharges with 1.5 cm < L_p < 4.0 cm). When the probe was held in this position, the measured electric field is always a maximum at H = H_{23}. Then the region II transmission line circuits are (1) 0.248 of a TEM wavelength and (2) 0.18 of a coaxial TM_{01} wavelength. Thus, both transmission lines can produce important impedance transformations required to sustain a plasma discharge. Both modes are Φ-symmetric and thus, both excite the TM_{01} circular waveguide mode in region III.

The measured electric field strengths shown in Figure 7.4 indicate that the cavity applicator length L_s was varied until two matched modes (mode 1 and mode 2) were achieved. When matched, the impedance is known to be 50 Ω at the H = H_{12} plane. The measured electric fields for both modes 1 and 2 indicate that (1) a standing wave field maximum occurs at the H = H_{23} plane and (2) the standing wave electric field patterns between the H = H_{23} and H_{34} indicate that the plasma impedance is inductive reactive.

The experimental measurements indicate that the highest density operation, i.e. mode 1, occurs when the empty waveguide section, L_3, is adjusted to be very short. Two factors contribute to the higher densities. First, the applicator is shorter than mode 2 by $\lambda_g/2$ and, thus, coupling wall losses are less. Second, and most importantly, when the probe plane H = H_{23} is closer to the discharge

plane H = H_{34}, propagating as well as evanescent fields can interact with the discharge. For example, the evanescent EM field depth, δ, shown in Table 8.1, indicates TM_{02} and other mode fields can interact directly with the discharge.

Finally, if we ignore the admittances of the waveguide discontinuities at planes H = H_{12} and H_{23} and the small resistance of TM_{01} transmission line, the plasma loaded waveguide impedance Z_p for mode 2 can be estimated using a Smith Chart™ to determine transmission line impedance transformations. Z_p for mode 2 is in the range of (190 to 430 + j 100 to 230) Ω, where the magnitude of the real and imaginary part of the impedance decreases as the pressure or absorbed power increases. Thus the collective behavior of the plasma loaded waveguide, i.e. the ECR discharge is not only resistive but has an inductive component probably due to the inductive effects of the motion of the charged particles (ions and electrons). However, it appears that these impedances may change considerably if the admittances Y_{12} and Y_{23} are included. The analysis of this part of the circuit is complex and must be left for future analytical and numerical investigations.

8.4 Concluding Remarks and Proposed Design Improvement

In this chapter, a microwave equivalent circuits for the end feed cavity applicator under EM resonant condition was presented. Various characteristic impedances and electrical lengths for best matching are analyzed. The circuit is

able to easily maximize the transfer microwave power into plasma discharge. Due to the excitation structure configuration, only TM fields are generated inside the end feed applicator. This may provide a hint to why the side feed applicator is easier to sustain plasma discharge at very low pressure than the end feed applicator.

The normalized wave impedances of propagating TM and TE waves are displayed in Figure 8.2. The TM wave impedance is always smaller than the intrinsic impedance of dielectric medium but the TE wave impedance is always larger. The conductivity of a discharge usually is smaller at lower pressure and hence its plasma impedance is usually higher. Therefore, it is easier for TE waves to match to the higher impedance of low pressure plasma. And TE modes are easily excited by the side feed applicator. However, it has been assumed thus far that the discontinuity susceptances in the stepped transformer are neglected.This is approximately true in a low-frequency coaxial line, but not in a high-frequency coaxial line or waveguide. The presence of the discontinuity susceptances has two effects. First, it increases slightly in the magnitudes of the individual step reflections. Second, it introduces shifts of phase angle in the reflection and transmission coefficients of the steps. In most cases, the physical result of this correction is to decrease the spacings between steps to somewhat less than $\lambda_g/4$, as measured in this study in region II.

It is particularly important for the current reactor to maintain a good match whenever operating at very low discharge pressures. To increase the versatility of cavity applicator, an extendible optimum multi-stepped-transmission-line

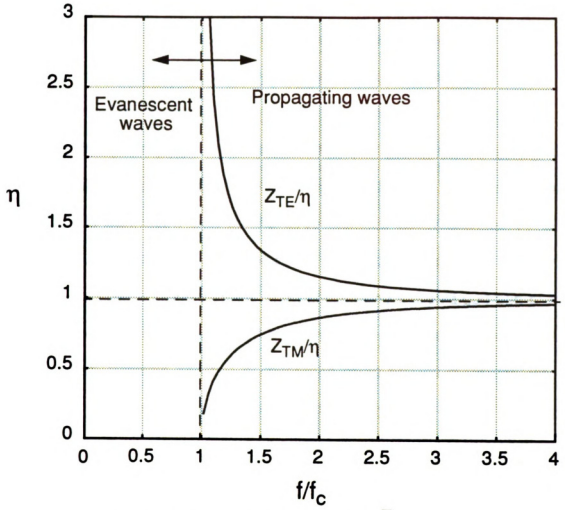

Intrinsic impedance of the medium: $\eta = \sqrt{\frac{\mu}{\varepsilon}}$

Cutoff frequency: $(f_c)^{TM}_{nl} = \frac{p_{nl}}{2\pi a\sqrt{\mu\varepsilon}}$, $(f_c)^{TE}_{nl} = \frac{p_{nl}'}{2\pi a\sqrt{\mu\varepsilon}}$

where a is the radius of the circular waveguide,

p_{nl} and p_{nl}' are the lth root of $J_n(x) = 0$ and $J_n'(x) = 0$ respectively.

TM wave impedance: $Z_{TM} = \eta\sqrt{1-\left(\frac{f_c}{f}\right)^2}$

TE wave impedance: $Z_{TE} = \eta/\sqrt{1-\left(\frac{f_c}{f}\right)^2}$

Figure 8.2 Normalized TE and TM wave impedances versus normalized frequency.

transformer structure for matching a wide-range of nonlinear plasma loaded cavity discharge is proposed here. Figure 8.3 (a) shows a schematic of an n-section stepped-transmission-line transformer. The transmission line may be of any type, coaxial or waveguide. The ϕ_i (i=1,2,..., n) stands for the electrical lengths of each section (usually an integer multiple of quarter guided wavelength). Each section is doing impedance transformation gradually to avoid large discontinuity jumps. This is particularly true for the large diameter cavity such as 14" dia. MPDR™-325. In practice, one of the proposed end feed applicators is displayed in Figure 8.3 (b). The additional sliding short section and the enlarged end of the excitation probe would give smother transitions. More tuning elements of L_1, L_2, r_{1o} and r_{2i} are available and this configuration could provide more degrees of freedom to match a wide range of plasma loaded cavity.

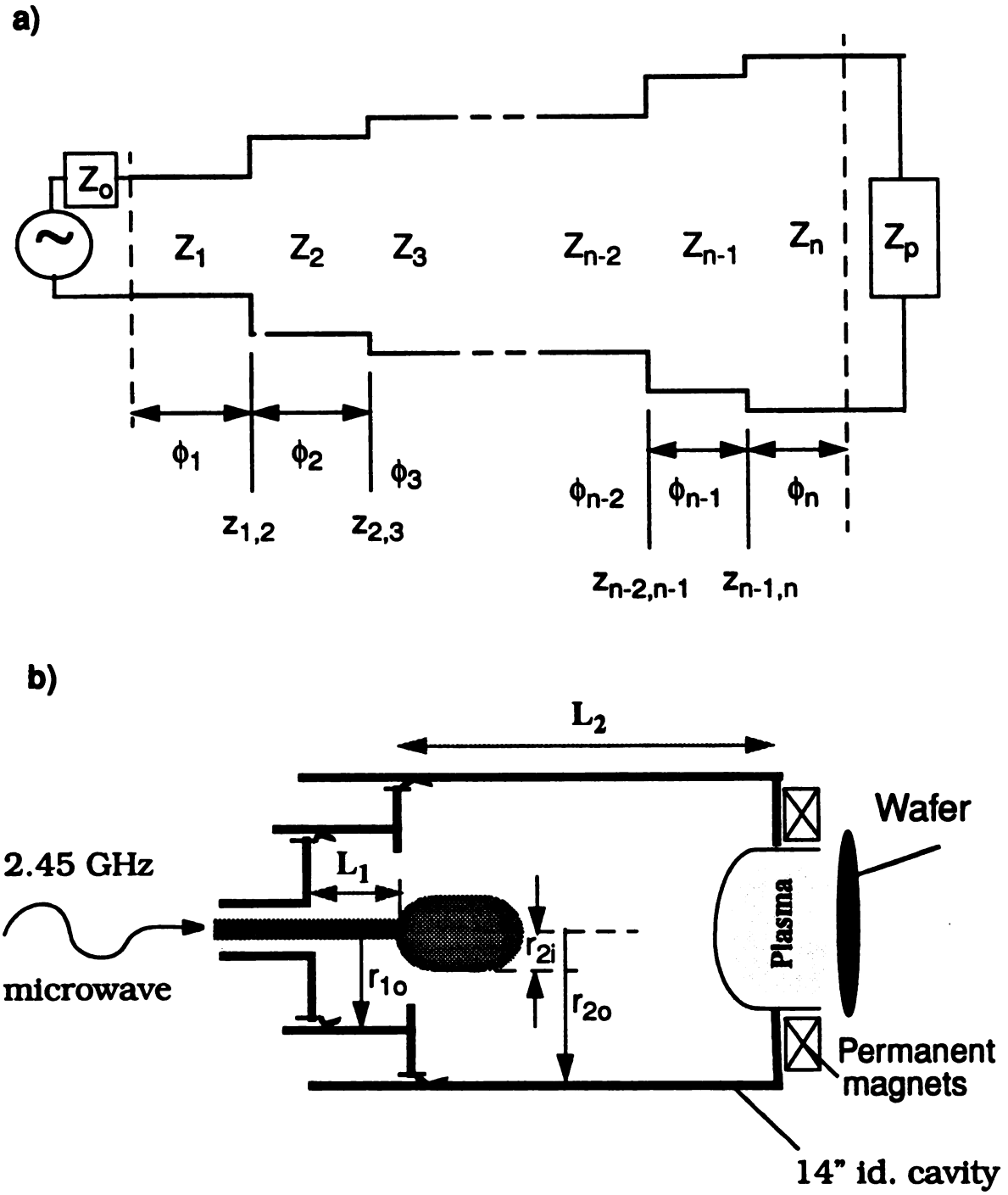

Figure 8.3 (a) Schematic of optimum stepped transmission line transformer, (b) A proposed version of end feed applicator.

Chapter 9

Experimental Hysteresis of Multipolar ECR Plasma Source and Control Sensors

- 9.1 Introduction
- 9.2 Experimental Hysteresis Results
  - 9.2.1 End feed hysteresis versus cavity height
  - 9.2.2 Side feed hysteresis on L_s, L_p and p
  - 9.2.3 Application to plasma control sensors
- 9.3 Argon Soft Sputter Control Processing Example
  - 9.3.1 Experiment preparation and sensors selection
  - 9.3.2 Experimental sequence and result
- 9.4 Concluding Remarks

Chapter 9

Experimental Hysteresis of Multipolar ECR Plasma Source and Control Sensors

9.1 Introduction

The low pressure, high density resonant cavity-type multipolar ECR plasma source and its variations [31] have been used for various micro-fabrication applications including silicon [76-79], III-V integrated circuits [158,159], and photonic devices [160]. Several studies [17,54,157] conducted over the past few years have concentrated on plasma source performance under the minimum reflected power operations. However, little was mentioned on how the well-known hysteresis and multiple steady states associated with microwave discharges can be controlled and avoided? Furthermore, operation at minimal *de facto* reflected power may not be guaranteed as the optimum state for reliable and repeatable plasma processes.

Low pressure, high density ECR plasma sources have been noted as being susceptible to plasma mode jumps, hysteresis of operation conditions, and multiple steady states [8, 161-166]. We usually refer to distinct plasmas separated by sudden transitions as "modes" or "operations". This chapter is motivated by the

application in processing semiconductor substrate, especially for the plasma discharge control to avoid those jumps or hystereses. As mentioned in Chapter 4, knowing the internal state of the applicator that relates to input and output variables would be more deterministic than the direct nonlinear relationship between input and output variables of the plasma source due to the possible multiple steady states. Thus, in this chapter, hysteresis phenomena are studied by examining the discharge absorbed power P_{abs} and downstream ion densities n_i versus the different input variables (P_{inc}, p, impedance matching circuit: L_s, L_p). In the end feed reactor, the investigation was concentrated only on the P_{abs} & n_i vs. L_s. In the side feed reactor, the hysteresis on cavity height, input coupling probe depth, and chamber pressure are addressed. Their experimental hysteresis responses provide an important database of sensor control for plasma processing. Knowing the hysteresis data aids the user/experimenter in the selection of proper internal or output variables as the control sensors for repeatable plasma processes. Finally, as an example, a simple argon soft sputter control experiment is presented to demonstrate a reproducible plasma process. Only 8P/8M magnet configuration and pure argon gas were used in the experiments presented in this chapter.

9.2 Experimental Hysteresis Results

Hysteresis or plasma with multiple steady states usually happen whenever one or more input variables (P_{inc}, p, tuning circuit; L_s, L_p, etc.) are changing back and forth. Figure 9.1 shows the schematic of the plasma hysteresis phenomenon. As shown, when the input variable(s) are varied back and forth, the desired output variable(s) trace out a cycle. Therefore, there is probably more than one output values corresponding to the same set of input variables. In this section, focus is put on the hysteresis investigation to the major impedance matching element, L_s in the end feed plasma source. Hysteresis on other variables such as pressure and probe depth are then highlighted next in the side feed applicator. Based on the measured hysteresis results, sensors to plasma control for reproducible process is suggested.

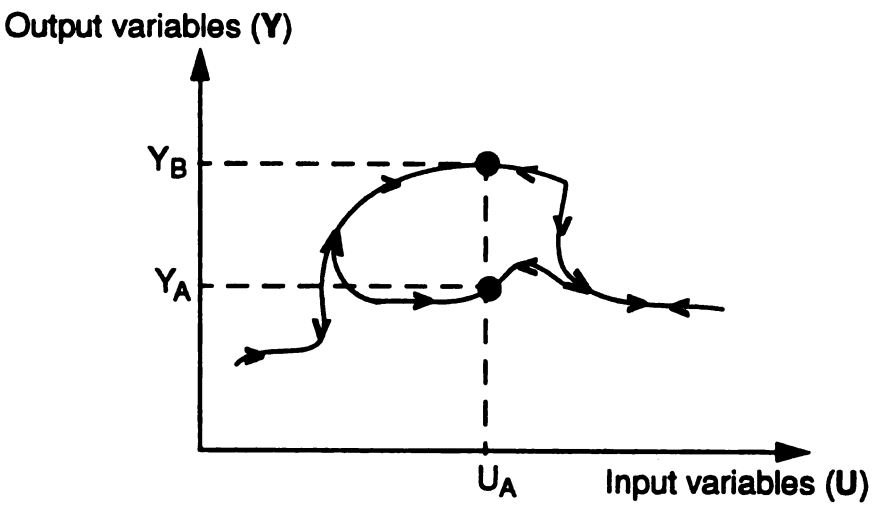

Figure 9.1 Schematic of a hysteresis cycle in plasma system variables.

9.2.1 End feed hysteresis versus cavity height

9.2.1.A General description of P_{abs} and n_i hysteresis on cavity height

Figures 9.2 and 9.3 show typical measurements of the absorbed power (P_{abs}) and downstream ion density (n_i) at (0, 0, 3 cm) versus cavity height (L_s) as the sliding short was increased (the ◊ data points) and then decreased (the + data points) in the end feed plasma source. The argon pressure was fixed at 5 mTorr, and the incident power was around 274 W. The arrows in the figures indicate the direction of motion of the sliding short. Despite their complex nonlinear appearance, they were reproducible within measurement error. Although a discharge was always present as the sliding short was varied back and forth from L_s = 69 to around 170 mm, the plasma density changed by almost a factor of five while the absorbed power varied from a low of approximately 25 W, i.e., a very poor match, to an almost perfect match where essentially 100% of the 274 Watt incident power was coupled into the plasma loaded applicator. Two broad regions ($L_s \cong$ 70-90 mm and 140-155 mm) of high absorbed power, which are over 70% of incident power, are identified as resonant mode 1 and mode 2. These correspond to the conditions for high density operation while the low density operation lies in all L_s values with usually at $L_s \cong$ 90-130 mm or $L_s >$ 155 mm. For the cavity height ranges of high density operations, experimental results in Section 7.2.2 indicate that mode 1 and 2 operations are primarily the TM_{011} and TM_{012} electromagnetic resonant modes excited inside the discharge loaded cavity applicator.

The upward and downward motion of sliding short results in abrupt jumps in both P_{abs} and ion density. As shown in mode 2 of Figures 9.2 and 9.3, the jump

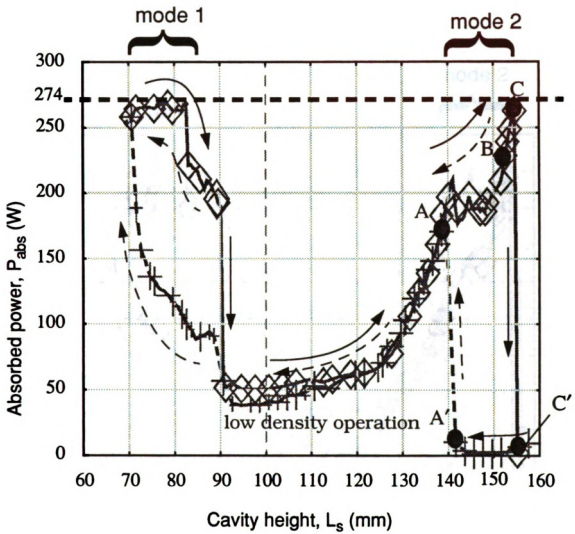

Figure 9.2 Absorbed power vs. cavity height for an end feed ECR MPDR-13 argon discharge. The chamber pressure was fixed at 5 mTorr, microwave incident power was fixed at ~ 274 W.
Solid line with ◊ symbol: when L_s is increasing, dashed line with + symbol: when L_s is decreasing.

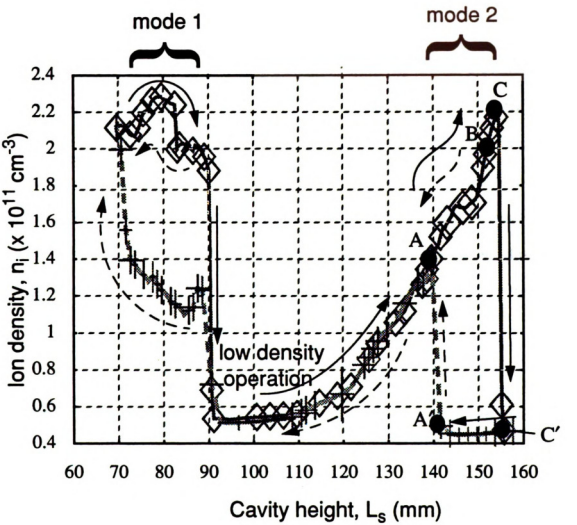

Figure 9.3 Ion density at (0, 0, 3 cm) vs. cavity height for an end feed ECR MPDR-13 argon discharge. The chamber pressure was fixed at 5 mTorr, microwave incident power was fixed at ~ 274 W. Solid line with ◊ symbol: when L_s is increasing, dashed line with + symbol: when L_s is decreasing.

down from state C to C' as the cavity length is first increased and then jumps up from state A' to A as the cavity length is decreased. Therefore, the region of L_s = 140-155 mm can either be high or low density operations. These hystereses and multiple steady states are also observed when L_s = 70-90 mm as the sliding short position first increases and then decreases.

Figures 9.2 and 9.3 give a very illustrated example on the important role that internal variables in the plasma system. Even with the identical input variables (incident power is fixed at 274 W, p = 5 mTorr, etc.) the plasma reactor can have two different output densities (high and low plasma operations) at certain L_s. The internal variable of P_{abs} provides the insight to the system. As shown in Figures 9.2 and 9.3, the plasma source output density follows closely to the internal variable of P_{abs} as the input variable L_s varies. This is consistent with the simple global discharge model described in Chapter 10.

9.2.1.B Hysteresis on cavity height versus incident power and pressure

In order to gain more hysteresis information on end feed MPDR™, the data were collected across a parameter space consisting of three levels of input microwave power (185, 231, and 277 W) and seven levels of chamber pressure (1, 2, 3, 4, 5, 6, and 7 mTorr). Figures 9.4 and 9.5 show the source characteristics on cavity height at a constant pressure of 5 mTorr for three constant incident power levels of 185, 233, and 277 W, and at constant incident power of 275 W for the different pressures of 1, 5, 7 mTorr, respectively. They all have sudden jumps at slightly different cavity height locations.

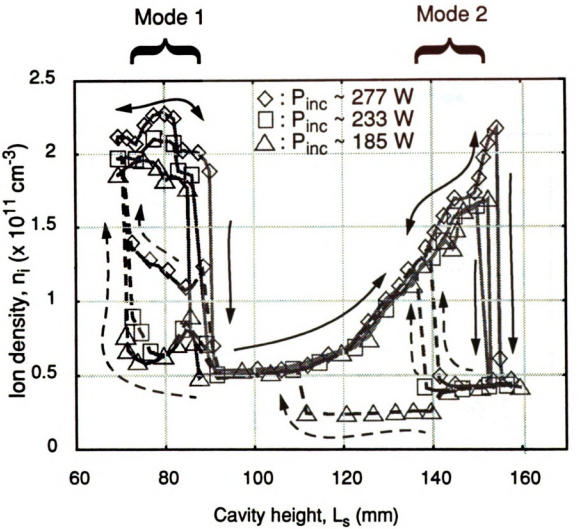

Figure 9.4 Ion density at (0, 0, 3 cm) vs. cavity height at different incident power for an end feed ECR MPDR-13 argon discharge. The chamber pressure was fixed at 5 mTorr.
Solid line: when L_s is increasing, dashed line: when L_s is decreasing.

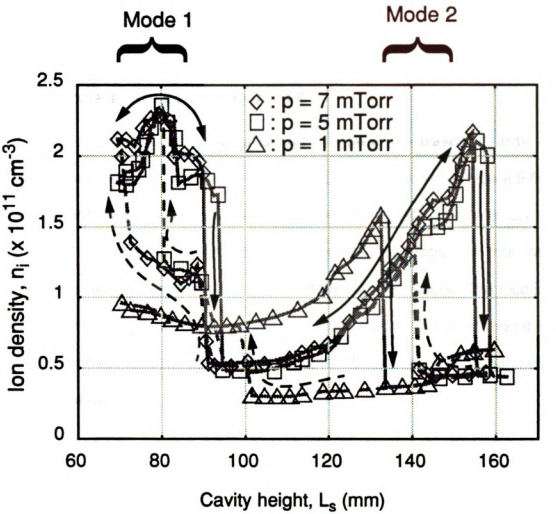

Figure 9.5 Ion density at (0, 0, 3 cm) vs. cavity height at different chamber pressure for an end feed ECR MPDR-13 argon discharge. The microwave incident power was fixed at ~275 W.
Solid line: when L_s is increasing, dashed line: when L_s is decreasing.

As shown in Figures 9.4 and 9.5, the high density operation regions vary with different input power and pressure. However, the average cavity height for high density operation in mode 1 remains roughly the same when power or pressure were altered. This insensitiveness to power and pressure in mode 1 gives an operational advantage over mode 2. This stable mode 1 is probably affected by the interaction between evanescent EM modes and plasma since no similar phenomena were observed in mode 2.

In order to avoid sudden degradation change in the plasma density and recovery from low density mode, the locations (L_{s1} & L_{s2}, shown in Figure 9.6) at which the abrupt transition occurs must be known in advance. Basically, L_{s1} and L_{s2} define the hysteresis boundaries on the variable L_s. Table 9.1 lists these locations over the aforementioned experimental parameter space. The locations shift upwards as incident power or pressure increases. A statistical model has been established to project these boundaries based on the experimental measurement data [173].

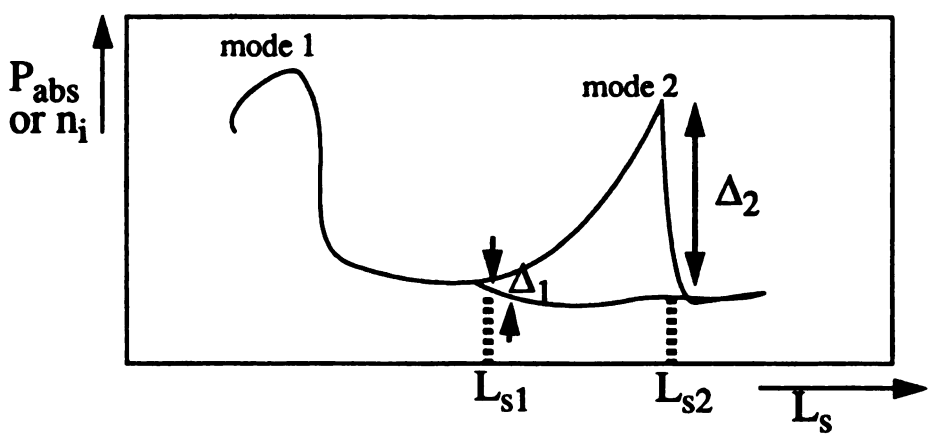

Figure 9.6 Schematic to illustrate the boundaries of a resonant mode.

Table 9.1 Measured transition locations for mode 2 plasma hysteresis on cavity height in end feed applicator.

L_{s1}/ L_{s2} (mm)		Incident microwave power (W)		
		185 W	231 W	277 W
Pressure (mTorr)	1	104.3/129.6	104.5/143.1	102.6/113.9
	2	113.6/142	117.3/142.4	138.1/143
	3	114.6/143.7	114.4/149.1	137.9/152.2
	4	110/153.4	135.2/153.3	140.9/154
	5	110.4/153.4	138.5/155.2	141.6/156.2
	6	111.1/153.2	137.9/157.7	142.3/158.2
	7	132.9/158.3	140.3/158.5	142.6/159.7

If high density operation is defined as over 50% of the incident power being absorbed by the discharge, the boundaries of a high density operation can be determined by the minimum and maximum cavity height at a given incident power and pressure. A typical Response Surface Methodology (RSM) model developed in MSU [173] is given here

$$L_s\,(max) = A + B^*(P_{inc}) + C^*(P_{inc})^2 + D^*(p) + E^*(p)^2 + F^*(P_{inc})^*(p) \text{ and} \quad (9.1)$$

$$L_s\,(min) = A + B^*(P_{inc}) + C^*(P_{inc})^2 + D^*(p) + E^*(p)^2 + F^*(P_{inc})^*(p) + G^*(p)^3, \quad (9.2)$$

where A, B, C, D, E, F are constant parameters to fit these 2nd and 3rd order models with the experimental data and the units in P_{inc} and p are Watts and mTorr, respectively. Figure 9.7 shows both the minimum and maximum cavity height positions for mode 1 predicted by the model versus the incident power and

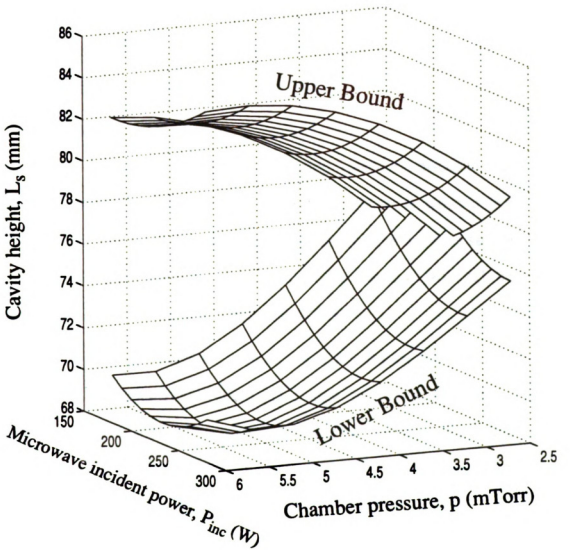

Figure 9.7 Response surface methodology model of minimum and maximum cavity heights for a high density plasma source operation. (Model fits to the mode 1 data for end feed ECR MPDR-13 plasma source)

chamber pressure. The coefficient of determination (a measure of fitness) between the model and the measured data is 0.94 for the minimum L_s and 0.95 for the maximum L_s. As shown in Table 9.1 or Figure 9.7, the ranges for high density operation (mode 1 and mode 2) are broader whenever the incident power or pressure is higher. This is consistent because higher power or pressure at this regime is easier to sustain a high density discharge.

9.2.1.C Discussion

Similar "jumps" and hystereses in tuning have been discussed for various microwave discharges [162-170] and occur also for other types of discharges [171,172]. The nonlinear discharge hysteresis behavior in previous section can be explained and understood by referring to earlier studies [167-172]. Thus, this behavior is only described briefly below for MPDR™-13.

The earlier investigations pointed out that a steady state microwave or rf discharge is characterized by both (1) charge density conservation, i.e., the number of charged species created per unit volume must equal those lost per unit volume by volume recombination and the net diffusion of charged species out of the volume, (2) power conservation, i.e., power absorbed by the plasma per unit volume equals power lost per unit volume. These losses are mainly caused by elastic collisions, inelastic ionization, excitation collisions, and energy transported to the walls by the various species in the discharge.

Steady state microwave discharge behavior can be described using a power loss load line [167,168]; i.e., as the absorbed power increases there is a corresponding increase in charge species that can be described by a curve,

identified as a load line, that characterizes the power absorbed versus the plasma density for the discharge. As described later in Chapter 10, this power loss line is a function of discharge geometry, gas types, and pressure. The steady state maintenance of a microwave discharge is only possible when there is a stable intersection between the discharge power-loss curve and the linear power absorbed curves of the plasma loaded applicator [167-172].

Figure 9.8 displays two such experimental plasma loss load lines. One is constructed from all the experimental data points shown in Figure 9.5 for a pressure of 7 mTorr while the other is constructed from similar experiments carried out at 1 mTorr. For each pressure, a dashed load line is drawn to provide the best fit of the experimental data. The differences between the different densities for a given pressure and P_{abs} may be caused by (1) errors in density and P_{abs} measurement, by (2) slightly different distributions in the impressed electric field and in the resulting different spatial variations in density, and by (3) the excitation of dipole resonance modes within the discharge [136]. It is useful to note that even after accounting for measurement errors, there appears to be some second order influences in the power loss curve that are caused by differences in the spatial nonuniformities of the impressed electric field and the associated plasma density profiles.

Two completely different plasmas can be operated with the same set of input variables because of the plasma hysteresis. In fact, a plasma discharge should be better described as a plasma state that is defined uniquely by all the current input variables plus its previous internal variables.

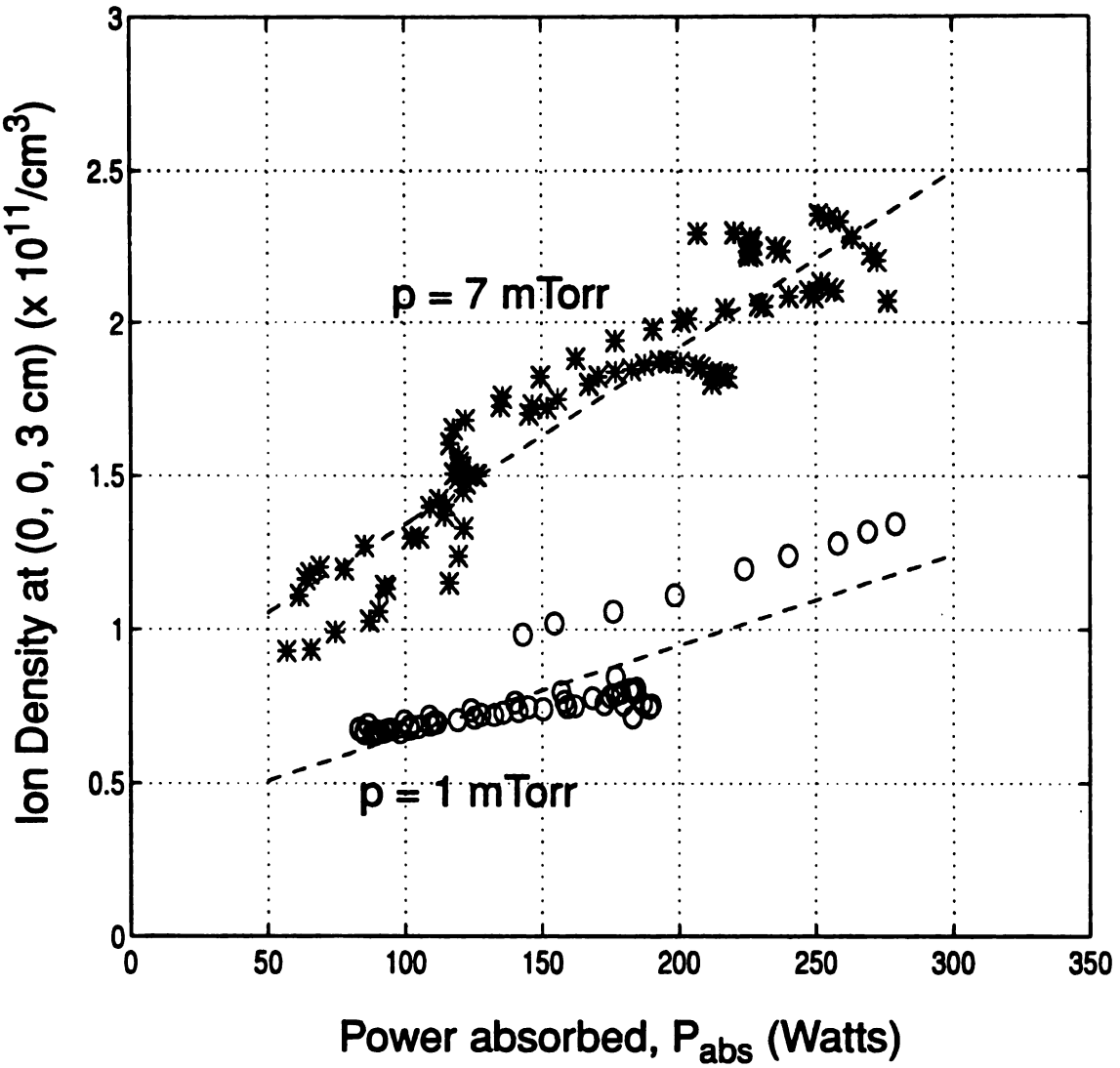

Figure 9.8 Plasma loss load lines for two different pressures for end feed reactor with 8P/8M ECR magnet.

The jumps and hysteresis behavior shown in Figures 9.2 to 9.5 then define the stable operating regions for the discharge circuit. When the discharge jumps out of one state (for example from C to C' in Figure 9.3), its shifts along the power loss load line from one stable condition to another. If it is desired to return to the original state (say B in Figure 9.3), one of the independent variables, P_{inc}, p, or L_s, must be varied appropriately. For example, when the sliding short is lowered to the H = A' position, the discharge jumps back to the higher density state A. Then, by increasing L_s, the higher density operation at B is restored. As long as P_{inc}, p, and L_s are adjusted to the appropriate conditions (based on the hysteresis database on particular plasma source), the discharge can remain in the stable high density operating condition. As shown, very stable operation occurs when the discharge operates with some excess reflected power. Thus to avoid jumps and hystereses it is best not to bring the discharge to a perfect match, i.e., operate at a condition such as point B.

When the discharge is at low density operation mode, the discharges look much dimmer, with low absorbed power and low ion density. Therefore, for reproducible high throughput plasma processing applications, it is not suggested to operate/maintain this plasma source at the edge of high density plasma operation.

The above situation describes the hysteresis effect over a single variable only. If two or more variables are involved, the scenario will become more complicated. However, the load line explanation is still valid using the two-dimensional curve. A general rule of thumb to return to the corresponding

high density operation state from its low density operation counterpart state is (1) alter the input variables appropriately using the hysteresis database (usually in the conditions that favor in producing more plasma) until experience a recover transition, (2) then change the inputs back to the original operation condition. For an alternate recovery in previous example, suppose you are in state A', you can go back to state A by increasing the pressure to ~ 10 mTorr, experience a jump (in brightness, density or absorbed power), then return back to 5 mTorr. Also raising the absorbed power and then lowering the power later will bring back to the original high density operation state. The load-line explanation can be equally well applied to the side feed plasma source described in the next section only with the different characteristic power-loss curve.

9.2.2 Side feed hysteresis on cavity height, probe depth and chamber pressure

For the experiments performed in side-feed plasma hysteresis characteristics, ion saturation currents were used instead of absolute plasma density. Ion saturation current is a good index of density based on the reasons mentioned in Section 7.3.3. The side applicator has the input coupling probe location at (H ~ 37 mm and $\Phi = 0^{o}$). Therefore possible TE_{111} mode may be excited in discharge loaded cavity. However, the applicator cavity height is shorter than the one listed in Table 7.2 and can only go up to H ~ 110 mm; and therefore, no long resonant mode data is available. The intention here is only to demonstrate some of side feed applicator hysteresis over several variables such as input

coupling probe depth, cavity height and chamber pressure. No modeling were done on the side applicator yet.

9.2.2.A Side feed hysteresis on cavity height position

Figure 9.9 shows an expanded view short resonant mode characteristics in the side feed plasma source for the cavity height range from 62 to 87 mm at 1.0 mTorr with 165 W incident power. Similar to the end feed plasma source, hysteresis events happen when L_s is first increasing and then decreasing. These two peaks correspond to the TE_{111} and TE_{211} electromagnetic modes inside the cavity. Once again, the ion saturation currents follow closely to the discharge absorbed power. However, the width of the hysteresis cycle in the side feed is much smaller than those in the end feed plasma source.

9.2.2.B Side feed hysteresis on input coupling probe depth

The side feed hysteresis on input coupling probe depth is displayed in Figure 9.10. The experimental conditions were cavity height 77.6 mm, 235 W incident power, 1.0 mTorr chamber pressure in the side feed plasma source. Both the ion saturation current and absorbed power were slightly decreasing when the probe was pulling out from 27 mm to around 8 mm, then experienced a sudden jump down as L_p is shortened. The return to the high density operation will not happen until the probe depth was increasing to around 14 mm.

9.2.2.C Side feed hysteresis on chamber pressure

Figure 9.11 presents the side feed plasma hysteresis on the chamber pressure. With argon flow rate at 18 sccm, the chamber pressure was manually controlled by throttling the gate valve. Under the experimental conditions of

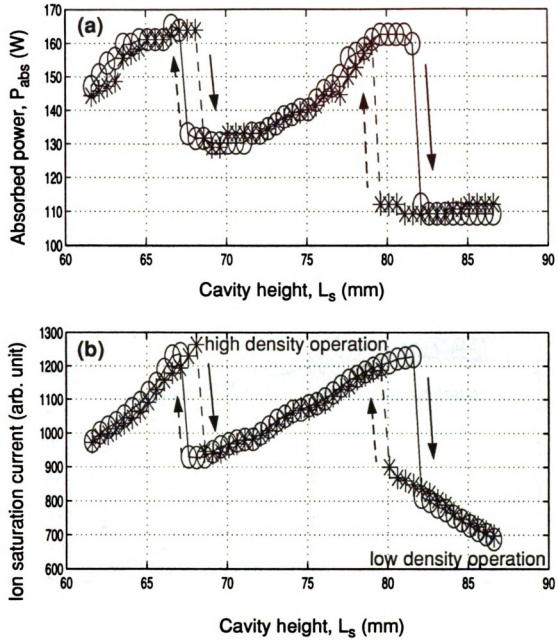

Figure 9.9 Side feed 8P/8M MPDR-13 hysteresis on cavity height, (a) absorbed power vs. cavity height, (b) ion saturation current vs. cavity height. The experimental conditions were L_p = 22.7 mm, P_{inc} ~ 165 W, 24 sccm argon gas, and p = 1 mTorr.
Solid line and O symbol: when L_s is increasing, Dashed line and ✳ symbol: when L_s is decreasing.

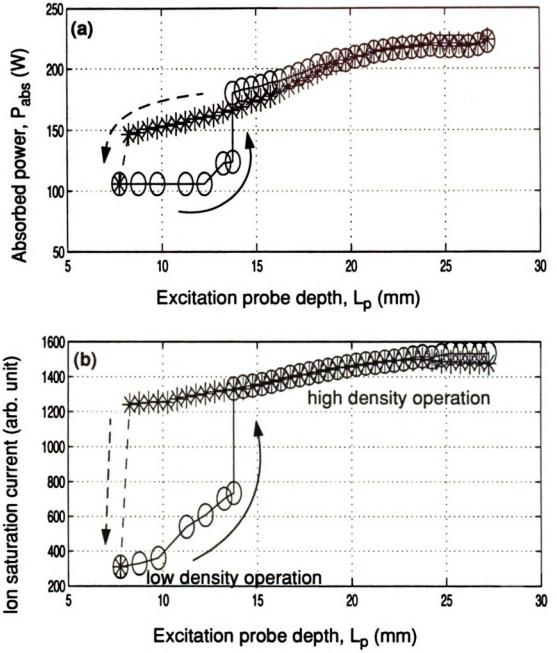

Figure 9.10 Side feed 8P/8M MPDR-13 hysteresis on depth of input coupling probe (a) absorbed power vs. L_p, (b) ion saturation current vs. L_p. The experimental conditions were L_s = 77.6 mm, P_{inc} ~ 235 W, 24 sccm argon gas, and p = 1 mTorr.
Solid line and O symbol: when L_p is increasing, Dashed line and ✳ symbol: when L_p is decreasing.

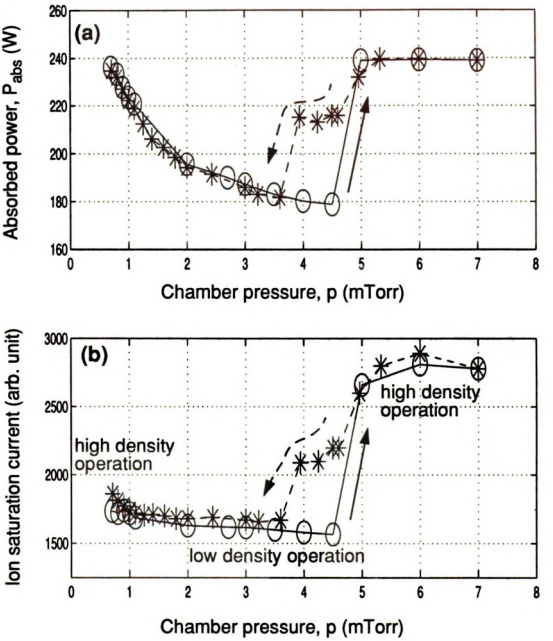

Figure 9.11 Side feed8P/8M MPDR-13 hysteresis on chamber pressure. The experimental conditions were L_s = 77.6 mm, L_p = 22.25 mm, P_{inc} ~ 240 W, and 18 sccm argon gas. Solid line and 0 symbol: when p is increasing, dashed line and ✳ symbol: when p is decreasing

L_s = 77.6 mm, L_p ~ 22.3 mm and P_{inc} ~ 240 W, there is a hysteresis cycle between 3.5 and 5 mTorr of chamber pressure. When the pressure is decreased from 7 mTorr to 5 m Torr, discharge stays in high density operation. As further decreasing the pressure, a sudden jump down in absorbed power or ion saturation current occurs at between 4 and 4.6 mTorr. Without altering other input variables (such as to retune the cavity or to increase input power), the chamber pressure has to increase to reach around 5 mTorr in order to return back to high density operation.

Note that identification on high and low density operations may not be so apparent during the pressure changes. Looking merely at the plasma source output ion density (or ion saturation current) is not a good criterion. Instead, judging the internal variable absorbed power is more accurate. Figure 9.11 (b) illustrates the current/ion density is still low at chamber pressure around 1 mTorr. However, Figure 9.11 (a) shows at that chamber pressure (~1 mTorr), most of the incident power has been absorbed. Recall within this pressure regime, the measured ion density depends heavily upon the pressure (see Figure 7.20) and is insensitive to the flow rate (see Figure 7.21). The available species for ionization/excitation at < 1 mTorr is about 2 to 4 times less than that in its low density operation neighbor, which is at 2- 4 mTorr. When compared to Figure 7.20, the density that is achievable at < 1mTorr in Figure 9.11 is already no less than its neighbor (2-4 mTorr). Therefore, for the hysteresis performance on chamber pressure, discharge absorbed power percentage is a better index for high density operation than the absolute plasma output density itself.

9.2.3 Application to plasma control sensors

Having hysteresis is unavoidable in any plasma discharge. Focus should be placed on operating the discharge optimally for plasma processes. In fact, simple stable operation is possible even if the experimental operating behavior for the particular gas is not completely understood. One such method of discharge operation is suggested by observing the database of plasma hystereses. For example, if mode 2 in Figure 9.3 is chosen as the desirable high density operating mode, stable operation can then be achieved by first igniting the discharge by adjusting L_s to an empty cavity resonance and then by length tuning the cavity height, L_s to mode 2. Then, by always operating with excess incident microwave power, i.e., in a slightly mismatched condition, the discharge can be maintained in the high density condition even the power or pressure is slightly changed for unexpected reasons. At each operating pressure, the discharge can be adjusted to the desired density by varying L_s over 120-155 mm or the incident power. As a good match is approached, the L_s tuning should not be increased to a perfect match in order to prevent a jump to a lower density state. This simple method has been automated using a computer controlled matching system used in next section (Section 9.3).

Control of a plasma source has the goal of creating a reliable and reproducible plasma process [174]. Real-time control is usually preferred because it can correct and modify the process immediately. The real-time control of a plasma process, shown in Figure 9.12, is habitually the use of sensors to measure *in-situ* output variables and adjust the inputs to obtain a desired output.

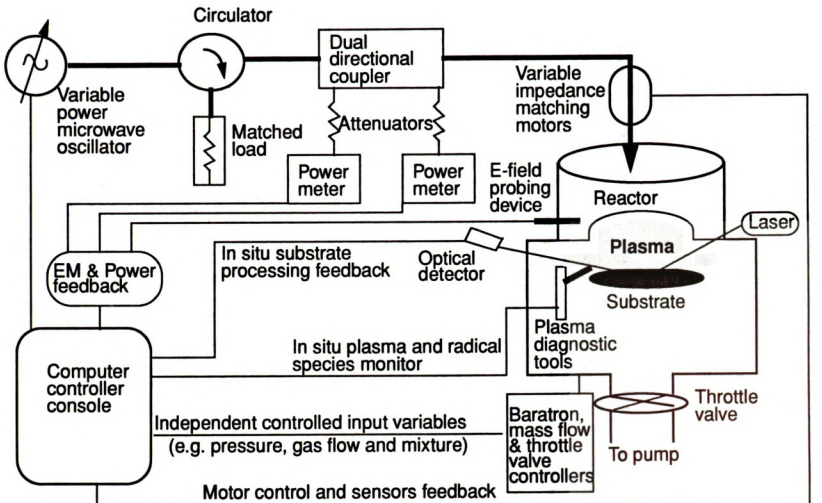

Figure 9.12 Microwave plasma processing control diagram

However, in many cases, the direct measurement of some desired processing outputs on a substrate is too expensive or impractical; so an alternative is to measure the internal variables of the plasma source/process. This is especially true that the internal variables have demonstrated important roles in previous sections.

On the other hand, the modeling the experimental database would aid in computer plasma process automation. Model like eqs. (9.1) and (9.2) give good predictions on the lower and upper bound of the high density mode. Moreover, modeling on the variation of internal variables and output variables with respect to the input variables can give information to computer for better controlling the plasma system. For example, the microwave electric field strengths at the end feed applicator wall operated within mode 1 have been modeled [173] with a RSM model as a function of chamber pressure, cavity height and incident microwave power as follows:

$$E^2\,(H = 38\text{ mm}, \Phi = 90^0) = A + B^*(P_{inc}) + C^*(p) + D^*(L_s) + E^*(P_{inc})^2 + F^*(p)^2 + G^*(L_s)^2 + H^*(P_{inc})^*(p) + I^*(P_{inc})^*(L_s) + J^*(p)^*(L_s). \quad (9.3)$$

Figure 9.13 displays the field strengths as a function of (a) cavity height and pressure at fixed incident power at 240 W, (b) cavity height and incident power at fixed pressure at 4 mTorr. The coefficient of determination is still good at around 0.77. More modeling work is ongoing by co-workers in our group.

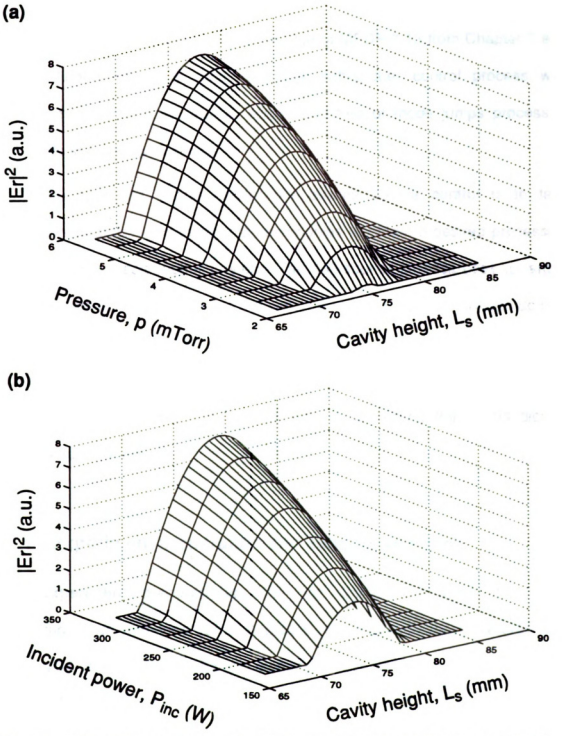

Figure 9.13 Response surface methodology model of the radial electric field at the wall (r = 8.89 cm, $\Phi = 90^{o}$, H= 38 mm) for a high density plasma source operation (mode 1 in end feed). (a) vs. L_s and p at P_{inc} = 240 W, (b) vs. L_s and P_{inc} at p = 4 mTorr.

9.3 Argon Soft Sputter Control Processing Example

Having the comprehensive knowledge of MPDR™-13 from Chapter 7 and aforementioned hysteresis data, a simple soft-sputter control process was conducted to demonstrate that a reliable and free of mode jumps process is achievable in our plasma source.

The approach in this section for plasma source control is to take measurement of selected internal state variables to obtain a desired processing rate for an argon soft-sputter process. The soft-sputter process uses an argon discharge with a rf bias applied to the wafer, which results in an induced dc bias that accelerates the positive ions to the wafer surface. This ion bombardment cleans the surface of the wafer by removing the top epidermal layer. The demonstration of this process is examined by quantifying the silicon dioxide removed from a wafer.

9.3.1 Experiment preparation and sensors selection

Experiment preparations: The soft sputter experiment set up is conducted in an end feed (8P/8M) plasma processing machine displayed in Figure 9.14. Initially, a set of 75-mm diameter silicon wafers were cleaned by the standard buffered oxide etch solution (34.6% (by wt) NH_4F/6.8% HF/58.6% H_2O) to remove the residual oxide and contamination on the silicon wafer. The oxide were then thermally (steam) grown on these wafers in a 1000 ^{0}C the furnace for about two hours. After the steam oxidation process, their visual colors appeared

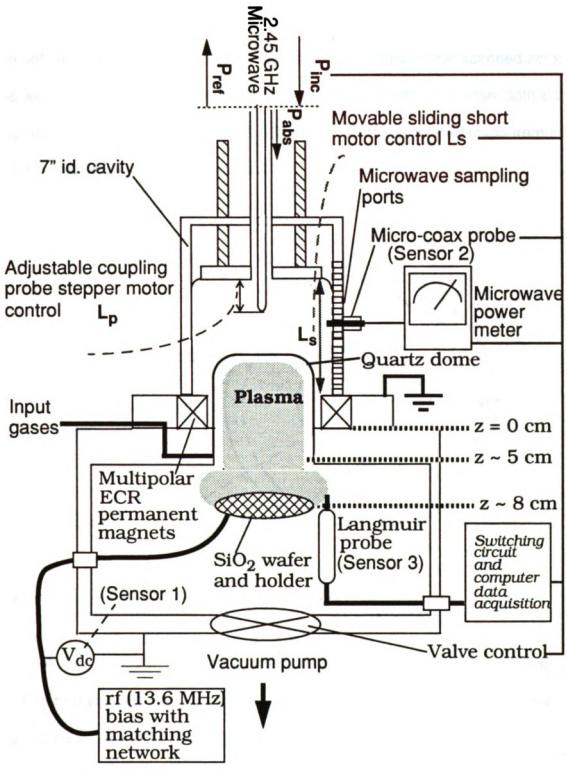

Figure 9.14 Experimental set up for soft sputter experiments.

to be blue and so their oxide thickness is expected to the order of 1100 A.

To acquire accurate spatial oxide thickness that has been removed from the soft sputter process, a Gaertner Scientific Corp. ellipsometer scanned across the wafers to provide a record of oxide thickness and refractive index both prior and after the sputtering of each wafer. The ellipsometer performed measurements at 9-point locations, shown in Figure 9.15.

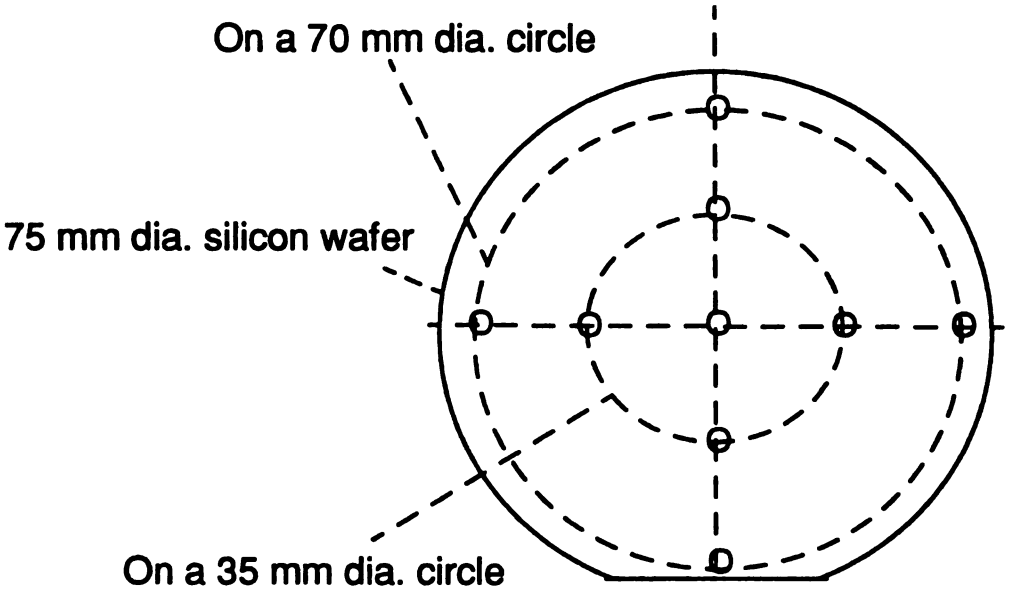

Figure 9.15 9-point locations for oxide thickness measurements

A 3.5" diameter aluminum wafer holder, which has a 1.5 mm deep 3" diameter central slot, was mounted inside the center of processing chamber at around z = 8 cm downstream. During the sputtering experiments, the wafer sat in the slot of wafer holder and no wafer clamping or adhesive glue were needed. Hence, the least contamination was added into the system. In order to control the

ion energy impinging to the oxide independently, a Plasma-Therm. Inc. HFS-500E rf (13.56 MHz, CW) power generator with a L-C matching network supplied the rf power through a vacuum coaxial feedthrough into the wafer holder. The supply rated maximum output power is 500 Watts. The induced dc bias on the aluminum wafer was monitored by a voltage meter.

Sensors selection: Three different sensors were selected for our soft sputter experiments. (1) We adjusted the output rf power (~30 W) to give an induced dc substrate bias at around -60 V (with respective to the chamber wall) during the experiments. (2) An E-probe was inserted into a hole at H =3.8 mm, Φ = 90° to read the relative electric field strengths near the cavity wall. (3) A 0.94 mm dia., 5.2 mm long cylindrical single Langmuir probe was placed ~1 cm away from the substrate holder edge to monitor the *in-situ* ion saturation current. They are distributively displayed as Sensors 1, 2, 3, in Figure 9.14.

9.3.2 Experimental sequence and result

The sputter process proceeded according to the following sequence:

(1) Measure the oxide thickness prior to the process.

(2) Place the wafer on the substrate holder located at 8 cm.

(3) Pump the processing chamber to 10^{-6} Torr, then turn on the argon flow.

(4) Ignite the argon discharge by applying microwave power and let it stable in one of the high density plasma operation modes that not too close to the hysteresis jump.

(5) Start the rf power supply and adjust the power to give -60 V dc bias to begin to time the sputter process.

(6) Control the input variables (including microwave power, rf power, and cavity height tuning) to maintain, a constant induced substrate bias at -60 V, a constant relative electric field strength (~6.8 mW) at the cavity call, and a constant probe saturation current (~ 137 μA) on the peripheral Langmuir probe during the sputter process.

(7) Run the soft-sputtering process in step (6) for 18 minutes.

(8) Turn off the rf power first, then the microwave power. Vent the processing chamber and remove the wafer.

(9) Measure the postprocessing thickness of the oxide.

The results of performing this processing sequence three times are shown in Table 9.2. Primarily, the two input settings needing real-time adjustment were the rf power and microwave input power. The rf power was adjusted to maintain a -60V substrate bias while the adjustment of the input microwave power was generally sufficient to maintain the constant probe saturation current.

Table 9.2 Soft sputter oxide removal experiments

Run	Chamber pressure, p (mTorr)	Sliding short position, L_s (mm)	Microwave incident power, P_{inc}(W)	Average oxide removed (nm)
A	4	75.6 (mode1)	varied around 235	37.5
B	4	153.1 (mode 2)	varied around 325	34.5
C	4	72.6 (mode 1)	varied around 248	35.1

The use of the sensor units in combination with real-time processing adjustments of the microwave input power allowed the processing rate to be well controlled. Specifically, the amount of oxide removed varied from only 34.5 to 37.5 nm for the various 18 min runs. The run-to-run repeatability of 2% was achieved.

9.4 Concluding Remarks

This chapter has employed reactor absorbed power and downstream ion density as the plasma source control sensors to study the plasma hysteresis on several input variables including the cavity height, excitation probe depth and chamber pressure. Both side feed and end feed plasma source exhibit repeatable hysteresis phenomena.

End feed reactor shows that two high density operation regions exist versus cavity height. Its hysteresis on cavity height were studied with different incident power and chamber pressure. Generally speaking, the measured boundaries in cavity height position increase with increasing pressure and power. In addition, their hysteresis boundaries in mode 1 have also been modeled as a function of incident power and pressure based on the measured data.

A side feed plasma source has similar hysteresis behavior on cavity height, input coupling probe depth, and chamber pressure. The hysteresis cycle on cavity height is narrower in side feed plasma source than in end feed. When varying the chamber pressure, the determination of a high density operation is better judged by the absorbed power as a percentage of the incident power.

Finally, the study of plasma hysteresis leads to better understanding and then to optimal operation of this plasma source. And hence the control sensor for plasma processing can be wisely selected. Argon soft sputtering control experiments performed in an end feed plasma processing machine were presented as an example to achieve a repeatable processing rate. The sensors were (1) induced dc bias, (2) microwave electric field near the applicator wall, and (3) the ion saturation current near the edge of wafer. Reproducible results from run to run were achieved even at different operation modes and vacuum to atmosphere process cycle.

Chapter 10

Plasma Global Model and Comparison of Various ECR Plasma Sources

- 10.1 Introduction
- 10.2 Review of the Simple Global Plasma Model
  - 10.2.1 Charged particle balance and average electron temperature
  - 10.2.2 Power balance and plasma load line
- 10.3 Performance Comparison Between Global Plasma Model Predictions and Experimental Data
  - 10.3.1 Performance comparison between global plasma model predictions and measured data of MPDR™-13
  - 10.3.2 Performance comparison between global plasma model predictions and experimental data from four different ECR plasma sources
- 10.4 Concluding Remarks

(The symbol L is equal to ℓ in this chapter)

Chapter 10

Plasma Global Model and Comparison of Various ECR Plasma Sources

(The symbol L is equal to ℓ in this chapter)

10.1 Introduction

As discussed in Chapter 2, many high density plasma sources have been developed over the past decade. Interest in the further development of these high density sources continues. Thus there is a need to understand their behavior and performance versus changes in the many experimental input variables. Especially important knowledge is the relationship between the controllable input variables, U_1, the reactor geometry variables, U_2, and the output source performance, Y_1. One method that is used to develop a understanding of plasma source performance makes extensive experimental plasma source diagnostic measurements such as those that were described in Chapters 7 and 9. However, while some experimental evaluation is always necessary, the numerous measurements presented in Chapters 7 and 9 are clearly tedious and time consuming. Thus if relatively simple theoretical models could be found to predict

the approximate plasma source behavior versus the U_1 and U_2 variables, then considerable time would be saved in plasma source design. In this chapter the use of simple plasma models to evaluate and predict source behavior is investigated. A simple plasma theoretical model, identified here as a global plasma model [176], is first described. Then this model is compared to the experimental performance data of MPDR™-13 presented in this thesis. Global plasma model predictions are also compared to the experimental performance data available from the literature for the four different ECR plasma source designs that were reviewed in Chapter 2.

10.2 Review of the Simple Global Plasma Model

If the working gas(es) are known, plasma global models are relatively simple methods to relate the average electron temperature and plasma density to the discharge geometry, pressure, and discharge absorbed power. They are based on the conservation of discharge species and absorbed power inside the discharge chamber. The idea of using species conservation and energy balance to understand discharge behavior has been recorded as far back as the 1929 [177,178] and by other subsequent researchers. Von Engel first organized some of these global model concepts into a classic book [179]. Until recently, global models were mostly applied to electropositive discharges in low pressure discharge regime. Recently, a research group in University of California at Berkerley led by Lieberman [176] has modified and expanded the use of global

models to include electronegative discharges [180], discharges containing reactive species [181], time-modulated plasmas [182,183], and electro-negative discharges operating in intermediate-pressures (0.1-1 Torr) [184]. Since argon gas discharges were mostly used in this thesis, only the simple plasma global models for low pressure (< 50 mTorr), electropositive discharges are briefly reviewed here. More detailed information on global models for more complex gas discharges can be found in aforementioned references.

10.2.1 Charged particle balance and average electron temperature

The first basic equation in global discharge model is ion conservation, i.e., the ion creation equals the ion loss in every differential volume throughout the discharge volume. In a mono-atomic gas, such as a noble gas, plasma global models are quite simple due to the lack of the molecular processes such as dissociation, attachment, rotational and vibrational excitations. The model usually assumes a Maxwellian electron energy distribution described by a temperature, T_e, and also assumes that electron collision rates are uniform throughout the discharge volume. Electron and ion motion is governed by collisional ambipolar diffusion at high pressure and free fall diffusion at low pressure. At pressures below 50 mTorr, volume recombination is unlikely and diffusion losses dominate.

The global plasma model is applied to the plasma reactor discharge chamber defined in Figure 2.4 by the radius **R** and ℓ. This chamber is bounded by the top and side walls where the charged species recombine and the **z** = 0 is

the plane through which the charged and radical species diffuse from the discharge region into the process chamber.

The exact diffusion process depends upon the relationship between the ion-neutral mean-free-path, λ_i, and the dimensions **R** and ℓ of the discharge. The mean-free-path, λ_i, can be estimated [185] by

$$\lambda_i = \frac{1}{n_g \sigma_i} \approx \frac{1}{3p}(m), \quad (p \text{ in Torr}) \tag{10.1}$$

where n_g is the neutral gas density and σ_i is the collisional cross section, which can be evaluated from the cross section database [186-188].

Low pressure or free fall diffusion occurs when $\lambda_i > (R, \ell)$. High pressure diffusion occurs when $\lambda_i < (T_i/T_e) \cdot (R, \ell)$. For 1 mTorr argon gas, $\lambda_i \sim 3$ cm is considered to be in low to intermediate pressure regime in the ECR reactors discussed here. Since most of the ECR discharge performance discussed here was examined at the 0.5 - 5 mTorr pressure regime, diffusion processes for these discharges are governed by either free-fall diffusion or fall in between the free-fall and the high pressure diffusion. However, since the objective here is to describe an approximate model that gives insight into discharge behavior we will adopt only the simpler free-fall uniform plasma diffusion model to compare with the chosen ECR plasma sources.

The name global model comes from the assumptions that plasma variables are spatially averaged. Several major assumptions in this model are (1) netural species density (n_g) is uniform throughout the discharge, (2) ion density profile is uniform over the entire discharge except at the sheath region near the walls (see

Figure 10.1), (3) diffusion flux to the wall is approximated by the product of the Bohm velocity times the plasma edge density, i.e., $\Gamma_i = n_{is} u_B$ [100].

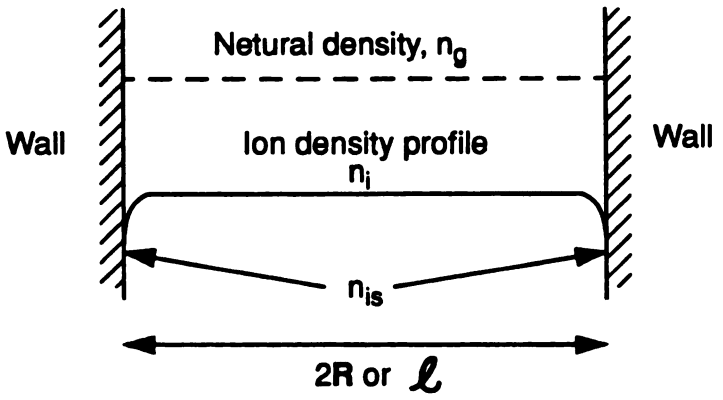

Figure 10.1 Assumed density profile in simple plasma global model

Godyak and Maximov [189] have solved the diffusion equations analytically to determine the plasma density at the sheath edges related to the center plasma density at the low and intermediate pressure regime:

$$h_L \equiv \left.\frac{n_{is}}{n_i}\right|_{axial} \approx \frac{0.86}{\sqrt{3.0 + \frac{L}{2\lambda_i}}}, \tag{10.2}$$

$$h_R \equiv \left.\frac{n_{is}}{n_i}\right|_{radial} \approx \frac{0.8}{\sqrt{4.0 + \frac{R}{\lambda_i}}}. \tag{10.3}$$

The terms h_L and h_R account for the variation in the density profile in the axial and radial direction respectively.

Two different cylindrical discharge volumes are considered: (1) a magnetic field free chamber, and (2) a chamber where a very strong radially confining magnetic field is applied. The first represents a simple discharge without magnetic confinement where diffusion takes place equally in all directions and diffusion through the z = 0 plane is assumed to be similar to the diffusion that occurs when an absorbing wall is present there. The second case approximately represents a chamber where radial diffusion is greatly reduced, such as the divergent field or the DECR reactors, and charged particle losses occur mainly through the discharge end surfaces. For simplicity, in this model, it is assumed that when radial magnetic field confinement is present there are no radial diffusion losses.

For the first case of low pressure diffusion without an applied magnetic field, ion conservation in the discharge reduces to the following **particle balance** equation [176],

$$\frac{K_{iz}(T_e)}{u_B(T_e)} = \frac{1}{n_g d_{eff}}, \tag{10.4}$$

where K_{iz} is the electron ionization rate constant, u_B is the Bohm velocity for ions, d_{eff} is the characteristic discharge length and is given by

$$d_{eff} = \frac{1}{2}\frac{RL}{(Rh_L + Lh_R)} = \frac{\pi R^2 L}{A_{eff}}. \tag{10.5}$$

Note that d_{eff} can also be viewed as the ratio of discharge volume to effective confinement area, A_{eff}, given by

$$A_{eff} = 2\pi R(Rh_L + Lh_R). \tag{10.6}$$

Note all terms on the left hand side of eq. (10.4) are functions of electron temperature. Thus given n_g and d_{eff}, T_e can be solved from eq. (10.4). This equation indicates that the electron temperature of the discharge is determined by ion conservation, is only a function of the n_g and d_{eff} product and is independent of the input power.

For experimental convenience, pressure (p) is the most frequent used variable instead of n_g. From the ideal gas law, the neutral gas density, n_g, equals $p/(kT_g)$, where p is the pressure, k is Boltzman's constant and T_g is the neutral gas temperature (~400 K from [101]). A solution of eq. (10.4) for argon gas without magnetic confinement is displayed as the solid curve in Figures 10.2 and 10.3. Thus at a given pressure and gas type, the reactor dimensions **R** and ℓ uniquely determine T_e, independent of input power.

If a very strong radially confining magnetic field is applied and radial diffusion losses are reduced to zero eq. (10.4) remains the same except the characteristic discharge length (or effective confinement surface) becomes d_{eff}' (A_{eff}'), given by

$$d_{eff}' \equiv L/(2h_L) \text{ and } A_{eff}' \equiv 2\pi R^2 h_L. \qquad (10.7)$$

The solution to eq. (10.4) for this magnetized ECR plasma source is represented as the dashed line in Figure 10.3. Note that $d_{eff} < d_{eff}'$ and the left hand side of eq. (10.4) is roughly inversely proportional to T_e. Any axial or multipolar magnetic confinement fields associated with a plasma source concept should produce a low electron temperature discharge. A comparison between the

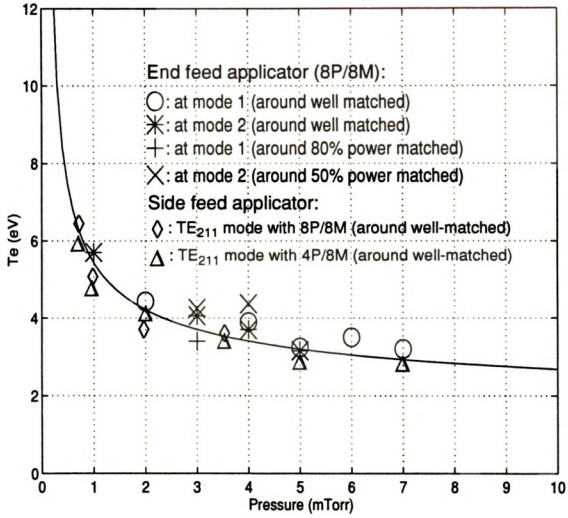

Figure 10.2 A comparison of experimental electron temperatures (data points) with the electron temperatures (solid curve) predicted from the global plasma model.

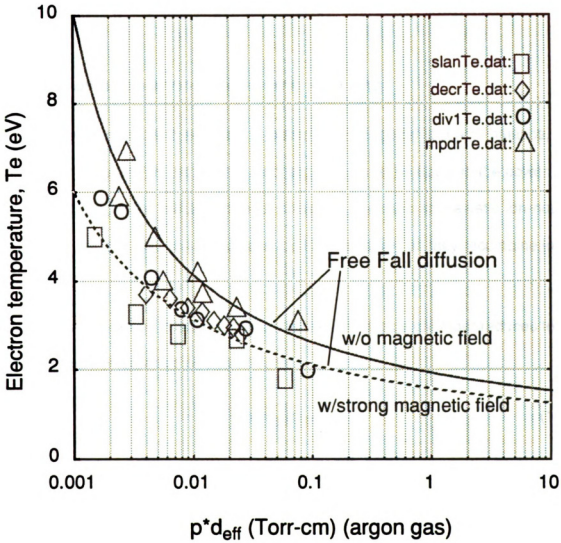

Figure 10.3 Comparison of electron temperatures between global model prediction and measured data in different plasma sources.

solid and dashed curves shows that for a given pressure a radially magnetically confined discharge has a lower electron temperature than the same reactor without an applied magnetic field. Thus, as expected, reducing the radial diffusion losses by the application of a static magnetic field lowers the plasma potentials.

10.2.2 Power balance and plasma load line

The second basic equation in plasma global model is power balance, i.e., the power absorbed by the plasma discharge, P_a, must be equal to the power loss from electron gas by electron-neutral collisions, inelastic and elastic ion-neutral collisions, and the loss of electron and ion kinetic energy as they recombine in the walls.

Power balance in the magnetic field-free discharge chamber reduces to the following **power balance** equation [176]

$$P_a = n_i e u_B A_{eff} E_T, \tag{10.8}$$

where E_T represents the total energy lost per electron-ion pair lost from the discharge. E_T is the sum of the collisional energy lost (E_c), the kinetic energy lost to the walls by the electrons (E_e), and the kinetic energy lost by the ions (E_i) as they fall through the sheath, i.e.,

$$E_T = E_c + E_e + E_i. \tag{10.9}$$

The collisional energy losses account for the loss of electron energy due to ionization, excitation and elastic collisions. E_c can be calculated via the various

atomic energy levels and reaction rate constants [190] and therefore is a function of electron temperature. The mean kinetic energy lost for ion-electron recombination at the wall is approximately $2kT_e$ [191] for Maxwellian electrons. The mean kinetic energy lost per ion consists the kinetic energy of ions lost at the plasma sheath edge plus the energy they gain as they fall through the sheath potential. For argon in insulating wall, $E_i \sim 5.2kT_e$ [176]. Figure 10.4 gives the approximate estimate of the total energy losses and its various components versus the electron temperature in argon gas. The collisional losses dominate for low energy electrons (usually in high pressure environment) while the kinetic energy losses are significant for high electron temperature argon discharges. Recall that the electron temperature can be determined by the particle balance equation described in the previous section. Using the experimentally measured discharge absorbed power, the average ion density can be estimated by eq. (10.8) with the calculated E_T and the electron temperature.

Note that in Figure 10.4, there is a minimum of E_T in the electron temperature range between 3 and 4 eV. Since u_B is a weak function of T_e, the minimum of E_T gives the best ion density for a given discharge absorbed power by eq. (10.8). Hence, the plasma global model can aid to design to improve plasma reactor design and is discussed in the concluding remarks of this chapter.

The power balance equation (10.8) describes the relationship between power absorbed by the discharge and average plasma density. Experimental measurements usually identify this equation as the power loss line or power load line. It can be rewritten in terms of average discharge power density, $\langle P_a \rangle$, i.e.,

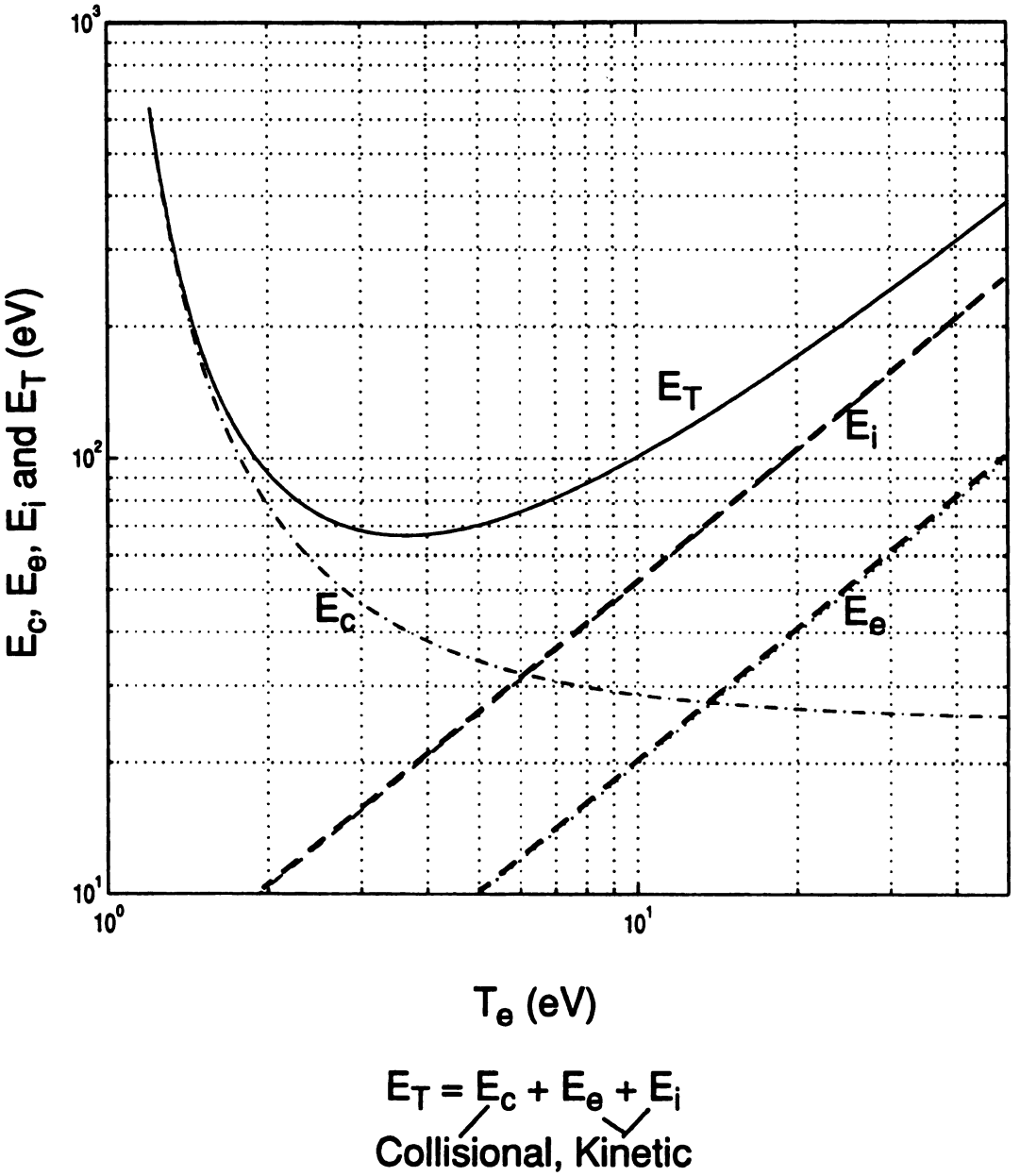

Figure 10.4 Collisional and kinetic energy losses per electron-ion pair created versus electron temperature in argon.

$$\langle P_a \rangle \equiv \frac{P_a}{\pi R^2 L} = \frac{n_i e u_B E_T}{d_{eff}}. \qquad (10.10)$$

Equation (10.10) describes a discharge power density loss line for an average discharge volume. In the presence of an axial confining magnetic field, eq. (10.10) is still true provided that d_{eff} is replaced by d_{eff}', which is given by eq. (10.7). Thus magnetic confinement increases the discharge efficiency and lowers the plasma potentials.

10.3 Performance Comparison Between Global Plasma Model Predictions and Experimental Data

10.3.1 Performance comparison between global discharge model predictions and measured data of MPDR™-13

It is interesting to compare the experimental data presented in Chapters 7 and 9 with the performance predictions from global plasma models described in previous section. It is assumed that the microwave discharge in the reactor shown in Figure 3.3 occurs in a cylindrical shaped volume of radius **R** = 6.25 cm and a height of 8.5 cm. Using eqs. (10.2), (10.3) and (10.5), the characteristic discharge length for this geometry dimension is calculated and is plotted in Figure 10.5 as a function of pressure. Over the 0.5 - 10 mTorr pressure regime an argon discharge produced in this volume is classified as a low pressure discharge [176]. Solving the charged particle balance diffusion equation eq. (10.4) in argon gas for the characteristic discharge length shown in Figure 10.5 yields a curve that uniquely

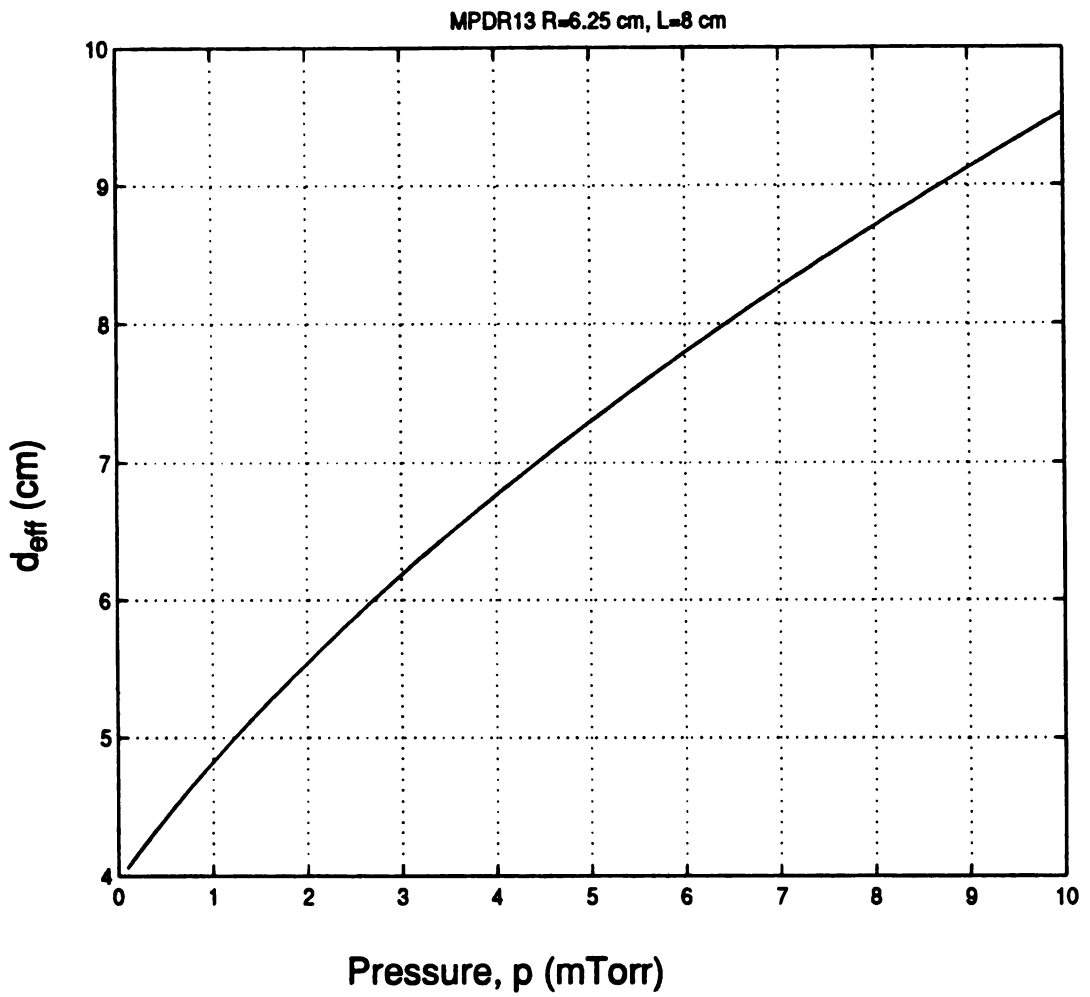

Figure 10.5 Characteristic discharge length vs. pressure in MPDR-13.

defines the electron temperature versus pressure. This curve is plotted as the solid line in Figure 10.2. Measured experimental temperatures versus pressure when operating in well-matched modes 1 and 2 in end feed applicator with 8P/8M configuration and TE_{211} in side feed applicator with 4P/8M or 8P/8M

configurations, as well as other measured electron temperatures for unmatched conditions, are also plotted as data points on Figure 10.2. These experimentally measured temperatures for the MPDR™-13 display excellent agreement with the global discharge model.

Applying discharge power balance over the same pressure regime produces the family of power loss line curves displayed in Figure 10.6. A unique power loss load line is plotted for each pressure. A comparison of the theoretical power loss load lines with the experimentally measured power loss data shown in Figure 9.8 indicates differences between theory and experiments. The magnitude of the difference depends on where the measured plasma density location z is. The closer the measured ion density location (z = constant plane) to the active discharge region, the less the discrepancy between the model prediction and the measured data. At a pressure of 1 mTorr the measured plasma densities at z = 3 cm are about a factor of 2-2.5 lower than the values by the global model while the measured densities at 7 mTorr are a factor of 2.8-4 smaller than those predicated by the global discharge models. The slopes of both experimental curves are lower than the slopes of global model. As noted earlier in Chapter 9, these differences can be partially accounted for by noting that densities shown in Figure 9.8 were measured at 3 cm downstream away from the active discharge. The discharge densities in the active discharge region, especially at the higher pressure with slower diffusion, are expected to be at least twice those shown in Figure 9.8. In conclusion, the global discharge model provides a good estimate of the MPDR™-13 plasma source performance.

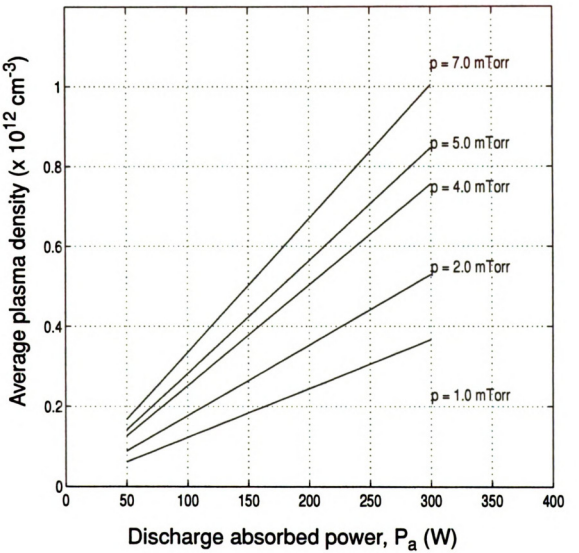

Figure 10.6 Plasma density vs. discharge absorbed power as calculated from the global plasma model in MPDR-13 reactor.

10.3.2 Performance comparison between global discharge model predictions and experimental data from four different ECR plasma sources

Nowadays, there are many different ECR reactor concepts (e.g., see Section 2.4) in the market and even a single specific reactor concept can be constructed in many different sizes (e.g. MPDR™s, SLANs, Div, SLAN, etc.). An analysis of the experimental measurements from these different reactors reveals that the performance varies considerably from one ECR reactor concept to another and also varies as the dimensions of the specific reactor configuration are changed. Sze and Asmussen [192] have compared the plasma performance of several sizes of MPDR™s. In this section the electron temperature, the ion production cost and plasma load line of four different ECR plasma sources are compared with the predictions from global discharge models. The different reactors along with their published experimental data are (1) the divergent field ECR plasma source [193], (2) the distributed ECR plasma source [45], (3) the slot antenna ECR plasma source [46,47], and (4) the multipolar ECR plasma sources [192] with the abbreviations of Div., DECR, ECR-SLANs and ECR-MPDR™s respectively. The microwave coupling efficiency could not be compared because it has not yet been estimated or published for most ECR plasma sources.

Table 10.1 lists the radius, height, d_{eff}, and plasma volume in plasma excitation regions for the various reactors. The MPDR™-5 has the smallest characteristic discharge length d_{eff} of 1.71 cm while the DECR is the largest at 11.88 cm.

Table 10.1 Geometric dimensions of various ECR plasma sources.

Reactors	ECR-MPDR™s			ECR-SLANs		Div.	DECR
variations	MPDR -5	MPDR -13	MPDR -325	μSLAN	SLAN-I	--	--
symbols	▲	s	D	S	q	O	‡
R (cm)	2.4	6.25	12	2	8	10	14
L (cm)	~3.27	~8	~9	6.12	6.12	19.7	16
Plasma volume (cm^3)	59	982	4000	77	1230	6190	9850
d_{eff} (cm) @ 1 mTorr	1.71	4.82	7.32	1.96	4.59	10.62 (24.7 cm for d_{eff}')	11.88

The measured electron temperatures of these plasma sources are plotted in Figure 10.3 along with the global model predictions. As shown in the figure, the strongly magnetized divergent field, DECR, and ECR-SLAN-I reactors have low electron temperatures which are comparable to the dashed curve derived from the global discharge model for an axially magnetized reactor. Overall, all other experimental electron temperatures data matches favorably to the electron temperatures predicted by the plasma global models using free-fall diffusion theory.

Power density loss lines are calculated for each of the four ECR reactor concepts and also for the several variations of ECR-MPDR™ and ECR-SLAN.

Individual curves for each of these different reactors for constant but different d_{eff} are displayed in Figure 10.7 as solid curves. Each curve displays the relationships between $<P_a>$ vs. n_i for a constant discharge dimensions **R** and ℓ. The dashed curve is for the strong axial magnetic field divergent field ECR reactor case. The data matches with the same trend as predicted by plasma global model. All experimental data lies above the corresponding global model curves by factors of 1.5 to 5. The discrepancies may be due to (1) that the plasma density in the active discharge region of the plasma source is actually higher than the measured density data at z ~ 0 cm location which is far from the active excitation area (or the center region in DECR case), (2) that the microwave coupling wall losses may be high for some reactors and are included in the P_a used to calculate the $<P_a>$, and (3) that the actual discharge volume is larger than the volumes defined by **R** and ℓ. Considering the assumptions and approximations made in the plasma global model as well as the accuracy of the experimental measurements, the experimental data agrees quite well with the global discharge models.

Figure 10.8 shows the ion production cost versus chamber pressure for different ECR sources. With 300 Watts of input power the average absorbed power density is 0.048 W/cm^3 in the divergent field ECR source. Its ion production costs vary from ~ 500 to 250 eV/ion as the pressure increases from 0.2 to 5 mTorr. The MPDR™-325 discharges operated with absorbed power densities of 0.08 - 0.2 W/cm^3 have the ion production costs of 350 - 210 eV/ion as the pressures change from 0.5 to 1.0 mTorr. The ion production costs for DECR source operating with absorbed power density of 0.16 W/cm^3 were in the range of ~1200

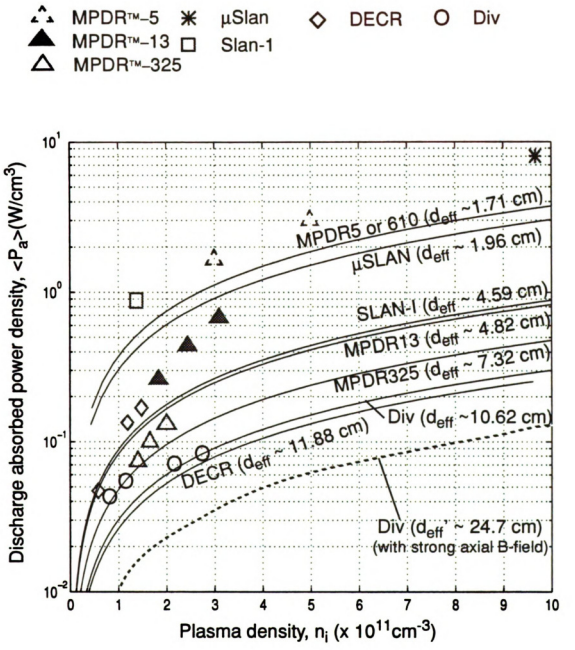

Figure 10.7 <P_a> vs. n_i in different argon discharges and plasma load loss lines calculated from global discharge models.

All measured data are in the range between 0.75 to 1.0 mTorr.

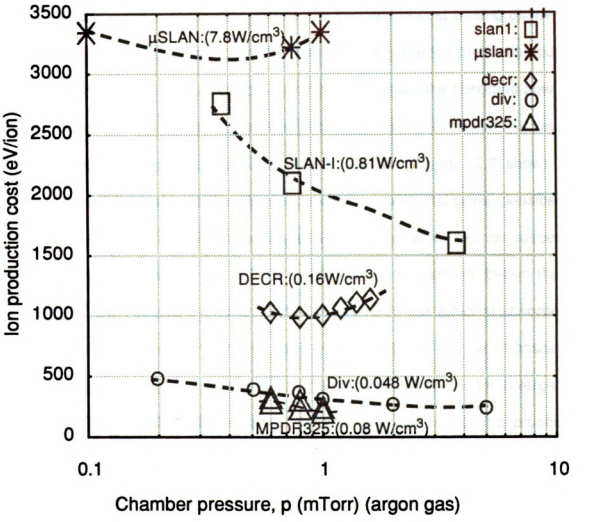

Figure 10.8 Ion production costs vs. pressure for different ECR plasma sources.

to 1000 eV/ion in 0.6 - 1.6 mTorr pressure regime. The ion production costs for a SLAN-I reactor operating in argon gas at pressures from 0.75 to 3.75 mTorr and an input power density of 0.81 W/cm^3 vary from 2700 to 1600 eV/ion.

Clearly, there is a large difference in ion production cost among different plasma sources. As shown in Section 7.3 and Ref. [192], the ion production cost within the same plasma reactor concept will increases when the absorbed power density increases or the chamber pressure decreases. It is believed that this trend should be the same even for different plasma sources. Figure 10.8 shows a reasonable result if we also account for the different experimental power densities. Therefore, one should not solely use Figure 10.8 to judge which reactor concept design is better. However, the MPDR™-325 seems to perform better than divergent field ECR source even though the MPDR™-325 has a higher absorbed power density. The reason for that may be: (1) there is about 4 cm thick transition region between the discharge chamber and the process chamber in the divergent field plasma source [193] (the reported value is near the top of the process chamber, not the bottom of discharge chamber), and (2) the microwave coupling efficiency in the divergent field plasma source may not be good, it may have significant microwave power lost in the wall surface of the applicator or lost in the coupling at the stub tuners.

10.4 Concluding Remarks

While direct comparison between dissimilar systems are difficult, the comparison of electron temperature, plasma load line, and ion production cost gives reasonably agreement (at least to the 1st order) with the plasma global model. Even though the global models do not give a completely detailed particle kinetics model, this simple but useful model can be applied to improve plasma reactor design. Electron temperature and plasma density are readily estimated and surprisingly **independent** the method of power coupling, as illustrated with different microwave ECR plasma sources described in Section 10.3.2. Also, the global models are independent of the method of coupling electrical power, i.e. independent of microwave, rf, uhf, dc power supplies and applicators. The measured plasma load lines for each plasma source follow the trend predicted by global plasma model. MPDR™s and divergent field reactors seem to have the edge in terms of plasma production efficiency. But other criteria such as ease of operation and scalability can overshadow the ion production cost in the overall preference one over the other.

Beside the assumptions made in the global models, several factors need to be considered to improve the global discharge models. The perfectly cylindrical geometry of the chamber used in this model is also modified for reasons (1) the open ended effect around $z = 0$ cm, (2) the dome shaped top end of the discharge region, (3) the physical intrusion (if any) of the substrate, plasma diagnostics and their supporting objects. These factors should be taken into account by improving the global discharge models.

For an initial reactor design or selection, engineers can apply plasma global model to achieve a head-start on the source design. One of the design strategies to optimize the discharge efficiency is outlined in a flow chart format, shown in Figure 10.9. It starts the selection of the reactor size and plasma chemistry from the desired processing wafer size and process material. From the process material, the gas(es) are chosen based on the plasma chemistries. Using the reaction rate constants of the chosen gases, an optimum electron temperature $(T_e)_{opt}$ for minimizing the total energy lost (E_T) per electron-ion pair lost from the discharge is calculated. On the other hand, the size of wafer would lead to the choice of reactor size R and ℓ. If we use the standard diffusion length (Λ) as the initial d_{eff}, the corresponding initial optimum operating pressure can be found by eq. (10.4) from previous $(T_e)_{opt}$ and d_{eff}. Then a new d_{eff} is calculated by using this pressure and eqs. (10.2), (10.3), and (10.5). A new operating pressure is then obtained by using the new d_{eff} with the $(T_e)_{opt}$. This calculation process continues until the difference between the new d_{eff} and the previous d_{eff} is within a preset tolerance. Then the optimum operation pressure for best ion production cost is found. Note that this is only an approximate design to maximize the plasma density production. Other reactor performance measures (such as ease of operation, costs of ownership, etc.) should also be taken into account. Also, the calculated pressure would affect the chemical rate constant. More iterations including this effect should be added.

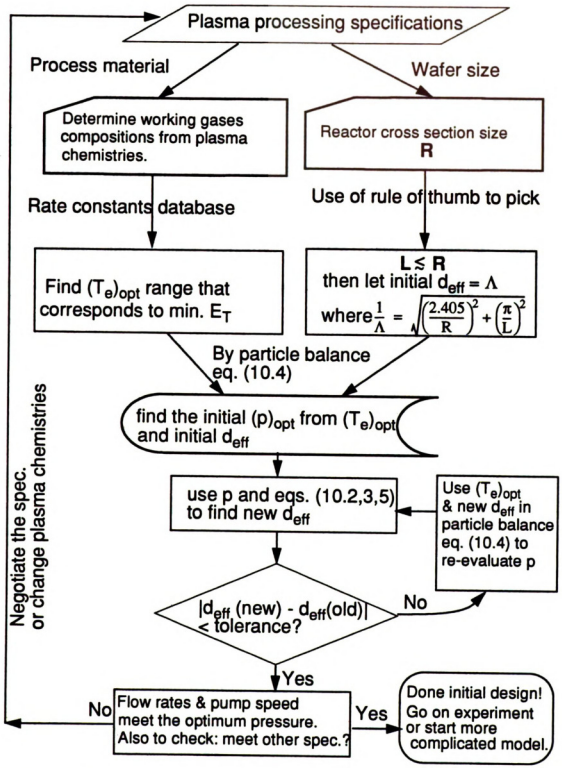

Figure 10.9 Strategy to design low pressure high density plasma source using global model at the initial stage.

The global discharge model does not consider the power coupling method, which is one of the beauty of this model. This leaves the choice of impedance matching network, applicator design and other factors such as ease of operation wide open. Furthermore, in order to the further understanding of the behavior of various plasma sources, complex numerical simulations [194-196] and experimental studies are under development to provide more detailed plasma variables variation and also to aid in reactor design. However, these take considerable computational resources or quite costly equipment. Therefore, global discharge models are useful as a simple tool to estimate plasma source performance.

Chapter 11

Summary

- 11.1 Work Done Highlights
- 11.2 Recommendation for Future Research
  - 11.2.1 Diagnostic techniques
  - 11.2.2 Microwave input coupling structure variations
  - 11.2.3 Plasma source operating with pulse-time power supply
  - 11.2.4 Reactor geometry design
- 11.3 Conclusion and Outlook

Chapter 11

Summary

11.1 Work Done Highlights

In this thesis, a number of tasks listed below has been accomplished:

(1) The baseplate and quartz bell jar for 7" cylindrical cavity were redesigned to enlarge the 9 cm diameter discharge to 12.5 cm. This baseplate and discharge design is widely used in both etching and deposition machines.

(2) The performance of several design variations of the new discharges versus a selection set of input variables was experimentally explored. The design variations include side feed and end feed applicators, and four different ECR magnetic field configurations (4P/8M, 8P/8M, 4P/4M and allN/8M). The different plasma source designs have been compared by evaluating the microwave coupling efficiency and ion production costs. Other performance evaluations such as ion density and its uniformity are also determined.

(3) The side feed and end feed cavity ECR applicators were comprehensively experimentally characterized by the magnitude and spatial variation of the electric fields in the discharge loaded cavity.

(4) The microwave equivalent circuit for the end feed reactor was developed from the electric field measurements.

(5) The magnetic fields in four different ECR magnetic configurations were simulated. The simulated results compared very well with measured magnetic field data.

(6) The plasma parameters at the downstream discharge region were experimentally measured versus input power, chamber pressure, dc bias effect. The measured plasma parameters include the electron temperature, EEDF, plasma potential, ion density and ion energy.

(7) The plasma hysteresis behavior of the MPDR™-13 was experimentally examined and this knowledge was used to develop plasma source control strategies.

(8) The experimental plasma source performance of different ECR HDP sources was compared with the performance predictions from global plasma models.

(9) The no-magnet case for MPDR™ discharge operated at low pressure (< 10 mTorr) was briefly "re-discovered" and investigated (see Appendix D).

This experimental investigation of MPDR™-13 plasma source has provided deep understanding the fundamentals of low pressure HDP ECR source physics and performance. The main conclusion results are listed in the following categories.

ECR static magnet field simulation: Simulations of the magnetic flux density on four different ECR configurations (namely 8P/8M, 4P/8M, 4P/8M, and allN/8M) have been performed. These simulations provide information on both the 875 Gauss ECR region spatial location and the magnetic field patterns. Computation results agree favorably with the experimental data. Therefore this simulation technique can be used in future ECR reactor design.

EM mode excitations: The electromagnetic fields inside the plasma load cavity have been examined with the E-field probe technique, which has been discussed in detail in Section 5.3 and Appendix A. TE_{211} and TE_{311} modes are likely to be excited for the side feed applicator, while TM_{011} and TM_{012} modes are the primarily excitations in the end feed applicator. The location of the input coupling probe influences greatly on the EM field excited inside the applicator cavity.

Best performance over the design variations: For the end feed applicator, the best microwave coupling efficiency in 8P/8M magnet configuration reaches around 98% when operating at TM_{011} mode excitation. For the side feed applicator, the best microwave coupling efficiency reaches 98-99% operating with the TE_{211} mode with both 4P/8M and 8P/8M magnet configurations. Both applicators show excellent microwave coupling efficiency (>90%).

The best ion production cost performance occurs with either the end feed (TM_{011} mode) or the side feed (TE_{211} mode) with 8P/8M magnet configuration. Their ion production costs are ~300-400 eV/ion.

Macroscopic plasma behavior and properties: The macroscopic properties of the side feed and end feed multipolar ECR plasma sources have been comprehensively measured. The typical measured downstream plasma parameters are ion density (>10^{11} cm^{-3}), electron temperature (2.5 to 8 eV), plasma sheath potential (12 to 32 V) and the ion energy (12 to 26 eV) impinging on a conducting substrate. These values of plasma parameters are perfectly suitable for the stringent requirements of state-of-the-art IC fabrication having deep sub-micron feature size.

The ion density measured in 8P/8M magnet configuration for both end feed and side feed applicators is the highest (2-4 x $10^{11}/cm^3$) due to efficient power coupling and the good multipolar magnetic confinement of 8P/8M configuration. The measured plasma potential and ion energy in 4P/8M configuration is the lowest, resulting also in the lowest ion impinging energy. However, 8P/8M magnetic field configuration together with the end feed (TM_{011} mode) and side feed (TE_{211} mode) applicators produce the best and acceptable overall plasma source performance (ion densities, ion energies, plasma potentials, and etc.).

The response of these plasma parameters to various input variables has also investigated in an electro-positive argon gas and they basically follow the prediction of global discharge model. Ion density increases when the pressure increases, or the power increases, or the z values decreases. Plasma potential and average ion energy impinging on substrate surface decrease when the pressure increases, or the z value increases and do not vary much over the incident power. FWHH of IEDF increases at further downstream area or when the

pressure goes down. The electron temperature in both end feed and side feed configurations is a weak function of incident power, but strongly depends upon the chamber pressure. The electron temperature decrease rapidly as the pressure increases, as predicted from the global discharge model.

Finally, at very low pressure (< 1 mTorr), plasma discharge maintenance in side feed plasma source is more easier than in end feed discharge. However, the plasma density of end feed plasma discharge is more uniform than the density in the side feed. This is true especially in high power operation.

Equivalent circuit: The end feed applicator is divided into four regions. The electric fields are examined in detail for each region. Different portions in the applicator are represented by electrical lump circuit elements. An equivalent circuit based on these circuit elements has been proposed. Based on the equivalent circuit, not only are the various components losses identified but also the EM wave transfer paths are shown. Impedance matching limits and constraints on the end feed ECR plasma source have been also discussed. This equivalent circuit approach provides information that is handy for impedance matching and applicator design.

Plasma hysteresis: The plasma hysteresis versus tuning (L_s, L_p) and pressure were investigated in MPDR™-13. Stable high density operation and plasma control sensors were identified. Hysteresis phenomena have confirmed that internal variables are important to understand and operate the plasma discharge. The high density operation can be stably operated for reproducible plasma process applications. As an example, argon soft sputter experiment

demonstrated the controllability of the plasma source and leads to a repeatable plasma process performance.

Global discharge model and comparison of various ECR reactors: Simple plasma global models were reviewed and were used as a norm to compare with the measured data in MPDR™-13 and with the published data for different ECR reactors. Despite the various ECR technologies, the measured electron temperatures match with global model prognosis. The agreement between the trend of the measured load lines and global model prediction encourages the usage of the simple global model in the initial plasma source design stage.

Plasma visual images: The vivid plasma images of MPDR™-13 are displayed in Appendix C. For these low pressure regime (< 50 mTorr), the static magnetic field patterns predominately influence the image appearance due to the magnetic confinement effect. This phenomenon is particularly pronounced when using different ECR magnet configurations. The visually dense discharges usually concentrate on the magnetic cusp regions generated by the strong ECR magnets. The EM field excited in cavity effect on the images plays secondary role in the picture. The image of "low density operation" processes lopsided brightness which corresponds to the measured electric field strength near the cavity wall.

As the pressure increases from 3 to 45 mTorr, the bright regions of ECR discharge images contract due to increasing collision frequency. The bright center region of non ECR microwave cavity discharge images extends to the wall as the pressure increases from low pressure (3 mTorr) to high pressure (45 mTorr).

11.2 Recommendation for Future Research

11.2.1 Diagnostic techniques

H-field probe: Instead of using the E-probe to measure the EM fields inside the cavity, a small loop antenna, called H-probe [137], can pick up the ϕ or z-component of magnetic fields to study the detail EM fields near the wall. The H-probe should be designed such that it can snug fit into the sampling holes (described in Section 5.3 and Figure 5.1) and is also rotatable while keeping excellent electrical contact with the applicator wall.

Basically, the function of H-probe technique is almost identical to the E-probe technique in terms of EM mode pattern identification. However, H-probe is particularly important to diagnose those EM fields which do not have the radial electric field component at the wall such as TE_{0n} modes. These two techniques (E-probe and H-probe) can be used to confirm each other on the excited EM fields inside the applicator.

B-dot probe: The EM field inside the plasma can be obtained by inserting a small conducted loop [142] inside the plasma location of interest. The local EM fields can be derived from the measured magnetic flux and Maxwell's equations. Careful design [145] should be enforced so that the local plasma is not disturbed significantly. The probe must also be strong enough to survive in the plasma harsh environment.

High resolution digital camera: As computer technology continues to evolve, high resolution digital camera has become affordable to many

experimentalists. It has the advantage to capture the emission signature of plasma discharge in digitized formats. Also, depending on the choice of sensor elements, the digital camera can provide spectrum that covers more than visual spectrum. The fine feature and out of visual spectrum range radiation such as infrared or ultra-violet can be spatially investigated. With more refinement, this non-invasion technique could be used as a control sensor for plasma processing.

11.2.2 Microwave input coupling structure variations

As mention in Chapter 7, the EM fields excited in the discharge loaded cavity depend heavily on the microwave launching locations and coupling structure. In this thesis, microwave is coupled into plasma reactor by a probe antenna at two locations in the applicator. Other excitation methods can also be used. For example, placing two or more probe antennas at different locations of the cavity might produce more uniform plasma by adjusting their relative phase of microwave launching.

A loop excitation is also possible implemented by attaching a loop conductor at the end of center conductor of the coaxial cable. The other end of the loop conductor must have excellent electrical contact with the applicator wall (or sliding short). The launching location, shape, size and orientation of the loop provide four tuning ways to excite various EM modes in the reactor. Initial experiments [141] have also demonstrated loop coupling can excite both TE and TM modes, depending on the launching locations.

Finally, waveguide aperture coupling, similar the SLAN applicator in Section 2.4, is an another option to couple high EM power into the applicator. The best structure is not known yet among these three methods of coupling (probe antenna, loop or waveguide aperture). Further careful studies should be conducted.

11.2.3 Plasma source operating with pulse-time power supply

The recent high power pulse HDP source studies [197-199] have caused a surge of interest in using pulse-time power supply instead of the conventional CW power energy. Results have indicated that a lower electron temperature and higher ion density production can be achieved (in the time-average sense) by using the pulse-time power source on the same machines than by CW power. Pulse time period and duty cycle play a role in optimization and further studies are needed. Plasma global models for pulse modulated plasma are also available [182-183].

11.2.4 Reactor geometry design

Since the size of semiconductor wafer has steadily increased well above ten centimeter in diameter, the original size of MPDR™-9 or MPDR™-13 discharge does not satisfy the industrial size requirement. One direction for improving MPDR™ is simply to enlarge the size of the whole reactor by a multiplication factor [54]. Figure 11.1 shows several possible sizes of variation. Lower commercial

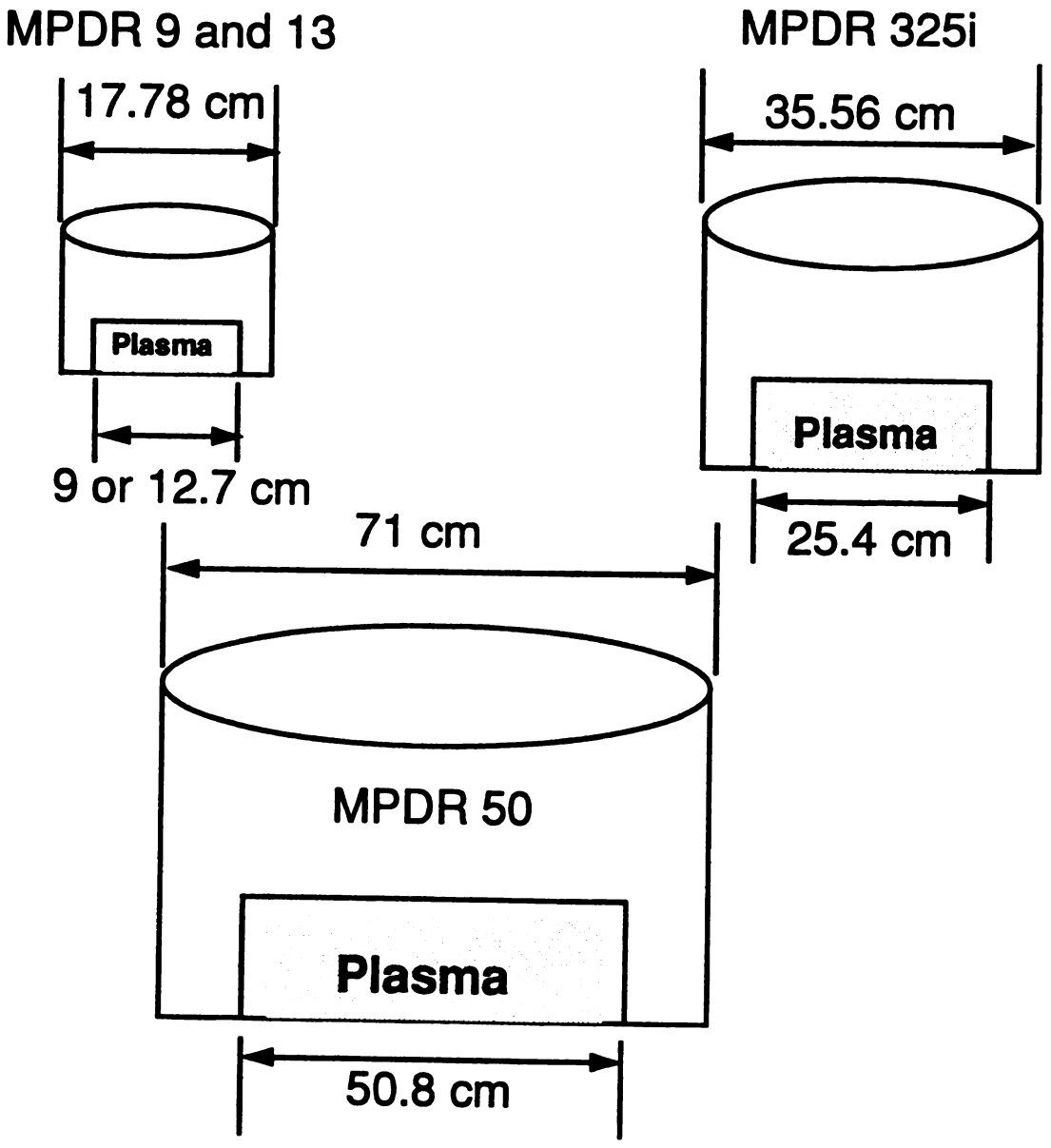

Figure 11.1 Several possible scale-up versions of MPDR.

frequency (e.g. 915 MHz) was also used [55] to control the EM mode excitation. As expected, the large reactor performance [200] has shown promising result in both dry etching uniformity and ion production cost.

Plasma global model is a handy tool to aid in reactor geometry design and to predict plasma behavior. It can be used to analyze scaling laws for plasma sources. More detailed models concerned with both the discharge generation and process chamber diffusion should be considered.

One of the most neglected but important factor of low pressure HDP design for etching application is the gas flow and the gas feed location (gas nozzle) [201]. More studies should be directed to this variable.

Finally, if optimization of Sections 11.2.2 to 11.2.3 are found, we can apply the knowledge to a larger reactor for even better performance.

11.3 Conclusion and Outlook

Finally, it is my belief that the research in this thesis has lead to a better understanding of both the fundamental and operational aspects of the multipolar MPDR™ plasma sources. The techniques and understandings presented in this thesis can also be applied to the scaled up versions for larger area processing machines (e.g. 300 mm dia. wafer) with predictable uniformity. Minimal damage on tiny and shallow critical devices can be controlled and hence optimized processing machines for delicate materials and deep submicron device processing can now be built and operated with ease.

APPENDICES

Appendix A

Calibration of E-probe in an Electromagnetic Cavity

- A.1 Introduction
- A.2 Quality Factors in Empty Cavity
- A.3 Formulation of the Proportional Constant for Absolute Electric Field Measurement

Appendix A

Calibration of E-probe in an Electromagnetic Cavity

A.1 Introduction

This appendix provides the details on the calibration of E-probe left out in Section 5.3.1 In the next section, the effect of non ideal cavity contributions to the quality factor are briefly presented. Then, the comparison between the measured quality factor values and the ideal cavity quality factor gives the estimate of the coupling wall loss in the cavity. Lastly, using the TM_{01q} EM mode pattern in the empty cavity experiments, the proportional calibration constants in eqs. (5.5) and (5.6) are obtained. In this appendix, only an end-feed applicator and the TM_{01q} mode (q = 1, 2, 3,...) were used. Similar derivations can proceed with a side feed applicator and other EM mode fields.

A.2 Quality Factors in Empty Cavity

As outlined in Section 5.3.1, the first step in making a nearly ideal cavity is to replace the discharge baseplate by a solid brass end plate at the bottom of the cavity. Therefore, this resulting cylindrical empty cavity (radius a, height L_s) has an

aluminum shell as the side wall and is terminated on both ends by solid brass plates. However, the bottom end plate available has a step structure of 1/2" height, as shown in Figure A.1. Therefore, the vertical coordinate values of the "high ring" and "low ring" sampling hole locations (shown in Figure 5.1) are 1/2" lower than the values shown in the Figure 5.1.

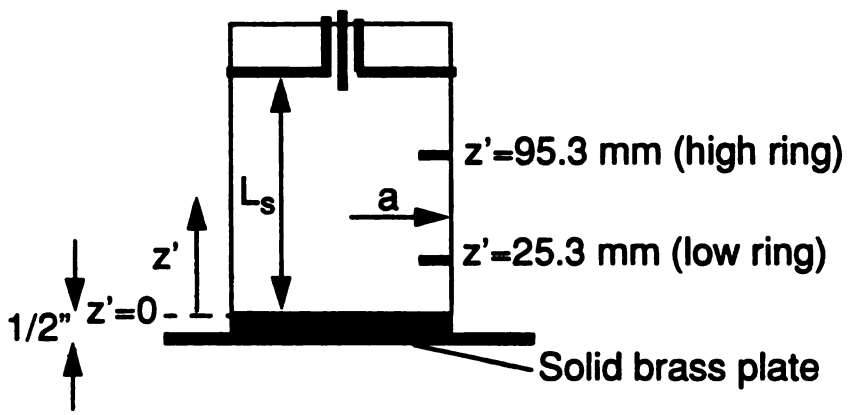

Figure A.1 The empty cavity configuration for E-field calibration.

In order to simplify the mathematics involved in the calibration procedure, the cavity is tuned to operate at the TM_{01q} mode. From the basic EM book, the r.m.s. electromagnetic fields inside the cavity obey the following equations:

$$E_z = E_{oz} * J_0(k_c r) * \cos(q*\pi*z'/L_s) \tag{A.1}$$

$$E_r = j\,(q*\pi*z'/k_c)*E_{oz}*J_1(k_c r)*\sin(q*\pi*z'/L_s) \tag{A.1a}$$

$$H_r, H_z, E_\phi = 0 \tag{A.1b}$$

$$H_\phi = (\omega*\varepsilon_0/k_c)*E_{oz}*J_1(k_c r)*\cos(q*\pi*z'/L_s) \tag{A.1c}$$

where E_{oz} is the maximum z-component value of electric field along the center axis, $\omega = 2\pi f_o$ is the angular applied frequency, L_s is the total cavity height, ε_o is the permittivity of free space, J_o is the zeroth order Bessel Function of First Kind, and $k_c = x_{01}/a$ is the radial wave number of TM_{01} modes. Note that $x_{01} = 2.405$, is the first zero of the $J_o = 0$.

The definition of the quality factor (Q) is given [96] by

$$Q = \omega U/\overline{P}_L \tag{A.2}$$

where U represents the EM stored energy and $\overline{P}_L$ stands for the time average power loss. For our non ideal cavity, the measured quality factor obeys the following equation:

$$\frac{1}{Q_o} = \frac{1}{Q_w} + \frac{1}{Q_{oth}} \tag{A.3}$$

where Q_o is the measured empty quality factor, Q_w is the ideal quality factor due to the excited EM mode wall loss, and Q_{oth} is the quality factor due to other imperfection losses (coupling probe launching structure, sampling holes, finger stocks joint contacts, etc.). The total power losses (P_{loss}) in the applicator cavity are the sum of EM mode loss (P_w) and other losses (P_{oth}). Inserting eq. (A.2) into eq. (A.3), we can have the power loss ratio in terms of their Q's

$$\frac{P_w}{P_{loss}} = \frac{Q_o}{Q_w}. \tag{A.4}$$

In the rest of this section, the ideal quality factor (Q_w) is first calculated by perturbation theory from the standard EM textbook [97]. The measured Q_o, the power loss distribution is then estimated. For sinusoidal fields, U can be written as

$$U = \int_v \varepsilon_o |\vec{E}|^2 dV \tag{A.5}$$

Substituting eq. (A.1) for eq. (A.5), after integration and simplification, we obtain

$$U = 0.5*(\pi a^2 L_s)*[J_1(x_{01})]^2*[1+(q\pi/(k_c*L_s))^2]*|E_{oz}|^2 \tag{A.6}$$

$$\text{or } U = 0.5*(\text{volume})*[J_1(x_{01})]^2*[1+(q\pi/(k_c*L_s))^2]*|E_{oz}|^2 \tag{A.6a}$$

On the other hand, using the perturbation methods for low loss conducting surfaces mentioned in Section 5.3.1, the average EM mode wall loss $\langle P_w \rangle$ is given by

$$\langle P_w \rangle = \int_S (\Re_s \cdot |H_t|^2) dS \tag{A.7}$$

Placing eq.(A.1) into eq.(A.7), after integration and simplification, we obtain

$$\langle P_w \rangle = [1/2*(2\pi a L_s)*\Re_{side} + (2*\pi a^2)*\Re_{end}]* [J_1(x_{01})]^2*[\omega*\varepsilon_o /k_c]^2*|E_{oz}|^2 \tag{A.8}$$

$$\text{or } \langle P_w \rangle = [1/2*(A_{side})*\Re_{side} + (A_{end})*\Re_{end}]* [J_1(x_{01})]^2*[\omega*\varepsilon_o /k_c]^2*|E_{oz}|^2 \tag{A.8a}$$

where A_{side} and A_{end} are the areas of the resonant cylindrical cavity side wall and two end plates, respectively; $\Re_{side}$ and $\Re_{end}$ represent the surface resistivities of the cylindrical side and the end plate respectively. Both eqs. (A.6) and (A.8) show energy stored and the EM wall loss has a form of a constant times the $|E_{0z}|^2$. The

constant is only related to the geometrical dimensions, operational mode, applied frequency, and material characteristics.

Hence, inserting eqs. (A.6) and (A.8) into eq. (A.2), the ideal cavity Q for TM_{01q} mode is

$$Q_{01q}^{TM} = \frac{\eta\sqrt{x_{01}^2 + ((q\pi a)/L_s)^2}}{2\Re_{side}\left(1 + \frac{\Re_{end}}{\Re_{side}}\frac{2a}{L_s}\right)} \tag{A.9}$$

where $\eta = 377\ \Omega$ is the intrinsic impedance of free space. From the material supplier's catalogs [202], $\Re_{side} = \Re$(6001 type Al) ~ 0.0161Ω at 2.45 GHz and $\Re_{ends} = \Re$(300 series brass) ~ 0.0248 Ω at 2.45 GHz. We obtain the ideal quality factor (Q_w) for TM_{012}, which is about 18414.

On the other hand, the measured empty (ultra-clean) cavity quality factor (Q_0) using sweep oscillation is about 8750. Therefore, at the worst case, around half of the power is dissipated into non ideal portions of the cavity beside the expected EM mode wall loss. A similar result is observed in TM_{011} mode (Q_w = 11124 and Q_0 = 5444). Hence, eqs. (5.5) and (5.6) of $P_w = K^*P_{abs}$ (with K between 1/2 and 3/4) are reasonable estimate formulas [203] for an empty cavity. However, when the applicator cavity is loaded with a plasma discharge, most of the input power will dissipate into the lossy discharge and only a small portion of power goes into the coupling structures or walls (see Section 7.2).

A.3 Formulation of the Proportional Constant for Absolute Electric Field Measurement

It is well known that the power sampled by the E-probe is linearly proportional to the square [102]of the local normal electric field: i.e.

$$P_s = C\,|E_r|^2 \tag{A.10}$$

$$\text{or } |E_r| = C'\sqrt{P_s} \tag{A.10a}$$

where C' = 1/sqrt(C). If the constant C (or C') is known, then the absolute field strength can be obtained from the above equation. In the following calibration, we excited the TM_{012} mode and picked two holes at the "low ring": one is located at $\Phi = 45^o$ and the other $\Phi = 90^o$. Two different E-probes were also used for the absolute electric field strength calibration process, one is flush with the inner wall and the other (namely probe 3) has a small center conductor penetration depth. The selection of the TM_{012} mode and the low ring locations is preferred because the sampling locations are farther away from the coupling launching probe to reduce the near field effect. For the TM_{012} mode, the experimental critically coupled condition is $L_s = 144.6$ mm and $L_p = -1.5$ mm,

The relationship ($\langle P_w \rangle \cong (1.29\text{x}10^{-8})\,|E_{oz}|^2$) between the P_w and E_{oz} can be found by evaluating eq. (A8) for the TM_{012} mode. Recall what we measured is the normal field component near the wall, namely E_r(hole), instead of E_{0z}. The relationship between E_r(hole) and E_{oz} for TM_{012} mode can be evaluated from eq. (A.1a). We get $|E_r(\text{hole})| \cong 0.7484\,|E_{0z}|$. Hence, the relationship between P_w and $|E_r(\text{hole})|$ is established as the following:

$$\langle P_w \rangle \cong (2.303 \times 10^{-8})\, |E_r(\text{hole})|^2 \qquad \text{(A.11)}$$

By writing $\langle P_w \rangle = K\, P_{abs}$ (K is between 1/2 and 3/4) and combining eq. (A.11) into eq. (A.10a), we can get C' from

$$C' = \sqrt{\frac{K}{2.303 \times 10^{-8}} \left(\frac{P_{abs}}{P_s} \right)} \qquad \text{(A.12)}$$

Table A.1 displays the sampled power P_s from two different E-probes at two calibration locations as the input power was varied. Note, the recorded values are the actual net power sampled at the wall. The loss (1.25 dB or 1.33) of the small cable (RG58C/U) from the E-probe to the power sensor is deducted for calculation. As shown in the Table A.1, the power ratio (P_s/P_{abs}) during the calibration should keep small (< 2%) in order not to perturb the normal electromagnetic resonant nature inside the cavity. The slight variation in the power ratio (P_s/P_{abs}) is believed due to the imperfection of the cavity wall thickness (see Appendix B).

Table A.2 displays the proportional constant values from eq. (A.12) by using the average experimental values in Table A.1, and for K=1/2. Hence, eq. (5.5) is derived. Similarly, using K = 1/4, eq. (5.6) can also be obtained.

Table A.1 Sample powers for two different probes

	Flushed probe				Penetration probe 3			
P_{abs}	P_s at 90°	P_s/P_{ab} $_s$ at 90°	P_s at 45°	P_s/P_{ab} $_s$at 45°	P_s at 90°	P_s/P_{ab} $_s$at 90°	P_s at 45°	P_s/P_{ab} $_s$at 45°
0.76 W	25.6 μW	3.37 x 10^{-5}	28.3 μW	3.72 x 10^{-5}	8.357 mW	1.10 x 10^{-2}	8.66 mW	1.14 x 10^{-2}
0.95 W	33.2 μW	3.49 x 10^{-5}	34.6 μW	3.64 x 10^{-5}	10.37 mW	1.092 x 10^{-2}	11.17 mW	1.177 x 10^{-2}
1.7 W	56.5 μW	3.33 x 10^{-5}	59 μW	3.47 x 10^{-5}	19.17 mW	1.128 x 10^{-2}	20.28 mW	1.193 x 10^{-2}
2.626 W	90.9 μW	3.46 x 10^{-5}	94.6 μW	3.603 x 10^{-5}	29.49 mW	1.123 x 10^{-2}	30.08 mW	1.145 x 10^{-2}
Average		3.413 x 10^{-5}		3.608 x 10^{-5}		1.111 x 10^{-2}		1.164 x 10^{-2}

Table A.2 Proportional constants for two E-probes

C'	at 45°	at 90°
Using Flushed probe	7.76 x 10^5	7.96 x 10^5
Using penetration probe 3	43.19 x 10^3	44.21 x 10^3

Appendix B

Measurements of Cavity Wall Thickness and Probe Lengths

- B.1 The End Feed Cavity Wall Thickness Near the E-field Sampling Holes
- B.2 Measured Electrode Lengths in Array of Probes

Appendix B

Measurements of Cavity Wall Thickness and Electrodes Lengths in Langmuir Probe Array

B.1 The End Feed Cavity Wall Thickness Near the E-field Sampling Holes

Since the EM sampled power is directly proportional to penetration depth of the E-probe, assuring the same depth around the cavity holes is extremely important for accurate measurement. Some experimental results of E-field data have demonstrated the location-preferred non-uniformity phenomena even in an empty cavity. Having inspect and consider many possible measurement error locations, wall thickness may be the suspect. However, once the cavity is constructed, wall thickness variation is beyond our control capability. Using the special calipers in Electrical Engineering Department Shop, the specific wall thickness (measuring area of around 2mm by 2mm) near the holes of the end feed aluminum shell cavity was measured. They are listed in the Table B.1 for reference purpose. The "low ring" and "high ring" are referred to the Figure 5.1.

Table B.1 Wall thickness (in inch) around the E-field sampling holes

Circumferential angle	Low ring at L_s = 38 mm	High ring at L_s =108 mm
0°	0.2605	0.2605
10°	0.261	0.261
20°	0.262	0.261
30°	0.262	0.26
40°	0.26	0.263
50°	0.257	0.2605
60°	0.262	0.261
70°	0.2626	0.262
80°	0.263	0.262
90°	0.263	0.263
100°	0.2615	0.2625
110°	0.261	0.261
120°	0.26	0.263
130°	0.259	0.262
140°	0.259	0.258
150°	0.259	0.258
160°	0.2575	0.257
170°	0.2565	0.2555
180°	0.257	0.2555

Table B.1 (Cont'd).

Circumferential angle	Low ring at H = 38 mm	High ring at H =108 mm
190°	0.257	N.A.
200°	0.257	
210°	0.257	
220°	0.255	
230°	0.255	
240°	0.256	
250°	0.253	
260°	0.2525	
270°	0.252	
280°	0.2515	
290°	0.254	
300°	0.256	
310°	0.256	
320°	0.256	
330°	0.2575	
340°	0.2575	
350°	0.2595	

From the low-ring measurement listed in Table B.1, the average thickness is around 0.256" and it has shown slightly thicker at $\Phi = 20^{o}$, 30° and 60°-90° and slightly thinner at $\Phi = 220^{o}$-290°. Therefore, if we use the same E-probe, the sampled EM power at the thicker wall would be lower than the values sampled around the thinner wall area. One of the uniformity figure of merit is "min-max" uniformity, which is defined as the half difference of maximum and minimum divided by their average. The min-max uniformity of low-ring thickness is about 2.2%. The thin locations in high-ring area are $\Phi = 140^{o}$ to 180°. Hence, the sampled EM powers over there are slightly higher.

B.2 Measured Electrode Lengths in Array of Probes

According to the eq. (5.13), the measured ion current density is proportional to the Langmuir prober area. For the same diameter tungsten wire, the area is proportional to the electrode probe length. Therefore, the electrode lengths in array of probes, shown in Figure 5.6, are listed in Table B.2 for accurate ion current/density uniformity measurement.

Table B.2 Electrode lengths in Langmuir probe array

Probe number (binary logic #)	Length in inch
1 (00001)	0.214"
2 (00010)	0.215"
3 (00011)	0.19"
4 (00100)	0.212"
5 (00101)	0.201"
6 (00110)	0.19"
7 (00111)	0.215"
8 (01000)	0.216"
9 (01001)	0.202"
10 (01010)	0.203"
11 (01011)	0.219"
12 (01100)	0.215"
13 (01101)	0.218"
14 (01110)	0.205"
15 (01111)	0.216"
16 (10000)	0.217"
17 (10001)	0.218"
18 (10010)	0.2"
19 (10011)	0.208"
20 (10100)	0.215"
21 (10101)	0.222"
22 (10110)	0.212"
23 (10111)	0.222"
24 (11000)	0.201"
25 (11001)	0.228"
26 (11010)	0.186"
27 (11011)	0.212"
28 (11100)	0.206"
29 (11101)	0.223"

Appendix C

Visual Image of Microwave Gas Discharges

- C.1 Introduction
- C.2 Experimental Set Up
- C.3 Experimental Results
  - C.3.1 Side feed images for different ECR magnet configurations
  - C.3.2 End feed 8P/8M ECR plasma images
  - C.3.3 Non magnetized microwave cavity plasma images
- C.4 Discussion and Summary

Appendix C

Visual Images of Microwave Gas Discharges

C.1 Introduction

The word plasma derives from the Greek Plásma, which means "something formed or molded" and was first suggested by Langmuir's observation of the manner in which the positive column of a glow discharge tended to mold itself. Another version of the plasma name story is that when Langmuir was investigating electrons and ions in the plasma, he was struck by their very different properties which are due to their disparate masses (the minimum ion/electron mass ratio is the one of proton/electron, or 1836 to 1, which is significantly more than that between a bowling ball and a marble). This reminded him of small red cells and big white ones in blood fluid, which by then was already called "plasma" in medical community.

Anyway, humans have long been fascinated by the light existing in and emitting by plasmas. The plasma state occupies 99% of the Universe. However, plasmas are minorities in this beautiful planet -- Earth. Since the glow phenomenon is the most direct indication of gas discharges, the "visual image" of a plasma is a natural way to study this special type of matter. A plasma radiates a

wide range of electromagnetic energy from deep infrared to deep ultra-violet. However, due to the limited human perception, the naked human eyes can only detect a certain limited range of the electromagnetic spectrum (wavelength range from 400 nm to 700 nm). And that is the reason why we call this range visible spectrum.

In this appendix, the spatial cross sectional radiation patterns of the ECR discharge are described as a number of reactor input parameters are varied. The input control parameters are incident microwave power, chamber pressure, different ECR configurations, side feed and end feed applicator configurations, rotation of the ECR magnet and the tunings (L_s, L_p) of the cavity resonant modes. The main output is the "visual image" of the plasma. Of course, there are as many different ways to describe the "visual images" of the plasma. Here photographs of the discharge cross section are used to identify the discharge state. The interpretation of these color images presented in this chapter will be described in later sections. Even though we may miss some valuable information of the gas discharges due to the limited human and film sensitivity limitation, visualization is still a good way to examine the plasma due to its handiness and convenience.

C.2 Experimental Set Up

As shown in Figure C.1, a "mirror-like" light reflecting object is placed inside the process chamber, underneath the plasma source, to reflect the light coming from plasma out of the process chamber windows for photo-taking. Either a big

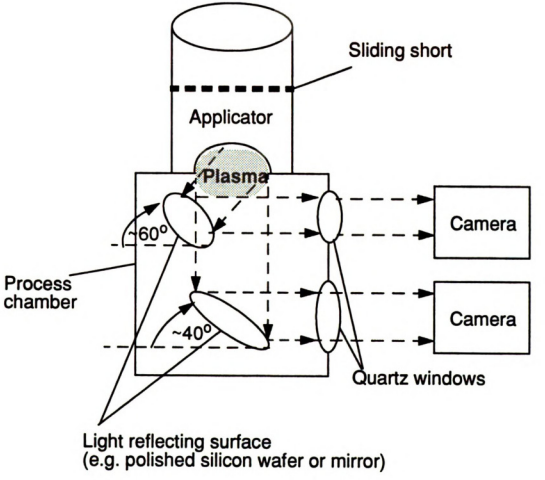

Figure C.1 Discharge picture-taking schematic in MPDR-13.

mirror or a four-inch diameter silicon wafer served as mirror. A silicon wafer is preferred because the back side coating of a regular mirror may contaminate the chamber under direct plasma exposure. A SLR Pentax camera collected the light transmitted through the window (either 6 or 7 in Figure 3.5). If the top window is used for picture-taking, this image gives a closer look at the discharge and the light reflecting plate was located closer to the source and inclined at approximately 60^0 from horizontal surface. When the lower window was used to take picture, the light reflecting surface was placed at an angle of about 40^0 from horizontal surface to yield a cross sectional view of the plasma discharge. During the picture taking process, only Kodak Gold 100 or 200 films were used. Shutter speeds and their respective apertures were also recorded at the same time. When developing the pictures, a fixed process was employed to ensure (at least within the same period of processing) every print has no other hidden compensation factor. Due to the concern of repeatability and the preferred requirement for MSU dissertation format, photographs were scanned via a HP4C scanner into a digital image file for reproduction. No modifications were added during the scan process. Photographs of argon microwave discharges were used in all the reported images.

Source of errors: Note that silicon is an indirect bandgap (about 1.12 eV) material. By $E = hc/\lambda$ we get silicon absorption wavelength of ~1110 nm, which belongs to infrared range, and is out of visual range. Thus using silicon wafer as a mirror should not be an interference factor on the visual image. Hence, the sources of errors are (1) the limited individual human perception, (2) film

sensitivity, and (3) the scanner process which do not give 100% fidelity of the original photographs. Another concern is that (4) the actual "visual image" of plasma should be in three dimensional space. The convenience of this set up only provides a two-dimensional image, viewing from the bottom of the plasma source. This adds another uncertainty to the images described in this appendix. However, visual plasma pictures provide some usual descriptive information of the discharge. For example, in an argon discharge, an overall pink Ar-discharge indicates existence of mostly excited atoms while the overall bluish Ar-plasma has more ions in it.

C.3 Experimental Results

Inside a plasma, the various processes (ionization, recombination, radiation, charge exchange, etc.) are invariably occurring among particles. The electromagnetic radiation into the surrounding external neighbors are the unavoidable by-products of the discharge. In this appendix, a basic assumption is made is that the bright glowing regions are the locations of a large number of energetic electrons which are trapped by the multipolar magnetic fields and thus have many inelastic collisions in these glowing volumes. The glowing discharge images are characterized by (1) their relative brightness, (2) their relative size, and (3) their shape.

C.3.1 Side feed images for different ECR magnet configurations

C.3.1.a TE_{211} mode

If an external magnetic field is applied to the plasma, the movement of the charged particles will be directly affected by the Lorentz force. The electrons move along the magnetic field lines and in the presence of an electric field also experience an E x B drift. The ions follow the electrons due to he Coulomb force between these two charged species. As a result, the drifts and diffusions of charged particles is spatially modified by the applied magnetic fields.

Figure C.2 shows different discharge cross sectional images for three different multipolar ECR magnet configurations operating at TE_{211} mode. There exists a pie shaped bright region between each pair of adjacent magnets. This is one of the visual features observed in all of our low pressure multipolar ECR plasma sources. However, the plasma lobes roughly have two different sizes. Viewed from the bottom, the bigger one always occurs between the two magnets when rotating in the counter clockwise direction or traveling from the magnetic north pole to south pole. In the 8P/8M case, 4 big and 4 small bright pie shaped regions are alternately observed. The large and small bright pie shaped regions occur because (1) the excited TE_{211} mode fields match better with four of the eight magnetic poles, and (2) they are partially due to the E x B drifts of the electrons described in Section C.4. In 4P/8M and 4P/4M cases, the number of bright regions reduces to four because of the reduction of the number of magnetic poles. The locations of the big and small bright zones for the 4P/4M and 4P/8M magnet configurations are still located according to the rules mentioned above.

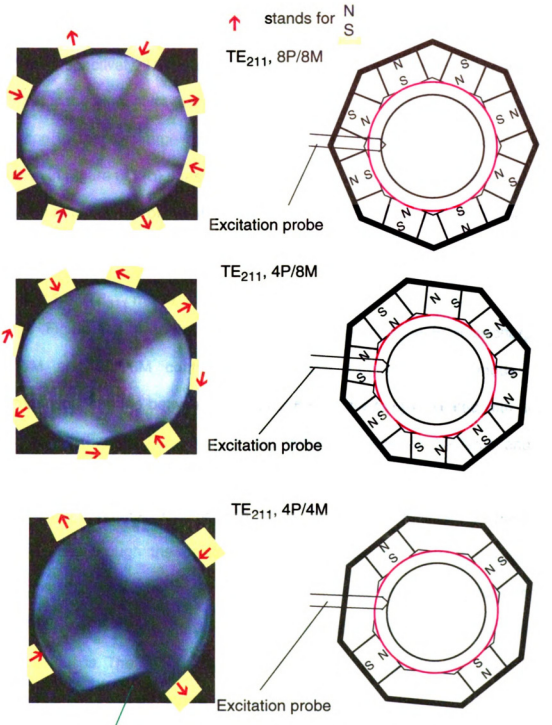

The small obstacle that appears in every picture in front of the image is the support for the mirror-like object from falling down.

All are with P_{inc} ~ 240 W, p =0.84 mTorr

Figure C.2 Discharge pictures for different ECR magnet configurations in side feed applicator operating at TE_{211} mode.

One other point was also observed. The appearance ratio of big pie to small pie radiating areas was roughly 1.75, 2.9 and 4.6 for 8P/8M, 4P/8M and 4P/4M respectively. The reason to this might be the gradient of magnetic field in 8P/8M is the highest so that it is not as easy for accelerated charged particles to escape to the discharge center. Also the 875-Gauss ECR zone of 4P/4M, as shown in Figure 6.4 (b) does not even form a close surface within discharge cross section at the center plane of the magnets. Therefore, its ratio is the largest.

C.3.1.b TE_{311} mode

Figure C.3 gives the cross sectional pictures of the ECR discharge with 8P/8M and allN/8M configurations excited with the TE_{311} mode. When comparison is made between the similar 8P/8M discharges excited with different TE modes (Figures C.2 and C.3), the difference between the large and small bright pie sizes is blurred by the impressed TE_{311} mode electric fields. That means the impressed electric field has at least 2nd order effect on the plasma image even though the basic pie structure caused by magnetic field cusps remains at low pressure regime. On the other hand, the plasma visual image of allN/8M does not have the pie shape bright region due to the lack of multipolar magnet cusps. The brightest spot for the allN/8M configuration happens to be a ring region close to the quartz wall. In addition, the plasma appears to be stream out from plasma region into the process region.

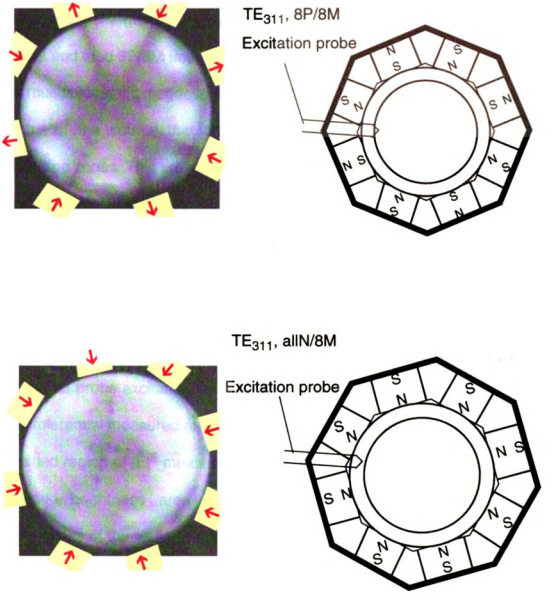

Figure C.3 Discharge pictures for different ECR magnet configurations in side feed applicator operating at TE_{311} mode.

C.3.2 End feed 8P/8M ECR plasma images

C.3.2.a High density mode and low density mode images

The end feed 8P/8M cross sectional images for the high density (mode 1) and low density (next to mode 1) discharges are shown in Figure C.4. For the typical end feed 8P/8M image, the pie shape bright area are still there because of the multipolar static magnetic fields. In addition, there exists a bright zone near the centre of the source that can extend into the four large bright pie shaped discharge zones. This probably is due to the non-zero axial electric field of the TM mode pattern. In contrast, the TE mode fields are purely transverse and do not have an axial electric field. This center bright discharge region near the top of the quartz bell jar affects the tuning characteristics from the empty cavity as mentioned in Section 7.2.4.A. Note that this center bright zone effect is more significant in mode 1 than mode 2 because of the near electric fields coupling by the center probe excitation antenna. Figure C.4 also displayed the corresponding circumferential measured relative electric fields at the wall. It is interesting that the lopsided region of $|E|^2$ measurement in low density mode is closely related to the lopsided brightness area in plasma image. Even though there is some unevenness of the wall thickness (shown in Appendix B), the electric fields of the high density mode are not perfectly Φ-symmetric due to the reason mentioned in Section 7.2.2.B. However, the image looks rather symmetric beside the pie shaped influenced by static magnetic field. This indicates that electric field at the wall is a more sensitive variable (sensor) than the visual plasma image.

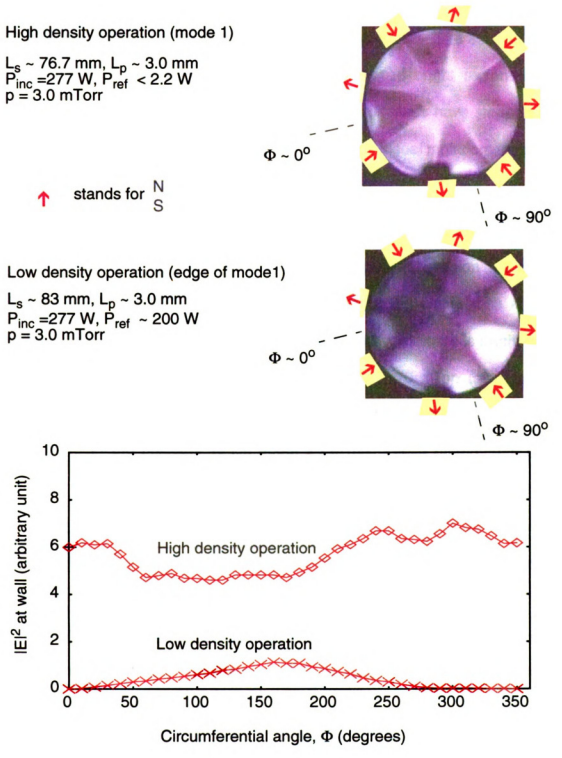

Figure C.4 High density and low density operation mode plasma images in end feed applicator with 8P/8M ECR manget configurations.

C.3.2.b Pressure effect

Figure C.5 presents the end feed 8P/8M plasma images at 7, 10, 25, 45 mTorr pressures. The pie shaped bright region gradually contracts as pressure goes up. At 45 mTorr, even though the pie shaped bright regions still exist between the magnetic cusp, various collisional processes have stepped in such that their pie shape sizes are roughly the same. The visual radiation does not exist in the center of the discharge.

If you carefully examine the 7 mTorr image in Figure C.5 and 3 mTorr image (mode 1) in Figure C.4, you can see that the big pie bright region in 3 mTorr has more structure than the 7 mTorr. Each of the four big pie regions at 3 mTorr contains a bright core region like the small pie does, plus there is bright region at the big pie boundary. When pressure goes up to 7~10 mTorr (also see Figure C.11), the plasma begins to fill up within the whole big pie region. It then starts to contract after the pressure reach about 25 mTorr. These phenomena probably relate to the mean free path variations at different pressures.

C.3.2.c Rotation effect of ECR magnets

Figure C.6 gives a series of plasma pictures for the 8P/8M, end feed, plasma source operating at mode 2 as the ECR magnets were rotated circumferentially at different angles. In these low pressure ECR discharges, magnetic fields clearly dominate the "visual image" of the plasma. As ECR magnets rotate, the shape will follow accordingly. Also Figure C.7 shows the P_{ref}/P_{inc} and the sampled radial electric field. The relative changes are relatively small versus Φ.

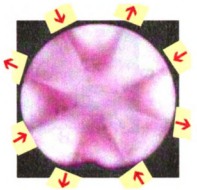

p = 7 mTorr

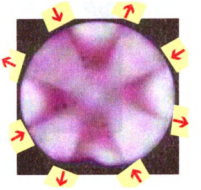

p = 10 mTorr

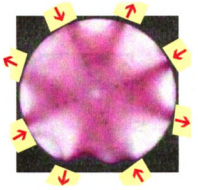

p = 25 mTorr

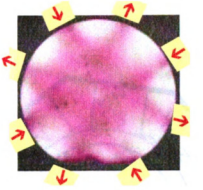

p = 45 mTorr

↑ stands for N / S

P_{inc} ~ 277 W, mode 1, 8P/8M ECR magnet configuration

Figure C.5 End feed visual images vs. pressure.

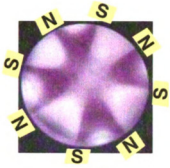

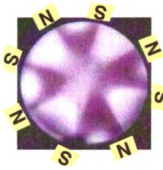

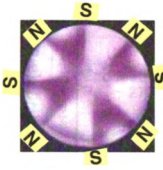

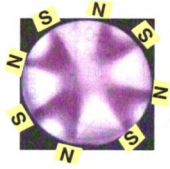

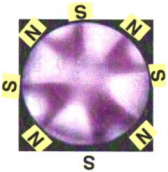

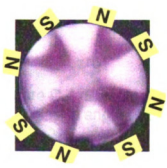

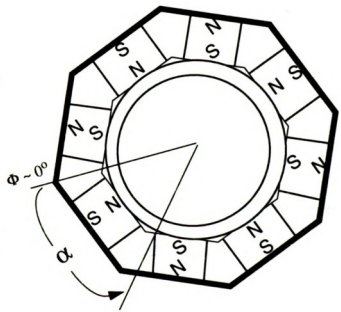

Bottom view

Figure C.6 Visual images vs. rotation of ECR magnets in end feed plasma source.

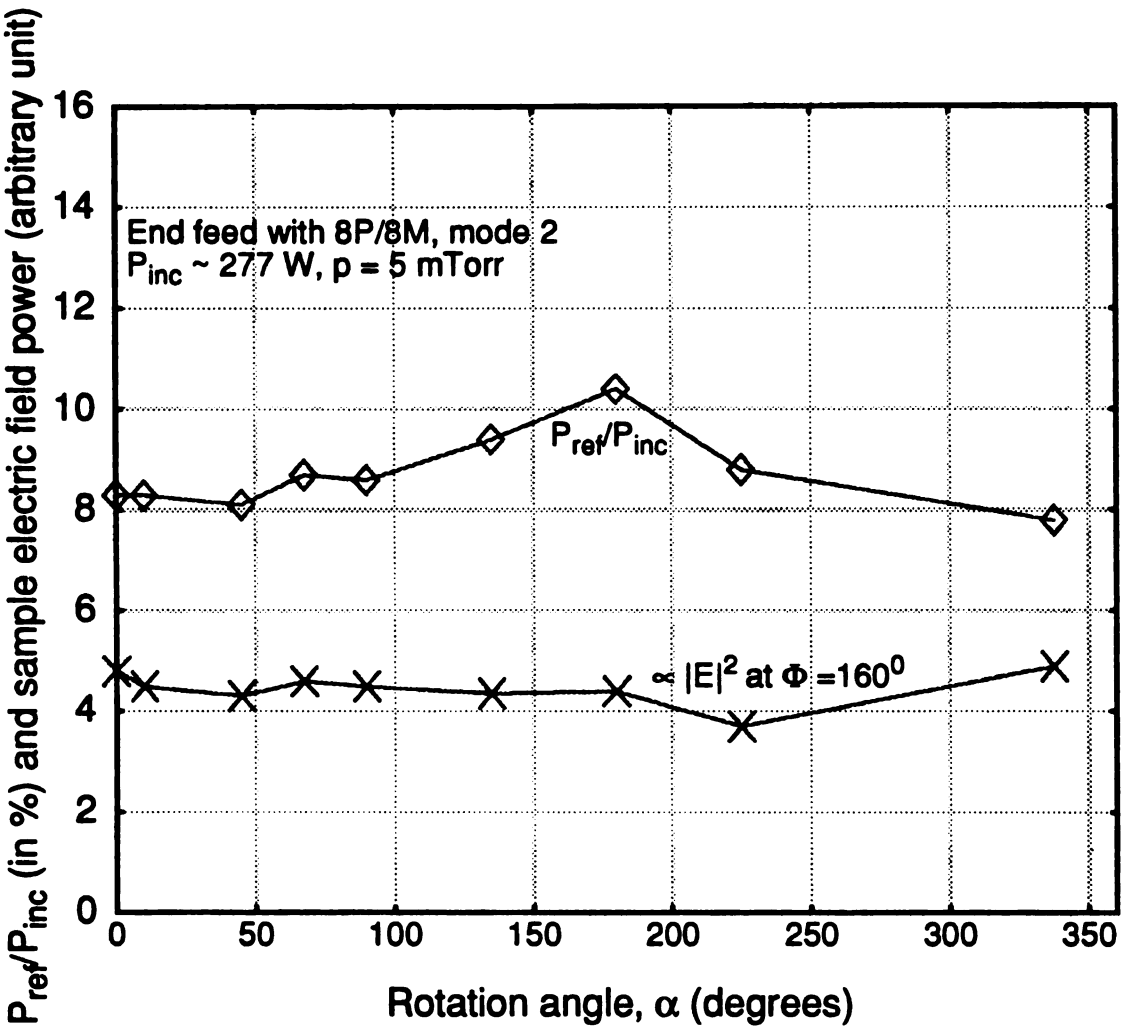

Figure C.7 Sample electric field power and percent of reflected power vs. rotation angle of ECR magnets.

C.3.3 Non magnetized microwave cavity plasma images

The physical structure of non magnetized microwave cavity plasma source is identical to the MPDR™-13 but the permanent magnet s are removed. Only end feed excitations was investigated. Its preliminary measured data is presented in Appendix D. Figures C.8 and C.9 display the plasma images from 5 to 45 mTorr for two resonant modes. The images are totally different from the ECR plasma discharges'. First the images of the non magnetized microwave plasma source do not have the pie shaped bright region due to lack of magnetic field cusps. At low pressure (several mTorr), the visual image is bright in the center of the discharge region. Contrary to the ECR discharges, as the pressure goes up, the center bright area extends to the wall when it reaches 45 mTorr. The detail heating mechanism is still not completely understood. Future experiments are needed for these non ECR microwave plasma sources.

C.4 Discussion and Summary

In this type of multipolar ECR reactor, magnetic fields have two roles: one confines the plasma (pie shape evidence) and the other is to provide necessary ~875 Gauss layer for electromagnetic ECR coupling to take place (bright lobes). Once the electrons obtain enough energy, they transfer their energy to the "plasma species" by the molecular and ion excitations, and ionization by electron impact collision. If the applied electric field is circumferentially symmetric, the intuitive "visual image" of the plasma would be symmetrical too. This can be seen

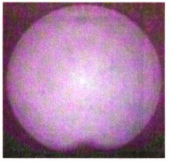

p = 5 mTorr

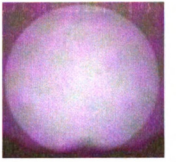

p = 7 mTorr

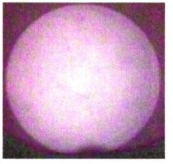

p = 10 mTorr

p = 15 mTorr

p = 26 mTorr

p = 45 mTorr

P_{inc} ~ 277 W, end feed applicator without magnet.

Figure C.8 Plasma pictures vs. pressure in non magnetized reactor at mode 1.

p = 5 mTorr

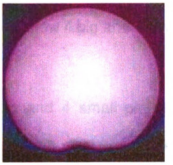

p = 7 mTorr

p = 10 mTorr

p = 15 mTorr

p = 25 mTorr

p = 45 mTorr

P_{inc} ~ 277 W, end feed applicator without magnet.

Figure C.9 Plasma pictures vs. pressure in non magnetized reactor at mode 2.

from the images of no magnet configuration. In ECR plasma source, observation of the bright plasma do not look this way. They show 4 big and 4 small pie shaped images instead of eight equally large zones.

An plausible explanation to the 4 big and 4 small pie shaped plasma appearance is given here. In the magneto-plasma discharges, electrons gyrate along the magnetic fields in helical paths. The ions are not significantly influenced by the magnetic field. Ion can diffuse quicker perpendicular to the magnetic fields than electrons. The net result is that plasma has charged more positively in the low magnetic field area (which is around the center region of the plasma discharge in our ECR plasma source). On the other hand, electrons follow the magnetic field wandering more closely to the chamber wall. This builds up an net electric field which tends to hold in electrons and drive out ions. That is to say an ambipolar electric field pointing radially outwards to the strong magnetic field areas from the center exists. As a result, both electrons and ions follow the E x B drift [204].

For example, at z = -1.27 cm plane (center plane of ECR magnets), the E x B drifts cause part of the plasma move upwards or downwards, depending on the direction of the magnetic field. Region 1 in Figure C.10 has an E x B drift to the top quartz bell jar and E x B drift in region 2 pulls plasma down to process chamber. Objects that are further away appear to be smaller than close objects. In addition, the plasma which goes upwards will quickly be confined by the curve shaped portion of the bell jar. This might adds to the explanation why 4 big and 4 small pie shape phenomenon. This plausible explanation is partially attributed to the

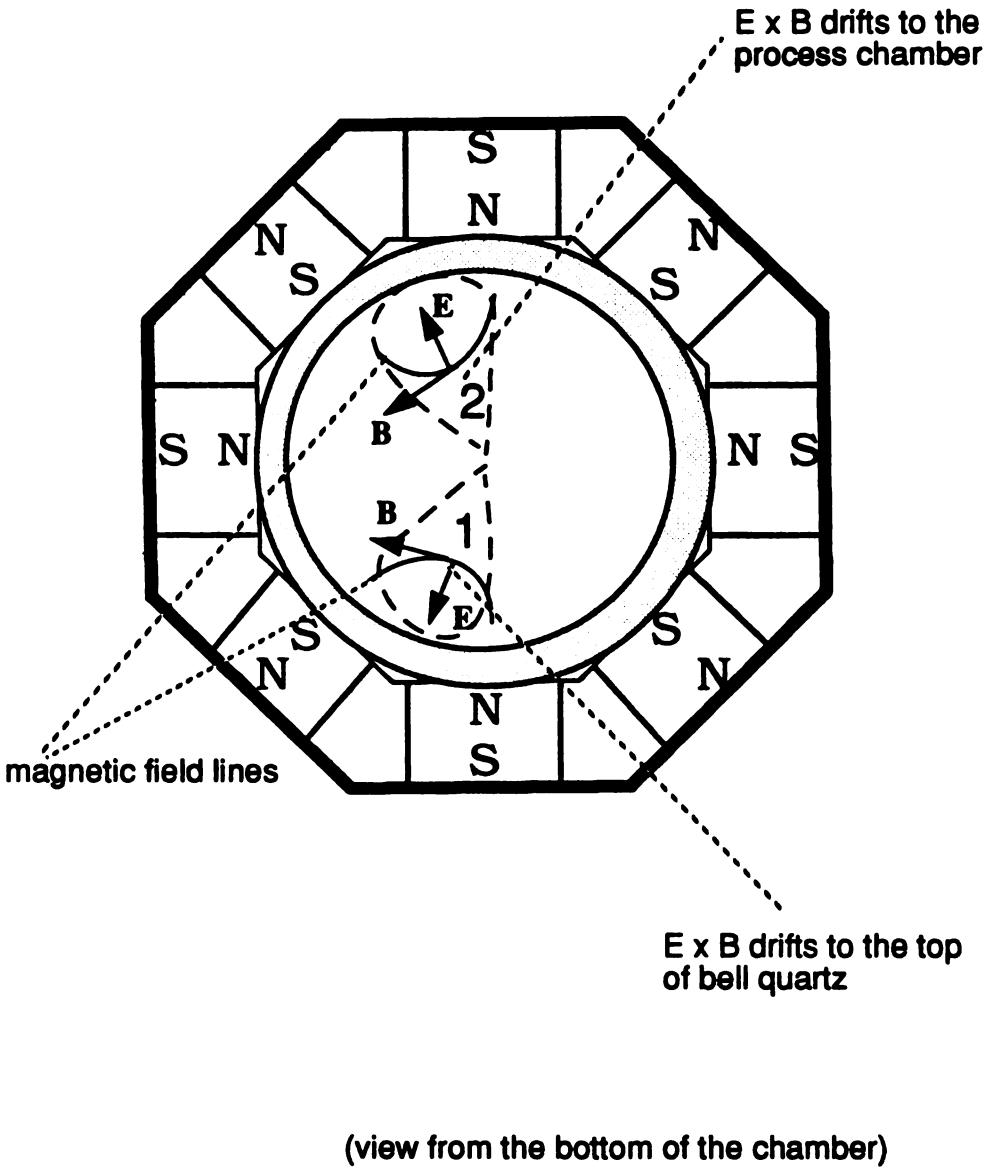

Figure C.10 Demonstration of the plasma movement due to the E x B drift.

different images in different ECR configurations such as Figure C.1.

In reality, things are not so clear-cut. The discharge is situated in a nonuniform magnetic field in three dimensional space. When location is not at the central cross section, the E x B drift will direct the discharge to go obliquely. Therefore, in our ECR discharges, observation of the individual semi-spheres attaching cusp field between the magnets, as shown in Figure C.11.

In summary, the plasma images of the low pressure ECR discharges depend heavily on the static magnetic field pattern. The plasma discharges are usually trapped between the magnetic cusp fields. The EM mode inside the applicator plays the 2nd order effect on the plasma images. Low density lopsided visual image corresponds to the lopsided electric field measurement at the cavity wall. As pressure increases, the bright discharge regions in ECR discharges starts to shrink while the non magnetized discharge extends.

For the price and performance of nowadays digital camera with charge-coupled device (CCD) detectors, it will provide a new popular and aesthetic way for future plasma characterization [205]. Also these technologies will eliminate the error during the process of scanning a regular picture.

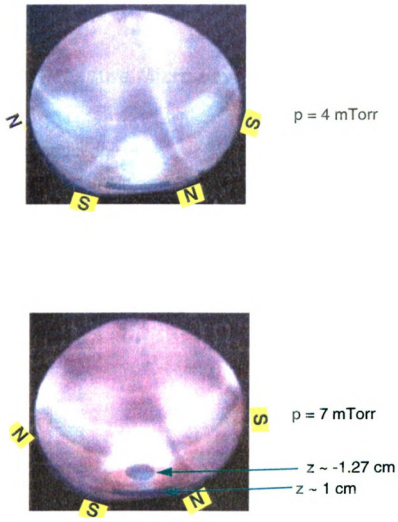

P_{inc} ~ 277 W, mode 1 (L_s = 76.7 mm, L_p = 30.4 mm) end feed applicator.

Figure C.11 Detail images vs. pressurer in the end feed plasma with 8P/8M ECR magnet configuration.

Appendix D

Low Pressure Microwave Cavity Plasma Discharges

- D.1 Introduction
- D.2 Experimentals and Comparison Principle
- D.3 Results and Discussions
  - D.3.1 Plasma density and electron temperature
  - D.3.2 Electric fields comparison
- D.4 Concluding Remarks

Appendix D

Low Pressure Microwave Cavity Plasma Discharges

D.1 Introduction

Traditionally, physicists or engineers generate plasma discharges either capacitively or inductively [206] by collisional heating, also called Ohmic heating. ECR and Ion Cyclotron Resonance (ICR) techniques were then developed to alternately produce plasma discharges. Until the late 1980s, people in the plasma community believed that ECR heating is the most efficient way to ignite and sustain a plasma discharge at very low pressure regime (< 10 mTorr). Collisionless electron heatings have been shown lately in low pressure discharges [207-209]. Recently, Popov has given an excellent comprehensive review [35] on various microwave heating mechanisms in various plasma discharges. One of them is referred to as stochastic heating [210], which is a result of plasma sheath movement near the wall. Plasma sheath near the wall is oscillating with the applied EM field. If the sheath moves towards the electrons, the energy increases. For an oscillating sheath, some electrons gain energy and others lose energy. However, averaging over an oscillation period, the net effect is an energy gain. These phenomena were reported both theoretically [210,211] and experimentally

[212]. This electron heating mechanism is usually referred to as stochastic, collisionless, or anomalous.

Therefore in this appendix, experiments were carried out to explore the existence of collisionless heating in microwave plasma discharges as pressure is varied from moderate to very low pressure. Both unmagnetized and magnetized (8P/8M only) discharges are compared to an assumed discharge sustained only with pure collisional heating mechanism. Preliminarily data on the investigation of the no-magnet microwave cavity discharge is reported at a pressure range of 3 to 45 mTorr. Only pure argon gas was used in this appendix. The intent is not to provide the details on the exact heating mechanisms, but to identify that there are other heating mechanisms than Ohmic heating occurring inside the microwave cavity unmagnetized and magnetized discharges. Some visual images are presented in Appendix C.

D.2 Experimentals and Comparison Principle

The experimental setup for the no-magnet microwave cavity source is identical to the MPDR-13 described in Chapter 3 except that there are no ECR or downstream magnets there. The main controlled input variables were chamber pressure (3 to 45 mTorr) and 2.45 GHz CW microwave incident power (120 to 400 W). The measured variables were the electric field strength at the applicator wall, downstream plasma density, and electron temperature.

Assuming a pure collisional cold steady-state discharge, the time average absorbed power density is governed by the following equation:

$$\bar{P}_a = \frac{N_{oe} e^2}{2 m_e \nu_e} \cdot \left[\frac{\nu_e^2}{\omega^2 + \nu_e^2} \right] \cdot |E|^2 \qquad (D.1)$$

where N_{oe} is the time average electron density, e is electron charge, m_e is the electron mass, ν_e is effective collision frequency for electrons, ω is the angular frequency of the applied energy source, and |E| represents the magnitude of the electric field strength.

In order to estimate the electric field magnitude in a pure Ohmic heated discharge, all other quantities in eq. (D.1) are needed. For simplicity, we assume that the electron density and temperature are uniform throughout the plasma excitation region except near the wall. Also, we approximate the time average absorbed power density by spatial average power density, i.e. $\bar{P}_a = \langle P_{abs} \rangle = P_{abs}/(\pi R^2 \ell)$, assuming uniformly absorption. Using the measured electron temperature data, an estimate of ν_e is assumed to be the electron elastic collision frequency [176], assuming a neutral gas temperature of 350 K. The expected electric field strength values required for pure Ohmic heating discharge can then be calculated through eq. (D.1) together with other experimental data (P_{abs} & N_{oe}). This expected electric field is then compared with the impressed electric field measurements using the techniques described in Chapters 5 and 7. Even this comparison method carries a number of oversimplified assumptions,

differences can still indicate if additional heating mechanisms other than the Ohmic heating are present.

D.3 Results and Discussions

D.3.1 Plasma density and electron temperature

Figure D.1 displays the measured electron temperature versus the pressure for the ECR and no-magnet microwave plasma sources. The non ECR electron temperature is slightly higher than the ECR's. No clear explanation is available at this moment. Also, the solid line given in the figure represents the prediction from the global discharge model. All the data falls within the same order of magnitude of the simple global discharge model described in Chapter 10.

Figure D.2 shows the load line curves (i.e. plasma density vs. absorbed power) for no-magnet configuration at different chamber pressures. As expected in the figure, the plasma density increases as absorbed power increases. Also, the plasma density increases with pressure at this low pressure regime. As indicated, even at the low pressure regime the no-magnet microwave plasma source has the same order of magnitude of plasma density ($10^{11}/cm^3$) as in the ECR plasma source. However, it is quite sensitive for the no-magnet reactor to sustain the plasma below 5 mTorr, where a lopsided electric field pattern was observed, shown in Figure D.3. At the same time, the input coupling probe is very close to the discharge quartz bell jar. It is speculated that some kind of local wave resonance happens there to sustain no magnetic field discharge at several mTorr

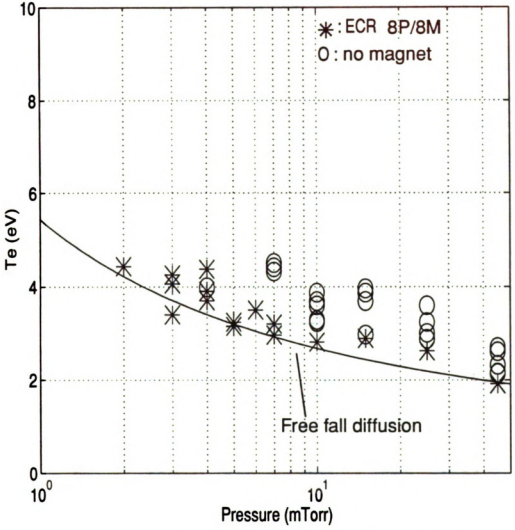

Figure D.1 Comparison of experimental electron temperatures (both ECR & no magnet) with global discharge model prediction in argon discharge.

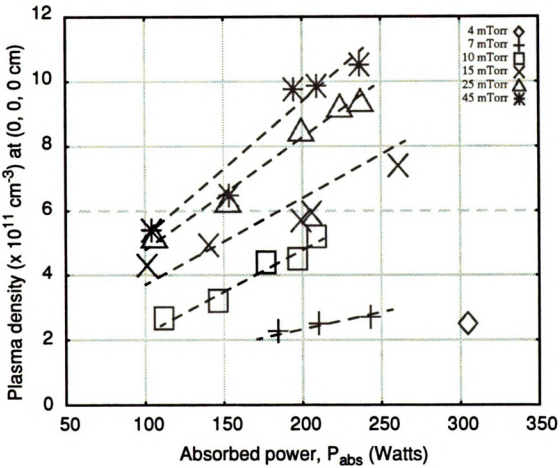

Figure D.2 Plasma density vs. absorbed power (argon pressure as a parameter) for the unmagnetized MPDR-13 plasma source.

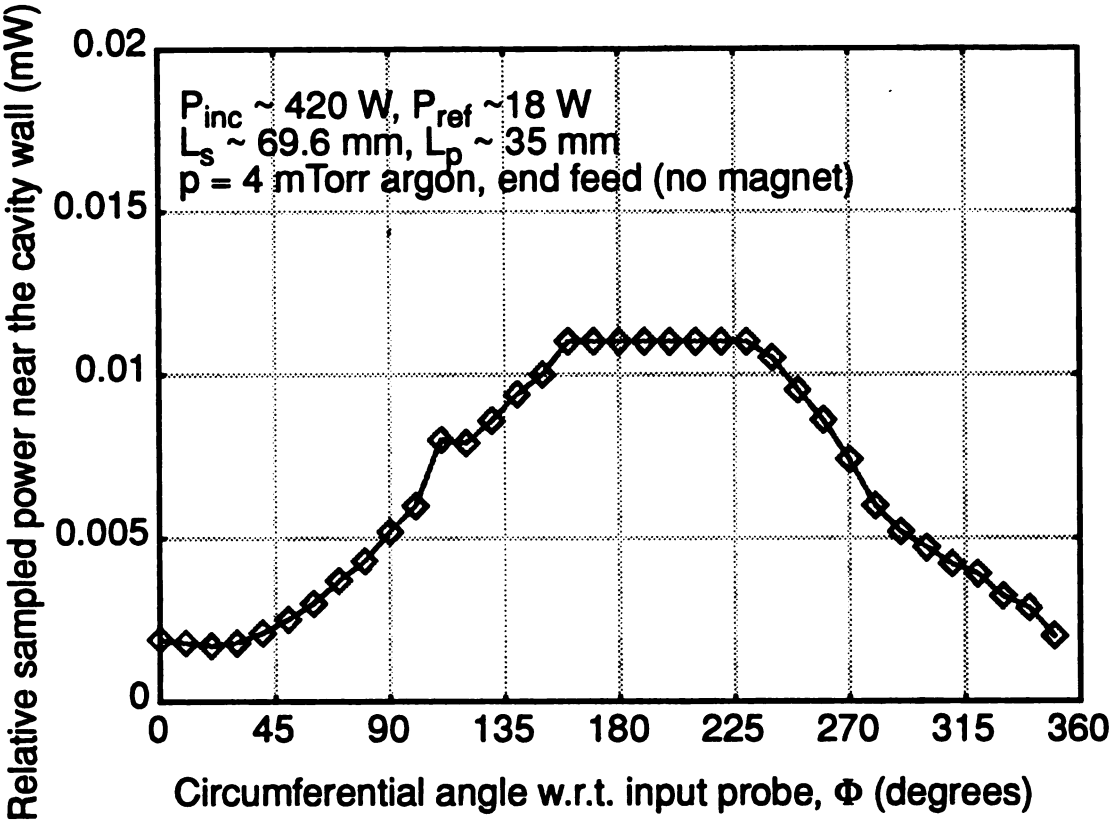

Figure D.3 Measured EM mode pattern in the unmagnetized MPDR-13 plasma source.

pressure. The ease of sustaining low pressure discharge with strong magnetic field suggests that ECR heating definitely plays an important role in maintaining the discharge at pressures below 1 mTorr. The effect of the magnetic field on the EM wave breakdown of gases [213] provides both energy resonance and the modification of diffusion. Of course, how low the plasma can be generated in the no-magnet case is absorbed power dependent. The higher the power, the lower

the pressure that the plasma can be maintained. Due to the capability of the MicroNow power supply and the microwave delivery configuration described in Chapter 3, the maximum power delivered to the reactor is limited to around 400 W after deduction from the losses in the microwave power monitor and transmission circuit described in Section 3.2.2. In the future, this source should be investigated at higher powers.

D.3.2 Electric field comparison

Using the previous density and temperature data, the expected electric field inside the plasma that is purely sustained by Ohmic heating can be calculated through eq. (D.1). Figures D.4 and D.5 display the comparison of the measured impressed electric fields from both magnetized and unmagnetized plasma sources with the calculated electric field from the ideal pure Ohmic heating discharge with similar electron density and temperature. As pressure drops from 45 to around 3 mTorr, the estimated impressed electric field based on E-probe measurement (denoted by * in Figure D.4) stayed around 4 - 5 kV/m in ECR plasma source. On the other hand, the estimated impressed electric field based on E-probe measurement (denoted by O in Figure D.5) in unmagnetized plasma also remained around 4 - 5 kV/m from 45 to 10 mTorr. Then it dropped to ~400 V/m at 7 and 4 mTorr. This anomalous low electric field in the no-magnet case may be partly due to the lopsided electric field distribution at cavity wall, and partly due to some kind of collisionless resonance heating mechanism happening there. The corresponding expected electric field (denoted by X in both

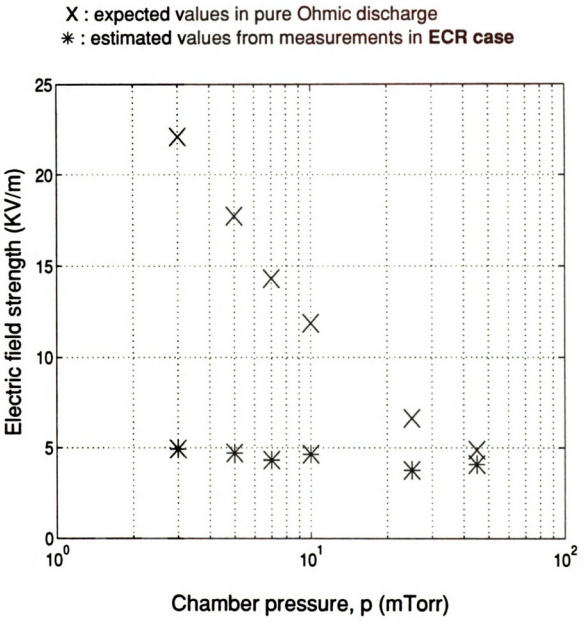

Figure D.4 Comparison of the measured electric field of 8P/8M ECR multipolar plasma source and the expected values sustained only by pure ohmic heating.

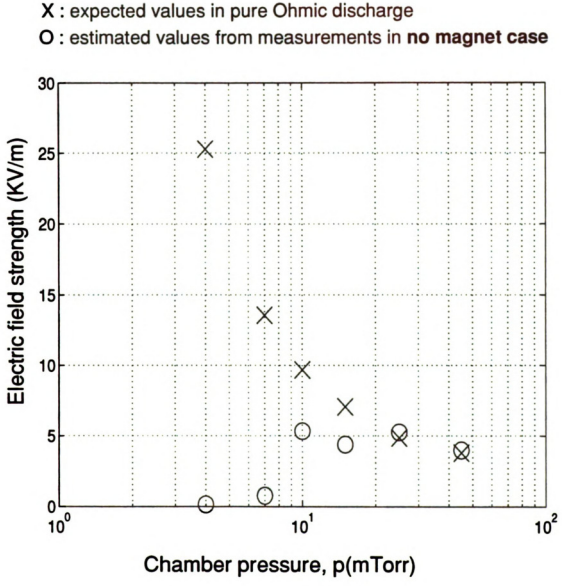

Figure D.5 Comparison of the measured electric field of the unmagnetized microwave cavity plasma source and the expected values sustained only by pure ohmic heating.

Figures D.4 and D.5) in pure Ohmic discharges rise from 5 to 23 kV/m over the pressure range. Also note that, for both magnetized and unmagnetized cases, the estimated electric field from E-probe measurement and the expected electric field correspond quite well at the moderate pressure (45 mTorr). This indicates that Ohmic heating may be dominant about 45 mTorr. As the pressure goes down, the expected electric field is always higher than the estimated impressed electric field from E-probe measurements. These experimental measurements suggest collisionless heating occurs in both ECR and no-magnet discharges at low pressure.

D.4 Concluding Remarks

From the electric field strength comparison, this phenomenon (high density at low pressure) occurs without extremely high applied microwave fields suggesting that other non-ohmic heating mechanisms occur inside both ECR and non ECR discharges. The extremely low electric field data suggests the existence of a resonance behavior in the no-magnet discharge especially at several mTorr pressure range. Strong ECR magnetic field plays important role to sustain plasma at sub-mTorr pressure regime.

Even without the magnetic field, the microwave-cavity type plasma source (MPDR™-13 without magnets) can generate a dense argon plasma (over $10^{11}/cm^3$) at a microwave power under 400 W in the several mTorr range. The

no-magnet configuration operates well as a low pressure high density plasma source without using any external magnetic field.

Additional future experiments (higher power and density uniformity studies) with this unmagnetized microwave cavity source are required to understand the basic plasma science and its possible applications. Also, modifying (both shape and size, e.g. a bigger knob at the end) the end of the excitation probe similar to Ref. [214] would improve both source efficiency and plasma density uniformity.

Finally, this no static magnetic field discharge is expected to be scalable to larger sizes (500 mm dia.) with a lower excitation frequency (915 MHz) for future low pressure high density single wafer plasma processing. Because magnets are not needed, the baseplate can be made in an extremely thin (~15 mm) shape to reduce unnecessary recombination at the wall.

BIBLIOGRAPHY

BIBLIOGRAPHY

[1] J. M. Cook and K. Donohoe, "Etching issues at 0.35 μm and below," Solid State Technol. 34(4), 119-124 (1991).

[2] P. Singer, "Looking down the road to quarter-micron production," Semicond. Int. 18(1), 46-52 (1995).

[3] J. M. E. Harper, J. J. Cuomo, P. A. Leary, G. M. Summa, H. R. Kaufman, and F. J. Bresnock, "Low energy ion beam etching," J. Electrochem. Soc. 128(5), 1077-1083 (1982).

[4] H.-C. Scheer, "Ion sources for dry etching: Aspects of reactive ion beam etching for Si technology," Rev. Sci. Instrum. 63 (5), 3050-3057 (1992).

[5] D. L. Flamm, "Trends in plasma sources and etching," Solid State Technol. 34(3), 47 (1991).

[6] P. Mak, G. King, T. A. Grotjohn, and J. Asmussen, "Investigation of the influence of electromagnetic excitation on electron cyclotron resonance discharge properties," J. Vac. Sci. Technol. A 10(4), 1281-1287 (1992).

[7] G. King, F.C. Sze, P. Mak, T. A. Grotjohn, and J. Asmussen, "Ion and neutral energies in a multipolar electron cyclotron resonance plasma source," J. Vac. Sci. Technol. A 10(4), 1265-1269 (1992).

[8] J. Asmussen and P. Mak, "Control of multipolar electron cyclotron resonance discharges using internal cavity impedance matching," Rev. Sci. Instrum. 65(5), 1753-1756, (1994).

[9] P. Mak, M.-H. Tsai, J. Natarajan, B. L. Wright, T. A. Grotjohn, F. M. A. Salam, M. Siegel, and J. Asmussen, "Investigation of multipolar electron cyclotron resonance plasma source sensors and models for plasma control," J. Vac. Sci. Technol. A 14(3), 1894-1900 (1996).

[10] P. Mak and J. Asmussen, "Experimental investigation of the matching and impressed electric field of a multipolar electron cyclotron resonance

discharge," J. Vac. Sci. Technol. A 15(1), 154-168 (1997).

[11] J. Asmussen, P. Mak and M. A. Perrin, "The design and application of electron cyclotron resonance discharges," accepted to publish in IEEE Trans. on Plasma Sci. (1997).

[12] P. Mak, G. King, J. Hopwood, T. A. Grotjohn and J. Asmussen, "Influence of Static Magnetic Field Configuration and EM Field Pattern on ECR Discharge Performance," the 18th IEEE Int. Conf. on Plasma Sci. Williamsburg, Virginia, CAT#91CH3037-9, p.195, June 3-5, (1991).

[13] P. Mak, G. King, T. A. Grotjohn and J. Asmussen, "Investigation of the Influence of Electromagnetic Excitation in Electron Cyclotron Resonance Discharge Properties," the 38th National Symposium of the American Vacuum Society, Seattle, Washington, Nov. 11-15, (1991).

[14] P. Mak, W. Tan, F.C. Sze, T. A. Grotjohn and J. Asmussen, "Study of the Electron Gas Behavior in an ECR multipolar Plasma Source," the 19th IEEE Int. Conf. on Plasma Sci., Tampa, Florida, CAT#92TH0460-6, p.115, June 1-3, (1992).

[15] W. Tan, P. Mak and T. A. Grotjohn, "Analysis of the Electromagnetic Excitation of the Discharge in an ECR multipolar Plasma Source," the 19th IEEE Int. Conf. on Plasma Sci., Tampa, Florida, CAT#92TH0460-6, p.126, June 1-3, (1992).

[16] P. Mak, G. King, M. Ulczynski, J. Zhang, T. Grotjohn and J. Asmussen, "Experimental Diagnosis of Low-Pressure Microwave Discharges during Diamond Thin Film Deposition" the 3rd Int. Conf. on the New Diamond Sci. and Technol., Heidelberg, Germany, Sept. 1-4, (1992).

[17] G. L. King, P. Mak, T. A. Grotjohn and J. Asmussen, "SF_6-Argon Plasma Properties and Behavior in a multipolar ECR Plasma Source," the 39th National Symposium of the American Vacuum Society, Chicago, Illinois, Nov. 9-13, (1992).

[18] J. Asmussen and P. Mak, "Methods of and Problems Associated with Process Control of Microwave Discharges," the 20th IEEE Int. Conf. on Plasma Sci., Vancouver, B.C., Canada, CAT# 93CH3334-0, p. 147, June 7-9, (1993).

[19] P. Mak and J. Asmussen, "An Evaluation of an End-Excited Electron Cyclotron Resonance Plasma Source," the 21st IEEE Int. Conf. on Plasma Sci., Santa Fe, New Mexico, CAT#94CH3465-2, p.85, June 6-8, (1994).

[20] P. Mak and J. Asmussen, "Experimental Measurement of the Impressed

Electric Field in a multipolar ECR Plasma Source," the 22nd IEEE Int. Conf. on Plasma Sci., Madison, Wisconsin, CAT#95CH35796, p.85, June 5-8, (1995).

[21] P. Mak, M.-H. Tsai, J. Natarajan, B. L. Wright, T. A. Grotjohn, F. M. A. Salam, M. Siegel and J. Asmussen, "Investigation of multipolar ECR Plasma Source Sensors and Models for Plasma Control," the 42nd National Symposium of the American Vacuum Society, Minneapolis, Minnesota, Oct. 16-20, (1995).

[22] P. Mak and J. Asmussen, "Experimental Evaluation of the Nonlinear Relationships between the Input, Internal and Output Variables of a multipolar ECR Plasma Source," the 42nd National Symposium of the American Vacuum Society, Minneapolis, Minnesota, Oct. 16-20, (1995).

[23] P. Mak, T. A. Grotjohn and J. Asmussen, "Experimental investigation of Collisional and Collisionless Heatings in Low Pressure Microwave Plasma Discharges," the 43rd National Symposium of the American Vacuum Society, Philadelphia, Pennsylvania, Oct. 14-18, (1996).

[24] J. Asmussen and P. Mak, "Microwave Plasma Processing Discharges: Microwave equivalent circuits and Global plasma models," presented in Russia (Aug. 1996), and presented in the First World Congress on Microwave Processing, Lake Buena Vista, Florida, U.S.A. Jan. 5-9, (1997).

[25] For examples, (i) R. N. Noyce, "Semiconductor device-and-lead structure," U.S. patent # 2,918,877 (Apr. 25, 1961). (ii) J. A. Hoerni, "Method of manufacturing semiconductor devices," U.S. patent # 3,025,589 (Mar. 20, 1962). (iii) J. S. Kilby, "Miniaturized electronic circuits," U.S. patent # 3,138,743 (June 23, 1964).

[26] K. Suzuki, S. Okudaira, N. Sakudo, and I. Kanomato, "Microwave plasma etching," Jpn. J. Appl. Phys. 16(11),1979-1984 (1977).

[27] L. Bardos, G. Longar, I. Stoll, J. Musil, and F. Zacek, "A method of formation of thin oxide films on silicon in a microwave magnetoactive plasma," J. Phys. D: Appl. Phys. 8, L195-197 (1975).

[28] J. T. C. Lee, "A comparison of HDP sources for polysilicon etching," Solid State Technol. 39 (8), 63-66 (Aug 1996).

[29] S. J. Pearton and F. Ren, "Review science of dry etching of III-V materials," J. Mater. Sci. Mater. Electron. 5, 1-12 (1994).

[30] R. Geller, "Electron cyclotron resonance multiply charged ion sources,"

IEEE Trans. Nucl. Sci. NS-23 (2), 904-912 (1976).

[31] J. Asmussen, "Microwave plasma disk processing machines," Ch. 6 in High Density Plasma Sources (O. A. Popov ed.), Park Ridge, NJ: Noyes Pub. (@1995).

[32] J. W. Coburn, "Mechanisms in plasma-assisted etching," Phys. Scr. T23, 258-263 (1988).

[33] J. Musil, "Microwave plasma: its characteristics and applications in thin film technology," Vacuum, 36, no.1-3, 161-169 (1986).

[34] J. Asmussen, "Electron cyclotron resonance microwave discharges for etching and thin-film deposition," J. Vac. Sci. Technol. A 7(3), 883-893 (1989).

[35] O. A. Popov, "Electron cyclotron resonance plasma sources and their use in plasma-assisted chemical vapor deposition of thin films," in Physics of Thin Films, Vol. 18, (M. H. Francombe and J. L. Vossen, eds.) New York, NY: Academic (@1994).

[36] S. Samukawa, K. Mori and M. Sasaki, "Ion current density and its uniformity at the electron cyclotron resonance position in electron cyclotron resonance plasma," J. Vac. Sci. Technol. A 9(1), 85-90 (1991).

[37] O. A. Popov, and A. O. Westner, "Electron cyclotron resonance sources for wide and narrow plasma streams," Rev. Sci. Instrum. 61(1), 303-305 (1990).

[38] J. E. Stevens, Y. C. Huang, R. L. Jarecki, and J. L. Cecchi, "Plasma uniformity and power deposition in electron cyclotron resonance etch tools," J. Vac. Sci. Technol. A 10(4), 1270-1275 (1992).

[39] T. D. Mantei and S. Dhole, "Characterization of a permanent magnet electron cyclotron resonance plasma source," J. Vac. Sci. Technol. B 9(1), 26-33 (1991).

[40] A. Narai, T. Hashimoto, T. Ichihashi, H. Shincho, Y. Horioko, "Compact electron cyclotron resonance plasma-etching reactor employing permanent magnet," Jpn. J. Appl. Phys. 30 (11B), 3159-3163 (1991).

[41] M. Sadowski, "Plasma Confinement with Spherical Multipole Magnetic Field," Phys. Lett. 25A(9), 695 (1967).

[42] R. Limpaecher, K. R. Mackenize, "Magnetic multipole containment of large uniform collisionless quiescent plasmas," Rev. Sci. Instrum. 44 (6), 726-731

(1973).

[43] M. Pichot, A. Durandet, J. Pelletier, Y. Arnal, and L. Vallier, "Microwave multipolar plasmas excited by distributed electron cyclotron resonance: Concept and performance," Rev. Sci. Instrum. 59(7), 1072-1075 (1988).

[44] R. Burke, and C. Pomot, "Microwave multipolar plasma for etching and deposition," Solid State Technol. 31(2), 67-71, (1988).

[45] J. Pelletier, Ch. 8 in High Density Plasma Sources (Ed. O. A. Popov), p. 411-417, (Noyes Pub., Park Ridge, NJ), (@1995). or J. Pelletier, "Device for Distributing a Microwave Energy for Exciting a Plasma," French Patent No. 9100894 (Jan. 22, 1994), US Patent No. 5,216,329 (June 1, 1993).

[46] J. Engemann, M. Schott, F. Werner, and D. Korzec, "Large volume electron cyclotron resonance plasma generation by use of the slotted antenna microwave source," J. Vac. Sci. Technol. A13(3), 875-882 (1995).

[47] D. Korzec, F. Werner, R. Winter and J. Engemann, "Scaling of microwave slot antenna (SLAN): a concept for efficient plasma generation," Plasma Sources Sci. Technol. 5, 216-234 (1996).

[48] F. Werner, D. Korzec and J. Engemann, "Slot antenna 2.45 GHz microwave plasma source," Plasma Sources Sci. Technol. 3, 473-481 (1994).

[49] G.Lisitano, R. A. Ellis, Jr., W. M. Hooke, and T.H. Stix, "Production of Quiescent Discharge with High Electron Temperatures," Rev. Sci. Instrum. 39(3), 295-297, (1968).

[50] K.-H. Kretschmer, K. Matl, G. Lorenz, I. Kessler, and B. Dumbacher, "An Electron Cyclotron Resonance (ECR) Plasma Source," Solid State Technol. 33, 53-55, (1990).

[51] G. Neumann, and K.-H. Kretschmer, "Characterization of a new electron cyclotron resonance source working with permanent magnets," J. Vac. Sci. Technol. B 9(2), 334-338 (1991).

[52] L. Mahoney and J. Asmussen, "A compact, resonant cavity, five centimeter, multicusp, ECR broad-beam ion source," Rev. Sci. Instrum. 61(1), 285-287 (1990).

[53] J. A. Hopwood, Ph.D. Dissertation, Michigan State Univ., (June 1990).

[54] F.C. Sze, D. K. Reinhard, B. Musson, J. Asmussen and M. Dahimene, "Experimental performance of a large-diameter multipolar microwave

plasma disk reactor," J. Vac. Sci. Technol. B 8(6), 1759-1762 (1990).

[55] J. Asmussen, J. Hopwood and F.C. Sze, "A 915 MHz/2.45 GHz ECR plasma source for large area ion beam and plasma processing," Rev. Sci. Instrum. 61(1), 250-252 (1990).

[56] O. A. Popov ed., High Density Plasma Sources, Park Ridge, NJ: Noyes Pub. (@1995).

[57] J. Hopwood, C. R. Guarnieri, S. J. Whitehair and J. J. Cuomo, "Electromagnetic fields in a radio-frequency induction plasma," J. Vac. Sci. Technol. A 11(1), 147-151 (1993).

[58] J. Hopwood, C. R. Guarnieri, S. J. Whitehair and J. J. Cuomo, "Langmuir probe measurements of a radio-frequency induction plasma," J. Vac. Sci. Technol. A 11(1), 152-156 (1993).

[59] J. Hopwood, "Planar RF induction plasma coupling efficiency," Plasma Sources Sci. Technol. 3, 460-464 (1994).

[60] J. Hopwood, "Ion bombardment energy distributions in a radio frequency induction plasma," Appl. Phys. Lett. 62(9), 940-942 (1993).

[61] K. Yoshida, H. Miyamoto, E. Ikawa and Y. Murao, "Gate electrode etching using a transformer coupled plasma," Jpn. J. Appl. Phys. 34(4B), 2089-2091 (1995).

[62] T. Okumura and I. Nakayama, "New inductively coupled plasma source using a multispiral coil," Rev. Sci. Instrum. 66(11), 5262-5265 (1995).

[63] U. Kortshagen, and M. Zethoff, "Ion energy distribution functions in a planar inductively coupled RF discharge," Plasma Sources Sci. Technol. 4, 541-550 (1995).

[64] J. Hopwood, Research Report, IBM Research Division, T. J. Watson Research Center (unpublished).

[65] M. Tuszewski and J. A. Tobin, "Characterization of a low-frequency inductively coupled plasma source," J. Vac. Sci. Technol. A 14(3), 1096-1101 (1996).

[66] D. L. Flamm, D. E. Ibbotson, W. L. Johnson, "Processes depending on plasma generation using a helical resonator," U.S. Patent #4,918,031, (Apr. 17, 1990).

[67] K. Niazi, A. J. Lichtenberg, M. A. Lieberman and D. L. Flamm, "Operation of

a helical resonator plasma source," Plasma Sources Sci. Technol. 3, 482-495 (1994).

[68] J.T.C. Lee, N. Layadi, K. V. Guinn, H. L. Maynard, F. P. Klemens, D. E. Ibbotson, and I. Tepermeister, "Comparison of advanced plasma sources for etching applications. V. Polysilicon etching rate, uniformity, profile control, and bulk plasma properties in a helical resonator plasma source," J. Vac. Sci. Technol. B 14(4), 2510-2518 (1996).

[69] R. W. Boswell, "Plasma production using a standing helicon wave," Phys. Lett. 33 A(7), 457-458 (Dec. 1970). or his Ph.D. Thesis, Flinders University of South Australia, (1970).

[70] A. J. Perry, D. Vender, and R. W. Boswell, "The application of the helicon source to plasma processing," J. Vac. Sci. Technol. B 9(2), 310-317 (1991).

[71] A. R. Ellingboe and R. W. Boswell, "Capacitive, inductive and helicon-wave modes of operation of a helicon plasma source," Phys. Plasmas, 3 (7), 2797-2804 (1996).

[72] F. F. Chen, "Helicon plasma sources," Ch.1 in High Density Plasma Sources, (O. A. Popov ed.), Park Ridge, NJ: Noyes Pub. (@1995) and references quoted therein.

[73] T. Shoji, Y. Sakawa, S. Nakazawa, K. Kadota, and T. Sato, "Plasma production by helicon waves," Plasma Sources Sci. Technol. 2(1), 5-10 (1993) and references quoted therein.

[74] M. Moisan and Z. Zakrzewski, "Plasma sources based on the propagation of electromagnetic waves," J. Phys. D: Appl. Phys. 24, 1025-1048 (1991).

[75] S. Bechu, C. Boisse-Laporte, P. Leprince, and J. Marec, "Homogeneity characterization of a large microwave plasma," J. Vac. Sci. Technol. A 15(3), 668-672 (1997).

[76] I. Tepermeister, N. Blayo, F. P. Klemens, D.E. Ibbotson, R. A. Gottscho, J. T. C. Lee, and H. H. Sawin, "Comparison of advanced plasma sources for etching applications. I. Etch rate, uniformity, and profile control in a helicon and a multipolar electron cyclotron resonance source," J. Vac. Sci. Technol. B 12(4), 2310-2321 (1994).

[77] I. Tepermeister, D.E. Ibbotson, J. T. C. Lee and H. H. Sawin, "Comparison of advanced plasma sources for etching applications. II. Langmuir probe studies of a helicon and a multipolar electron cyclotron resonance source,"

J. Vac. Sci. Technol. B 12(4), 2322-2332 (1994).

[78] G. W. Gibson, H. H. Sawin, I. Tepermeister, D.E. Ibbotson and J. T. C. Lee, "Comparison of advanced plasma sources for etching applications. III. Ion energy distribution functions for a helicon and a multipolar electron cyclotron resonance source," J. Vac. Sci. Technol. B 12(4), 2333-2341 (1994).

[79] N.Blayo, I. Tepermeister, J. L. Benton, G. S. Higashi, T. Boone, A.Onuoha, F. P. Klemens, D.E. Ibbotson, J. T. C. Lee and H. H. Sawin, "Comparison of advanced plasma sources for etching applications. IV. Plasma induced damage in a helicon and a multipolar electron cyclotron resonance source," J. Vac. Sci. Technol. B 12(3),1340-1350 (1994).

[80] Jung-Hun Kim, Ho-Jun Lee, Youn-Taeg Kim, Ki-Woong Whang, Jung-Hoon Joo, "Effects of the axial external magnetic field on the reduction of the dielectric window damage due to capacitive coupling in the inductively coupled plasma," J. Vac. Sci. Technol. A15(3), 564-567 (1997).

[81] J. Root and J. Asmussen, "MSU Microwave Ion Source," presented at the MSU/NASA workshop on Advanced Propulsion Concepts using Time Varying ELectromagnetic Fields, East Lansing, Michigan, Feb. 24-25 (1982).

[82] J. Asmussen and J. Root, "Characteristics of a microwave plasma disk ion source," Appl. Phys. Lett. 44(4), 396-398 (1984).

[83] J. Asmussen and J. Root, "Ion generation apparatus and methods for the use thereof," U.S. Patent #4,507,588, (Mar. 26,1985).

[84] J. Asmussen, R. Mallavarpu, J. R. Hamann and H.C. Park, "The design of a microwave plasma cavity," Proc. IEEE, 62(1), 109-117 (1974).

[85] M. Dahimene and J. Asmussen, "The performance of a microwave ion source immersed in a multicusp static magnetic field," J. Vac. Sci. Technol. B 4(1), 126-130 (1986).

[86] J. Asmussen and M. Dahimene, "The experimental test of a microwave ion beam source in oxygen," J. Vac. Sci. Technol. B5(1), 328-331 (1987).

[87] Available on line: http://www.fcc.gov/

[88] G. Adishian, P. Miller and E. Maier, "RF Power Generator Performance Parameters for Plasma Applications," Semiconductor Int.16, 80-85 (Oct

1993).

[89] S. Samukawa, T. Nakamura, T. Ishida and A. Ishitani, "Optimally stable electron cyclotron resonance plasma generation and essential points for compact plasma source," Jpn. J. Appl. Phys. 31(12B), 4348-4356 (1992).

[90] G. T. Salbert, Ph.D. Dissertation, Michigan State Univ. p. 97, (June 1992).

[91] J. Zhang, Ph.D. Dissertation, Michigan State Univ., June (1993).

[92] R. Keller, "Ion extraction" of Ch. 3 in The Physics and Technology of Ion Sources, ed. by I. G. Brown, New York, NY: Wiley, (1989).

[93] J. Asmussen, H. H. Lin, B. Manring, and R. Fritz, "Single-mode or controlled multimode microwave cavity applications for precision materials processing," Rev. Sci. Instrum. 58 (8), 1477-1486 (1987).

[94] J. R. Rogers, Ph.D. Dissertation, Michigan State Univ., (1982).

[95] J. D. Jackson, Classical Electrodynamics, New York, NY: Wiley, 2nd Ed. (@1975), p.357.

[96] R. F. Harrington, Time Harmonic Electromagnetic Fields, New York, NY: McGraw-Hill, (@1961). p.73, 255

[97] S. Ramo, J. R. Whinnery, and T. Van Duzer, Fields and Waves in Communication Electronics, New York, NY: Wiley, 2nd Ed. (@1984), p.155, 432, 428

[98] J. R. Brophy and P. J. Wilbur, "Simple performance model for ring and line cusp ion thrusters," AIAA Journal, 23(11),1731-1736 (1985).

[99] For examples, O. Auciello and D. L. Flamm Eds, Plasma Diagnostics: Plasma parameters and chemistry, San Diego, CA: Academic Press, (@1989).

[100] B. N. Chapman, Glow discharge processes, New York, NY: Wiley, (@1980).

[101] G. L. King, Ph.D. Dissertation, Michigan State Univ. (June 1994).

[102] W. Altar, F. B. Marshall, and L. P. Hunter, "Probe error in standing wave detectors, "Proc. I.R.E. 34(1), 33-44 (1946).

[103] S. Burkart, "Coaxial E-field probe for high-power microwave measurement,"

IEEE Trans. Microwave Theory Tech. MTT-33 (3), 262-265 (1985).

[104] I. Langmuir, "Positive ion currents in the positive column of the mercury arc," Gen. Elec. Rev. 26(11), 731-735 (1923). or "The pressure effect and other phenomena in gaseous discharges," J. Frank. Inst. 196(6), 751-762 (1923).

[105] I. Langmuir and H. Mott-Smith, "Studies of Electric Discharges in Gases at Low Pressures, Part I to V," Gen. Elec. Rev. 27(7, 8, 9, 11,12), 449-455, 538-548, 617-623, 762-771, 810-820 (1924).

[106] H. M. Mott-Smith and I. Langmuir, "The Theory of Collectors in Gaseous Discharges," Phys. Rev. 28, 727-763 (1926).

[107] F. F. Chen, "Electric Probes," Ch. 4 in Plasma Diagnostic Techniques, (eds. R. H. Huddlestone and S. L. Leonard), New York, NY: Academic, (@1965).

[108] J. D. Swift and M. J. R. Schwar, Electrical probes for plasma diagnostics, New York, NY: American Elsevier, (@1969).

[109] P. M. Chung, L. Talbot and K. J. Touryan, Electric Probes in Stationary and Flowing Plasmas: Theory and Applications, New York, NY: Springer-Verlag, (@1975).

[110] B. E. Cherrington, "The use of electrostatic probes for plasma diagnostics --- a review," Plasma Chem. Plasma Process. 2(2), 113-140 (1982).

[111] For examples, J. G. Laframboise, "Theory of spherical and cylindrical Langmuir probes in a collisionless, Maxwellian plasma at rest," University of Toronto, UTIAS Report No. 100, (1996). or A. Brockhaus, C. Borchardt, and J. Engemann, "Langmuir probe measurements in commercial plasma plants," Plasma Sources Sci. Technol 3, 539-544 (1994). or J. E. Allen, "Probe theories and applications: modern aspects,", Plasma Sources Sci. Technol. 4, 234-241, (1995). and etc.

[112] F. C. Sze, Ph.D. Dissertation, Michigan State Univ. (May 1993).

[113] E. O Johnson and L. Malter, "Double-probe method for determination of electron temperatures in steady and time-varying gas discharges," Phys. Rev. 76, 1411-1412 (1949). or E. O Johnson and L. Malter, "A floating double probe method for measurements in gas discharges," Phys. Rev. 80(1), 58-68 (1950).

[114] Both the data acquisition and analyzing programs were first written by L. J. Mahoney, then they are continuously edited and improved by F. C. Sze and

the author of this thesis.

[115] E. W. Peterson and L. Talbot, "Collisionless electrostatic single-probe and double-probe measurements," AIAA J. 8(12), 2215-2219 (1970).

[116] M. J. Druyvesteyn, "Der Niedervoltbogen," Z. Phys. 64, 781-798 (1930) (in German).

[117] H. W. Rundle, D. R. Clark, J. M. Deckers, "ELectron energy distribution functions in an O_2 glow discharge," Can. J. Phys. 51, 144-148 (1973).

[118] R. C. Woods and I. D. Sudit, "Theory of electron retardation by Langmuir probes in anisotropic plasmas," Phys. Rev. E: 50, 2222-2238 (1994).

[119] A. A. Sonin, "Free-molecule Langmuir probe and its use in flow-field studies," AIAA J. 4(9), 1588-1596 (1966).

[120] I. D. Sudit and R. C. Woods, "A study of the accuracy of various Langmuir probe theories," J. Appl. Phys. 76(8), 4488-4498 (1994).

[121] K. Suzuki, S. Okudaira, and I. Kanomata, "The roles of ions and neutral active species in microwave plasma etching," J. Electrochem. Soc. 126(6), 1024-1028 (1979).

[122] I. H. Hutchinson, Principles of Plasma Diagnostics, Cambridge, England: Cambridge University Press (@1987), p.81.

[123] L. Tonks, H. M. Mott-Smith and I. Langmuir, "Flow of ions through a small orifice in a charged plate," Phys. Rev. 28, 104-128 (1926).

[124] The data acquisition program was written by A. K. Srivastava and the author of this thesis.The data analyzing programs were first written by F. C. Sze.

[125] C. Bohm and J. Perrin, "Retarding-field analyzer for measurements of ion energy distributions and secondary electron emission coefficients in low-pressure radio frequency discharges," Rev. Sci. Instrum. 64(1), 31-44, (1993).

[126] Y. Sakai and I. Katsumata, "An energy resolution formula of a three plane grids retarding field energy analyzer," Jpn. J. Appl. Phys. 24(3), 337-341 (1985).

[127] The program is in the language Fortran 77 format. It was initially written with the great help from Dr. T. A. Grotjohn.

[128] Catalogs from Magnet Sales & Manufacturing Inc. in Culver City, CA

(http://www.magnetsales.com/) or PERMAG, Magnetic Material Division, Dexter Corporation in Toledo, Ohio. (http://www.thomasregister.com:8000/olc/dextermagnetic/)

[129] J. Strikwerda, Finite difference schemes and partial differential equations, Pacific Grove, CA: Wadsworth & Brooks/Coles Math. Series (@1989).

[130] P. G. Ciarlet, Introduction to numerical linear algebra and optimisation, English translation @Cambridge Univ. Press: Cambridge, England, (@1989), Ch. 5.

[131] L. Solyman and D. Walsh, Lectures on the Electrical Properties of Materials, New York, NY: Oxford Univ. Press, 4th Ed. (@1988), p. 7

[132] ibid. p. 248

[133] F. C. Trutt, E. A. Erdelyi, and R. F. Jackson, "The non-linear potential equation and its numerical solution for highly saturated electrical machines," IEEE Trans. on Aerospace, AS-1 (2), 430-440, (1963).

[134] I. P. Shkarofsky, T. W. Johnston, and M. P. Bachynski, The particle kinetics of plasmas, Reading, MA: Addison-WEsley, @1966, p. 29

[135] L. J. Mahoney, M.Sc. Thesis, Michigan State University, (1989).

[136] M. A. Lieberman, and R. W. Bosewell, "Modeling the Transitions from capacitive to inductive to wave-sustained RF discharges," 7th ICOP conference jointed with 5th International conference of diamond and related materials, France, Sept. (1997).

[137] E. L. Ginzton, Microwave Measurements, New York, NY: McGraw-Hill (@1957), p. 243

[138] S. A. Cohen, "An introduction to plasma physics for material processing," Ch. 3 in Plasma Etching: An introduction (D. M. Manos and D. L. Flamm Ed.) San Diego, CA: Academic Press. (@1989), p.213 and p. 216.

[139] M. Dahimene, Ph. D. Thesis.Michigan State University, (1987).

[140] J. Zhang, B. Huang, D. K. Reinhard, and J. Asmussen, "An investigation of electromagnetic field patterns during microwave plasma diamond thin film deposition," J. Vac. Sci. Technol. A 8(3), 2124-2128 (1990).

[141] M. A. Perrin, private communication at East Lansing, Michigan.

[142] R. H. Lovberg, "Magnetic probes," Ch. 3 in Plasma Diagnostic Techniques,

(eds. R. H. Huddlestone and S. L. Leonard), New York, NY: Academic, (@1965).

[143] J. A. Meyer and A. E. Wendt, "Measurements of electromagnetic fields in a planar radio-frequency inductively coupled plasma source," J. Appl. Phys. 78(1), 90-96 (1995).

[144] J. Hopwood, "Inductively coupled plasma discharges," presentation at MSU for the satellite course EE989A (NTU-IC734-MS), June 26, (1995).

[145] R. Piejak, V. Godyak, and B. ALexamdrovich, "The electric field and current density in a low-pressure inductive discharge measured with different B-dot probes," J. Appl. Phys. 81(8), 3416-3421 (1997).

[146] E. W. McDaniel and E. A. Mason, The mobility and diffusion of ions in gases, New York, NY: John Wiley & Sons, (@1973), Section 1-11.

[147] R. F. Whitmer and G. F. Herrmann, "Effects of a velocity-dependent collision frequency on wave-plasma interactions," Phys. Fluids, 9(4), 768-773 (1966).

[148] J. C. Sprott, "Electron cyclotron heating in toroidal octupoles," Phys. Fluids, 14(8), 1795 -1802 (1971).

[149] P. C. Clemmow and J. P. Dougherty, Electrodynamics of Particles and Plasmas, New York, NY: Addison-Wesley, (@1969), reissued (@1989).

[150] W. P. Allis, S. J. Buchsbaun, and A. Bers, Waves in anisotropic plasmas, Cambridge, MA: MIT Press, (@1963).

[151] C. K. Birdsall and A. B. Langdon, Plasma Physics via computer simulation, New York, NY: McGraw-Hill, (@1985).

[152] J. M. Dawson, V. Decyk, R. Sydora, and P. Liewer, "High-performance computing and Plasma Physics," Physics Today, 46(3), 64-70 (1993).

[153] N. Marcuvitz, Waveguide Handbook, New York, NY: McGraw-Hill (@1951), p.310

[154] J. R. Whinnery and H. W. Jamieson, "Equivalent circuits for discontinuities in transmission lines," Proc. I.R.E., 32, 98-115 (1944).

[155] J. R. Whinnery, H. W. Jamieson, and T.E. Robbins, "Coaxial-line discontinuities," Proc. I.R.E., 32, 695-709 (1944).

[156] P. I. Somlo, "The computation of coaxial line step capacitances," IEEE

Trans. on Microwave Theory Tech. MTT-15(1), 48-53 (1967).

[157] J. Hopwood, D. K. Reinhard, and J. Asmussen, "Charged particle densities and ion energy distributions in a multipolar electron cyclotron resonant plasma etching source," J. Vac. Sci. Technol. A 8(4), 3103-3112 (1990).

[158] S. J. Pearton, U. K. Chakrabarti, A. Katz, A. P. Perley, W. S. Hobson, and M. Geva, "Hybrid electron cyclotron resonance-radio-frequency plasma etching of III-V semiconductors in Cl_2-based discharges. Part I. GaAs and related compounds & Part II. InP and related compounds," Plasma Chem. Plasma Process. 11(4) 405-422 & 423-438, (1991).

[159] F. Ren, S. Pearton, C. R. Abernathy, and J. R. Lothian, "Nanoscale structures in III-V semiconductors using sidewall masking and high ion density dry etching," J. Vac. Sci. Technol. A 13(3), 753-757 (1995).

[160] S. J. Pearton, W. S. Hobson, and A. F. J. Levi, "Comparison of plasma chemistries for patterning InP-based laser structures," Plasma Sources Sci. Technol. 3,19-24 (1994).

[161] P. K. Shuffebotham and D. J. Thomson, "Diagnostic techniques for plasma stability in electron cyclotron resonance plasma processing," J. Vac. Sci. Technol. A 8(5), 3713-3719 (1990).

[162] O. A. Popov, "Electron cyclotron resonance plasmas excited by rectangular & circular microwave modes," J. Vac. Sci. Technol. A 8(3), 2909-2912 (1990).

[163] S. M. Gorbatkin, L. A. Berry, and J. B. Roberto, "Behavior of Ar plasmas formed in a mirror field electron cyclotron resonance microwave ion source," J. Vac. Sci. Technol. A 8(3), 2893-2899 (1990).

[164] D. A. Carl, M. C. Williamson, M. A. Lieberman, and A. J. Lichtenberg, "Axial radio frequency electric field intensity and ion density during low to high mode transition in argon electron cyclotron resonance discharges," J. Vac. Sci. Technol. B 9(2), 339-347 (1991).

[165] S. Minomo, K. Kondo, Y. Yoshizako, Y. Ishida and M. Taniguchi, "Characterization and stabilization of an electron cyclotron resonance plasma source using an automatic microwave tuner," Rev. Sci. Instrum. 63(4), 2547-2549 (1992).

[166] E. S. Aydil, J. A. Gregus, and R. A. Gottscho, "Multiple steady states in electron cyclotron resonance plasma reactors," J. Vac. Sci. Technol. A

11(6), 2883-2892 (1993).

[167] R. M. Fredericks and J. Asmussen, "Returning and hysteresis effects of a rf plasma in a variable size microwave cavity," J. Appl. Phys. 42(9), 3647-3649 (1971).

[168] J. Asmussen, R. Mallavarpu, J. R. Hamann, and H. C. Park, "The design of a microwave plasma cavity," Proc. IEEE, 62(1),109-117 (1974).

[169] Y.A. Lebedev, "Some properties of the tunable cavity microwave plasma source," Plasma Sources Sci. Technol. 4, 474-481 (1995).

[170] M. Moisan and J. Pelltier, Microwave Excited Plasmas, Amsterdam: Elsevier (@1992), p. 112-115

[171] A. J. Hatch and L. E. Heuckroth, "Returning effect and dynamic instability of a radio-frequency capacitive discharge," J. Appl. Phys. 41(4), 1701-1706 (1970).

[172] J. Taillet, "Resonance-sustained radio frequency discharges," Am. J. Phys. 37(4), 423-440 (1969).

[173] M.-H. Tsai, and T. A. Grotjohn, Private communications at Michigan State University.

[174] N. Hershkowitz and H. L. Maynard, "Plasma characterization and process control diagnostics," J. Vac. Sci. Technol. A 11(4), 1172-1175 (1993).

[175] G. G. Barna, M. M. Moslehi, Y. J. Lee, "Sensor needs for IC manufacturing," Solid State Technol. 38, 57-61 (1994).

[176] M. A. Lieberman and A. J. Lichtenberg, Principles of Plasma Discharges and Materials Processings, New York, NY: Wiley-Interscience (@1994), Ch. 3 and 10.

[177] L. Tonks and I. Langmuir, "A general theory of the plasma of an arc," Phys. Rev. 34, 876-922 (1929).

[178] M. J. Druyvesteyn and N. Warmoltz, "Energy balance, electron temperature, and voltage gradient in the positive column in mixture of Na vapour with Ne, He and Ar," Phil. Mag. 17, 7th Ser., 1-27 (1934).

[179] A. Von Engel, Ionized Gases, Oxford: Clarendon Press (@1955).

[180] A. J. Lichtenberg, V. Vahedi, M. A. Lieberman, and T. Rognlien, "Modeling electronegative plasma discharges," J. Appl. Phys. 75(5), 2339-2347

(1994).

[181] C. Lee and M. A. Lieberman, "Global model of Ar, O_2, Cl_2, and Ar/O_2 high-density plasma discharges," J. Vac. Sci. Technol. A 13(2), 368-380 (1995).

[182] S. Ashida, C. Lee, and M. A. Lieberman, "Spatially averaged (global) model of time modulated high density argon plasmas," J. Vac. Sci. Technol. A 13(5), 2498-2507 (1995).

[183] M. A. Lieberman and S. Ashida, "Global models of pulse-power-modulated high density, low-pressure discharges," Plasma Sources Sci. Technol. 5, 145-158 (1996).

[184] Y. T. Lee, M. A. Lieberman, A. J. Lichtenberg, F. Bose, H. Baltes, and R. Patrick, "Global model for high pressure electronegative radio-frequency discharges," J. Vac. Sci. Technol. A 15(1), 113-126 (1997).

[185] E. A. McDaniel, Collisional phenomena in ionized gases, New York, NY: Wiley @1964.

[186] D. Rapp and P. Englander-Golden, "Total cross sections for ionization and attachment in gases by electron impact. Pt. I: Positive ionization & Pt. II: Negative-ion formation," J. Chem. Phys. 43(5), 1464-1479 & 1480-1489 (1965).

[187] L. R. Peterson and J. E. Allen Jr., "Electron impact cross sections for argon," J. Chem Phys. 56(12), 6068-6076 (1972).

[188] W. L. Morgan, "A critical evaluation of low-energy electron impact cross sections for plasma processing modeling. Pt. I: CH_2, F_2 and HCl & Pt. II: CF_4, SiH_4 and CH_4," Plasma Chem. Plasma Process. 12(4), 449-476 & 477-493 (1992).

[189] V. A. Godyak, Soviet Radio Frequency Discharge Research, Fall Church, VA: Delphic Associates, Inc. @1986, Ch. 5

[190] F. Kannari, M. Obara, and T. Fujioka, "An advanced kinetic model of electron-beam-excited KrF lasers including the vibrational relaxation in KrF*(B) and collisional mixing of KrF*(B,C)," J. Appl. Phys. 57(9), 4309-4322 (1985).

[191] V. E. Golant, A. P. Zhilinsky, I. E. Sakharov, and S. C. Brown, Fundamentals of Plasma Physics, New York, NY: Wiley (@1980).

[192] F.C. Sze and J. Asmussen, "Experimental scaling laws for multipolar

electron cyclotron resonance plasma source," J. Vac. Sci. Technol. A11(4), 1289-1295 (1993).

[193] K. Shirai, I. Takashi, and S. Gonda, "Electric probe measurements in an ECR plasma CVD apparatus," Jpn. J. Appl. Phys. 28(5), 897-902 (1989).

[194] M. Surendra, "Radio frequency discharge benchmark model comparison," Plasma Sources Sci. Technol. 4, 56-73 (1995).

[195] Special issue on *Modeling Collisional Low-Temperature Plasmas*, (Guest Editors: M. J. Kushner and D. B. Graves), IEEE Trans. on Plasma Sci. PS-19(2), (Apr. 1991).

[196] Special issue on *Modeling and Simulation of Collisional Low-Temperature Plasmas*, (Guest Editors: C. H. J. Wu, M. Meyyappan, and D. J. Economou), IEEE Trans. on Plasma Sci. PS-23(4), (Aug. 1995).

[197] M. Meguappan, "Analysis of pulse-time modulated high-density discharges", J. Vac. Sci. Technol. A 14 (4), 2122-2126, (1996).

[198] R. L. Papenbreer and J. Engemann, "Pulsed operation of a MPDR-type ECR plasma source for high power applications", Rev. Sci. Instrum. 63(4), 2550-2552, (1992).

[199] C. Charles & R. W. Boswell, "Breakdown, steady state, and decay regions in pulsed oxygen helicon diffusion plasmas", J. Appl. Phys. 78 (2), 766-773 (1995).

[200] B. D. Musson, F. C. Sze, D. K. Reinhard and J. Asmussen, "Anisotropic etching of submicron silicon features in a 23 cm diameter microwave multicusp electron cyclotron resonance plasma reactor," J. Vac. Sci. Technol. B9(6), 3521-3525 (1991).

[201] G.I. Font and I. D. Boyd, "Numerical study of the effects of reactor geometry on a chlorine plasma helicon etch reactor," J. Vac. Sci. Technol. A 15(2), 313-319 (1997).

[202] Catalogs from Copper and Brass Sales, Inc. Detroit, MI. (http://www.copperandbrass.com/) and Uniform Tubes, Inc., Collegeville, PA 19426 (http://www.uniformtubes.co.uk/)

[203] Jes Asmussen, Private communications, Michigan State University, E. Lansing, MI 48824.

[204] S. Seshadri, Fundamental of Plasma Physics, New York, NY: American

Elsevier, (@1973).

[205] Special issue on *Images in Plasma Science*, (Guest Editors: M. J. Kushner & D. N. Ruzic), IEEE Trans. on Plasma Sci., PS-24(1), (Feb. 1996).

[206] Plasma & Technology of Low Temperature Plasmas, (Russian Ed. S. V. Dresvin, English Ed. H. V. Eckert), Ames, IA: Iowa State Univ. Press (@1977).

[207] M. M. Turner, "Collisionless Electron Heating in an Inductively Coupled Discharges," Phys. Rev. Lett. 71(12), 1844-1847 (1993).

[208] V. Vahedi, M. A. Lieberman, G. DiPeso, T. D. Rognlien, and D. Hewett, "Analytic model of power deposition in inductively coupled plasma sources," J. Appl. Phys. 78, 1446 (1995).

[209] V. A. Godyak, R. B. Piejak, and B. M. Alexandrovich, "The electron-energy distribution function in a shielded argon radiofrequency inductive discharge," Plasma Sources Sci. Technol. 3, 332-336 (1995).

[210] M. A. Lieberman, "Analytical solution for capacitive RF sheath," IEEE Trans. Plasma Sci. PS-16(6), 638-644 (1988).

[211] M. A. Lieberman and A. J. Lichtenberg, "Stochastic and Adiabatic Behavior of Particles Accelerated by Periodic Forces," Phys. Rev. A 5(4), 1852-1866 (1972).

[212] O. A. Popov and V.A. Godyak, "Power dissipated in low-pressure radio-frequency discharge plasmas," J. Appl. Phys. 57(1), 53-58 (1985).

[213] B. Lax, W. P. Allis, and S. C. Brown, "The Effect of Magnetic Field on the Breakdown of Gases at Microwave Frequencies," J. Appl. Phys. 21, 1297-1304 (1950).

[214] K. Yokogawa, N. Itabashi, and S. Tachi, "Large volume, ultra-high frequency electron cyclotron resonance plasma for microelectronics processings," the 42nd National Symposium of the American Vacuum Society, Minneapolis, Minnesota, Oct. 16-20, (1995.)

MICHIGAN STATE UNIV. LIBRARIES
31293015706140